

Annual Research Briefs – 2002

Center for Turbulence Research

December 2002

20030328 482



DISTRIBUTION STATEMENT A
Approved for Public Release
Distribution Unlimited

CONTENTS

Preface	1
A G-equation formulation for large-eddy simulation of premixed turbulent combustion. H. PITSCHE	3
A numerical scheme for the large-eddy simulation of turbulent combustion using a level-set method. L. DUCHAMP DE LAGENESTE and H. PITSCHE	15
On the role of quasi-one-dimensional dissipation layers in turbulent scalar mixing. N. PETERS and P. TROUILLET	27
Modelling turbulence-radiation interactions for large sooting turbulent flames. J.-F. RIPOLL and H. PITSCHE	41
Inverse parabolicity of PDF equations in turbulent flows - reversed-time diffusion or something else. A.Y. KLIMENKO	53
Filtered density-function modeling for large-eddy simulations of turbulent reacting flows. C. CHA and P. TROUILLET	63
Transported PDF modeling of turbulent premixed combustion. C. CHA	77
Comparison of turbulent premixed flames at different turbulence levels. L. DUCHAMP DE LAGENESTE and H. PITSCHE	91
An Eulerian level-set/vortex-sheet method for two-phase interface dynamics. M. HERRMANN	103
Progress toward large-eddy simulation of turbulent reacting and non-reacting flows in complex geometries. K. MAHESH, G. CONSTANTINESCU, S. APTE, G. IACCARINO, F. HAM and P. MOIN	115
Consistent boundary conditions for integrated LES/RANS simulations: LES inflow conditions. J. U. SCHLUTER	143
Integration of RANS and LES flow solvers: interface validation. J. U. SCHLUTER, S. SHANKARAN, S. KIM, H. PITSCHE and J. J. ALONSO	155

Grid-independent large-eddy simulation in turbulent channel flow using three-dimensional explicit filtering. J. GULLBRAND	167
Wall modeling for large-eddy simulation using an immersed boundary method. F. TESSICINI, G. IACCARINO, M. FATICA, M. WANG and R. VERZICCO	181
Towards LES wall models using optimization techniques. J. TEMPLETON, M. WANG and P. MOIN	189
Optimal aeroacoustic shape design using approximation modeling. A. MARSDEN, M. WANG and P. KOUMOUTSAKOS	201
Towards sail shape optimization of a modern clipper ship. T. DOYLE, M. GERRITSEN and G. IACCARINO	215
An experimental investigation of high aspect ratio 2D sails. A. CROOK, M. GERRITSEN and N. N. MANSOUR	225
Turbulence modelling in large-eddy simulations of the cloud-topped atmospheric boundary layer. M. P. KIRKPATRICK	239
Secondary shear instability as a source of turbulence in the solar tachocline. K. PETROVAY	255
Numerical simulation of 2D compressible heat-driven convection. K. V. PARCHEVSKY	267
Numerical simulation of magnetoconvection in a stellar envelope. S. D. USTYUGOV and A. N. ANDRIANOV	281
Vortex dynamics and angular momentum transport in accretion disks. H. LIN, J. A. BARRANCO and P. S. MARCUS	289
Interaction between turbulent flow and free surfaces. Y.-N. YOUNG, F. E. HAM, M. HERRMANN and N. MANSOUR	301
Simulation of flows over wavy rough boundaries. A. NAKAYAMA and K. SAKIO	313
Image-based computational modeling of blood flow in a porcine aorta bypass graft. V. FAVIER and C. A. TAYLOR	325
Hemodynamic changes induced by stenting in elastic arteries. F. NICOUD	335

Wavelet analysis of blood flow singularities by using ultrasound data. P. MAY	349
Flow around cactus-shaped cylinders. S. TALLEY and G. MUNGAL	363
Numerical simulation of turbulent polymer solutions. Y. DUBIEF	377
Flat-plate boundary-layer transition in hypersonic flows. C. STEMMER	389
Simple stochastic model for laminar-to-turbulent subcritical transition. S. FEDOTOV, I. BASHKIRTSEVA and L. RYASHKO	397
An analytical model for predicting airfoil self-noise using wall-pressure statistics. M. ROGER, S. MOREAU and M. WANG	405
Turbulence modeling in an immersed-boundary RANS method. G. KALITZIN and G. IACCARINO	415
Skin friction estimation at high Reynolds numbers and Reynolds number effects for transport aircraft. A. CROOK	427
Appendix: Center for Turbulence Research 2002 Roster	439

Preface

This volume contains the 2002 Annual Progress Reports of the postdoctoral fellows and visiting scholars of the Center for Turbulence Research. In 2002 CTR sponsored 18 resident Postdoctoral Fellows, 12 visiting scholars and 5 doctoral students and hosted 10 Research Associates. The 35 reports contained in this volume cover a wide range of subjects representing NASA's wide ranging interests. The papers are roughly classified into six different groups, although many treat two or more subjects. In addition, in the summer of 2002, CTR sponsored its ninth biennial Summer Program which was the largest ever with fifty participants from ten countries. A separate volume containing the proceedings of this Summer Program was published earlier this year.

Turbulent combustion remains the largest component of the CTR's core program. This program and several related activities at CTR are supported by NASA's Ultra Efficient Engine Technology Program. It is also intimately connected with the Department of Energy's ASCI program at Stanford which develops the technology for numerical simulation of realistic aircraft engines using state of the art massively parallel computers. In combustion modeling the attention has been directed to the modeling of higher levels of complexity such as spray dynamics, radiation and soot formation. Major aircraft engine manufacturers have shown considerable interest in this program; in particular, a significant active collaboration exists between CTR and the Pratt & Whitney Corporation. CTR's combustion program is essentially based on the large-eddy simulation technique, LES, which is actively being pursued at CTR for this and many other applications. Important accomplishments in LES included simulations with three-dimensional filters, which result in grid independent calculations (that is why we call it "true" LES), and the development of the methodology for integration of LES and Reynolds Averaged computations. Optimization techniques are being studied and used for the important problem of wall boundary conditions for LES as well as for optimal shape design for aeroacoustic and aerodynamic performance gains.

Turbulence in geophysical and astrophysical applications is receiving increased attention at CTR and is expected to occupy a larger fraction of the CTR's core program. We believe that CTR is poised to contribute significantly to this area especially by providing improved subgrid scale models, high fidelity numerical methods, advanced computer programming tools and insights in turbulence physics in multi-phase and reacting flows. CTR is broadening its scope of research to more general non-linear multi-scale phenomena. One such area is computational biology which is a fast developing field involving very intensive computing. This year the work at CTR focused on cardiovascular fluid dynamics using imaging techniques, and aerodynamics of natural phenomena. Hypersonic transition with real gas effects is of interest to NASA for space transportation and is an area of active research at CTR.

We thank Millie Chethik and Marlene Lomuljo-Bautista for their day-to-day management of the Center. Special thanks are due to Dr. Massimiliano Fatica for his help with the final preparation of this report.

We dedicate this volume to the memory of the enormous contributions of Charles David Pierce. Charles was a student and later a Research Associate at CTR. His dissertation was the pioneering step that launched CTR's program in large eddy simulation of turbulent combustion. Charles' legacy computer codes and original ideas in modeling turbulent combustion and numerical methods remain at the heart of CTR's research enterprise.

Parviz Moin
Nagi N. Mansour
Peter Bradshaw (editor)

This volume is available as a .pdf file on the Web at <http://ctr.stanford.edu>

A G -equation formulation for large-eddy simulation of premixed turbulent combustion

By H. Pitsch

1. Motivation and objectives

Premixed turbulent combustion in technical devices often occurs in thin flame fronts. The propagation of these fronts, and hence, for instance, the heat release, are governed by the interaction of transport processes and chemistry within the front. In flamelet models this strong coupling is expressed by treating the flame front as a thin interface propagating with a laminar burning velocity s_L . The coupling of transport and chemistry is reflected in the scaling of the laminar burning velocity, which can be expressed as $s_L \sim \sqrt{D/t_c}$, where D is the diffusion coefficient and t_c is the chemical time scale. Flamelet models for premixed turbulent combustion have been extensively used in the past and different models have been formulated for Reynolds averaged (Bray *et al.* (1985); Peters (2000)) and large-eddy simulations (LES) (Hawkes & Cant (2000); Kim & Menon (2000); Chakravarthy & Menon (2001); Pitsch & Duchamp de Lageneste (2002)).

The G -equation model proposed by Williams (1985) is based on the flamelet modeling assumptions and uses a level-set method to describe the evolution of the flame front as an interface between the unburned and burned gases. The level-set function G is a scalar field defined such that the flame front position is at $G = G_0$, and that G is negative in the unburned mixture. The instantaneous and local G -equation can be derived by considering the instantaneous flame surface. An implicit representation of this surface can be given as

$$G(\mathbf{x}, t) - G_0 = 0, \quad (1.1)$$

which defines the level-set function G . Here, \mathbf{x} is the vector of space coordinates. Differentiating Eq. (1.1), one obtains

$$\frac{\partial G}{\partial t} + \frac{d\mathbf{x}_f}{dt} \cdot \nabla G = 0, \quad (1.2)$$

where \mathbf{x}_f is the flame front location. If the curvature radius of the instantaneous flame front is locally larger than the flame thickness, the flame is in the corrugated flamelets regime, and the flame front propagation speed is given by

$$\frac{d\mathbf{x}_f}{dt} = \mathbf{v} + s_L \mathbf{n}. \quad (1.3)$$

Here, \mathbf{v} is the local flow velocity and s_L is the laminar burning velocity. The flame normal vector \mathbf{n} is defined to be directed into the unburned mixture and can be expressed as

$$\mathbf{n} = -\frac{\nabla G}{|\nabla G|}. \quad (1.4)$$

Combining Eqs. (1.2) and (1.3) yields the instantaneous G -equation

$$\frac{\partial G}{\partial t} + \mathbf{v} \cdot \nabla G = s_L |\nabla G|. \quad (1.5)$$

Since this equation has been derived from Eqs. (1.1) and (1.3), which both only describe the flame surface, also Eq. (1.5) is valid at the flame surface only. The remaining G -field is arbitrary and commonly defined to be a distance function.

The location of G_0 can be defined to be anywhere in the flame, for instance at a given temperature iso-surface. Then, in Eq. (1.5), the velocity v is evaluated at that location, and the laminar burning velocity s_L has to be defined with respect to that location as well. Typically, G_0 is defined to be either immediately ahead of the flame in the unburned, or immediately behind the flame in the burned gases. The burning velocities defined with respect to the unburned and burned are denoted as $s_{L,u}$ and $s_{L,b}$, respectively.

Peters (1992, 1999, 2000) has developed an appropriate theory for premixed turbulent combustion describing the corrugated flamelets and the thin reaction zones regimes based on the G -equation formulation. Peters (2000) and Oberlack *et al.* (2001) pointed out that, since the G -field has physical meaning only at $G = G_0$, in order to derive the Reynolds averaged G -equation, conventional averaging of the G -field cannot be applied. For LES, this implies that not only is it impossible to obtain a filtered G -field from filtering the instantaneous resolved field, but also that the filter kernels, which are usually being used for filtering the velocity and scalar fields cannot be applied. In the application of the G -equation in LES, these facts have not been considered in the past. Hence, we first need to develop a filter kernel that takes information only from the instantaneous resolved flame surface. This will be done in the next section. Thereafter, the equation for the filtered flame front position will be derived. The resulting equation has two unclosed terms, a flame front conditionally averaged flow velocity appearing in the convection term, and the sub-filter burning velocity. To relate the conditional velocity to the unconditionally filtered velocity, which is known from the solution of the momentum equations, a model for this quantity will also be developed. Finally, we will derive an equation for the sub-filter flame front wrinkling, which will lead to an analytic model for the sub-filter burning velocity.

2. G -Equation for the filtered flame location valid in the corrugated flamelets regime

Peters (2000) and Oberlack *et al.* (2001) have pointed out that for the derivation of a G -equation for the ensemble or time averaged flame location the traditional averaging of the entire G -field cannot be applied. Because the G -field has physical significance only for $G = G_0$, only the G_0 iso-surface can be of relevance in the averaging procedure and the remaining G -field, which can be arbitrarily defined, must not be used. Instead, Peters (2000) has proposed an averaging procedure that only uses the probability density function (pdf) of finding $G = G_0$ at a particular location. This procedure was described only for the one-dimensional case. Oberlack *et al.* (2001) developed a rigorous averaging procedure for the three-dimensional case. Through the consistent application of this averaging procedure, a G -equation for the averaged flame location and an equation for the flame brush thickness have been derived for the corrugated flamelets regime. In this section, we will first develop an appropriate LES filter and then derive a G -equation for the filtered flame front location in the corrugated flamelets regime by using similar arguments as given by Oberlack *et al.* (2001). The resulting G -equation will be extended to the thin reaction zones regime in the following section.

A parametric representation of the flame surface \mathcal{F} can be given as

$$\mathbf{x}_f = \mathbf{x}_f(\lambda, \mu, t), \quad (2.1)$$

where \mathbf{x}_f is the flame front location, and λ and μ are curvilinear coordinates along the flame surface forming an orthogonal coordinate system moving with the flame front. Considering a point P_0 on the flame surface, which is given by the coordinates (λ_0, μ_0) , $\mathbf{x}_f(\lambda_0, \mu_0, t)$ describes the temporal development of the location of the point P_0 in physical space as function of time t . The coordinates λ and μ are hence parameters of the function \mathbf{x}_f and will in the following be written as $\Lambda = (\begin{smallmatrix} \lambda \\ \mu \end{smallmatrix})$.

For a given set of parameters Λ , a spatial filter \mathcal{H} can then be defined as

$$\mathcal{H}(\Lambda - \Lambda') = \begin{cases} a(\Lambda), & \text{if } |\mathbf{x}_f(\Lambda) - \mathbf{x}_f(\Lambda')| \leq \frac{\Delta}{2} \\ 0, & \text{otherwise} \end{cases}, \quad (2.2)$$

where Δ is the filter width and $a(\Lambda)$ is a normalization factor that is determined by the normalization condition

$$\int_{\mathcal{F}} \mathcal{H}(\Lambda - \Lambda') d\Lambda' = 1. \quad (2.3)$$

This filter function is substantially different from the conventionally applied filter kernels for scalar quantities. Since the flame is only defined on a surface, the filter also has to move along this surface and cannot be used at an arbitrary point in space. The coordinates used in the filter function are therefore not spatial, but flame surface coordinates. Then, a spatial filtering operation for the flame front location can be defined as

$$\hat{\mathbf{x}}_f(\Lambda, t) = \int_{\mathcal{F}} \mathbf{x}_f(\Lambda', t) \mathcal{H}(\Lambda - \Lambda') d\Lambda'. \quad (2.4)$$

This filtering operation should be described in more detail for clarity. The surface coordinates Λ are defined along the instantaneous flame surface. To obtain the filtered front location, for each point $\mathbf{x}_f(\Lambda)$ on the instantaneous flame surface, the filtering operation Eq. (2.4) yields a corresponding mean flame front location $\hat{\mathbf{x}}_f(\Lambda)$. These locations define the filtered flame front position. Note, that although $\hat{\mathbf{x}}_f$ is expressed as a function of Λ , these parameters are still defined through the unfiltered front.

Applying the filter operation to Eq. (1.3) leads to

$$\frac{d\hat{\mathbf{x}}_f}{dt} = \hat{\mathbf{v}} + \widehat{s_L \mathbf{n}}, \quad (2.5)$$

where the conditionally filtered flow velocity and propagation speed are given by

$$\hat{\mathbf{v}}(\Lambda, t) = \int_{\mathcal{F}} \mathbf{v}(\Lambda', t) \mathcal{H}(\Lambda - \Lambda') d\Lambda'. \quad (2.6)$$

and

$$\widehat{s_L \mathbf{n}}(\Lambda, t) = \int_{\mathcal{F}} s_L(\Lambda', t) \mathbf{n}(\Lambda', t) \mathcal{H}(\Lambda - \Lambda') d\Lambda'. \quad (2.7)$$

To obtain an equation for the filtered flame front location, the implicit representation of the filtered flame surface, given as

$$\check{G}(\mathbf{x}, t) = G_0, \quad (2.8)$$

is differentiated and the displacement speed of \check{G} appearing in this equation is associated

with the filtered displacement speed of the unfiltered front. This results in

$$\frac{\partial \check{G}}{\partial t} + \frac{d\hat{x}_f}{dt} \cdot \nabla \check{G} = 0. \quad (2.9)$$

Note that the $\hat{\cdot}$ -quantities are a direct result of the filtering operation Eq. (2.4), whereas \check{G} is just the level-set representation of the filtered flame front location. Therefore, the filtered flame front is not yet defined by Eq. (2.8). Indeed, this equation and its differentiated form could describe any iso-surface. Only by choosing the propagation speed of this surface equal to the filtered propagation speed from Eq. (2.5), this surface is identified with the filtered flame front location. Introducing Eq. (2.5) into Eq. (2.9) yields the G -equation for the mean flame front location as

$$\frac{\partial \check{G}}{\partial t} + \hat{v} \cdot \nabla \check{G} = -\widehat{s_L n} \cdot \nabla \check{G}. \quad (2.10)$$

As proposed by Oberlack *et al.* (2001), the propagation term defined in Eq. (2.7) can be modeled by the turbulent burning velocity, here the sub-grid burning velocity, s_T , and the gradient of the resolved G -field as

$$\widehat{s_L n} = s_T \check{n} = -s_T \frac{\nabla \check{G}}{|\nabla \check{G}|}, \quad (2.11)$$

where \check{n} is the normal vector of the filtered flame front position

$$\check{n} = -\frac{\nabla \check{G}}{|\nabla \check{G}|}. \quad (2.12)$$

Note that according to the definition of G_0 the conditional velocity is either the filtered velocity in the immediate unburned or burned gases, which will be denoted by \hat{v}_u and \hat{v}_b , respectively. Similarly, the turbulent burning velocity has to be defined with respect to the unburned or burned gases, denoted by $s_{T,u}$ and $s_{T,b}$. With these notations, depending on the definition of G_0 , Eq. (2.10) can be written as either

$$\frac{\partial \check{G}}{\partial t} + \hat{v}_u \cdot \nabla \check{G} = s_{T,u} |\nabla \check{G}| \quad (2.13)$$

or

$$\frac{\partial \check{G}}{\partial t} + \hat{v}_b \cdot \nabla \check{G} = s_{T,b} |\nabla \check{G}|. \quad (2.14)$$

The evolution of the filtered flame front location can be described by either one of the Eqs. (2.13) and (2.14). To solve these equations, models for the sub-filter burning velocity and the flame front conditioned, filtered velocity have to be provided. The latter quantity has to be modeled in terms of the Favre-filtered velocities, which are known from the solution of the Favre-filtered momentum equations. Models for these quantities will be provided in subsequent sections.

3. G -equation for the filtered flame location valid in the corrugated flamelets and the thin reaction zones regime

In the derivation for the instantaneous G -equation for the thin reaction zones regime, Peters (2000) starts from the instantaneous temperature equation and develops a level-set equation for a temperature iso-surface given by $T(\mathbf{x}, t) = T^0$, where T^0 is the inner layer

temperature. The expression for the propagation speed is similar to Eq. (1.3), where, following Gibson (1968), the displacement speed, s_d , can be written as

$$s_d = \left(\frac{\nabla \cdot (\rho D_T \nabla T) + \omega_T}{\rho |\nabla T|} \right)_{T=T^0}. \quad (3.1)$$

Here, ρ is the density, D_T is the temperature diffusivity, and ω_T is the chemical source term. With the temperature iso-surface normal vector $\mathbf{n}_T = -\nabla T / |\nabla T|$, the transport term in Eq. (3.1) can be expressed by its components normal and tangential to the T^0 surface and the displacement speed becomes

$$s_d = -(D_T \nabla \cdot \mathbf{n}_T)_{T=T^0} + \left(\frac{-\mathbf{n}_T (\rho D_T |\nabla T|) - \omega_T}{|\nabla T|} \right)_{T=T^0} = s_\kappa + (s_n + s_r). \quad (3.2)$$

Peters *et al.* (1998) have shown that $(s_n + s_r)$, which for an unstrained premixed flame is the laminar burning velocity, is not significantly changed by turbulence, and therefore, in the thin reaction zones regime, is small compared with the contribution from curvature s_κ . Since the temperature iso-surface $T = T^0$ will be described by $G = G_0$, s_κ can be written as

$$s_\kappa = -D_T \nabla \cdot \mathbf{n} = D_T \nabla \cdot \left(\frac{\nabla G}{|\nabla G|} \right). \quad (3.3)$$

The combined displacement velocity valid in the corrugated flamelets and the thin reaction zones regime is given by an expression similar to Eq. (1.3), but with the laminar burning velocity s_L replaced by $s_L + s_\kappa$. Filtering this expression with the filter operation given by Eq. (2.4) leads to

$$\frac{d\hat{\mathbf{x}}_f}{dt} = \hat{\mathbf{v}} + \widehat{(s_L + s_\kappa) \mathbf{n}}. \quad (3.4)$$

Introducing Eq. (3.4) into Eq. (2.9) leads to the G -equation valid for the corrugated flamelets and the thin reaction zones regime

$$\frac{\partial \check{G}}{\partial t} + \hat{\mathbf{v}} \cdot \nabla \check{G} = -\widehat{(s_L + s_\kappa) \mathbf{n}} \cdot \nabla \check{G}. \quad (3.5)$$

As in Eq. (2.11), the propagation term can again be modeled by a turbulent burning velocity and the normal vector of the mean flame front position as

$$\widehat{(s_L + s_\kappa) \mathbf{n}} = s_T \check{\mathbf{n}} = -s_T \frac{\nabla \check{G}}{|\nabla \check{G}|}. \quad (3.6)$$

It is important to note that in the modeling of the turbulent burning velocity, the effect of curvature, most important in the small scale turbulence regime, and the effect of laminar flame propagation, important in the large scale turbulence regime, have to be considered. It is also interesting to note that in the present derivation of the G -equation, the term proportional to the eddy diffusivity and the curvature of the mean field, which in Peters (2000) and Pitsch & Duchamp de Lageneste (2002) arises from the scalar flux term in the thin reaction zones regime, does not appear. This term always leads to a stabilization of the mean flame front and hence, to a decrease in the resolved scale turbulent burning velocity.

4. Model for the conditionally filtered flow velocity

A consistency requirement for the conditional velocities model is imposed by the fact that Eqs. (2.13) and (2.14) are equivalent. After applying a model for \hat{v}_u in Eq. (2.13) and \hat{v}_b in Eq. (2.14), these still have to have the same solution. In the following, we will therefore first develop a model for the conditional velocities, and then show that applying the model to both equations leads to equivalent formulations.

The conditional velocity \hat{v} is the velocity at the flame front, weighted with the filter function \mathcal{H} and averaged over the entire flame surface within the filter volume. Physically, this averaged velocity, as it appears in the convection term in Eq. (2.10), leads to the convection of the entire sub-filter flame surface. Hence, it is important only to capture the large-scale velocity motion in the model for the conditional velocities, and not the small scale velocity fluctuations, which only lead to sub-grid flame wrinkling, but not to convection on the resolved scales. Then, the local unfiltered velocities can be assumed to be constant in the burned and the unburned part of the sub-filter volume. These velocities are then equal to the respective conditional velocities. This can be written as

$$\mathbf{v}(G) = \begin{cases} \hat{v}_u & \text{if } G < G_0 \\ \hat{v}_u & \text{if } G = G_0 \text{ and } G_0 \text{ defined in the unburned} \\ \hat{v}_b & \text{if } G = G_0 \text{ and } G_0 \text{ defined in the burned} \\ \hat{v}_b, & \text{if } G > G_0 \end{cases} \quad (4.1)$$

where it has to be distinguished, whether G_0 is defined to be in the unburned or the burned mixture. The unconditional Favre-filtered velocity can then be expressed by

$$\bar{\rho}\tilde{\mathbf{v}} = \int_{-\infty}^{\infty} \rho\mathbf{v}(G)P(G)dG = \rho_u \hat{v}_u \int_{-\infty}^{G_0} P(G)dG + \rho_b \hat{v}_b \int_{G_0}^{\infty} P(G)dG, \quad (4.2)$$

where $P(G)$ is the pdf of finding a particular value of G . Introducing the probability of finding burned mixture as

$$p_b = \int_{G_0}^{\infty} P(G)dG, \quad (4.3)$$

the unconditional velocity can be written as

$$\bar{\rho}\tilde{\mathbf{v}} = \rho_u \hat{v}_u (1 - p_b) + \rho_b \hat{v}_b p_b. \quad (4.4)$$

Similarly, the unconditionally filtered density can be derived as

$$\bar{\rho} = \rho_u (1 - p_b) + \rho_b p_b. \quad (4.5)$$

To express \hat{v}_b by \hat{v}_u , we will use the jump condition for the mass balance across the mean flame interface, given by

$$\rho_u \tilde{\mathbf{n}} \cdot \left(\hat{v}_u - \frac{\partial \hat{x}_f}{\partial t} \right) = \rho_b \tilde{\mathbf{n}} \cdot \left(\hat{v}_b - \frac{\partial \hat{x}_f}{\partial t} \right). \quad (4.6)$$

The displacement speed can be expressed by Eqs. (3.4) and (3.6), where the choice of the conditional velocity and the burning velocity depend on the location of G_0 with respect to the flame. If G_0 is defined to be in the unburned mixture, \hat{v}_u and $s_{T,u}$ have to be used. However, if G_0 is in the burned gases, then the appropriate values are given by \hat{v}_b

and $s_{T,b}$. For the velocity jump across the flame front this results in

$$\check{\mathbf{n}} \cdot (\hat{\mathbf{v}}_u - \hat{\mathbf{v}}_b) = \frac{\rho_u - \rho_b}{\rho_b} s_{T,u}, \quad (4.7)$$

if G_0 is defined to be in the unburned mixture, and

$$\check{\mathbf{n}} \cdot (\hat{\mathbf{v}}_u - \hat{\mathbf{v}}_b) = \frac{\rho_u - \rho_b}{\rho_u} s_{T,b}, \quad (4.8)$$

if G_0 is in the burned gases. Introducing Eqs. (4.7) and (4.8) into Eq. (4.4) results in expressions for the conditional velocities in terms of the unconditional velocities as

$$\check{\mathbf{n}} \cdot \hat{\mathbf{v}}_u = \check{\mathbf{n}} \cdot \tilde{\mathbf{v}} + \frac{\rho_u - \rho_b}{\bar{\rho}} s_{T,u} p_b \quad (4.9)$$

and

$$\check{\mathbf{n}} \cdot \hat{\mathbf{v}}_b = \check{\mathbf{n}} \cdot \tilde{\mathbf{v}} - \frac{\rho_u - \rho_b}{\bar{\rho}} s_{T,b} (1 - p_b). \quad (4.10)$$

In order to make use of these relations in the G -equation given by Eqs. (2.13) and (2.14), we first split the convection term into a flame normal and a flame tangential part. Since the flame tangential part only leads to a parallel translation of the flame front and has no influence on the flame propagation, it can be neglected. The convection term from Eq. (2.13), for instance, can then be written as

$$\hat{\mathbf{v}}_u \cdot \nabla \check{G} = (\check{\mathbf{n}} \cdot \hat{\mathbf{v}}_u) \check{\mathbf{n}} \cdot \nabla \check{G}. \quad (4.11)$$

After introducing Eq. (4.9) into the normal convection term, only the normal component of the unconditional velocity appears, which can again be complemented by the tangential part without changing the solution, which leads to

$$\frac{\partial \check{G}}{\partial t} + \tilde{\mathbf{v}} \cdot \nabla \check{G} = s_{T,u} |\nabla \check{G}| \left(1 + \frac{\rho_u - \rho_b}{\bar{\rho}} p_b \right) \quad (4.12)$$

and

$$\frac{\partial \check{G}}{\partial t} + \tilde{\mathbf{v}} \cdot \nabla \check{G} = s_{T,b} |\nabla \check{G}| \left(1 - \frac{\rho_u - \rho_b}{\bar{\rho}} (1 - p_b) \right). \quad (4.13)$$

With Eq. (4.5), the equations for the filtered flame front position can be written as

$$\frac{\partial \check{G}}{\partial t} + \tilde{\mathbf{v}} \cdot \nabla \check{G} = \frac{\rho_u}{\bar{\rho}} s_{T,u} |\nabla \check{G}| \quad (4.14)$$

and

$$\frac{\partial \check{G}}{\partial t} + \tilde{\mathbf{v}} \cdot \nabla \check{G} = \frac{\rho_b}{\bar{\rho}} s_{T,b} |\nabla \check{G}|. \quad (4.15)$$

It is easily seen that these equations satisfy some important limits. If Eq. (4.14) is evaluated in the unburned mixture, then $\tilde{\mathbf{v}} = \hat{\mathbf{v}}_u$ and $\bar{\rho} = \rho_u$. Hence, Eq. (2.13) is recovered. If, on the other hand, this equation is evaluated in the burned gases, $\tilde{\mathbf{v}} = \hat{\mathbf{v}}_b$, $\bar{\rho} = \rho_b$, and, since the mass conservation through the flame requires

$$\rho_u s_{T,u} = \rho_b s_{T,b}, \quad (4.16)$$

the right hand side goes to $s_{T,b} |\nabla \check{G}|$. Therefore, in the burned gases, Eq. (2.14) is recovered. By using Eq. (4.16), it can also be shown easily that Eqs. (4.14) and (4.15) are equivalent.

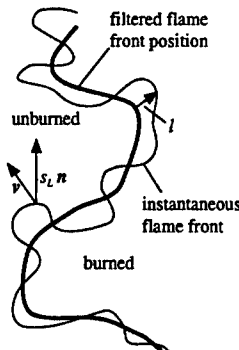


FIGURE 1. Instantaneous and filtered flame front position

5. Equation for the sub-filter flame brush thickness

We now want to derive an equation for the length-scale of the sub-filter flame front fluctuations l , which might be associated with the sub-filter flame brush thickness. This equation will then be used to derive a model for the turbulent burning velocity. The flame front fluctuation l will here be defined as the distance of the instantaneous flame front to the filtered flame front in the direction normal to the filtered flame surface, as indicated in Fig. 1. Then, l is simply the distance between the points \mathbf{x}_f and $\hat{\mathbf{x}}_f$ given by

$$l = |\mathbf{x}_f - \hat{\mathbf{x}}_f|. \quad (5.1)$$

For a given point $\hat{\mathbf{x}}_f$ on the filtered flame surface, the appropriate location on the instantaneous surface is then defined with the filtered front normal vector at $\hat{\mathbf{x}}_f$ as

$$l \hat{\mathbf{n}} = \mathbf{x}_f - \hat{\mathbf{x}}_f. \quad (5.2)$$

It is easy to see that this definition of the length scale satisfies the important criterion that l tends to zero, if the flame front wrinkling is completely resolved, since this implies that \mathbf{x}_f and $\hat{\mathbf{x}}_f$ are the same. Other choices could be made to define the length-scale of the sub-filter flame front wrinkling. For instance, the length-scale could be evaluated at constant value of Λ as $l = \mathbf{x}_f(\Lambda) - \hat{\mathbf{x}}_f(\Lambda)$, which would correspond to the definition used in Oberlack *et al.* (2001). However, this definition does not necessarily tend to zero, if the flame is resolved.

Similar to the G -variance equation given in Peters (2000), the equation for flame front fluctuations has a production term, active on the large scales, and two dissipation terms, the kinematic restoration term, important in the corrugated flamelets regime, and the scalar dissipation term, important in the thin reaction zones regime. The length scale equation should therefore actually be derived and modeled separately in each of these regimes and combined subsequently. Here, for brevity, only the combined equation, valid in both regimes, will be derived. However, the modeling of each dissipation term will be done in the limit, where only this particular term is important.

Differentiating Eq. (5.2) and using Eq. (3.4) and the corresponding unfiltered equation, an expression for l can be derived as

$$\frac{dl \hat{\mathbf{n}}}{dt} = \frac{d\mathbf{x}_f - \hat{\mathbf{x}}_f}{dt} = \mathbf{v} - \hat{\mathbf{v}} + s_L \mathbf{n} - \widehat{s_L \mathbf{n}} + s_\kappa \mathbf{n} - \widehat{s_\kappa \mathbf{n}}. \quad (5.3)$$

The equation for the length scale of the sub-filter flame front fluctuations can then be obtained by multiplying Eq. (5.3) by $l \hat{\mathbf{n}}$ and applying the filtering operation, given by

Eq. (2.4). This leads to

$$\frac{d\hat{l}^2}{dt} = 2\check{\mathbf{n}} \cdot \widehat{lv'} + 2\check{\mathbf{n}} \cdot \widehat{l(s_L n)'} + 2\check{\mathbf{n}} \cdot \widehat{l(s_\kappa n)'}, \quad (5.4)$$

where the sub-filter velocity fluctuation has been introduced as $\mathbf{v}' = \mathbf{v} - \hat{\mathbf{v}}$ and the turbulent burning velocity fluctuations as $(s_L n)' = s_L n - \widehat{s_L n}$ and $(s_\kappa n)' = s_\kappa n - \widehat{s_\kappa n}$. Since \hat{l}^2 is a quantity that is defined at the filtered flame front only, the rate of change can be described in an Eulerian frame of reference such that

$$\frac{d\hat{l}^2}{dt} = \frac{\partial \hat{l}^2}{\partial t} + \frac{d\hat{x}_f}{dt} \cdot \nabla \hat{l}^2, \quad (5.5)$$

which, using Eq. (2.5), leads to

$$\frac{\partial \hat{l}^2}{\partial t} + (\hat{\mathbf{v}} + \widehat{s_L n}) \cdot \nabla \hat{l}^2 = 2\check{\mathbf{n}} \cdot \widehat{lv'} + 2\check{\mathbf{n}} \cdot \widehat{l(s_L n)' + l(s_\kappa n)'}. \quad (5.6)$$

The convective transport term can again be modeled as described earlier using Eqs. (2.11) and (4.9), which leads to

$$\frac{\partial \hat{l}^2}{\partial t} + \left(\tilde{\mathbf{v}} + \frac{\rho_u}{\bar{\rho}} s_T \check{\mathbf{n}} \right) \cdot \nabla \hat{l}^2 = 2\check{\mathbf{n}} \cdot \widehat{lv'} + 2\check{\mathbf{n}} \cdot \widehat{l(s_L n)' + l(s_\kappa n)'}. \quad (5.7)$$

In Eq. (5.7), the terms on the left hand side describe the rate of change and the transport of the length scale due to the flame displacement. The first term on the right hand side describes the production of flame front wrinkling due to the turbulence, whereas the second and third terms on the right hand side are the flame surface dissipation due to flame propagation and diffusive curvature effects, respectively.

To model the production term in Eq. (5.7), we have to consider the scalar flux term $\check{\mathbf{n}} \cdot \widehat{lv'}$, which would typically be expressed using a gradient transport assumption, involving a turbulent eddy viscosity and the spatial gradient of the scalar. However, since the flame front fluctuation l is defined at the mean flame front position only, spatial gradients of this quantity are not defined. The length scale l will therefore first be related to fluctuations of the scalar field G , which for small l or constant $|\nabla \check{G}|$ around the flame front can be written as

$$l = \frac{G'}{|\nabla \check{G}|}. \quad (5.8)$$

Note that constant $|\nabla \check{G}|$ can be required, because the definition of the \check{G} -field away from $\check{G} = G_0$ is arbitrary, and that l is certainly still independent of the definition of this field. The scalar flux term then becomes

$$\check{\mathbf{n}} \cdot \widehat{lv'} = \widehat{\frac{\check{\mathbf{n}}}{|\nabla \check{G}|} \cdot G' v'} = -\frac{\check{\mathbf{n}}}{|\nabla \check{G}|} D_{t,G} \cdot \nabla \check{G}, \quad (5.9)$$

where the right hand side has been obtained by invoking a gradient transport assumption for G . With the definition of the mean flame front normal vector, Eq. (2.12), the turbulent production term can then be modeled by

$$\widehat{\check{\mathbf{n}} \cdot lv'} = D_{t,G}. \quad (5.10)$$

$D_{t,G}$ would generally be called the eddy diffusivity of G . This is misleading, since the scalar G is non-diffusive. However, $D_{t,G}$ appears not in a diffusion type term in the

modeled form of the length scale equation, but as a source term, which, since a turbulent diffusivity really describes turbulent transport rather than diffusion, accounts for the production of flame surface through turbulent mixing. This also implies that $D_{t,G}$ has no contribution from a molecular diffusion coefficient. It should therefore be called turbulent transport coefficient rather than eddy diffusivity. Since the definition of G outside $G = G_0$ is arbitrary, this coefficient cannot be simply determined using the dynamic procedure for scalar quantities as proposed by Moin *et al.* (1991). Instead, a constant Schmidt number assumption with a Smagorinsky-type model for the sub-filter eddy viscosity will be used for $D_{t,G}$, which results in

$$D_{t,G} = \frac{C_\nu \Delta v'_\Delta}{Sc_{t,G}}, \quad (5.11)$$

where $C_\nu \Delta$ is a sub-filter length-scale given by the filter width Δ and the Smagorinsky coefficient C_ν , the latter of which is determined by a dynamic model as described by Moin *et al.* (1991). According to Pitsch & Steiner (2000), the Schmidt number has been chosen to be $Sc_{t,G} = 0.5$.

Since both dissipation terms act on the small scales, the scaling relations for these terms provided by Peters (1999) in a Reynolds averaged context can also be applied here. In the corrugated flamelets regime, the kinematic restoration term is the dominant dissipation term. This term should be independent of small scale quantities such as the laminar burning velocity, but scales with the mean propagation term and can be expressed as

$$\widehat{\check{\mathbf{n}} \cdot l(s_L \mathbf{n})'} = c_2 C_\nu \Delta \check{\mathbf{n}} \cdot \widehat{s_L \mathbf{n}} = -c_2 C_\nu \Delta s_T, \quad (5.12)$$

where the turbulent burning velocity has been introduced using Eq. (2.11).

Similarly, also the scalar dissipation term, dominant in the thin reaction zones regime, is assumed to scale with the respective mean propagation term. Since a dissipation term can be written independently of the large scales, the missing length scale is obtained from the small scale quantities and it follows

$$\widehat{\check{\mathbf{n}} \cdot l(s_\kappa \mathbf{n})'} = c_1 \frac{l_F}{s_L} (\check{\mathbf{n}} \cdot \widehat{s_\kappa \mathbf{n}})^2 = -c_3 \frac{l_F}{s_L} s_T^2. \quad (5.13)$$

Introducing Eqs. (5.10), (5.12), and (5.13) into Eq. (5.7), and assuming that production equals dissipation in that equation, an expression for the turbulent burning velocity can be obtained as

$$D_{t,G} - c_2 C_\nu \Delta s_T - c_3 \frac{l_F}{s_L} s_T^2 = 0. \quad (5.14)$$

This leads to

$$\frac{s_T - s_L}{s_L} = -\frac{b_3^2 C_\nu}{2b_1 Sc_{t,G} l_F} \frac{\Delta}{l_F} + \sqrt{\left(\frac{b_3^2 C_\nu}{2b_1 Sc_{t,G} l_F} \frac{\Delta}{l_F} \right)^2 + \frac{b_3^2 D_t}{s_L l_F}}. \quad (5.15)$$

Here, the laminar burning velocity has been added to satisfy the laminar limit. The constants c_2 and c_3 have been determined such that Eq. (5.15) results for $\Delta/l_F \rightarrow 0$ in Damköhler's small-scale limit

$$\frac{s_T - s_L}{s_L} = b_1 \frac{v'_\Delta}{s_L}, \quad (5.16)$$

and for $\Delta/l_F \rightarrow \infty$ in the large-scale limit

$$\frac{s_T - s_L}{s_L} = b_3 \sqrt{\frac{D_t}{D}}. \quad (5.17)$$

The resulting expressions for the constants are $c_2 = 1/(b_1 \text{Sc}_{t,G})$ and $c_3 = 1/b_3^2$, where the constants b_1 and b_3 have been taken from Peters (2000) to be $b_1 = 2.0$ and $b_3 = 1.0$.

Finally, in light of these results, the scaling used in the modeling of the dissipation terms in the length scale equation should be discussed. To derive the models given in Eqs. (5.12) and (5.13), dimensional arguments have been used, which, if used differently, could also have led to different results. In particular, for the kinematic restoration, a linear dependence of the propagation term has been assumed, while for the scalar dissipation term a quadratic dependence is used. As an example for a different scaling possibility, the latter could also have been expressed as linearly dependent on the propagation term times the small scale length scale l_F . Such a scaling has been used in Pitsch & Duchamp de Lageneste (2002), which then led to a similar, but different expression for the turbulent burning velocity. The quadratic relation, which for the scaling used in this study is given by Eq. (5.14), has then no linear term, and can be solved more easily. However, the choice of the particular scaling used here and also in Peters (2000) is motivated by results from direct numerical simulations by Wenzel (2000), who studied the evolution of the G-equation in forced isotropic turbulence. Unfortunately, the scaling of the dissipation terms in the length scale equation has not been investigated, but the scaling of the corresponding terms in an equation for the flame surface area ratio $\sigma = |\nabla G|$ has been given. It is found that the kinematic restoration term depends quadratically, the scalar dissipation rate cubically on σ . These dependencies can be translated to the length scale equation. Since $\sigma \sim G'$, it follows that $\frac{dG'^2}{G'^2} \sim \frac{d\sigma}{\sigma}$, which, using Eq. (5.8), leads to $dl^2 = \frac{G'^2}{\sigma} d\sigma$. This shows that compared with the transport equation for σ given in Peters (2000), in the equation for l^2 , given by Eq. (5.7), the power of σ in the dissipation terms should be decreased by one. This results in the scaling employed in Eqs. (5.12) and (5.13), since, using the present filtering procedure, σ appears in form of the normal vector.

6. Conclusions and future work

In the present paper a consistent formulation of the G-equation approach for LES has been developed. It has been discussed that the instantaneous unfiltered G-equation is valid only at the instantaneous flame front location. In a filtering procedure, applied to derive the appropriate LES equation, only states on the instantaneous unfiltered flame surface can hence be considered. A new filter kernel has been provided here that averages only states along the flame surface. The filter has been used to derive the G-equation for the filtered flame front location. This equation has two unclosed terms involving a flame front conditionally averaged flow velocity and a turbulent burning velocity. A model for the conditional velocity is derived expressing this quantity in terms of the Favre-filtered flow velocity, which is usually known from the flow solver. This model leads to the appearance of a density ratio in the propagation term of the G-equation. Due to the application of the new filtering procedure, also a propagation term proportional to the curvature of the mean front does not appear. This is an important difference to the mean G-equation given by Pitsch & Duchamp de Lageneste (2002), since the term has a stabilizing effect on the flame front and will therefore lead to a decreased resolved

turbulent burning velocity. An equation for the length-scale of the sub-filter flame front wrinkling is derived and leads to a model for the turbulent burning velocity. In the future, we will validate the present formulation in LES of turbulent premixed combustion experiments and assess the importance of the differences in the present formulation. Also, having provided a sound filtering procedure, dynamic models for the turbulent burning velocity can now be developed.

7. Acknowledgments

The authors gratefully acknowledge funding by the US Department of Energy within the ASCI program and by Snecma Moteurs. The author also thanks Marcus Herrmann for many inspiring discussions.

REFERENCES

- BRAY, K. N. C., LIBBY, P. A. & MOSS, J. B. 1985 Unified modeling approach for premixed turbulent combustion. I. general formulation. *Combust. Flame* **61**, 87–102.
- CHAKRAVARTHY, V. K. & MENON, S. 2001 Large-eddy simulation of turbulent premixed flames in the flamelet regime. *Comb. Sci. Tech.* **162**, 175.
- GIBSON, C. H. 1968 Fine structure of scalar fields mixed by turbulence. I. Zero-gradient points and minimal gradient surfaces. *Phys. Fluids* **11**, 2305.
- HAWKES, E. R. & CANT, R. S. 2000 A flame surface density approach to large-eddy simulation of premixed turbulent combustion. *Proc. Combust. Inst.* **28**, 51–58.
- KIM, W. W. & MENON, S. 2000 Numerical modeling of turbulent premixed flames in the thin-reaction-zones regime. *Comb. Sci. Tech.* **160**, 119–150.
- MOIN, P., SQUIRES, K., CABOT, W. & LEE, S. 1991 A dynamic subgrid-scale model for compressible turbulence and scalar transport. *Phys. Fluids A* **3**, 2746–2757.
- OBERLACK, M., WENZEL, H. & PETERS, N. 2001 On symmetries and averaging of the *G*-equation for premixed combustion. *Comb. Theory Modelling* **5** (4), 1–20.
- PETERS, N. 1992 A spectral closure for premixed turbulent combustion in the flamelet regime. *J. Fluid Mech.* **242**, 611–629.
- PETERS, N. 1999 The turbulent burning velocity for large scale and small scale turbulence. *J. Fluid Mech.* **384**, 107–132.
- PETERS, N. 2000 *Turbulent Combustion*. Cambridge University Press.
- PETERS, N., TERHOEVEN, P., CHEN, J. H. & ECHEKKI, T. 1998 Statistics of flame displacement speeds from computations of $2-d$ unsteady methane-air flames. *Proc. Combust. Inst.* **27**, 833–839.
- PITSCH, H. & DUCHAMP DE LAGENESTE, L. 2002 Large-eddy simulation of premixed turbulent combustion using a level-set approach. *Proc. Combust. Inst.* **29**, accepted for publication.
- PITSCH, H. & STEINER, H. 2000 Large-eddy simulation of a turbulent piloted methane/air diffusion flame (Sandia flame D). *Phys. Fluids* **12** (10), 2541–2554.
- WENZEL, H. 2000 Direkte numerische Simulation der Ausbreitung einer Flammenfront in einem homogenen Turbulenzfeld. PhD thesis, RWTH Aachen.
- WILLIAMS, F. A. 1985 Turbulent combustion. In *The Mathematics of Combustion* (ed. J. D. Buckmaster), pp. 197–1318. Society for Industrial & Applied Mathematics.

A numerical scheme for the large-eddy simulation of turbulent combustion using a level-set method

By Laurent Duchamp de Lageneste AND Heinz Pitsch

1. Introduction

In premixed combustion, fuel and air are fully mixed before entering the combustion chamber. When a heat source is introduced (spark or pilot flame), combustion takes place in the form of a thin front propagating through the mixture. If turbulence levels are such that the reaction zone is still smaller than the Kolmogorov scale, the flame is in the flamelet regime (Peters 2000) and can be viewed as a thin interface separating two different states thus making it a suitable candidate for the use of a level-set approach.

The level-set methodology has been used in recent years to describe the dynamic evolution of fronts and discontinuities. Comprehensive overviews can be found in Sethian (1996) or Osher & Fedkiw (2002), including different possible numerical approaches and examples of applications to problems ranging from multiphase flows to image reconstruction.

The first application of this approach to the description of reacting flows is due to Williams (1985) who proposed an equation for the propagation of a flame front separating burnt from unburnt gases: the G -equation. This equation describes the evolution of a continuous field G of which a particular iso-level G_0 gives the location of the reaction front. This G_0 level is advected with the external velocity field \mathbf{U} , while propagating normally to itself with the laminar burning velocity s_L . The G -equation is then:

$$\frac{\partial G}{\partial t} + \mathbf{U} \cdot \nabla G = s_L |\nabla G|. \quad (1.1)$$

Once the position of the front is defined, one can write jump relations through the front to take gas expansion due to heat release into account, and compute all the thermochemical quantities simply from the position relative to the flame front.

Although this approach is simple and requires considerably less computational resources than solving the full system of conservation equations for the reacting species with detailed chemistry, the numerical treatment of (1.1) is generally not trivial. One difficulty arises in particular from the fact that (1.1) is strictly valid only at the particular iso-surface G_0 as can be seen by considering that the laminar burning velocity s_L can only be defined at G_0 . An immediate consequence is that away from the front, the values of G are arbitrary and that the ansatz chosen should not affect the results. Theoretical considerations concerning the derivation of proper averaging procedures which respect the particular symmetries of the G -equation are discussed in Oberlack *et al.* (2001).

A common practice is to define the G field as the signed distance to the flame front (Sethian 1996). Since (1.1) will not in general conserve G as a distance as the calculation progresses, a specific procedure has to be implemented to re-assign the value of the signed distance function to points away from the front after each time step.

The numerical methods to solve the level-set equation can therefore be divided in two major steps:

- time-advance the level-set equation,
- reinitialize G to a distance function.

Because of the necessary use of upwind differencing at each stage, level-set methods have a tendency to lose surface in under-resolved regions of the flow. For applications in the RANS context (Peters 2000; Herrmann 2000) the consequences of this drawback can be expected to be small because of the relative smoothness of the mean flame front. However, the impact of these inaccuracies will grow in LES applications, where the effect of small-scale wrinkling must be retained. Attempts to improve surface conservation have led to various techniques; see Sethian (1996), Sussman & Fatemi (1999), Russo & Smereka (2000) or Peng *et al.* (1999). We will show that it is necessary to take these improvements into account if one is considering applying the level-set methodology to the LES of turbulent premixed combustion.

In this paper, we will first present the numerical methods used to advance the level-set equation in the context of LES of turbulent premixed combustion. We will then focus on some of the potential problems associated particularly with the reinitialization procedure. A detailed description of this procedure will be given, as well as some of the necessary modifications of the base algorithm that have been introduced in order to improve surface conservation properties. Finally, an example of application of the resulting method to the simulation of a laminar Bunsen flame will be presented.

2. Numerical treatment of the level-set approach for premixed combustion

In the laminar case, the G -equation flamelet model proposed by Williams (1985) yields the following equation describing the propagation of an instantaneous flame surface:

$$\frac{\partial G}{\partial t} + \mathbf{U} \cdot \nabla G = s_L |\nabla G|, \quad (2.1)$$

where \mathbf{U} is the convection velocity, and s_L is the laminar burning velocity. If curvature effects are taken into account, an additional curvature correction term appears on the right-hand side of (2.1) as described by Pelce & Clavin (1982) and Matalon & Matkowsky (1982):

$$\frac{\partial G}{\partial t} + \mathbf{U} \cdot \nabla G = s_L |\nabla G| - D_M \kappa |\nabla G|, \quad (2.2)$$

where D_M is the Markstein diffusivity and κ the curvature.

In the LES framework, Pitsch & Duchamp de Lageneste (2002) derived the following equation for the motion of the filtered G_0 level:

$$\bar{\rho} \frac{\partial G}{\partial t} + \bar{\rho} \tilde{\mathbf{U}} \cdot \nabla G = \frac{\rho_u}{\bar{\rho}} (s_T |\nabla G| - D_t \kappa |\nabla G|), \quad (2.3)$$

where $\tilde{\mathbf{U}}$ is the filtered convective velocity, s_T is the modeled turbulent burning velocity and κ is the curvature of the filtered front. Here, a model for the conditionally filtered velocity derived by Pitsch in a companion article in the present volume has been introduced. In this form, (2.3) is a Hamilton-Jacobi equation with an additional parabolic curvature term.

While solutions of this equation for a given initial condition are generally not unique, Crandall & Lions (1983) showed that a unique viscosity solution can be obtained through the use of the appropriate monotone scheme. As strictly-monotone schemes are limited to first-order accuracy and are therefore too dissipative, Osher & Sethian (1988) have introduced a class of high-order upwind schemes for the Hamilton-Jacobi equation based

on the ENO polynomial reconstruction procedure previously developed by Harten *et al.* (1987) and extended by Shu & Osher (1989) in the context of conservation laws.

Here, additional difficulties can arise from local mesh refinement and the use of cylindrical coordinates. In particular, the explicit numerical treatment of the advective term would lead to unacceptably low timestep restrictions in refined regions and close to the centerline. Thus the use of an implicit scheme to treat at least parts of the advective terms is necessary.

Using mass conservation, the advective part can be rewritten in the more advantageous conservative form

$$\frac{\partial \bar{\rho}G}{\partial t} + \nabla \cdot (\bar{\rho}UG) = \rho_u s_T |\nabla G| - \bar{\rho} D_t \kappa |\nabla G|. \quad (2.4)$$

The appropriate part of the convective terms is then treated using a semi-implicit version of the QUICK scheme described by Akselvoll (1996) and Pierce & Moin (2001) to alleviate the CFL restriction.

The propagation term appearing on the right-hand side of (2.4) is then discretized using a third-order-accurate version of the ENO scheme described by Shu & Osher (1989).

The remaining parabolic curvature term is treated accordingly, using central differences.

We will now describe the discretization of the propagation and curvature terms in more detail. The reader is referred to Akselvoll (1996) and Pierce & Moin (2001) for a thorough description of the semi-implicit scheme used to discretize the convective terms.

2.1. Discretization of the propagation term

Various schemes have been derived for the numerical treatment of the propagation term appearing in (2.4). The two most popular variants are the Engquist-Osher entropy-satisfying scheme and the Godunov scheme.

Our objective is to discretize the term $s_T \cdot |\nabla G|$ appearing in (2.4), rewritten in the following form:

$$s_T \cdot |\nabla G| = \max(s_T, 0) \nabla^+ + \min(s_T, 0) \nabla^-. \quad (2.5)$$

The Engquist-Osher scheme to obtain ∇^+ and ∇^- would then read

$$\begin{aligned} \nabla^+ = & \left[\max(D_{-x}^{i,j,k}, 0)^2 + \min(D_{+x}^{i,j,k}, 0)^2 \right. \\ & + \max(D_{-y}^{i,j,k}, 0)^2 + \min(D_{+y}^{i,j,k}, 0)^2 \\ & \left. + \max(D_{-z}^{i,j,k}, 0)^2 + \min(D_{+z}^{i,j,k}, 0)^2 \right]^{1/2}, \end{aligned} \quad (2.6)$$

and

$$\begin{aligned} \nabla^- = & \left[\max(D_{+x}^{i,j,k}, 0)^2 + \min(D_{-x}^{i,j,k}, 0)^2 \right. \\ & + \max(D_{+y}^{i,j,k}, 0)^2 + \min(D_{-y}^{i,j,k}, 0)^2 \\ & \left. + \max(D_{+z}^{i,j,k}, 0)^2 + \min(D_{-z}^{i,j,k}, 0)^2 \right]^{1/2}, \end{aligned} \quad (2.7)$$

while the Godunov scheme is given by:

$$\begin{aligned} \nabla^+ = & \left[\max(\max(D_{-x}^{i,j,k}, 0)^2, \min(D_{+x}^{i,j,k}, 0)^2) \right. \\ & \left. + \max(\max(D_{-y}^{i,j,k}, 0)^2, \min(D_{+y}^{i,j,k}, 0)^2) \right]^{1/2} \end{aligned} \quad (2.8)$$

$$+ \max(\max(D_{-z}^{i,j,k}, 0)^2, \min(D_{+z}^{i,j,k}, 0)^2) \Big]^{1/2},$$

and

$$\begin{aligned} \nabla^- = & \left[\max(\max(D_{+x}^{i,j,k}, 0)^2, \min(D_{-x}^{i,j,k}, 0)^2) \right. \\ & + \max(\max(D_{+y}^{i,j,k}, 0)^2, \min(D_{-y}^{i,j,k}, 0)^2) \\ & \left. + \max(\max(D_{+z}^{i,j,k}, 0)^2, \min(D_{-z}^{i,j,k}, 0)^2) \right]^{1/2}, \end{aligned} \quad (2.9)$$

where $D_{\pm x, \pm y, \pm z}^{i,j,k}$ are third-order ENO approximations to the gradient of G in each direction.

Although both methods should give equivalent results, the Godunov scheme is generally considered to be slightly less dissipative near sonic points than the Engquist-Osher scheme, and will be used to discretize the propagation term.

2.2. Discretization of the curvature term

The curvature term, being parabolic in nature, is accordingly discretized using second-order central differencing (Sethian 1996).

Introducing the mean curvature as

$$\kappa_M = \nabla \cdot \mathbf{N}_G = -\nabla \cdot \frac{\nabla G}{|\nabla G|}, \quad (2.10)$$

where $\mathbf{N}_G = -\nabla G / |\nabla G|$ is the normal to each iso-level of G , the term $D_t \kappa |\nabla G|$ in (2.3) is discretized as

$$D_t \kappa |\nabla G| = D_t \kappa_M^{i,j,k} [(D_{cx}^{i,j,k})^2 + (D_{cy}^{i,j,k})^2 + (D_{cz}^{i,j,k})^2]^{1/2}, \quad (2.11)$$

where $\kappa_M^{i,j,k}$ is a central-difference approximation of the expression given in (2.10) and $D_{cx, cy, cz}^{i,j,k}$ is the second-order central-difference approximation of the components of the gradient of G in each direction.

3. Reinitialization

In problems such as turbulent combustion, it is impossible to maintain the level-set function as a signed distance from the moving G_0 surface because of the turbulent nature of the advective flow field. Flat or steep regions develop as the interface moves, rendering computation at these places inaccurate. It is therefore necessary to introduce a procedure that will reset the G -field to the signed distance from G_0 in a pre-defined neighborhood of G_0 . Such a procedure is called reinitialization and several variants have been proposed by Sethian (1996), Sussman & Fatemi (1999), Russo & Smereka (2000) and Peng *et al.* (1999).

In LES, where the effects of small-scale motion on the front must be retained, special attention must be paid to using a procedure that preserves the position of the G_0 -surface accurately.

3.1. General procedure

In order to reset the G field to the signed distance from the G_0 surface, the following equation has to be solved to a steady state:

$$\phi_0 = G(x, 0) \quad (3.1)$$

$$\frac{\partial \phi}{\partial t} = S(\phi_0)(1 - |\nabla \phi|), \quad (3.2)$$

where $S(\phi_0)$ is a smoothed sign function defined by

$$S(q) = \frac{q}{\sqrt{q^2 + \Delta x^2}}. \quad (3.3)$$

It is possible to rewrite (3.2) as an advection equation,

$$\frac{\partial \phi}{\partial t} + \mathbf{w} \cdot \nabla \phi = S(\phi_0) \quad (3.4)$$

$$\mathbf{w} = S(\phi_0) \frac{\nabla \phi}{|\nabla \phi|}. \quad (3.5)$$

A suitable numerical scheme can then be derived from those developed for solving the advection equation.

We use a third-order ENO scheme presented in Shu & Osher (1989) or Sussman & Fatemi (1999) for the spatial derivatives, while time advancement is done using the corresponding third-order optimal Runge-Kutta scheme.

One then obtains the following Godunov scheme for the reinitialization (expressed for a first-order time discretization, for simplicity):

$$\phi_0 = G(x, 0) \quad (3.6)$$

$$\phi^{n+1} = \phi^n + dt [max(S(\phi_0), 0)\nabla^+ + min(S(\phi_0), 0)\nabla^-], \quad (3.7)$$

with

$$\begin{aligned} \nabla^+ = 1 - & [max(max(D_{-x}^{i,j,k}, 0)^2, min(D_{+x}^{i,j,k}, 0)^2) \\ & + max(max(D_{-y}^{i,j,k}, 0)^2, min(D_{+y}^{i,j,k}, 0)^2) \\ & + max(max(D_{-z}^{i,j,k}, 0)^2, min(D_{+z}^{i,j,k}, 0)^2)]^{1/2}, \end{aligned} \quad (3.8)$$

and

$$\begin{aligned} \nabla^- = 1 - & [max(max(D_{+x}^{i,j,k}, 0)^2, min(D_{-x}^{i,j,k}, 0)^2) \\ & + max(max(D_{+y}^{i,j,k}, 0)^2, min(D_{-y}^{i,j,k}, 0)^2) \\ & + max(max(D_{+z}^{i,j,k}, 0)^2, min(D_{-z}^{i,j,k}, 0)^2)]^{1/2}, \end{aligned} \quad (3.9)$$

where $D_{\pm x, \pm y, \pm z}^{i,j,k}$ are third-order ENO approximations of the components of the gradient of ϕ in each direction.

Once a stationary solution is obtained for ϕ , G is simply replaced by ϕ .

3.2. Reinitialization in presence of high or low gradients

3.2.1. General procedure

When advected by a turbulent velocity field, regions of high or low gradient are likely to develop around the G_0 -surface. When the procedure outlined above is applied, Peng *et al.* (1999) have shown that large straying of the G_0 surface may occur, especially in high gradient regions, while convergence in regions of low gradients tends to be slow.

Peng *et al.* (1999) proposed a modification of this method, designed to avoid these drawbacks by taking the local value of the gradient into account in smoothing of the sign function.

In this variant, the sign function is now given by:

$$S(q) = \frac{q}{\sqrt{q^2 + |\nabla G|^2 \Delta x^2}}. \quad (3.10)$$

As noted by Osher & Fedkiw (2002), for this procedure to work well it is necessary to update $S(q)$ continuously as the calculation progresses.

An illustration of the improvements achieved using this formulation is given in the next section.

3.2.2. Validation: one time reinitialization of a distorted field

To assess the ability of this method to conserve the initial location of the G_0 level if regions of high or low gradient are present, we compare the results of the reinitialization of the ϕ_0 field (Russo & Smereka 2000),

$$\phi_0 = f(x, y) \left[\sqrt{\frac{x^2}{A^2} + \frac{y^2}{B^2}} - 1 \right], \quad (3.11)$$

to a signed distance function.

Here, $f(x, y) = \epsilon + (x - x_0)^2 + (y - y_0)^2$, with $A = 4$, $B = 2$, $\epsilon = 0.1$, $x_0 = 3.5$, and $y_0 = 2$. Hence, the $\phi_0 = 0$ surface is an ellipse and is surrounded by both high and low gradients (see figure 1).

The computational domain is $\Omega = [-5, 5] \times [-5, 5]$ and a coarse, 50×50 , grid is used.

Results of the reinitialization using the sign function defined in (3.3) are presented in figure 1. Reinitialization across the $\phi_0 = 0$ surface results in undesired perturbations that can be considerable in regions of larger gradients.

In figure 2, results using the sign function defined by (3.10) show that straying of the $\phi_0 = 0$ surface is avoided in the high-gradient zone.

Another positive side-effect of this modification can be observed in low-gradient regions where the modification of the sign function leads to faster convergence of the procedure. This is particularly apparent in the comparison of the results obtained in the upper-right corner region after ten iterations with both methods.

3.3. Enforcing volume conservation

The procedure outlined above is a third-order space- and time-accurate method to achieve reinitialization of the G -field. However, as pointed out by Sussman & Fatemi (1999), because of its upwind nature, its direct application may lead to unwanted dissipation of the G_0 -surface. Furthermore, the reinitialization error is likely to accumulate as the number of time steps grows.

This effect can be expected to be even more pronounced when G exhibits regions of locally-large curvature like small wrinkles of the flame surface.

Sussman & Fatemi (1999) proposed a constraint that prevents straying of the G_0 surface, and has the additional advantage that the error introduced is independent of the number of time steps required to reinitialize the G -field.

Noting that the volume enclosed in the G_0 surface can be evaluated by

$$V = \int S(G) dx, \quad (3.12)$$

where $S(G)$ is the smoothed approximation of the sign function appearing in (3.2), volume

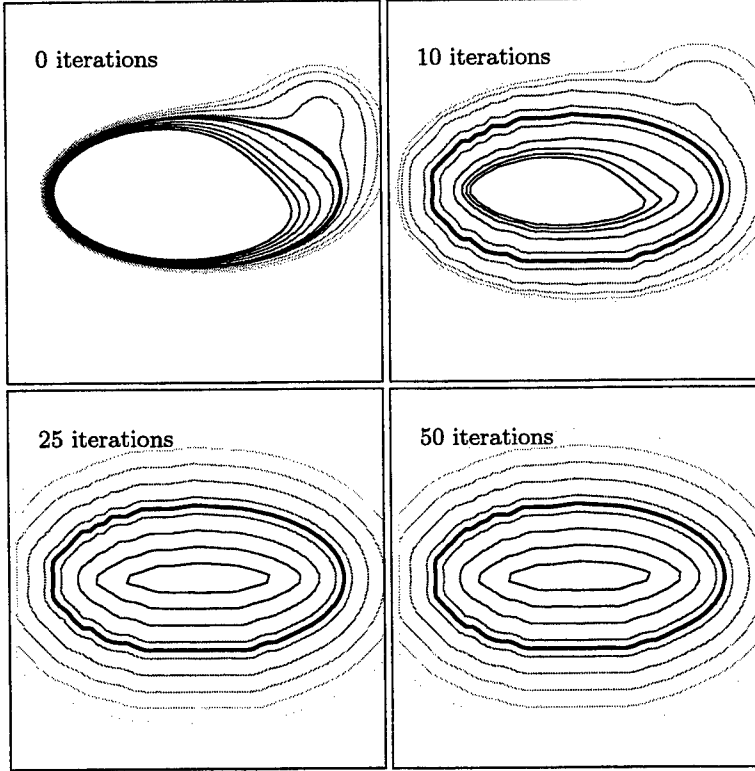


FIGURE 1. One time reinitialization with sign function defined by (3.3) on a 50×50 grid. From left to right and top to bottom, reinitialized field after 0, 10, 25 and 50 iterations. The $G_0 = 0$ level is displayed as a bold line.

conservation is enforced by requiring that

$$\partial_t \int S(G) d\mathbf{x} = 0. \quad (3.13)$$

By introducing the operator $L(\phi_0, \phi) = S(\phi_0)(1 - |\nabla \phi|)$, the reinitialization procedure becomes

$$\frac{\partial \phi}{\partial t} = L(\phi_0, \phi) + \lambda f(\phi), \quad (3.14)$$

where λ is obtained by requiring that

$$\partial_t \int S(G) = \int S'(\phi) \frac{\partial \phi}{\partial t} = \int S'(\phi) (L(\phi_0, \phi) + \lambda f(\phi)) = 0. \quad (3.15)$$

Taking $f(\phi) = S'(\phi)|\nabla \phi|$ leads to

$$\lambda = \frac{- \int S'(\phi) L(\phi_0, \phi)}{\int S'(\phi)^2 |\nabla \phi|}, \quad (3.16)$$

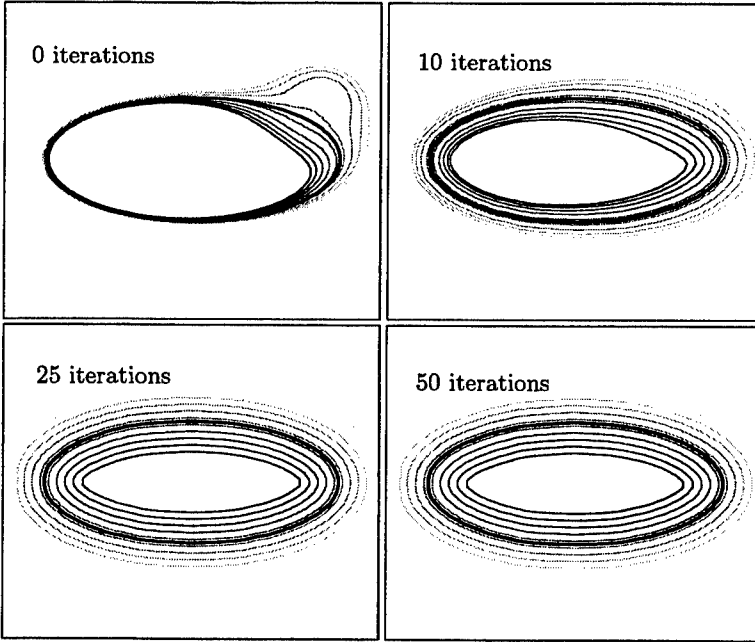


FIGURE 2. One time reinitialization with sign function defined by (3.10) on a 50×50 grid. From left to right and top to bottom, reinitialized field after 0, 10, 25 and 50 iterations. The $G_0 = 0$ level is displayed as a bold line.

with

$$S'(q) = \frac{\Delta x^2}{[q^2 + \Delta x^2]^{\frac{3}{2}}}. \quad (3.17)$$

This leads to the new procedure:

(a) Solve $\tilde{\phi}_{n+1} = \phi_n + dt L(\phi_0, \phi)$ using the same third-order ENO scheme described in section 3.1.

(b) Solve $\phi_{n+1} = \tilde{\phi}_{n+1} + dt \lambda S'(\phi_0) |\nabla \phi_0|$ to get the constrained solution of the reinitialization sub-step where the terms $S'(\phi)$, $L(\phi_0, \phi)$ and $f(\phi)$ appearing in (3.14) and (3.16) are discretized as $S'(\phi_0)$, $\frac{\tilde{\phi}_{n+1} - \phi_0}{dt}$, and $S'(\phi_0) |\nabla \phi_0|$ respectively.

When a Runge-Kutta fractional step method is used for the time discretization, the constraint is enforced only once at the end of each time step. All the integrals are evaluated using a third-order Simpson's rule on a nine-point stencil.

An illustration of the improvements obtained using this constraint is provided in the next section.

3.3.1. Zalesak's problem

Zalesak's problem involves the rotation of a notched circle and constitutes a good test of how well the reinitialization handles regions of high curvature.

The domain is a square of 100×100 , where a notched circle is centered at $(25, 0)$. The

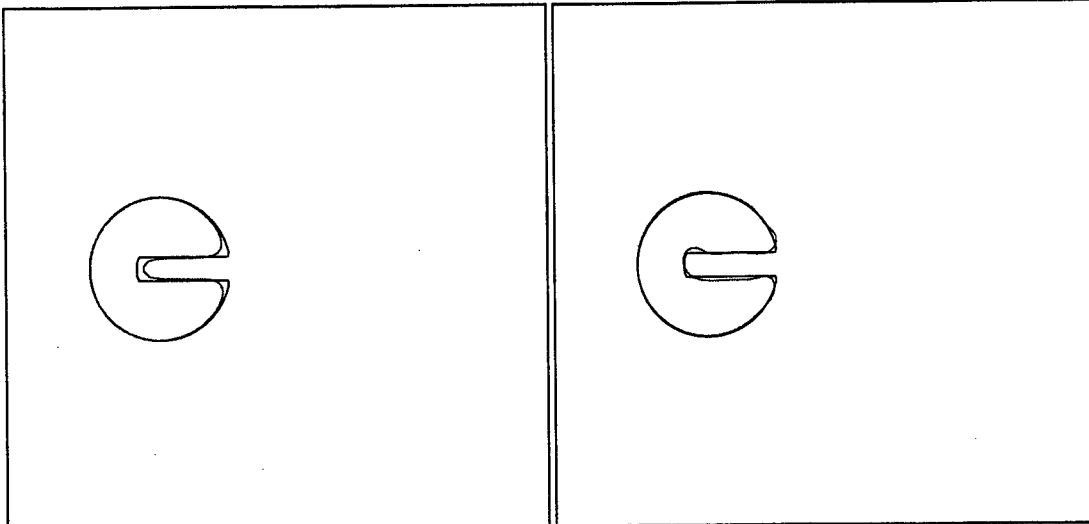


FIGURE 3. Zalesak's problem after one full revolution on a 100×100 grid, reinitialization alone (left) and reinitialization with volume-preservation constraint (right).

velocity field is constant in time and is defined as

$$U = \frac{(50 - y)\pi}{314},$$

$$V = \frac{(x - 50)\pi}{314}.$$

The results after one full revolution around the center of rotation are shown in figure 3. On the left side is the result obtained using reinitialization without the constraint, and on the right is the result of the computation using the constraint. Both results are compared to the analytical solution. While results of both methods are very good for the circular region of the object, important differences are found in the rectangular region where the method without constraint is shown to round off the sharp corners, leading to a surface loss of nearly 10%.

Using the constraint, sharp corners are better preserved and surface loss is only about 2%.

4. Validation: numerical simulation of a laminar Bunsen flame (Echekki & Mungal 1990)

As a first validation of the numerical scheme we use in the case of reacting flows, we present results obtained from the numerical simulation of a laminar Bunsen flame in this section.

This configuration has been studied experimentally by Echekki & Mungal (1990) and consists of a rectangular 2-D slot burner with an exit section width of $H = 6.8$ mm. The exit velocity is $U_0 = 1.5$ m/s and the fuel is a stoichiometric mixture of methane and air.

The 2-D numerical simulation domain is $6H$ long and $6H$ wide. The inlet profile is set to be a top-hat profile and a boundary layer is allowed to develop for $1H$ before the flow exits the burner.

Figure 4 shows a comparison of the position of the flame front observed in the experiment with the results of the simulation, together with a visualization of the streamlines.

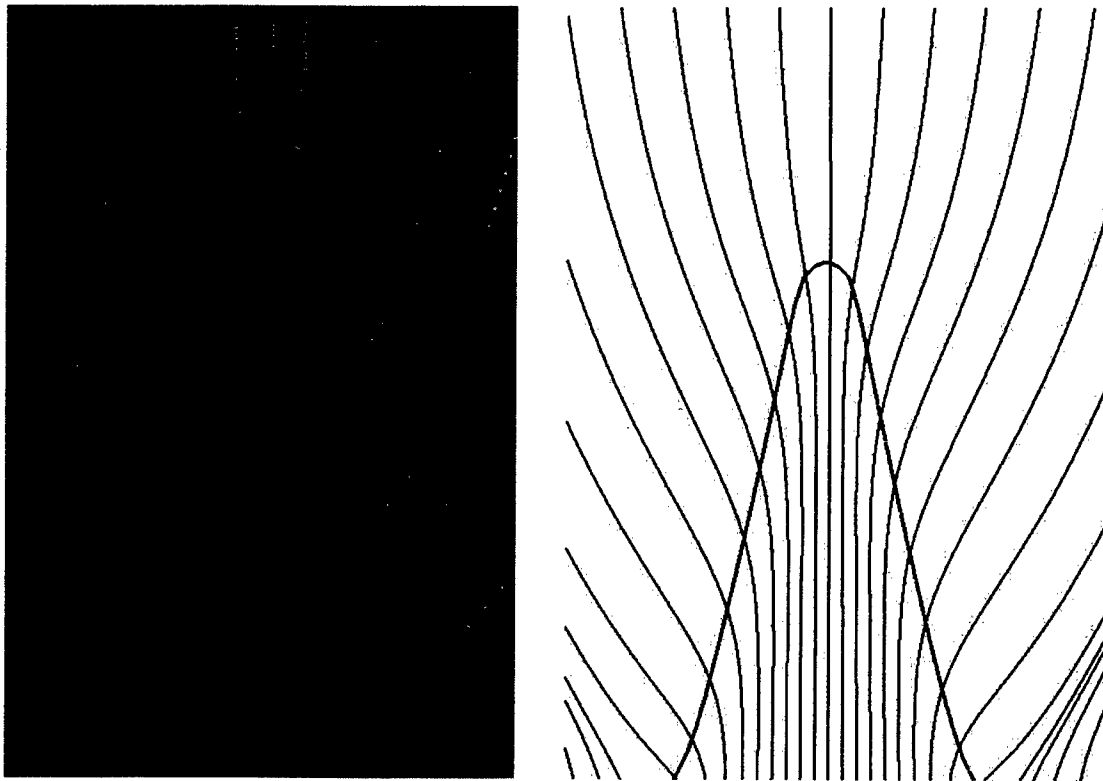


FIGURE 4. Laminar Bunsen flame: flame position and streamlines. Experiment (left) and simulation (right).

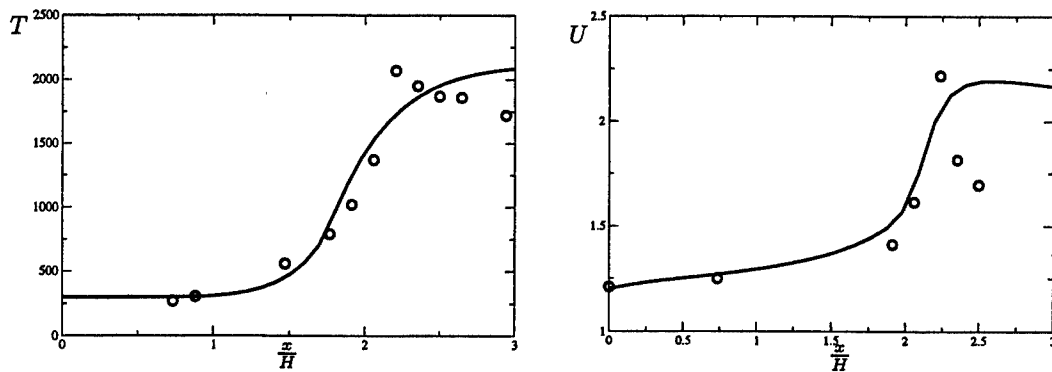


FIGURE 5. Laminar Bunsen flame: Temperature (left) and velocity (right). Experimental results (symbols) and numerical simulation (solid lines).

Good agreement is obtained for the flame length as well as for the curvature at the tip of the flame, showing that the increase in flame speed due to curvature is well reproduced by the simulation. A similar divergence of the streamlines in the burned region of the flame can be observed, showing that the simulation also predicts the effect of heat release on the flow field correctly.

Figure 5 shows the evolution of temperature (left) and axial velocity (right) along

the axis of symmetry of the flame. The temperature rise along the axis as well as the simultaneous velocity increase are well predicted by the simulation until the tip is reached. Behind the flame tip however, the temperature in the experimental data drops slowly due to radiation, which is neglected in our simulation. The simulation therefore predicts nearly-constant temperature behind the tip.

As a consequence, the fast deceleration of the gas downstream of the tip is also underestimated in the simulation.

5. Conclusion

In this report, we have presented numerical methods to solve the level-set equation for premixed combustion in LES. In particular, we have described the third-order ENO scheme used to discretize the normal propagation term as well as the numerical schemes used for the remaining terms.

We have then stressed that the reinitialization procedure used to keep G as a distance function is a key factor in the development of an accurate level-set model for LES of turbulent premixed combustion. The overall method, including its discretization by an higher-order ENO scheme has been introduced. Examples of potential problems generated by the application of this algorithm to the case of turbulent combustion have been given. Consequently, a first modification of the procedure has been introduced to avoid undesired straying of the interface due to the creation of regions of low or high gradients due to the turbulence. An additional constraint has been implemented in order to enforce volume conservation around the flame surface.

A first validation of the resulting scheme has finally been presented for the case of a laminar Bunsen flame, showing reasonable agreement with experimental data.

Further applications of this method in LES of turbulent premixed flames are reported in a companion paper in this volume.

Acknowledgments

The authors gratefully acknowledge funding by the US Department of Energy within the ASCI program and by SNECMA Moteurs.

REFERENCES

- AKSELVOLL, K. 1996 An efficient method for temporal integration of the navier-stokes equations in confined axisymmetric geometrie. *J. Comp. Phys.* **125**, 454–463.
- CRANDALL, M. G. & LIONS, P. L. 1983 Viscosity solutions of Hamilton-Jacobi equations. *Trans. Amer. Math. Soc.* **277**, 1–42.
- ECHEKKI, T. & MUNGAL, M. G. 1990 Flame speed measurements at the tip of a slot burner: effects of flame curvature and hydrodynamic stretch. In *23rd Symposium on Combustion* (ed. T. C. Institute), pp. 455–461.
- HARTEN, A., ENGQUIST, B., OSHER, S. & CHAKRAVARTHY, S. 1987 Uniformly high order accurate essentially non-oscillatory schemes III. *J. Comp. Phys.* **71**, 231–303.
- HERRMANN, M. 2000 Numerische simulation vorgemischter und teilweise vorgemischter turbulenten flamen. PhD thesis, RWTH, Aachen.
- MATALON, M. & MATKOWSKY, B. J. 1982 Flames as gasdynamic discontinuities. *J. Fluid Mech.* **124**, 239–259.

- OBERLACK, M., WENZEL, H. & PETERS, N. 2001 On symmetries and averaging of the G -equation for premixed combustion. *Comb. Theo. and Model.* **5**, 1–20.
- OSHER, S. & FEDKIW, R. 2002 *Level set methods and dynamic implicit surfaces*, *Applied Mathematical Sciences*, vol. 153. Springer, Berlin.
- OSHER, S. & SETHIAN, J. 1988 Fronts propagating with curvature dependant speed: algorithms based on Hamilton-Jacobi formulations. *J. Comp. Phys.* **79**, 12–49.
- PELCE, P. & CLAVIN, P. 1982 Influence of hydrodynamic and diffusion upon the stability limits of laminar premixed flames. *J. Fluid Mech.* **124**, 219–237.
- PENG, D., MERRIMAN, B., OSHER, S., ZHAO, H. & KANG, M. 1999 A PDE-based fast local level set method. *J. Comp. Phys.* **155**, 410–438.
- PETERS, N. 2000 *Turbulent Combustion*. Cambridge University Pres.
- PIERCE, C. D. & MOIN, P. 2001 Progress-variable approach for large eddy simulation of turbulent combustion. *Tech. Rep. TF-80*. Dept. Mech. Eng., Stanford University.
- PITSCH, H. & DUCHAMP DE LAGENESTE, L. 2002 Large-eddy simulation of premixed turbulent combustion using a level-set approach. In *Proceedings of the 29th Symposium on Combustion*. The Combustion Institute: accepted for publication.
- RUSSO, G. & SMEREKA, P. 2000 A remark on computing distance functions. *J. Comp. Phys.* **163**, 51–67.
- SETHIAN, J. A. 1996 *Level Set Methods : Evolving Interfaces in Geometry, Fluid Mechanics, Computer Vision and Material Science*. Cambridge University Press.
- SHU, C. W. & OSHER, S. 1989 Efficient implementation of essentially non-oscillatory shock capturing schemes, II. *J. Comp. Phys.* **83**, 32–78.
- SUSSMAN, M. & FATEMI, E. 1999 An efficient, interface-preserving level set re-distancing algorithm and its application to interfacial incompressible fluid flow. *SIAM Journ. Sci. Comp.* **20**, 1165–1191.
- WILLIAMS, F. A. 1985 Turbulent combustion. In *The Mathematics of Combustion* (Frontiers in Applied Mathematics, vol. 2, J. Buckmaster, ed.) SIAM, Philadelphia, pp. 97–131.

On the Role of Quasi-one-dimensional Dissipation Layers in Turbulent Scalar Mixing

By N. Peters † AND P. Trouillet

1. Motivation and background

Ever since Carl Gibson (1968) analyzed the fine scale structure of scalar mixing in terms of zero gradient points there has remained the question how these findings can be related to mixing models. Existing turbulent mixing models ignore the existence of minimal points. They are intuitively based on the picture that turbulent mixing is controlled by two processes: Stirring of the scalar field by turbulence and subsequent molecular diffusion. The general idea is that at sufficiently intense turbulence, stirring is the rate determining process and that molecular diffusion just completes the sequence. This follows from the hypothesis of a cascade process for scalar mixing, which suggests the use of the flow time to model scalar dissipation. This hypothesis is supported by experimental and DNS data, but since it recurs essentially to dimensional scaling only, it leaves open the question about the precise mechanism by which the interaction between turbulent stirring and molecular diffusion takes place.

There are a number of unresolved questions in scalar mixing. In pdf methods based on one-point statistics, for instance, the modeling of molecular mixing represents a challenging problem. The challenge lies in the existence of an exact form for the pdf equation of the conserved scalar which, however, is not well posed. For the special case of homogeneous turbulence this pdf equation reads (cf. O'Brien, 1980)

$$\frac{\partial P_Z}{\partial t} = -\frac{1}{2} \frac{\partial^2}{\partial Z^2} (\chi_Z P_Z) . \quad (1.1)$$

Here Z is the mixture fraction which stands for a conserved scalar that is normalized such that it varies between $0 \leq Z \leq 1$, P_Z is its probability density function and χ_Z is the conditional scalar dissipation rate defined as

$$\chi_Z = 2D \langle (\nabla Z')^2 | Z \rangle , \quad (1.2)$$

where D is the diffusion coefficient and Z' is the mixture fraction fluctuation. In most situations in turbulent mixing the definition (1.2) can be replaced by

$$\chi_Z = 2D \langle (\nabla Z)^2 | Z \rangle , \quad (1.3)$$

because the square of the mean gradient $(\nabla \bar{Z})^2$ is small compared to that of the fluctuating mixture fraction $(\nabla Z')^2$. Since χ_Z represents the gradient and therefore requires two-point information, it must be modelled. As pointed out by Pope (2000), the assumption of a constant conditional scalar dissipation rate equal to its mean unconditional value in (1.1) leads to an anti-diffusion equation, which is not well-posed, because it is non-realizable for arbitrary initial conditions. In most pdf methods the anti-diffusion term is therefore replaced by intuitively derived mixing models that do not make use of

† Institut für Technische Mechanik - Aachen, Germany (n.peters@itm.rwth-aachen.de)

the exact formulation. From a fundamental point of view this is certainly unsatisfactory. Hence, the following questions may be posed: Is there an exact formulation for the molecular mixing process in a mathematically realizable form? If there is such a form, would this allow to model the process of stirring by the turbulent flow field and the subsequent molecular mixing process in a straight forward way? We will answer the first question in the affirmative and will outline aspects of the modeling below.

In the following, we will first derive an equation for the functional form of the scalar dissipation rate valid in a local region between a minimum and a maximum point in mixture fraction space. This equation exhibits analytical unsteady and quasi-steady state solutions which correspond in physical space to local convective-diffusive structures in which unsteady diffusion is enhanced by compressive strain (cf. Ashurst et al., 1987). We will call these structures quasi-one-dimensional dissipation layers (Q1DL). The distribution function of the mixture fraction within these layers is analytically related to the local scalar dissipation rate. In search of these Q1DLs we will then analyze the scalar DNS data of a time-evolving turbulent mixing layer by Rogers and Moser (1994) by generating trajectories between minimum and maximum points. Choosing a particular quasi-steady solution (the one that corresponds to a sine function in physical space) we will then reconstruct the probability density function of the mixture fraction P_Z and the conditional scalar dissipation rate χ_Z using the joint pdf of minimum and maximum mixture fraction values of trajectories. Finally, we will derive an exact form for the joint distribution function of minimum and maximum mixture fractions, expressed in terms of their algebraic mean and their difference.

2. Theory

We consider a small local fluid element with initial size of the order of πL_0 centered around its midpoint $O(x_0, t)$ which is convected by the velocity $\mathbf{v}(x_0, t)$ within a constant density turbulent flow field. We also introduce a local cartesian coordinate system, unit vectors $\mathbf{i}, \mathbf{j}, \mathbf{k}$, aligned with the principal axis of strain ($\partial u / \partial x, \partial v / \partial y, \partial w / \partial z$) and a relative coordinate at $O(x_0, t)$ to the fluid element as $(x, y, z) = \mathbf{x} - \mathbf{x}_0$. The velocity field within the small fluid element can be expanded as

$$\mathbf{v}(\mathbf{x}, t) = \mathbf{v}(\mathbf{x}_0, t) + \mathbf{i} \frac{\partial u}{\partial x} x + \mathbf{j} \frac{\partial v}{\partial y} y + \mathbf{k} \frac{\partial w}{\partial z} z. \quad (2.1)$$

We denote the most compressive rate of strain as $a = -\partial v / \partial y$ and assume that the scalar gradient is locally aligned with the most compressive rate of strain. This assumption is based on the DNS analysis by Ashurst et al. (1987) who found that "there is an increased probability for the scalar gradient to align with the most compressive strain direction and that the average gradient is larger when pointing into that direction". Therefore we will conduct a one-dimensional analysis based on the scalar equation

$$\frac{\partial Z}{\partial t} - a y \frac{\partial Z}{\partial y} = D \frac{\partial^2 Z}{\partial y^2}, \quad (2.2)$$

where D is assumed constant.

By differentiating (2.2) with respect to y and multiplying it with $2 \partial Z / \partial y$ an equation for the square of the mixture fraction gradient can be derived

$$\frac{\partial}{\partial t} \left(\frac{\partial Z}{\partial y} \right)^2 - a y \frac{\partial}{\partial y} \left(\frac{\partial Z}{\partial y} \right)^2 - 2 a \left(\frac{\partial Z}{\partial y} \right)^2 = 2 \frac{\partial Z}{\partial y} \frac{\partial}{\partial y} \left(D \frac{\partial^2 Z}{\partial y^2} \right). \quad (2.3)$$

Using the one-dimensional form of the scalar dissipation rate as

$$\chi_L = 2D(\partial Z/\partial y)^2, \quad (2.4)$$

and multiplying (2.3) with $2D$ we obtain an equation for χ_L

$$\frac{\partial \chi_L}{\partial t} - a y \frac{\partial \chi_L}{\partial y} - 2a \chi_L = D \frac{\partial^2 \chi_L}{\partial y^2} - \frac{1}{4} \left(\frac{\partial \chi_L}{\partial Z} \right)^2. \quad (2.5)$$

Here the identity

$$\frac{\partial^2 Z}{\partial y^2} = \frac{1}{2} \frac{\partial}{\partial Z} \left(\frac{\partial Z}{\partial y} \right)^2 \quad (2.6)$$

has been used. We call χ_L the local dissipation rate within the quasi-one-dimensional dissipation layer.

In general a Q1DL lies between minimum and maximum values of the mixture fraction that differs from 0 and 1, respectively

$$0 \leq Z_{min}(t) \leq Z \leq Z_{max}(t) \leq 1. \quad (2.7)$$

Therefore we introduce the normalized coordinate

$$Z^* = \frac{Z - Z_{min}}{\Delta Z}, \quad (2.8)$$

where

$$\Delta Z = Z_{max} - Z_{min}. \quad (2.9)$$

We now introduce a flamelet-type transformation (cf. Peters, 2000) by replacing y by Z^* as independent variable and by setting the new time variable $\tau = t$. Using the transformation rules

$$\frac{\partial}{\partial t} = \frac{\partial Z^*}{\partial t} \frac{\partial}{\partial Z^*} + \frac{\partial}{\partial \tau}, \quad (2.10)$$

$$\frac{\partial}{\partial y} = \frac{\partial Z^*}{\partial y} \frac{\partial}{\partial Z^*} \quad (2.11)$$

on (2.5) we obtain

$$(\Delta Z)^2 \frac{\partial \chi_L}{\partial \tau} = \frac{\chi_L}{2} \frac{\partial^2 \chi_L}{\partial Z^{*2}} + 2a^* \chi_L - \frac{1}{4} \left(\frac{\partial \chi_L}{\partial Z^*} \right)^2 + [b^* - Z^*(c^* + b^*)] \frac{\partial \chi_L}{\partial Z^*}. \quad (2.12)$$

This equation has several interesting features: The first term on the r.h.s. is a transport term where χ_L itself is the diffusivity in Z^* -space. For $a > 0$ the second term may be interpreted as a productive term, while the third term resembles a dissipation term since it contains the square of derivatives. The last term, finally, results from the time dependence of Z_{min} and Z_{max} defined by the quantities b and c

$$b = \frac{1}{\Delta Z} \frac{\partial Z_{min}}{\partial t}, \quad c = -\frac{1}{\Delta Z} \frac{\partial Z_{max}}{\partial t}, \quad (2.13)$$

with the parameters

$$b^* = b(\Delta Z)^2, \quad c^* = c(\Delta Z)^2. \quad (2.14)$$

appearing in (2.12). Let us note here that the time evolution of ΔZ can be calculated from (2.13) by

$$\frac{d \Delta Z}{dt} = -(b + c) \Delta Z = -2\hat{b} \Delta Z \quad (2.15)$$

where $\hat{b} = (b + c)/2$. This shows that the parameter \hat{b} describes the rate at which minima and maxima mixture fraction points move closer towards each other. We will therefore call \hat{b} the mixing rate.

Analytical solutions of (2.12) can be readily derived. For $Z_{min} = 0$ and $Z_{max} = 1$, for instance, the steady-state solution is given by eq. (3.47) in Peters (2000). For the unsteady case with $a = 0$ a closed form solution is also derived. For $Z_{min} = 0$ but $Z_{max}(t) \neq 1$ some unsteady solutions have recently been presented by Villermaux (2002).

Since we are dealing with a one-dimensional structure the local distribution function of Z^* within the Q1DL, denoted by P_L , is analytically related to that of χ_L . This follows directly from the relation (cf. Papoulis, p. 95)

$$P_L(Z^*) = \frac{P(y)}{|\partial Z^*/\partial y|}, \quad (2.16)$$

where $P(y)$ is uniform. With the definition (2.4) and D being constant this leads to

$$\chi_L(Z^*)^{1/2} \cdot P_L(Z^*) = const. \quad (2.17)$$

For the local structure this relation can be used to derive from (2.12) an equation for $P_L(Z^*)$

$$(\Delta Z)^2 \frac{\partial P_L}{\partial t} = -\frac{1}{2} \frac{\partial^2 (\chi_L P_L)}{\partial Z^{*2}} + [b^* - Z^*(c^* + b^*)] \frac{\partial P_L}{\partial Z^*} - a^* P_L, \quad (2.18)$$

where τ has been set equal to t again. In (2.18) the first term on the r.h.s. is reminiscent of the anti-diffusion term in (1.1). This will be used in section 4 below.

We now ask the question if there is a particular solution of (2.12) which is most likely to occur in a turbulent mixing field. For that purpose we need to go back to the original scalar equation (2.2). It is well known that, starting from an arbitrary initial condition for $Z(y, t)$ at $t = 0$, higher order harmonics in the solution of a parabolic equation will die out very rapidly and the first harmonic representing a sine function will remain (cf. Kervokian, 1990, p.35, for example). For the reconstruction in section 4 we will therefore choose for $Z(y, t)$ the particular form of a sine function in the interval between Z_{min} and Z_{max} . Because of symmetry $b = c = \hat{b}$ and the origin are placed at the center of the one-dimensional layer at $Z = Z_m$ where Z_m is defined by

$$Z_m = \frac{Z_{max} + Z_{min}}{2}. \quad (2.19)$$

The zero gradient points Z_{min} and Z_{max} are placed at $y = -\pi L/2$ and $y = +\pi L/2$, respectively, where πL is the width of the layer. Since the velocity v at any position y is $-ay$ we obtain for the change of L

$$v(L) = \frac{dL}{dt} = -aL, \quad (2.20)$$

which may be integrated as

$$L(t) = L_0 e^{-\int_0^t a(t) dt}. \quad (2.21)$$

A Lagrangian form of (2.2) may be obtained by introducing the new coordinates

$$\eta = y/L(t), \quad \tau = t. \quad (2.22)$$

This leads with the transformation rules

$$\frac{\partial}{\partial y} = \frac{1}{L} \frac{\partial}{\partial \eta}, \quad \frac{\partial}{\partial t} = a\eta \frac{\partial}{\partial \eta} + \frac{\partial}{\partial \tau} \quad (2.23)$$

to

$$\frac{\partial Z}{\partial \tau} = \frac{D}{L^2(t)} \frac{\partial^2 Z}{\partial \eta^2}. \quad (2.24)$$

It is easily seen that the sine function solution

$$Z = Z_m + \frac{\Delta Z}{2} \sin \eta, \quad (2.25)$$

equivalent to

$$Z^* = \frac{1}{2} (1 + \sin \eta), \quad (2.26)$$

satisfies (2.24). Inserting (2.25) into (2.24) and using (2.19) it is seen that there exists the following relation between \hat{b} , L and D

$$2 \hat{b} = \frac{D}{L^2}. \quad (2.27)$$

This shows that the mixing rate \hat{b} increases as $L(t)$ decreases. This will occur if the time integral in the exponent of (2.21) is positive, i.e. if the strain is compressive on time average. This is generally the case under turbulent conditions. Therefore compressive strain increases the mixing rate \hat{b} and thereby enhances mixing.

The scalar dissipation rate is calculated from (2.25) as

$$\chi_L = 2 D \left(\frac{\partial Z}{\partial y} \right)^2 = \frac{D(\Delta Z)^2}{2 L^2} \cos^2 \eta = \hat{b}^* \cos^2 \eta, \quad (2.28)$$

where $\hat{b}^* = \hat{b}(\Delta Z)^2$. By replacing the cosine function by the sine function it is seen with (2.26) that χ_L can be expressed in terms of Z^* as

$$\chi_L = 4 \hat{b}^* Z^* (1 - Z^*), \quad (2.29)$$

This solution satisfies for $b = c$ the balance of the last two terms in (2.12). Inserting it into the remaining part of (2.12) leads with $\tau = t$ to

$$\frac{d \hat{b}^*}{dt} = \hat{b}^* (2a - 4 \hat{b}). \quad (2.30)$$

Combining (2.27), (2.20) and (2.19) shows that (2.30) is satisfied for any prescribed function $a(t)$.

χ_L can also be written as

$$\chi_L = 4 \hat{b}^* (Z - Z_{min})(Z_{max} - Z). \quad (2.31)$$

Since \hat{b} , Z_{min} and Z_{max} depend on time we call this a quasi-steady-state solution. Also, using (2.17) we can calculate the local distribution function of Z within the Q1DLs as

$$P_L(Z; Z_{min}, Z_{max}) = \frac{\pi^{-1}}{(Z - Z_{min})^{1/2}(Z_{max} - Z)^{1/2}}, \quad (2.32)$$

where normalization has led to the elimination of the parameter \hat{b}^* . In the following we will use (2.31) and (2.32) to reconstruct the pdf $P_Z(Z)$ and the conditional scalar dissipation rate χ_Z in the DNS data.

Box	<i>x</i>	<i>y</i>	<i>z</i>
1	[78, 90]	[-1.3, 1.3]	[3.2, 7.7]
2	[29, 41]	[-1.3, 1.3]	[3.2, 7.7]
3	[49, 61]	[-1.3, 1.3]	[7.7, 12.2]
4	[15, 26]	[-1.3, 1.3]	[7.7, 12.2]

TABLE 1. Location of the boxes used to extract the DNS fields. The global dimensions of the DNS domain are [0, 100], [-4, 4] and [0., 24.7] in the *x*, *y* and *z* directions respectively.

3. A-priori testing using DNS data

The testing will be based on instantaneous flow and scalar fields extracted from the DNS of a time-evolving mixing layer performed by Rogers and Moser (1994). This DNS was computed using a pseudo-spectral method to solve the 3D incompressible Navier-Stokes equations on a $512 \times 210 \times 192$ Fourier/Jacobi modes domain. A transport equation for a scalar with Schmidt number 1.0 was carried along in the simulation. After an initial development, the mixing layer becomes self-similar from $t = 87.5$ to $t = 150$ in non-dimensional units. During the simulation, the Reynolds number based on the vorticity thickness $Re_\omega = \Delta U \delta_\omega / \nu$ grows from 1370 to 10800.

Data from several times during this interval were used to test the theory. For each time, both velocity and scalar fields were extracted from four boxes centered around the midpoint $y = 0$ of the mixing layer. Table 1 gives a description of these subdomains. A conversion from Fourier space to physical space was performed. In physical space, the velocity and scalar fields were discretized on a regular structured grid with a resolution Δx which is of the order of the Kolmogorov scale.

The ensemble of the four boxes was then used to demonstrate the existence and relevance of the Q1DL structures presented in the theory above and to reconstruct both the pdf P_Z and the conditional scalar dissipation rate χ_Z . For brevity, we will only report data and analysis for one particular time, namely $t = 150$.

3.1. Evidence of one-dimensional dissipation layers

In Fig. 1 we show a portion of the scalar field $Z(\mathbf{x}, t)$ extracted from one of the boxes and in Fig. 2 the corresponding field of the instantaneous scalar dissipation rate $\chi(\mathbf{x}, t)$ defined by

$$\chi = 2 D (\nabla Z)^2. \quad (3.1)$$

Fig. 1 shows fairly large structures in the scalar field. At their edges these structures generate steep gradients and therefore thin layers with high values of the scalar dissipation rate as shown in Fig. 2. These layers have been observed both experimentally and in many DNS simulations and are the subject of the present analysis.

3.2. Trajectories

In order to analyze the local dependence of the local scalar dissipation rate on mixture fraction, thereby identifying Q1DL structures, we calculate, starting from at every grid point in the boxes listed in Table 1, the direction of the scalar gradient (∇Z). We follow

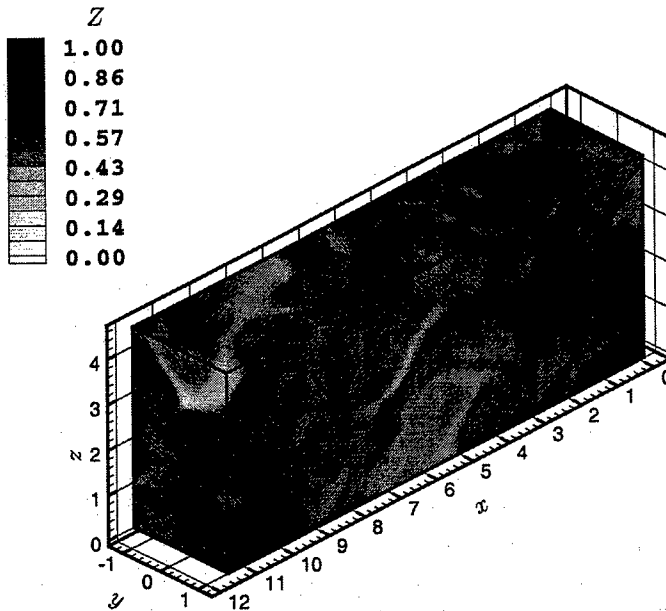


FIGURE 1. Mixture fraction field in a box extracted from the center of the mixing layer

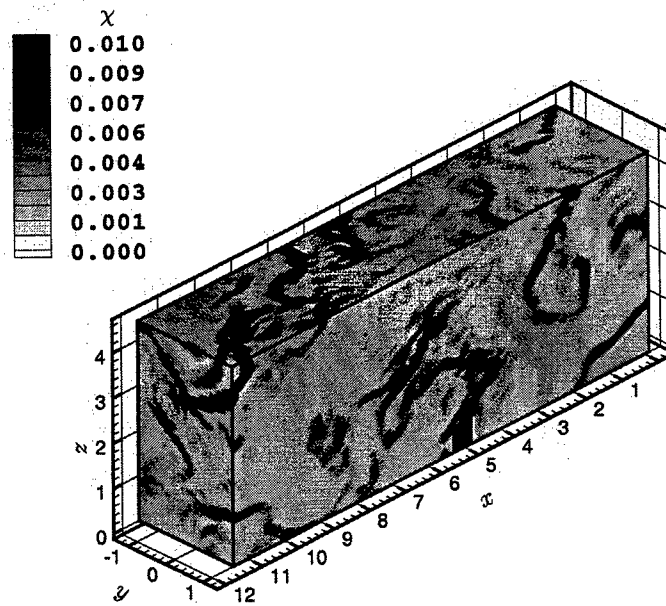


FIGURE 2. Instantaneous scalar dissipation rate field from the same box as Fig. 1

this direction using a large number of small spatial steps of the order of $1/10$ of the grid resolution Δx , recalculating the scalar gradient after each step. The scalar field between the grid points is computed by tri-linear interpolation. With this procedure we move in the direction of increasing as well as decreasing values of the mixture fraction until we find a maximum as well as a minimum point. These extremal points correspond to the location where a continuation of the trajectory in the direction calculated at the previous

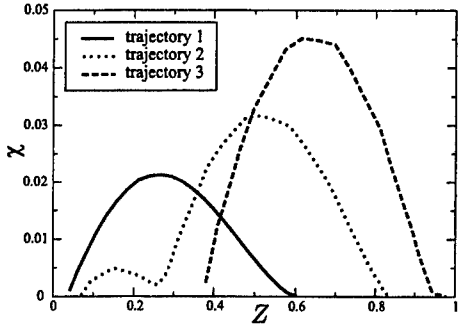


FIGURE 3. Scalar dissipation rate χ extracted along three representative trajectories

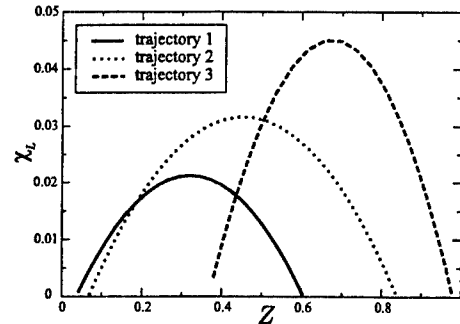


FIGURE 4. Reconstructed scalar dissipation rate χ_L along the same trajectories as Fig. 3

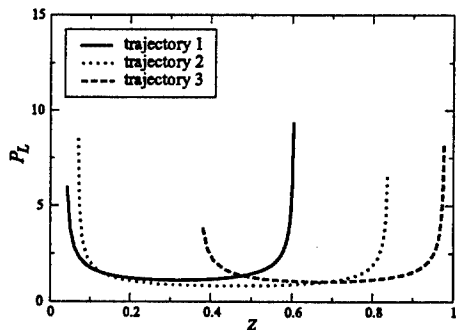


FIGURE 5. Reconstructed pdf $P_L(Z)$ along the three trajectories of Fig. 3

step would lead to a change in sign of the mixture fraction gradient. A further criterion for having reached a zero gradient point is that the scalar dissipation rate χ should be less than 0.0005. Trajectories which leave the box without ending at a minimum as well as a maximum point are not counted. Thereby we obtain from 21 million grid points within the four boxes 5 million trajectories. As a consequence of not counting trajectories that leave the box without reaching the two extremal points we will not capture the spike in the mixture fraction pdf at $Z = 0$ in figure 19 b for $\xi = 0$ in Rogers and Moser (1994).

For the trajectories that were completed within the box we obtain one minimum and one maximum point associated with the original starting point of the trajectory. It is important to note that we are not considering physical zero gradient points as such, but end points of trajectories. They are weighted by the number of starting points and their joint pdf reflects the trajectories rather than that of the zero gradient points themselves.

We calculate the scalar dissipation rate χ along the trajectory using the definition (3.1). The rates b and c defined by (2.13) are calculated by using the balance of the last two terms of (2.12) in the limit $\chi_L \rightarrow 0$. This leads to

$$b = \frac{1}{4 \Delta Z} \frac{\partial \chi}{\partial Z}, \quad c = \frac{1}{4 \Delta Z} \frac{\partial \chi}{\partial Z} \quad (3.2)$$

for $Z^* \rightarrow 0$ and $Z^* \rightarrow 1$, respectively.

In Fig. 3 we show three calculated scalar dissipation rate profiles along trajectories between different minima and maxima points Z_{min} and Z_{max} . With these values and the mixing rate \hat{b} calculated as the algebraic average of b and c we reconstruct in Fig. 4 the local scalar dissipation rate χ_L using (2.31). Using (2.32) we can also calculate the local distribution function P_L which we show in Fig. 5. It is seen that, with the exception of trajectory 2, the shapes of χ in Fig. 3 are close to the inverse parabolas χ_L in Fig. 4. We believe that trajectory 2 passes close to a saddle point in the 3-D mixture fraction field, with the intermediate minimum of χ occurring in the vicinity of that saddle point. Trajectories with intermediate minima of χ were found quite frequently in the numerical analysis of the DNS data. They could have been split into two or more trajectories to obtain a closer agreement with the theory, but we believe that this would have introduced some additional arbitrariness.

The shapes of the local pdf P_L shown in Fig. 5 are symmetric with respect to Z_m of that trajectory and show singularities at their corresponding values Z_{min} and Z_{max} . These singularities follow directly from $\chi_L = 0$ in (2.17) and indicate that the trajectories have long tails in physical space where the scalar gradients are small.

We will now use (2.32) to reconstruct the pdf P_Z of the mixture fraction using values from those points only from which complete trajectories have been started. For that purpose we calculate the joint pdf $Q(Z_{min}, Z_{max}, \hat{b})$ from the trajectories in the four boxes at time $t = 150$. The reconstructed pdf $P_{Z,r}$ is then obtained from

$$P_{Z,r} = \int_0^1 \int_0^1 P_L(Z; Z_{min}, Z_{max}) \int_0^\infty Q(Z_{min}, Z_{max}, \hat{b}) d\hat{b} dZ_{min} dZ_{max}. \quad (3.3)$$

The comparison is shown in Fig. 6. The agreement is remarkably good, indicating that the symmetric shape of P_L in (2.31) is sufficiently accurate to reconstruct the scalar pdf. Other symmetric shapes have also been used but the resulting pdf seems to be quite insensitive to that choice. It is remarkable that the reconstruction is successful even though the shape of the local pdf P_L is bimodal with singularities at Z_{min} and Z_{max} and P_Z has a bell-shaped form. The ability to reconstruct P_Z is a strong argument in favor of the predominance of Q1DLs in the mixing process.

In a similar way we reconstruct χ_Z by using (2.31) and the joint pdf $Q(Z_{min}, Z_{max}, \hat{b})$. The reconstructed conditional scalar dissipation rate $\chi_{Z,r}$ follows from

$$\chi_{Z,r} = \int_0^1 \int_0^1 \int_0^\infty \chi_L(Z; Z_{min}, Z_{max}, \hat{b}) Q(Z_{min}, Z_{max}, \hat{b}) dZ_{min} dZ_{max} d\hat{b}. \quad (3.4)$$

and is denoted as "reconstruction 1" in Fig. 7. The comparison is not as favorable as that in Fig. 6, when we take the mixing rate \hat{b} from the trajectories. It is seen that "reconstruction 1" does not reproduce the two humps of the DNS around $Z = 0.2$ and $Z = 0.8$. As an alternative we could use the maximum value of χ from each trajectory to parameterize (2.31). Rather than to take these values directly we will derive an approximate relation between the maximum of χ and \hat{b}^* and correct \hat{b}^* in (2.31) accordingly.

It is evident that the sine function solution and therefore χ_L in (2.29) does not capture the initial unsteady development of the Q1DLs. With the solution of (2.15) there exists a monotonic relation between the time and ΔZ of a Q1DL. Therefore one may parameterize the additional time dependence of χ_L by a correlation for \hat{b}^* in (2.29) that depends on ΔZ only. The analysis of the trajectories from the DNS shows in fact that the maximum values of χ , which occur at $Z^* = 0.5$ and therefore according to (2.29) would be equal to

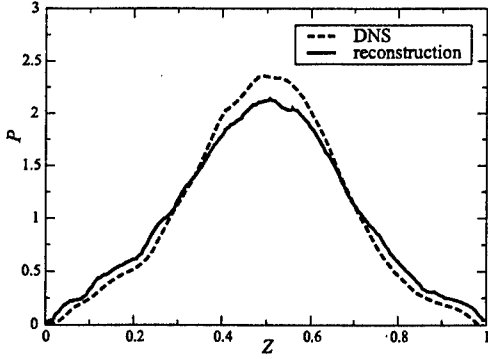


FIGURE 6. Comparison of the DNS and the reconstructed pdfs of mixture fraction

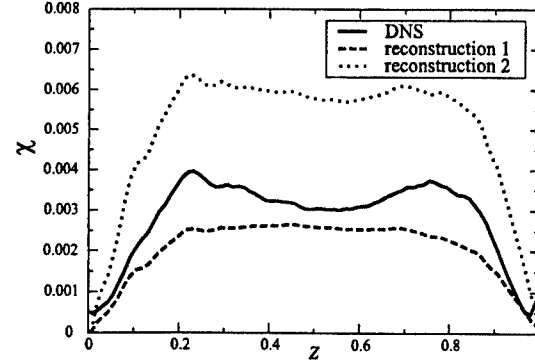


FIGURE 7. Comparison of the DNS and the reconstructed scalar dissipation rates

\hat{b}^* , can reasonably well be approximated by

$$\chi_{max}/\hat{b}^* = 1.0 + 2.0 \Delta Z / (\Delta Z)_{max} \quad (3.5)$$

Here the maximum values of ΔZ are :

$$(\Delta Z)_{max} = \begin{cases} 2 - 2Z_m & \text{for } Z_m \geq 0.5 \\ 2Z_m & \text{for } Z_m < 0.5 \end{cases} \quad (3.6)$$

which follow from (4.5) below for $Z = 0$, $Z^* = 0$ and $Z = 1$, $Z^* = 1$, respectively. Dissipation layers that extend to $Z = 0$ and $Z = 1$ will therefore have dissipation rates which are significantly larger than predicted by (2.31).

In the second reconstruction, shown as "reconstruction 2" in Fig. 7, we have multiplied (2.31) by the approximation of the r.h.s. of (3.5). This curve shows higher values than the DNS curve, but also shows its characteristic humps. By comparison with "reconstruction 1" we conclude that the humps in the χ_Z profile result from dissipation layers that extend either to $Z = 0$ or to $Z = 1$. Similar profiles of χ_Z with two humps, for instance, are found in the constant density DNS data of Pantano et. al. (2002).

4. An equation for the joint distribution function of Z_m and ΔZ

Rather than considering the joint pdf of minimum and maximum points we will derive an equation for the joint distribution function of Z_m and ΔZ from first principles. The corresponding normalized pdf calculated from the Z_m and ΔZ values of the 5 million trajectories is shown in Fig. 8.

Based on (2.9), (2.13) and (2.19) the substantial changes of Z_m and ΔZ are

$$\frac{dZ_m}{dt} = \frac{b-c}{2} \Delta Z, \quad \frac{d\Delta Z}{dt} = -(b+c) \Delta Z. \quad (4.1)$$

We realize that depending on the sign of $(b - c)$ the value of Z_m either increases or decreases with time, while ΔZ always decreases. We also note that (cf. Gibson, 1968) minimum and maximum points are convected by the flow field but due to their nature, they do not diffuse. This is also valid for Z_m and ΔZ . In a flow field Z_m and ΔZ are therefore governed by the following convective-reactive equations

$$\frac{\partial Z_m}{\partial t} + \mathbf{v} \cdot \nabla Z_m = \frac{b-c}{2} \Delta Z, \quad \frac{\partial \Delta Z}{\partial t} + \mathbf{v} \cdot \nabla \Delta Z = -(b+c) \Delta Z. \quad (4.2)$$

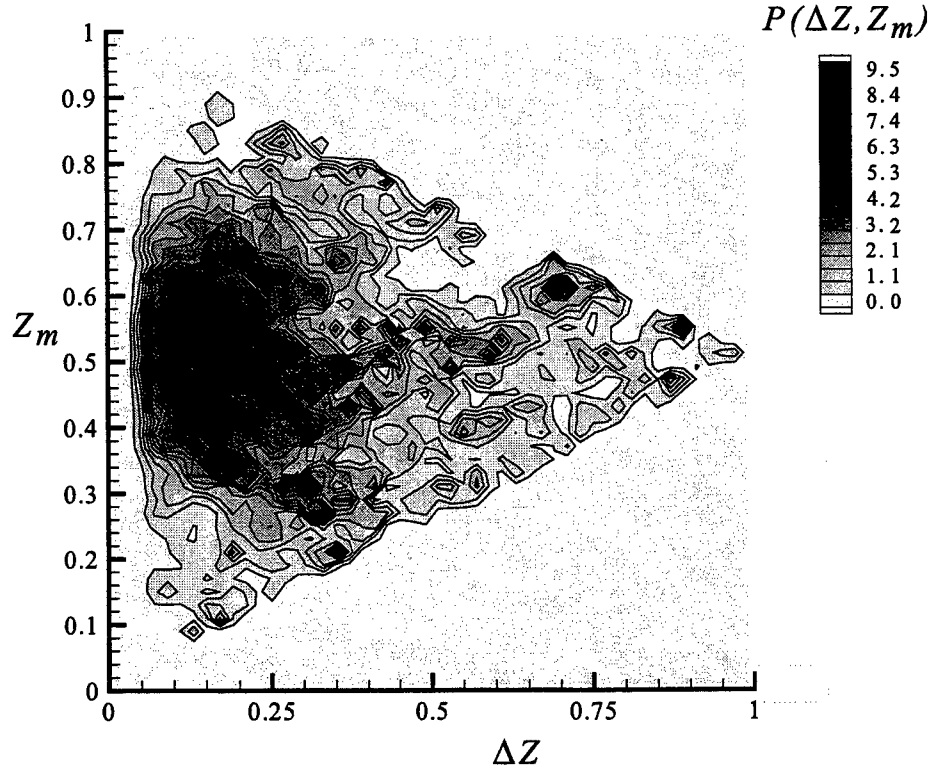


FIGURE 8. Isocontour lines of the joint pdf of Z_m and ΔZ

In deriving the joint distribution function of Z_m and ΔZ , we follow O'Brien (1980) who considered the pdf of a reactive-diffusive scalar. In such a derivation the formulation of the reaction term is exact while the diffusion term must be modelled. We are fortunate that Z_m and ΔZ are non-diffusive such that, based on (4.2), the equation for the joint distribution function P of Z_m and ΔZ becomes

$$\frac{\partial P}{\partial t} + \langle \mathbf{v} \cdot \nabla P \rangle + \frac{1}{2} \frac{\partial ((b - c) \Delta Z P)}{\partial Z_m} - \frac{\partial ((b + c) \Delta Z P)}{\partial \Delta Z} = \Sigma(Z_m, \Delta Z). \quad (4.3)$$

Here a yet unknown source term $\Sigma(Z_m, \Delta Z)$ has been added on the r.h.s. The convective term containing the fine-grained joint density P must be modelled. The rates $(b - c)$ and $(b + c)$ in (4.3) are assumed to be fixed quantities that are known.

Gibson (1968) discussed the initial production of zero gradient points by vortices that are strong enough to overturn the imposed scalar gradient. He also argued that secondary splitting would continuously generate new zero gradient points. Based on these considerations we expect that the production term $\Sigma(Z_m, \Delta Z)$ in the equation for P must depend on properties of the turbulent flow field. Since the only quantity representing the flow field in the theory developed above is the strain rate a , we expect that $\Sigma(Z_m, \Delta Z)$ will depend on this quantity.

We want to show that, knowing the joint distribution function $\mathbf{P}(Z_m, \Delta Z)$, we would be able to reconstruct P_Z . One way to do this is to reproduce in the homogeneous limit the exact equation (1.1) which governs P_Z . For that purpose we make use of our knowledge about the local distribution function P_L following from (2.18). We first multiply (4.3) by P_L to obtain

$$\begin{aligned} P_L \frac{\partial \mathbf{P}}{\partial t} + \langle \mathbf{v} \cdot \nabla (P_L \mathbf{P}) \rangle + \frac{1}{2} \frac{\partial ((b-c) \Delta Z P_L \mathbf{P})}{\partial Z_m} - \frac{\partial ((b+c) \Delta Z P_L \mathbf{P})}{\partial \Delta Z} \\ = \mathbf{P} \left[\frac{1}{2} (b-c) \Delta Z \frac{\partial P_L}{\partial Z_m} - (b+c) \Delta Z \frac{\partial P_L}{\partial \Delta Z} \right] + P_L \Sigma(Z_m, \Delta Z) . \end{aligned} \quad (4.4)$$

With the definition

$$Z^* = \frac{1}{2} + \frac{Z - Z_m}{\Delta Z} \quad (4.5)$$

the grouping in square brackets in the third term on the r.h.s. of (4.4) becomes

$$\frac{1}{2} (b-c) \Delta Z \frac{\partial P_L}{\partial Z_m} - (b+c) \Delta Z \frac{\partial P_L}{\partial \Delta Z} = - [b - Z^*(b+c)] \frac{\partial P_L}{\partial Z^*} . \quad (4.6)$$

Combining (2.18) and (4.4) with (4.6) then leads to

$$\begin{aligned} \frac{\partial P_L \mathbf{P}}{\partial t} + \langle \mathbf{v} \cdot \nabla (P_L \mathbf{P}) \rangle = - \frac{1}{2} \frac{\partial^2 (\chi_L P_L \mathbf{P})}{\partial Z^2} + \\ - \frac{1}{2} \frac{\partial ((b-c) \Delta Z P_L \mathbf{P})}{\partial Z_m} + \frac{\partial ((b+c) \Delta Z P_L \mathbf{P})}{\partial \Delta Z} - a P_L \mathbf{P} + P_L \Sigma(Z_m, \Delta Z) \end{aligned} \quad (4.7)$$

Integration over Z_m and ΔZ shows that the third and the fourth term on the r.h.s. cancel after integration because \mathbf{P} must be zero at the boundaries. Furthermore, the last two terms cancel if the source in (4.3) satisfies the condition

$$\int_0^1 \int_{(\Delta Z)_{\min}}^{(\Delta Z)_{\max}} (\Sigma(Z_m, \Delta Z) - a \mathbf{P}) P_L d\Delta Z dZ_m = 0 . \quad (4.8)$$

If (4.8) is to be valid for any form of P_L it follows immediately that

$$\Sigma(Z_m, \Delta Z) = a \mathbf{P} . \quad (4.9)$$

With the definitions

$$P_Z = \int_0^1 \int_{(\Delta Z)_{\min}}^{(\Delta Z)_{\max}} P_L \mathbf{P} d\Delta Z dZ_m \quad (4.10)$$

$$\mathcal{P}_Z = \int_0^1 \int_0^{(\Delta Z)_{\max}} P_L \mathbf{P} d\Delta Z dZ_m \quad (4.11)$$

integration of (4.7) over Z_m and ΔZ leads to a pdf equation for Z in the form

$$\frac{\partial P_Z}{\partial t} + \langle \mathbf{v} \cdot \nabla \mathcal{P}_Z \rangle = - \frac{1}{2} \frac{\partial^2 \chi_Z P_Z}{\partial Z^2} , \quad (4.12)$$

which reduces to (1.1) in the limit of homogeneous turbulence as anticipated. In (4.12)

$$\chi_Z P_Z = \int_0^1 \int_0^{(\Delta Z)_{\max}} \chi_L P_L \mathbf{P} d\Delta Z dZ_m , \quad (4.13)$$

which is consistent with the use of Bayes' theorem by O'Brien (1980) in the definition of

χ_Z as a conditional mean scalar dissipation rate. O'Brien also introduced a gradient flux approximation for the convective term which reads for the convective term in (4.3)

$$\langle \mathbf{v} \cdot \nabla \mathcal{P} \rangle = \langle \mathbf{v} \rangle \cdot \nabla \mathcal{P} - \nabla D_t \cdot \nabla \mathcal{P}, \quad (4.14)$$

where D_t is the turbulent diffusivity. Equation (4.3) then becomes with (4.9) and (4.14)

$$\frac{\partial \mathcal{P}}{\partial t} + \langle \mathbf{v} \rangle \cdot \nabla \mathcal{P} - \nabla D_t \cdot \nabla \mathcal{P} + \frac{1}{2} \frac{\partial ((b-c)\Delta Z \mathcal{P})}{\partial Z_m} - \frac{\partial ((b+c)\Delta Z \mathcal{P})}{\partial \Delta Z} = a \mathcal{P}. \quad (4.15)$$

Apart from the modeling of the convective term this equation is exact if the rates a, b and c are assumed to be fixed known quantities.

5. Modeling aspects

In the present analysis we have replaced the direct formulation for the scalar pdf equation for Z by an indirect formulation for the joint distribution function of Z_m and ΔZ . Both are exact as far as the scalar field is concerned. The former is not well-posed and therefore requires ad-hoc modeling of the molecular mixing term. In transported pdf models this modeling is usually based on the assumption of a constant scalar-to-flow time scale ratio, (cf. Pope, 2000). On the contrary, in the present formulation molecular mixing occurs exclusively within the Q1DLs. The independent variables in the present formulation are Z_m and ΔZ , where Z_m represents Z in a certain way while ΔZ captures non-local effects since the Q1DLs may span over a large distance within the turbulent flow. Modeling is required for the mixing rate $\hat{b} = (b+c)/2$, the asymmetry coefficient $(b-c)$ and the strain rate a . In the case of constant density turbulence the statistics of a are determined entirely by the velocity field, with the mean of a being proportional to ε/k where ε is the viscous dissipation and k is the kinetic energy of turbulence. The influence of the statistics of a on \hat{b} and $(b-c)$ can in principle be determined by solving (2.2) with the use of (2.13) for various initial conditions. Such an approach will, to a certain extend, be problem-dependent. Since the mean of the mixing rate \hat{b} represents the inverse of the scalar time and k/ε represents the flow time, the approach offered here appears somewhat less empirical than the assumption of a constant scalar-to-flow time scale ratio used in current modeling approaches for the scalar pdf P_Z .

Details of the modeling will be addressed in a more complete paper on the subject.

6. Conclusions

By identifying quasi-one-dimensional dissipation layers as key elements we have outlined a non-local theory of turbulent mixing. In this theory molecular mixing and its enhancement by compressive strain occurs exclusively within the local Q1DLs, while their transport by turbulence and their formation and disappearance is described by a pdf transport equation. That equation remains to be modeled. The main assumption of the theory is that the layers are one-dimensional and that they can be parametrized by four parameters, the minimum and the maximum mixture fraction and the mixing rates b and c .

This has been tested by generating trajectories and by reconstructing the mixture fraction pdf and the conditional scalar dissipation rate from DNS data of Rogers and Moser. The reconstructed scalar pdf $P_{Z,r}$ shows good agreement with the scalar pdf P_Z of the starting points of the trajectories. The reconstruction of the scalar dissipation

rate turns out to be quite sensitive to the mixing rate \hat{b} and its dependence on other parameters of the problem.

Acknowledgements

The authors acknowledge generous financial support by the Center for Turbulence Research. They want to thank Mike Rogers for advice in using the DNS data. They also enjoyed permanent discussions with Heinz Pitsch and Chong Cha and final discussions with Rodney Fox during the CTR summer program.

REFERENCES

- Ashurst, W. T, Kerstein, A. R., Kerr, R. M. and Gibson, C. H. 1987 *Alignment of vorticity and scalar gradient with strain rate in simulated Navier-Stokes turbulence*. Phys. Fluids **30**, 2343-2353.
- Gibson, C. H. 1968 *Fine structure of scalar fields mixed by turbulence. I. Zerogradient points and minimal gradient surfaces*. Phys. Fluids **11**, 2305-2317.
- Kervokian, J. 2000 *Partial Differential Equations*. Springer Verlag.
- O'Brien, E. E. 1980 *The probability density function (pdf) approach to reacting turbulent flows*. "Turbulent Reacting Flows", (P. A. Libby and F. A. Williams, Eds.), 185-218, Springer Verlag.
- Pantano, C., Sarkar, S. and Williams, F. 2002 *The interaction of scalar mixing and heat release in a reacting shear layer*. "Turbulent Mixing and Combustion", (A. Pollard and S. Candel, Eds.), 137-148, Kluwer Academic Publications.
- Papoulis, A. 1984 *Probability, Random Variables and Stochastic Processes*. McGraw-Hill, Inc.
- Peters N. 2000 *Turbulent Combustion*. Cambridge University Press.
- Pope, S. B. 2000 *Turbulent Flows*. Cambridge University Press.
- Rogers, M.M. and Moser, R.D. 2000 *Direct Simulation of a self-similar turbulent mixing layer*. Phys. Fluids **6**, 903-923.
- Villermaux, E. 2000 *Mixing as an Aggregation Process*. "Turbulent Mixing and Combustion", (A. Pollard and S. Candel, Eds.), 1-21, Kluwer Academic Publications.

Modelling turbulence-radiation interactions for large sooting turbulent flames

By J.-F. Ripoll AND H. Pitsch

1. Motivation and objectives

Large-scale turbulent flames and fires are strongly influenced by radiative energy transport. Especially in fires, fluid dynamics are governed by buoyancy, and hence, by the density and temperature distribution (Joulain (1998); Drysdale (1999); Tieszen (2001)). In pool fires, also the fuel mass flow rate is determined through radiative energy transfer from the flame to the liquid fuel, which thereby determines the evaporation rate. An accurate description of radiative energy transfer, which, in fires, is mainly caused by soot radiation, is therefore mandatory in numerical simulations.

Since a detailed description of radiation using, for instance, a discrete ordinate method is usually very expensive in numerical simulations, radiation is most commonly described using simplified models, such as the Milne-Eddington diffusion equations, valid in the limit of isotropic radiation, the Rosseland model, valid for high opacity media, or the optically thin model, valid for non absorbing media. Another simplification that is often made is neglecting turbulence-radiation interactions (TRI), although these have been found to be important, for instance, in pool fires (Tieszen (2001)). The aim of this paper is to provide a closed averaged radiation model accounting for TRI, which is simple and cost effective enough to be applied in numerical simulations.

A macroscopic radiation model, the M_1 -model, which has also been called the maximum entropy closure radiation model, has been developed successively by Minerbo (1978), Levermore (1984), Anile *et al.* (1991), Muller & Ruggeri (1993), Fort (1997), Dubroca & Feugeas (1999), and Brunner & Holloway (2001). This model provides field equations for the radiative energy and the radiative flux vector. The major advantage of this model is that it remains valid independently of the opacity. Ripoll (2002) has developed an averaged form of the M_1 -model for turbulent flows. The resulting formulation, however, is very complex and expensive to solve. In the present paper, we develop a simplified formulation of this model, which is better suited for combustion problems, and particularly for fire simulations. It will be shown how various levels of simplified models can be obtained from the M_1 -model with mean absorption coefficients (Ripoll *et al.* (2001)), and from these, closed form averaged models will be provided at different approximation levels.

The paper is organized as follows. First, in section 2, we will give a short overview of the M_1 radiation model and define the mean absorption coefficients. In section 3, different approximations will be provided for the mean absorption coefficients and the Eddington tensor, which is the most complex term in the M_1 -model. An averaged form of the M_1 -model for turbulent flows and closure for various terms will be presented in section 4. The variance of the radiative temperature remains as the only unknown. Finally, in section 5, models of various complexity for this quantity will be provided and discussed.

2. Radiative transfer equations

2.1. The M_1 radiation model with mean absorption coefficients

The M_1 radiation model developed by Minerbo (1978), Levermore (1984), Anile *et al.* (1991), Muller & Ruggeri (1993), Fort (1997), Brunner & Holloway (2001), and Dubroca & Feugeas (1999) describes the evolution of the radiative energy E_R and the radiative flux \vec{F}_R of a non-scattering gray medium. Considering a total radiative intensity $I(\vec{r}, t, \vec{\Omega}, \nu)$, where \vec{r} is the position, t the time, $\vec{\Omega}$ the normalized direction vector and ν the frequency, $E_R(\vec{r}, t) = \langle I \rangle_{\Omega, \nu}$ and $\vec{F}_R(\vec{r}, t) = \langle \vec{\Omega} I \rangle_{\Omega, \nu}$ describe the first two moments of the $I(\vec{r}, t, \vec{\Omega}, \nu)$ distribution according to the direction and the frequency. When the medium follows a Rayleigh law, the M_1 -model with mean absorption coefficients, developed by Ripoll *et al.* (2001), is written as

$$\partial_t E_R + \vec{\nabla} \cdot \vec{F}_R = c[\sigma_P a T^4 - \sigma_E E_R] \quad (2.1)$$

$$\frac{1}{c} \partial_t \vec{F}_R + c \vec{\nabla} \cdot (\vec{D}_R E_R) = -\sigma_F \vec{F}_R \quad (2.2)$$

where T is the temperature of the medium, c is the speed of light and the constant a is defined by $a = \frac{8}{15} \frac{\pi^5 k^4}{h^3 c^3} = \frac{4\sigma_{sb}}{c}$. Here, k is the Boltzmann constant, h is the Planck constant, and σ_{sb} is the Stefan-Boltzmann constant.

The mean absorption coefficients, which represent the opacity at the macroscopic level, are denoted by σ_P for the Planck mean absorption coefficient, and σ_E and σ_F for the two effective mean absorption coefficients defined below. The radiative flux is defined by $\vec{F}_R = (F_R^x, F_R^y, F_R^z)^T$ in \mathbf{R}^3 . The Eddington tensor \vec{D}_R is computed in terms of the Eddington factor $\chi(\|f\|)$ and of the anisotropic factor \vec{f} , given by $\vec{f} = (f_x, f_y, f_z)^T = \vec{F}_R/(cE_R)$ as

$$\vec{D}_R = \frac{1-\chi}{2} \vec{\text{Id}} + \frac{3\chi-1}{2} \vec{n} \otimes \vec{n}, \quad \text{with } \vec{n} = \frac{\vec{f}}{\|f\|}. \quad (2.3)$$

Here, $\|g\|$ denotes the Euclidian norm of a vector \vec{g} , $\vec{\text{Id}}$ is the identity matrix, \otimes stands for the dyadic product, and χ is defined by

$$\chi(\vec{f}) = \frac{3 + 4\|f\|^2}{5 + 2\sqrt{4 - 3\|f\|^2}}. \quad (2.4)$$

The radiative pressure is defined from the Eddington tensor as $\vec{P}_R = \vec{D}_R E_R$ and the radiative temperature is defined through the radiative energy as

$$T_R = \left(\frac{E_R}{a} \right)^{\frac{1}{4}}. \quad (2.5)$$

This macroscopic model is hyperbolic and has two equations describing the relaxation towards the radiative equilibrium, which is given by $E_R = aT^4$ and $\vec{F}_R = 0$. Another important property is that the norm of the anisotropic factor \vec{f} is bounded ($\|f\| \in [0, 1]$), which implies that the radiative flux is controlled by the speed of light. At the equilibrium, the anisotropic factor $\|f\|$ is equal to zero, while $\|f\|$ tends to 1 (i.e. $\|\vec{F}_R\| = cE_R$), when the emission is anisotropic. This corresponds to the transparent limit. This property ensures that the M_1 -model stays valid for all values of the opacity, since the speed of light is never exceeded and both opaque and transparent limits are given by the Eddington

tensor. The expression for the Eddington tensor D_R , which plays the role of a flux limiter, is derived from an underlying spectral radiative intensity. This intensity can describe a beam (by a Dirac function) as well as an isotropic emission (by a Planck function), and can hence be applied in both the transparent and the opaque limit. Therefore, this model can be applied in fire simulations, where the main difficulty in modeling radiative heat transfer comes from the wide range of opacities of the medium, which leads to anisotropic radiation. This makes the commonly used diffusion models, such as the Milne-Eddington and Rosseland models, and the optically thin model inapplicable.

An interesting alternative formulation of the M_1 -model with mean absorption coefficients can be derived by neglecting the time dependent terms in (2.1) and (2.2). Then, a diffusion equation for the radiative energy can be derived by eliminating the radiative flux from these equations as

$$\vec{\nabla} \cdot \left(\frac{1}{\sigma_F} \vec{\nabla} \cdot (\vec{D}_R E_R) \right) = c [\sigma_P a T^4 - \sigma_E E_R]. \quad (2.6)$$

Similarly, by eliminating the radiative energy, a diffusion equation for the radiative flux is obtained as

$$-\vec{\nabla} \cdot \left(\frac{\vec{D}_R}{\sigma_E} \vec{\nabla} \cdot \vec{F}_R \right) + \sigma_F \vec{F}_R = -c \vec{\nabla} \cdot \left(\frac{\sigma_P}{\sigma_E} \vec{D}_R a T^4 \right). \quad (2.7)$$

Note that taken separately, these equations are unclosed.

2.2. Definition of the mean absorption coefficients

For sooting flames, a Rayleigh diffusion law for the spectral absorption coefficient can be employed, and provides the opacity σ as a linear function of the frequency ν as $\sigma(\nu) = C_1 \nu$. The factor C_1 depends then on the soot volume fraction C_s , and can be defined as (Lee & Tien (1981); Mullins & Williams (1987))

$$C_1 = \frac{1}{c} \frac{36\pi n p C_s}{(n^2 - p^2 + 2)^2 + 4n^2 p^2} = 9.859475 \times 10^{-9} C_s \quad \text{with } n = 2, p = 0.40. \quad (2.8)$$

The mean absorption coefficients, derived in Ripoll *et al.* (2001), take this frequency dependence of the opacity of the medium into account. They represent the opacity at a macroscopic level and have a strong influence on radiative heat transfer (Siegel & Howell (2001)). The mean absorption coefficients are given by

$$\sigma_P = 360 C_1 \frac{k \zeta_5}{\pi^4 h} T = C_P T \quad \text{with} \quad C_P = 360 \frac{k \zeta_5}{\pi^4 h} C_1 \quad (2.9)$$

$$\sigma_E = 3\sigma_P \frac{1 + \|A\|^2}{B(3 + \|A\|^2)(1 - \|A\|^2)} \quad \text{and} \quad \sigma_F = \frac{\sigma_P}{4} \frac{5 + \|A\|^2}{B(1 - \|A\|^2)}, \quad (2.10)$$

with $\zeta_5 = 1.03692$. \vec{A} and B are defined as

$$\vec{A} = \frac{2 - \sqrt{4 - 3\|f\|^2}}{\|f\|^2} \vec{f} \quad \text{and} \quad B = \frac{T}{T_R} \left[\frac{3 + \|A\|^2}{3(1 - \|A\|^2)^3} \right]^{\frac{1}{4}}. \quad (2.11)$$

3. Simplifications of the M_1 -model with mean absorption coefficients

3.1. Expansion of the absorption coefficients

To simplify the effective mean coefficients σ_E and σ_F , first the expression for B , given in (2.11), is introduced into (2.10), such that σ_E and σ_F are functions of $\|f\|$ only through

A. Since A tends to zero for small $\|f\|$, with (2.11) we then write A as a second order Taylor series expansion for small $\|f\|$, which is given by

$$\|A\| = 3/4\|f\| + O(f^3). \quad (3.1)$$

After developing σ_E and σ_F in a Taylor series expansion for small A and replacing A using (3.1), we obtain

$$\sigma_E = C_P G_E(f) T_R, \quad (3.2)$$

$$\sigma_F = C_P G_F(f) T_R, \quad (3.3)$$

with

$$G_E(f) = 1 + \frac{15}{32}\|f\|^2 + O(\|f\|^4) \quad (3.4)$$

and

$$G_F(f) = \frac{5}{4} \left(1 + \frac{33}{200}\|f\|^2 + O(\|f\|^4) \right). \quad (3.5)$$

The isotropic limit for these coefficients can be obtained taking $\|f\| = 0$ in (3.4) and (3.5), which leads to $G_E \simeq 1$ and $G_F \simeq 5/4$. For the mean absorption coefficients in the isotropic limit follows

$$\sigma_E = C_P T_R \quad \text{and} \quad \sigma_F = 5/4 C_P T_R. \quad (3.6)$$

3.2. Expansion of the Eddington tensor

The Eddington tensor D_R has a complex form, which leads to various problems. For instance, the Jacobian matrix and the eigenvalues cannot be expressed easily for multi-dimensional problems. Then, the development of numerical schemes, particularly of implicit methods, is not straight forward. Even in one dimension, the Eddington tensor has to be treated in a special way, as, for instance, in the numerical scheme proposed by Brunner & Holloway (2001). Moreover, if an averaged form of the M_1 -model is being developed, this tensor must be simplified without modifying its main properties. Here, the Eddington tensor is expanded in a Taylor series around the directional equilibrium $f = 0$ and around the anisotropic limit $f = 1$. The two limits are then connected.

Combining (2.4) and (2.11) leads to $\chi(A) = (1 + 3\|A\|^2)/(3 + \|A\|^2)$. With this expression, the Eddington tensor (2.3) can be rewritten as

$$\vec{\vec{D}}_R = \frac{1 - \|A\|^2}{3 + \|A\|^2} \vec{\vec{\text{Id}}} + \frac{4\|A\|^2}{3 + \|A\|^2} \vec{n} \otimes \vec{n}. \quad (3.7)$$

Expanding the Eddington tensor of the M_1 -model as given by (3.7) for small $\|A\|$ and then replacing $\|A\|$ by Eq. (3.1) leads to

$$\vec{\vec{D}}_R \simeq \frac{1}{3} \left[(1 - \frac{3}{4}\|f\|^2) \vec{\vec{\text{Id}}} + \frac{9}{4}\|f\|^2 \vec{n} \otimes \vec{n} + O(\|f\|^4) \right]. \quad (3.8)$$

An even more simplified form of the Eddington tensor can be achieved by considering only the diagonal contributions of both terms in (3.8), i.e. $(D_R^{a,b})_{a,b=x,y} \simeq (D_R^{a,a})_{a=x,y}$. This leads to the following approximation

$$\vec{\vec{D}}_R \simeq \frac{1}{3} \left[1 + \frac{3}{2}\|f\|^2 + O(\|f\|^4) \right] \vec{\vec{\text{Id}}}. \quad (3.9)$$

Similar to the expansions for the mean absorption coefficients, also here it is obvious that these expansions for small $\|f\|$ cannot describe the anisotropic limit. It can easily

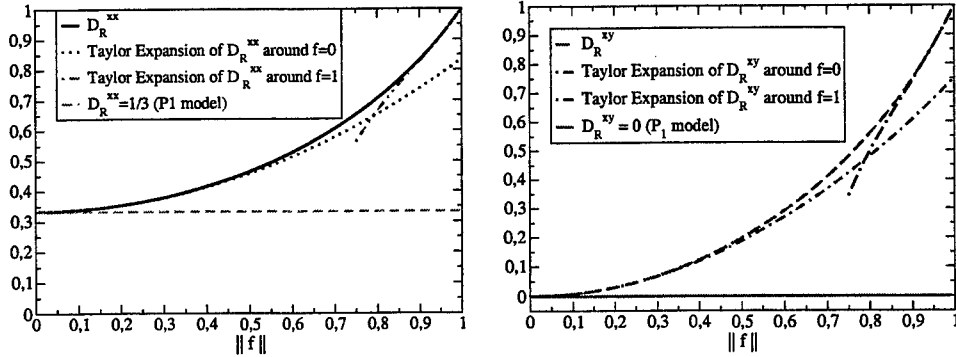


FIGURE 1. Left: Diagonal component D_R^{xx} of the Eddington tensor D_R and its Taylor series expansions.
Right: Deviatoric component D_R^{xy} of the Eddington tensor D_R and its Taylor series expansions

be seen in (2.3) that, in the anisotropic limit, when f goes to 1, the first part of this tensor is zero, and that the second part tends to $f \otimes f$. Here, this property is lost and the diagonal part does not become zero in this limit. Hence, this model is not able to describe strong disequilibrium effects. This can be seen in Fig. 1, where the components of the Eddington tensor and their Taylor expansions are plotted.

However, this limit can be described by an expansion of the Eddington tensor for $\|f\| \rightarrow 1$. Again, since $\|A\| = 1$ for $\|f\| = 1$, we first expand (3.7) for $\|A\| \rightarrow 1$, and then replace $\|A\|$ by the expansion of $\|A\|$ for $\|f\| \rightarrow 1$, given by

$$\|A\| = 1 + 2(\|f\| - 1) + 4(\|f\| - 1)^2 + O((\|f\| - 1)^3). \quad (3.10)$$

The resulting expression for the Eddington tensor in the limit $\|f\| \rightarrow 1$ is

$$\vec{D}_R \simeq \vec{n} \otimes \vec{n} + (\vec{\text{Id}} - 3\vec{n} \otimes \vec{n})(-6\|f\|^3 + 16\|f\|^2 - 15\|f\| + 5) + O((\|f\| - 1)^4). \quad (3.11)$$

It is shown in Fig. 1 that the Eddington tensor can be approximated by the two Taylor series expansions obtained for small $\|f\|$ and for $\|f\| \rightarrow 1$. To achieve good accuracy, the third order of (3.11) has to be retained.

4. Averaged M_1 -model with mean absorption coefficients

The main purpose here is to develop an ensemble-averaged formulation of the radiation model, which accounts for turbulence-radiation interactions, but is still not too complex or numerically costly, so that it can be used in fire simulations. An averaged form of the M_1 -model with mean absorption coefficients has already been derived by Ripoll (2002). However, because of the complexity of the averaged quantities, this model cannot be applied directly in numerical simulations. Here, a simplified form of this model will be derived.

The following mean quantities are introduced:

$$\bar{T} = \int_{\mathcal{D}_T} T \mathcal{P}_T(T) dT, \quad \bar{T}_R = \int_{\mathcal{D}_{T_R}} T_R \mathcal{P}_{T_R}(T_R) dT_R, \quad (4.1)$$

$$\bar{f}_i = \int_{\mathcal{D}_{f_i}} f_i \mathcal{P}_{f_i}(f_i) df_i, \quad \forall i = x, y, z, \quad \text{and} \quad \bar{C}_s = \int_{\mathcal{D}_{C_s}} C_s \mathcal{P}_{C_s}(C_s) dC_s, \quad (4.2)$$

where the integration domains are given as $\mathcal{D}_T = \mathcal{D}_{T_R} =]-\infty, +\infty[$, $\mathcal{D}_f =]-1, 1[$, and $\mathcal{D}_{C_s} =]0, 1[$. The probability density functions $\mathcal{P}_T(T)$, $\mathcal{P}_{T_R}(T_R)$, $\mathcal{P}_{C_s}(C_s)$, and $\mathcal{P}_{f_i}(f_i)$, $\forall i = x, y, z$ are assumed to be given by the following Gaussian and β functions:

$$\mathcal{P}_T(T) = \frac{1}{\sqrt{2\pi T' T'}} e^{-\frac{(T-\bar{T})^2}{2T' T'}}, \quad \mathcal{P}_{T_R}(T_R) = \frac{1}{\sqrt{2\pi \bar{T}'_R \bar{T}'_R}} e^{-\frac{(T_R-\bar{T}_R)^2}{2\bar{T}'_R \bar{T}'_R}}, \quad (4.3)$$

$$\mathcal{P}_{f_i}(f_i) = \frac{(f_i+1)^{\alpha_{f_i}-1}(1-f_i)^{\beta_{f_i}-1}}{2^{\alpha_{f_i}+\beta_{f_i}-1}} \frac{\Gamma(\alpha_{f_i}+\beta_{f_i})}{\Gamma(\alpha_{f_i})\Gamma(\beta_{f_i})}, \quad \forall i = x, y, z, \quad (4.4)$$

$$\mathcal{P}_{C_s}(C_s) = (C_s)^{\alpha_s-1}(1-C_s)^{\beta_s-1} \frac{\Gamma(\alpha_s+\beta_s)}{\Gamma(\alpha_s)\Gamma(\beta_s)} \quad (4.5)$$

$$\text{with } \alpha_{f_i} = \bar{f}_i \gamma_{f_i}, \quad \beta_{f_i} = (1-\bar{f}_i) \gamma_{f_i}, \quad \gamma_{f_i} = \frac{\bar{f}_i(1-\bar{f}_i)}{\bar{f}'_i \bar{f}'_i} - 1, \quad \forall i = x, y, z, \quad (4.6)$$

$$\alpha_s = \bar{C}_s \gamma_s, \quad \beta_s = (1-\bar{C}_s) \gamma_s, \quad \gamma_s = \frac{\bar{C}_s(1-\bar{C}_s)}{\bar{C}'_s \bar{C}'_s} - 1, \quad \Gamma(x) = \int_0^\infty e^{-t} t^{(x-1)} dt. \quad (4.7)$$

The direct integration of the Gaussian functions leads to the moments of T_R and T in the following form

$$\begin{aligned} \bar{X}^9 &= 945 \bar{X}' \bar{X}'^4 \bar{X} + 1260 \bar{X}' \bar{X}'^3 \bar{X}^3 + 378 \bar{X}' \bar{X}'^2 \bar{X}^5 + 36 \bar{X}' \bar{X}' \bar{X}^7 + \bar{X}^9, \\ \bar{X}^8 &= 105 \bar{X}' \bar{X}'^4 + 420 \bar{X}' \bar{X}'^3 \bar{X}^2 + 210 \bar{X}' \bar{X}'^2 \bar{X}^4 + 28 \bar{X}' \bar{X}' \bar{X}^6 + \bar{X}^8, \\ \bar{X}^5 &= 15 \bar{X}' \bar{X}'^2 \bar{X} + 10 \bar{X}' \bar{X}' \bar{X}^3 + \bar{X}^5, \\ \bar{X}^4 &= 3 \bar{X}' \bar{X}'^2 + 6 \bar{X}' \bar{X}' \bar{X}^2 + \bar{X}^4, \end{aligned} \quad (4.8)$$

where X stands for T_R or T , and $\bar{X}' \bar{X}'$ for $\bar{T}'_R \bar{T}'_R$ or $\bar{T}' \bar{T}'$.

To obtain a closed form of the averaged equations, two assumptions have to be made in the following. First, we assume that the soot volume fraction is uncorrelated from the radiative energy and flux and from the matter temperature. This assumption can be justified for fires, considering the experimental results given by Coppalle & Joyeux (1994). Note however, that correlations of the radiative properties of soot and other quantities are retained.

Secondly, it is assumed that the anisotropic factor and the radiative temperature are uncorrelated. This assumption is difficult to justify, although in the limit, where radiation is isotropic and the anisotropic factor tends to zero, also the correlation becomes small. Note however, that the assumption of uncorrelated anisotropic factor and radiative temperature does not imply that radiative flux and radiative energy are uncorrelated, since $\bar{E}_R \bar{F}_R = c \bar{f} \bar{E}_R^2 \neq \bar{E}_R \bar{F}_R$.

According to the definition of the ensemble averages and the above assumptions, the mean radiative energy and flux can be determined as

$$\bar{E}_R = \bar{a} \bar{T}_R^4 = \int_{\mathcal{D}_{T_R}} a T_R^4 \mathcal{P}_{T_R}(T_R) dT_R \quad \text{and} \quad \bar{F}_R = c \bar{f} \bar{E}_R. \quad (4.9)$$

It is convenient to introduce turbulent effective mean absorption coefficients defined as

$$\sigma_P^t = \frac{\overline{\sigma_P T^4}}{\overline{T}^4} = \overline{C}_P \frac{\overline{T^5}}{\overline{T}^4}, \quad (4.10)$$

$$\sigma_E^t = \frac{\overline{\sigma_E E_R}}{\overline{E}_R} = \overline{C}_P \overline{G}_E \frac{\overline{T_R^5}}{\overline{T_R}^4}, \quad \text{and} \quad \sigma_F^t = \frac{\overline{\sigma_F F_R}}{\overline{F}_R} = \overline{C}_P \frac{\overline{G_F f}}{\overline{f}} \frac{\overline{T_R^5}}{\overline{T_R}^4}. \quad (4.11)$$

Then, the averaged M_1 -model with mean absorption coefficients can be written as

$$\partial_t \overline{E}_R + \nabla \cdot \overline{F}_R = c[\sigma_P^t a \overline{T^4} - \sigma_E^t \overline{E}_R], \quad (4.12)$$

$$\frac{1}{c} \partial_t \overline{F}_R + c \nabla \cdot (\overline{D}_R(f) \overline{E}_R) = -\sigma_F^t \overline{F}_R, \quad (4.13)$$

where for $a, b = x, y, z$

$$\overline{D}_R^{ab}(f) = \int_{\mathcal{D}_f} D_R^{ab}(f_x, f_y, f_z) \mathcal{P}_f(f) df. \quad (4.14)$$

Here, $\mathcal{P}_f(f)$ is the joint pdf of f_x, f_y, f_z , which can in principle be modeled as a multi-variate β -function, depending on the mean components and the variances and co-variances of f_x, f_y , and f_z . These can be computed at shown below. However, since the evaluation of this pdf is very complex, the further assumption that the components of the anisotropy factor are uncorrelated leads to

$$\overline{D}_R^{ab}(f) = \int_{\mathcal{D}_{f_x}} \int_{\mathcal{D}_{f_y}} \int_{\mathcal{D}_{f_z}} D_R^{ab}(f_x, f_y, f_z) \mathcal{P}_{f_x}(f_x) \mathcal{P}_{f_y}(f_y) \mathcal{P}_{f_z}(f_z) df_x df_y df_z, \quad (4.15)$$

where the pdfs of the individual components can be modeled according to (4.4).

This system is closed, if the variances of the radiative energy and of the anisotropic factor are known. The variance of the anisotropic factor only appears in the expressions for \overline{G}_E , \overline{G}_F , and \overline{D}_R . If the variance of the anisotropic factor is assumed to be small, it follows that only the variances of the radiative energy is needed. Indeed, if $\overline{f}^{a'} f^{a'} \simeq 0$, $\forall a = x, y, z$, then $\overline{G}_E(f) \simeq G_E(\overline{f})$, $\overline{G}_F(f) \simeq G_F(\overline{f})$, and $\overline{D}_R(f) \simeq D_R(\overline{f})$. This assumption will be discussed in section 5.2. The model then becomes

$$\partial_t \overline{E}_R + \nabla \cdot \overline{F}_R = c \overline{C}_P \left(a \overline{T^5} - a G_E(\overline{f}) \overline{T_R^5} \right), \quad (4.16)$$

$$\frac{1}{c} \partial_t \overline{F}_R + c \nabla \cdot D_R(\overline{f}) \overline{E}_R = -c \overline{C}_P G_F(\overline{f}) a \overline{T_R^5} \overline{f}. \quad (4.17)$$

Similarly to the derivation of the diffusion formulation of the M_1 -model given by (2.6) and (2.7), an averaged diffusion formulation can be obtained from (4.12) and (4.13). The diffusion equation for the mean radiative flux then becomes

$$-\vec{\nabla} \cdot \left(\frac{\overline{D}_R(f)}{\sigma_E^t} \vec{\nabla} \cdot \overline{F}_R \right) + \sigma_F^t \overline{F}_R = -c \vec{\nabla} \cdot \left(\frac{\sigma_P^t}{\sigma_E^t} \overline{D}_R(f) a \overline{T^4} \right). \quad (4.18)$$

5. Model for the variances of the radiative variables

In the averaged M_1 -model, given by (4.12) and (4.13), the variance of both the radiative temperature and the anisotropy appear, and models for these quantities have to be provided. Expressions for the variances have been derived by Ripoll (2002). Here, simplified formulations for these quantities will be developed.

5.1. General formulation

Using the assumption made in the previous section that the radiative energy and the anisotropy factor are uncorrelated, the variances of the radiative variables can be written as

$$\overline{E'_R E'_R} = \overline{(E_R - \bar{E}_R)^2} = \overline{E_R^2} - \bar{E}_R^2, \quad (5.1)$$

$$\overline{F'_R F'_R} = \overline{(c f E_R - c \bar{f} \bar{E}_R)^2} = \overline{(c f E_R - c \bar{f} \bar{E}_R)^2} = c^2 \bar{f}^2 \overline{E_R^2} - c^2 \bar{f}^2 \bar{E}_R^2. \quad (5.2)$$

Introducing $\bar{f}' \bar{f}' = \bar{f}^2 - \bar{f}^2$ into (5.2), leads to an expression relating the variances of the radiative flux, the anisotropy factor, and the radiative energy as

$$\overline{F'_R F'_R} = c^2 \bar{f}' \bar{f}' \overline{E_R^2} + c^2 \bar{f}^2 \overline{E'_R E'_R}. \quad (5.3)$$

Ripoll (2002) has derived transport equations for the variances of radiative energy and radiative flux. However, in their general form, mainly because of the different integral terms of the Eddington tensor, these equations are complex and not easily applicable. If in the variance equation of the radiative flux, the directional equilibrium assumption is applied for the Eddington tensor, and if, according to $\|f\| \rightarrow 0$ in (3.4) and (3.5), $\bar{G}_E \simeq 1$ and $\bar{G}_F \simeq 5/4$, the equations for $\overline{E'_R E'_R}$ and $\overline{F'_R F'_R}$ become

$$\begin{aligned} \frac{1}{2} \partial_t \overline{E'_R E'_R} + c \nabla \cdot (\overline{E'_R E'_R} \bar{f}) - \frac{c}{2} \bar{f} \cdot \nabla (\overline{E'_R E'_R}) = \\ c \bar{C}_P (a^2 \bar{T}^9 + \frac{15}{32} a^2 \bar{T}^9 \|f\|^2 - a \bar{T}^5 \bar{E}_R) - c \bar{C}_P (a^2 \bar{T}_R^9 - a \bar{T}_R^5 \bar{E}_R), \end{aligned} \quad (5.4)$$

$$\frac{1}{c} \partial_t \overline{F'_R F'_R} + \frac{c^2}{3} \bar{f} \nabla \overline{E'_R E'_R} = -c^2 \frac{5}{2} \bar{C}_P (\bar{f}^2 a^2 \bar{T}_R^9 - \bar{f}^2 a \bar{T}_R^5 \bar{E}_R). \quad (5.5)$$

5.2. Simplification around the equilibrium

With (5.4) and (5.5), in three-dimensional simulations, four equations need to be solved to describe the spatial distribution of the variances of the radiative energy and the components of the radiative flux.

A major simplification can be achieved by assuming that the variance of the anisotropic factor is negligible. This implies that $\overline{f_a^2} = \bar{f}_a^2, \forall a = x, y, z$, and hence the variance of the radiative flux can be expressed by the variance of the radiative temperature as $\overline{F'_R F'_R} = c \bar{f}_a^2 \overline{E'_R E'_R}, \forall a = x, y, z$. This assumption has already been used in section 4 to simplify the mean absorption coefficients and the Eddington tensor. It is noteworthy that neglect the variance of the anisotropy factor is not equivalent to neglect the variance of the radiative flux.

It can be shown that this assumption also implies that $\|\bar{f}^2\| = \|\bar{f}\|^2$, which also simplifies the second term on the right hand side in the equation for the radiative energy (5.4), leading to

$$\begin{aligned} \frac{1}{2} \partial_t (\overline{E'_R E'_R} (1 + 3\|\bar{f}\|^2)) + c \nabla \cdot (\overline{E'_R E'_R} \bar{f}) = c \bar{C}_P (a^2 \bar{T}^9 + \frac{15}{32} a^2 \bar{T}^9 \|\bar{f}\|^2 - a \bar{T}^5 \bar{E}_R) \\ - c \bar{C}_P (1 + \frac{15}{4} \|\bar{f}\|^2) (a^2 \bar{T}_R^9 - a \bar{T}_R^5 \bar{E}_R). \end{aligned} \quad (5.6)$$

This equation is now closed. The radiative energy is known from the solution of the equation for the mean radiative temperature, the matter temperature and the soot volume fraction are given by the flow solver, and averages of powers of the radiative temperature can be obtained from (5.1), (4.8), and definition of the radiative temperature (2.5).

5.3. Algebraic model for the variance of the radiative energy

Solving the transport equation for the variance of the radiative energy (5.6) can be avoided by introducing further simplifications. If the equation for the variance of the radiative energy is non-dimensionalized with the speed of light and a characteristic opacity σ , all terms are of the same order. This shows that the time needed to achieve a steady state scales with $(\sigma c)^{-1}$, which is typically much smaller than the flow time scales that perturb the steady state of (5.6). The unsteady term in the variance equations can therefore be neglected.

If it is assumed that production is equal to dissipation in the equation for the variance, an algebraic expression for the radiative temperature can be obtained as

$$\overline{T^9} \left(1 + \frac{15}{32} \|\bar{f}\|^2\right) - \left(1 + \frac{15}{4} \|\bar{f}\|^2\right) \overline{T_R^9} + \left(1 + \frac{15}{4} \|\bar{f}\|^2\right) \overline{T_R^4} (\overline{T_R^5} - \overline{T^5}) = 0, \quad (5.7)$$

where the definition of the radiative temperature (2.5) has been used. This leads in the limit $\|f\| \rightarrow 0$ to

$$\overline{T^9} - \overline{T_R^9} + (\overline{T_R^5} - \overline{T^5}) \overline{T_R^4} = 0. \quad (5.8)$$

Using (4.8), the algebraic model (5.7) can be written in a polynomial form as

$$A \overline{T'_R T_R'}^4 + B \overline{T'_R T_R'}^3 + C \overline{T'_R T_R'}^2 + D \overline{T'_R T_R'} + E = 0 \quad (5.9)$$

with

$$A = -900 \left(1 + \frac{15}{4} \|\bar{f}\|^2\right) \overline{T_R}, \quad B = -1140 \left(1 + \frac{15}{4} \|\bar{f}\|^2\right) \overline{T_R^3}, \quad (5.10)$$

$$C = -300 \left(1 + \frac{15}{4} \|\bar{f}\|^2\right) \overline{T_R^5} - 3 \overline{T^5}, \quad E = \overline{T^9} \left(1 + \frac{15}{32} \|\bar{f}\|^2\right) - \overline{T^5} \overline{T_R^4}, \quad (5.11)$$

$$D = -20 \left(1 + \frac{15}{4} \|\bar{f}\|^2\right) \overline{T_R^7} - 6 \overline{T^5} \overline{T_R^2}. \quad (5.12)$$

This algebraic model is easy to solve and can be pre-tabulated in terms of \overline{T} , $\overline{T_R}$, $\overline{T' T'}$, and $\|\bar{f}\|$. In the following we will demonstrate the consistency of this model in some relevant limits. To fully assess the validity of the algebraic model, which is based on equilibrium assumptions, it will have to be compared with solutions of the variance transport equation (5.6).

5.3.1. Case $\|\bar{f}\| = 0$

Results from the solution of (5.9) for $\|\bar{f}\| = 0$ and $\overline{T} = 2000$ K are shown in Fig. 2. It can be observed that for any combination of the parameters a positive solution for $\overline{T'_R T_R'}$ is obtained as long as $0 \leq \overline{T_R} \leq \overline{T}$. Three comments can be made regarding Fig. 2. Firstly, when $\overline{T} \neq \overline{T_R}$, there exists a non-zero positive $\overline{T'_R T_R'}$, which is always larger than $\overline{T' T'}$, even if $\overline{T' T'} = 0$. Secondly, both variances of radiative temperature and matter temperature are equal when $\overline{T} = \overline{T_R}$, which is shown by the solid line. This is consistent with the radiative equilibrium in the instantaneous M_1 -model. Finally, when $\overline{T} \neq \overline{T_R}$ nonlinear solutions are obtained.

Even simpler models for the variance of the radiative temperature could be constructed from (4.8) by assuming that some higher moments of the radiative temperature and the matter temperature are equal. To assess this assumption, results from the algebraic model (5.8), denoted "A1" are shown for two values of the mean radiative temperature, $\overline{T_R} = 1900$ K and 1700 K in Fig. 2. Also shown are two simple approximations given by

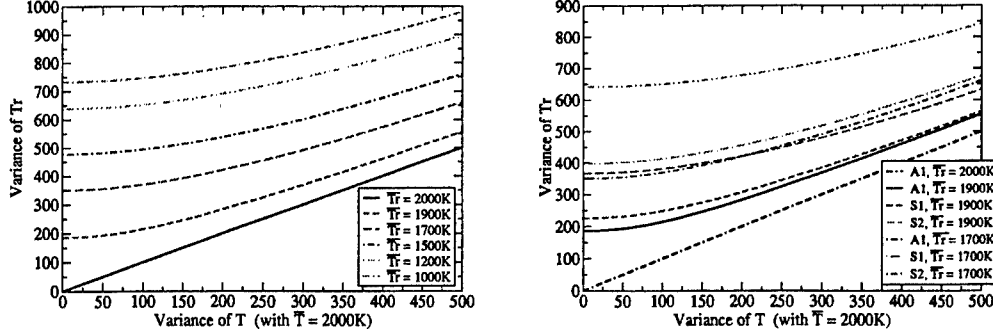


FIGURE 2. Left: solution of the algebraic model for $\|\vec{f}\| = 0$. Right: comparison of the algebraic model with other moment equations.

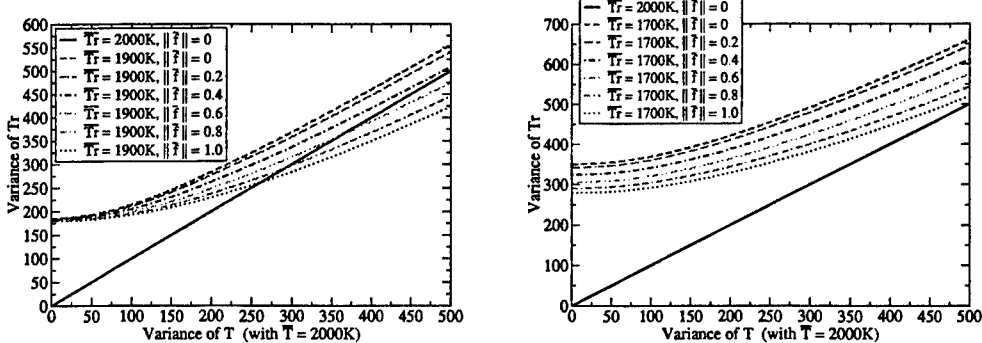


FIGURE 3. Solution of the algebraic model for different values of $\|\vec{f}\|$ with $\bar{T}_R = 1900\text{K}$ (left) and $\bar{T}_R = 1700\text{K}$ (right).

$\bar{T}_R^9 = \bar{T}^9$ and $\bar{T}_R^4 = \bar{T}^4$, which are denoted as “S1” and “S2”, respectively. The solution of “A1” for $\bar{T} = \bar{T}_R = 2000\text{K}$, implying $\bar{T}'\bar{T}' = \bar{T}'_R\bar{T}'_R$ is also shown, since it could also be used as a simple approximation for the variance of the radiative temperature.

It appears that model “S2” largely overpredicts the variance, while model “S1” yields a variance approximately 50 K too high, if compared to the algebraic model. It can hence be concluded that the algebraic equation should be used, since it is not more difficult to solve than the simple models.

5.3.2. Case $\|\vec{f}\| \neq 0$

Results from the solution of the algebraic model (5.7) with $\|\vec{f}\| \neq 0$ are given in Fig. 3 for two different values of the radiative temperature, $\bar{T}_R = 1700\text{K}$ and 1900K , a variation of the anisotropic factor from $\|\vec{f}\| = 0$ to $\|\vec{f}\| = 1$, and a matter temperature of $T = 2000\text{K}$. Again, it is obvious that positive solutions for the variance of the radiative temperature exist throughout the entire parameter range.

It is interesting to note that for stronger anisotropic disequilibrium ($\|f\| \neq 0$), the variance of the radiative temperature becomes smaller, while it becomes larger for stronger energetic disequilibrium ($T_R \neq T$).

6. Coupling with the Navier-Stokes equations

In the previous sections, a closed form of the averaged M_1 -model with mean absorption coefficients has been presented, where closure has been introduced at various levels, such that models of different complexity and accuracy can be used. The only remaining unclosed terms are the mean matter temperature and its variance and the mean soot volume fraction. These quantities have to be provided from a combustion model, which is a part of the flow solver. Most combustion models, such as flamelet models (Peters (1984); Pitsch *et al.* (2000)), conditional moment closure models (Klimenko & Bilger (1999)), or pdf transport models (Pope (1985)) would allow to compute these quantities. However, most combustion models compute for Favre-averaged quantities, while the present formulation of the radiation model is based on Reynolds-averages. However, if the density is known, the appropriate pdfs can be converted to yield either Favre-averaged or Reynolds-averaged quantities. As an example, using a flamelet model and neglecting the variance of the scalar dissipation rate, the Favre-averaged temperature would be computed according to

$$\tilde{T} = \int_0^1 T(Z) \tilde{P}(\tilde{Z}, \tilde{Z''^2}) dZ, \quad (6.1)$$

where Z is the mixture fraction, and the tilde denotes Favre-averages. Since the Favre pdf is defined as $\tilde{P}(Z; \tilde{Z}, \tilde{Z''^2}) = \rho(Z)P(Z; \bar{Z}, \bar{Z''^2})/\bar{\rho}$ with ρ being the density, the Reynolds averaged temperature can be obtained as

$$\bar{T} = \int_0^1 T(Z) \frac{\bar{\rho}}{\rho(Z)} \tilde{P}(\tilde{Z}, \tilde{Z''^2}) dZ. \quad (6.2)$$

Using other combustion models, the appropriate quantities can be obtained accordingly.

7. Conclusions

In this paper, an ensemble-averaged version of the M_1 radiation model with mean absorption coefficients is proposed for describing radiation in large sooting flames. Closure is provided from transport equations for the variances of the radiative quantities, presumed pdf assumptions, and the assumption that the anisotropic factor and the radiative temperature are uncorrelated. This latter assumption is equivalent to the uncoupling the directional and energetic disequilibrium and seems to be a reasonable way to provide a closed and usable form of an averaged macroscopic radiative model.

REFERENCES

- ANILE, M., PENNISI, S. & SAMMARTINO, M. 1991 A thermodynamical approach to Eddington factors. *J. Math. Physics* **32** (2).
- BRUNNER, T. A. & HOLLOWAY, J. P. 2001 One-dimensional Riemann solvers and the maximum entropy closure. *J. Quant. Spectrosc. Radiat. Transfer* **69**, 543–566.
- COPPALLE, A. & JOYEUX, D. 1994 Temperature and soot volume fraction in turbulent

- diffusion flames: Measurements of mean and fluctuating values. *Combust. and Flame* **96**, 275–285.
- DRYSDALE, D. 1999 *An introduction to Fire Dynamics*. Wiley, New York.
- DUBROCA, B. & FEUGEAS, J.-L. 1999 Etude théorique et numérique d'une hiérarchie de modèles aux moments pour le transfert radiatif. *C. R. Acad. Sci. Paris* **329**, 915–920.
- FORT, J. 1997 Information-theoretical approach to radiative transfer. *Phys. A* **243**, 275–303.
- JOULAIN, P. 1998 The behavior of pool fires: state of the art and new insights. *27th Sympo. (Int.) on Comb.*. The Combustion Institute. pp. 2691–2706.
- KLIMENKO, A. Y. & BILGER, R. W. 1999 Conditional moment closure for turbulent combustion. *Prog. Energy Combust. Sci.* **25**, 595–687.
- LEE, S. C. & TIEN, C. L. 1981 Optical constants of soot in hydrocarbon flames. In *Eighteenth Symposium International on Combustion*, pp. 1159–1166. The Combustion Institute.
- LEVERMORE, D. 1984 Relating Eddington factors to flux limiters. *J. Quant. Spectrosc. Radiat. Transfer* **31**, 149–160.
- MINERBO, G. N. 1978 Maximum entropy eddington factors. *J. Quant. Spectrosc. Radiat. Transfer* **20**, 541–545.
- MULLER, I. & RUGGERI, T. 1993 *Extended Thermodynamics*. Springer, New York.
- MULLINS, J. & WILLIAMS, A. 1987 The optical properties of soot: a comparison between experimental and theoretical values. *Fuel* **68**, 277–280.
- PETERS, N. 1984 Laminar diffusion flamelet models in non-premixed turbulent combustion. *Prog. Energy Combust. Sci.* **10**, 319–339.
- PITSCH, H., RIESSMEIER, E. & PETERS, N. 2000 Unsteady flamelet modeling of soot formation in turbulent diffusion flames. *Comb. Sci. Tech.* **158**, 389–406.
- POPE, S. B. 1985 Pdf methods for turbulent reactive flows. *Prog. Energy Combust. Sci.* **11**, 119.
- RIPELL, J.-F. 2002 An averaged formulation of the m_1 radiation model with presumed probability density functions for turbulent flows. Submitted for publication.
- RIPELL, J.-F., DUBROCA, B. & DUFFA, G. 2001 Modelling radiative mean absorption coefficients. *Comb. Th. and Mod.* **5**, 261–275.
- SIEGEL, R. C. & HOWELL, J. R. 2001 *Thermal radiation heat transfer*. 4th ed., Taylor and Francis, London.
- TIESZEN, S. R. 2001 On the fluid dynamics of fires. *Annu. Rev. Fluid Mech.* **33**, 67–92.

Inverse parabolicity of PDF equations in turbulent flows – reversed-time diffusion or something else

By A. Y. Klimenko †

1. Motivation

The focus of the present work is the well-known feature of the PDF transport equations in turbulent flows – the inverse parabolicity of the equations. While it is quite common in fluid mechanics to interpret equations with direct (forward-time) parabolicity as either diffusion or a combination of diffusion and other processes (for example convection and reaction), the possibility of a similar interpretation for the equations with inverse parabolicity is not clear. In the present work, we investigate whether the inverse-parabolic terms in PDF equations can be treated as an “inverse diffusion”. In other words, we look for a physical process which can be modeled by this inverse diffusion while complying with the major laws of nature and turbulence.

2. The PDF transport equations

The PDF techniques, which have been developed for last thirty years, represent an effective tool for deriving and analyzing the PDF transport equations in turbulent flows (Pope 1985, Kuznetsov & Sabelnikov 1989, Dopazo 1894, Klimenko & Bilger 1999, Pope 2000). The PDF transport equation

$$\frac{\partial P}{\partial t} + \frac{\partial \hat{u}_i P}{\partial x_i} + \frac{\partial \hat{A}_I P}{\partial z_I} + \frac{\partial^2 \hat{B}_{IJ} P}{\partial z_I \partial z_J} = 0 \quad (2.1)$$

specifies the evolution of a joint PDF $P = P(\mathbf{z}; \mathbf{x}, t)$ of the values $\mathbf{Z} = (Z_1, \dots, Z_n)$ which are transported by the turbulence according to

$$\frac{\partial Z_I}{\partial t} + \frac{\partial v_i Z_I}{\partial x_i} - D \frac{\partial^2 Z_I}{\partial x_i \partial x_i} = W_I \quad (2.2)$$

Here we introduce the conditional expectation $\hat{u}_i(\mathbf{z}, \mathbf{x}, t)$ of velocity $v_i(\mathbf{x}, t)$, the conditional dissipation $\hat{B}_{IJ}(\mathbf{z}, \mathbf{x}, t)$, which is, by definition, symmetric and positive semidefinite and the conditional “drift” coefficient $\hat{A}_I(\mathbf{z}, \mathbf{x}, t)$ according to the following equations

$$\hat{u}_i \equiv \langle v_i | \mathbf{Z} = \mathbf{z} \rangle, \quad \hat{B}_{IJ} \equiv \langle D \nabla Z_I \cdot \nabla Z_J | \mathbf{Z} = \mathbf{z} \rangle, \quad \hat{A}_I \equiv \langle W_I | \mathbf{Z} = \mathbf{z} \rangle \quad (2.3)$$

By default, the lower case indices run over physical coordinates (that is $i = 1, 2, 3$) while the upper case indices run over all dimensions of the transported quantities (that is $I = 1, 2, 3, 4, \dots, n$). Vector notation is used to denote vectors of maximal dimension introduced for a particular quantity. For example, $\mathbf{x} = (x_1, x_2, x_3) = (x_i; i = 1, 2, 3)$ and $\mathbf{Z} = (Z_1, \dots, Z_n) = (Z_I; I = 1, \dots, n)$. The sample space variable for \mathbf{Z} is denoted by \mathbf{z} . The convention of summation over repeated indices applies throughout the paper. The gradient operators are calculated in the physical space $\nabla = (\partial / \partial x_i, i = 1, 2, 3)$. For simplicity,

† Mech. Eng. Dept., The University of Queensland, Qld. 4072, Australia; email: klimenko@mech.uq.edu.au

we assume that the density ρ is constant, and that the Reynolds number is high so that the terms involving transport by molecular diffusion (such as those specified by the term $D\nabla^2 P$) and differential-diffusion effects can be neglected. Apart from these conventional assumptions, equation (2.1) is exact and can be derived from (2.2) by standard PDF techniques (Pope 1985, Kuznetsov & Sabelnikov 1989, Dopazo 1994, Klimenko & Bilger 1999 and Pope 2000). The physical meaning of the values W_I depends on the actual physical meaning of the variables Z_I : for reactive scalars W_I would represent a chemical source term while for velocity components W_I denotes the pressure gradient. For the sake of certainty, we assume that the first three components of Z_I represent the velocity components, while the rest of the values Z_I (that is Z_4, \dots, Z_n) are reactive scalars. Thus we have

$$v_i = Z_i, \hat{u}_i = z_i, W_i = -\frac{1}{\rho} \frac{\partial p}{\partial x_i} \quad (2.4)$$

while the other source terms $W_\alpha = (W_4, \dots, W_n)$ are assumed to be functions of the scalar variables $W_\alpha = W_\alpha(Z_4, \dots, Z_n)$ and their particular forms are not stipulated in the present work. By default, the Greek indices run over the "scalar quantities" $\alpha = 4, \dots, n$.

The most interesting feature of (2.1) is its inverse parabolicity, determined by the positive sign of the last term. While direct parabolic equations are quite common in fluid mechanics and other areas of engineering, inverse-parabolic equations seem quite unusual for any physical process but they are most common for the PDF equations in turbulent flows. The objective of the present work is to find a reasonable physical interpretation of this strange but common feature of the PDF equations.

3. The reversed-time diffusion model

The terms with conventional direct parabolicity, such as the last term on the left-hand side of (2.2), are called the diffusion terms, since these terms may normally be associated with some diffusive Markov processes (or random-walk processes). For example, the diffusion of a small amount of dye in stationary fluid is governed by (2.2) with $v = 0$ and $W = 0$. In this case the word "diffusion" reflects existence of the physical molecular diffusion process represented by a random walk of the dye molecules causing spreading of the dye into uncolored fluid. The Markov diffusion process specified by the Ito stochastic equation $dx_i^* = (2D)^{1/2} dw_i^*$ would represent a good mathematical model of this molecular random-walk provided the value D matches the physical value of the diffusion coefficient (here w_i^* represent independent Wiener processes which are commonly used in constructing stochastic models). We should note that the Markov diffusion process is not necessarily identical to the physical random-walk of the dye molecules but the former would certainly represent an adequate mathematical model of the latter. Thus the physical interpretation of the equations involving direct parabolicity is, usually, not very difficult: using the Ito equations, one can build a Markov diffusion process which corresponds to the original diffusion equation. This Markov process should represent a reasonable model of the physical process which is described by the diffusion equation, provided that the coefficients of the Ito equation are matched well with the corresponding physical properties.

On the face of the problem the physical interpretation of the inverse-parabolic equation (2.1) is only marginally more complicated than the problems considered in the previous paragraph. One needs to introduce the reversed time $\tau \equiv -t$ and rewrite (2.1) as an

equation with direct parabolicity,

$$\frac{\partial F^-}{\partial \tau} + \frac{\partial u_i^- F^-}{\partial x_i} + \frac{\partial A_I^- F^-}{\partial z_I} - \frac{\partial^2 \hat{B}_{IJ} F^-}{\partial z_I \partial z_J} = 0 \quad (3.1)$$

where

$$A_I^- \equiv -A_I, \quad u_i^- \equiv -\dot{u}_i, \quad \tau \equiv -t.$$

Equation (3.1), obviously, satisfied by $F^- = P$ and, at the same time, it can be interpreted as the reversed-time Fokker-Planck equation (with drift coefficients u_i^- and A_I^- and the diffusion coefficients \hat{B}_{IJ}) which governs the transitional probabilities for the Ito equation represented by the following system of stochastic equations

$$dx_i^- = u_i^- d\tau, \quad dz_I^- = A_I^- d\tau + b_{IJ} \overset{\text{Ito}}{\cdot} dw_J^- \quad (3.2)$$

where $\hat{B}_{IJ} = b_{IK} b_{JK}/2$ and w_J^- represents the Wiener processes driving the stochastic processes z_I^- and x_i^- backward in time. The symbol “Ito” indicates that the product should be evaluated in the “Ito sense” backward in time, that is, if $d\tau$ is positive, b_{IJ} is evaluated at τ but not at $\tau + d\tau$. This interpretation of the PDF equation is formally correct – the PDF of the constructed Markov process should coincide with P (provided the values of the coefficients \dot{u}_i , A_I and \hat{B}_{IJ} are specified in agreement with their physical definitions (2.3) and the initial distribution for the stochastic trajectories are set in accordance with P). We use a new function F^- in (2.1), since in addition to $F^- = P$, the function F^- may represent other solutions of the Fokker-Planck equation, depending also on normalization and the initial conditions (for example, the transitional probabilities).

Although the constructed stochastic process models the PDF P well, we must refrain from claiming any deeper similarity between the model and some physical processes in turbulent flows (as we did while considering molecular diffusion of dye controlled by equations with direct parabolicity). It is not obvious if (and how) the stochastic trajectories specified by (3.2) can be associated with some physical trajectories. Indeed, all physical processes evolve forward in time while the constructed model develops backward in time, and it would be very difficult to specify a physical process which can correspond to the model. In order to illustrate this difficulty we introduce the following notation:

- *Realization of the process* – a particular trajectory represented by a specific solution of the Ito equation;
- *Markov process* – combines many realizations according to their probabilities. The Markov process is characterized by the diffusion and drift coefficients and by a certain PDF (such as P) which satisfies the Fokker-Planck equation and certain initial conditions;
- *Markov family* – is characterized by certain diffusion and drift coefficients but comprise many Markov processes which correspond to different solutions of the same Fokker-Planck equation with different initial conditions. The family does not correspond to a single PDF (such as P) but to all possible PDFs satisfying a given Fokker-Planck equation.

In the case of dye diffusion, we found that not only a particular Markov process, but also its family, correspond well to the physics of the problem (indeed, let us consider diffusion of the dye as a passive substance with different initial conditions). In the case of the reversed-time process, only the modeling Markov process is assigned a certain physical significance, not its family. This can be illustrated by the following consideration. Let us assume that at $t = t_0$ (and $\tau = \tau_0 \equiv -t_0$) the PDF is slightly altered due to some external influence $F^- = P + F'$ instead of $F^- = P$. Physically, the F^- would be different

from its original prognosis P for some time after t_0 (that is for $t > t_0$) while the PDF F^- of the process specified by (3.1) and (3.2) would differ for some time before t_0 (that is $\tau > \tau_0$). This illustrates that the coefficients of (3.1) and (3.2) must change for $t > t_0$ if the PDF is disturbed at $t = t_0$. Hence, although the Markov process $F^- = P$ models the actual joint PDF P , the other processes from the same Markov family (represented by the other solutions of the same equation (3.1)) do not correspond well to the physical processes in turbulent flows.

4. The forward-time diffusion model

The difficulties that we experienced in the previous section in finding a good physical interpretation of the reversed-time diffusion model are, obviously, related to the fact that physical processes develop forward in time. Thus, it would be desirable to reverse the reversed-time process and force it to develop forward in time. We have a Markov process with the PDF $F^- = P$ which evolves backward in time, and we wish to find another Markov process which evolves forward in time and which is equivalent to the original process. That is, if the trajectories of the first process are shown on a photograph, they are indistinguishable from the trajectories of the second process. However, one can easily distinguish the processes while watching their animated evolutions – they will propagate in opposite directions. The possibility of reversing a Markov process is not obvious, but is proved in the special Anderson (1982) theorem. It should also be noted that only a specific Markov process, but not its whole Markov family, can be reversed in time, and the original and reversed processes may belong to different Markov families. The original and reversed processes form adjoint couples – an attempt to reverse the reversed process once more yields the original process. It should be noted that, although the Fokker-Planck equation is essentially the same as the direct Kolmogorov equation of a Markov process, the inverse Kolmogorov equation of the same process should not be confused with the Fokker-Planck equation of the reversed-time process. The inverse Kolmogorov equation deals with transitional probabilities of the process, which are not specifically considered in this section.

The Anderson (1982) equations, applied to the reversed-time diffusion model specified by $F^- = P$ and by (3.1) – (3.2), indicate that the Fokker-Planck equation for the forward-time diffusion model is given by

$$\frac{\partial F^+}{\partial t} + \frac{\partial u_i^+ F^+}{\partial x_i} + \frac{\partial A_I^+ F^+}{\partial z_I} - \frac{\partial^2 \hat{B}_{IJ} F^+}{\partial z_I \partial z_J} = 0 \quad (4.1)$$

where

$$A_I^+ \equiv \hat{A}_I + \frac{2}{P} \frac{\partial \hat{B}_{IJ} P}{\partial z_J}, \quad u_i^+ \equiv \hat{u}_i$$

The Ito equation, which corresponds to (4.1), is specified by

$$dx_i^+ = u_i^+ dt, \quad dz_I^+ = A_I^+ dt + b_{IJ} \overset{\text{Ito}^+}{\cdot} dw_J^+ \quad (4.2)$$

The symbol “Ito⁺” indicates that the product should be evaluated as an Ito product forward in time, and $\hat{B}_{IJ} = b_{IK} b_{JK}/2$. The Anderson theorem provides even the possibility to reverse particular realizations of a Markov process, that is $x_i^+(-\tau) = x_i^-(\tau)$ and $z_i^+(-\tau) = z_i^-(\tau)$ provided the forward and backward Wiener processes are linked by the

equation

$$dw_J^+ = dw_J^- + \Phi_A(\mathbf{z}^-(\tau), \mathbf{x}^-(\tau), \tau) d\tau, \quad \Phi_A(\mathbf{z}, \mathbf{x}, -t) \equiv \frac{1}{P} \frac{\partial b_{IJ} P}{\partial z_I} \quad (4.3)$$

We emphasize that, of course, all differentials in this equation (and in other equations of the present work) are evaluated in the same direction in time. The proof that the stochastic process w_J^+ defined by (4.3) may be treated as a Wiener process is far from trivial and can be found in Anderson (1982).

The trajectories specified by s (3.2) and (4.2) can be conventionally called "the stochastic particles". Although the stochastic trajectories specified by (4.2) coincide with the stochastic trajectories of the reversed-time model, the process (4.2) is more convenient for our purposes, since it evolves forward in time. In the following sections, we demonstrate that, for the Markov family specified by (4.2) and (4.2), its physical analog (i.e. a physical process in a turbulent flow which can reasonably be modelled by the family) can be found. The family of stochastic trajectories, which are specified by (4.2), can be associated with some physical trajectories in a turbulent flow.

5. The physical process

We consider the Lagrangian fluid particles transported by a turbulent flow jointly with the fields specified by (2.2), and introduce the following conditional expectation:

$$Q = Q(\mathbf{z}, \mathbf{x}, t) \equiv \langle f | \mathbf{Z} = \mathbf{z} \rangle \quad (5.1)$$

where $f = f(\mathbf{x}, t)$ represents the concentration of the fluid particles. The fluid particles are transported according to the equations

$$dx_i^* = v_i(\mathbf{x}^*(t), t) dt, \quad \frac{\partial f}{\partial t} + \frac{\partial v_i f}{\partial x_i} = 0 \quad (5.2)$$

The second equation in (5.2), representing the transport equation for f , is equivalent to the first equation in (5.2) specifying the fluid particle trajectories $\mathbf{x}^*(t)$. The function f also allows us to select some of the fluid particles (f set to 1 for the selected fluid particles and f set to 0 for others) or assign each fluid particle a certain weight f .

At this point we declare that the stochastic particles of the forward-time diffusion model are considered to be a model for the turbulent transport of fluid particles. In order to be accurate in this declaration, we should state how the properties of the particle transport are simulated by the model. Specifically, we assume that $F^+ = QP$, that is, F^+ is a model for QP . The different Markov processes which belong to the family of (4.1) are interpreted as variations of Q , while P remains the same for the whole family. Since $f = 1$ obviously satisfies (5.2) and $F^+ = P$ satisfies (4.1), the forward-time model is trivial if it is restricted only to $F^+ = P$. The assumed similarity of turbulent transport of fluid particles and a forward-time process is a hypothesis which is expected to be valid for any reasonable initial $Q \neq 1$.

The physical interpretation of modeling stochastic trajectories needs some clarification. Let us assume that the PDF $P = P(\mathbf{z}, \mathbf{x}, t)$ is represented by a very large number of trajectories of the stochastic particles on the time interval $t_1 \leq t \leq t_2$. These trajectories can be obtained equivalently by a) solving (3.2) backward in time from the initial distribution of the particles in \mathbf{z} - \mathbf{x} -space at $t = t_2$ specified by $P(\mathbf{z}, \mathbf{x}, t_2)$; or b) solving s (4.2) forward in time from the initial distribution of the particles in \mathbf{z} - \mathbf{x} -space at $t = t_1$ specified by $P(\mathbf{z}, \mathbf{x}, t_1)$. We wish to select some of the stochastic particles so that their

distribution $F(\mathbf{z}, \mathbf{x}, t)$ models the distribution of marked fluid particles in \mathbf{z} - \mathbf{x} -space for $t_1 \leq t \leq t_2$ (i.e. $F = QP$ but $Q \neq 1$ since f is different for marked and non-marked fluid particles). In order to find $F(\mathbf{z}, \mathbf{x}, t)$, we can select the stochastic particles so that their distribution at $t = t_1$ is given by $F(\mathbf{z}, \mathbf{x}, t_1)$. The particles must be selected solely on the basis of their positions in \mathbf{z} - \mathbf{x} -space at $t = t_1$ (i.e. by ignoring their future trajectories). The distribution of the selected stochastic particles for $t_1 \leq t \leq t_2$ corresponds to $F(\mathbf{z}, \mathbf{x}, t)$. (The same effect can be achieved by assigning the initial weights of $Q(\mathbf{z}, \mathbf{x}, t_1)$ to all stochastic particles. Here, \mathbf{z} and \mathbf{x} are determined by the location of each stochastic particle at $t = t_1$.) It should be noted that selecting the stochastic trajectories on the basis of particle positions at $t = t_2$ and the distribution $F(\mathbf{z}, \mathbf{x}, t_2)$ would not, generally, give the expected distribution $F(\mathbf{z}, \mathbf{x}, t)$ for the time interval $t_1 \leq t < t_2$. The suggested interpretation allows us to model stochastic behavior of a single fluid particle with a given initial location $\mathbf{z}_1, \mathbf{x}_1$ in \mathbf{z} - \mathbf{x} -space. This can be done by selecting $Q \sim \delta(\mathbf{z} - \mathbf{z}_1)\delta(\mathbf{x} - \mathbf{x}_1)$, where the Delta function applied to the vector arguments denotes the product of the Delta functions applied to the components.

In the next section, we assess the pluses and minuses of the forward-time diffusion model and its physical interpretation. This can be done by introducing a model which belongs to the same class as the forward-time diffusion model and, to the best of our knowledge, is the optimal model from this class.

6. The optimal diffusion model

Assuming that the evolution of the function $F^+ = QP$ can be specified by the following equation

$$\frac{\partial F^+}{\partial t} + \frac{\partial u_i F^+}{\partial x_i} + \frac{\partial A_I F^+}{\partial z_I} - \frac{\partial^2 B_{IJ} F^+}{\partial z_I \partial z_J} = 0 \quad (6.1)$$

with the coefficients $u_i(\mathbf{z}, \mathbf{x}, t)$, $A_I(\mathbf{z}, \mathbf{x}, t)$ and $B_{IJ}(\mathbf{z}, \mathbf{x}, t)$ which are not known a priori, the goal of this section is to find the definitions of these coefficients which comply with known properties of turbulence. The coefficients are then to be compared with the corresponding coefficients of the forward-time diffusion model. First, we note that integration of (6.1) over all z_I should result in the averaged scalar-transport equation, $\partial \langle f \rangle / \partial t + \operatorname{div} \langle \mathbf{v} f \rangle = 0$. This condition implies that

$$\int u_i Q P dz = \int \hat{u}_i Q P dz.$$

Since these integrals must be the same for any Q we conclude that

$$u_i = \hat{u}_i. \quad (6.2)$$

The second constraint is that $F^+ = P$ (i.e. $Q = 1$) is a solution of (6.1). This condition can be satisfied if

$$A_I = \hat{A}_I + \frac{1}{P} \frac{\partial (\hat{B}_{IJ} + B_{IJ}) P}{\partial z_J} \quad (6.3)$$

Here we use the fact that P is governed by (2.1). The third constraint is related to the Kolmogorov (1941) theory of small-scale turbulence and the Richardson (1926) law of turbulent dispersion. According to the Kolmogorov theory, the turbulent dispersion of particles at small scales (although exceeding the viscous scales of turbulence) is determined by the average dissipation of energy and, if any scalar fields are involved, by the average scalar dissipation. Since the characteristics considered here are conditional, we

assume that the conditional dissipation terms \hat{B}_{IJ} are to be used. The evolution of F^+ with sharp initial conditions (e.g. $F^+ \sim \delta(\mathbf{z} - \mathbf{z}_1)\delta(\mathbf{x} - \mathbf{x}_1)$ as previously considered) is determined by the diffusion term of (6.1) which is characterized by the coefficient B_{IJ} . Thus we can write

$$\mathbf{B} \sim \hat{\mathbf{B}} \quad (6.4)$$

The vector-type notation used in this equation indicates a certain link or a general compatibility of magnitudes between the values B_{IJ} and \hat{B}_{IJ} and it does not mean that B_{IJ} and \hat{B}_{IJ} are the same.

In order to investigate the other constraints which can be applied to the coefficients, it is convenient to rewrite (6.1) as an equation for Q

$$\frac{\partial Q}{\partial t} + \hat{u}_i \frac{\partial Q}{\partial x_i} + A_I^\circ \frac{\partial Q}{\partial z_I} - B_{IJ} \frac{\partial^2 Q}{\partial z_I \partial z_J} = S \quad (6.5)$$

where $S \equiv 0$,

$$A_I^\circ \equiv A_I - \frac{2}{P} \frac{\partial B_{IJ} P}{\partial z_J} = \hat{A}_I + \frac{1}{P} \frac{\partial (\hat{B}_{IJ} - B_{IJ}) P}{\partial z_J} \quad (6.6)$$

and we take into account s (2.1), (6.2) and (6.3). Equation (6.5) corresponds to Conditional Moment Closure (CMC — Klimenko & Bilger 1999) with multiple velocity-scalar conditioning. Another constraint, which can be called “the linear constraint”, is conventional in CMC and explores similarity between scalars f and Z_4, \dots, Z_n . Indeed, since we neglect all differential diffusion effects, the conditional characteristics of the scalar f , which satisfies the equation

$$\frac{\partial f}{\partial t} + \frac{\partial v_i f}{\partial x_i} - D \frac{\partial^2 f}{\partial x_i \partial x_i} = S \quad (6.7)$$

should be similar to these of the scalar f , which satisfies (5.2). Effectively, the replacement of (5.2) by (6.7) introduces the diffusing particles of Dreeben & Pope (1997), transported by the turbulence according to

$$dx_i^* = v_i(\mathbf{x}^*(t), t) dt + \sqrt{2D} dw_i^* \quad (6.8)$$

The Brownian-type fluctuations, which are induced by the Wiener processes w_i^* , simulate the molecular-diffusion effects. In addition, if $S = S(Z_4, \dots, Z_n) \neq 0$, the particles are allowed to appear (for $S > 0$) or disappear (for $S < 0$). The extension of the forward-time Markov model to these particles is reasonable since, if the Lagrangian trajectories in the phase space of the scalars Z_4, \dots, Z_n are well-represented by the Markov process $z_4^+(t), \dots, z_n^+(t)$, then any deterministic function $S = S(z_4^+, \dots, z_n^+)$ should also possess the Markov property. (Here we assume that, as in the chemical reactions, the source term S and the other source terms W_α are deterministic functions of the scalars Z_4, \dots, Z_n). The purpose of the extension is to utilize the similarity of turbulent transport of scalars f and Z_4, \dots, Z_n by making the transport equation for f similar to (2.2). At this point we note that $f = a_\alpha Z_\alpha + a_0$, $S = a_\alpha W_\alpha$ form a solution of (6.7) where a_α and a_0 are arbitrary constants. Hence $Q = a_\alpha Z_\alpha + a_0$, $S = a_\alpha W_\alpha$ must satisfy (5.1). This constraint leads us to the relation $A_\alpha^\circ = \hat{A}_\alpha$ which, if we take into consideration (6.6), means in practice that

$$B_{\alpha I} = \hat{B}_{\alpha I} \quad (6.9)$$

Note that the matrices B_{JI} and \hat{B}_{JI} are symmetric.

Although application of the linear constraint to the scalar quantities is a common

practice in Conditional Methods, a similar constraint should not be applied to the velocity components z_i ($i = 1, 2, 3$) (Klimenko 1998, Weinman & Klimenko 2000). Due to the specific nature of the pressure gradient, which cannot be expressed as a deterministic function of velocities and scalars, the turbulent transport of momentum is quite different from the turbulent transport of scalars. This point can be illustrated by assuming, in the spirit of (6.4), that

$$B_{ij} = \frac{3}{2} C_0 \hat{B}_{ij} \quad (6.10)$$

where C_0 is, effectively, the so-called Kolmogorov constant. The linear constraint applied to velocities would require $C_0 = 2/3$. Although this value was suggested in one of the early works (Krasnoff & Peskin 1971), the value of $C_0 = 2/3$ is not consistent with DNS and experiments for particle diffusion in turbulent flows. DNS indicate that C_0 is about 2 (Yeung & Pope 1989, Weinman & Klimenko 2000) while it is expected that $C_0 \sim 7$ when the Reynolds number becomes very large (Sawford 1991). These acceptable values for C_0 are noticeably larger than 2/3.

Comparison of the optimal diffusion model with the forward-time model indicates that all coefficients are the same with exception of B_{ij} – the 3×3 matrix of the diffusion rate in the velocity phase space. The forward-time diffusion model corresponds to $C_0 = 2/3$ which significantly underestimates the diffusion rate in the velocity space.

7. Conclusions

The transport equations for joint velocity/scalar PDFs are considered and the possibility of interpreting the inverse-parabolic terms in these equations as reversed-time diffusion has been investigated. This interpretation presumes that the reversed-time diffusion process (that is, a Markov diffusion process which corresponds to the PDF equation) can be interpreted as a model for certain physical processes in turbulence. Although we found that the physical process of Lagrangian dispersion of fluid particles in a turbulent flow may be modeled by the trajectories of the diffusion process mentioned above, this possibility needs certain qualifications:

1) Since the trajectories of the reversed-time diffusion process are propagating backwards in time, they have to be reversed in time to match the properties of fluid particles which, obviously, develop forward in time. We call the result of reversing the reversed-time diffusion process the “forward-time diffusion model”.

2) The forward-time diffusion model also represents a Markov process, although it belongs to a different Markov family (i.e. the transport coefficients of the model and the original PDF equation are not the same). The forward-time diffusion process is naturally associated with the original PDF transport equation and, at the same time, has a direct link to the equations used in the Conditional Moment Closure methods.

3) The forward-time diffusion model does generally comply with theoretical expectations for a Markov model of this kind. However, the forward-time diffusion model underpredicts the rate of diffusion in velocity space, while the prediction for the rate of diffusion in scalar space is accurate. These diffusion rates affect predictions for the turbulent dispersion from a localized source.

4) The optimal diffusion model (i.e. the best model from the same class of models) largely coincides with the forward-time diffusion model, except for the coefficients B_{ij} determining the diffusion rate in the velocity space. These coefficients should be 3 to 10 times larger in the optimal model.

Acknowledgments

This work has been performed during the sabbatical stay of the author at CTR. This stay has been supported by CTR and The University of Queensland.

REFERENCES

- ANDERSON, B. 1982 Reverse-time diffusion equation models. *Stochastic Processes and their Application* **12**, 313–326.
- DOPAZO, C. 1994 Recent developments in Pdf methods. In *Turbulent Reacting Flows*, (P. A. Libby & F. A. Williams, eds.) Academic Press, London, pp. 375–474.
- DREEBEN, T. D. & POPE, S. B. 1997 Probability density function and Reynolds-stress modeling of near-wall turbulent flows. *Phys. Fluids* **9**, 154–163.
- KLIMENKO, A. & BILGER, R. 1999 Conditional moment closure for turbulent combustion. *Prog. Energy Combust. Sci.* **25**, 595–687.
- KLIMENKO, A. Y. 1998 Conditional methods in application for Lagrangian modelling. *Phys. Fluids* **10**, 922–927.
- KOLMOGOROV, A. N. 1941 The local structure of turbulence in incompressible viscous fluid for very large Reynolds numbers. *C.R. Acad. Sci. U.S.S.R.* (4), 301–305.
- KRASNOFF, E. & PESKIN, R. L. 1971 The Langevin model for turbulent diffusion. *Geophys. Fluid Dyn.* **2**, 123.
- KUZNETSOV, V. & SABELNIKOV, V. 1989 *Turbulence and combustion*. Hemisphere/McGraw-Hill, New York.
- POPE, S. 1985 Pdf methods for turbulent reactive flows. *Prog. Energy Combust. Sci.* **11**, 119–192.
- POPE, S. B. 2000 *Turbulent Flows*. Cambridge University Press.
- RICHARDSON, L. F. 1926 Atmospheric diffusion shown on a distance-neighbour graph. *Proc. Roy. Soc.* pp. 709–737.
- SAWFORD, B. L. 1991 Reynolds number effects in Lagrangian statistical models of turbulent dispersion. *Physics of Fluids* **A-3**, 1577.
- WEINMAN, K. A. & KLIMENKO, A. Y. 2000 Estimation of the Kolmogorov constant c_0 by DNS of a continuous scalar. *Physics of Fluids* **11**, 3205–3220.
- YEUNG, P. K. & POPE, S. 1989 Lagrangian statistics from direct numerical simulations of isotropic turbulence. *J. Fluid Mech.* **207**, 531–586.



Filtered density-function modeling for large-eddy simulations of turbulent reacting flows

By Chong M. Cha AND Philippe Trouillet

1. Motivation and objectives

Large-eddy simulations (LES) have become practical for describing turbulent mixing in flows of engineering interest. At high Reynolds numbers, the response of small-scale mixing dynamics to the large-scale eddies is thought to be universal. Since only the unresolved small-scale (or subgrid-scale) processes require modeling in an LES, it is believed to be more robust than Reynolds-averaged (RANS) turbulence modeling, which also models the large-scale dynamics and hence must be tuned for different geometries.

In turbulent reacting flows of practical interest, the chemical scales can be even smaller than the smallest turbulence scales. With initially-nonpremixed reactants, the separation of chemical and turbulence scales allows a presumed beta PDF and the steady flamelet model to describe the subgrid-scale mixing and reaction processes, respectively, in a LES (Cook & Riley 1994; Cook *et al.* 1997; Cook & Riley 1997). (The unsteady response of flamelets to residence-time effects in an LES has been accounted for by Pitsch & Steiner (2000a,b).) The feedback of these subgrid-scale processes create significant density changes which impact the large-scale dynamics which, in turn, drive the modeled small-scale processes. Thus, a breakdown of flamelet modeling at the subgrid scale, for example when local extinction and reignition events become significant (Sripakagorn *et al.* 2000), would invalidate the entire LES calculation.

With regard to local extinction, fluctuations due to internal intermittency have yet to be accounted for in an LES of any turbulent reacting flow. Although of little importance for first- and second-order moment predictions without reaction (Pope 2000), their effect has a nontrivial impact on stable burning, either in a flamelet or distributed reaction mode. This is especially important with present implementations based on flamelet modeling, where no entirely satisfactory mechanism for reignition yet exists (Pitsch *et al.* 2002).

The present work focuses on the filtered-density-function (FDF) approach and its variants (Colucci *et al.* 1999; Jaberi *et al.* 1999). In the FDF approach, subgrid-scale processes are described by Lagrangian Monte Carlo calculations of the “large-eddy probability density function” (Gao & O’Brien 1993) for, most generally, the joint large-eddy PDF of velocity, the reacting scalars, and the dissipation. (The additional dissipation dimension would be required to account for intermittency effects (Pope 1990).)

The dominant mechanism by which local reignition occurs in a turbulent flow is not completely understood. DNS with initially-nonpremixed reactants in three-dimensional turbulence (Sripakagorn *et al.* 2000) seem to suggest that reignition occurs primarily by convective transport. Alternatively, triple-flame propagation may be the dominant mechanism, as seen in two-dimensional “turbulence” simulations of autoignition (Domingo & Vervisch 1996). Accounting for the latter mechanism in an FDF approach may be prohibitively expensive computationally. For turbulence at high Reynolds number, the

expectation is that the former mechanism will dominate (Hewson & Kerstein 2001). Reignition by distributed combustion can be described by the FDF approach.

These potentially attractive features of the family of FDF approaches, e.g., for describing local extinction and reignition, motivate the present work. "FDF" is henceforth used to represent any of the variations of the transported large-eddy PDF approaches (Colucci *et al.* 1999; Jaber *et al.* 1999) that also exist analogously in the RANS case (Pope 1985). In the FDF approach, the time-dependent structure of the turbulence down to the Taylor scale is reproduced; changes at finer resolution are accounted for by modeling the effective diffusion at the unresolved scales. This is represented by the conditionally-averaged molecular mixing term in the joint PDF equation. Closure is obtained by modeling this term with the available single-point information, which then requires the spatial correlation to be prescribed *via* a characteristic length or time scale. Current micro-mixing models for reacting scalars ignore the influence of chemistry on this time scale by using the turbulent time scale of a conserved scalar in place of the reacting-scalar time scale. This implicitly assumes distributed combustion. With realistic, Arrhenius kinetics, the large activation temperature steepens the local gradients of a reacting scalar, decreasing its length or time scale as compared to the conserved scalar under the same turbulent velocity field. Thus, for sufficiently fast chemistry, the generally used estimate of substituting the time scale of the reacting scalar by that of a conserved scalar can significantly overestimate the true mixing time for the reacting scalar.

An improved approach for modeling the time scale of a turbulent reacting scalar, valid in both the flamelet and distributed-combustion limits, has been developed by Cha (2001) and Cha & Trouillet (2002) within a RANS framework. The model can readily be applied to any existing micro-mixing model where the time scales of the reacting scalars appear explicitly. This would include classic linear-mean-square estimation (LMSE) (Dopazo 1975), extended LMSE (Sabel'nikov & Gorokhovski 2001), and the variants of Curl's approach (Norris & Pope 1991), to name a few. The issues arising from its application with a RANS turbulence model are discussed in Cha (2001) and Cha & Trouillet (2002). For inhomogeneous turbulent flows, the assumption of local homogeneity and isotropy within a computational volume was made.

The objective of the present work is to validate the analogous time-scale model for a reacting scalar in an LES framework. At present, the phenomena of local extinction and reignition are not addressed. Note that to describe local extinction with a mixing-limited combustion mode, a subgrid-scale mixing model must first be able to treat flamelet combustion, by definition. The new modeling presented in this paper addresses this specific issue. The expectation is better performance in a LES framework as compared to the RANS case, as the assumption of local homogeneity and isotropy below the Taylor scale (for LES) *vis-à-vis* at the sub-integral scale (for RANS) would be more accurate. The modeling validation is performed using the direct numerical simulation (DNS) of a turbulent reacting jet (Boersma 1999), which was also used for the RANS validation case in Cha & Trouillet (2002).

The paper is organized as follows. In the next section, the numerical experiment of Boersma (1999), which simulates a reacting jet with a single-step reaction, is described. In section 3, the micro-mixing model is described within the LES framework. In section 4, results of the modeling study using the DNS of the jet flame are presented and discussed. Conclusions are given in section 5.

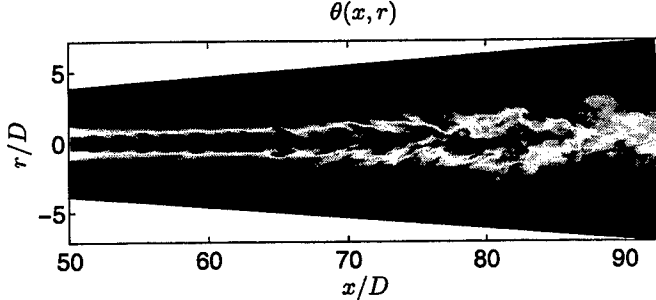


FIGURE 1. Temperature field from the turbulent reacting jet DNS of Boersma (1999). The planar slice shown lies on the jet centerline. Axial and radial distances are nondimensionalized by D , the jet nozzle diameter. The Reynolds number based on fuel-nozzle exit conditions is 4,000.

2. Numerical experiment

The *a priori* validation study uses the DNS of a turbulent reacting jet performed by Boersma (1999). Briefly, the Reynolds number based on fuel-nozzle exit conditions is 4,000. A global, second-order, irreversible reaction where one mole of fuel (F) reacts with one mole of oxidizer (O) to form two moles of product (P) is considered:



The chemical source terms for fuel, oxidizer, and product are $\dot{s}_F = -\dot{s}$, $\dot{s}_O = -\dot{s}$, and $\dot{s}_P = 2\dot{s}$, respectively, where

$$\dot{s} = k\rho\psi_F\psi_O \quad (2.1b)$$

$$k = A \exp \left[-\frac{Ze(1-\theta)}{1-\alpha(1-\theta)} \right]. \quad (2.1c)$$

Here, ψ_j represents the mass fraction of the j -th species ($j = F, O$, or P), ρ is the mixture density, A is an effective frequency factor, $\alpha \equiv (T_f - T_\infty)/T_f$ is the heat-release parameter, $Ze \equiv \alpha T_a/T_f$ is the Zeldovich number, and $\theta \equiv (T - T_\infty)/(T_f - T_\infty)$ is the normalized temperature with T_a , T_f , and T_∞ the activation, flame, and reference temperatures, respectively. The chemical-kinetic rate parameters were chosen to approximate methane/air combustion with 300 K temperatures for the initially segregated F and O streams: $A = 10^5$, $\alpha = 0.8$, and $Ze = 8.0$. The Schmidt number is 0.75 and Lewis numbers are unity. Heat release is accounted for, with a maximum density ratio of approximately 5. The molecular diffusivities and viscosity are temperature-dependent. See Boersma (1999) for details of the simulation.

Bilger's mixture fraction for this system can be written as

$$\xi = \frac{1}{2}(\psi_F - \psi_O + 1),$$

one of three linear combinations of the reactive scalars (Shvab-Zeldovich coupling functions) for this case, which eliminates the chemical source term and conveniently normalizes this passive scalar such that it is unity in pure fuel and zero in pure oxidizer (Bilger 1980). For the present case, fuel and oxidizer are in stoichiometric proportion at $\xi = \xi_{st} = 1/2$. The dissipation rate of passive-scalar energy is represented by $\chi \equiv 2\mathcal{D}(\nabla\xi)^2$, where \mathcal{D} is the diffusion coefficient of ξ . In a turbulent flow, χ reduces the variance of ξ , thus characterizing the rate of mixing which drives ξ to its mean value. For nonpremixed systems, the local $\chi(t, \xi)$ describes the flux of fuel and oxidizer into the reaction zone at $\xi = \xi_{st}$ (Peters 1984). For the present kinetic rate parameters, if χ exceeds a value of 4.2 sec^{-1} , the rate of mixing in ξ phase space exceeds the chemical

production rate and extinguishes the flame. That is, 4.2 is the quenching value of the scalar dissipation rate, $\chi = \chi_q$, as given by the steady flamelet solution (Peters 1984).

Figure 1 shows the typical, instantaneous spatial distribution of the temperature field, θ , from the DNS of the jet flame. The typical LES computational grid would not resolve the entire range of turbulent scales shown. Accounting for the unresolved turbulent structure is a turbulence modeling issue. Accounting for the unresolved spatial structure of the reactive scalars is a combustion modeling issue and is discussed next.

3. Modeling

Within an LES computational volume, the transport equation for the subgrid-scale variance of the j -th reacting scalar can be written as

$$\frac{1}{\langle \psi_j'^2 \rangle} \frac{d\langle \psi_j'^2 \rangle}{dt} - \frac{\langle s'_j \psi'_j \rangle}{\langle \psi_j'^2 \rangle} = -\frac{\langle 2D(\nabla \psi_j)^2 \rangle}{\langle \psi_j'^2 \rangle} \equiv \frac{1}{T_j}. \quad (3.1)$$

where local homogeneity and isotropy have been assumed. Here, $\langle (\cdot) \rangle$ denotes the LES filtering operation, $\langle \psi_j'^2 \rangle \equiv \langle \psi_j^2 \rangle - \langle \psi_j \rangle^2$ is the subgrid-scale variance, $\langle s'_j \psi'_j \rangle \equiv \langle s_j \psi_j \rangle - \langle s_j \rangle \langle \psi_j \rangle$ is the subgrid-scale covariance of s_j , the chemical source term of the j -th species, with ψ_j , and $\langle 2D(\nabla \psi_j)^2 \rangle \equiv \chi_j$ is the scalar dissipation rate of the j -th scalar. The time scale of the j -th reactive scalar, T_j , is then $T_j = \langle \psi_j'^2 \rangle / \langle \chi_j \rangle$. If $s_j = 0$, then ψ_j is a conserved or passive scalar, ξ , by definition. We denote the time scale of the passive scalar by $T = \langle \xi'^2 \rangle / \langle \chi \rangle$, which can be related to the time scale of the turbulence (Pope 1985).

The limit of infinitely-fast chemistry of a simple chemistry case is worth elucidating: For a global, one-step, irreversible reaction, $s_j = 0$ outside an infinitely-thin reaction zone, transport is then governed by turbulent mixing and $T_j = T$. In the frozen chemistry limit, $s_j \equiv 0$ and trivially $T_j = T$. Current particle-interaction models used in Lagrangian Monte Carlo simulations are valid in these limits.

In the slow-chemistry limit, the transport of a reacting scalar is governed primarily by advective stirring (distributed combustion) and $T_j \approx T$. Then, for unity Schmidt number, the time scale of ψ_j can be constructed with the relevant turbulent length scale and diffusivity. For an LES, $T \sim \Delta^2 / \nu_t$ (Jaberi *et al.* 1999), where Δ is the grid width and ν_t the subgrid eddy viscosity. In the fast, but not infinitely fast, chemistry limit (flamelet combustion), T_j can deviate from T by an order of magnitude over an integral time scale (Cha 2001; Cha & Trouillet 2002);

Thus, current particle-interaction models, which replace the mixing time scale of a reactive scalar by the turbulence time scale, are not valid in this limit. Formulation of the model for the T_j/T ratio for the LES case readily follows from the work of Cha (2001) and Cha & Trouillet (2002). The model is based on (i) mapping closure, which describes the effects from the mixing at the sub-Taylor scale in this LES case, and (ii) flamelet modeling, which relates the mapping functions for the passive and reactive scalars. The synthesis of these modeling elements is described in the following subsections.

3.1. Passive-scalar mixing

Mapping closure was originally conceived by Chen *et al.* (1989) to describe the probability distribution of a passive scalar field advected by Navier-Stokes turbulence. Briefly, mapping closure provides the transformation from a standard, Gaussian reference field, z_0 , enforcing the exact transport equation for ξ of a binary mixing problem. Denoting the

transformation by $z_0 \xrightarrow{X} \xi$, the generally nonlinear mapping, X , then describes the deviation of p_ξ from the standard, Gaussian distribution of z_0 , $p_{z_0} \equiv (1/2\pi)^{1/2} \exp(-z_0^2/2)$. Using X , the fine-scale mixing and probability distribution of ξ at scales below which $\langle(\cdot)\rangle$ is defined can be directly calculated using (Chen *et al.* 1989)

$$\langle D(\nabla \xi)^2 | \xi = \eta \rangle = \langle D(\nabla \xi)^2 \rangle \frac{(\partial X / \partial z_0)^2}{\langle (\partial X / \partial z_0)^2 \rangle} \quad (3.2a)$$

$$p_\xi = \frac{1}{\partial X / \partial z_0} p_{z_0}, \quad (3.2b)$$

respectively. With local homogeneity and isotropy assumed within an LES computational cell, the analytical developments of Gao (1991*b,a*) and O'Brien & Jiang (1991) can be applied to give (Cha & Trouillet 2002)

$$X(z_0) = \xi^- + \frac{1}{2} (\xi^+ - \xi^-) \left\{ 1 + \text{erf} \left[\frac{z_0}{\sqrt{2}\Sigma} - \beta \text{erf}^{-1} \left(2 \frac{\xi^+ - \langle \xi \rangle}{\xi^+ - \xi^-} - 1 \right) \right] \right\} \quad (3.3a)$$

$$p_\xi(\eta) = \Sigma \exp \left\{ \gamma^2 - \Sigma \left[\gamma + \beta \text{erf}^{-1} \left(2 \frac{\xi^+ - \langle \xi \rangle}{\xi^+ - \xi^-} - 1 \right) \right]^2 - \log(\xi^+ - \xi^-) \right\} \quad (3.3b)$$

valid for each LES computational cell, with the spatial average $\langle \xi \rangle$, subgrid rms ξ' and $\langle \chi \rangle$ given by a suitable SGS turbulence model. Here, ξ^- and ξ^+ are the minimum and maximum values of ξ in each LES computational cell, Σ is determined from the subgrid-scale variance, η is the sample space variable of ξ , $\gamma \equiv \text{erf}^{-1}(2(\eta - \xi^-)/(\xi^+ - \xi^-) - 1)$, and $\beta \equiv (1 + 1/\Sigma^2)^{1/2}$. In an LES using the FDF approach, the values of $\langle \xi \rangle$ and $\langle \xi'^2 \rangle$ are known at each time in each cell. Estimates of ξ^- and ξ^+ are known from the information carried by the ensemble of notional particles.

The current standard modeling practice in LES calculations is to construct passive-scalar mixing statistics from $\langle \xi \rangle$ and $\xi' \equiv \langle \xi'^2 \rangle^{1/2}$ only, using an assumed beta PDF shape to approximate the large-eddy PDF. *A priori* studies show that the assumed beta PDF distribution well approximates filtered DNS data of homogeneous turbulence (Cook & Riley 1994) and the present, nonhomogeneous case of the turbulent reacting jet (Wall *et al.* 2000). For practical purposes, (3.3b) with $\xi^- = 0$ and $\xi^+ = 1$ yields distributions essentially identical to the beta PDF (Cha & Trouillet 2002). (This can be readily verified by direct calculation, substituting the various possible values of $\langle \xi \rangle \in [0, 1]$ and $\xi'^2 \in [0, 1/4]$ into (3.3b), the PDF from mapping closure, against the well-known presumed beta PDF.)

The beta PDF has not been related to first principles: its motivation lies only in describing a bounded random variable whose first and second moments can be enforced by an LES (or RANS) turbulence model. In contrast, mapping closure describes the assumptions leading to (3.3b), beginning with the exact transport equation for ξ (Chen *et al.* 1989). In the late stages of mixing ($\xi' \rightarrow 0$), the two approaches are demonstrably consistent. For $\xi' \rightarrow 0$, or equivalently, $\langle \chi \rangle \rightarrow 0$, the beta PDF can be shown to asymptote to the Gaussian distribution (Girimaji 1991). This behavior is the fundamental modeling assumption on which mapping closure is based. In the late stages of mixing, the mapping becomes linear and (3.3b) asymptotes to a normal distribution, $\Sigma p_\xi((\eta - \langle \xi \rangle)/\Sigma) \rightarrow p_{z_0}$. Thus, at the late stages of mixing, it is clear that only the first two moments of ξ characterize the entire, approximately-Gaussian, probability density function of ξ and the beta PDF and mapping closure are consistent (for $\xi' \rightarrow 0$).

3.2. Reactive scalar mixing

In the flamelet regime, the mapping function of the j -th scalar, Y_j , depends only on a single reference field and can be obtained from the flamelet equations and the mapping function of the passive scalar (Cha 2001). Analogous to the passive scalar case, the mapping functions Y_j allow multi-point information at scales below $\langle(\cdot)\rangle$ to be determined from multi-point information about the reference field, *e.g.*, $\nabla\psi_j = (\partial Y_j / \partial z_0) \nabla z_0$. Whence,

$$\langle D(\nabla\psi_j)^2 | \psi_j = \phi \rangle = \frac{\langle \chi \rangle}{2} \frac{(\partial Y_j / \partial z_0)^2}{\langle (\partial X / \partial z_0)^2 \rangle} \quad (3.4a)$$

$$p_{\psi_j} = \frac{1}{|\partial Y_j / \partial z_0|} p_{z_0} \quad (3.4b)$$

follow, analogous to (3.2). With given Y_j and X , the time-scale ratio of a reactive to a passive scalar can be readily written as

$$T_j/T \equiv \frac{\langle \psi_j'^2 \rangle / \langle \chi_j \rangle}{\langle \xi'^2 \rangle / \langle \chi \rangle} = \frac{\langle \psi_j'^2 \rangle / \langle (\partial Y / \partial z_0)^2 \rangle}{\langle \xi'^2 \rangle / \langle (\partial X / \partial z_0)^2 \rangle} \quad (3.5)$$

or, in terms of the flamelet solution, as (Cha 2001)

$$\frac{T_j}{T} = \frac{\langle \psi_j'^2 \rangle}{\langle \xi'^2 \rangle} \frac{\langle (\partial X / \partial z_0)^2 \rangle}{\int_{-\infty}^{+\infty} (\partial \psi_j / \partial \xi)^2 (\partial X / \partial z_0)^2 p_{z_0} dz_0}. \quad (3.6)$$

Here, ψ_j is taken to be the steady flamelet solution, which would allow T_j/T to be pretabulated in practice. The mapping function of the passive scalar, X , is given by (3.3a).

Implementations of the flamelet equations (steady or unsteady) usually employ additional, simplifying assumptions to model $\chi(t, \xi)$, the local mixing orthogonal to the reaction zone, *i.e.*, in ξ phase space. No entirely satisfactory method of accounting for intermittency effects in a flamelet approach currently exists. The present work is no exception: As is traditionally done, the local, instantaneous scalar dissipation rate is replaced by the spatial average conditional on mixture fraction, thereby neglecting intermittency effects. For all practical purposes, the resulting flamelet model would be constrained by the same limitations as the quasi-steady conditional-moment closure model (Cha & Kosály 2000).

3.3. Implementation issues

Implementation issues of (3.6) in Lagrangian particle Monte Carlo calculations, for the joint FDF of the reactive scalars say, are described. The T_j/T ratio can be pretabulated as a function of $\langle \xi \rangle$, ξ' , and $\langle \chi \rangle$. During the LES calculation, $\langle \xi \rangle$ and ξ' are known in each computational cell from the subgrid-scale FDF. Well-known models exist for $\langle \chi \rangle$. Then, for a given computational cell, the T_j/T ratio simply multiplies the passive scalar time scale to obtain the time scale to be used for the j -th reacting scalar for a given particle interaction model.

The restriction imposed by the quasi-steady flamelet assumption, namely that the time scale for $\langle \chi \rangle$ be much greater than the time taken for the unsteady flamelet solution to relax to its steady counterpart (Cha & Kosály 2000), requires an *ad hoc* implementation strategy when this assumption is not met at a particular computational grid point. For example, the effects of extinction are important when $\langle \chi | \xi_{st} \rangle \gtrsim \chi_q$; reignition events

ensue when the dissipation rate drops back below χ_q (Cha *et al.* 2001). This hysteresis effect would necessitate a binary “switch” for every computational volume to ensure that the proper time scale was being used in the Monte Carlo simulations to describe reignition by distributed combustion, as discussed in the Introduction to this paper. (Note that the conditional scalar dissipation rate is known from (3.2a) and (3.3a).) The available time-developing information from the Monte Carlo simulations, *e.g.*, the filtered temperature conditional at ξ_{st} , could then be used to switch back to 3.6 when the flamelet regime is reached in a given computational grid point.

4. Results and discussion

Validation of the time-scale model uses the DNS of the turbulent reacting jet, already described in section 2. At a fixed time, t , the spatially-averaged statistics are calculated using the typical LES grid for this flow used to investigate the presumed beta PDF subgrid mixing model in Wall *et al.* (2000). Here, only results from Favre, or density-weighted, averaging is presented. Define an “LES grid point” as a single fixed point centered within a three-dimensional volume defined by the LES grid. (A “DNS grid point” is of course defined by the DNS calculation (Boersma 1999).) At a fixed axial distance, x , from the jet nozzle, a “sliding” filter is used to maximize the use of the DNS data, as is conventionally done for *a priori* validation studies of LES models. That is, each DNS grid point also corresponds to an LES grid point with consecutive LES volumes then overlapping. For the present study, we are interested in a subset of these LES grid points that contain the stoichiometric isosurface. For a given x , define an index I to label a DNS grid point following the stoichiometric isocontour, $\xi = \xi_{st}$, in the azimuthal direction. This will also correspond to an LES grid point due to the sliding filter. Two sets of calculations are performed: one in which the exact local values of ξ^- and ξ^+ from the ensemble of DNS points at an LES grid point are used, and a second set of calculations where ξ^- and ξ^+ are set to zero and one, respectively. The values for ξ^- and ξ^+ will be unique for a given I and will generally vary with I .

Figure 2 shows the volume-averaged scalar dissipation rates of ξ and ψ_p along the stoichiometric isocontour, indexed by I , at various axial distances from a jet nozzle of diameter D . Results are at the same instant of time as figure (1). Symbols are the spatially-averaged DNS data, solid lines are modeling results using the exact local values of ξ^- and ξ^+ within each LES volume, and dash-dash lines are modeling results with $\xi^- = 0$ and $\xi^+ = 1$. The spatially-filtered dissipation rate of ξ would be input into the model in practice. Here, $\langle \chi \rangle$ is calculated directly from the DNS data to circumvent any errors that could be made with the usual LES modeling, *i.e.*, neglecting its transient response to the large-scale mixing. In the near-field of the jet ($x/D \lesssim 15$), the turbulence is not fully developed and $\langle \chi \rangle$ is fairly uniform circumnavigating the stoichiometric isocontour (*i.e.*, as a function of I). Approximate axisymmetry can be observed in this region by inspection of figure 1. In the mid-field ($x/D \approx 25$) and far-field ($x/D \approx 35$) regions of the jet, $\langle \chi \rangle$ can fluctuate by an order-of-magnitude with I . The developed turbulent structures in these regions can cause $\langle \chi \rangle$ along some regions of the stoichiometric isocontour to be comparable in magnitude to values found in the near-field of the jet.

Figure 2 shows that the values of ξ^- and ξ^+ can be set to 0 and 1 in (3.3a) without significantly influencing the modeling results for the reactive-scalar dissipation rate $\langle \chi_p \rangle = \langle \chi \rangle \langle (\partial Y_p / \partial z_0)^2 \rangle / \langle (\partial X / \partial z_0)^2 \rangle$. The $\langle \chi_p \rangle$ predictions are generally in good agreement with the spatially-filtered DNS data. In the near-field of the jet, intermittency effects

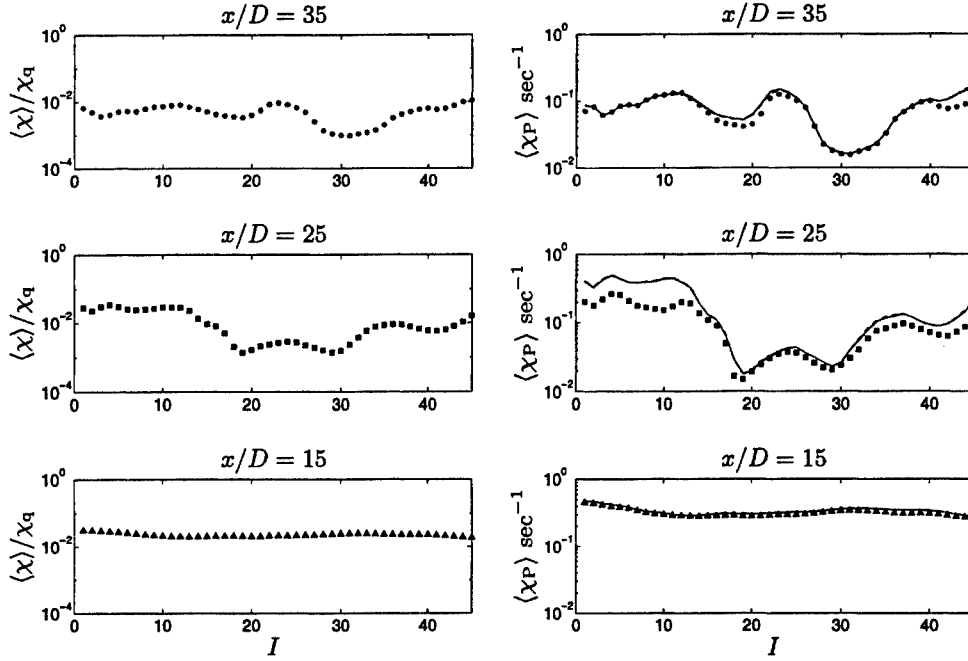


FIGURE 2. Spatially-filtered dissipation rates of the passive scalar, ξ , and the reacting scalar, χ_P , at three representative axial distances from the jet nozzle: $x/D = 15$ (near-field), $x/D = 25$ (mid-field), and $x/D = 35$ (far-field). Results are at the same instant of time as in figure 1. Symbols are filtered DNS data circumnavigating the stoichiometric isocontour, $\xi = \xi_{st}$, for a given x ; I is just a convenient label along the isocontour. Lines are corresponding modeling predictions: Solid lines are modeling results using the exact local values of ξ^- and ξ^+ within each LES volume at a given I , dash-dash lines are modeling results with $\xi^- = 0$ and $\xi^+ = 1$.

are absent and both mapping closure and the present implementation of flamelet modeling are accurate. As is well known, residence-time effects are negligible in the near-field and steady flamelets are valid. Accurate modeling predictions of $\langle \chi_P \rangle$ are thus ensured in the near-field given the validity of the component models (mapping closure and flamelet modeling) used in describing $\langle \chi_P \rangle$.

Some deviations between the $\langle \chi_P \rangle$ data and predictions are seen where the turbulence is developed. Figure 2 shows the representative behavior in the mid-field ($x/D = 25$) and far-field ($x/D = 35$) regions of the jet. In particular, the deviations are conspicuous only for relatively large $\langle \chi \rangle$, and hence for relatively large ξ' .

To investigate the effect of the relatively large $\langle \chi \rangle$ or ξ' on each of the two modeling components (flamelet modeling and mapping closure), the DNS is used to give insight into the subgrid-scale structure of the reacting and passive scalar mixing fields. Figure 3 shows the mass fraction of subgrid-scale product at three representative LES grid points: $x/D = 35$, $I = 45$ (where the maximum deviation between the modeling and filtered data occurs in the far-field region of the jet), at $x/D = 25$, $I = 10$ (where the maximum deviation occurs in figure 2), and at an arbitrary, reference position of $x/D = 25$, $I = 19$ (where good agreement between the modeling and data is seen in figure 2). Also shown are the corresponding local values of $\chi(\xi)$ at the subgrid-scales properly nondimensionalized by χ_q for the present discussion.

With regard to the flamelet model, the neglect of the subgrid-scale spatial fluctuations of χ contributes to the deviations between the filtered DNS data and the modeling predic-

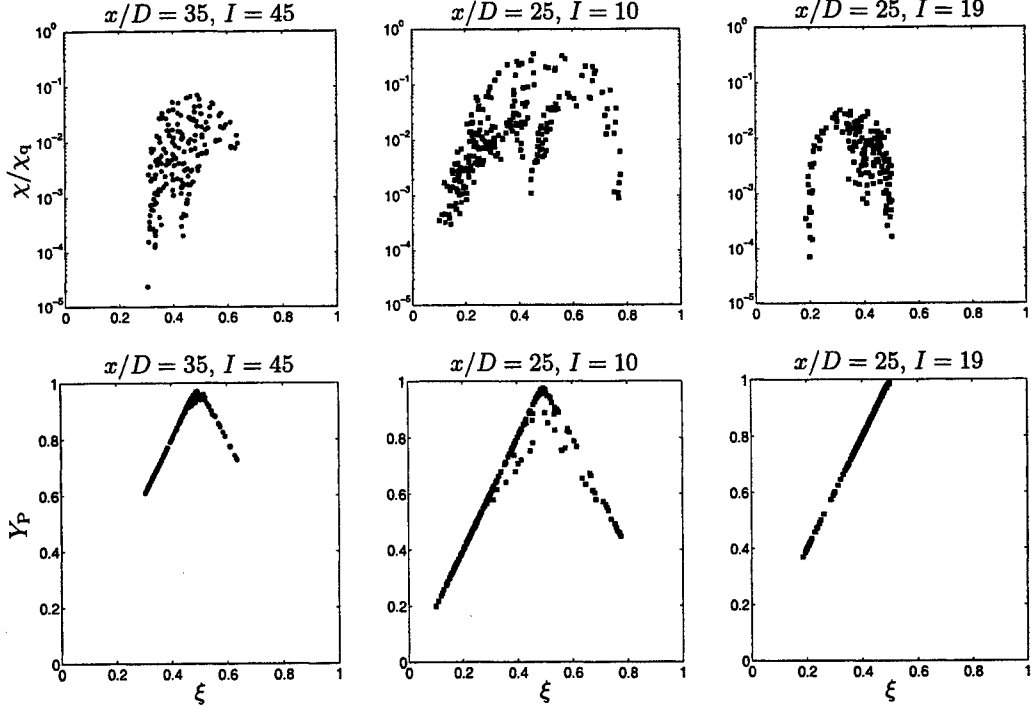


FIGURE 3. Exact subgrid-scale values of χ , the dissipation rate of ξ , and the corresponding local product mass fractions, ψ_P , at three representative LES grid points in figure 2: $x/D = 35$, $I = 45$ (stars), $x/D = 25$, $I = 10$ (squares), and $x/D = 25$, $I = 19$ (squares). The dissipation rate of ξ is nondimensionalized by χ_q , the quenching value of χ for the present chemistry case as defined by the steady flamelet solution.

tions of figure 2. Figure 3 shows that when local values of χ are large, local extinction is observed in the corresponding product mass fractions. Note that locally, $\chi \sim \chi_q$ although $\langle \chi \rangle \ll \chi_q$ (for subplot $x/D = 25$, $I = 10$), which follows from the fine-scale structure of the dissipation rate. For smaller $\langle \chi \rangle$ (subplots $x/D = 35$, $I = 45$ and $x/D = 25$, $I = 19$), the subgrid-scale fluctuations of χ are not large enough to reach local extinction and the flamelet solution is accurate.

With regard to mapping closure, in regions of the flow where the turbulence is developed and where relatively large values of ξ' occur (subplot $x/D = 25$, $I = 10$ in figure 3), multi-scale mixing processes are occurring. In these regions, a unique set of ξ^+ and ξ^- values misrepresents the true subgrid-scale structure of the mixing. This is because, for developed turbulence, the large difference between global ξ^+ and ξ^- , proportional to ξ' , necessarily result in additional length scales corresponding to the distribution of local ξ^- and ξ^+ . Thus, ξ^- and ξ^+ as defined by mapping closure less accurately represents the true subgrid-scale mixing.

With RANS turbulence modeling, the effect of neglecting the true values of ξ^- and ξ^+ had a negligible influence on the modeling results (Cha & Trouillet 2002): At a given \mathbf{x} , for time-averaged ξ values close to either 0 or 1, the variance of ξ will be small and hence $\xi^+(\mathbf{x})$ and $\xi^-(\mathbf{x})$ could be set to 1 and 0, respectively. At intermediate $\langle \xi \rangle$ values, the effect of intermittency drives $\xi^- \rightarrow 0$ and $\xi^+ \rightarrow 1$ in the statistically stationary limit, and again ξ^- and ξ^+ could be set to 0 and 1 without significantly influencing modeling results within a RANS turbulence modeling framework. Here, for the LES case, accounting for

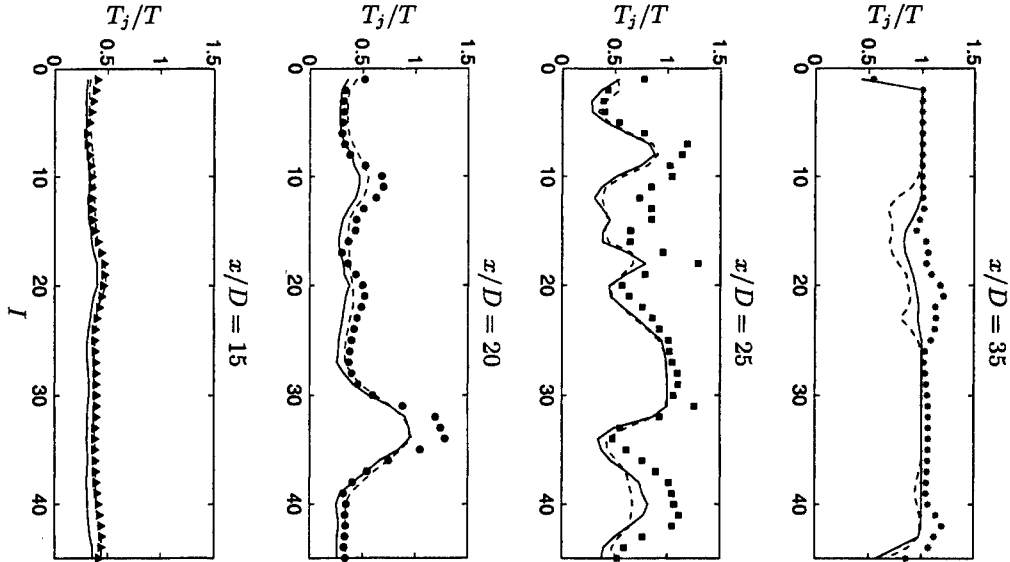


FIGURE 4. Time scale ratio of the reactive to passive scalar for increasing axial distances from the jet nozzle, from $x/D = 15$ to $x/D = 35$, the approximate time-averaged stoichiometric flame-length. Symbols are filtered DNS data. Lines are corresponding modeling predictions: Solid lines are modeling results using the exact local values of ξ^- and ξ^+ within each LES volume at a given I , dash-dash lines are modeling results with $\xi^- = 0$ and $\xi^+ = 1$.

(spatial) intermittency effects can sometimes be important when the subgrid variance of ξ is sufficiently large, as illustrated above. For the typical LES grid spacing employed in the present case (Wall *et al.* 2000), the subgrid variance is generally small and the effect of neglecting ξ^- and ξ^+ has negligible impact on the overall modeling performance. In practice, the expectation is that ξ^- and ξ^+ can be set to 0 and 1 in (3.3) as the subgrid-scale variance of ξ will generally be small in a large-eddy simulation.

Figure 4 shows the modeling predictions (lines) of the time scale ratio, (3.6), versus the experimental data obtained from the filtered DNS (symbols). The comparisons are made for the same grid points as in figure 2 (and for the same axial distances as in the RANS case of Cha & Trouillet (2002)). Again, solid lines are modeling results using the exact local values of ξ^- and ξ^+ within each LES volume at a given I , and dash-dash lines are modeling results with $\xi^- = 0$ and $\xi^+ = 1$. As was also seen in the reactive scalar dissipation rate predictions, ξ^- and ξ^+ can be set to 0 and 1 in (3.3a) without significantly influencing the modeling results, here for the time scale ratio. The T_j/T predictions are in excellent agreement in the near-field of the jet. The deviations in the mid- and far-fields of the jet occur when ξ' or $\langle \chi \rangle$ is sufficiently large, which follows directly from the above discussion of Figs. 2 and 3. Overall, the results show that T_j can be significantly less than T , even in the mid- and far-field regions of the jet for the LES case. The new modeling represents a significant improvement over simply approximating T_j by T alone.

5. Summary and conclusions

Transported probability-density-function approaches for the large-eddy PDF, known as the “filtered density function approach” (FDF), require modeling of the mixing processes at the subgrid-scale. For large-eddy simulations of initially nonpremixed turbulent

reacting flows, the current FDF approaches can, strictly, treat only distributed combustion (small Damköhler number flows) because of the limitations imposed by neglecting the effects of chemistry on the mixing process. Thus many problems of practical engineering interest, where Arrhenius kinetics are used and the chemistry is relatively fast, are beyond the reach of FDF. The merits of the FDF approach include the potential to describe local reignition events among others. To describe local extinction from a mixing-limited combustion mode, the model must first be able to treat flamelet combustion, by definition. A model for the time scale of reactive scalar mixing at the subgrid-scale that is valid both for flamelet and distributed combustion has been developed, (3.6) in this paper. The model is based on mapping closure, to describe the subgrid-scale mixing of the passive scalar, and flamelet modeling, to describe the mixing of the reactive scalars in mixture fraction space. Application to Lagrangian particle Monte Carlo calculations has been described.

The modeling results using spatially-filtered DNS data of a turbulent reacting jet (with one-step, Arrhenius chemical kinetics, and heat release) show generally good predictions of the reactive scalar time scale, which can be significantly less than the passive scalar time scale even in the mid-field regions of the jet. Mapping closure does not account for intermittency, nor does the present, conventional implementation of steady flamelet modeling needed to obtain the reactive scalar mapping functions. In regions of the jet flame where the turbulence is developed and the subgrid variance and dissipation rate of the passive scalar are relatively large, some deviation between the data and modeling predictions occur.

Acknowledgements

The authors express gratitude to Bendiks Boersma for making his DNS database available to us.

REFERENCES

- BILGER, R. W. 1980 Turbulent flows with nonpremixed reactants. In *Turbulent Reacting Flows, Topics in Applied Physics* 44, chap. 3, pp. 65–113. Springer.
- BOERSMA, B. J. 1999 Direct numerical simulation of a turbulent reacting jet. *Annual Research Briefs*, Center for Turbulence Research, NASA Ames/Stanford Univ., pp. 59–72.
- CHA, C. M. 2001 Transported pdf modeling of turbulent nonpremixed combustion. *Annual Research Briefs*, Center for Turbulence Research, NASA Ames/Stanford Univ., pp. 79–86.
- CHA, C. M. & KOSÁLY, G. 2000 Quasi-steady modeling of turbulent nonpremixed combustion. *Combust. Flame* **122**, 400–421.
- CHA, C. M., KOSÁLY, G. & PITSCHE, H. 2001 Modeling extinction and reignition in turbulent nonpremixed combustion using a doubly-conditional moment closure approach. *Phys. Fluids* **13**, 3824–3834.
- CHA, C. M. & TROUILLET, P. 2002 A model for the mixing time scale of a turbulent reacting scalar. *Phys. Fluids* (submitted).
- CHEN, H., CHEN, S. & KRAICHNAN, R. H. 1989 Probability distribution of a stochastically advected scalar field. *Phys. Rev. Lett.* **63**, 2657–2660.

- COLUCCI, P. J., JABERI, F. A., GIVI, P. & POPE, S. B. 1999 Filtered density function for large eddy simulation of turbulent reacting flows. *Phys. Fluids* **10**, 499–515.
- COOK, A. W. & RILEY, J. J. 1994 A subgrid model for equilibrium chemistry in turbulent flows. *Phys. Fluids* **6**, 2868–2870.
- COOK, A. W. & RILEY, J. J. 1997 Subgrid-scale modeling for turbulent, reacting flows. *Combust. Flame* **112**, 593–606.
- COOK, A. W., RILEY, J. J. & KOSÁLY, G. 1997 A laminar flamelet approach to subgrid-scale chemistry in turbulent flows. *Combust. Flame* **109**, 332–341.
- DOMINGO, P. & VERVISCH, L. 1996 Triple flames and partially premixed combustion in autoignition of non-premixed turbulent mixtures. *Proc. Combust. Inst.* **26**, 233–240.
- DOPAZO, C. 1975 Probability density function approach for a turbulent axisymmetric heated jet. Centerline evolution. *Phys. Fluids A* **18**, 397–404.
- GAO, F. 1991a An analytical solution for the scalar probability density function in homogeneous turbulence. *Phys. Fluids A* **3**, 511–513.
- GAO, F. 1991b Mapping closure and non-Gaussianity of the scalar probability density functions in isotropic turbulence. *Phys. Fluids A* **3**, 2438–2444.
- GAO, F. & O'BRIEN, E. E. 1993 A large-eddy simulation scheme for turbulent reacting flows. *Phys. Fluids* **5**, 1282–1284.
- GIRIMAJI, S. S. 1991 Assumed β -pdf model for turbulent mixing: Validation and extension to multiple scalar mixing. *Combust. Sci. and Tech.* **78**, 177–196.
- HEWSON, J. C. & KERSTEIN, A. R. 2001 Stochastic simulation of transport and chemical kinetics in turbulent CO/H₂/N₂ flames. *Combust. Theory Modelling* **5**, 669–697.
- JABERI, F. A., COLUCCI, P. J., JAMES, S., GIVI, P. & POPE, S. B. 1999 Filtered mass density function for large-eddy simulation of turbulent reacting flows. *J. Fluid Mech.* **401**, 85–121.
- NORRIS, A. T. & POPE, S. B. 1991 Turbulent mixing model based on ordered pairing. *Combust. Flame* **83**, 27–42.
- O'BRIEN, E. E. & JIANG, T. L. 1991 The conditional dissipation rate of an initially binary scalar in homogeneous turbulence. *Phys. Fluids A* **3**, 3121–3123.
- PETERS, N. 1984 Laminar diffusion flamelet models in non-premixed turbulent combustion. *Prog. Energy Combust. Sci.* **10** (3), 319–339.
- PITSCH, H., CHA, C. M. & FEDOTOV, S. 2002 Flamelet modeling of non-premixed turbulent combustion with local extinction and re-ignition. *Combust. Theory Modelling* (submitted).
- PITSCH, H. & STEINER, H. 2000a Large-eddy simulation of a turbulent piloted methane/air diffusion flame (Sandia flame D). *Phys. Fluids* **12**, 2541–2554.
- PITSCH, H. & STEINER, H. 2000b Scalar mixing and dissipation rate in large-eddy simulations of non-premixed turbulent combustion. *Proc. Combust. Inst.* **28**, 41–49.
- POPE, S. B. 1985 PDF methods for turbulent reacting flows. *Prog. Energy Combust. Sci.* **11**, 119–192.
- POPE, S. B. 1990 Computations of turbulent combustion: Progress and challenges. *Proc. Combust. Inst.* **23**, 591–612.
- POPE, S. B. 2000 *Turbulent Flows*. Cambridge.
- SABEL'NIKOV, V. A. & GOROKHOVSKI, M. 2001 Extended LMSE and Langevin models of the scalar mixing in the turbulent flow. In *Second International Symposium on Turbulence and Shear Flow Phenomena*. Royal Institute of Technology (KTH), Stockholm, Sweden, vol. 3, pp. 257–262.

- SRIPAKAGORN, P., KOSÁLY, G. & PITSCHE, H. 2000 Local extinction-reignition in turbulent nonpremixed combustion. *Annual Research Briefs*, Center for Turbulence Research, NASA Ames/Stanford Univ., pp. 117–128.
- WALL, C., BOERSMA, B. J. & MOIN, P. 2000 An evaluation of the assumed beta probability density function subgrid-scale model for large eddy simulation of nonpremixed turbulent combustion with heat release. *Phys. Fluids* **12**, 2522–2529.

Transported PDF modeling of turbulent premixed combustion

By Chong M. Cha

1. Motivation and objectives

Computational implementation of transported PDF methods for turbulent reacting flows (Pope 1985, 1990) use an ensemble of “notional” particles to represent the joint probability density function (PDF) of, most generally, the velocity, reacting scalars, and their dissipation rates. Following Pope (1997), the evolution equation for the i -th notional particle, among N_p total particles in an unresolved subdomain of the flow field, can be written as

$$\frac{d}{dt} \psi^{(i)}(t) = (\mathcal{M} + \mathcal{S})\psi^{(i)}, \quad (1.1)$$

where ψ represents a set of numbers defining the state space, \mathcal{M} is the mixing or transport operator, and \mathcal{S} is the source/sink operator. The operators map the state space onto itself. For simplicity, consider only the thermochemical state (a composition of N_s total species, the temperature or enthalpy, and pressure). Then ψ contains $N_s + 2$ elements. \mathcal{S} is known *a priori* for a given chemical-kinetic scheme and heat-loss model (e.g. for radiation). For many practical engineering applications, these are highly nonlinear, but depend only on the single-point information of ψ . \mathcal{M} , on the other hand, contains the spatial derivatives of ψ at scales below that of the subdomain and hence must be modeled. This is generally done with the available single-point information only, by specifying the spatial or temporal correlation. For practical engineering applications, current (and future) computational limitations demand that \mathcal{M} describe turbulent as well as molecular transport. For example, in the simplest of these mixing models (Dopazo 1994),

$$\mathcal{M}\psi^{(i)} = -\frac{\psi^{(i)} - \frac{1}{N_p} \sum_{i=1}^{N_p} \psi^{(i)}}{T_{\text{mix}}},$$

where T_{mix} is an effective mixing time scale accounting for the enhanced diffusion due to turbulence. In application with RANS, T_{mix} is given by the integral timescale of the turbulence; with LES, by the micro-timescale.

In practice, (1.1) is usually integrated using a “time-splitting” method (Pope 1985): To calculate the change in $\psi^{(i)}$ over a Δt , the \mathcal{M} and \mathcal{S} operations are applied separately, and each repeatedly in inverse proportion to the inherent time scales associated with each operator. For example, if the smallest chemical time scale is much smaller than the mixing time scale, the majority of the computational overhead will then be spent repetitively applying the \mathcal{S} operator, *i.e.*, integrating

$$\frac{d}{dt} \psi^{(i)}(t) = \mathcal{S}\psi^{(i)}. \quad (1.2)$$

In practical applications, (1.2) is “stiff”, that is, a large difference between the maximum and minimum absolute eigenvalues of the Jacobian of \mathcal{S} exists. Physically, this is due to a large separation of the chemical time scales. Denote the chemical time scales by

T_{chem} . Typically, in engineering applications, the minimum $T_{\text{chem}} \sim 10^{-9}$ sec as compared to $T_{\text{mix}} \sim 10^{-3}$ to 10^{-4} sec (Pope 1997) and hence most of the computational costs are spent integrating (1.2). Sophisticated software packages are generally available to integrate large systems of stiff equations (Byrne & Hindmarsh 1987). Due to the Jacobian evaluations, the computational time and storage requirements in solving (1.2) scale with N_s^2 , seriously debilitating this approach for practical engineering applications where N_s is usually large. Parallelization of (1.2) is non-trivial.

Alternatively, a stochastic algorithm has been developed by Bunker *et al.* (1974) and Gillespie (1992) to solve (1.2). Briefly, the stochastic algorithm interprets the chemical reactions as random queuing events. The occurrence of a single reaction event follows a Poisson process, whose time scale depends upon the local state of the system. Thus, changes in “ $\psi^{(i)}$ ” do not occur over a fixed Δt , but follow from

$$\Delta t = \min\{(\Delta t)_1, (\Delta t)_2, \dots, (\Delta t)_{N_r}, \} \quad (1.3)$$

where Δt is now a random variable defined by the set of exponentially distributed $(\Delta t)_k$, which describes the next time-of-arrival of the k -th reaction among the total number of reactions, N_r . Note that k and Δt are not independent random variables due to the min function of (1.3). With the arrival of each reaction event, the relevant species “concentrations” are updated accordingly. Note that, Jacobian evaluations are not required and, on average, the algorithm will automatically update changes in the faster species more often. The algorithm actually updates extrinsic values; the (intrinsic) concentrations are defined according to a system size (van Kampen 1992; Gardiner 1983). A review and formulation of the chemical Master equation by Poisson processes is described in Gardiner (1983). The computational time of the stochastic algorithm at an accuracy fixed by a number of realizations and/or number of stochastic particles will scale linearly with N_r . Storage requirements scale only linearly with N_s . These attributes make it ideal for systems with a large number of species. Parallelization of the algorithm is trivial, allowing essentially arbitrary tolerances (with unlimited processor number).

For the same computational time under serial computation, the stochastic algorithm yields less accurate solutions as compared to the deterministic approach or direct integration of (1.2). However, Bunker *et al.* (1974) report that, with acceptable statistical errors, the computational gain using the stochastic chemistry algorithm is a factor of 10 faster than direct integration. A reduced chemistry mechanism with $N_s = 6$ was used. Extrapolating to larger chemical kinetic mechanisms, a 10-fold increase in the number of species would result in a 10^2 -fold increase in the computational time for direct integration and thus a total of a 100-fold gain in computational speed for the stochastic algorithm over direct integration assuming a 10-fold increase in the number of reactions.

The current state-of-the-art of the stochastic chemistry algorithm includes only zero-dimensional applications, *e.g.*, well-stirred reactor calculations, but apply realistic, Arrhenius and multi-step kinetic models. No transport model with the stochastic chemistry algorithm exists, motivating the present work. Following (1.3), the most straightforward method of introducing transport is through additional queuing events. In this paper, this is done by incorporating random walks and/or triplet maps into the algorithm. Representation of continuous laminar diffusive systems by stochastic methods (*i.e.*, jump process approximations for molecular diffusion and chemical reaction) are well-known, but limited to simple reaction (Gardiner 1983). Here, realistic, Arrhenius kinetics are also considered as well as turbulent transport.

At present, the main issues remaining in transported PDF modeling of turbulent premixed and nonpremixed combustion include:

- (i) Accounting for the small-scale structure of turbulence in the micro-mixing models,
- (ii) extension to the flamelet combustion regimes (another modeling issue), and
- (iii) computational feasibility (predominantly an implementation issue).

The objectives of the paper are to address the latter two issues for applications to turbulent premixed combustion. Modeling approaches with regard to issue (i) usually employ stochastic methods to describe intermittency effects (Pope & Chen 1990; Fox 1997). With regard to issue (ii), Cha & Trouillet (2002a,b) have extended transported PDF modeling to the flamelet regime for nonpremixed combustion; no significant additional computational demands are required in correcting the reactive scalar timescales for many existing micro-mixing models. For the premixed case, Pope & Anand (1984) have treated flamelet combustion, but only in Damköhler's large-scale turbulence limit. Their method preserves the unmodified convective-diffusive flame structure of the preheat zone and is thus limited to the corrugated flamelet regime. Extension of their method to Damköhler's small-scale limit is described in this paper; again, no significant additional computational demands would be required over that of their existing approach of describing the corrugated flamelet regime. The present formulation of a transported PDF model for turbulent premixed combustion is applicable in both flamelet regimes and for distributed combustion (and the entire transition in between) with one unifying transport model: Kerstein's one-dimensional turbulence. Applications of Kerstein's one-dimensional turbulence concept to premixed flames using direct integration for the chemistry have been performed by Menon and co-workers with Fickian molecular diffusion replaced by a laminar flame propagation process (Menon & Kerstein 1992) and, more recently, by explicit finite differencing of the diffusion term (Smith & Menon 1996). Here, the one-dimensional turbulence concept with stochastic chemistry is developed.

The paper is organized as follows. In the next section, the canonical problem of a reaction-diffusion wave is described and the regimes of turbulent premixed combustion reviewed. Section 3 presents the results from two validation studies: (i) in the laminar case, one-dimensional premixed flames are simulated and their laminar flame speeds compared to exact solutions; and (ii) for an isotropic turbulence case, the scaling of the turbulent burning velocity is compared with the well-known relations in Damköhler's small- and large-scale turbulence limits. Conclusions are given in the final section.

2. Background

2.1. The laminar premixed flame

The simplest model, still preserving the underlying physics (enhanced transport due to chemical reaction, in this case), can be written as

$$\frac{\partial \Theta}{\partial t} = s \frac{\partial \Theta}{\partial z} + D \frac{\partial^2 \Theta}{\partial z^2} + \dot{S} \quad (2.1)$$

for travelling wave solutions. Here, s is the propagation velocity (defined below), which is generally time-dependent, and \dot{S} is the nonlinear source term of Θ . A transformation into a co-moving reference frame, $z \equiv x - st$, has been made from the laboratory reference frame, x , assuming waves travelling left to right. For a flame, this equation describes the transport of Θ from a "burnt" temperature $\Theta = \Theta_b$, $\dot{S} = 0$ at one boundary ($x = -\infty$) into the "unburnt" temperature $\Theta = \Theta_u$, $\dot{S} = 0$ at the other boundary ($x = +\infty$) with

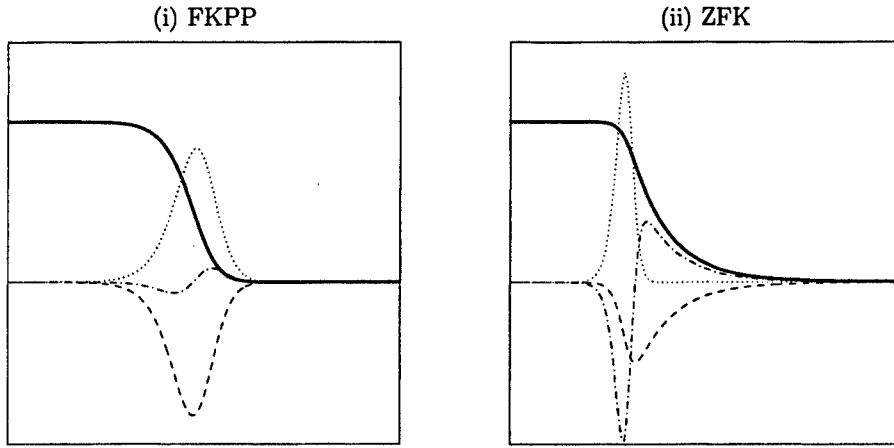


FIGURE 1. Structure of a one-dimensional laminar reaction-diffusion wave. Bold solid lines show the wave which travels left to right. Dash-dot lines are the convection term, dash-dot diffusion, and dot-dot the source term. Subplot (i) shows the structure of the Fisher (1937) and Kolmogorov *et al.* (1937) flame (FKPP); subplot (ii) the structure of the Zeldovich & Frank-Kamenetsky (1938) flame (ZFK).

$\Theta_u \leq \Theta \leq \Theta_b$, $\Theta > 0$. Two nonlinear source terms are considered based on the logistic form of $\dot{S} = k(\Theta - \Theta_u)(\Theta_b - \Theta)/(\Theta_b - \Theta_u)^2$ for (i) constant $k = A$ and (ii) for the Arrhenius formula $k = A \exp(-\Theta_a/\Theta)$ with large activation temperatures, $\Theta_a \gg \Theta_b$, and constant A . The former source term is well-known in the natural sciences since its formulation by Fisher (1937) to describe a limiting case for the propagation of advantageous genes in a population; the latter, in combustion science following the pioneering work of Zeldovich & Frank-Kamenetsky (1938). See Williams (1985) and Clavin (1994) for details.

No known general analytical solution exists for the Zeldovich & Frank-Kamenetsky case, henceforth referred to as “ZFK” for convenience. Asymptotics (for large Θ_a) is described in Williams (1985) and Clavin (1994); clever iterative numerical strategies in Williams (1985). For the Fisher equation, the approximate analytical solution is due to Kolmogorov *et al.* (1937). We henceforth refer to this case as “FKPP”. For both cases, the approximate solutions initialize finite-differenced numerical computations to yield their steady-state profiles. The Monte Carlo simulations (with the stochastic chemistry algorithm) are compared to these solutions (in section 3).

Defining $\theta \equiv (\Theta - \Theta_u)/(\Theta_b - \Theta_u)$ and the relevant length and time scales of the premixed flame as ℓ_F and T_F , respectively, yields the following nondimensionalized equations

$$\text{FKPP: } 0 = \mu \frac{d\theta}{d\xi} + \frac{d^2\theta}{d\xi^2} + T_F A \theta(1 - \theta) \quad (2.2a)$$

$$\text{ZFK: } 0 = \mu \frac{d\theta}{d\xi} + \frac{d^2\theta}{d\xi^2} + T_F A \exp \left[-\frac{\text{Ze}(1 - \theta)}{1 - \alpha(1 - \theta)} \right] \frac{\theta(1 - \theta)}{1 - \alpha(1 - \theta)} \quad (2.2b)$$

where space has been nondimensionalized by ℓ_F (e.g., $\xi \equiv z/\ell_F$) and time by T_F . With hindsight (Williams 1985; Clavin 1994; Kolmogorov *et al.* 1937), for $T_F A = 1/4$ in (2.2a), $\mu = 1$ and for $T_F A = \text{Ze}^2/2$ in (2.2b), $\mu = 1 - \mathcal{O}(1/\text{Ze})$ with $\text{Ze} \gg 1$ and $\alpha \approx 1$. Here, $\alpha \equiv 1 - \Theta_u/\Theta_b$ is the heat-release parameter and $\text{Ze} \equiv \alpha\Theta_a/\Theta_b$ is the Zeldovich number

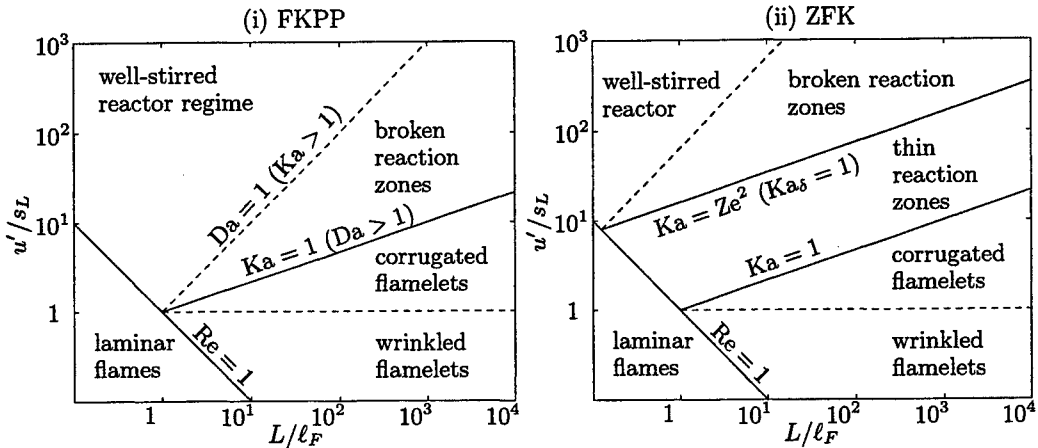


FIGURE 2. Turbulent premixed flame regime diagram (Bray & Peters 1994; Peters 2000) showing isolines of the various nondimensional numbers: $u'/s_L = \text{Re} (L/\ell_F)^{-1}$, $u'/s_L = \text{Da}^{-1} (L/\ell_F)$, and $u'/s_L = \text{Ka}^{2/3} (L/\ell_F)^{1/3} = \text{Ze}^{4/3} \text{Ka}_s^{2/3} (L/\ell_F)^{1/3}$. Of course, with respect to the definitions of the Re and Da (and $\text{Ka} = \text{Ze}^2 \text{Ka}_s = \text{Re}^{1/2} \text{Da}^{-1}$), the regimes must be identical for the two cases. However, physical and semantic differences are to be distinguished for $\text{Ka} > 1$ (Damköhler's small-scale turbulence limit) between the two cases. For the ZFK case, the additional regime of thin reaction zones (Peters 1999) is also a flamelet regime for the present one-step chemistry case (see discussion in section 3.2.)

(Williams 1985). In dimensional units, $s = \ell_F/T_F \equiv s_L$ (for the laminar case) are

$$\text{FKPP: } s_L \approx \sqrt{\mathcal{D} \frac{A}{1/4}} \quad \text{and} \quad \text{ZFK: } s_L \approx \sqrt{\mathcal{D} \frac{A}{\text{Ze}^2/2}} \quad (2.3)$$

for the FKPP and ZFK cases, respectively.

Figure 1 shows the laminar flame structure for the FKPP and ZFK solutions. In subplot (ii), and in all subsequent calculations throughout the paper, $\alpha = 0.85$ and $\text{Ze} = 8$. As is well known, for the ZFK case the large $\text{Ze} \gg 1$ confines the chemical source term to an inner reactive-diffusive zone of width $\ell_S \sim \mathcal{O}(\ell_F/\text{Ze})$, resulting in a convective-diffusive balance within the outer zone (of thickness ℓ_F). For the FKPP case, a single convective-reactive zone dominates the entire flame thickness, as seen in figure 1 (i).

2.2. The turbulent premixed flame

Figure 2 reviews the various regimes of turbulent premixed combustion (Bray & Peters 1994; Peters 2000). We ignore the “well-stirred reactor” regime in both cases, as simple models already exist for this regime. Recall the definitions

$$\text{Re Sc} \equiv \frac{u'L}{\mathcal{D}} \quad \text{and} \quad \text{Da} \equiv \frac{L/u'}{T_F}$$

which delineate the various regimes of turbulent premixed combustion. Here, u' is the turbulent velocity scale. Note that a single Damköhler number can be defined irrespective of the complexity of the chemistry (multiple chemistry times) by using the flame time. Unity Schmidt number is assumed ($\text{Sc} = 1$). The so-called “wrinkled flamelets” regime, where $u' < s_L$, is also ignored. The remaining regimes then include the “thin reaction zones” (Peters 1999), broken reaction zones (formerly “distributed reaction zones” (Bray & Peters 1994)) and “corrugated flamelet” regimes which are divided by the unity Karlovitz

number line. Recall the definition of the Karlovitz number, $Ka \equiv T_F/T_\eta$, where T_η is Kolmogorov's inner turbulence time scale. Following Peters (1999), for the ZFK case, the zone between $1 \leq Ka \leq Ze^2$ defines the regime of thin reaction zones. For the FKPP case and $Ka > 1$, the broken reaction zones regime is a distributed combustion regime. For either the ZFK or FKPP case, $Ka < 1$ is referred to as the corrugated flamelets regime (see figure 2).

The Karlovitz number is important as it distinguishes the scaling in Damköhler's small- and large-scale turbulence limits for another set of validation studies which predict the s_t/u' scaling with Da. Recall that, in Damköhler's small-scale turbulence limit, $\eta < \ell_F$ ($T_\eta < T_F$ or $Ka > 1$) and the small-scale turbulence will modify the laminar flame structure. Employing an eddy diffusivity argument, $s_t \sim \sqrt{D_t A}$ which follows from (2.3) with constant D_t or by dimensional analysis. Thus, it readily follows, with $Re = D_t/D$, that

$$\frac{s_t}{u'} \sim Da^{1/2}. \quad (2.4a)$$

This scaling is expected to be valid for the ZFK case (assuming the Kolmogorov eddies to be larger than $\ell_\delta \equiv \ell_F/Ze$, the diffusive-reactive zone thickness). This is because eddy diffusivity successfully describes transport when convective-diffusive processes dominate. However, the scaling is questionable for the FKPP case as the leading-order solution, with or without all higher-order corrections, reveal an ever dominating convective-reactive balance.

In Damköhler's large-scale turbulence limit, $\eta > \ell_F$ ($T_\eta > T_F$ or $Ka < 1$) and the laminar flame structure is preserved on average by definition. Due to this separation of the laminar flame and turbulence scales, the enhanced transport will be dominated by turbulence rather than reaction. This is because enhanced transport by turbulence is generally much more effective than enhanced transport due to chemical reaction and diffusion. A purely "kinematic scaling" is thus expected with s_t/u' then independent of Da (more precisely, the unmodified characteristic flame time):

$$s_t \sim u'. \quad (2.4b)$$

Recall that the BML model (Bray & Libby 1994) is strictly valid in Damköhler's (very) large-scale turbulence limit only: It follows that for $\eta \gg \ell_F$, the details in the laminar flame structure are unimportant and a composite delta function PDF representation of the premixed flame would be sufficient.

3. Results and discussion

3.1. Laminar premixed flame

As a queuing process, incorporating Fickian diffusion by random walks in (2.1) is a straightforward extension of the stochastic chemistry algorithm. For simplicity, assume a uniformly-discretized grid of spacing Δx . Define the random variable Δt on the lhs of (1.3) as $(\Delta t)_{\text{chem}}$, the random time increment to the next reaction event. Then, the time increment to the next reaction or diffusion event is given by the random variable

$$\Delta t = \min\{(\Delta t)_{\text{diff}}, (\Delta t)_{\text{chem}}\} \quad (3.1)$$

With $T_{\text{diff}} \equiv (\Delta x)^2/D/2$ taken to be a deterministic time-of-arrival of a random walk (Feller 1970), $(\Delta t)_{\text{diff}}$ is the remaining time to the next random displacement event. For the uniform grid spacing and a given D , T_{diff} is independent of x . Thus, random walks are

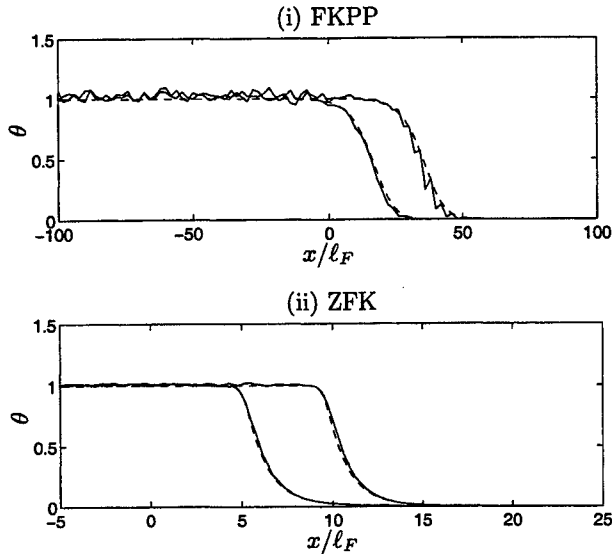


FIGURE 3. Typical realizations from the Monte Carlo simulations of the laminar FKPP and ZFK premixed flames. Solid lines are the simulation results. For the (i) FKPP case, the two solutions are between 20 nondimensional time units t/T_F with dash-dash lines from deterministic, finite-differenced solutions. For the (ii) ZFK case, between 5 nondimensional time units with dash-dash lines from finite-differenced solutions.

applied at every grid point every T_{diff} . Update of the species populations follow the jump process as described by the stochastic chemistry algorithm at every grid point. Values of the species populations can be converted to and from concentrations *via* van Kampen's system size. For example, the initial (intrinsic) concentration, $\theta(x)$, are converted to extrinsic (integer) values, M , for every subvolume, Δx , following $M = \text{round}\{\Omega \times \theta\}$, where $\Omega = n_p \Delta x$ and $n_p(x)$ is the number of particles in a cell. Sensitivity to the system size, or n_p for fixed Δx , is described below.

Figure 3 compares the Monte Carlo simulation results to the exact and approximate flame solutions for the FKPP and ZFK cases, respectively. Qualitatively, the Monte Carlo simulations are in good agreement with the deterministic solutions for the flame structure. Defining a single realization as a simulation with duration of approximately $10 T_F$, a quantitative assessment can be made using flame-speed calculations.

For numerical simulations of a reaction-diffusion wave (Monte Carlo or otherwise), a practical measure of the flame speed is first required. One can be derived by integrating the governing equations in lab coordinates from a reference position in the burnt region, x_b say. Leibniz's rule gives $\frac{d}{dt} \int_{x_b}^{\infty} \Theta dx + \frac{dx_b}{dt} \Theta_b = \int_{x_b}^{\infty} \dot{S} dx$, where x_b is sufficiently upstream from the flame that $(d\Theta/dx)_{x_b} = 0$ holds. Since $s = \int \dot{S} dx$, it follows that

$$s = \frac{d}{dt} \int_{x_b}^{\infty} \Theta dx \quad (3.2)$$

for a fixed x_b . Thus, $s(t)$ can be estimated by the local time derivative of $\int \Theta dx \equiv H(t)$. At "steady-state", characterized by a constant wave speed, $H(t)$ will be linear and s given by its slope. Note, this is valid for calculating the flame speed for both the laminar case ($s = s_L$) and the flame speed for a turbulent Θ field ($s \rightarrow s_t$) along the mean direction of propagation, also denoted by x . For the latter case, although pedagogically misleading, we refer to s_t as a "turbulent flame speed". (The definition of s_t and its distinction from s for the turbulent case is described later in section 3.2.)

For Monte Carlo simulations, convergence of the statistical errors from the flame speed

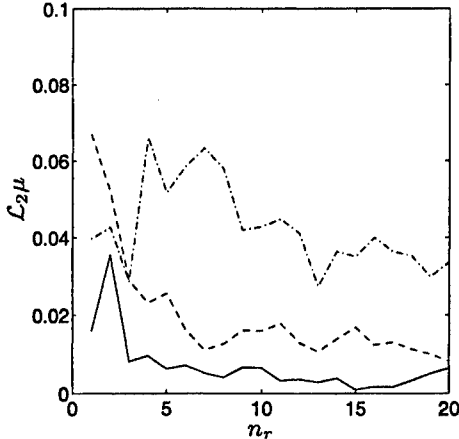


FIGURE 4. Monte Carlo statistical errors with the number of realizations, n_r , for the laminar flame speed calculated from (3.2). The figure shows three sets of calculations: $n_p = 10^3$ (dash-dot line), 10^4 (dash-dash), and 10^5 (solid line). The FKPP case is shown. Results for the ZFK case are comparable.

calculation procedure can be gauged using the \mathcal{L}_2 error estimator

$$\mathcal{L}_2\mu \equiv \left[\left(\frac{1}{n_r} \sum_{k=1}^{n_r} \mu^{(k)} - 1 \right)^2 \right]^{1/2},$$

where $\mathcal{L}_2\mu$ is a function of n_r , the number of realizations, and $\mu^{(k)} \equiv s^{(k)} T_F / \ell_F$ is the nondimensional flame speed for the k -th realization calculated using (3.2).

Figure 4 shows the convergence of the statistical errors with n_p (with Δx fixed) and n_r for the laminar flame-speed calculation procedure. For a fixed and sufficiently large n_r , the figure just shows the well-known $1/n_p^{1/2}$ scaling of the Monte Carlo statistical errors. For a fixed system size, the figure shows that the flame-speed calculation procedure requires only a few realizations to reach the asymptotic error at $n_r \gg 1$. The figure can be interpreted as follows: The flame-speed calculation procedure yields less than, for example, a 5% error using $n_p \sim 10^3$ and $n_r \gtrsim 10$, or $n_p \sim 10^4$ and $n_r \gtrsim 1$, etc.

3.2. Turbulent premixed flame

Kerstein's linear-eddy variant (Kerstein 1991a,b) of his one-dimensional turbulence concept is incorporated with the stochastic chemistry and mixing algorithm of section 3.1. This is straightforward as the advective stirring processes are already represented by a queuing process through the triplet mapping procedure. Define the Poisson random variable $(\Delta t)_{\text{stir}}$ as the next time-of-arrival of each eddy or mapping event. Then, the time increment to the next reaction, molecular diffusion, or advective stirring event is given by the random variable

$$\Delta t = \min\{(\Delta t)_{\text{stir}}, (\Delta t)_{\text{diff}}, (\Delta t)_{\text{chem}}\}, \quad (3.3a)$$

where $(\Delta t)_{\text{diff}}$ and $(\Delta t)_{\text{chem}}$ have been defined with regard to (3.1).

The resulting one-dimensional turbulent premixed flame model is an abstraction. However, the expected qualitative features of the turbulence-chemistry interaction are reproduced by the Monte Carlo simulations. Figure 5 shows typical realizations of the flame structure in Damköhler's small- and large-scale turbulence limits in subplots (i) and (ii), respectively, for the FKPP reaction-diffusion wave. Single realizations are shown by the solid lines; the ensemble average summed over 10^2 realizations at the same time are shown by the dash-dash lines. In both subplots, $Re = 100$. In subplot (i), $Da = 5$, and in

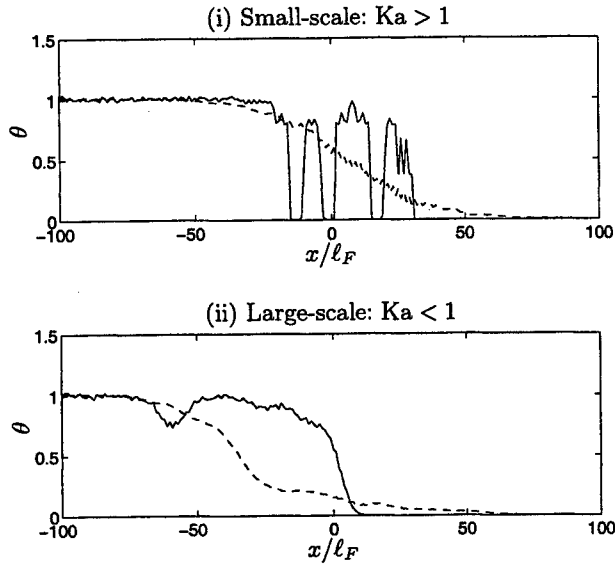


FIGURE 5. Typical realizations from the Monte Carlo simulations of the turbulent FKPP premixed flame. Solid lines are the simulation results; dash-dash lines are ensemble averages of 10^2 realizations at the same time. Turbulent transport is modeled using Kerstein's linear eddies. The corresponding laminar results are shown in figure 3. In both figures, $Re = 100$. In subplot (i), $Da = 5$ (hence $Ka = Re^{1/2}/Da = 2$); in subplot (ii), $Da = 50$ (hence $Ka = 0.2$).

subplot (ii), $Da = 50$. Thus, in subplot (i), $Ka > 1$ and the smallest turbulent eddies will modify the laminar flame structure since $\eta < \ell_F$. This is clearly observed in the single realizations (solid lines) of figure 5 (i). Figure 3 (i) shows the corresponding laminar case. In figure 5 (ii), $Ka < 1$ and the turbulence does not modify the laminar flame structures. Preservation of the laminar flame scales is visibly apparent upon comparing the single realizations (solid lines) in figure 5 (ii) with the corresponding laminar case in Fig. 3 (i). The qualitative features of the turbulence-chemistry interaction for the ZFK case are similar.

The expected quantitative results for the “turbulent flame speed” are also reproduced by the stochastic model. Figure 6 shows the turbulent flame speed calculated using (3.2) over a range of Damköhler numbers, for the ZFK reaction-diffusion wave. Each point represents a single realization; big dots are the conditional (on Da) average. “ s_t ” is used to distinguish this average from the “ s ” of each realization from figure 3.2. The unity Karlovitz number line is demarcated by the bold dot-dot line. Subplot (i) shows on log-log scale the subset of realizations in subplot (ii) for which $Ka > 1$. For $Ka > 1$ ($\eta < \ell_F$), subplot (i) shows that the modeling predicts the expected s_t/u' dependence on Da as given by (2.4a) for Damköhler's small-scale turbulence limit. For $Ka < 1$ ($\eta > \ell_F$), s_t/u' becomes independent of Da for increasing Da , validating the model in Damköhler's large-scale turbulence limit as well.

We note in passing the increasing scatter of s with Da in figure 6. For a given Da bin size, the number of realizations are too large for the observed scatter to be solely due to statistical error. Following the analysis of the statistical errors for the flame-speed calculation procedure in the previous subsection, the statistical errors would only account for a small fraction of the scatter (even for a Da bin size which includes only 10 realizations). Physically, the increasing scatter in s/u' with Da is to be expected since, for fixed Re , the increasing range of turbulent length scales would create an increasing variation in the s “measurements” taken at the same time amongst an increasing number of realizations. Evidently, the intermittency effects on s , also observed in experimental data, are captured by the present modeling.

To introduce the less-computationally-expensive Taylor diffusion model into the sim-

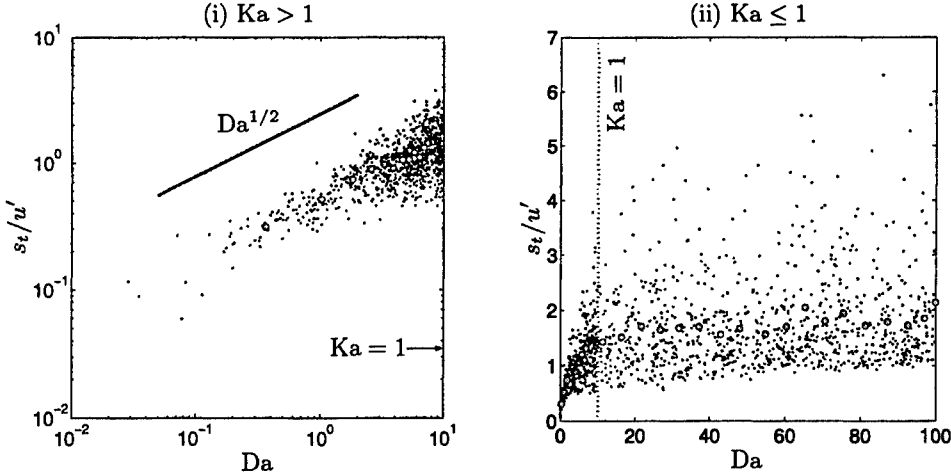


FIGURE 6. Scaling of s_t/u' with Da in Damköhler's small- ($Ka > 1$) and large-scale ($Ka \leq 1$) turbulence limits for the ZFK premixed flame. A subset of the same data in subplot (ii) is shown in subplot (i), which shows Damköhler's small-scale turbulence scaling of $s_t/u' \sim Da^{1/2}$ for $Ka > 1$. Recall that $Da Ka = Re^{1/2}$.

ulations in place of Kerstein's linear eddy model, consider the ZFK case in Damköhler's small-scale turbulence limit, whose scaling is given by (2.4a). Representing the classic engineering approach, the main motivating idea behind Taylor diffusion here is to reproduce the turbulent flame-speed scaling directly without performing multiple realizations for a fixed Da . This scaling is thus trivially reproduced by simulating a "laminar" flame but with the molecular diffusivity replaced by an "eddy diffusivity". In other words, instead of using (3.3a), turbulent and molecular transport can be simulated together following

$$\Delta t = \min\{(\Delta t)_{\text{mix}}, (\Delta t)_{\text{chem}}\} \quad (3.3b)$$

which is analogous to (3.1) but with \mathcal{D} in $(\Delta t)_{\text{diff}}$ replaced by $\mathcal{D}_t = Re \mathcal{D}$ for $(\Delta t)_{\text{mix}}$. Equation (2.3) then gives the turbulence enhanced flame speed, s_t , and so the scaling given by (2.4a) is trivially reproduced (although without intermittency). It is interesting and useful to ask what is lost with the faster computations resulting from replacing T_{stir} , the range of turbulent timescales, and T_{diff} by T_{mix} alone (besides losing the true scatter in the turbulent flame-speed predictions)? It is argued that this question is equivalent only to asking: When is the regime of thin reaction zones a true flamelet regime? Consideration of the limitations of Taylor diffusion for the corrugated flamelet regime yields a simple transported PDF model for turbulent premixed combustion valid in both Damköhler's small- and large-scale turbulence limits.

For the regime of thin reaction zones, consider again the ZFK case with one-step chemistry. Recall that Taylor diffusion works when advective and diffusive processes are unmodified by reaction. That reaction does not directly impact the enhanced convective-diffusive transport in the modified preheat zone is guaranteed by the high activation temperature ($Ze \gg 1$) of the reaction. This is because, with the one-step reaction, only temperatures between $(1 - 1/Ze) < \theta < 1$, which have a low probability of occurrence in the modified preheat zone under the defined restrictions, will lead to a non-negligible reaction rate. Thus, only convective-diffusive effects remain important outside the inner reactive-diffusive boundary layer. This is clear for the present one-step chemistry case. For multi-step chemistry, assume that T_{chem} , the range of chemistry timescales, and T_{diff}

yield a well defined flame time scale irrespective of the modified preheat zone. Taylor diffusion would thus be valid so long as the inner zone remains intact. The repercussions of this assumption being valid are significant. For example, consider the transported PDF model of Pope & Anand (1984), where the combined contributions from the diffusion and chemical source terms in the transported PDF equation for a reacting scalar, ψ say, are modeled together by a known function $h(\psi)$. In Damköhler's large-scale turbulence limit then, $h(\psi)$ is the response of the convection term of the steady planar laminar premixed flame and is known ahead of time for a given chemical kinetic scheme. Extension to the thin reaction zones regime can simply be done by parameterizing $h(\psi) \rightarrow h_t(\psi)$ by $D \rightarrow D_t$, where $h_t(\psi; D_t)$ would be pretabulated in practice for an expected range of D_t . It is no surprise that such a tabulation over a "parameter" governed by the large scales can be performed if the thin reaction zones regime is a flamelet regime.

In the corrugated flamelet regime, the less computationally-expensive algorithm represented by (3.3b) will obviously give the wrong scaling for the turbulent flame speed. This is of minor concern, as s_t/u' changes little with large Da due to the weak $Da^{1/2}$ dependence in Damköhler's small-scale turbulence limit. (Of major concern would be the neglect of the increasing level of s fluctuations with Da.) Or, if this regime is of practical interest, and the transition between Damköhler's small- and large-scale turbulence limits can be neglected, the above tabulation procedure can readily be modified to yield a unique $h_t(\psi; D_t) = h(\psi)$ for all values of D_t above a threshold value. (Of course, the effect of the largest fluctuations in s , which occur in the large-scale limit, would also have to be negligible as well.) Certainly, semi-empirical or purely empirical correlations for s_t/u' from a given application can also be used to pretabulate $h_t(\psi; D_t)$ as well, since s_t can be related to D_t . A semi-empirical correlation for s_t/u' has been developed and applied by Peters (1999) to convect a level-set surface representing the inner reaction zone. If intermittency effects must be accounted for, the present transported PDF model with Taylor diffusion becomes questionable as it incorrectly assumes that the turbulent flame speed (or turbulent diffusivity) is a well-defined, physical quantity.

4. Conclusions and future work

Currently, transported PDF methods of turbulent combustion discount the flame structures which can modify the unresolved mixing processes. Accounting for flamelet combustion in micro-mixing models for turbulent nonpremixed combustion is described in Cha & Trouillet (2002a,b). Here, for the premixed case, enhanced molecular transport due to reaction as well as turbulence must be accounted for. Pope & Anand (1984) have treated turbulent premixed combustion in the corrugated flamelet regime by a transported PDF method; here, their method is extended to the "thin reaction zones" regime (Peters 1999). In the thin reaction zones regime, the characteristic laminar flame scales are modified by the turbulence, but the inner layer reaction zone and turbulence scales remain separated due to a large activation energy. Neglecting intermittency effects, this allows the turbulence broadened preheat zone to be described by eddy diffusivity and hence the response of the flame structure to the turbulent mixing processes to be pretabulated for a given chemistry scheme in practice.

For distributed combustion, the interaction with the range of chemistry time scales must be accounted for and the issue of computational feasibility of transported PDF modeling arises if detailed kinetics are required. The stochastic chemistry algorithm of Bunker *et al.* (1974) and Gillespie (1992) is extended to treat transport to help off-

set the significant computational demands required for describing complex chemistry in transported PDF methods. Molecular and turbulent transport are integrated into the stochastic chemistry algorithm as queuing processes. For simplicity, a freely propagating premixed flame driven by a one-step chemical reaction is considered. Two nonlinear source terms, with and without high activation energy and referred to as the FKPP and ZFK cases, respectively, define two representative nonconservative systems for model investigation and validation (see (2.2) in this paper).

For the laminar cases, results from the Monte Carlo simulations are compared to exact deterministic, finite-differenced solutions and validate the approach for molecular transport and transport by eddy diffusivity. For the turbulent case, Kerstein's one-dimensional turbulence concept is used to incorporate the entire dynamic range of turbulent motions in the more general, but more computationally-expensive, model. (The model is general because it can be applied without *ad hoc* knowledge of the regime.) The resulting simulations are able to reproduce the expected scalings in Damköhler's small- and large-scale turbulence limits. Results, not presented here, also show good agreement with the experimental data sets of Abdel-Gayed & Bradley (1981) and Bradley *et al.* (1992). If intermittency effects can be neglected, Taylor diffusion represents a less physical, but less computationally-expensive model of turbulent transport. The ZFK case exemplifies an ideal scenario where the thin reaction zones regime is a flamelet regime on average and Taylor diffusion modeling of transport is valid. In contrast, distributed combustion occurs in the FKPP case when the smallest turbulent scales interact with the characteristic flame scale.

In immediate future work, the general algorithm represented by (3.3a) can be applied to study distributed combustion. Results for the FKPP case, not presented here, yield a counter-intuitive, reaction independent $s_t/u' \sim Da^{1/2}$ scaling (as the Taylor diffusion model would yield by definition)! In other future work, the computational savings which result from using stochastic chemistry can be spent on multi-step chemistry and/or multi-dimensional simulations. For example, describing local sources/sinks by a queuing process offers a straightforward means of incorporating chemical reaction in cellular automata or lattice Boltzmann simulations.

REFERENCES

- ABDEL-GAYED, R. G. & BRADLEY, D. 1981 A two-eddy theory of premixed turbulent flame propagation. *Phil. Trans. Roy. Soc. Lond. A* **301**, 1–25.
- BRADLEY, D., LAU, A. K. C. & LAWES, M. 1992 Flame stretch as a determinant of turbulent burning velocity. *Phil. Trans. Roy. Soc. Lond.* **338**, 359–387.
- BRAY, K. N. C. & LIBBY, P. A. 1994 Recent developments in the BML model of premixed turbulent combustion. In *Turbulent Reacting Flows*, chap. 3, pp. 115–151. Academic, New York.
- BRAY, K. N. C. & PETERS, N. 1994 Laminar flamelets in turbulent flames. In *Turbulent Reacting Flows*, chap. 2, pp. 63–113. Academic, New York.
- BUNKER, D. L., GARRETT, B., KLEINDIENST, T. & III, G. S. L. 1974 Discrete simulation methods in combustion kinetics. *Combust. Flame* **23**, 373–379.
- BYRNE, G. D. & HINDMARSH, A. C. 1987 Stiff ODE solvers: A review of current and coming attractions. *J. Comput. Phys.* **70**, 1–62.
- CHA, C. M. & TROUILLET, P. 2002a A model for the mixing time scale of a turbulent reacting scalar. *Phys. Fluids* (submitted).

- CHA, C. M. & TROUILLET, P. 2002b A subgrid mixing model for large-eddy simulations of turbulent reacting flows using the filtered density function. *Phys. Fluids* (submitted).
- CLAVIN, P. 1994 Premixed combustion and gasdynamics. In *Annu. Rev. Fluid Mech.* bf 26, 321–352.
- DOPAZO, C. 1994 Recent developments in PDF methods. In *Turbulent Reacting Flows* (P. A. Libby & F. A. Williams, eds.), chap. 7, pp. 375–474. Academic, New York.
- FELLER, W. 1970 *An Introduction to Probability Theory and Its Applications*, 3rd edn. Wiley, New York.
- FISHER, R. A. 1937 The wave advance of advantageous genes. *Ann. Eugenics* 7, 355–369.
- FOX, R. O. 1997 The Lagrangian spectral relaxation model of the scalar dissipation in homogeneous turbulence. *Phys. Fluids* 9 (8), 2364–2386.
- GARDINER, C. W. 1983 *Handbook of Stochastic Methods for Physics, Chemistry and the Natural Sciences*. Springer New York.
- GILLESPIE, D. T. 1992 *Markov Processes*. Academic, New York.
- VAN KAMPEN, N. G. 1992 *Stochastic Processes in Physics and Chemistry*. Amsterdam: North-Holland.
- KERSTEIN, A. R. 1991a Linear eddy model of turbulent scalar transport. Part 6: Microstructure of diffusive scalar mixing fields. *J. Fluid Mech.* 231, 361.
- KERSTEIN, A. R. 1991b Linear-eddy modeling of turbulent transport. Part V: Geometry of scalar interfaces. *Phys. Fluids A* 3, 1110–1114.
- KOLMOGOROV, A. N., PETROVSKY, I. G. & PISCOUNOV, N. S. 1937 Study of the diffusion equation with a source term and its application to a biological problem. *Bull. State Univ. Moscow* 1, 1–25.
- MENON, S. & KERSTEIN, A. R. 1992 Stochastic simulation of the structure and propagation rate of turbulent premixed flames. *Proc. Combust. Inst.* 24, 443–450.
- PETERS, N. 1999 The turbulent burning velocity for large scale and small scale turbulence. *J. Fluid Mech.* 384, 107–132.
- PETERS, N. 2000 *Turbulent Combustion*. Cambridge University Press.
- POPE, S. B. 1985 PDF methods for turbulent reacting flows. *Prog. Energy Combust. Sci.* 11, 119–192.
- POPE, S. B. 1990 Computations of turbulent combustion: Progress and challenges. *Proc. Combust. Inst.* 23, 591–612.
- POPE, S. B. 1997 Computationally efficient implementation of combustion chemistry using *in situ* adaptive tabulation. *Combust. Theory Modelling* 1, 41–63.
- POPE, S. B. & ANAND, M. S. 1984 Flamelet and distributed combustion in premixed turbulent flames. *Proc. Combust. Inst.* 20, 403–410.
- POPE, S. B. & CHEN, Y. L. 1990 The velocity-dissipation pdf model for turbulent flows. *Phys. Fluids A* 2, 1437.
- SMITH, T. & MENON, S. 1996 Model simulations of freely propagating turbulent premixed flames. *Proc. Combust. Inst.* 26, 299–306.
- WILLIAMS, F. A. 1985 *Combustion Theory*. Benjamin-Cummings, San Francisco..
- ZELDOVICH, Y. B. & FRANK-KAMENETSKY, D. A. 1938 A theory of thermal propagation of flame. *Acta Physicochim. URSS* 9, 341–350.

Comparison of turbulent premixed flames at different turbulence levels

By Laurent Duchamp de Lageneste AND Heinz Pitsch

1. Introduction

In the flamelet regime, turbulent combustion is characterized by a reaction-zone thickness much smaller than the Kolmogorov length scale (Peters 2000). Thus the internal flame structure remains unaffected by turbulence, and can be approximated by a thin interface separating burnt from unburnt gases.

An equation describing the dynamics of such a surface has been presented in Williams (1985) and is now known as the G -equation. It is based on the flamelet assumption and uses the general level-set methodology described in detail in Sethian (1996) and Osher & Fedkiw (2002). Variants of this model have been used in conjunction with Reynolds-averaged Navier-Stokes models (RANS) (Peters 2000; Herrmann 2000) or large-eddy simulation models (LES) (Smith & Menon 1997; Kim & Menon 2000; Chakravarthy & Menon 2000; Sankaran & Menon 2000; Duchamp de Lageneste & Pitsch 2001).

Pitsch & Duchamp de Lageneste (2002) have formulated a level-set method based on the G -equation for LES of premixed turbulent combustion in which a specific filtering procedure respecting the particular symmetries of the G -equation (Oberlack *et al.* 2001) has been used.

As a validation of the model and to demonstrate the benefits of LES in turbulent combustion modeling, we report in the present paper on the LES of two Bunsen flames, the F3-flame and the F2-flame from the series of experiments by Chen *et al.* (1996). These flames are nominally in the regime of thin reaction zones (Peters 2000) but F2, which has a higher turbulence level and hence a higher Karlovitz number, is closer to the regime of distributed reaction zones than F3.

After briefly recalling the main equations used in the level-set modeling of premixed turbulent combustion, we will compare results from the simulations to the experimental data of Chen *et al.* (1996). As a first step, results from the cold-flow simulations will be presented to ensure that adequate boundary conditions are used in the LES. This cold flow will also be used as a validation of the flow solver as well as a reference computation, to be used later to assess the ability of the LES to capture flow changes due to combustion.

We will then present and discuss results concerning the reacting cases, where time-averaged quantities such as axial velocity, turbulent kinetic energy and temperature will be compared to the data of Chen *et al.* (1996).

2. Level-set method

We briefly recall here the main equations and models involved in the level-set LES of premixed turbulent combustion. The derivation and discretization of this method is discussed in detail in previous reports. In the following equations, all symbols denote filtered quantities unless otherwise noted.

The level-set equation (or G -equation) for LES is written as:

$$\frac{\partial G}{\partial t} + \mathbf{U} \cdot \nabla G = \frac{\rho_u}{\rho} (s_T - D_t \kappa) |\nabla G|, \quad (2.1)$$

where \mathbf{U} is the convection velocity, s_T the turbulent burning velocity, ρ_u the unburnt density, and κ the curvature.

An algebraic model similar to the one derived for RANS by Peters (2000) is used for the turbulent burning velocity:

$$\frac{s_T - s_L}{s_L} = -\frac{C_\nu b_3^2}{2b_1 S c_{t,G} l_F} \frac{\Delta}{l_F} + \left[\left(\frac{C_\nu b_3^2}{2b_1 S c_{t,G}} \right)^2 + \frac{b_3^2 D_t}{s_L l_F} \right]^{\frac{1}{2}}, \quad (2.2)$$

where Δ is the filter width, $D_t = C_\nu \Delta v'_\Delta / S c_{t,G}$ the turbulent diffusivity computed with a constant turbulent Schmidt number of $S c_{t,G} = 0.5$ according to Pitsch & Steiner (2000), v'_Δ being the turbulent velocity fluctuation, and s_L and l_F the laminar burning velocity and flame thickness respectively. The constants b_1 and b_3 are evaluated by Peters (2000) as $b_1 = 2.0$ and $b_3 = 1.0$.

In the case where dilution or partial-premixing effects are to be considered, an equation for the conserved mixture fraction Z is also solved together with an equation for the reduced temperature $\theta = (T - T_u)/(T_b - T_u)$. If heat losses are included in the model, an equation for the enthalpy H is also used. These equations are:

$$\rho \frac{\partial Z}{\partial t} + \rho \mathbf{U} \cdot \nabla Z = \nabla \cdot (\rho D_t^Z \nabla Z), \quad (2.3)$$

$$\rho \frac{\partial \theta}{\partial t} + \rho \mathbf{U} \cdot \nabla \theta = \nabla \cdot (\rho D_t^\theta \nabla \theta) + \rho \omega, \quad (2.4)$$

and:

$$\rho \frac{\partial H}{\partial t} + \rho \mathbf{U} \cdot \nabla H = \nabla \cdot (\rho D_t^H \nabla H). \quad (2.5)$$

On the burnt side, the temperature is given as a function of Z and its subgrid variance by pre-computing a laminar flamelet library similar to the one classically used in non-premixed combustion (Peters 2000). Although, since an equation for the temperature is already solved, it may seem redundant to use an extra equation for the enthalpy, H is used only as a parameter in the generation of the flamelet library to take possible heat losses into account. On the unburnt side, the temperature is simply given by the solution of (2.4). Hence, (2.4) is really only solved in the unburnt region, with the burnt temperature evaluated from the flamelet library acting as a boundary condition at the flame surface.

In order to distinguish between burnt and unburnt regions, the probability of burning $P_b = P_{G \geq G_0}$ is defined using an assumed PDF approach. Assuming a Gaussian sub-filter distribution for G , this PDF is given by:

$$P_{G \geq G_0} = \int_{\xi=G_0}^{\infty} \frac{1}{\sqrt{2\pi G''^2}} \exp \left[-\frac{(G - \xi)^2}{2G''^2} \right] d\xi. \quad (2.6)$$

The filtered source term appearing in (2.4) is expressed as: $\omega = P_b(\theta - \theta_{flamelet})$, thus setting the temperature to the value prescribed by the flamelet library ($\theta_{flamelet}$) on the burnt side while vanishing on the unburnt side.

All subgrid quantities such as the subgrid variances Z''^2 and G''^2 or the turbulent

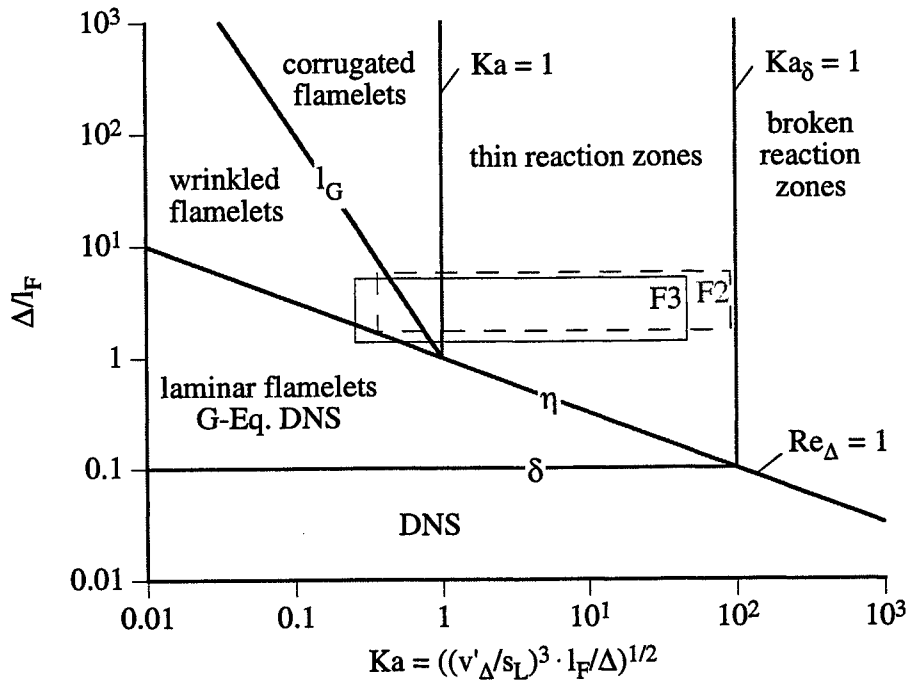


FIGURE 1. LES regime diagram. The non-dimensional filter width is plotted as a function of the Karlovitz number. The areas covered by the values of the parameters computed along an instantaneous flame surface for F2 and F3 are shown as rectangles.

diffusivities $D_t^{\theta, H, Z}$ are computed using the dynamic approach developed by Moin *et al.* (1991) and Pierce & Moin (1998).

3. Numerical simulation

3.1. Experimental setup

Flame F2 and F3 are turbulent Bunsen flames, studied experimentally by Chen *et al.* (1996). The experimental setup is the same in both cases, and consists of an axial-symmetric central jet of diameter $D = 12$ mm surrounded by a large pilot flame. A stoichiometric mixture of methane and air is used for the central jet as well as the pilot flame. The whole apparatus is surrounded by air at rest.

The mean exit velocity of the central jet is different in each case, with $U_0 = 50$ m/s for F2 and $U_0 = 30$ m/s for F3. Experimental data are available for the cold flow as well as the reacting flow at different downstream stations.

Chen *et al.* (1996) have shown that both flames are mainly in the regime of thin reaction zones. This is confirmed by showing in figure 1 the values of the non-dimensional filter width and corresponding Karlovitz number computed along an instantaneous flame surface for F2 and F3. The rectangles in figure 1 are used to represent the area covered by the parameter values in both cases, and F2 is shown to have on average a higher Karlovitz number than F3.

3.2. Grid and boundary conditions

We use the structured code developed at CTR by Pierce & Moin (2001), in which the low-Mach-number approximation to the Navier-Stokes equations is solved using a second-order finite-volume scheme on a staggered cylindrical grid.

The computational domain extends $20D$ downstream of the nozzle and $4D$ in the radial direction. The grid of $256 \times 96 \times 64$ nodes corresponds to approximately 1.6 million cells, and is refined around the wall separating the central jet from the pilot in the radial direction.

Convective boundary conditions (Akselvoll 1996) are prescribed at the outlet, while instantaneous profiles, obtained from a separate, fully-developed turbulent pipe flow LES, are prescribed at the central jet inlet. The surrounding pilot is considered to be a laminar inflow with a prescribed mean velocity, computed using the mean mass-flow rate given in the experiment.

Before discussing the results, a few remarks concerning the experimental results and their subsequent consequences on our modeling assumptions are worth making:

- In the experiment, the pilot nozzle consists of an array off small jets issued through a cooled perforated plate (1175 holes of 1 mm in diameter), forming a flat flame above the plate's surface. This configuration leads to heat losses at the plate surface which are modeled in the simulation by choosing an appropriate enthalpy for the fluid issuing from the pilot to give the correct temperature distribution at the first measurement station downstream of the nozzle, which is located at $x/D = 0.25$.
- While the inlet profiles used in the simulation of the central jet are those of a fully developed pipe flow, experimental data close to the inlet section show that the flow may not be fully developed. Nevertheless, it will be shown that these differences are small and are unimportant further downstream.
- Since the only difference between F2 and F3 is the mean velocity of the central jet, the only parameter that has been changed in our simulations is the Reynolds number.

4. Results and discussion

In this section we present some comparisons between the results from the LES and the experimental data reported by Chen *et al.* (1996). In particular, we discuss predictions of mean quantities such as mean axial velocity or temperature, as well as turbulent quantities like the turbulent kinetic energy and turbulent flame-brush thickness.

We first focus briefly on cold-flow results before presenting a more detailed study of reacting-flow simulations.

4.1. Cold flow

In this section, we compare some of the LES results for the non-reacting flows with corresponding experimental data. The purpose of this comparison is twofold:

- It serves as a validation of the flow solver, insuring that grid and boundary conditions are properly chosen,
- By comparing the cold-flow results with reacting-flow results presented below, the data will be used to assess the ability of the LES to capture flow changes generated by the combustion process.

4.1.1. Mean axial velocity

Figure 2 shows a comparison between computed (solid lines) and measured (symbols) radial profiles of mean axial velocity at two downstream locations. As expected, the

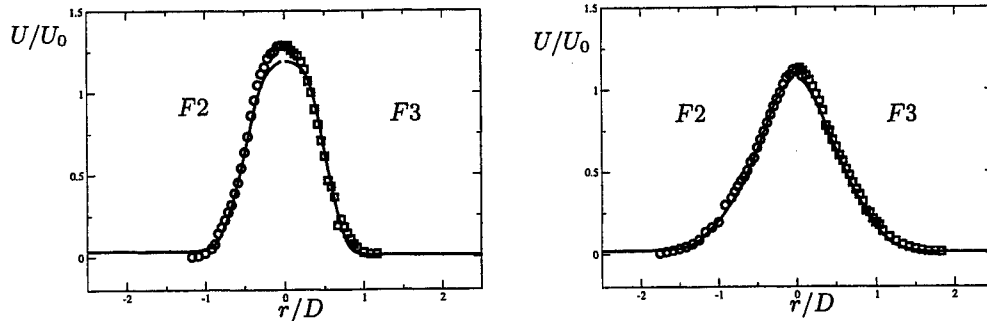


FIGURE 2. Cold flow. Radial profiles of mean axial velocity. Solid lines denote the LES results, symbols denote experimental data. Stations: $x/D = 2.5$ (left) and $x/D = 6.5$ (right).

experimental data shows the spreading of the jet corresponding to the development of the lateral shear layers. The end of the potential core is observed at roughly $x/D = 4.5$, and the maximum mean velocity decreases from thereon as the jet expands in the radial direction.

The LES captures these effects very accurately. Some discrepancies in the maximum jet velocity can be seen at the first station and indicate that our assumption of a fully developed pipe flow at the inflow may not have been fully realized in the experiment. Nevertheless, these small discrepancies vanish further downstream and do not seem to affect the accuracy of the results.

With proper non-dimensionalization, very little difference can be observed between F2 and F3, underlining the self-similar development of the jets.

Overall, the agreement between the LES and the experimental data is very good.

4.1.2. Turbulent kinetic energy

Figure 3 shows radial profiles of turbulent kinetic energy for the same downstream locations as in the previous section. These profiles also show the radial spreading of the lateral shear layers surrounding the central jet and it can be seen that radial mixing increases, both outwards and inwards, with distance from the nozzle. In particular, the increase of turbulent kinetic energy close to the centerline indicates the merging of the lateral shear layers and thus the end of the potential core. It is to be noted that the peak turbulent kinetic energy is constant up to $x/D = 6.5$ and that, again, no significant differences can be observed between F2 and F3.

The results extracted from the LES capture the downstream evolution of the turbulent kinetic energy with very good accuracy.

4.2. Reacting flow

In this section, results from the LES of flames F2 and F3 are compared to experimental data from Chen *et al.* (1996). Comparisons are shown between cold and reacting flows, but also between the two reacting flows, to assess the ability of the LES to predict not only the impact of combustion on the flow field but also the changes with Reynolds number.

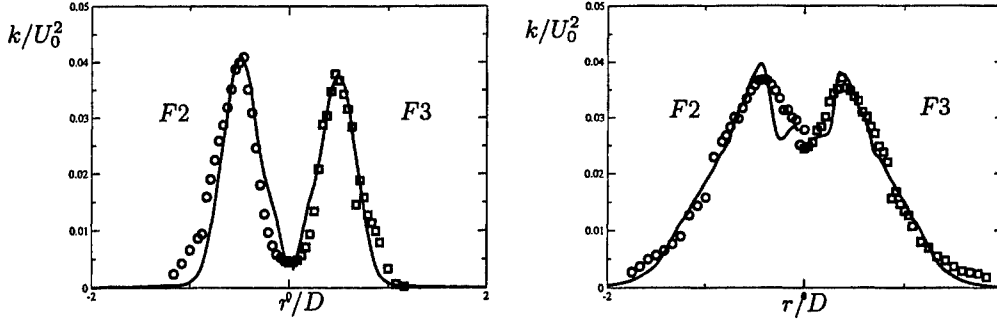


FIGURE 3. Cold flow. Radial profiles of turbulent kinetic energy. Solid lines denote the LES results, symbols denote experimental data. Stations: $x/D = 2.5$ (left) and $x/D = 6.5$ (right).

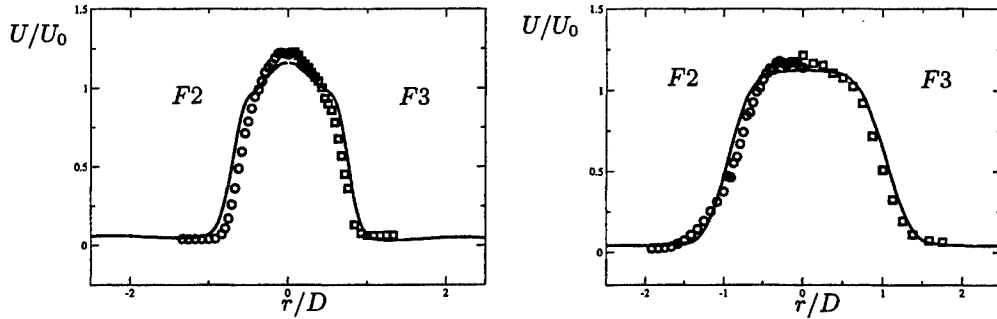


FIGURE 4. Reacting flow. Radial profiles of mean axial velocity. Solid lines denote the LES results, symbols denote experimental data. Stations: $x/D = 2.5$ (left) and $x/D = 6.5$ (right).

4.2.1. Mean axial velocity

Figure 4 shows radial profiles of the mean axial velocity at the two downstream stations $x/D = 2.5$ and $x/D = 6.5$. Results for flame F2 are on the left side while those for F3 are on the right. Symbols represent experimental data, solid lines the numerical results.

A first interesting comparison can be made between figure 4 and figure 2 concerning the ability of the LES to capture the effect of heat release on the mean flow pattern. In this respect, the experimental data show that the presence of combustion has qualitatively the same effect on the mean velocity profiles for both flames:

- radial profiles are broadened because of the divergence of the mean streamlines due to gas expansion,
- the maximum velocity observed around the centerline stays approximately constant up to the axial position where the fuel is almost completely consumed, showing an extension of the potential core in the reacting case.

These significant differences between cold and reacting cases are particularly apparent if one compares figure 4 to figure 2 for the downstream station $x/D = 6.5$. It can also be seen in these figures that the LES reproduces these effects accurately.

We will now focus on the specific differences between the two reacting cases. The main

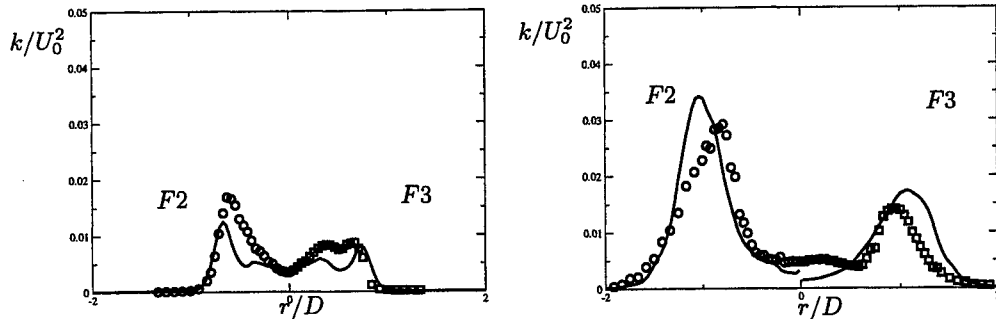


FIGURE 5. Reacting flow. Radial profiles of turbulent kinetic energy. Solid lines denote the LES results, symbols denote experimental data. Stations: $x/D = 2.5$ (left) and $x/D = 6.5$ (right).

difference from the experimental data is the apparent larger broadening of the axial velocity profile in the F3 case compared with F2. This phenomenon can be observed at both stations and is well predicted by the simulation. It is consistent with the lower jet exit velocity for F3, leading to a relatively faster flame. F3 being shorter than F2, its angle with the burner is smaller and leads to a wider spreading of the jet.

The overall quantitative agreement between computation and experiment is good, although one can observe in figure 4 a slight overprediction of the jet spreading rate in both cases. An explanation for this discrepancy will be given in section 4.2.3.

4.2.2. Turbulent kinetic energy

Figure 5 displays radial profiles of turbulent kinetic energy at stations $x/D = 2.5$ and 6.5 and can be compared to figure 3. Large differences can be observed between the cold and the reacting cases.

First, the turbulent fluctuations are greatly reduced in the reacting case due to the increased viscosity and the dilatation caused by the heat release. This is especially apparent at $x/D = 2.5$, where the peak intensity was found experimentally to be reduced by 58% for F2 and 75% for F3 compared to the cold case. This trend is well reproduced by the simulation although to a slightly higher extent as reductions of 66% and 77% are observed for F2 and F3 respectively.

Furthermore, computational and experimental results shown in figure 3 show an increasing turbulent kinetic energy close to the centerline for the cold case, but figure 5 shows relatively constant levels for both reacting cases. This indicates that the shear layer surrounding the jet are deflected outward in the reacting cases due to heat release, extending the potential core up to the axial position where most of the fuel is consumed, and therefore prevents radial mixing.

In addition, it was noted in section 4.1.2 that turbulent kinetic energy levels for the cold cases were relatively constant up to $x/D = 6.5$. In contrast, the peak intensity computed in the LES increases in the downstream direction for both reacting cases, and follows the trend observed experimentally, levels for F2 are always higher than for F3.

It was also reported in section 4.1.2 that no significant difference could be found between the F2 and F3 turbulent kinetic energy profiles for the cold cases, whereas results and experimental data show large qualitative and quantitative differences for the reacting cases. For instance, at the first station $x/D = 2.5$, the experimental results for F3 show

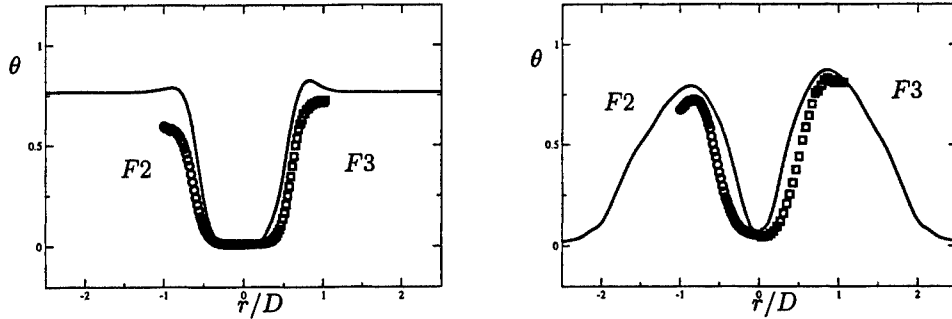


FIGURE 6. Reacting flow. Radial profiles of reduced mean temperature. Solid lines – LES results, symbols – experimental data. Stations: $x/D = 2.5$ (left) and $x/D = 6.5$ (right).

that the radial profile exhibits two peaks. The first one, located on the burnt side of the flame, is also observed in the F2 results and increases along the streamwise direction whereas the second one, found on the unburnt side, is not observed for F2, and vanishes further downstream. This particular behavior is qualitatively well predicted by the LES as shown in figure 5.

While the overall quantitative predictions from the LES are reasonable, figure 5 shows that the LES slightly underpredicts turbulent kinetic energy levels at $x/D = 2.5$ while it overpredicts this same quantity at $x/D = 6.5$, this trend can be observed for both F2 and F3.

4.2.3. Mean temperature

Figure 6 shows the radial profiles of the mean reduced temperature defined by

$$\theta = \frac{T - T_u}{T_b - T_u}, \quad (4.1)$$

where T_u is the unburnt temperature and T_b the burnt temperature.

At $x/D = 2.5$, the most important difference between F2 and F3 reported by Chen *et al.* (1996) is the considerably lower mean temperature observed for flame F2. Whereas flame F3 is already found to be at a reduced temperature approximately 25 % lower than the adiabatic flame temperature due to heat losses at the burner surface, F2 temperature is even lower (about 45 %). This difference can be explained by the combined effect of heat losses at the burner exit and increased fluctuations of the flame front.

As shown in figure 6, LES results for F3 are overpredictions, but still reasonable with a maximum discrepancy around 10 % whereas those for F2 show a maximum discrepancy of around 25 %. This tendency of the LES to overpredict the mean temperature is consistent with the overprediction of the jet spreading rate noted in section 4.2.1, as well as with the lower predicted turbulence intensities observed at $x/D = 2.5$ (section 4.2.2). However, it is observed in figure 6 that the predictions tend to become better further downstream, such that results at $x/D = 6.5$ are in reasonable agreement with experimental data. Thus, the major discrepancies observed between our simulations and the experimental data of Chen *et al.* (1996) are found to be confined to the first few diameters downstream of the jet exit.

Since heat losses at the burner exit are taken into account in both simulations and are

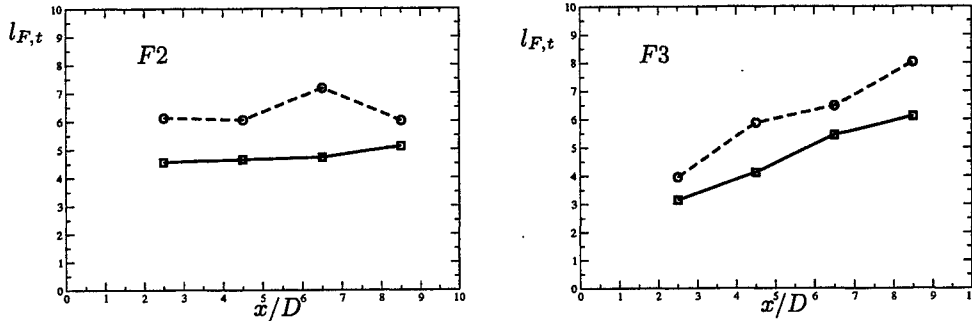


FIGURE 7. Downstream evolution of the mean turbulent flame-brush thickness $l_{F,t}$. Solid lines denotes LES, dashed lines experimental results. F2 flame (left) and F3 flame (right).

not expected to be very different from F3 to F2, we will now focus on the predictions of the flame front fluctuations.

4.2.4. Turbulent flame-brush thickness

In Chen *et al.* (1996), the turbulent flame-brush thickness is defined as a measure of the flame-front fluctuations and is computed as

$$l_{F,t} = \left[\frac{\partial \bar{\theta}}{\partial r} \right]_{\max}^{-1}. \quad (4.2)$$

Figure 7 shows the values of $l_{F,t}$ extracted from the experimental data of Chen *et al.* (1996) at four different downstream stations $x/D = 2.5$, $x/D = 4.5$, $x/D = 6.5$ and $x/D = 8.5$ for flames F2 and F3 compared with the corresponding values obtained from the LES.

It is immediately apparent that the LES underpredicts the turbulent flame-brush thickness at every station for both flames. If one considers only the results for the first station $x/D = 2.5$, it is seen that the experiment predicts an increase of the turbulent flame brush of nearly 60% when going from F3 to F2, whereas the LES shows an increase closer to 45%. Thus LES underpredicts the turbulent flame-brush thickness of flame F2 by almost 30%, which could explain the overprediction of the mean temperature at $x/D = 2.5$. A possible reason for this systematic underprediction of the flame-surface wrinkling could be the presence of a curvature term in (2.1). This term tends to damp any small instability occurring at the flame front. Pitsch (2002) presents a new derivation of the G -equation for LES where this curvature term does not appear. Further validation of this new formulation with the F2 and F3 cases will assess the impact of the curvature on the flame-front wrinkling and is in progress.

On a more qualitative level, the results shown in figure 7 also show significant differences in the downstream evolution of l_F for F2 and F3. While $l_{F,t}$ increases linearly with distance from the burner for F3, it seems to stay constant for F2. This behavior is also observed in the LES, and can be linked to the higher Reynolds number of flame F2.

5. Conclusions

This paper presents results from the LES of two turbulent Bunsen flames at different Reynolds and Karlovitz numbers. A level-set method has been used as a model for turbulent premixed combustion and comparison are made with the experimental data of Chen *et al.* (1996). As a validation of the flow solver, computations of the corresponding cold cases have been carried out and used as references to assess the ability of the LES to predict the changes of the flow patterns due to combustion.

From the cold-flow simulations, it has been shown that inflow and boundary conditions are properly chosen, and that the flow solver predicts results in very good agreement with experimental data.

Subsequent comparisons of the reacting-flow characteristics have shown that the level-set approach is able to reproduce the main characteristics of the turbulent flames studied. In particular, the changes in the mean flow pattern due to heat release, such as the increased spreading of the jet and decreased turbulent kinetic energy, are well captured. Furthermore, the main flow differences between F3 and F2, such as the higher spreading rate and lower turbulent kinetic energy of F3 compared with F2, are reasonably well reproduced by the LES.

Nevertheless, mean temperature profiles were shown to be overpredicted in the first few diameters downstream of the nozzle, especially for F2. These discrepancies were traced to an underprediction of the turbulent fluctuations of the flame front and a possible link with the presence of a curvature term in the *G*-equation was suggested.

Acknowledgments

The authors gratefully acknowledge funding by the US Department of Energy within the ASCI program, and by SNECMA Moteurs.

REFERENCES

- AKSELVOLL, K. 1996 An efficient method for temporal integration of the navier-stokes equations in confined axisymmetric geometries. *J. Comp. Phys.* **125**, 454–463.
- CHAKRAVARTHY, V. K. & MENON, S. 2000 Subgrid modeling of turbulent premixed flames in the flamelet regime. *Flow, Turb. and Comb.* **5**, 23–45.
- CHEN, Y. C., PETERS, N., SCHNEEMANN, G. A., WRUCK, N., RENZ, U. & MANSOUR, M. S. 1996 The detailed flame structure of highly stretched turbulent premixed methane-air flames. *Comb. and Flame* **107**, 233–244.
- HERRMANN, M. 2000 Numerische simulation vorgemischter und teilweise vorgemischter turbulenten flammen. PhD thesis, RWTH, Aachen.
- KIM, W. W. & MENON, S. 2000 Numerical modeling of turbulent premixed flames in the thin-reaction zones regime. *Comb. Sci. Tech.* **172**, 1–32.
- DUCHAMP DE LAGENESTE, L. & PITSCHE, H. 2001 Progress in large-eddy simulation of premixed and partially-premixed turbulent combustion. In *Annual Research Briefs*, Center for Turbulence Research, NASA Ames/Stanford Univ., pp. 97–107.
- MOIN, P., SQUIRES, K., CABOT, W. & LEE, S. 1991 A dynamic subgrid-scale model for compressible turbulence and scalar transport. *Phys. Fluids A*, 2746–2757.
- OBERLACK, M., WENZEL, H. & PETERS, N. 2001 On symmetries and averaging of the *G*-equation for premixed combustion. *Comb. Theo. and Model.* **5**, 1–20.

- OSHER, S. & FEDKIW, R. 2002 *Level set methods and dynamic implicit surfaces*, *Applied Mathematical Sciences*, vol. 153. Springer, New York.
- PETERS, N. 2000 *Turbulent Combustion*. Cambridge University Pres.
- PIERCE, C. D. & MOIN, P. 1998 Large eddy simulation of a confined jet with swirl and heat release. *AIAA Paper* 98-2892.
- PIERCE, C. D. & MOIN, P. 2001 Progress-variable approach for large eddy simulation of turbulent combustion. *Tech. Rept. TF-80*. Dept. Mech. Engg., Stanford University.
- PITSCH, H. 2002 A *G*-equation formulation for large-eddy simulation of premixed turbulent combustion. In *Ann. Research Briefs*, Center for Turbulence Research, NASA Ames/Stanford Univ.,
- PITSCH, H. & DUCHAMP DE LAGENESTE, L. 2002 Large-eddy simulation of premixed turbulent combustion using a level-set approach. In *Proceedings of the 29th Symposium on Combustion*. The Combustion Institute. Accepted for publication.
- PITSCH, H. & STEINER, H. 2000 Large eddy simulation of a turbulent piloted methane/air diffusion flame. *Phys. Fluids* **12** (10), 2541–2553.
- SANKARAN, V. & MENON, S. 2000 Structure of premixed flame in the thin-reaction zones regime. In *Proceedings of the 28th Symposium on Combustion*. The Combustion Institute, Pittsburg, pp.123–129.
- SETHIAN, J. A. 1996 *Level Set Methods : Evolving Interfaces in Geometry, Fluid Mechanics, Computer Vision and Material Science*. Cambridge University Press.
- SMITH, T. M. & MENON, S. 1997 One-dimensional simulations of freely propagating turbulent premixed flames. *Comb. Sci. Tech.* **128**, 99–130.
- WILLIAMS, F. A. 1985 Turbulent combustion. In *Math. of Comb.* (Frontiers in Applied Mathematics, vol 2, J. Buckmaster, ed.) SIAM, Philadelphia

An Eulerian level-set/vortex-sheet method for two-phase interface dynamics

By M. Herrmann

1. Motivation and objectives

Two-phase interface dynamics play an important role in a wide variety of technical applications, for example direct injection IC-engines, LOX/H₂ rocket engines, or spray painting. The dynamics at the interface determine the atomization process, i.e. the process by which an initially-liquid jet or sheet is broken up into individual small drops. This atomization process can be the rate-determining factor for combustion processes where the fuel and/or the oxidizer are initially in liquid form. The correct physical modeling of the atomization process, usually in a turbulent environment, is therefore crucial for the overall simulation of such combustion systems.

The atomization process of liquid jets/sheets is usually divided into two consecutive steps, the primary and the secondary atomization. The initial breakup of the liquid jet/sheet into large and small structures is called the primary atomization, whereas the subsequent breakup of these structures into ever-smaller drops is called secondary atomization.

The objective of this paper is to lay down a framework for the development of a Large Surface Structure (LSS) model to correctly describe the primary atomization process in turbulent environments. To this end, a simplified system of equations describing the instantaneous interface dynamics is derived, which forms the basis for the introduction of filtering and the derivation of closure models in future work. Coupling of this LSS model with both a subsequent spray model, describing the secondary atomization and evaporation, and a Large Eddy Simulation (LES) turbulence model will provide a sound physical model for the simulation of the entire atomization process.

In the present work, the simplified system of equations describing the instantaneous interface dynamics is derived. Then, the employed numerical methods are presented. Finally, the approach is validated by calculating vortex sheets without surface tension, the linear regime of the Kelvin-Helmholtz instability, and its long-time behavior.

2. Governing equations

To simplify the following derivations and discussion, we will limit ourselves to the two-dimensional case. The extension to three dimensions is straightforward.

The focus of this paper is the motion of the interface Γ between two inviscid, incompressible fluids 1 and 2, as shown in Fig. 1. In this case, the velocity on either side i of the interface Γ is determined by the incompressible Euler equations given here in dimensionless form as

$$\nabla \cdot \mathbf{u}_i = 0, \quad (2.1)$$

$$\frac{\partial \mathbf{u}_i}{\partial t} + (\mathbf{u}_i \cdot \nabla) \mathbf{u}_i = -\frac{1}{\rho_i} \nabla p, \quad (2.2)$$

subjected to the boundary conditions at the interface Γ ,

$$[(\mathbf{u}_1 - \mathbf{u}_2) \cdot \mathbf{n}] \Big|_{\Gamma} = 0, \quad [p_2 - p_1] \Big|_{\Gamma} = \frac{1}{We} \kappa, \quad (2.3)$$

and in the far field,

$$\lim_{y \rightarrow \pm\infty} \mathbf{u}_i = (\pm U_{\infty}, 0)^T. \quad (2.4)$$

Here, \mathbf{n} is the vector normal to the interface, $We = \rho_{ref} u_{ref}^2 / \Sigma L_{ref}$ is the Weber number, Σ is the surface-tension coefficient, ρ_{ref} , u_{ref} , L_{ref} are reference density, velocity and length respectively, and κ is the curvature of Γ . An interface subjected to the above boundary conditions is called a vortex sheet; see Saffman & Baker (1979). Parameterizing the interface location by

$$\mathbf{x}(\alpha, t) \Big|_{\Gamma} = (x(\alpha, t), y(\alpha, t))^T \Big|_{\Gamma}, \quad (2.5)$$

the velocity \mathbf{u} at a point \mathbf{x} away from the interface is given by

$$\mathbf{u}(\mathbf{x}, t) = \int_{\Gamma} \eta^*(\alpha, t) \mathbf{e}_z \times \frac{\mathbf{x} - \mathbf{x}(\alpha, t)}{|\mathbf{x} - \mathbf{x}(\alpha, t)|^2} d\alpha, \quad (2.6)$$

where η^* is the unnormalized vortex-sheet strength and \mathbf{e}_z is the unit vector in the third dimension. The normalized vortex-sheet strength η defines the jump in tangential velocity across the interface Γ ,

$$\eta = \frac{\eta^*}{\partial_{\alpha} s} = [(\mathbf{u}_2 - \mathbf{u}_1) \cdot \mathbf{t}] \Big|_{\Gamma}, \quad (2.7)$$

where \mathbf{t} is the interface tangential vector and

$$\partial_{\alpha} s = \frac{\partial s}{\partial \alpha} = \sqrt{\left(\frac{\partial x}{\partial \alpha}\right)^2 + \left(\frac{\partial y}{\partial \alpha}\right)^2} \quad (2.8)$$

is the arc-length metric. Combining (2.6) and (2.7), \mathbf{u} can also be calculated from a line integral of the vortex-sheet strength,

$$\mathbf{u}(\mathbf{x}, t) = \int_{\Gamma} \eta(s, t) \mathbf{e}_z \times \frac{\mathbf{x} - \mathbf{x}(s, t)}{|\mathbf{x} - \mathbf{x}(s, t)|^2} ds. \quad (2.9)$$

2.1. Lagrangian formulation

Parameterizing the interface by (2.5), denoting by \mathbf{u}_{Γ} the velocity on the interface calculated from the principal-value integration of (2.6), and assuming equal densities of both fluids, the evolution equation for the interface location is given by

$$\frac{\partial \mathbf{x}}{\partial t} = \mathbf{u}_{\Gamma}, \quad (2.10)$$

$$\frac{\partial \eta^*}{\partial t} = \frac{1}{We} \frac{\partial \kappa}{\partial \alpha}. \quad (2.11)$$

Equation (2.11) can be derived by combining the Euler equations (2.1) and (2.2) with the boundary conditions (2.3)-(2.4) and the velocity at the interface (2.6); see for example Baker *et al.* (1982); Hou *et al.* (1994).

2.2. Eulerian formulation

Instead of parameterizing the interface Γ by (2.5), the interface may also be represented by the iso-surface of a scalar field $G(\mathbf{x}, t)$, as shown in figure 1. Setting

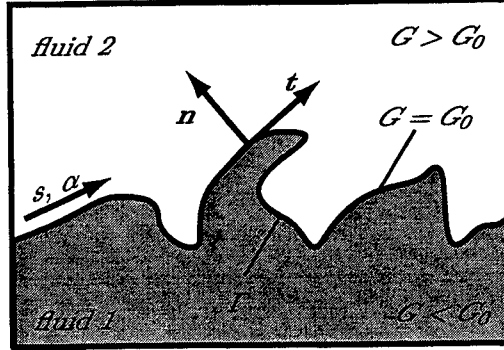


FIGURE 1. Interface definition.

$$G(\mathbf{x}, t)|_{\Gamma} = G_0 = \text{const}, \quad (2.12)$$

$G(\mathbf{x}, t) < G_0$ in fluid 1, and $G(\mathbf{x}, t) > G_0$ in fluid 2, an evolution equation for the scalar G can be derived by simply differentiating (2.12) with respect to time and using (2.10),

$$\frac{\partial G}{\partial t} + \mathbf{u} \cdot \nabla G = 0. \quad (2.13)$$

This equation is called the level-set equation and goes back to Osher & Sethian (1988). It is easy to see, that (2.13) is independent of the choice of G away from the interface. However, to facilitate the numerical solution of (2.13), G is chosen to be a distance function away from the interface, i.e.

$$|\nabla G| \Big|_{G \neq G_0} = 1. \quad (2.14)$$

Transforming (2.11) to an Eulerian frame results in

$$\frac{\partial \eta^*}{\partial t} + \mathbf{u} \cdot \nabla \eta^* = \frac{1}{\text{We}} \partial_\alpha s \nabla \kappa \cdot \mathbf{t}. \quad (2.15)$$

Making use of the level-set scalar G , the curvature κ can be expressed as

$$\kappa = \nabla \cdot \mathbf{n} = \nabla \cdot \frac{\nabla G}{|\nabla G|}, \quad (2.16)$$

and the interface tangential vector \mathbf{t} and normal vector \mathbf{n} are

$$\mathbf{t} = \frac{1}{|\nabla G|} \begin{pmatrix} -\partial_y G \\ \partial_x G \end{pmatrix}, \quad \mathbf{n} = \frac{\nabla G}{|\nabla G|}. \quad (2.17)$$

Strictly speaking, (2.15) has physical meaning only at the location of the interface itself, i.e. $G = G_0$, since only there is the surface tension term on the right-hand side defined. Again, as is the case for the level-set scalar G , a reinitialization operation for values away from the interface should be prescribed. Here, the redistribution condition

$$\nabla \eta^* \cdot \nabla G = 0 \quad (2.18)$$

is used, setting $\eta^* = \eta^* \Big|_{G=G_0} = \text{const.}$ in the direction normal to the interface.

Since (2.9) involves η instead of η^* it is useful to derive a transport equation for the vortex-sheet strength. To do this, the arc-length metric has to be expressed in terms of the level-set scalar G . Following the arguments in Harabetian & Osher (1998), let us

introduce a function ϕ , such that the pair (G, ϕ) forms an orthogonal coordinate system near $G = G_0$,

$$\phi(\mathbf{x}(\alpha), t) = \alpha. \quad (2.19)$$

Differentiating (2.12) and (2.19) with respect to α and solving the resulting system leads to

$$\partial_\alpha \mathbf{x} = J^{-1} (-\partial_y G, \partial_x G)^T, \quad (2.20)$$

where J is the Jacobian of (G, ϕ) ,

$$J = \partial_x G \partial_y \phi - \partial_y G \partial_x \phi. \quad (2.21)$$

Inserting (2.20) into (2.8) and abbreviating $\sigma = |\nabla G| \Big|_{G=G_0}$ results in

$$\partial_\alpha s = \frac{1}{|J|} \sigma. \quad (2.22)$$

A transport equation for J has been derived by Harabetian & Osher (1998). In the case analyzed here, this reduces to

$$\frac{\partial J}{\partial t} + \mathbf{u} \cdot \nabla J = 0. \quad (2.23)$$

The evolution equation for σ can be derived by applying the ∇ operator to (2.13) and multiplying the resulting equation with $\mathbf{n} = \nabla G / |\nabla G|$, which yields

$$\frac{\partial \sigma}{\partial t} + \mathbf{u} \cdot \nabla \sigma = -(\mathbf{n} \cdot \nabla \mathbf{u} \cdot \mathbf{n}) \sigma. \quad (2.24)$$

Finally, combining this equation with (2.7), (2.15), (2.22), and (2.23) gives, after some algebraic manipulations, the transport equation for the vortex-sheet strength η

$$\frac{\partial \eta}{\partial t} + \mathbf{u} \cdot \nabla \eta = (\mathbf{n} \cdot \nabla \mathbf{u} \cdot \mathbf{n}) \eta + \frac{1}{We} \nabla \kappa \cdot \mathbf{t}. \quad (2.25)$$

Here, the terms on the left-hand side describe temporal changes and convective transport, respectively. The first term on the right-hand side describes the effect of stretching of the vortex sheet and the second term accounts for the influence of surface tension. Again, the above equation has meaning only at the interface location itself. Away from the interface, the redistribution equation

$$\nabla \eta \cdot \nabla G = 0 \quad (2.26)$$

is employed.

Finally, to close the system of (2.13) and (2.25), the velocity \mathbf{u} has to be calculated from the vortex-sheet strength η . Two different approaches can be used to evaluate this coupling. First, \mathbf{u} can be evaluated by a surface integral according to (2.9). Noting that any surface integral along $G = G_0$ can be transformed to a volume integral by

$$\int_{\Gamma} f(s) ds = \int_V f(\mathbf{x}') \delta(G(\mathbf{x}') - G_0) |\nabla G(\mathbf{x}')| d\mathbf{x}', \quad (2.27)$$

where δ is the delta function, (2.9) can be rewritten as

$$\mathbf{u}(\mathbf{x}, t) = \int_V \eta(\mathbf{x}', t) \mathbf{e}_z \times \frac{\mathbf{x} - \mathbf{x}'}{|\mathbf{x} - \mathbf{x}'|^2} \delta(G(\mathbf{x}') - G_0) |\nabla G(\mathbf{x}')| d\mathbf{x}'. \quad (2.28)$$

Using the latter formulation has the advantage that no explicit reconstruction of the interface location from the level-set scalar field is required. It should be pointed out

however that (2.9) and (2.28) are computationally expensive since they involve a surface integration volume integration, respectively, for each grid node near the interface.

Second, following the vortex-in-cell approach, see Christiansen (1973), the velocity \mathbf{u} can be calculated from a stream function ψ ,

$$\mathbf{u}(\mathbf{x}, t) = \int_V \delta(\mathbf{x} - \mathbf{x}') (\partial_y \psi(\mathbf{x}', t), -\partial_x \psi(\mathbf{x}', t))^T d\mathbf{x}', \quad (2.29)$$

where ψ is given by

$$\Delta \psi(\mathbf{x}, t) = \omega(\mathbf{x}, t), \quad (2.30)$$

and the vorticity ω is

$$\omega(\mathbf{x}, t) = \int_{\Gamma} \eta^*(\alpha, t) \delta(\mathbf{x} - \mathbf{x}(\alpha, t)) d\alpha = \int_{\Gamma} \eta(s, t) \delta(\mathbf{x} - \mathbf{x}(s, t)) ds, \quad (2.31)$$

see Cottet & Koumoutsakos (2000). Using this vortex-in-cell approach significantly speeds up the computation of the velocity \mathbf{u} as compared to the integral formulation (2.9) respectively (2.28). Employing (2.27) the above relation can be rewritten as

$$\omega(\mathbf{x}, t) = \int_V \eta(\mathbf{x}', t) \delta(\mathbf{x} - \mathbf{x}') \delta(G(\mathbf{x}') - G_0) |\nabla G(\mathbf{x}')| d\mathbf{x}'. \quad (2.32)$$

The inclusion of the apparently superfluous integration over a delta function in (2.29) is in fact necessary to allow for a consistent numerical spreading operator, (2.32), and interpolation operator, (2.29), operator. Again, (2.32) is preferable to (2.31), because no reconstruction of the exact interface location is needed.

To summarize, (2.13), (2.25), and either (2.9), (2.28), or (2.29), form the system of equations describing the interface dynamics.

3. Numerical method

The system of equations describing the interface dynamics is solved on an equidistant, cartesian grid. However, instead of solving the equations everywhere in the whole computational domain, a tube approach is employed to significantly speed up the computations. Following arguments by Peng *et al.* (1999), five distinct tubes around the $G = G_0$ level set, called the \mathcal{I} , \mathcal{I}_2 , \mathcal{B} , \mathcal{T} and \mathcal{N} tubes are introduced. A grid node (i, j) lies in a specific tube, when

$$(i, j) \in \begin{cases} \mathcal{I} & \text{if } |G_{i,j}| \leq \alpha_I \Delta x \\ \mathcal{I}_2 & \text{if } |G_{i,j}| \leq 2\alpha_I \Delta x \\ \mathcal{B} & \text{if } |G_{i,j}| \leq \alpha_B \Delta x \\ \mathcal{T} & \text{if } |G_{i,j}| \leq \alpha_T \Delta x \\ \mathcal{N} & \text{if any } (i_0, j_0) \in \mathcal{T} \text{ with } i_0 \in [i-3, i+3], j_0 \in [j-3, j+3] \end{cases} \quad (3.1)$$

with Δx the grid size and typically $\alpha_I = 4$, $\alpha_B = \alpha_I + 3$, and $\alpha_T = \alpha_B + 3$. The use of the individual tubes will be discussed in the following sections.

3.1. Convective terms

The level-set equation (2.13) is a Hamilton-Jacobi equation. In this work, the fifth-order WENO scheme for Hamilton-Jacobi equations of Jiang & Peng (2000) is used. A Roe flux with local Lax-Friedrichs entropy correction is employed to solve both the level-set equation and the convective term of the η equation (2.25), see Shu & Osher (1989) and

Osher & Shu (1991). Integration in time is performed by the third-order TVD Runge-Kutta time discretization of Shu (1988).

Solution of the convective terms is restricted to the \mathcal{T} -tube, where, as suggested by Peng *et al.* (1999), \mathbf{u} in (2.13) and (2.25) is replaced by

$$\mathbf{u}_{\text{cut}} = c(G)\mathbf{u}, \quad (3.2)$$

with the cutoff function

$$c(G) = \begin{cases} 1 & : |G| \leq \alpha_B \Delta x \\ \frac{(|G|/\Delta x - \alpha_T)^2(2|G|/\Delta x + \alpha_T - 3\alpha_B)}{(\alpha_T - \alpha_B)^3} & : \alpha_B \Delta x < |G| \leq \alpha_T \Delta x \\ 0 & : |G| > \alpha_T \Delta x \end{cases}. \quad (3.3)$$

This ensures that no artificial oscillations are introduced at the \mathcal{T} -tube boundaries.

3.2. Source terms

Both the stretching term and the surface-tension term in the η equation (2.25) constitute simple source terms and are integrated in time within the convective TVD Runge-Kutta scheme. Evaluation of the source terms is limited to the \mathcal{T} -tube.

3.3. Reinitialization

The reinitialization procedure employed here to solve (2.14) is the one originally proposed by Sussman *et al.* (1994), where the Hamilton-Jacobi equation

$$\frac{\partial H(\mathbf{x}, t^*)}{\partial t^*} + S(H(\mathbf{x}, t^*))(|\nabla H(\mathbf{x}, t^*)| - 1) = 0, \quad \mathbf{x}_{i,j} \in N \quad (3.4)$$

$$H(\mathbf{x}, t^* = 0) = G(\mathbf{x}, t) - G_0 \quad (3.5)$$

is solved until

$$\|H(\mathbf{x}, t^*) - H(\mathbf{x}, t^* - \Delta t^*)\|_{\infty} < \epsilon_1, \quad \mathbf{x}_{i,j} \in B \quad (3.6)$$

with, typically, $\epsilon_1 = 10^{-3} \Delta x$. In (3.4), $S(H)$ is an approximation to the sign function. As pointed out by Peng *et al.* (1999), the choice of this approximate sign function is crucial to minimize undesired movement of the $H(\mathbf{x}, t^*) = G_0$ interface while solving (3.4). Here, we will use the approximate sign function by Peng *et al.* (1999),

$$S(H) = \frac{H}{\sqrt{H^2 + |\nabla H|^2 (\Delta x)^2}} \quad (3.7)$$

with a second-order central-difference approximation for ∇H . Equation (3.4) is solved by the fifth-order WENO scheme used to solve the convective terms, but employing a Godunov flux function instead of the Roe-LLF flux function. Again, the solution in time is advanced by the third-order Runge-Kutta scheme.

Reinitialization is limited to the \mathcal{N} -tube, which is three cells larger in each direction than the \mathcal{T} -tube. Peng *et al.* (1999) proposed an extension of the \mathcal{T} -tube by only one cell. However, it was found, that this still might introduce fluctuations in the solution. The convergence criterium (3.6) is evaluated only inside the \mathcal{B} -tube.

3.4. Redistribution

The redistribution procedure employed here to solve (2.26) is that described by Chen & Steen (1997) and Peng *et al.* (1999). The Hamilton-Jacobi equation

$$\frac{\partial \vartheta(\mathbf{x}, t^*)}{\partial t^*} + S(G(\mathbf{x}, t) - G_0) \mathbf{n}(\mathbf{x}, t) \cdot \nabla \vartheta(\mathbf{x}, t^*) = 0 \quad \mathbf{x}_{i,j} \in T, \quad (3.8)$$

$$\vartheta(\mathbf{x}, t^* = 0) = \eta(\mathbf{x}, t) \quad (3.9)$$

is solved using a first-order-upwind flux approximation and a simple first-order time advancement until

$$||\delta(G(\mathbf{x}, t) - G_0)[\vartheta(\mathbf{x}, t^*) - \vartheta(\mathbf{x}, t^* - \Delta t^*)]||_\infty < \epsilon_2 \cdot ||\eta(\mathbf{x}, t = 0)||_\infty, \quad \mathbf{x}_{i,j} \in I \quad (3.10)$$

with typically $\epsilon_2 = 10^{-4}$. This specific convergence criterion ensures convergence of the vorticity ω , see (3.17). The sign function in (3.8) is again approximated by (3.7).

Solution of (3.8) is limited to the T -tube, whereas the convergence criterion (3.10) is evaluated only within the I -tube.

3.5. Velocity evaluation

Three different methods, denoted M_1 through M_3 , are used to calculate the velocity \mathbf{u} . Method M_1 is based on the line integral (2.9), whereas methods M_2 and M_3 are based on the vortex-in-cell approach, employing (2.31) and (2.32) respectively.

3.5.1. Line-integral formulation

Equation (2.9) is used to calculate the velocity \mathbf{u} at every grid point in the T -tube. The problem that the integral can become singular for $\mathbf{x}(s) \rightarrow \mathbf{x}$ is circumvented by adding a positive constant $4\varepsilon^2$ to the denominator as proposed by Krasny (1986). For interfaces periodic in the x -direction, (2.9) can be transformed to

$$u(x, y, t) = \frac{1}{2} \int_0^L \eta(s, t) \frac{\sinh 2\pi(y - y(s, t))}{\cosh 2\pi(y - y(s, t)) - \cos 2\pi(x - x(s, t)) + 4\varepsilon^2} ds, \quad (3.11)$$

$$v(x, y, t) = \frac{1}{2} \int_0^L \eta(s, t) \frac{\sin 2\pi(x - x(s, t))}{\cosh 2\pi(y - y(s, t)) - \cos 2\pi(x - x(s, t)) + 4\varepsilon^2} ds, \quad (3.12)$$

see Milne-Thomson (1968). The above equations are solved by first reconstructing the location of the interface $G = G_0$ in each grid cell containing it. Grid cells containing part of the interface are easily identified by

$$\neg \left(\min_{i^* \in [i, i+1], j^* \in [j, j+1]} G_{i^*, j^*} > G_0 \vee \max_{i^* \in [i, i+1], j^* \in [j, j+1]} G_{i^*, j^*} < G_0 \right). \quad (3.13)$$

The entry and exit coordinates of the interface into these cells are calculated by approximating G by cubic splines along the grid lines. The interface shape itself is assumed to be a straight line connecting the entry and exit points in each cell. The integration along these lines is performed by five-point Gaussian quadrature, with η at the quadrature points calculated from two-dimensional third-order B-splines. This approach to calculate the velocity by line integration will be called method M_1 .

The disadvantage of using method M_1 is the fact that it is computationally expensive and that the interface location must be reconstructed, thus in effect losing one of the benefits of the level-set approach.

3.5.2. Laplace formulation

In order to solve the Laplace equation for the stream function (2.30), the vorticity at each grid point in the computational domain has to be calculated by a numerical version of either (2.31) or (2.32). Approximating the δ function by a smoothed version, the vorticity, located solely at the interface location, is in fact spread out to the neighboring grid nodes. Hence, this approach is similar to the vortex-in-cell method that spreads the

vorticity of Lagrangian vortex particles to their surrounding grid nodes. Quite a number of spreading functions have been proposed to this end; see Ebiana & Bartholomew (1996). Here we will use

$$\delta(\mathbf{x} - \mathbf{x}(s)) = \delta_\varepsilon(x - x(s))\delta_\varepsilon(y - y(s)), \quad (3.14)$$

$$\delta(G(\mathbf{x}') - G_0) = \delta_\varepsilon(G(\mathbf{x}') - G_0), \quad (3.15)$$

with δ_ε as proposed by Peskin (1977)

$$\delta_\varepsilon(x) = \begin{cases} \frac{1}{2\varepsilon} \left[1 + \cos\left(\frac{\pi x}{\varepsilon}\right) \right] & : |x| \leq \varepsilon \\ 0 & : |x| > \varepsilon \end{cases}, \quad (3.16)$$

and $\varepsilon = \alpha_I \Delta x$.

If the vorticity is calculated by (2.31), the integration along the interface is calculated in the same way as for method \mathcal{M}_1 described in section 3.5.1. The above approach will be called method \mathcal{M}_2 .

Using (2.32), called method \mathcal{M}_3 below, avoids the necessary reconstruction of the interface location in method \mathcal{M}_2 . The integration itself is performed by first evaluating

$$\Omega(\mathbf{x}', t) = \eta(\mathbf{x}', t)\delta(G(\mathbf{x}') - G_0)|\nabla G(\mathbf{x}')| \quad (3.17)$$

for all cells within the \mathcal{I} -tube, and then integrating

$$\omega(\mathbf{x}, t) = \int_V \delta_\varepsilon(\mathbf{x} - \mathbf{x}')\Omega(\mathbf{x}', t)d\mathbf{x}'. \quad (3.18)$$

for all cells within the \mathcal{I}_2 -tube by a simple midpoint rule.

The Laplace equation (2.30) for the stream function is solved by the package FISHPACK throughout the whole computational domain.

The calculation of the velocity from the stream function is again a two-step process. First, an initial velocity \mathbf{U} is calculated at each grid node by simple central-difference approximation,

$$\mathbf{U}_{i,j} = \left(\frac{\psi_{i,j+1} - \psi_{i,j-1}}{2\Delta y}, -\frac{\psi_{i+1,j} - \psi_{i-1,j}}{2\Delta x} \right)^T. \quad (3.19)$$

Secondly, in order to be consistent with the spreading step of the vorticity (3.18), the same δ_ε and numerical-integration method has to be used in the interpolation step to calculate \mathbf{u} ,

$$\mathbf{u}(\mathbf{x}, t) = \int_V \delta_\varepsilon(\mathbf{x} - \mathbf{x}')\mathbf{U}(\mathbf{x}', t)d\mathbf{x}', \quad (3.20)$$

evaluated within the \mathcal{T} -tube.

4. Results

Two different cases have been calculated to validate the approach proposed in this paper. First, vortex sheets without surface tension were calculated. Secondly, the Kelvin-Helmholtz instability was calculated both to determine the linear growth and to evaluate the long-time evolution of the interface.

4.1. Vortex sheets

Pure vortex sheets constitute a special class of two-phase interfaces in that they do not exhibit any surface-tension forces and thus have constant unnormalized vortex-sheet

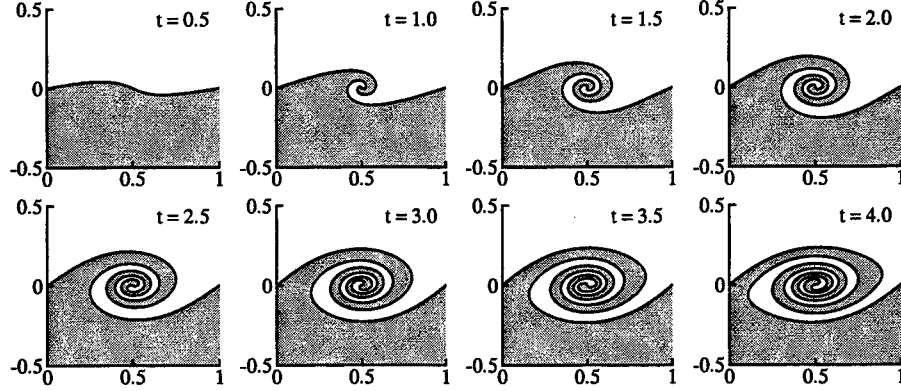


FIGURE 2. Temporal evolution of the vortex sheet, 256×256 grid, method \mathcal{M}_3 , $\varepsilon = 8\Delta x$.

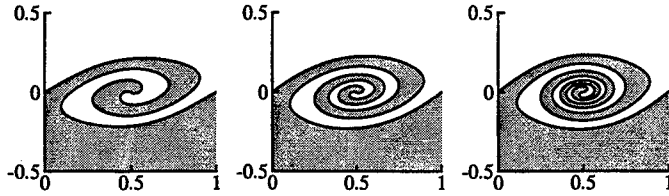


FIGURE 3. Vortex sheet at $t = 4$, 256×256 grid, method \mathcal{M}_3 , $\varepsilon = 32\Delta x$ (left), $\varepsilon = 16\Delta x$ (center), $\varepsilon = 8\Delta x$ (right).

strength η^* ; see (2.11). An initially-sinusoidal perturbed planar interface exhibits a characteristic central roll-up region; see Krasny (1986). The initial conditions used here are those of Krasny (1986), where the initial shape of the interface

$$x(\alpha, t = 0) = \alpha + A_0 \sin 2\pi\alpha, \quad (4.1)$$

$$y(\alpha, t = 0) = +A_0 \sin 2\pi\alpha, \quad (4.2)$$

is represented by the initial G field

$$G(\mathbf{x}, t = 0) = y - A_0 \sin \left(\frac{2\pi}{L} \left[x - A_0 \sin \frac{2\pi}{L} x \right] \right), \quad (4.3)$$

with initial amplitude $A_0 = 0.01$, interface length L , and

$$\eta_{VS}(\mathbf{x}, t = 0) = \frac{\eta^*}{\sqrt{1 + \frac{4\pi A_0}{L} \cos \frac{2\pi}{L} x + 2 \left[\frac{2\pi A_0}{L} \cos \frac{2\pi}{L} x \right]^2}} \quad (4.4)$$

with $\eta^* = 1$. Calculations were performed in a 1×1 box on an equidistant 256×256 cartesian grid with periodic boundary conditions at the left and right, and slip walls at the bottom and top.

Figure 2 shows the temporal evolution of the vortex sheet with $\varepsilon = 8\Delta x$ and velocity-calculation method \mathcal{M}_3 . Similar to the findings of Krasny (1986), reducing the spreading factor ε generates ever more turns in the central core region, while retaining the outer shape of the roll-up region; see figure 3, where ε is reduced from $\varepsilon = 32\Delta x$ down to $\varepsilon = 8\Delta x$. The maximum number of possible turns is limited by the single-valued nature

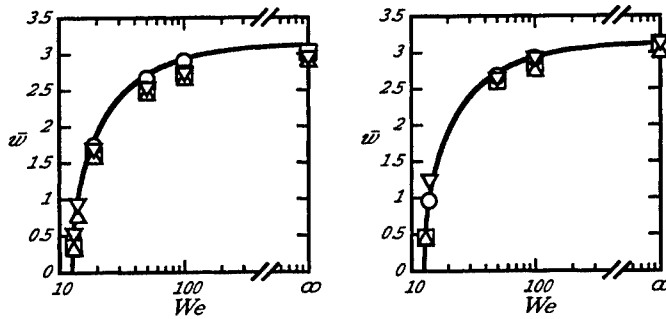


FIGURE 4. Growth rates \bar{w} for 128×128 (left) and 256×256 (right) grid and method M_1 , $\epsilon = 0$ (\circ); M_1 , $\epsilon = 4\Delta x$ (\square); M_2 , $\epsilon = 4\Delta x$ (\triangle); M_3 , $\epsilon = 4\Delta x$ (∇), and linear theory (line).

of the level-set scalar; since no two interface fronts may exist in the same grid cell, automatic merging and hence pinching will occur. The number of turns generated in the central core region is less than those achieved by Krasny (1986) with a vortex-blob method or Tryggvason (1989) with a vortex-in-cell method, but is comparable to those reported by Harabetian *et al.* (1996) and Peng *et al.* (1999) using a level-set-based approach.

4.2. Kelvin-Helmholtz instability

4.2.1. Linear growth

Calculations of the linear growth rate of the Kelvin-Helmholtz instability are initialized by the sinusoidal perturbed planar interface (4.3) and a modified distribution of vortex-sheet strength taking the effect of surface tension into account,

$$\eta(\mathbf{x}, t=0) = \beta (\eta_{VS}(\mathbf{x}, t=0) - \eta^*) + \eta^*, \quad (4.5)$$

where β is chosen such that the initial normal-velocity profile at $G = G_0$ calculated by method M_1 and $\epsilon = 0$ is that of the linear solution; see Chandrasekhar (1961). The boundary conditions are those of the vortex-sheet calculation.

Figure 4 shows the calculated growth rates \bar{w} ,

$$\bar{w} = \frac{1}{t_1} \int_0^{t_1} w(t) dt, \quad (4.6)$$

for an initial amplitude of $A_0 = 0.0001$ for both the 128×128 (left) and the 256×256 (right) grid case. Here, t_1 is chosen to be either $t_1 = 1$ or, for larger Weber numbers, the time when smaller wavelengths start to visibly pollute the linear solution. Although the calculated growth rates are generally less than linear theory predicts, the agreement between linear solution and numerical simulation is good. The calculated growth rate is smaller due to the spreading operation of the vorticity in methods M_2 and M_3 , and the de-singularization of the surface integral in method M_1 , respectively. Setting the de-singularization factor to $\epsilon = 0$ for method M_1 (circles) shows excellent agreement with the linear solution. Setting $\epsilon = 0$ is viable here, since for $t \leq t_1$ the interface does not come close to a grid node, thus the fractions in (3.11) and (3.12) stay finite.

4.2.2. Long-time evolution

Figure 5 shows snapshots of the interface for the long-time evolution of the Kelvin-Helmholtz instability for Weber numbers $We = 100$ and $We = 400$. Here, a 128×256 grid for a box of size 1×2 was used with the same boundary conditions as for the vortex-sheet calculation.

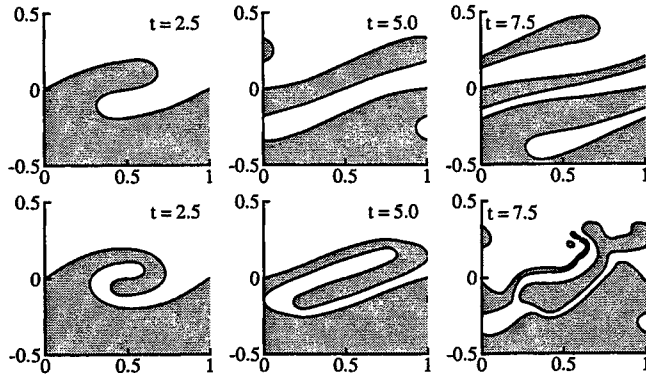


FIGURE 5. Interface at $t = 2.5, 5$, and 7.5 for $We = 100$ (top) and 400 (bottom), method \mathcal{M}_3 .

The results obtained are similar to those reported by Hou *et al.* (1997) who used a vortex-point method. As can be seen in the $We = 400$ case, pinching events occur and drops are formed.

5. Conclusions and future work

An Eulerian level-set/vortex-sheet method has been presented that allows for the calculation of two-phase interface dynamics taking surface-tension effects into account. This method shows good agreement with the linear theory of Kelvin-Helmholtz instability and is able to automatically handle complex topology changes of the interface, such as pinching and merging. Future work will extend the method to three dimensions, include the effect of different fluid densities, and introduce a coupling to an ambient turbulent velocity field. The presented method lays down a framework for the derivation of a Large Surface Structure model of the primary atomization interface dynamics in turbulent flow fields. The derivation of closure models for filtered versions of the equations presented will also be the focus of future work. Coupling of the presented method with a subsequent spray model for secondary atomization and evaporation will be achieved by combining the level-set approach with a transport equation for a volume of fluid scalar. Finally, coupling with an LES turbulence model will yield a consistent approach describing the complete atomization process, suitable for engineering applications.

Acknowledgments

The support of the German Research Foundation (DFG) is gratefully acknowledged.

REFERENCES

- BAKER, G. R., MEIRON, D. I. & ORSZAG, S. A. 1982 Generalized vortex methods for free-surface flow problems. *J. Fluid Mech.* **123**, 477–501.
- CHANDRASEKHAR, S. 1961 *Hydrodynamic and Hydromagnetic Stability*. Oxford University Press.
- CHEN, Y.-J. & STEEN, P. H. 1997 Dynamics of inviscid capillary breakup: Collapse and pinchoff of a film bridge. *J. Fluid Mech.* **341**, 245–267.

- CHRISTIANSEN, J. P. 1973 Numerical simulation of hydrodynamics by the method of point vortices. *J. Comput. Phys.* **13**, 363–379.
- COTTET, G.-H. & KOUMOUTSAKOS, P. D. 2000 *Vortex Methods*. Cambridge University Press.
- EBIANA, A. B. & BARTHOLOMEW, R. W. 1996 Design considerations for numerical filters used in vortex-in-cell algorithms. *Comp. Fluids* **25**, 61–75.
- HARABETIAN, E. & OSHER, S. 1998 Regularization of ill-posed problems via the level set approach. *SIAM J. Appl. Math.* **58**, 1689–1706.
- HARABETIAN, E., OSHER, S. & SHU, C. W. 1996 An Eulerian approach for vortex motion using a level set regularization procedure. *J. Comput. Phys.* **127**, 15–26.
- HOU, T. Y., LOWENGRUB, J. S. & SHELLY, M. J. 1997 The long-time motion of vortex sheets with surface tension. *Phys. Fluids* **9**, 1933–1954.
- HOU, T. Y., LOWENGRUP, J. S. & SHELLY, M. J. 1994 Removing the stiffness from interfacial flows with surface tension. *J. Comput. Phys.* **114**, 312–338.
- JIANG, G.-S. & PENG, D. 2000 Weighted ENO schemes for Hamilton-Jacobi equations. *SIAM J. Sci. Comput.* **21**, 2126–2143.
- KRASNY, R. 1986 Desingularization of periodic vortex sheet roll-up. *J. Comput. Phys.* **65**, 292–313.
- MILNE-THOMSON, L. M. 1968 *Theoretical Hydrodynamics*. MacMillan, London.
- OSHER, S. & SETHIAN, J. A. 1988 Fronts propagating with curvature -dependent speed: Algorithms based on Hamilton-Jacobi formulations. *J. Comput. Phys.* **79**, 12–49.
- OSHER, S. & SHU, C. W. 1991 High-order essentially nonoscillatory schemes for Hamilton-Jacobi equations. *SIAM J. Num. Anal.* **28**, 907–922.
- PENG, D., MERRIMAN, B., OSHER, S., ZHAO, H. & KANG, M. 1999 A PDE-based fast local level set method. *J. Comput. Phys.* **155**, 410–438.
- PESKIN, C. S. 1977 Numerical analysis of blood flow in the heart. *J. Comput. Phys.* **25**, 220–252.
- SAFFMAN, P. G. & BAKER, G. R. 1979 Vortex interactions. *Annu. Rev. Fluid Mech.* **11**, 95–122.
- SHU, C. W. 1988 Total-variation-diminishing time discretization. *SIAM J. Sci. Stat. Comput.* **9**, 1073–1084.
- SHU, C.-W. & OSHER, S. 1989 Efficient implementation of essentially non-oscillatory shock-capturing schemes, II. *J. Comput. Phys.* **83**, 32–78.
- SUSSMAN, M., SMEREKA, P. & OSHER, S. 1994 A level set method for computing solutions to incompressible two-phase flow. *J. Comput. Phys.* **119**, 146–159.
- TRYGGVASON, G. 1989 Simulations of vortex sheet roll-up by vortex methods. *J. Comput. Phys.* **80**, 1–16.

Progress toward large-eddy simulation of turbulent reacting and non-reacting flows in complex geometries

By K. Mahesh †, G. Constantinescu, S. Apte,
G. Iaccarino, F. Ham and P. Moin

1. Motivation and objectives

The large-eddy simulation (LES) approach is used to simulate the combustor of the gas turbine engine. LES was chosen because of its demonstrated superiority over RANS in predicting mixing, which is central to combustion. The combustor simulations have two major components - gas phase and sprays. The gas phase part of the project has developed a parallel, unstructured grid LES solver which has now been completely integrated with the spray module. As discussed in previous reports (Mahesh *et al.* 2000, 2001) the gas phase solver is non-dissipative and discretely conserves energy, thus insuring both accuracy and robustness for high Reynolds number simulations in complex geometries. A dynamic procedure is used to compute the coefficients in the additional terms that are present in the filtered momentum and scalar-transport equations. The objective of this work is to develop unstructured mesh technology for LES of reacting flow (including spray physics) in realistic configurations using massively-parallel computing platforms.

2. Accomplishments

Our progress in the last year was as follows:

- The gas-phase solver was made fully implicit, resulting in a significant overall speed-up for both non-reacting and reacting flow simulations. Overall reduction in CPU time is between six and ten. Compared to the explicit code, the time step is larger by factors of 10 – 20 while the increased overhead is 1.5 – 3.5.
- Development of a geometric multigrid approach to solving the Poisson equation was initiated and preliminary tests were completed.
- The cold-flow simulations in the complex Pratt & Whitney combustor and the front-end validation model that were initiated last year were completed. The LES results are shown to predict experimental data considerably better than RANS.
- Extension of the gas-phase solver to the reacting, variable-density, low-Mach-number equations was completed. The progress-variable approach of Pierce & Moin (2001) is used in the reacting-flow calculations. The LES module was rewritten to reduce memory use. Also, the CPU time per time step of the reacting module was reduced from approximately 25 % of the total to about 10 – 15 %.
- Validation of the low-Mach-number algorithm used for variable-density flow simulations was initiated. Comparison to the coaxial jet methane combustor of Spadaccini *et al.* (1976) is under way. Preliminary results show good qualitative agreement with the numerical simulations performed for the same conditions by Pierce & Moin (2001).

† Aerospace Engineering and Mechanics, University of Minnesota

- Reacting-flow simulation using JetA fuel in the complex Pratt & Whitney combustor geometry has been initiated. Extensive validation data is available for this test case.
- Validation simulations of particle-laden swirling flows in a coaxial combustor geometry (Sommerfeld & Qiu 1991) were completed, obtaining good agreement with the experimental data.
- A spray-atomization methodology for use with the Lagrangian schemes was developed. The secondary-breakup phenomenon is modeled to predict spray characteristics such as droplet distribution, penetration depth and spray angle.
- A novel hybrid approach involving tracking of individual droplets and parcels of droplets was developed to reduce the computational cost while retaining the essential dynamics of spray evolution.
- Validation of the secondary breakup model was performed and effectiveness of the hybrid scheme was demonstrated in a simplified combustor geometry.
- Validation of the spray-breakup model in Pratt & Whitney's front-end validation geometry was initiated.
- The combustor code was christened CDP in memory of the late Dr. Charles David Pierce who made several lasting contributions to the LES of reacting flows.

3. Implicit algorithm

As described in last year's progress report, the gas-phase solver used the explicit second-order Adams-Bashforth method to advance the equations in time. Algorithmic developments in the gas-phase solver emphasized spatial discretization, which resulted in the development of a non-dissipative, energy-conserving formulation in the absence of time-discretization errors. This explicit algorithm was successfully used to demonstrate the accuracy of the flow solver in both simple and exceedingly complex geometries such as the Pratt & Whitney combustor.

Last year, the gas-phase solver was sped up considerably by allowing the use of larger time steps. This was achieved by making the time advancement fully implicit. The need for implicit time-advancement was felt because numerical stability restrictions imposed by the Adams-Bashforth method were restricting the time step in the coaxial combustor simulations to be an order of magnitude less than the time step used by Pierce & Moin in their structured grid computations that treated the viscous terms implicitly. Also the simulations performed in the front-end model showed that the narrow passages in the fuel injector considerably accelerate the flow, and, as a result, the convective terms impose strict restrictions on the time step for an explicit scheme.

The second-order Crank-Nicolson scheme is used for both convection and viscous terms. The convection terms are linearized prior to solution. The implementation is such that the viscous terms alone can be implicitly advanced if so desired. At present successive over-relaxation is used to solve the implicit system. Typically 20 – 100 iterations are needed to converge the residuals. The use of multigrid techniques to solve the implicit system is under consideration. Results for some typical calculations are summarized in table 1. The savings are seen to be significant. For example, explicit calculation of the cold flow in a coaxial geometry required 320 hours \times 96 processors = 30,700 CPU hours on an IBM SP3 machine. The implicit code uses about 5,000 CPU hours, which is approximately a factor of four larger than the time taken by the highly-optimized structured-grid solver of Pierce & Moin which uses the same time step. The structured solver is of course incapable of handling geometries as complex as the Pratt & Whitney combustor. The

	Grid (10^6 cvs)	Processors	Explicit (CPU hours)	Implicit (CPU hours)
Coaxial combustor (Sommerfeld)	1.6	96	30700	5000
Turbulent channel $Re_\tau = 180$	0.9	32	2240	256
Pratt & Whitney combustor	1.4	32	13500	3200

TABLE 1. CPU time in hours for the explicit and implicit solvers.

above ratio of implicit to explicit time step also applies to the reacting-flow simulations. Reacting calculations of the Spadaccini experiment using the explicit solver would require about 600,000 CPU hours on an IBM SP3 machine, while the implicit solver requires approximately 70,000 CPU hours. This cost is comparable to that of a structured code (the physical time steps were identical and corresponded to a CFL number between 0.5 and 1.0) which required $\sim 50,000$ CPU hours on the ASCI RED machine. Further significant reduction of the CPU time in the unstructured LES code is expected, once a multi-level multigrid solver for the pressure and momentum equations in the predictor step of the fractional-step algorithm is implemented.

The calculations in complex geometries show significant speed-up due to the implicit algorithm. The time taken for the cold-flow calculations in the full Pratt & Whitney geometry is very reasonable (3,200 CPU hours, or about 100 wall-clock hours when the job is run on 32 processors). However, computations in the front-end model are still expensive (110,000 CPU hours) in spite of the implicit algorithm speed-up by a factor of six. This is because the time step is now limited by accuracy; it is limited by the high flow speeds through the channels of the three swirlers. In normalized terms, the time step at which the calculations are being currently run are the same as that for the simple coaxial combustor. The high cost for the front-end model is therefore the price paid by unsteady simulations in general (including unsteady RANS) and is not peculiar to LES. We are presently investigating the exact requirements of grid resolution and quality inside the injector region such that the time step could be increased without compromising accuracy.

4. Combustion model implementation in the unstructured code

In this section we present the motivation behind using the flamelet / progress-variable combustion model developed by Pierce & Moin (2001), together with an overview of their method, including the equations and the algorithm to calculate the subgrid momentum and scalar transport terms and its implementation in the unstructured code. Pierce & Moin's approach is based on "quasi-steady" flamelets in which the local flame state undergoes unsteady evolution through a sequence of stationary solutions to the flamelet equations.

A single-parameter flamelet library is first developed for the given combustor conditions

by looking for stationary solutions to the one-dimensional reaction-diffusion equations. The unstable and the lower branches of the S-shaped curve are included so that the complete range of flame states, from completely extinguished (mixing without reaction) to completely reacted (equilibrium chemistry), is represented in the library. Arbitrarily complex chemical-kinetic mechanisms as well as differential-diffusion effects can be included. The result is a complete set of flame states, given in terms of mixture fraction and a single flamelet parameter, denoted by λ :

$$y_k = y_k(Z, \lambda), \quad T = T(Z, \lambda), \quad \rho = \rho(Z, \lambda), \quad w_k = w_k(Z, \lambda). \quad (4.1)$$

where y_k are the mass fractions of the chemical species, T is the temperature, ρ the density, w_k are the reaction terms in the scalar transport equation for the chemical species and Z is the mixture fraction. One of the combustion variables, or some combination of the variables that is representative of the overall flame behavior, is chosen to serve as an overall reaction progress variable.

In this model in addition to the variable-density momentum and continuity equations (4.2) and (4.3), scalar-transport equations are solved for the mixture fraction Z , which is a conserved scalar (4.4), and for the progress variable C , which is a non-conserved scalar (4.5):

$$\frac{\partial \rho \mathbf{u}}{\partial t} + \nabla \cdot (\rho \mathbf{u} \mathbf{u}) = -\nabla p + \nabla \cdot [2\mu(\mathbf{S} - \frac{1}{3}\mathbf{I} \nabla \cdot \mathbf{u})], \quad (4.2)$$

$$\nabla \cdot (\rho \mathbf{u}) = -\frac{\partial \rho}{\partial t}, \quad (4.3)$$

$$\frac{\partial \rho Z}{\partial t} + \nabla \cdot (\rho \mathbf{u} Z) = \nabla \cdot (\rho \alpha \nabla Z), \quad (4.4)$$

$$\frac{\partial \rho C}{\partial t} + \nabla \cdot (\rho \mathbf{u} C) = \nabla \cdot (\rho \alpha \nabla C) + \rho w_C. \quad (4.5)$$

In the above equations, \mathbf{S} is the strain-rate tensor, \mathbf{I} is the identity tensor, μ is the molecular viscosity, α is the molecular diffusivity and w_C is the chemical-reaction source term.

The continuity equation acts as a constraint on the velocity field, with the time derivative of density as a source term. This constraint is enforced by the pressure, in a manner analogous to the enforcement of the incompressibility constraint for constant density flows.

Under the model assumptions, all the other fluid and flow variables (density, temperature, molecular viscosity, molecular diffusivity), chemical species and the reaction source terms in the scalar-transport equations are related to the mixture fraction and the progress variable through a flamelet library that is precalculated, given a specific fuel reaction mechanism and the flow conditions in the combustor. The only requirements for the quantity chosen to serve as progress variable are that it is representative of the overall gross flame behavior and that it varies monotonically with the flame state so that its value uniquely determines it. For instance, in the reacting-flow simulation of methane-air combustion in a coaxial jet combustor discussed below, the progress variable is chosen as the product mass fraction $C = y_{CO_2} + y_{H_2O}$ (Pierce & Moin 2001).

For turbulent simulations, the governing equations (4.2) to (4.5) are filtered. A major modeling requirement is for the nonlinear density function $\bar{\rho}$ obtained by filtering the

state relation for the density ρ in (4.1). While algebraic scaling laws and scale-similarity concepts can be expected to work for quadratic nonlinearities, the only acceptable closure for arbitrary nonlinearities appears to be the probability density function (PDF) approach. Here, the presumed subgrid PDF is used:

$$\bar{\rho}^{-1} = \int \rho^{-1}(Z, \lambda) \tilde{P}(Z, \lambda) dZ d\lambda \quad (4.6)$$

In addition, the filtered progress-variable equation contains a reaction source term \tilde{w}_C that must be closed. This is accomplished by writing

$$\tilde{w}_C = \int w_C(Z, \lambda) \tilde{P}(Z, \lambda) dZ d\lambda \quad (4.7)$$

and assuming that

$$\tilde{P}(Z, \lambda) = \delta(\lambda - \lambda_0) \cdot \beta(Z, \tilde{Z}, \widetilde{Z''^2}) . \quad (4.8)$$

That is, each subgrid state is represented by a single flamelet. For conserved scalars such as mixture fraction, the subgrid PDF is modeled using the beta distribution which is a reasonable assumption in the absence of further information about the subgrid state (Wall *et al.* 2000). The final step is to relate λ_0 to the filtered value of the progress variable, \tilde{C} , that is obtained by solving the corresponding transport equation:

$$\tilde{C} = \int C(Z, \lambda) \tilde{P}(Z, \lambda) dZ d\lambda . \quad (4.9)$$

After substitution of the presumed PDF and integrating, this yields

$$\tilde{C} = f(\tilde{Z}, \widetilde{Z''^2}, \lambda_0) \quad (4.10)$$

If C is a monotonic function of λ , then the above relation can be used to eliminate λ_0 from the problem. The final result is a closed specification of the chemical system and fuel properties (molecular viscosity and molecular diffusivity) in terms of three variables \tilde{Z} , $\widetilde{Z''^2}$ and \tilde{C} , which are chosen as the input variables in the chemical table for turbulent calculations:

$$y_k = y_k(\tilde{Z}, \widetilde{Z''^2}, \tilde{C}) , \quad T = T(\tilde{Z}, \widetilde{Z''^2}, \tilde{C}) , \quad \rho = \rho(\tilde{Z}, \widetilde{Z''^2}, \tilde{C}) , \quad w_k = w_k(\tilde{Z}, \widetilde{Z''^2}, \tilde{C}) . \quad (4.11)$$

$$\mu = \mu(\tilde{Z}, \widetilde{Z''^2}, \tilde{C}) , \quad \alpha = \alpha(\tilde{Z}, \widetilde{Z''^2}, \tilde{C}) . \quad (4.12)$$

The subgrid mixture-fraction variance $\widetilde{Z''^2}$ is obtained using the method proposed by Pierce & Moin:

$$\rho \widetilde{Z''^2} = C_Z \bar{\rho} \Delta^2 |\nabla \tilde{Z}|^2 . \quad (4.13)$$

where the coefficient C_Z is calculated dynamically. The subgrid momentum and scalar transport terms that appear from the filtering of (4.2), (4.4) and (4.5) must be modeled. The eddy viscosity μ_t and eddy diffusivity α_t that appear in these terms are evaluated as follows:

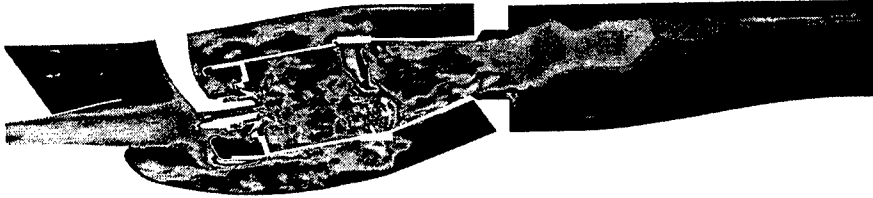


FIGURE 1. Computational domain in the $x - y$ symmetry plane, $z = 0$, with contours of the instantaneous absolute value of the velocity field for the flow in the Pratt & Whitney full-combustor geometry in the same plane

$$\mu_t = C_\mu \bar{\rho} \Delta^2 |\tilde{\mathbf{S}}| \quad (4.14)$$

$$\rho\alpha_t = C_\alpha \bar{\rho} \Delta^2 |\tilde{\mathbf{S}}| \quad (4.15)$$

where the coefficients C_μ and C_α are calculated dynamically.

All the operators in the scalar-transport equations are discretized in a similar fashion to that used in the momentum equations.

Finally, we describe the approach for the calculation of the coefficients in the expressions of the subgrid scalar variance, eddy viscosity and eddy diffusivity in the filtered momentum and scalar transport equations. It is well known that the prediction of negative values for the dynamically-calculated coefficients (C_μ , C_α and C_Z) coupled with the long time correlation of these coefficients can cause instability of the numerical solution. Negative values of these coefficients can be predicted by the dynamic procedure, especially in regions of high gradients and skewed meshes, two conditions that are often met in calculations of very complex turbulent flows using hybrid unstructured meshes. The usual way to avoid this problem is to clip these coefficients, so that the sum of the molecular and eddy viscosity (diffusivity) will remain positive. However, in our implementation we propose a more robust implementation, based on Germano's identity, in which the usual expression is used to compute the coefficients in the region where the predicted values for these coefficients are positive (e.g. $C_\mu \Delta^2 = 0.5 \langle L_{i,j} M_{i,j} \rangle / \langle M_{k,l} M_{k,l} \rangle$), while in regions where the least square is negative, by contracting Germano's identity with itself one obtains $C_\mu \Delta^2 = 0.5 \sqrt{\langle L_{i,j} L_{i,j} \rangle / \langle M_{k,l} M_{k,l} \rangle}$. The other advantage of using this approach is that it eliminates the need for averaging the terms of the form $\langle L_{i,j} M_{i,j} \rangle$, an operation that is generally needed to improve robustness. In an unstructured environment this operation is not trivial, even for problems in which the flow is homogeneous in one or two directions. Moreover, we are primarily interested in calculations of complex flows in which there are no homogeneous directions. Though several methods like Lagrangian averaging (Meneveau *et al.* 1996) were proposed to address this problem, the typical solution is to apply a locally-defined filter on the field of the computed values C_μ . Using the present approach to compute the coefficients in the dynamic procedure, we found that this step was not necessary.

Location	LES Error	LES Error	RANS Error	RANS Error
	% wrt expt.	% wrt inlet	% wrt expt.	% wrt inlet
OD dilution hole	3.1	0.8	11.4	3.2
ID dilution hole	3.5	0.5	7.5	1.1
Core (main swirler)	10.3	0.14	8.4	0.11
Second (OD) swirler	7.5	0.35	13.5	0.63
Third (Guide) swirler	0.4	0.02	18.9	0.84

TABLE 2. Comparison of mass-flow splits in the Pratt & Whitney full-combustor geometry

5. Cold-flow simulations in the Pratt & Whitney geometry

5.1. Complex combustor

Last year's report documented flow-visualization results from cold-flow calculations in the complex Pratt & Whitney combustor geometry. These computations were extended to include the effects of flow bleed and transpiration and detailed comparisons with experiment were made for mass-flow splits and pressure drop. The geometry in the symmetry plane $z = 0$ together with contours of the absolute value of the velocity field are shown in figure 1. The Reynolds number in the pre-diffuser inlet section, defined with the bulk velocity in the inlet section and a characteristic length scale $L = 1''$, is about 500,000 while it takes a value of about 150,000 in the main (core) swirler channel. Turbulent fluctuations from a separate calculation, in a periodic pipe sector of shape identical to the pre-diffuser inlet section, are fed in at the inlet. In the experiment, fuel is injected at the tip of the downstream part of the injector. The mass-flow rate for the fuel is matched in our simulation.

Interestingly, the RANS and LES predictions for the pressure drop across the different components of the combustor are very close (within 6,000 Pa for 5 out of the 6 stations). However, as shown in table 2, LES does a better job overall in predicting the mass-flow splits through the swirlers and the inner and outer dilution holes. LES predictions are within 10.5% of the experimental measured values for the mass splits through the swirlers, but more importantly within 4% for the total discharges through the swirlers, inner and outer dilution holes. The errors as a percentage of the total inlet discharge are much lower.

5.2. Front-end model

Cold-flow simulations were performed in the Pratt & Whitney front-end test-rig geometry. This geometry has the same fuel injector and combustion chamber as the complete combustor, but air is fed to the injector through a cylindrical plenum, the inner and outer diffuser channels are absent, and the main combustor chamber does not have dilution holes on the surrounding walls. The interest in simulating the flow in this geometry is the availability of detailed LDV velocity-profile measurements in the main combustion

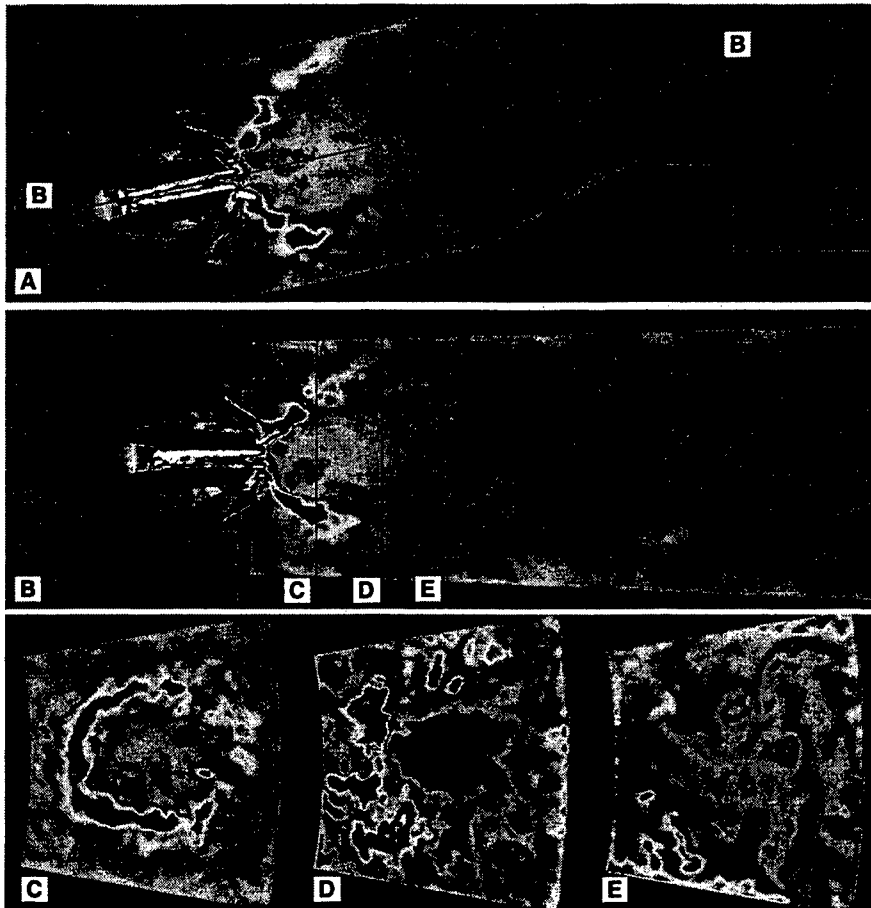


FIGURE 2. Fine-grid LES solution for the front-end rig geometry; Contours of the instantaneous streamwise velocity component (a) in the $x - y$ symmetry plane ($z=0$), (b) in a plane containing the main swirler symmetry axis, perpendicular on the $z = 0$ plane, and at several downstream locations (c) $x = 1.1''$, (d) $x = 2.2''$, (e) $x = 3.4''$

chamber, which can be used to fully validate the accuracy of our solver for a geometry of complexity comparable to the full combustor. The Reynolds number in the main swirler channel of the injector is close to 100,000.

The complexity of the geometry and flow inside the test rig is illustrated in figure 2 which shows some sections of the computational domain along with contours of the streamwise velocity in the symmetry plane ($z=0$), in a plane containing the main swirler symmetry axis, perpendicular to the $z = 0$ plane, and at several downstream locations, $x = 1.1''$, $x = 2.2''$ and $x = 3.4''$ from the injector, for the statistically-steady solution obtained on a fine mesh. The main feature observed in these plots is the formation of a relatively large recirculation region downstream of the injector, due to the swirling jet coming out from the injector into the main combustor chamber.

Prediction of the correct dimensions of the recirculation region, together with the variation of the jet width with distance from the injector, are two of the main challenges in simulating this flow. In particular, RANS calculations of this flow, conducted both at Pratt & Whitney using an in-house $\kappa - \epsilon$ code and at Stanford using a commercial

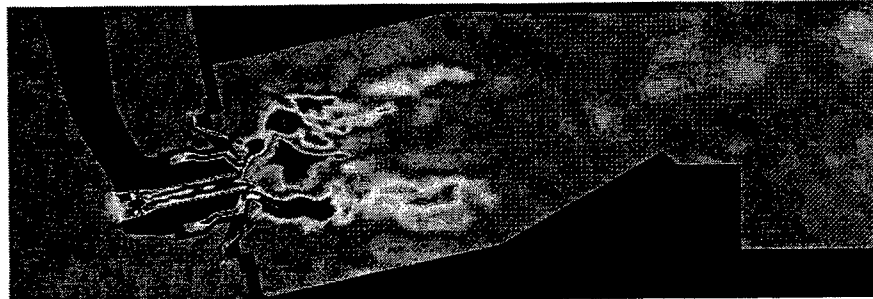


FIGURE 3. Coarse-grid LES solution; Contours of the instantaneous streamwise velocity component in the $x - y$ symmetry plane ($z = 0$)

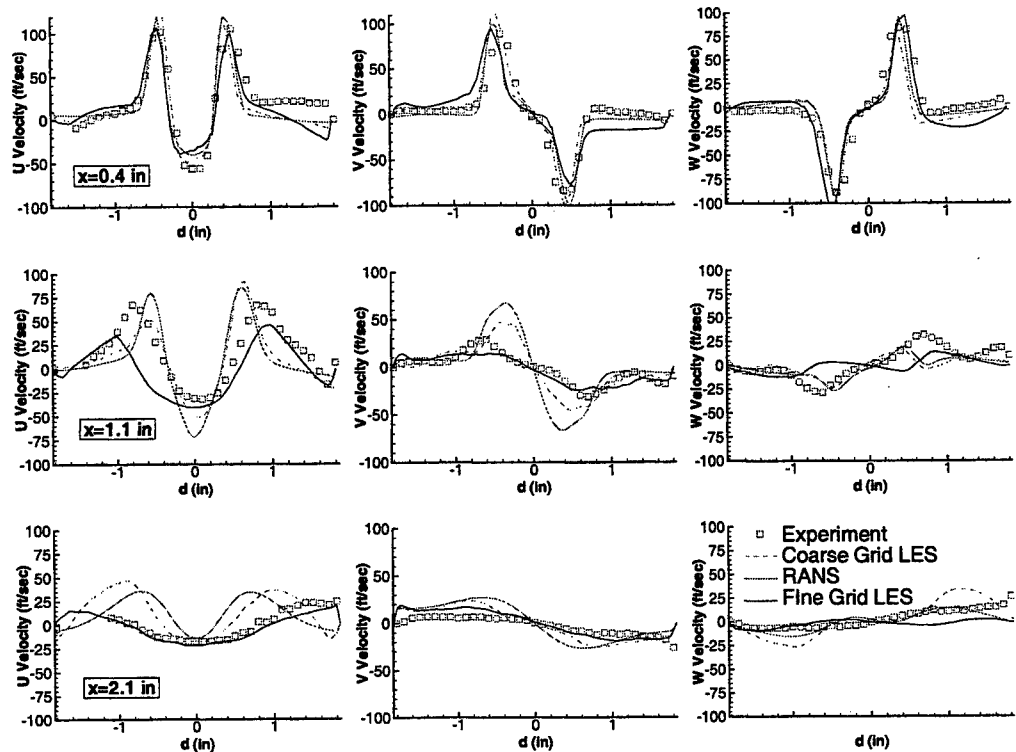


FIGURE 4. Comparison between fine-grid LES, coarse-grid LES, RANS (FLUENT) and experiment (Pratt & Whitney) for the gas-phase velocity (streamwise, radial and swirling components) in the Pratt & Whitney combustor at three stations situated at $x = 0.4''$, $x = 1.1''$ and $x = 2.1''$ downstream of the injector

software (FLUENT), failed to predict these quantities correctly away from the injector, though they were fairly successful in predicting all three velocity components immediately downstream of the injector. This is evident from comparison of the RANS profiles with the experimental data symbols in Fig. 4. Interestingly, the Pratt & Whitney RANS simulation was able to capture the pressure drop across the injector within 2%, while FLUENT yielded a much bigger error ($\sim 20\%$). This is attributed to different grid densities inside the injector.

Two grids were generated in the present LES simulations: a coarser grid containing about 2.2 million control volumes and a finer containing about 4.5 million control volumes. Contours of the instantaneous streamwise velocity component are shown in figures 3 and 2a for the solutions obtained on the two grids at a statistically steady state. Though for the simulation on the coarser mesh the prediction of the mean pressure drop across the injector (4588 Pa) was found to be very close to the experimental value (4500 Pa), the agreement with the experimental data for the velocity profiles was not much better than the results obtained from RANS calculations. In particular, the spreading of the jet away from the injector was substantially underpredicted. This can be seen by comparing the streamwise velocity profiles at the downstream station $x=2.1''$ from the injector in figure 4. The reason for this is that insufficient grid resolution causes the (conical) detached shear layers, which are initially shed at the correct angle from the injector (this is expected because all models do a fairly good job in predicting all the velocity components immediately downstream of the injector), to curve toward the injector centerline, due to a too-high rate of decay of azimuthal momentum inside the initial region of these layers. This results in a much smaller recirculation region compared to the fine grid solution (see figure 2) where the detached shear layers are seen to extend up to the lateral walls of the main combustor chamber. The angle between the injector axis and the conical shape corresponding to the detached layers is approximatively constant at 55° . The shedding of vortex tubes due to the Kelvin-Helmholtz instabilities in the detached shear layers is clearly observed. The fine-grid solution in figure 2 displays the right features corresponding to the flow in the test-rig geometry at the specified conditions. This also results in better quantitative predictions for the velocity profiles (see figure 4), especially away from the injector where, as clearly observed in the mean streamwise velocity profile at $x = 2.1''$ from the injector, the level of agreement between the LES fine-grid solution and the experiment is clearly superior to the one observed for the RANS or the LES coarse-grid solutions. However, some differences between the experiment and the fine-grid LES results remain (e.g. compare the streamwise velocity profiles at the $x = 1.1''$ station). These differences may occur because the flow is under-resolved in some regions. We plan to address this by performing one additional calculation on a very fine mesh (14 million cells).

6. Multigrid solution of the pressure-Poisson equation

In the present unstructured LES solver, the conjugate-gradient (cg) solution of the pressure-Poisson system is the most computationally-expensive component of the overall solution process, requiring from 50 to 80% of the total solution time. In this section we present some details of a multigrid solver for this Poisson system that will eventually replace the present cg solver. Tests using a single coarse grid (1-level multigrid) have demonstrated an overall reduction in computation time of 35 to 60% per time step. Once fully implemented, the pressure solver should become one of the least expensive components of the solution process, yielding reductions in overall computation time of 45 to 75% per time step.

6.1. Background

Multigrid methods are used extensively in the numerical solution of partial differential equations. They can exhibit an optimal complexity in terms of both work and storage — i.e. both work and storage scale linearly with problem size. They can also achieve very good parallel efficiency and scalability by the method of domain decomposition. For

standard multigrid methods involving point-relaxation smoothers and isotropic coarsening, however, the convergence factor is known to degenerate dramatically in the presence of coefficient anisotropy. Coefficient anisotropy can result from large cell aspect ratios, anisotropic material properties, or asymmetric operators. In the present case the anisotropy is primarily geometric, caused by the grid stretching used to resolve high-Reynolds number boundary layers.

In an effort to make multigrid methods more robust, several solutions have been proposed to this problem. Most of these solutions involve some combination of the following two ideas: 1) the use of semi-coarsening, where the coarsening is not isotropic, and 2) improvements to the smoother so that both high- and low-frequency components of the residual distribution are effectively reduced in at least one or two directions (i.e. the so-called line and plane smoothers of structured-grid methods). When the semi-coarsening and/or smoother improvements are properly matched, multigrid methods recover their optimality, even in the presence of strong coefficient anisotropies.

6.2. Proposed multigrid method

The multigrid method currently being integrated into the unstructured LES solver has the following characteristics:

- V-cycle multigrid with linear restriction and block correction.
 - Multi-color Gauss-Seidel smoothing on all grids except the coarsest; on the coarsest grid, the residual is reduced by approximately one order of magnitude using a coarse grid version of the present cg solver.
 - Coarse-grid control volumes are built by the agglomeration (sometimes called aggregation) of fine grid control volumes. The agglomeration procedure is performed once per computation, when the pressure solver is first called. Agglomeration avoids use of mesh generators to generate the coarse grids, and simplifies the restriction and prolongation operators.
 - Directional agglomeration (semi-coarsening) is used to prevent stalling of the multigrid method in the presence of large cell aspect ratios and the resulting coefficient anisotropy. At present, a greedy-type algorithm is used, similar to that described by Raw (1996) and Elias *et al.* (1997).
- Other authors have solved the coefficient-anisotropy problem by using uniform coarsening, combined with line-implicit smoothing in the direction of greatest coefficient strength (Brandt *et al.* 2002, Mavriplis & Pirzadeh 1999). While effective for certain problems, line-implicit smoothing combined with uniform coarsening will not yield an optimal multigrid method in general (Montero *et al.* 2001).
- Coarse-grid coefficients are calculated using the discretized coarse-grid approximation (i.e. geometric multigrid). Algebraic multigrid with first-order restriction (insertion) of the fine-grid coefficients was tested and found to yield significantly slower convergence rates. Algebraic multigrid with higher-order restriction was not considered because of the increase in bandwidth (neighbor connections) associated with coarser grids.

6.3. Results

A two-grid version of this multigrid method has been added to the parallel unstructured LES solver and tested on a number of problems, including the coaxial combustor (1.1 million control volumes, 32 processors). Figure 5 compares the normalized wall-clock time per time step for this problem, breaking out the pressure solver from the other components of the solution (scalar equations, momentum equations, chemistry, etc.). For

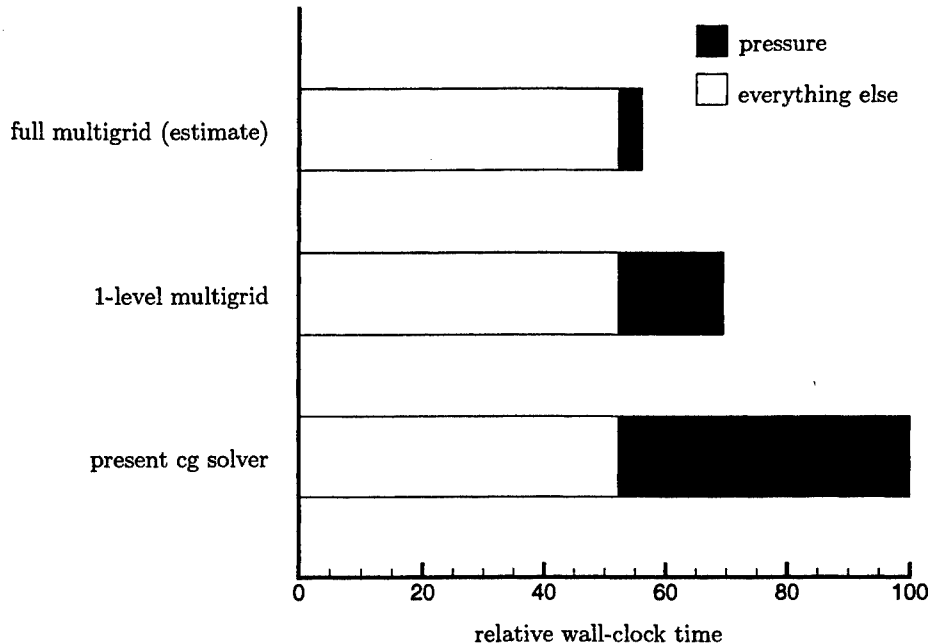


FIGURE 5. Normalized breakdown of total computation time for three different Poisson solvers: coaxial combustor problem with 1.1 million control volumes on 32 processors.

the coaxial-combustor problem, the pressure solution requires about 50% of the total solution time when the present cg solver is used.

The one-level multigrid solver is able to converge the pressure equation to the same tolerance in about 10 to 12 cycles: however each cycle is significantly more expensive than a fine-grid cg iteration, so the actual speed-up in pressure solution is about 2.7 times, corresponding to a reduction in overall solution time of about 30%. Most of the computational cost in this one-level multigrid is associated with the coarse-grid cg iterations, where 100 or more iterations may be necessary to reduce the coarse-grid residual by one order of magnitude. Extrapolating this demonstrated two-grid performance to multiple coarse grids, the speed-up in the pressure solution should be about 10 times, corresponding to a reduction in overall solution time of about 45% for this problem.

Figure 6 compares the convergence history of the the pressure solver for these three cases. The histories are plotted relative to "equivalent cg iterations", proportional to wall clock time.

7. Towards generating very large unstructured grids

In the framework of ASCI, the generation of unstructured meshes is carried out using the commercial software GAMBIT and the research code CUBIT (developed by Sandia National Laboratories); the former is usually preferred because it provides a more user-friendly interface. Grids ranging from one to five million elements have been produced for the geometries discussed above. At present, we simulate a 20° sector of the Pratt &

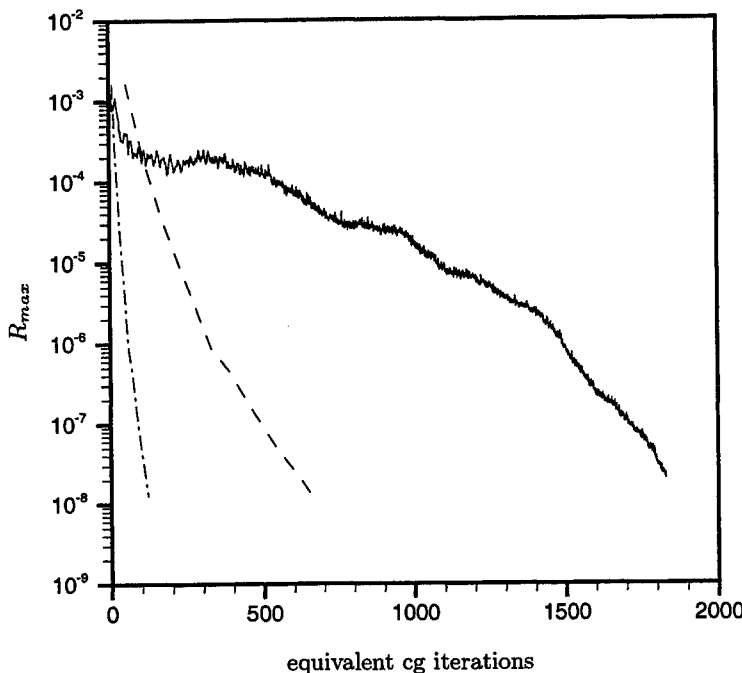


FIGURE 6. Comparison of pressure convergence history for three different Poisson solvers: — present cg solver; - - - 1-level multigrid; - - - full multigrid (estimate); coaxial combustor problem with 1.1 million control volumes on 32 processors.

Whitney combustor. Future simulations are planned that incorporate the entire combustor. In order to provide sufficient resolution for a geometry as complex as the Pratt & Whitney combustor, substantially larger meshes have to be generated. Grid generation is currently carried out on SGI workstations, and the largest grid that can be handled (because of the memory limit of 8 GB on these machines) is about 8 millions elements. There are two approaches that can be followed to overcome this limitation. The first is to generate a coarse grid and then subdivide all the elements along meridian planes: from a hexahedral eight smaller homothetical hexahedrals can be constructed splitting all the faces in four (halving the edges); similarly from one tetrahedra four hometical tetrahedrals can be generated (see figure 7).

This procedure can be easily performed on a multiprocessor machine. A subset of elements is assigned to each processor and the splitting is carried out independently. The major drawback of this process is inaccuracy in the representation of the physical boundaries of the domain. Notice that the splitting of an element requires the generation of an additional node on each face and on each edge. Consider a tetrahedral grid in a spherical volume; the boundary (spherical surface) is approximated by a tessellation of (planar) triangles. The accuracy of this representation can be evaluated by considering the distance between the circumcenter of each triangle and the spherical surface; finer grids correspond to higher accuracy. If the splitting procedure discussed above is used, refined grids will have the same accuracy (in representing the spherical surface) as the initial coarse mesh. The only way to improve the accuracy would be to project the nodes

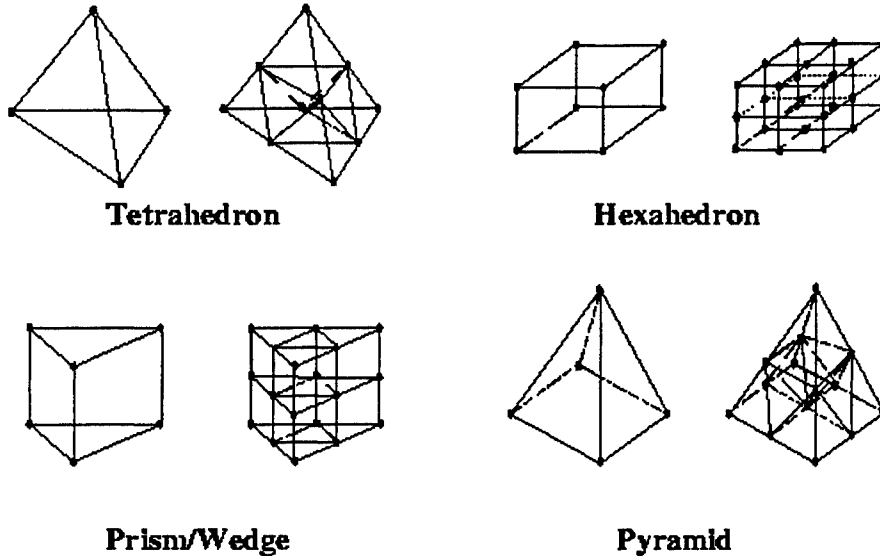


FIGURE 7. Grid generation by element splitting

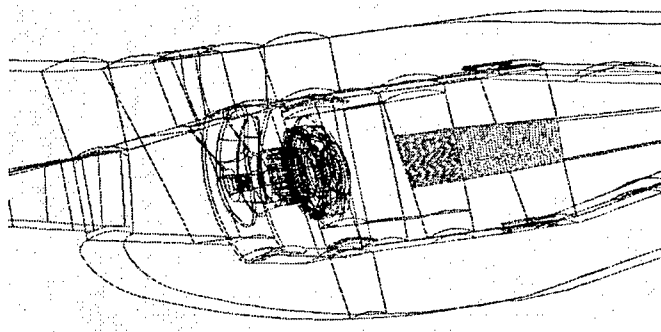


FIGURE 8. Subdomain-based grid generation

created by the splitting on the “real” boundary surface. The result is that to perform this procedure it is necessary to access the CAD representation of the computational domain and carry out projection operations for all the elements belonging to the boundaries. Therefore it is required to access to the CAD modules in GAMBIT with its related memory limitations. Note that neglecting this final boundary-fitting step produced highly distorted geometry representations in regions of high surface curvature.

The second approach consists in dividing the computational domain in subdomains (blocks); the surfaces between blocks are meshed first, and then fine grids (up to the desired resolution) are constructed independently (see figure 8). A *simple* (and intrinsically parallel) code can be written to merge together all the block grids without using GAMBIT and therefore without memory limitations. Initial tests of this second approach are encouraging.

8. Reacting flow simulations in a coaxial combustor geometry

The flamelet / progress-variable model described in a previous section was tested against experimental data for a methane-fueled coaxial-jet combustor corresponding to

COAXIAL COMBUSTOR - REACTING FLOW

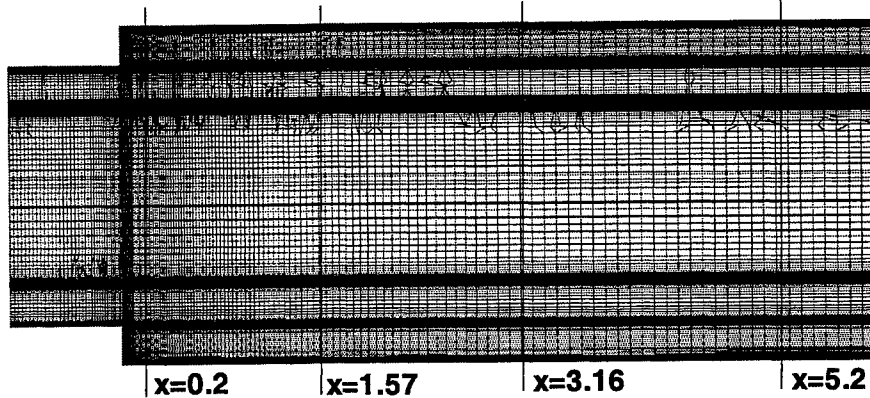


FIGURE 9. Computational domain and mesh section in an azimuthal plane

STREAMWISE VELOCITY (μ)

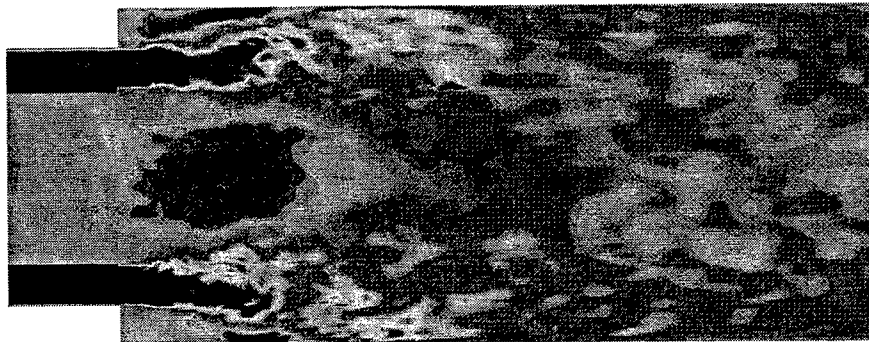


FIGURE 10. Instantaneous contours of the streamwise velocity component in an azimuthal plane

the experiment of Spadaccini *et al.* (1976). This experiment was chosen because of the relatively simple geometry, well-defined boundary conditions (confined jet simulation) coupled with a rather complex flow physics that mimics fairly well the complex-flow phenomena encountered in a realistic gas-turbine combustor. Results from a previous calculation using a structured code by Pierce & Moin (2001) are available, together with the original data of Spadaccini *et al.* (1976). This will allow a full validation of the reacting flow, including mean-velocity profiles, temperature and chemical species at several stations inside the main combustion chamber. A general view of the geometry and computational mesh in an azimuthal plane is given in figure 9. The fuel is introduced through a circular core section at a relatively low velocity, 0.93 m/s, while non-swirling air is introduced through a surrounding annulus at a much higher mean velocity of $U=20.6$ m/s. The mass flow rates of the fuel and air in the inlet sections are 0.0072 kg/s and 0.137 kg/s, respectively, the air temperature is 750 K, while the fuel temperature is 300 K. The mean pressure in the combustor is 3.8 atm. The fuel used in the experiment was natural

DENSITY

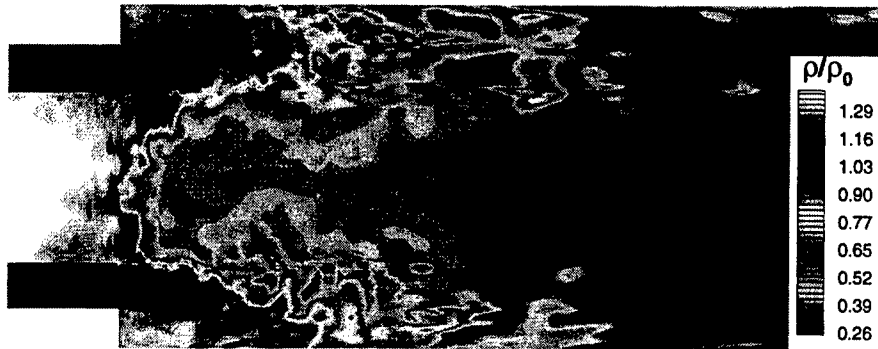


FIGURE 11. Instantaneous contours of the density in an azimuthal plane

MIXTURE FRACTION Z (exponential scale)



FIGURE 12. Instantaneous contours of the mixture fraction in an azimuthal plane

PRODUCT MASS FRACTION ($Y_{CO_2} + Y_{H_2O}$)



FIGURE 13. Instantaneous contours of the progress variable $y_{CO_2} + y_{H_2O}$ in an azimuthal plane

CO MASS FRACTION (Y_{CO})



FIGURE 14. Instantaneous contours of the carbon monoxide concentration y_{CO} in an azimuthal plane

gas but in the present investigation, as well as in the numerical simulation of Pierce & Moin, it was assumed to be pure methane. Because of the high air/fuel velocity ratio, a strong central recirculation region is formed in front of the fuel port, which appears to the surrounding air stream almost as a bluff body (see also figure 10 in which contours of the streamwise velocity component are shown). The recirculating combustion products provide a continuous ignition source for the relatively cold incoming reactants, thereby stabilizing the flame. Mixture fraction in the experiment was computed based on the total carbon and hydrogen atoms mass fractions, and the product mass fraction was computed from $C = y_{CO_2} + y_{H_2O}$.

A computational grid containing ~ 1.3 million hexahedra was generated to mesh the geometry that was used by Pierce & Moin in their simulations. Though they used approximately ~ 2.5 million points in their simulations, we were able to achieve roughly the same grid density in the important flow regions (mainly the upstream part of the main combustor) where turbulent mixing and combustion-related phenomena are important. The LES model is very similar in the two simulations, except the specific treatment in the estimation of the model coefficients due to the unstructured environment of our solver. The injector radius corresponding to the annular exterior radius ($R = 4.685D$ cm) and the mean air velocity in the inlet section were used for non-dimensionalization. The Reynolds number on the air side is $\sim 50,000$. The computational domain started at a distance of $1R$ upstream of the main combustor chamber, where fully-developed turbulent inflow conditions were specified using a precalculated database from a separate calculation for a periodic pipe and annular pipe domains at the corresponding Reynolds numbers. The computational domain was extended to a combustor length of $12R$, where convective outflow boundary conditions were used to convect the turbulent eddies out of the domain. Fully-developed incompressible velocity and mixing fields were obtained before the chemistry model was turned on. The initial progress-variable scalar field was set to its maximum allowed value determined from fast chemistry, so that initially the flame was fully ignited. A chemical table corresponding to methane and the specified combustor pressure was precalculated. The product mass fraction was chosen as the progress variable. The boundary conditions for the mixture fraction were $Z = 1$ in the fuel inlet section and $Z = 0$ in the air inlet section. The progress variable C in both the fuel and air

inlet sections was set to zero, as no reaction takes place at those locations. A time step of 0.005 R/U was used in the simulation using the implicit algorithm. About 80 inner iterations were needed to reduce the momentum residuals by five orders of magnitudes, while the conjugate-gradient pressure solver (no multigrid) needed about 1,700 iterations per time step to converge the pressure. About 50% of the CPU time per iteration was spent in the pressure solver, and $\sim 15\%$ in the combustion module. Based on Pierce & Moin's estimations we expect that ~ 500 R/U time units will be needed to obtain fully converged statistics. As mentioned in a previous section we expect to use $\sim 70,000$ CPU hours for this computation on an IBM SP3 machine.

At this point the calculation was run for ~ 120 R/U time units and the flow seems 'statistically steady' in the upstream part of the main combustor chamber. The streamwise velocity profile and its rms fluctuation in a section situated just downstream of the entrance into the main combustor chamber show good agreement with the similar profiles computed by Pierce & Moin. The statistics are still evolving downstream in the combustor. The flame location can be inferred from the temperature or the progress-variable contours shown in figure 13, as the progress variable essentially is tracking the reaction. In the experiment, the flame location was observed to lift off the burner and reattach intermittently in a highly-unsteady asymmetric manner. Our calculations also predict a lifted flame, and an animation of the progress-variable contours shows that our simulation is able to capture this behavior. At this point good qualitative agreement is obtained for the distribution of the mixture fraction and progress variable with the calculation of Pierce & Moin. Instantaneous contours of these variables in an azimuthal plane are shown in figure 12 and 13. Also shown are similar snapshots of the density (figure 11) and carbon monoxide concentrations (figure 14).

9. Integration with spray module

The spray models described in our progress reports from 1999, 2000 and 2001 have been fully integrated with the unstructured gas-phase solver. The droplets are modeled as point particles which satisfy Lagrangian equations. They influence the gas phase through source terms in the gas-phase equations. As the particles move, their position is located and each particle is assigned to a control volume of the gas-phase grid. The gas-phase properties are interpolated to the particle location and the particle equations are advanced. The particles are then relocated, particles that cross interprocessor boundaries are duly transferred, source terms in the gas-phase equation are computed, and the computation is further advanced. Validation of the Lagrangian particle-tracking approach, application of spray simulations to the Pratt & Whitney injector, and extension of the spray module to account for evaporation are described below.

9.1. Validation of Lagrangian Particle Tracking (LPT) Scheme in CDP

The flow in a swirl-stabilized coaxial combustor represents an important validation case. Sommerfeld & Qiu (1991) provide detailed measurements of this flow, which tests both the gas-phase solver and the spray module. A detailed validation of the gas-phase solver in this geometry was completed last year and was presented in an earlier ASCI report. The particle-laden flowfield was computed by injecting particles with a known size distribution at the inlet of the combustor. The primary jet of the combustor is laden with glass beads whose diameter varies from 10 microns to 120 microns. The particle phase was initialized by computing over a few flow-through times. About 1.2 million particles were obtained in the combustor. The particle statistics were then computed over two flow through times

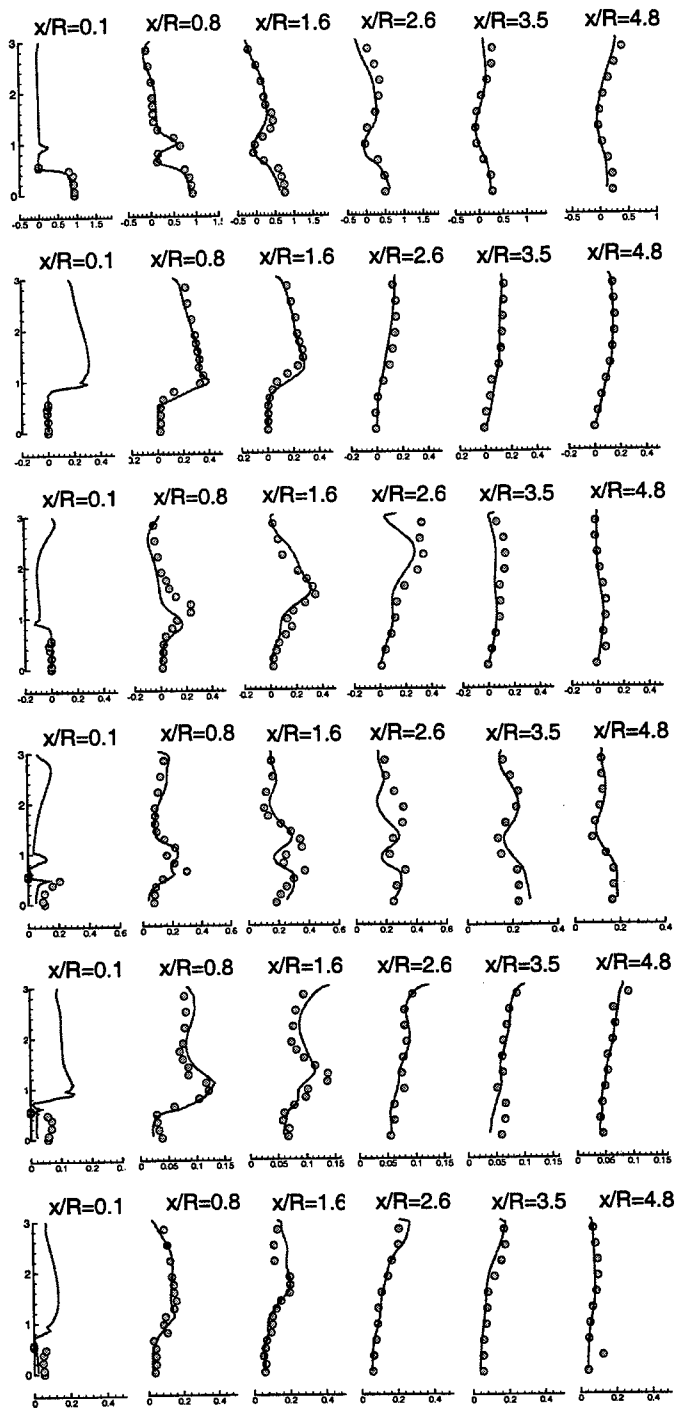


FIGURE 15. Comparison of particle phase properties between LES (—) and experiment (○, Sommerfeld & Qiu 1991) for swirling flow in a coaxial combustor. (a): mean axial velocity, (b): mean swirl velocity, (c): mean radial velocity, (d) rms of axial velocity, (e) rms of swirl velocity, (f) rms of radial velocity.

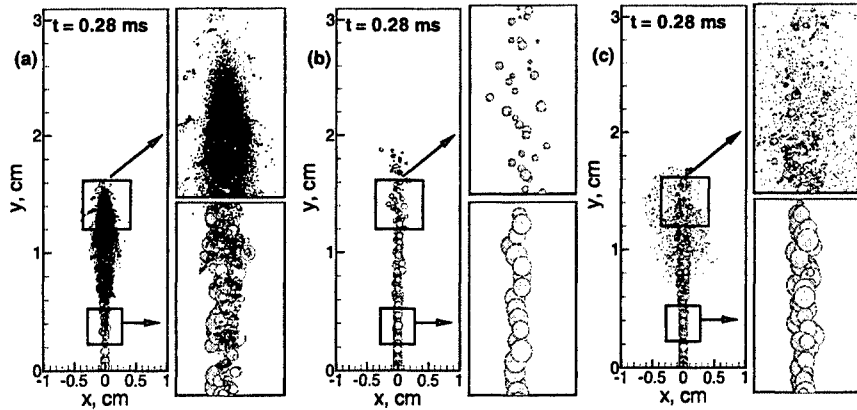


FIGURE 16. Comparison of the pure-droplet, pure-parcel, and hybrid approaches.

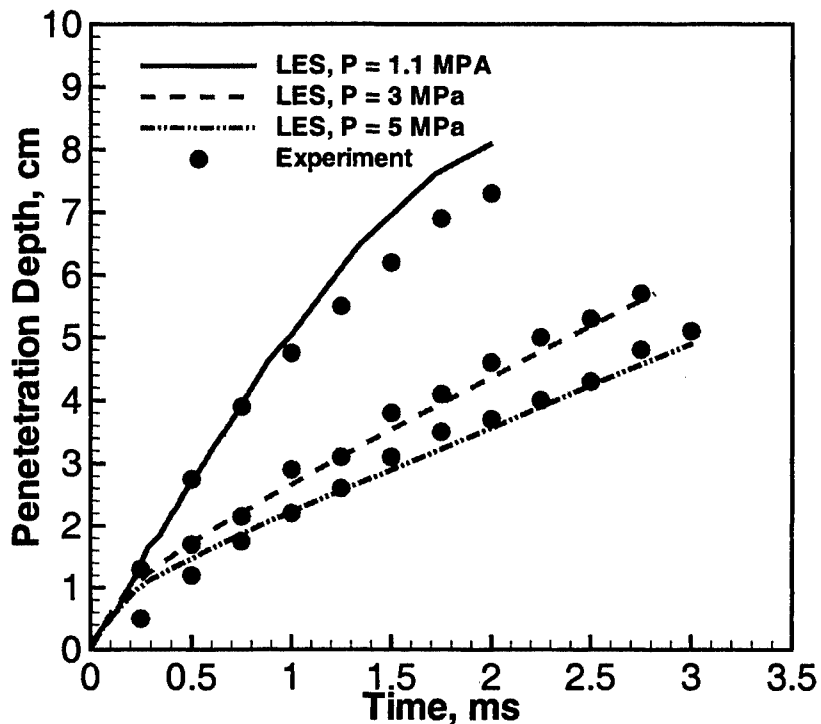


FIGURE 17. Comparison of the spray-penetration depth with experimental data.

in the region of interest. The agreement of mean and rms velocity components with the experiment is shown in figure 15. Very good agreement was also obtained for the mean and rms of diameter distribution at various axial locations. The present computation was performed on 96 processors using an explicit time-advancement procedure. The overhead due to the particle-phase was about 30%. Particle-dispersion characteristics were also obtained by tracking a large number of particles of different size classes. It was compared with the experimental data and analytical estimates to show good agreement. Details of this computation can be found in Apte *et al.* (2002). It was shown that the point-particle

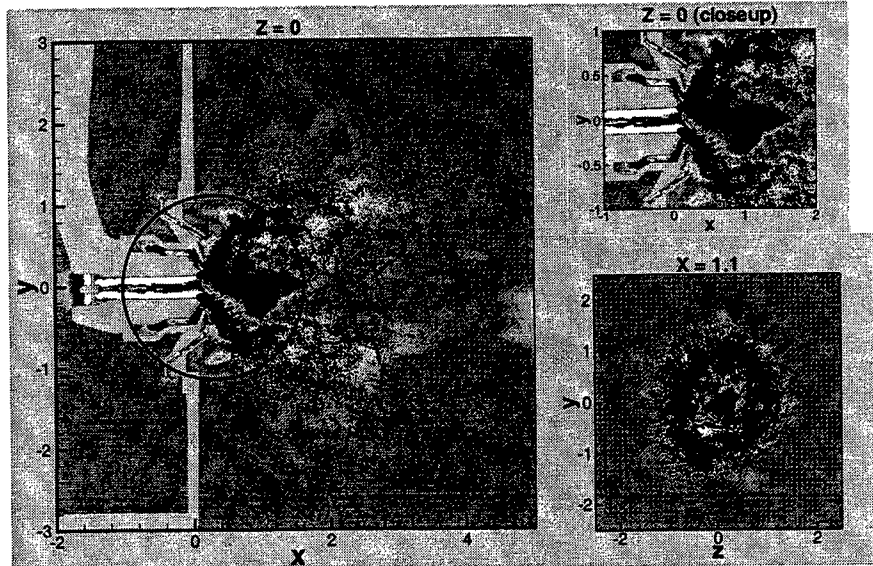


FIGURE 18. Evolution of spray from a PW injector: contours of axial velocity superimposed on particle scatter plot.

approximation of the dispersed phase was able to accurately predict the behavior of the solid phase for the particle loadings simulated. This study represents the first LES of two-phase flows in a coaxial combustor using the unstructured grid solver (CDP). After completing this comprehensive validation study, we focused on incorporating complex spray breakup and evaporation models in CDP.

10. Spray models for use in CDP

10.1. Stochastic model for secondary breakup

Liquid-spray atomization plays a crucial role in the combustion dynamics in gas-turbine combustors. In standard Lagrangian particle-tracking codes, emphasis is placed on obtaining the correct spray-evolution characteristics away from the injector. Only the global behavior of the primary atomization, occurring close to the injector, is considered and the details are not captured. The essential features of spray evolution, viz. droplet size distribution, spray angle, and penetration depth, are predicted away from the injector surface by secondary breakup models. Usually standard, deterministic breakup models based on Taylor Analogy Breakup (TAB) (O'Rourke & Amsden 1987) or wave (Reitz 1987) models are employed in RANS-type computations. Liquid 'blobs' with the size of the injector diameter are introduced into the combustion chamber and undergo atomization according to the balance between aerodynamic and surface-tension forces acting on the liquid phase. In the TAB model, oscillations of the parent droplet are modeled in the framework of a spring-mass system and breakup occurs when the oscillations exceed a critical value. In the wave model, new droplets are formed based on the growth rate of the fastest wave instability on the surface of the parent blob. Both models are deterministic, with 'single-scale' production of new droplets. In many combustion applications, however, injection of a liquid jet takes place at high relative velocity between the two phases (high initial Weber number). Under these conditions, intriguing processes

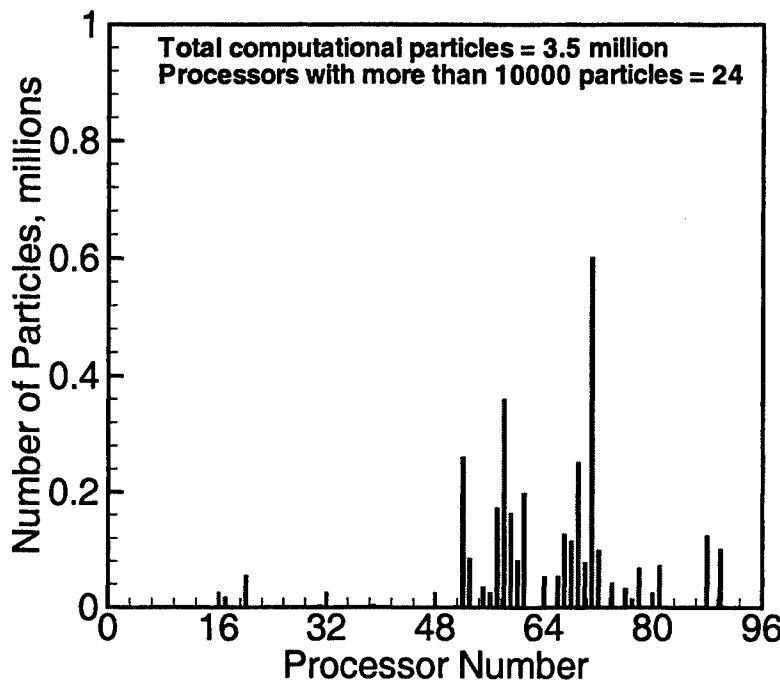


FIGURE 19. Load balance for spray-breakup simulation.

such as turbulence-induced breakup, multiple-droplet collisions in the dense-spray region, fluctuations due to cavitating flow inside the injector, etc., contribute to the process of atomization. This results in droplet formation over a large spectrum of droplet sizes and is not captured by the above models. Predicting the distribution of droplet sizes at each spray location is important for sheet-breakup modeling.

In order to predict the essential global features of these complex phenomena, a stochastic approach for droplet breakup which accounts for a range of product-droplet sizes is necessary. Specifically, for a given control volume, the characteristic radius of droplets is assumed to be a time-dependent stochastic variable with a given initial distribution function. The breakup of parent blobs into secondary droplets is viewed as the temporal and spatial evolution of this distribution function around the parent-droplet size. This distribution function follows a certain long-time behavior, which is characterized by the dominant mechanism of breakup. The size of new droplets is then sampled from the distribution function evaluated at a typical breakup time scale of the parent drop.

Owing to the complexity of the phenomenon, it is difficult to clearly identify such a dominant mechanism for breakup. Kolmogorov (1941) developed a stochastic theory for breakup of solid particles by modeling it as a discrete random process. He assumed that the probability to break each parent particle into a certain number of parts is independent of the parent-particle size. Using the central limit theorem, Kolmogorov pointed out that such a general assumption leads to a log-normal distribution of particle size in the long-time limit.

Based on Kolmogorov's hypothesis we have developed a numerical scheme for atom-

ization of liquid spray at large Weber number (Gorokhovski & Apte 2001). The discrete model of Kolmogorov is reformulated in terms of a Fokker-Planck (FP) differential equation for the evolution of the size-distribution function from a parent blob towards the log-normal law:

$$\frac{\partial T(x, t)}{\partial t} + \nu(\xi) \frac{\partial T(x, t)}{\partial x} = \frac{1}{2} \nu(\xi^2) \frac{\partial^2 T(x, t)}{\partial x^2}. \quad (10.1)$$

where the breakup frequency (ν) and time (t) are introduced. Here, $T(x, t)$ is the distribution function for $x = \log(r_j)$, where r_j is the droplet radius. Breakup occurs when $t > t_{breakup} = 1/\nu$. The value of the breakup frequency and the critical radius of breakup are obtained by the balance between the aerodynamic and surface tension forces. The secondary droplets are sampled from the analytical solution of equation (10.1) corresponding to the breakup time-scale. The parameters encountered in the FP equation ($\langle \xi \rangle$ and $\langle \xi^2 \rangle$) are computed by relating them to the local Weber and Reynolds numbers for the parent blob, thereby accounting for the capillary forces and turbulent properties. The capillary force prescribes a lower bound limit for the produced-droplet size through the local maximum stable (or critical) radius (r_{cr}). The velocity of the produced droplets is modeled using a Monte-Carlo procedure. As new droplets are formed, parent droplets are destroyed and Lagrangian tracking in the physical space is continued until further breakup events occur. The evolution of droplet diameter is basically governed by the local relative-velocity fluctuations between the gas and liquid phases. In this respect, LES plays a key role in providing accurate, local estimates of the gas-phase turbulent quantities. Although the mesh spacing used in a typical LES computation is larger than droplet size, the superiority of LES over RANS lies in accurate predictions of mixing and momentum transport from the gas phase to the spray field. The details of this model are given by Gorokhovski & Apte (2001).

10.2. Hybrid particle-parcel technique for spray simulations

Performing spray-breakup computations using Lagrangian tracking of each individual droplet gives rise to a large number of droplets ($> 50\text{-}100$ million) very close to the injector. Computing such a large number of droplet trajectories is a formidable task even with supercomputers. In parallel computation of complex flows utilizing standard domain-decomposition techniques, the load balancing per processor is achieved by distributing the number of grid cells equally among all processors. Lagrangian particle tracking, however, causes load imbalance owing to the varying number of droplets per processor.

In order to overcome the above load-balancing problem, the usual approach is to represent a group of droplets with similar characteristics (diameter, velocity, temperature etc.) by a computational particle or ‘parcel’. In addition, one carries the number of droplets per parcel as a parameter to be tracked. Since, a parcel represents a group of droplets (of the order of 100-1000), the total number of computational particles or trajectories to be simulated is reduced significantly. With breakup, the diameter of the parcel is sampled according to the procedure given above and the number of droplets associated with the particles is changed in order to conserve mass. This reduces the total number of particles per processor and increases the computational overhead with sprays by about 20% depending on the number of parcels used. Each parcel has all the droplet characteristics associated with it. The parcels methodology works well for RANS-type simulations where one is interested in time- or ensemble-averaged quantities. For LES,

however, we should ideally simulate as many droplet trajectories as possible in order to obtain time-accurate results.

A hybrid scheme involving the computation of both individual droplets and parcels is proposed. The difference between droplets and parcels is simply the number of particles associated with them, N_{par} , which is unity for droplets. During injection, new particles added to the computational domain are pure drops ($N_{par} = 1$). These drops move downstream and undergo breakup according to the above breakup model and produce new droplets. This increases the number of computational particles in the domain. In the dense-spray regime, one may obtain large number of droplets in a control volume and its immediate neighbors. The basic idea behind the hybrid approach is to collect all droplets in a particular control volume, and group them into bins corresponding to their size and other properties such as velocity, temperature etc. The droplets in bins are then used to form a parcel by conserving mass, momentum and energy. The properties of the parcel are obtained by mass-weighted averaging from individual droplets in the bin. For this procedure, only those control volumes are considered for which the number of droplets increases above a certain threshold value. The number of parcels created would depend on the number of bins and the threshold value used to sample them. The parcel thus created then undergoes breakup according to the above stochastic sub-grid model, however, does not create new parcels. On the other hand, N_{par} is increased and the diameter is decreased by mass conservation.

The effectiveness of this hybrid approach is demonstrated in the following computations. The implementation of this method in an unstructured LES code gives us the capability of testing and validating these models in realistic industrial geometries for various combustors with multiphase flows.

10.3. Spray-breakup simulations

Simplified combustor geometry

In order to validate the stochastic breakup model, a standard test case for spray atomization is simulated and compared with the experimental data of Hiroyasu and Kudota (1974) in a Diesel-engine configuration. The computational domain is a closed cylinder of length 13.8 cm and diameter 5.6 cm. A liquid jet is injected through a single-hole nozzle into this constant-pressure, room-temperature nitrogen chamber. Since the chamber temperature is low, evaporation of the liquid fuel is negligible. Large blobs of diameter 300 μm , corresponding to the injector size, are injected into the combustion chamber. Initially, there is no gas-phase flow inside the chamber. Gas-phase recirculation zones are created as the spray penetrates into the combustion chamber, through momentum-transfer between the gas and liquid phases. Three cases with different chamber pressures of 1.1, 3, and 5 MPa are simulated and compared with the experimental data. The corresponding flow parameters are indicated in table 3. The number of droplets injected per iteration is determined from the droplet diameter and time step by keeping the mass-flow rate constant. The time step used in the present simulation is 1.5 ms and a uniform grid of $64 \times 65 \times 65$ cells is found to capture the spray dynamics accurately.

The computations were performed using three different approaches: tracking and creation of all droplets, tracking of parcels, and the hybrid droplet-parcel algorithm. Results for the 1.1 MPa case are qualitatively compared in figures 16a-c, respectively. The size and location of each circle corresponds to that of the actual droplets in the computational domain. Figure 16a indicates that a broad spectrum of droplet sizes is present with the co-existence of large and small droplets. It should be noted that, when all droplet

Parameters	Case 1	Case 2	Case 3
P_{tiq} , MPa	10	10	10
P_{gas} , MPa	1.1	3	5
Injection diameter, μm	300	300	300
Injection time, ms	2.5	4	5
Injection velocity, m/s	102	90.3	86.4

TABLE 3. Validation cases for stochastic breakup model in Diesel-engine configuration; Hiroyasu & Kudota (1974).

trajectories are computed a large number of droplets ($\sim 2\text{-}3$ million) is obtained even at an early stage of the simulation. This simulation, however, depicts the complex interactions between the liquid and gas phases, the momentum coupling, and spray atomization due to stripping of small droplets. Figure 16b shows a similar simulation performed using the parcels-approach normally used in RANS-type computations. An extremely coarse (global) representation of the liquid core and atomization is obtained because new droplets are not created. Figure 16c, on the other hand, indicates the effectiveness of the hybrid approach. Here, the total number of computational particles is much smaller than those obtained when all the droplet trajectories are computed.

Close to the nozzle, the liquid core shows the existence of large and small droplets. Away from the nozzle, a global representation of droplets grouped to form parcels as well as small sparse droplets is observed. The computational overload due to the hybrid approach is significantly less (~ 50 times lower) in comparison with the computation of all droplet trajectories. The essential features of the spray dynamics are captured by the hybrid approach indicating its effectiveness and applicability in Eulerian-Lagrangian formulations.

Figure 17 shows the comparison of the spray-tip penetration depth as a function of time with the experimental data for the three cases investigated. Good agreement is obtained for all the three cases using the hybrid algorithm. The penetration depth decreases with increase in pressure. This could be attributed to the decreased injection velocity as well as strong damping of the liquid momentum by the denser gas-phase at higher pressures. The liquid core lengths were less than 2 mm in the above computations. The penetration depths predicted were weakly dependent on the grid size and the resolution used was sufficient to obtain good agreement with the experiments. The ligament-like liquid structures deflected outward are clearly visible and the spray angles produced for the three cases, 20, 23, and 25 degrees, respectively, are in close agreement with the experimental observations (Hiroyasu & Kudota 1974).

PW front end validation geometry

The stochastic model together with the hybrid particle-parcel approach were used to simulate the spray evolution from the Pratt & Whitney injector. The experimental data

set was obtained by mounting the injector in a cylindrical plenum through which gas with prescribed mass-flow rate was injected. The gas goes through the main and guide swirler to inject a swirling jet into the atmosphere. Liquid film is injected through the filer surface which forms an annular ring. The liquid mass-flow rate corresponds to certain operating conditions of the gas-turbine engine. Measurements were made of the droplet distribution and liquid mass flux in the radial direction at two different axial locations away from the injector. Gas-phase statistics for mean and rms velocities is also available at these locations. The outside air-entrainment rates were measured and prescribed as inflow conditions. A snapshot of the spray evolution in the $z = 0$ plane, together with the gas-phase axial velocity contours, is shown in figure 18. The hybrid approach used herein gives a dynamical picture with correct spray angle. Preliminary results show that the liquid mass fluxes at two downstream locations are in reasonable agreement with the experimental data. However, a longer-time sample is necessary to match the computational predictions with the experiments.

This computation was performed on 96 processors. The domain decomposition is based on the optimal performance of the Eulerian gas-phase solver. Due to breakup, a large number of droplets is created in the vicinity of the injector. With the hybrid approach, the total number of computational particles tracked after 6 ms is about 3.5 million, which represents approximately 13 million droplets. This includes about 150,000 parcels. The distribution of particles on 96 processors is shown by the histogram in figure 19. This implies that less than 30% of the total number of processors contain more than 10,000 computational particles. A preliminary solution to this problem is to use more processors, which would reduce the maximum number of computational particles per processor. A better approach is to develop an alternative domain-decomposition scheme with dynamic load balancing and additional weights for CVs containing particles.

11. Future plans

Our plans for the next year are as follows:

- Complete the simulation of reacting flow in the coaxial combustor geometry corresponding to the experiment of Spadaccini *et al.*
- Complete spray breakup simulation in Pratt & Whitney front-end validation geometry.
- Address the issue of load-balancing due to spray and investigate dynamic domain-decomposition techniques for Eulerian-Lagrangian computations of spray.
- Perform validation simulation for spray evaporation corresponding to the experiment of Sommerfeld & Qiu (1998).
- Implement a multi-level version of the geometric multigrid algorithm for the pressure-equation solver and investigate the advantages of using multigrid techniques to accelerate convergence of the momentum and scalar transport equations.
- Improve the agglomeration algorithm to optimize the geometric characteristics of agglomerated coarse grid control volumes. Alternate-directional agglomeration algorithms will be investigated.
- Implement commutative filters to estimate more accurately the filtered quantities that have to be evaluated in the dynamic procedure and to implement LES models with explicit filtering in which the filter width can be specified *a priori* by the user instead of being dictated by the local grid spacing.
- Generate the next-generation grids for the complex Pratt & Whitney combustor.

- Calculate the reacting flow in the full Pratt & Whitney geometry and validate by comparing with the experimental data provided by Pratt & Whitney. This calculation will involve testing not only the combustion model module but also the Lagrangian particle tracking module, evaporation and breakup modules.

Acknowledgments

We would like to acknowledge the Department of Energy's ASCI program for providing financial support for this work. We are also very grateful to the Pratt & Whitney combustor group for providing detailed experimental data to validate our code.

REFERENCES

- APTE, S.V., MAHESH, K., & MOIN, P. 2002 LES of particle-laden swirling flow in a coaxial combustor. To be submitted to *Int. J. Multiphase Flows*.
- BRANDT, A., DISKIN, B., & THOMAS, J. L. 2002 Recent advances in achieving textbook multigrid efficiency for computational fluid dynamics simulations. *ICASE Rept. No. 2002-16*.
- ELIAS, S. R., STUBLEY, G. D., & RAITHBY, G. D. 1997 An adaptive agglomeration method for additive correction multigrid. *Int. J. for Num. Methods in Engg.* **40**, 887–903.
- GOROKHOVSKI, M. & APTE, S.V. 2001 Stochastic sub-grid modeling of drop breakup for LES of atomizing spray. *Annual Research Briefs*, Center for Turbulence Research, NASA Ames/Stanford Univ., 169–176.
- HIROYASU & M., KUDOTA, T. 1974 Fuel droplet size distribution in diesel combustion chamber. *SAE Tech. Paper* 740715.
- KOLMOGOROV, A. N. 1941 On the log-normal distribution of particle sizes during break-up process. *Dokl. Akad. Nauk SSSR* **31**, 99–101.
- MAVRIPPLIS, D. J., & PIRZADEH, S. 1999 Large-scale parallel unstructured mesh computations for 3D high-lift analysis. *ICASE Rept. No. 1999-9*.
- MENEVEAU, C., LUND, T. S. & CABOT, W.H. 1996 A Lagrangian dynamic subgrid-scale model of turbulence. *J. Fluid Mech.* **319**, 353–385.
- MONTERO, R. S., LLORENTE, I. M., & SALAS, M. D. 2001 Robust Multigrid Algorithms for the Navier Stokes Equations. *J. Comp. Phys.* **173**, 412–432.
- O'ROURKE, P. J., & AMSDEN, A. A. 1987 The TAB method for numerical calculations of spray droplet breakup. *SAE Tech. Paper* 872089.
- PIERCE, C. D. & MOIN, P. 2001 Progress variable approach for large eddy simulation of turbulent combustion. *Report TF-80*, Mech. Engg. Dept., Stanford Univ.
- RAW, M. 1996 Robustness of coupled algebraic multigrid for the Navier-Stokes equations. *AIAA Paper* 96-0297.
- REITZ, R. D. 1987 Modeling atomization processes in high-pressure vaporizing sprays. *Atom. & Spray* **3**, 309–337.
- SOMMERFELD, M. & QIU, H. H. 1991 Detailed measurements in a swirling particulate two-phase flow by a phase-Doppler anemometer. *Int. J. Heat and Fluid Flow* **12**, 20–28.
- SOMMERFELD, M., & QIU, H.H. 1998 Experimental studies of spray evaporation in turbulent flow. *Int. J. Heat & Fluid Flow* **19**, 10–22.

142 *K. Mahesh, G. Constantinescu, S. Apte, G. Iaccarino, F. Ham & P. Moin*

- SPADACCINI, L.J., OWEN, F.K. & BOWMAN, C.T. 1976 Influence of aerodynamic phenomena on pollutant formation in combustion. (Phase I. Gaseous fuels). *U.S. Environmental Protection Agency Rept. EPA-600/2-76-247a.*
- WALL, C., BOERSMA, B.J. & MOIN, P. 2000 An evaluation of the assumed beta probability density function subgrid-scale model for large eddy simulation of nonpremixed, turbulent combustion with heat release. *Phys. Fluids* **12**, 2522–2529.

Consistent boundary conditions for integrated LES/RANS simulations: LES inflow conditions

By J. U. Schlüter

1. Motivation

Currently, a wide variety of flow phenomena are addressed with numerical simulations. Many flow solvers are optimized to simulate a limited spectrum of flow effects effectively, such as single parts of a flow system, but are either inadequate or too expensive to be applied to a very complex problem.

As an example, the flow through a gas turbine can be considered. In the compressor and the turbine section, the flow solver has to be able to handle the moving blades, model the wall turbulence, and predict the pressure and density distribution properly. This can be done by a flow solver based on the Reynolds-Averaged Navier-Stokes (RANS) approach. On the other hand, the flow in the combustion chamber is governed by large scale turbulence, chemical reactions, and the presence of fuel spray. Experience shows that these phenomena require an unsteady approach (Veynante and Poinsot, 1996). Hence, the use of a Large Eddy Simulation (LES) flow solver is desirable.

While many design problems of a single flow passage can be addressed by separate computations, only the simultaneous computation of all parts can guarantee the proper prediction of multi-component phenomena, such as compressor/combustor instability and combustor/turbine hot-streak migration. Therefore, a promising strategy to perform full aero-thermal simulations of gas-turbine engines is the use of a RANS flow solver for the compressor sections, an LES flow solver for the combustor, and again a RANS flow solver for the turbine section (figure 1).

2. Interface

The simultaneous computation of the flow in all parts of a gas turbine with different flow solvers requires an exchange of information at the interfaces of the computational domains of each part. Previous work has established algorithms, which ensure, that two or more simultaneously running flow solvers are able to exchange the information at the interfaces efficiently (Shankaran *et al.*, 2001, Schlüter *et al.*, 2002).

The necessity of information exchange in the flow direction from the upstream to the downstream flow solver is self-explanatory: the flow in a passage is strongly dependent on mass flux, velocity vectors, and temperature at the inlet of the domain. However, since the Navier-Stokes equations are elliptic in subsonic flows, the downstream flow conditions can have a substantial influence on the upstream flow development. This can easily be imagined by considering that, for instance, a flow blockage in the turbine section of the gas turbine can determine and even stop the mass flow rate through the entire engine. This means that the information exchange at each interface has to go in both, downstream *and* upstream, directions.

Considering an LES flow solver computing the flow in the combustor, information on the flow field has to be provided to the RANS flow solver computing the turbine as

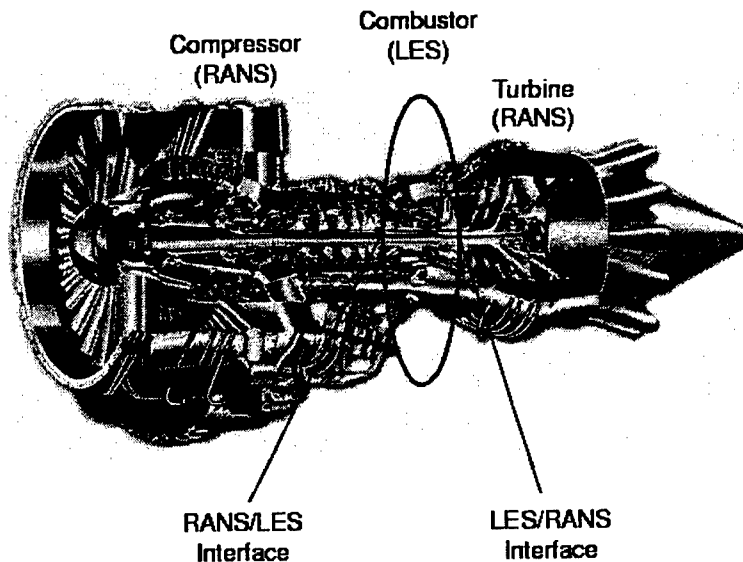
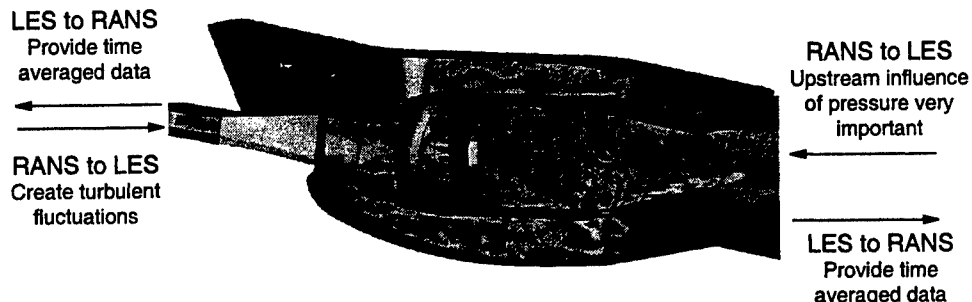


FIGURE 1. Gas turbine engine

FIGURE 2. Gas turbine combustor with interfaces. (LES of combustor from Mahesh *et al.*, 2001)

well as to the RANS flow solver computing the compressor, while at the same time, the LES solver has to obtain flow information from both RANS flow solvers (figure 2). The coupling can be done using overlapping computational domains for the LES and RANS simulations. For the example of the compressor/combustor interface this would imply that inflow conditions for LES will be determined from the RANS solution at the beginning of the overlap region, and correspondingly the outflow conditions for RANS are determined from the LES solution at the end of the overlap region.

However, the different mathematical approaches of the different flow solvers make the coupling of the flow solvers challenging. Since LES resolves large-scale turbulence in space and time, the time step between two iterations is relatively small. RANS flow solvers average all turbulent motions over time and predict ensemble averages of the flow. Even when a so-called unsteady RANS approach is used, the time step between two ensemble-averages of the RANS flow solver is usually larger by several orders of magnitude than that for an LES flow solver.

The specification of boundary conditions for RANS from LES data is relatively straight-

forward. The LES data can be averaged over time and used as boundary condition for the RANS solver.

Since LES computations have shown to be sensitive to outflow conditions (Moin, 1997, Pierce & Moin, 1998a), the adjustment of the LES solution near the outlet to the RANS solution of the downstream computation is of importance. Previous work investigated in detail LES outflow conditions (Schlüter and Pitsch, 2001, Schlüter *et al.*, 2002). A virtual body force is employed to drive the LES mean velocity field to the RANS solution in an overlap region. The turbulent quantities and the pressure field adjusts accordingly to the mean velocity field.

In the present study, the boundary conditions provided from an upstream RANS flow solver to a downstream LES flow solver is investigated. The inflow conditions have to be created such, that the time-averaged mean values of all computed quantities match the RANS solution at a given plane and meaningful turbulent fluctuations are added. LES computations of validation test cases are performed to assess the influence of the inflow boundary conditions.

3. Inflow Boundary conditions

The following section presents some possible LES inlet conditions, which are tested for use in integrated RANS-LES computations

3.1. Creation of database from auxiliary LES computation

The formulation of LES inflow conditions from time-averaged RANS data is similar to the definition of LES inflow conditions from experimental data, which is usually given in time-averaged form. An established procedure to create inflow boundary conditions is to perform an auxiliary LES computation prior to the actual LES of the desired domain (Pierce & Moin, 1998b). The auxiliary LES computation computes a periodic pipe and uses virtual body forces inside the domain to drive the flow to the desired velocity profiles. The time history of one plane of this computation is written into a database. The actual LES computation of the desired geometry then reads this database and uses its transient velocity field to define its own inlet velocity field.

This method is a well established procedure and shows good results in reproducing experiments (e.g. Duchamps & Pitsch, 2000, Schlüter, 2001). Hence, it will be used as a benchmark for all following proposed boundary conditions.

The advantage of this method is that the representation of the inlet turbulence is taken from a fully developed turbulent flow, which means all temporal and spatial correlations of the turbulent fluctuations are actual representations of eddies. The energy spectra in time and space have a natural energy distribution especially in the long wave range.

The creation of the database implies additional computational costs. However, using flow solver specialized to this task, the auxiliary computation usually takes less than an hour wall-clock time on a single processor, which is less than 1% of the computational costs for the LES of the actual geometries used in the current investigation.

The disadvantage of this procedure is that the mean velocity field at the inlet has to be known prior to the LES computation. In integrated RANS-LES computations the mean velocity field at the inlet of the changes in time, and hence, is unknown. This makes it impossible, to apply this procedure in this form for integrated RANS-LES computations.

3.2. No-fluctuations inflow conditions

The most simple way to define the inflow boundary conditions from RANS data is to neglect the turbulent fluctuations entirely. The velocity field at the inlet is then defined by the ensemble-averaged mean profiles of the RANS computation. This means, the incoming flow is laminar, but the shape of the velocity profiles is still that from a turbulent flow. It is easy to adapt this inflow condition during the LES computation to take variations of the ensemble-averaged flow field delivered by the RANS computation into account.

3.3. Random fluctuations

Early work in LES inlet boundary conditions report the usage of random fluctuations superposed to the mean velocity field at the inlet to simulate inflow turbulence. However, due to the lack of correlations in space and time of the fluctuations, these lack the energy in the long wave range. As a result of that, the fluctuations are usually in the high wave spectrum and hence, dissipated very quickly. The few tests in the current investigation which were made with this inlet condition agree with these findings. The flow laminarizes quickly behind the inlet and flow fields obtained with this inlet condition were indistinguishable from the flow fields obtained with the no-fluctuations inflow condition. Hence, they will not be shown here.

3.4. Mean velocity profiles with turbulent fluctuations from database

The method proposed here for integrated RANS-LES computations, uses the mean flow field from the RANS solution and adds meaningful turbulence from a database created by an auxiliary LES computation. This allows to vary the mean flow field during the LES computation in order to take temporal variations of the RANS solution into account. As for the inlet condition proposed in section 3.1, an auxiliary LES computation of a pipe flow is performed to define the turbulent fluctuations. The inlet condition is then defined as:

$$u_{i,\text{LES}}(t) = \underbrace{\bar{u}_{i,\text{RANS}}(\tau)}_I + \underbrace{(u_{i,\text{DB}}(t) - \bar{u}_{i,\text{DB}})}_{II} \cdot \underbrace{\frac{\sqrt{\overline{u_{(i)}^2}_{\text{RANS}}}(\tau)}{\sqrt{\overline{u_{(i)}^2}_{\text{DB}}}}}_{III} \quad (3.1)$$

with RANS denoting the solution delivered by the RANS computation and DB properties delivered by the database. The time-scale t is the time-scale used by the LES computation, and τ the time-scale used by the RANS computation. The RANS time-step $\Delta\tau$ is usually much larger than the LES time-step Δt , which means, that multiple LES inlet conditions are computed before the RANS solution is updated.

Term *II* of Eq. 3.1 computes the velocity fluctuation of the database. This turbulent fluctuation is scaled to the needed value with term *III*. Here, it is assumed that the value of $\overline{u_{(i)}^2}_{\text{RANS}}(\tau)$ is a known quantity. However, most RANS turbulence models do not compute the single components of the Reynolds-stress tensor, but more general turbulent quantities such as the turbulent kinetic energy k . In this case, the axial components of the Reynolds-tensor have to be approximated by:

$$\overline{u_{(i)}^2}_{\text{RANS}} = \frac{2}{3}k \quad (3.2)$$

Once the turbulent fluctuation is computed, it is then added to the time-averaged velocity field (term *I*) and a meaningful inlet velocity field is recovered.

The quality of the database can be measured in the necessity of term *III* to scale the

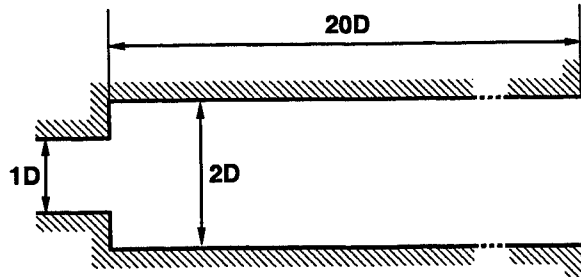


FIGURE 3. Geometry of test case

turbulent fluctuation. Since this scaling is linear, it is desirable, that the scaling factor is close to unity. Hence, in the creation of the database it is important to reproduce the expected inlet condition as closely as possible in order to keep scaling in the bounds of the validity of a linear extrapolation.

In the following test cases, inlet conditions computed with eqn. 3.1 are using databases with flow statistics strongly different from the desired values. This is solely to prove the robustness of the method and not advisable for the final application.

4. Validation test case

In order to validate the influence of different inflow boundary conditions, LES computations of a confined jet with and without swirl were performed. The considered geometry corresponds to the experiments of Dellenback (Dellenback, 1986, Dellenback *et al.*, 1988). The experiment investigates the flow at an axi-symmetric expansion (figure 3). Measurements upstream of the expansion allow a proper description of the inflow statistics and multiple measured velocity profiles downstream of the expansion give a good picture of the flow development.

Three different flow configurations are computed:

- (a) no swirl ($S = 0.0$) at a Reynolds-number $Re = 30,000$
- (b) strong swirl ($S = 0.6$), at $Re = 30,000$ and
- (c) weak swirl ($S = 0.3$), at $Re = 20,000$

with the swirl number S defined as:

$$S = \frac{1}{R} \frac{\int_0^R r^2 \bar{u}_x \bar{u}_\phi dr}{\int_0^R r \bar{u}_x^2 dr}, \quad (4.1)$$

where \bar{u}_x is the axial velocity component, \bar{u}_ϕ the azimuthal velocity component, and R the radius of the nozzle.

For the first two cases measurements are available and LES predictions can be compared with experimental data. For the last case, no measurements are available.

The computational meshes contain 1.58 million points (1.52 million cells) and are identical for all LES computations.

5. LES flow solver

In order to investigate the effects of different inflow boundary conditions, the various boundary conditions were implemented in an LES flow solver and tested. For this task, the LES flow solver developed at the Center for Turbulence Research (Pierce & Moin,

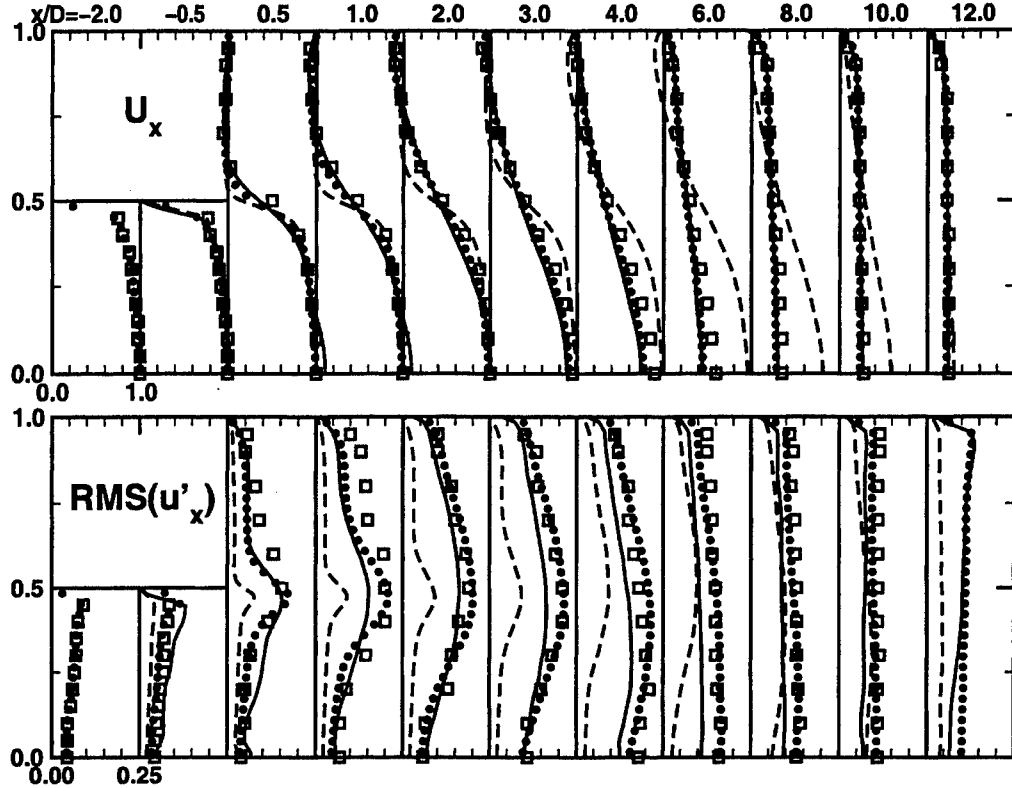


FIGURE 4. LES results for a confined jet. Squares: experiment; Dots: LES with inflow entirely from database (section 3.1); Dashed line: LES with no-fluctuations inflow (section 3.2); Solid line: LES with mean-flow + fluctuations from data-base (section 3.4)

1998a) has been used. The flow solver solves the filtered momentum equations with a low-Mach number assumption on an axisymmetric structured mesh. A second-order finite-volume scheme on a staggered grid is used (Akselvoll & Moin, 1996).

The subgrid stresses are approximated with an eddy-viscosity approach. The eddy viscosity is determined by a dynamic procedure (Germano *et al.*, 1991; Moin *et al.*, 1991).

6. Validation

6.1. Confined jet without swirl

The first test of the inlet boundary conditions is made for a confined jet without swirl. It is well known, that the spreading rate of the jet is dependent on the turbulence present in the jet flow.

Figure 4 shows the velocity fields obtained for this case. Experimental results are shown as square symbols. The two velocity profiles on the left are taken upstream of the step, and the leftmost profile defines the inlet conditions for the LES computations.

The first LES computation (black dots in figure 4) determines the inlet conditions entirely from a database (compare section 3.1). The database was created by an auxiliary computation with body forces driving the mean velocity field to the desired inlet velocity profile on the left. The usage of this boundary condition is possible in this case, since the time-averaged velocity field defining the inlet condition does not vary in time. It

can be seen, that this LES computation reproduces the experimental data well in mean values and turbulent fluctuations. The reattachment of the flow behind the step is well captured.

The second LES computation uses no-fluctuations inflow conditions (compare section 3.2). Since the initial turbulence in the flow does not reach the desired level near the step, the spreading rate of the jet is underestimated and the jet penetrates much further into the chamber (dashed lines in figure 4). The reattachment length is overestimated. As a result of the neglect of turbulence at the inlet, the axial turbulent fluctuations are underestimated throughout the domain.

The third LES computation uses the mean velocity field and turbulent fluctuations from a database (compare section 3.4). The database used is the database created for a swirling flow (first LES computation of the following chapter, section 6.2) and hence, is not adapted to this particular case. The correction of Eq. 3.1 is used to obtain the desired mean statistics. The results of this computation (solid lines) show a good agreement with the experiment and the first LES computation in the mean values. There are some discrepancies in turbulent fluctuations between this LES computation and the LES computation using a matching database due to the different description of turbulence at the inlet. However, both LES results are reasonably close to the experimental data.

This test case shows, that the proposed inflow condition (Eq. 3.1) is capable of reproducing the desired flow field, even when a low-quality database is used. The importance of turbulent fluctuations at the inlet is underlined with the failure of the no-fluctuations inlet condition to reproduce the flow field properly.

6.2. Confined jet with strong swirl

As a second test case a swirl flow at an expansion with a swirl number $S = 0.6$ is considered. Swirl flows with high swirl ($S > 0.25$) create central recirculation zones, and, as a result of that, flows with high shear are created which have a high level of turbulence production.

Figure 5 shows the results of this series of computations. The LES computation using a data-base with matching inlet velocity statistics (black dots) agrees well with the experiments (square symbols).

Surprisingly, the LES computation using the no-fluctuations inflow conditions (dashed lines) yields a comparable flow field and, despite some discrepancies, agrees reasonably well with the experiments. This can be explained with the fact, that the level of turbulence production is very high behind the expansion. The origin of the inner recirculation zone in highly swirling flows is fixed at the location of the expansion. This means, the zones of the turbulence production – the shear layers created by the recirculating fluid and the issuing jet – is well determined and independently of the inflow conditions. The turbulence level is then nearly entirely defined by the turbulence production behind the step.

The third LES computation uses a combined approach and the database from the previous test case of the flow *without* swirl (section 6.1). The particular shape of the axial velocity profile and the entire swirl component is imposed using Eq. 3.1. The LES computation recovers the LES solution using a matching database exactly.

This second test case shows, that situations exist, where the inlet turbulence plays a minor role, even when complex flow configurations are considered. In this special case, the high level of turbulence production inside the LES domain is dominant and its location and level are not determined by the inlet conditions.

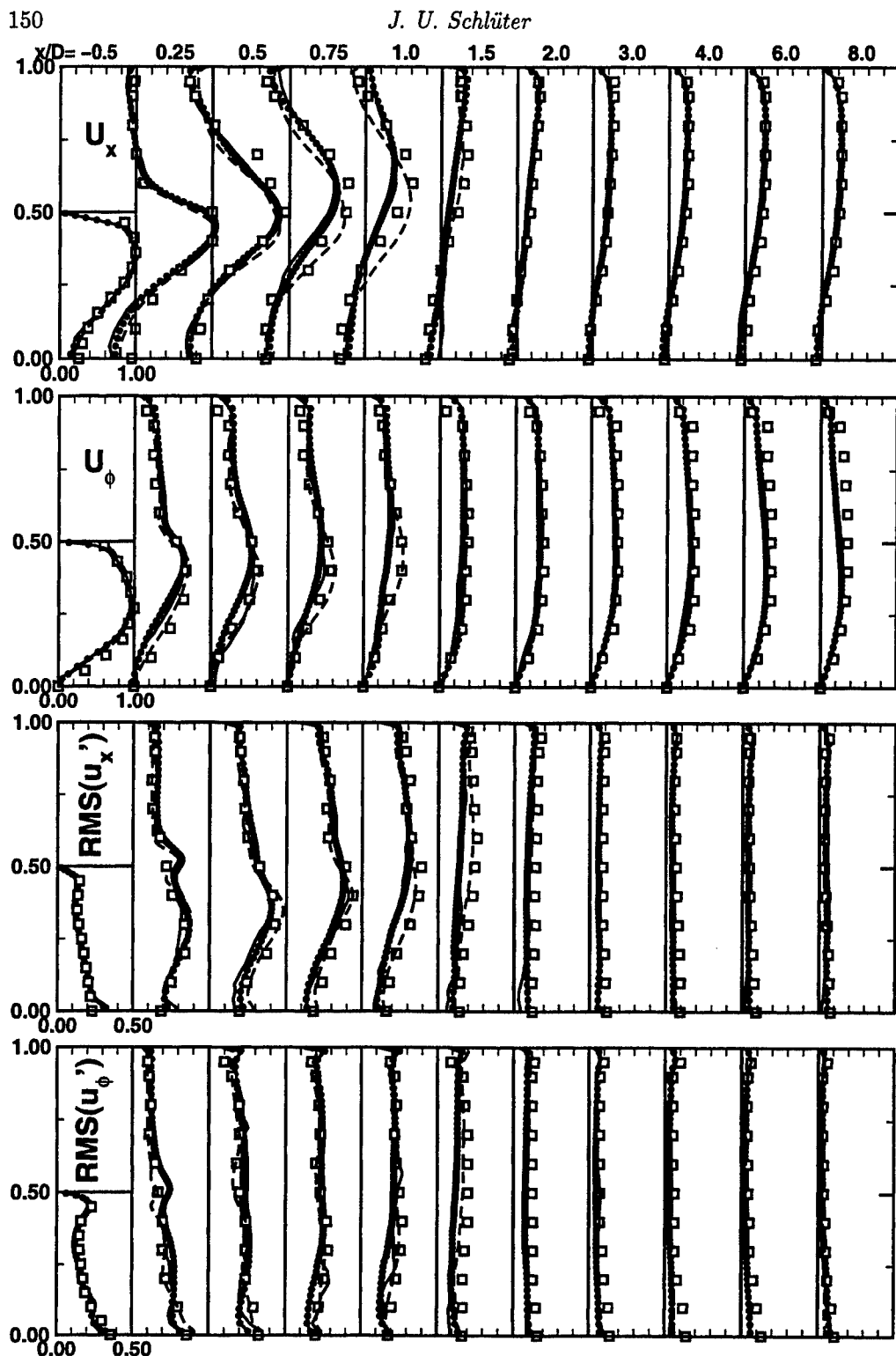


FIGURE 5. LES results for a jet with strong swirl ($S = 0.6$). Squares: experiment; Dots: LES with inflow entirely from database (section 3.1); Dashed line: LES with no-fluctuations inflow (section 3.2); Solid line: LES with mean-flow + fluctuations from data-base (section 3.4)

6.3. Confined jet with weak swirl

While in the previous case the strong swirl ensured a certain universality of the extent of the recirculation zone, weakly swirling flows are much more sensitive to inflow conditions (Gupta *et al.*, 1984). Since it is desirable for most flow applications, e.g. for gas turbine combustors, to keep the swirl number low in order to minimize the pressure drop over the swirler, these kinds of flows are of particular interest for industrial applications. Hence, a proper definition of LES inflow boundary conditions is crucial for the prediction of these flows and the optimization of swirler geometries.

The third test case considered in this investigation is a weakly swirling flow at a swirl number $S = 0.3$. The swirl number is just supercritical, meaning that an inner recirculation zone develops. Unfortunately, no experimental measurements are available for this case, but since the traditional method of generating inflow conditions by an auxiliary LES computation was very successful in the previous two cases, the results of this computation can be used as a reference.

Figure 6 shows the results of this series of LES computations. The LES computation with a database with matching mean flow statistics (black dots) shows the onset of the recirculation zone near the location of the expansion.

Using the no-fluctuations inflow condition (dashed lines), the location and extent of the recirculation zone changes dramatically. As a result of that, the mean flow field differs substantially from the previous LES computation. Due to the neglect of turbulence at the inlet, the turbulent fluctuations are underestimated throughout the near field of the expansion. As a result of the displacement of the zones of turbulence production, not even the shape of the profiles of turbulent fluctuations is reproduced.

Using Eq. 3.1 and the non-swirling database from the test case in section 6.1 (solid lines), all flow features are recovered. The origin and the extent of the recirculation zone are identical to the LES with the matching database. As a result of that, the turbulence production is also well represented and the prediction of turbulent fluctuations coincide.

This last test case shows most dramatically how the choice of LES inflow boundary conditions may alter the results of a computation. While the previous test case of the strongly swirling flow was remarkably robust to different inflow conditions, the present case shows that only a little change in flow parameters, the decrease of the swirl number, may result in flow configuration much more sensitive to inflow conditions.

7. Conclusions

The definition of LES inflow conditions from time-averaged statistical data has been subject of research for some time. The current investigation focuses on LES inflow boundary conditions for integrated RANS-LES computations, where the LES inflow conditions are prescribed by the solution of an upstream RANS solver. Here, the flow statistics, which have to be prescribed at the inlet of the LES domain, may vary in time.

A modification of the already widely used procedure, where an auxiliary LES computation creates a database for inflow conditions, was proposed. This inflow condition uses the unsteady mean velocity profiles at the inlet and superposes turbulent fluctuations from a database.

The proposed inflow condition was validated on three different flows. While one case, a strongly swirling flow, was surprisingly robust against different inflow conditions, the other two cases, a confined jet and a weakly swirling flow, underlined the necessity of a proper turbulence description at the inlet.

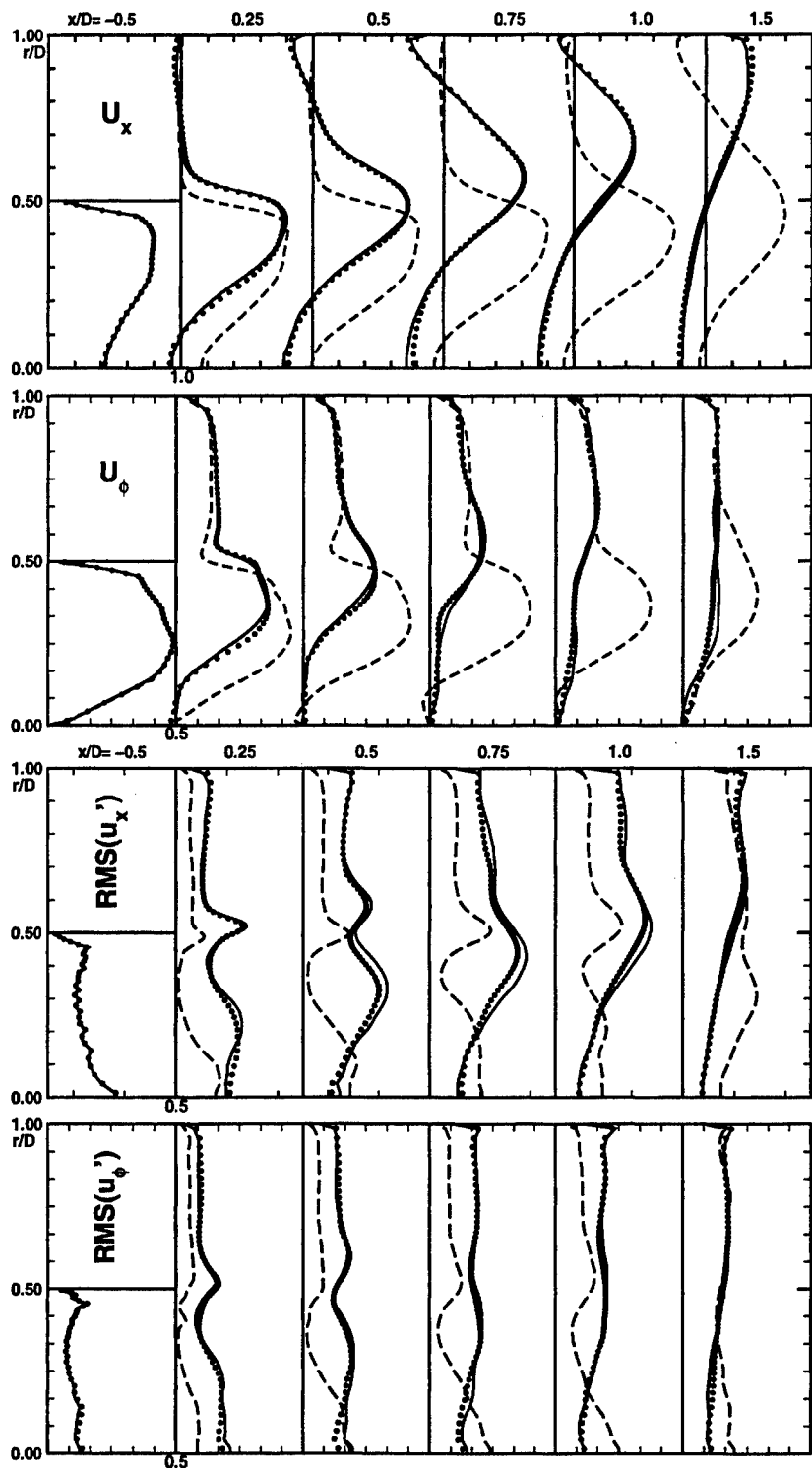


FIGURE 6. LES results for a jet with weak swirl ($S = 0.3$). Dots: LES with inflow entirely from database (section 3.1); Dashed line: LES with no-fluctuations inflow (section 3.2); Solid line: LES with mean-flow + fluctuations from data-base (section 3.4), no experimental data available

The inflow boundary condition proposed in the present study shows equivalent results to the commonly applied procedure using a database from an auxiliary LES computation. Its advantage over other methods is its flexibility to accommodate for time-dependent flow statistics at the LES inlet.

The definition of LES inflow boundary conditions for integrated RANS-LES computations is an important step towards integrated flow computations.

8. Acknowledgments

Support by the US Department of Energy under the ASCI program is gratefully acknowledged.

REFERENCES

- AKSELVOLL, K., & MOIN, P. 1996 Large-eddy simulation of turbulent confined coannular jets. *J. Fluid Mech.* **315**, 387–411.
- DELLENBACK, P. A., METZGER, D. E. & NEITZEL, G. P 1988 Measurements in turbulent swirling flow through an abrupt axisymmetric expansion. *AIAA J.* **26**, 669–681.
- DELLENBACK, P. A. 1986 *Heat transfer and velocity measurements in turbulent swirling flows through an abrupt axisymmetric expansion*. PhD thesis, Arizona State University.
- DUCHAMPS DE LAGENESTE, L. & PITSCHE, H. 2000 A level-set approach to large eddy simulation of premixed turbulent combustion. *Annual Research Briefs* Center for Turbulence Research, NASA Ames/Stanford Univ., 105–116.
- GERMANO, M., PIOMELLI, U., MOIN, P. & CABOT, W., 1991 A dynamic subgrid-scale eddy viscosity model. *Phys. Fluids A* **3**, 1760–1765.
- GUPTA, A. K., LILLEY, D. G. & SYRED, N. 1984 *Swirl Flows*. Abacus Press.
- MAHESH, K., CONSTANTINESCU, G., APTE, S., IACCARINO, G. & MOIN, P., 2001 Large-eddy simulation of gas turbine combustors *Annual Research Briefs*, Center for Turbulence Research, NASA Ames/Stanford Univ. 3–18.
- MOIN, P. 1997 Progress in large eddy simulation of turbulent flows. *AIAA Paper* 97-0749.
- MOIN, P., SQUIRES, K., CABOT, W. & LEE, S. 1991 A dynamic subgrid-scale model for compressible turbulence and scalar transport. *Phys. Fluids A* **(3)**, 2746–2757.
- PIERCE, C. D. & MOIN, P. 1998a Large eddy simulation of a confined coaxial jet with swirl and heat release. *AIAA Paper* 98-2892.
- PIERCE, C. D. & MOIN, P. 1998b Method for generating equilibrium swirling inflow conditions. *AIAA J.* **36**, 1325–1327.
- SCHLÜTER, J., 2001 Large-eddy simulations of combustion instability suppression by static turbulence control. *Annual Research Briefs* Center for Turbulence Research, NASA Ames/Stanford Univ. 119—130.
- SCHLÜTER, J., PITSCHE, H. 2001 Consistent boundary conditions for integrated LES/RANS simulations: LES outflow conditions. *Annual Research Briefs* Center for Turbulence Research, NASA Ames/Stanford Univ. 19–30.
- SCHLÜTER, J., SHANKARAN, S., KIM, S., PITSCHE, H., ALONSO, J. J. 2002 Integration

- of LES and RANS flow solvers: Interface validation. *Annual Research Briefs*, Center for Turbulence Research, NASA Ames/Stanford Univ.
- SCHLÜTER, J. U., PITSCHE, H., AND MOIN, P. 2002 Consistent boundary conditions for integrated LES/RANS simulations: LES outflow conditions. *AIAA paper* 2002-3121.
- SHANKARAN, S., LIOU, M.-F., LIU, N.-S., DAVIS, R., AND ALONSO, J. J. 2001 A multi-code-coupling interface for combustor/turbomachinery simulations. *AIAA paper* 2001-0974.
- VEYNANTE, D. AND POINSOT, T. 1996 Reynolds averaged and large eddy simulation modeling for turbulent combustion. In *New Tools in Turbulence Modelling*, Les éditions physiques. Springer, Berlin. pp. 105–140.

Integration of RANS and LES flow solvers: interface validation

By J. U. Schlüter, S. Shankaran, S. Kim, H. Pitsch AND J. J. Alonso

1. Introduction

The variety of flow problems encountered in complex flow systems - such as in aero-engine gas turbines - requires well adapted flow solvers for different parts of the system in order to predict the flow accurately and efficiently. Currently, many flow solvers are specialized to simulate one part of a flow system effectively, but are either inadequate or too expensive to be applied to a generic problem.

For the example of a gas turbine, in the compressor and the turbine section, the flow solver has to be able to handle the moving blades, model the wall turbulence, and predict the pressure and density distribution properly. This can be done by a flow solver based on the Reynolds-Averaged Navier-Stokes (RANS) approach. On the other hand, the flow in the combustion chamber is governed by large scale turbulence, chemical reactions, and the presence of fuel spray. Experience shows that predictions of such phenomena are strongly improved by the use of Large Eddy Simulations (LES).

While many design problems of a single flow passage can be addressed by separate computations, only the simultaneous computation of all parts can guarantee the proper prediction of multi-component phenomena, such as compressor/combustor instability and combustor/turbine hot-streak migration. Therefore, a promising strategy to perform full aero-thermal simulations of gas-turbine engines is the use of a RANS flow solver for the compressor sections, an LES flow solver for the combustor, and again a RANS flow solver for the turbine section (figure 1).

While it would be possible to use one single flow solver, which switches between different mathematical approaches depending on the flow section, the current choice is to use several separate flow solvers. The reason for that is, that currently a wide variety of validated flow solvers are in use. Merging two or more computer programs into a single code or extending a code to different modeling approaches is tiresome at best and prone to errors.

The usage of entirely separate flow solvers allows, for a given flow problem, to choose the best combination of a variety of existing flow solvers, which have been developed, optimized, and validated separately. Once these have been equipped with a generic interface, it is possible to continue the development of the flow solvers separately without compromising compatibility. The implementation of this interface into several flow solvers allows their modular exchange, which results in a high degree of flexibility.

The implementation of an interface for the simultaneous flow computation using separate flow solvers faces a number of challenges. These can be described as follows:

(a) *Establishing a contact between the flow solvers for information exchange:* The first obvious obstacle is to establish a real-time connection between two or more simultaneous running flow solvers over which the information can be exchanged. Most flow solvers are already parallelized using MPI (Message Passing Interface). Here, MPI will be used for peer-to-peer message passing as well.

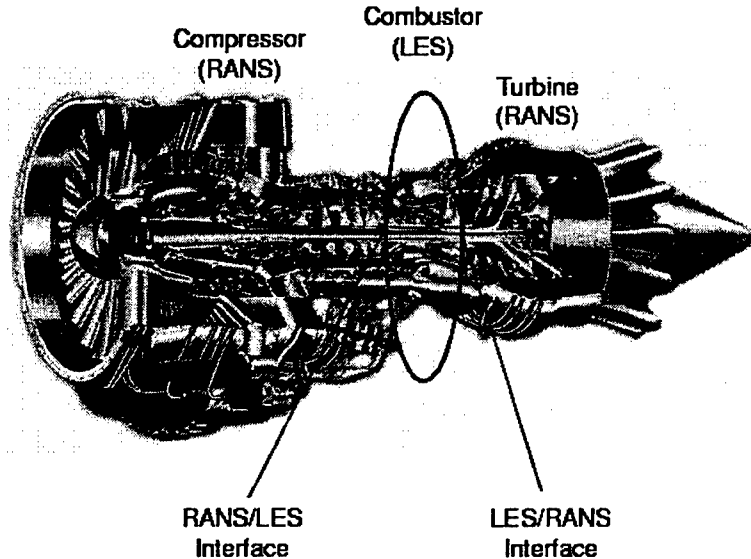


FIGURE 1. Gas turbine engine

(b) *Ensuring that each flow solver obtains the information needed on the boundaries:* A general procedure has to be defined, which ensures, that each flow solver knows, which information has to be sent where.

(c) *Processing of the obtained information to boundary conditions:* Finally, the physical problem of defining meaningful boundary conditions from the obtained data has to be addressed. This can be especially challenging, when two different modeling approaches, such as LES and RANS, are used.

The current investigation deals with these tasks and describes a successful coupling of RANS and LES flow solvers.

2. Peer-to-peer message passing

The message passing between two separate flow solvers (peer-to-peer message passing) is very similar to the information exchange between processors of a parallel computation. Many flow solvers are parallelized and use MPI for process-to-process message passing. MPI can be used for communication between different flow solvers as well.

Before establishing a contact between two flow solvers, it has to be ensured, that the commands for the internal message passing due to the parallelization of the two codes do not interfere with each other. With MPI it is possible to direct the range of the message passing with communicators. The most commonly used communicator of MPI is the standard communicator `MPI_COMM_WORLD` which includes all processors of all codes. Using this communicator for internal message passing will inevitably result in confusion between the two codes. Hence, each code has to create its own local communicator (*intra-communicator*) to encapsulate the internal message passing. All codes have to use their own intra-communicator for all MPI commands concerning the parallelization of the code instead of `MPI_COMM_WORLD`.

In the next step, a communicator is created for the peer-to-peer message passing (*inter-communicator*). Say, a case with three flow solvers is to be run with a first RANS code using three processors (ranks 0, 1, and 2, local root process 0), a LES code using four

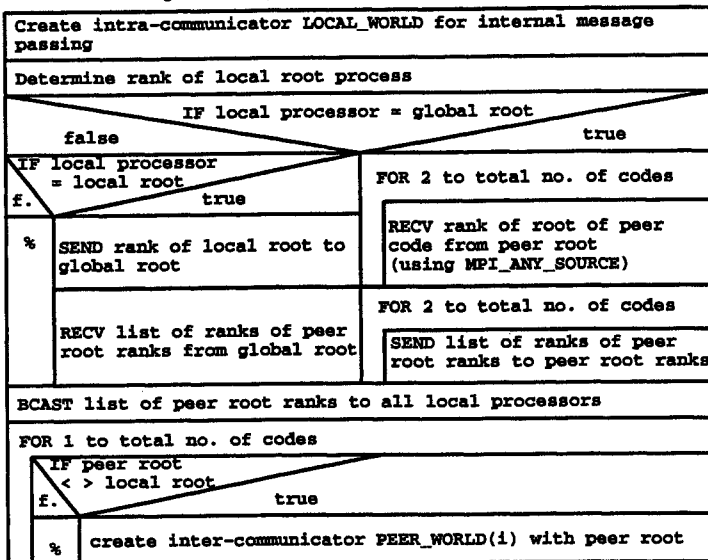


FIGURE 2. Structure Chart for exchange of root ranks needed for creation of inter-communicators

processors (ranks 3, 4, 5, and 6, local root process 3) and a second RANS code using two processors (ranks 7 and 8, local root process 7). In order to create the inter-communicator, it is necessary, that every processor knows the rank of the root processes of the other codes. A global root process is appointed (rank 0) which collects the ranks of the root processes of all codes (here: ranks 0, 3 and 7), compiles them into a list and sends them back to the local root processes. A structure chart for this procedure is shown in figure 2. Since there is no inter-communicator available yet, this communication has to be done with the standard communicator MPI_COMM_WORLD. With the knowledge of the ranks of all root processes it is possible to create the inter-communicators.

3. Handshake and communication procedures

3.1. Handshake

Efficient parallelizing of a flow solver seeks to limit the information exchange between parallel processes to a minimum, since the information exchange requires a large amount of time compared to the actual computation. Similarly, it is favorable to minimize the communication between several parallel running flow solvers. Since the flow solvers have to exchange flow information rather often, either after each iteration or after a chosen time-step, the aim is to minimize the communication efforts by an initial handshake, which optimizes the communication during the actual flow computation.

The most simple way to organize the information exchange would be to let only the root processes communicate. However, this would mean that prior to the peer-to-peer communication the root processes would have to gather the flow information to hand over from their own processes, and after the peer-to-peer communication would have to broadcast the obtained information back to their processes. The here reported solution avoids this additional communication by direct communication of the neighboring processors on the interface.

The initial handshake routine establishes the direct communication (figure 3). First, for

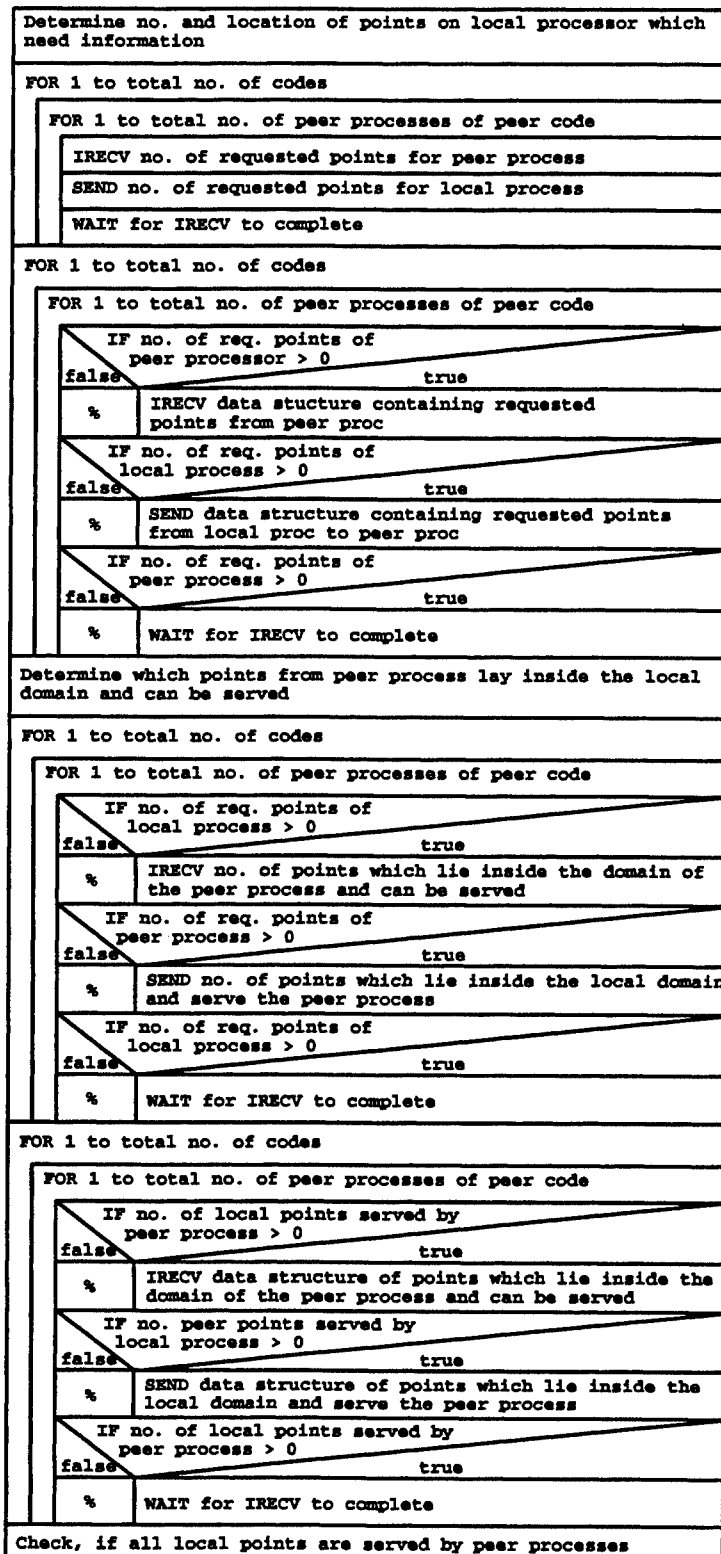


FIGURE 3. Structure Chart for the initial handshake to establish direct communication between interface processors.

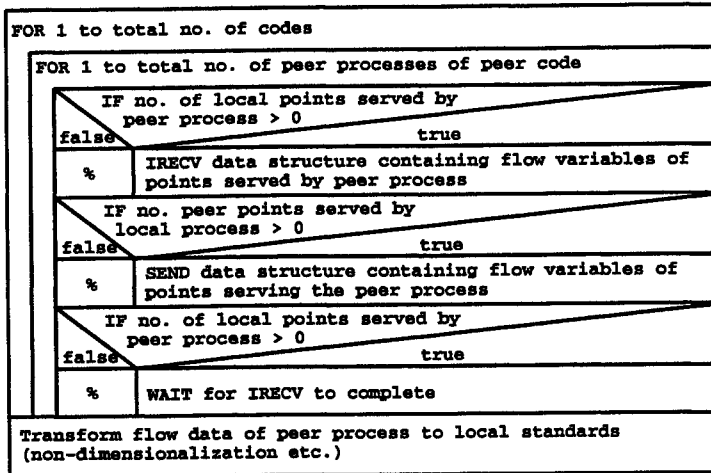


FIGURE 4. Structure Chart for the communication of flow data between iterations.

each code each processor has to identify all the points, which need flow information from the peers to define its interface boundary condition. The location of each of these points has to be stored in a data structure containing three integers and three double precisions. The three integers are an '*ip*' number, which determines what kind of flow variables are requested for this point, an '*id*' number, which contains a unique identification number for each point, and a '*flow solver*' number denoting the flow solver requesting this point. The three real numbers contain the *x*, *y*, *z*-coordinates of the point in Cartesian coordinates using metric dimensions.

The handshake takes place in four steps. First, each processor communicates the number of points in its own domain requesting flow data to each processor of a peer code. This allows each code to dynamically allocate arrays to store received information. In the second step each processor receives a data package containing the location of the requested points from each peer processor that request a non-zero number of points.

In an intermediate step, each processor identifies, whether a requested point lies within its own domain and can be served. During the identification, the interpolation schemes required to obtain the data for this point are also being determined and stored for later use.

In the third communication step each processor communicates to all peer-processes requesting data the number of points found. This allows again to dynamically allocate arrays for the following fourth step. In the fourth communication step, each processor sends out an array to each peer processor it can serve. The array consists of two integers containing *ip* and *id* of the point. Finally, each processor determines whether all of its requested point can be served by peer processors.

3.2. Communication

The communication of flow data between iterations is rather straight-forward once the handshake is completed (figure 4). Since it is known to every processor what kind of data has to be provided to which peer processor, and from which peer processor flow data can be expected, the data packages can be sent directly without going through the root process.

Each processor has to compile the data to be sent into a data structure. This data structure may vary between different flow solvers and has to be defined beforehand.

However, as a standard data structure a set of 7 variables has been established. These variables contain $\rho, \rho u, \rho v, \rho w, \rho E, k$, and ν_t in this order, with ρ being the density, u, v, w the velocity components in $x-, y-, z-$ direction, respectively, E the total Energy, k the turbulent kinetic energy, and ν_t the eddy viscosity. This set of variables gives the freedom to choose between several RANS turbulence models without changing the interface routines, e.g. boundary conditions can be defined from this set of data for $k-\epsilon$ and $k-\omega$ turbulence models likewise. More sophisticated data sets are possible steered by the data structure sent in the handshake routine.

4. Boundary conditions

4.1. LES Boundary conditions

The formulation of unsteady LES boundary conditions from ensemble-averaged RANS data is one of the biggest challenges in the coupling of two flow solvers based on such different mathematical approaches like LES and RANS. Unsteady LES boundary conditions have to be generated which fulfill the statistical properties of the time-averaged solution delivered by the RANS flow solver. Even if an unsteady RANS computation is assumed, the time-step of the unsteady RANS computation is usually larger than the LES time-step by several orders of magnitude. The LES boundary conditions then have to correspond to the ensemble-averages delivered by the RANS computation.

4.1.1. LES inflow boundary conditions

Specifying inflow conditions for LES from upstream RANS data is a similar problem as specifying LES inflow conditions from experimental data, which is usually given in time-averaged form, and has therefore been investigated in some detail in the past. A method that has been successfully applied is to generate a time-dependent database for the inflow velocity fields by performing a separate LES simulation, in which virtual body forces are applied to achieve the required time-averaged solution (Pierce & Moin, 1998b). However, since unsteady RANS flow solvers may deliver *unsteady* ensemble-averaged velocity profiles, a generation of such a data-base is impossible, since the mean velocity field at the inlet is unknown.

The here proposed LES inlet conditions use a data-base created by a separate LES computation and modifies then its statistical properties in order to match the RANS solution:

$$u_{i,\text{LES}}(t) = \underbrace{\bar{u}_{i,\text{RANS}}}_I + \underbrace{(u_{i,\text{DB}}(t) - \bar{u}_{i,\text{DB}})}_{II} \cdot \underbrace{\frac{\sqrt{u'^2_{(i),\text{RANS}}}}{\sqrt{u'^2_{(i),\text{DB}}}}}_{III} \quad (4.1)$$

with RANS denoting the solution delivered by the RANS computation and DB properties delivered by the database. Term *II* computes the velocity fluctuation of the database, while term *III* scales the fluctuation to the actual value needed. When added to term *I* a meaningful unsteady inlet condition is recovered. In order to keep corrections small, the generated inflow data-base should have statistical properties close to the actual prediction by the RANS flow solver, although it has been shown, that even very generic data-bases are able to recover meaningful LES inflow conditions (Schlüter, 2002).

4.1.2. LES outflow boundary conditions

In order to take upstream effects of the downstream flow development into account, LES outflow conditions have to be defined that can impose mean flow properties on the unsteady LES solution matching the statistical properties delivered by a downstream RANS computation. A method, that has been used in the past, employs virtual body forces to drive the mean velocity field of the LES solution to a RANS target velocity field (Schlüter and Pitsch, 2001, Schlüter *et al.*, 2002).

$$F_i(\mathbf{x}) = \frac{1}{\tau_F} (\bar{u}_{i,RANS}(\mathbf{x}) - \bar{u}_{i,LES}(\mathbf{x})), \quad (4.2)$$

with $\bar{u}_{i,RANS}$ being the solution of the RANS flow solver computed in an overlap region between LES and RANS domain, and $\bar{u}_{i,LES}$ is a time-average of the LES solution over a trailing time-window. This body force ensures that the velocity profiles at the outlet of the LES domain fulfill the same statistical properties as the velocity profiles in an overlap region computed by a RANS simulation downstream. This makes it possible to take upstream effects of the downstream flow into account.

4.2. RANS boundary conditions

The specification of RANS boundary conditions from LES data is essentially straightforward. The unsteady LES flow data is time-averaged over the time-step applied by the RANS flow solver and can be employed directly as a boundary condition.

In the current study, the compressible formulation of the RANS flow solver and the quasi-incompressible low-Mach-number formulation of the LES code posed a challenge. While the RANS code allows for acoustic waves to propagate in the limits of the RANS formulation and its turbulence models, the density field of the LES solution is entirely defined by chemical reactions and not by acoustics. This leads to the necessity of the RANS inflow and outflow condition to be able to fluctuate the density field at the boundaries in order to let acoustic waves leave the domain.

Currently, the mass-flux vector at every point of the inlet is being specified corresponding to the value delivered by the LES computation. This means ρu , ρv , ρw , (and T) are imposed at the boundaries. This allows the density ρ to fluctuate to account for the passing of acoustic waves. The velocity components u, v, w are adjusted accordingly in order to conserve the mass-flux. Variations of ρ are in the order of < 2%.

Other boundary conditions are possible, especially Navier-Stokes characteristic boundary conditions (Poinsot and Lele, 1992) which have a more accurate treatment of acoustic waves.

5. Validation of the interface

In order to validate the interface and the boundary conditions, a LES flow solver and a RANS flow solver were equipped with the interface and the newly developed boundary conditions. Integrated flow computations were performed in a LES-LES and LES-RANS environment.

5.1. The LES flow solver

The LES flow solver chosen for this work, is a code developed at the Center for Turbulence Research at Stanford by Pierce and Moin (Pierce & Moin, 1998a). The flow solver solves the filtered momentum equations with a low-Mach number assumption on an axi-symmetric structured single-block mesh. A second-order finite-volume scheme on

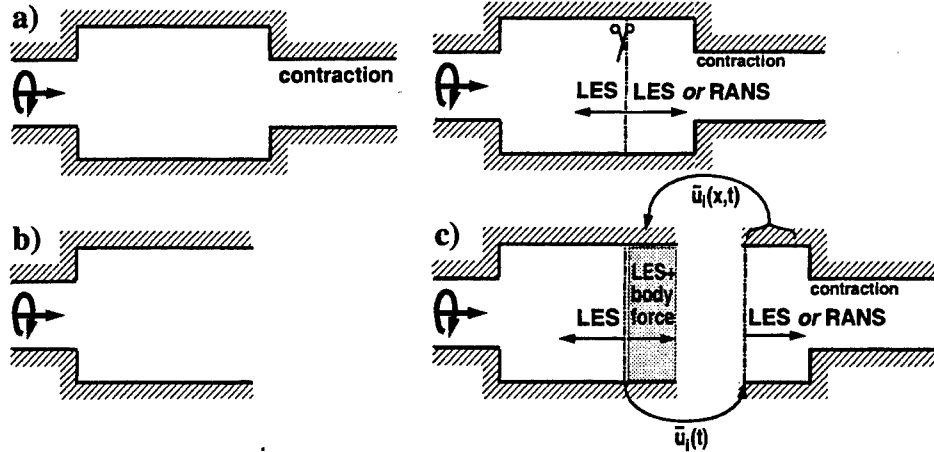


FIGURE 5. Geometry for integrated LES/RANS computations: a) full geometry, b) reduced LES domain, c) schematic splitting of domain to two computational domains

a staggered grid is used (Akselvoll & Moin, 1996). The subgrid stresses are approximated with an eddy-viscosity approach, where the eddy viscosity is determined by a dynamic procedure (Germano *et al*, 1991, Moin *et al*, 1991).

5.2. The RANS flow Solver

The RANS flow solver used for this investigation is the TFLO code developed at the Aerospace Computing Lab (ACL) at Stanford. The flow solver computes the unsteady Reynolds Averaged Navier-Stokes equations using a cell-centered discretization on arbitrary multi-block meshes (Yao *et al*, 2000).

The solution procedure is based on efficient explicit modified Runge-Kutta methods with several convergence acceleration techniques such as multi-grid, residual averaging, and local time-stepping. These techniques, multi-grid in particular, provide excellent numerical convergence and fast solution turnaround. Turbulent viscosity is computed from a $k - \omega$ two-equation turbulence model. The dual-time stepping technique (Jameson, 1991, Alonso *et al*, 1995, Belov *et al*, 1996) is used for time-accurate simulations that account for the relative motion of moving parts as well as other sources of flow unsteadiness.

5.3. Numerical experiment: swirl flow

The computation of a swirl flow presents a challenging test-case in order to validate the interface and the boundary conditions, due to the complexity of the flow and its sensitivity to inflow and outflow parameters. Yet, this test case is simple enough to perform a LES computation of the entire domain in order to obtain an 'exact' solution, which serves as a reference solution to assess the accuracy of integrated computations.

A swirl flow at an expansion with a subsequent contraction three diameter D downstream of the expansion is considered (figure 5a). Inlet velocity profiles are taken from an actual experiment in a similar geometry (Dellenback *et al*, 1988). The swirl number of the flow is $S = 0.3$, which is just supercritical, meaning that vortex breakdown takes place and a recirculation zone develops. The extension and strength of this recirculation zone is strongly influenced by the presence of the downstream contraction.

In a first computation the entire domain is computed by LES. A first computation of this study computed the entire domain. All subsequent computations assume, that this domain is to be computed by two or more separate flow solvers. The geometry is

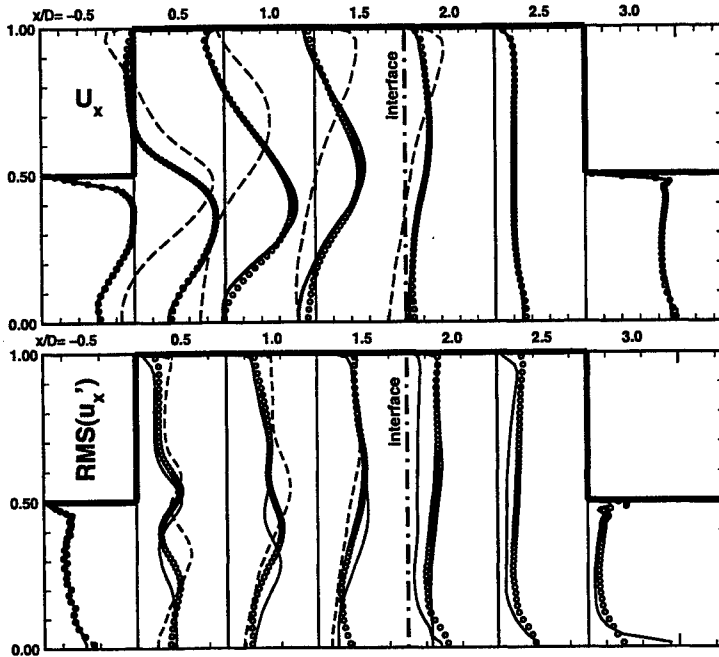


FIGURE 6. Integrated LES/LES computations. Velocity components for different downstream positions. circles: LES of full geometry (figure 5a), dashed line: LES of expansion (figure 5b), solid line: integrated LES-RANS computation (figure 5c)

split in two computational domains with a short overlap region. The expansion is to be computed with the LES code, while the contraction is computed either by a second instance of the LES code or by the RANS code (figure 5c). If the coupling of the two codes is done appropriately, then this coupled simulation should recover the solution of the LES performed for the entire domain.

5.4. Integrated LES/LES computations

The first test for the interface and the LES boundary conditions is to use a LES flow solver for the second part of the domain. In these integrated LES/LES computations the same LES flow solver is hence used twice. The time-interval can be chosen arbitrarily when communication between the two instances of the flow solver takes place. Each LES computation can chose a time-step to advance the solution between two iterations of its own, only limited by the CFL condition in its own domain. After several iterations, after both LES computations have computed the same physical time-span, an exchange of time-averaged quantities, the mean velocities $\bar{u}, \bar{v}, \bar{w}$ and the turbulent kinetic energy k , takes place. While it would have been possible in the case of two LES computations to exchange more information, especially about turbulent quantities, it was aim to prove the validity of the LES boundary conditions from section 4.1.

Figure 6 shows the velocity profiles for three different computations. The velocity profiles denoted by the circles represent the LES computation of the entire domain (figure 5a) and hence, the target for the integrated computations.

To show the importance of integrated computations for this case, the dashed lines show the velocity profiles of a LES computation of the expansion, without the computation of the contraction by a second flow solver (figure 5b). It can be seen, that the obtained

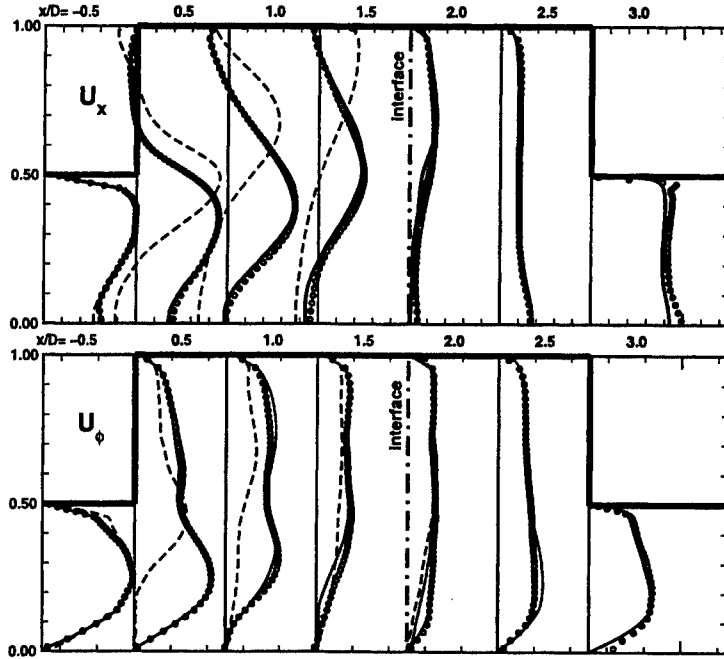


FIGURE 7. Integrated LES/RANS computations. Velocity components for different downstream positions. circles: LES of full geometry (figure 5a), dashed line: LES of expansion (figure 5b), solid line: integrated LES-RANS computation (figure 5c)

velocity field differs substantially from the first simulation, and hence, the influence of the downstream contraction can not be neglected.

The solid lines in figure 6 show the integrated LES/LES-computation using two LES solvers for the two domains (figure 5c). The location of the interface is denoted with a dot-dashed line, meaning, that the velocity profiles on the left-hand side of the interface are computed with the first LES computation and the profiles on the right hand-side from the second LES. The LES computation of the subsequent contraction delivers a mean flow field which is used to correct the outflow conditions of the upstream LES. As a result, the velocity profiles of the integrated LES/LES-computation tend towards the velocity profiles of the LES of the entire domain. The inlet conditions of the second LES are defined from the mean velocity profiles obtained from the upstream LES.

In the integrated LES/LES computation, the velocity fluctuations u'^2, v'^2, w'^2 are handed over as the turbulent kinetic energy $k = 0.5 \cdot (u'^2 + v'^2 + w'^2)$, and reconstructed as $u_i'^2 = 2k/3$. This explains a mismatch in the axial velocity fluctuations at the interface. Although it would have been possible in integrated LES/LES computations to hand over the entire Reynolds-stress tensor, the usage of the RANS standard data set allows better comparison with the following computations.

5.5. Integrated LES/RANS computations

The final step in assessing integrated flow computations is to perform a simulation, where the second LES flow solver is replaced by a RANS flow solver. The swirl flow at the expansion is computed by the LES flow solver while the contraction is computed with the RANS flow solver TFLO.

Figure 7 shows the mean velocity profiles obtained by an integrated LES-RANS com-

putation. The circles show the LES of the entire domain, and, for comparison, the dashed line represents the LES solution of the swirl flow without the computation of the contraction.

The integrated LES-RANS computation (solid lines) essentially matches the velocity profiles from the LES of the entire domain. This means, that integrated LES-RANS computations are able to successfully predict complex flows such as the swirl flow considered here.

The time advantage of integrated LES-RANS computations is strongly dependent on the chosen RANS time-step. For the present case, the RANS time step was chosen approximately $2 \cdot 10^3$ times longer than the LES time-step limited by the CFL condition. This resulted in a decrease of computational costs by a factor of ≈ 2 .

6. Conclusions

The increasing complexity of flow problems investigated with numerical methods calls for the integration of existing flow solvers, where each of the flow solvers is optimized to address a particular problem. In this study, an interface was developed and implemented that enables two or more flow solvers to run simultaneously and to exchange data at the overlapping boundaries.

The interface was tested on a swirl flow at an expansion with a subsequent contraction, which has been split into two parts, the upstream expansion and the downstream contraction part. Each of these is computed by a separate flow solver in a fully coupled simulation. The integrated LES-LES and LES-RANS computations have demonstrated to yield the same flow prediction as a LES computation of the entire domain.

The LES boundary conditions developed in earlier work were put to a real-time test. RANS boundary conditions were adapted to accommodate the different approaches (compressible/low-Mach number) on both sides of the interface.

The computation reported in this work proves the feasibility, accuracy and efficiency of integrated LES/RANS computations. LES and RANS flow solvers were successfully combined in order to improve the efficiency of the flow prediction without compromising the accuracy. This is an important step towards the application of this concept to industrial applications.

7. Acknowledgments

We gratefully acknowledge support by the US Department of Energy under the ASCI program.

REFERENCES

- AKSELVOLL, K., & MOIN, P. 1996 Large-eddy simulation of turbulent confined coannular jets. *J. Fluid Mech.* **315**, 387–411.
- J. J. ALONSO, L. MARTINELLI, AND A. JAMESON 1995 Multigrid unsteady Navier-Stokes calculations with aeroelastic applications. *AIAA Paper* 95-0048.
- A. BELOV, L. MARTINELLI, AND A. JAMESON 1996 Three-dimensional computations of time-dependent incompressible flows with an implicit multigrid-driven algorithm on parallel computers. In *Proc. 15th Int. Conf. on Num. Methods in Fluid Dyn.*
- DELLENBACK, P. A., METZGER, D. E. & NEITZEL, G. P 1988 Measurements in

turbulent swirling flow through an abrupt axisymmetric expansion. *AIAA J.* **26**, 669-681.

GERMANO, M., PIOMELLI, U., MOIN, P. & CABOT, W., 1991 A dynamic subgrid-scale eddy viscosity model. *Phys. Fluids A* (3), 1760-1765.

JAMESON, A. 1991 Time dependent calculations using multigrid, with applications to unsteady flows past airfoils and wings. *AIAA paper* 91-1596.

MOIN, P., SQUIRES, K., CABOT, W. & LEE, S. 1991 A dynamic subgrid-scale model for compressible turbulence and scalar transport. *Phys. Fluids A* (3), 2746-2757.

PIERCE, C. D. & MOIN, P. 1998a Large eddy simulation of a confined coaxial jet with swirl and heat release. *AIAA Paper* 98-2892.

PIERCE, C. D. & MOIN, P. 1998b Method for generating equilibrium swirling inflow conditions. *AIAA J.* **36**, 1325-1327.

T. J. POINSOT AND S. K. LELE 1992 Boundary conditions for direct simulations of compressible viscous reacting flows. *J. Comp. Phys.* (101):104-129

J. SCHLÜTER AND H. PITSCH 2001 Consistent boundary conditions for integrated LES/RANS simulations: LES outflow conditions. *Annual Research Briefs* Center for Turbulence Research, NASA Ames/Stanford Univ., 19-30.

J. U. SCHLÜTER, H. PITSCH, AND P. MOIN 2002 Consistent boundary conditions for integrated LES/RANS simulations: LES outflow conditions. *AIAA paper* 2002-3121

J. SCHLÜTER 2002 Consistent boundary conditions for integrated LES/RANS simulations: LES inflow conditions. *Annual Research Briefs* Center for Turbulence Research, NASA Ames/Stanford Univ.

S. SHANKARAN, M.-F. LIOU, N.-S. LIU, AND R. DAVIS ANF J. J. ALONSO 2001 A multi-code-coupling interface for combustor/turbomachinery simulations. *AIAA paper* 2001-0974.

D. VEYNANTE AND T. POINSOT 1996 Reynolds averaged and large eddy simulation modeling for turbulent combustion. In *New Tools in Turbulence Modelling*, Les edition physique. Springer, pp 105-140.

J. YAO, A. JAMESON, J. J. ALONSO, AND F. LIU 2000 Development and validation of a massively parallel flow solver for turbomachinery flows. *AIAA paper* 2000-0882.

Grid-independent large-eddy simulation in turbulent channel flow using three-dimensional explicit filtering

By Jessica Gullbrand

1. Motivation and objectives

In traditional large-eddy simulation (LES) solution methods, the computational grid and discretization operators are considered as “implicit” filtering of the Navier-Stokes equations. This LES procedure divides the turbulent flow field into resolved and unresolved scales, where the unresolved scales must be modeled.

When explicit filtering is used in LES, the filtering procedure of the governing equations is separated from the grid and discretization operations. This separation now divides the flow field into resolved filtered scale (RFS) motions, and subfilter-scale (SFS) motions. The SFS is itself divided into a resolved part (RSFS) and an unresolved part (USFS) (Zhou, Brasseur & Juneja 2001): see figure 1. The RFS motion is obtained by solving the filtered Navier-Stokes equations. The RSFS motions can theoretically be reconstructed from the resolved field and occur due to the use of a smooth (in spectral space) filter function. The USFS motions consist of scales that are not resolved in the simulation and need to be modeled. The explicitly-filtered governing equations were recently studied by Carati, Winckelmans & Jeanmart (2001).

The smallest resolved scales are often used to model the turbulence-closure term in LES, and therefore it is of great importance to capture these scales to high accuracy. The accuracy of the LES solution can be increased by using high-order numerical schemes. High-order methods will increase the accuracy of the important large energy-containing scales, but the small scales will still be contaminated with truncation errors when using non-spectral methods. These errors can be reduced or eliminated by using explicit filtering in LES (Lund 1997). This can be achieved either by using a large ratio between the filter width and the cell size, or by using a higher-order method, then the ratio need not be so large. In recent *a priori* studies by Chow & Moin (2003), a minimum ratio of filter width to cell size was determined to prevent the numerical error from becoming larger than the contribution from the turbulence closure term. They concluded that a fourth-order scheme should be used with a filter width of at least twice the cell size, and for a second-order scheme the filter width should be at least four times the cell size.

Using explicit filtering and high-order numerical schemes requires the filter functions to be commutative to at least the same order as the numerical scheme. The differentiation and the filtering operations must commute, to ensure that the filtered Navier-Stokes equations have the same structure as the unfiltered equations. In general, the operations do not commute when a variable filter width is used, as is needed in inhomogeneous flow fields. Ghosal & Moin (1995) showed that the commutation error is of the same order as the contribution from the turbulence closure term, $O(\Delta^2)$, where Δ is the filter width. Therefore, this error must be reduced or eliminated to avoid significant effects on the

LES solution. A general theory for constructing discrete high-order commutative filters was proposed by Vasilyev, Lund & Moin (1998).

Most previous studies of LES using explicit filtering in turbulent channel flow have used filtering in two dimensions (the homogeneous directions) and only a few studies have applied filtering in all three dimensions. Only investigations performed using smooth filter functions are discussed here. Two-dimensional filtering was investigated by Piomelli, Moin & Ferziger (1988), Najjar & Tafti (1996), Sarghini, Piomelli & Balaras (1999), and Gullbrand & Chow (2002) among others. Studies using three-dimensional filtering were performed by Cabot (1994), Gullbrand (2001), Winckelmans, Wray, Vasilyev & Jeanmart (2001), and Stolz, Adams & Kleiser (2001). However, most of the studies using three-dimensional filtering did not focus on minimizing the effect from the numerical errors. If care is not taken to reduce the errors, they may be larger than the contribution from the turbulence closure models. Therefore, it will not be possible to separate the effects from the numerics and the behavior of the turbulence closure models. Cabot (1994), for example, used a second-order finite-difference scheme and second-order filter functions with a ratio of two between the filter width and cell size. The error from the second-order scheme is probably larger than the turbulence closure contribution due to the small ratio of filter width to cell size used and, in addition, a second-order commutation error is present. Therefore, the LES results are highly affected by the numerical errors. Winckelmans *et al.* (2001) used a high-order finite-difference scheme (fourth-order) but applied a second-order filter with a ratio of filter width to cell size of $\sqrt{6}$. The use of a second-order filter introduces commutation errors of second-order which are of the same order as the turbulence model contribution in the simulations. A spectral method was used by Stolz *et al.* (2001), together with fourth-order commutative filter functions with a filter-grid ratio of approximately 1.5. The use of spectral methods clearly reduces the numerical errors in the simulation when compared to the studies previously mentioned. However, the use of explicit filtering in spectral methods is questionable. In spectral methods, the RSFS term can be exactly reconstructed from the filtered field, and truncation errors are not present in the small scales. Therefore, there is no need for explicit filtering when using spectral methods (Winckelmans & Jeanmart 2001). In addition, spectral methods can be applied only to specific geometries and cannot be used in flow fields of engineering interest, so they are not considered here. Gullbrand (2001) used fourth-order commutative filter functions, with a ratio of two between the filter width and cell size, in a fourth-order finite-difference code. The commutation error is then of the same order as the numerical scheme, which is of higher order than the turbulence closure contribution. According to the study by Chow & Moin (2003), the filter-grid ratio used ensures that the contribution from the turbulence closure term is larger than the numerical errors from the scheme. Thus, the fourth-order scheme using fourth-order commutative filters with a filter width of at least twice the cell size creates a numerically-clean environment where turbulence closure models can be tested and validated.

In this paper, turbulence closure models are evaluated using the “true” LES approach in turbulent channel flow. The study is an extension of the work presented by Gullbrand (2001), where fourth-order commutative filter functions are applied in three dimensions in a fourth-order finite-difference code. The true LES solution is the solution to the filtered governing equations. The solution is obtained by keeping the filter width constant while the computational grid is refined (figure 2). As the grid is refined, the solution will converge towards the true LES solution. The true LES solution will depend upon the filter width used, but be independent of the grid resolution. In traditional LES, because

the filter is implicit and directly connected to the grid spacing, the solution converges towards a direct numerical simulation (DNS) as the grid is refined, and not towards the filtered Navier-Stokes equations. The effect of turbulence closure models is therefore difficult to determine in traditional LES because, as the grid is refined, more length scales are resolved and less influence from the models is expected in the LES results. In contrast, in the true LES formulation, the explicit filter eliminates all scales that are smaller than the filter cutoff, regardless of the grid resolution. This ensures that the resolved length-scales do not vary as the grid resolution is changed. A resolution requirement for the true LES is that the cell size must be smaller than or equal to the cutoff length scale of the filter function.

The turbulence closure models investigated are the dynamic Smagorinsky model (DSM), the dynamic mixed model (DMM), and the dynamic reconstruction model (DRM). These turbulence models were previously studied using two-dimensional explicit filtering in turbulent channel flow by Gullbrand & Chow (2002). The DSM by Germano, Piomelli, Moin & Cabot (1991) is used as the USFS model in all the simulations, to be able to evaluate different reconstruction models for the RSFS stresses. The DMM (Zang, Street & Kossoff 1993) consists of the scale-similarity model (SSM) by Bardina, Ferziger & Reynolds (1983), which is the RSFS model, in linear combination with the DSM. In the DRM, the RSFS stresses are modeled by using an estimate of the unfiltered velocity in the unclosed term, while the USFS stresses are modeled by the DSM.

2. Governing equations

The governing equations for an incompressible flow field are the continuity equation together with the Navier-Stokes equations,

$$\frac{\partial u_i}{\partial x_i} = 0, \quad \frac{\partial u_i}{\partial t} + \frac{\partial u_i u_j}{\partial x_j} = -\frac{\partial p}{\partial x_i} + \frac{1}{Re_\tau} \frac{\partial^2 u_i}{\partial x_j \partial x_j}. \quad (2.1)$$

Here u_i denotes velocity, p pressure and Re_τ the Reynolds number based upon friction velocity, u_τ , and channel half-width, h . Einstein summation is applied to repeated indices.

In LES, the governing equations are filtered in space. The filtering procedure is applied to the flow-field variables according to

$$\bar{u}_i(x, \Delta, t) = \int_{-\infty}^{\infty} G(x, x', \Delta) u_i(x', t) dx', \quad (2.2)$$

where G is the filter function and Δ is the filter width.

Hence, the filtered governing equations can be written as

$$\frac{\partial \bar{u}_i}{\partial x_i} = 0, \quad \frac{\partial \bar{u}_i}{\partial t} + \frac{\partial \bar{u}_i \bar{u}_j}{\partial x_j} = \frac{\partial \bar{p}}{\partial x_i} + \frac{1}{Re_\tau} \frac{\partial^2 \bar{u}_i}{\partial x_j \partial x_j} - \frac{\partial \bar{\tau}_{ij}}{\partial x_j} \quad (2.3)$$

where the turbulent stresses are defined as $\bar{\tau}_{ij} = \bar{u}_i \bar{u}_j - \bar{u}_i \bar{u}_j$. The filtered equations are not closed because of the nonlinear term $\bar{u}_i \bar{u}_j$. Note that a second filtering is applied to the convective and turbulent stress terms (the nonlinear terms) in (2.3), to ensure that the wavenumber content is the same for every term in the equations. The product of the nonlinear terms ($\bar{u}_i \bar{u}_j$) introduces high wavenumbers that are beyond the wavenumber content of the filtered velocity field (\bar{u}_i). To prevent these high wavenumbers to influence the resolved wavenumbers, the nonlinear terms are explicitly filtered. A potential drawback of (2.3) is that the resulting equation is in general not Galilean-invariant. However, if an appropriate turbulence closure model is used, the problem can be avoided.

3. Subfilter-scale models

The turbulent flow field is divided into RFS motions and SFS motions when explicit filtering of the Navier-Stokes equations is applied. In figure 1, a sketch of a typical energy spectrum is shown. The solid line represents the energy captured by a fully resolved DNS, while the dashed line represents the LES energy. The vertical line at k_{cg} shows the filter cutoff in the LES. The filter cutoff is determined by where the filter function goes to zero and stays zero (in spectral space), *i.e.* no wavenumbers higher than the cutoff wavenumber are resolved in the simulation. The filter cutoff can be seen in figure 2. All wavenumbers smaller than the filter cutoff wavenumber are resolved in the simulations. However, they are damped by the filter function and have to be recovered by an inverse filter operation. This corresponds to the RSFS portion of the energy spectrum. The same terminology for the RSFS and the USFS was previously suggested by Zhou *et al.* (2001). In theory, the RSFS can be exactly recovered, but this is only possible when using spectral methods. If non-spectral methods are applied, there are numerical errors (NE) associated with the high wavenumbers and thus the recovered scales are contaminated with errors. The unresolved portion of the spectrum (the USFS) consists of wavenumbers that are higher than the filter cutoff wavenumber. The USFS motions need to be modeled. The USFS portion of the spectrum was previously called the subgrid-scale (SGS) portion in the study by Gullbrand & Chow (2002). However, the name is not valid here, since it is the filter function that determines the cutoff location and not the computational grid. The vertical lines in the figure represent the grid cutoff wavenumbers for two grid resolutions. The coarse grid cutoff, k_{cg} , happens to coincide with the filter cutoff, while the fine grid cutoff, k_{fg} , is located in the USFS portion of the spectrum. However, the USFS motions are the same in the two simulations, since the filter cutoff determines the wavenumbers resolved.

To recover the RSFS stresses, the iterative method of van Cittert (1931) is used in this study. This method was previously used by Stolz *et al.* (2001) in their approximate deconvolution procedure to reconstruct the unfiltered velocity field u_i from the filtered field \bar{u}_i . To fully recover the unfiltered velocity, an infinite number of iterations is needed. However, since this is not practical in numerical simulations, the unfiltered velocity field is approximated by a finite number of iterations. By varying this number, different models can be obtained to model the RSFS stresses.

Here, low-level reconstruction (the SSM) and reconstruction of level five using the approximate deconvolution model (ADM) by Stolz *et al.* (2001) are used to model the RSFS stresses. Further details of the reconstruction used are found in 3.3. In order to compare the different RSFS models, the same USFS model (the DSM) is used in all the simulations. The combinations of RSFS and USFS models used are described below.

3.1. Dynamic Smagorinsky Model

The DSM is a widely-used eddy viscosity USFS model (Smagorinsky 1963):

$$\tau_{ij} = -2\overline{\nu_e \bar{S}_{ij}} = -2\overline{(C\Delta)^2 |\bar{S}| \bar{S}_{ij}}, \quad (3.1)$$

where ν_e is the eddy viscosity, Δ the filter width and S_{ij} the strain rate tensor. The model parameter $(C\Delta)^2$ is calculated dynamically (Germano *et al.* 1991) using the least-square approximation of Lilly (1992). The model parameter is calculated by the same dynamic procedure as described in the papers previously mentioned. The explicit filtering of the nonlinear terms is not considered when the model parameter is calculated. The filtering

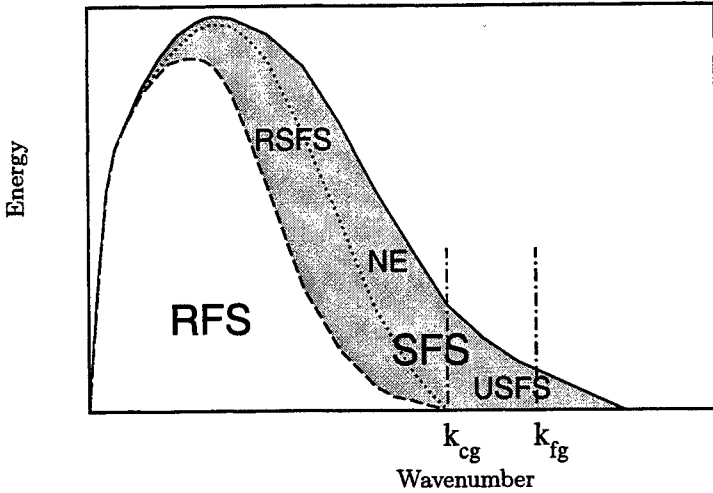


FIGURE 1. Schematic of velocity energy spectrum showing partitioning into resolved filtered scale (RFS), resolved subfilter-scale (RSFS), and unresolved subfilter-scale (USFS) motions. The numerical error (NE) region, denoted by -----, is a subregion of the RSFS. —— represents DNS energy, ----- LES energy, and - - - filter cutoff. The vertical line at k_{cg} represents the filter cutoff wavenumber, which corresponds to the smallest resolved wavenumber for the coarse grid. The vertical line at k_{fg} represents the wavenumber cutoff for the fine grid.

enters only in the final stage of the process, when τ_{ij} is introduced into the filtered Navier-Stokes equations.

3.2. Dynamic Mixed Model

Low-level reconstruction of the RSFS stresses can be performed by using the scale-similarity model proposed by Bardina *et al.* (1983). The SSM is obtained by substituting $u_i \approx \bar{u}_i$ into the definition of the turbulence stress tensor, $\bar{\tau}_{ij}$. Here the RSFS stress is modeled by the scale-similarity term and the DSM is used as the USFS model:

$$\bar{\tau}_{ij} = (\bar{u}_i \bar{u}_j - \bar{\bar{u}}_i \bar{\bar{u}}_j) - 2\overline{(C\Delta)^2 |S| \bar{S}_{ij}}, \quad (3.2)$$

to form the DMM. In the code, the SSM term is discretized with the same numerical scheme as the convective terms.

3.3. Dynamic Reconstruction Model

High-order reconstruction of the RSFS stress tensor can be achieved by the iterative deconvolution method of van Cittert (1931). The unfiltered quantities can be derived by a series of successive filtering operations (G) applied to the filtered quantities with

$$u_i = \bar{u}_i + (I - G) * \bar{u}_i + (I - G) * ((I - G) * \bar{u}_i) + \dots \quad (3.3)$$

where I is the identity matrix. The truncation order of the expansion determines the level of deconvolution, as discussed by Stolz *et al.* (2001). If the series includes the terms explicitly shown in (3.3), it corresponds to reconstruction of level two. An approximate unfiltered velocity (u_i^*) is obtained by the truncated series. u_i^* is substituted into the unclosed term $\bar{u}_i \bar{u}_j$, which results in $\bar{u}_i^* \bar{u}_j^*$. This reconstruction was used by Stolz *et al.*

(2001) to form the ADM. Here the ADM is used in linear combination with the DSM,

$$\bar{\tau}_{ij} = \overline{u_i^* u_j^*} - \overline{u_i} \overline{u_j} - 2\overline{(C\Delta)^2 |\bar{S}| \bar{S}}_{ij}, \quad (3.4)$$

which is called the dynamic reconstruction model (DRM). In the simulations, the same numerical scheme is used for the convective terms and the RSFS terms. The DRM yields a Galilean-invariant expression of (2.3), since the nonlinear terms $\overline{u_i} \overline{u_j}$ on the right-hand side and left-hand side of the equation cancel each other. A reconstruction series of level five is used in this study.

4. Filter functions

It is important that the explicit filter and the test filter, which is used in the dynamic procedure of the DSM, have similar shapes, since the dynamic procedure is based upon the scale-similarity assumption in the Germano identity (Germano *et al.* 1991). In the simulations presented here, the same filter function is used in all the simulations. It is only the filter width that is varied between the simulations. The base filter is a fourth-order commutative filter function with filter width $2\Delta_{cg}$, where Δ_{cg} is the grid cell size for the coarse-grid resolution. The computational domain and grid resolutions used in the simulations are discussed in section 6. It is not straightforward to determine the filter width of a high-order filter and different methods were studied by Lund (1997). Here, one of the methods suggested by Lund is applied. The filter width is defined as the location where the filter function reaches a value of $G(k) = 0.5$. The filter function used in the simulations was developed by Vasilyev *et al.* (1998) and is

$$\bar{\phi}_i = -\frac{1}{32}\phi_{i-3} + \frac{9}{32}\phi_{i-1} + \frac{1}{2}\phi_i + \frac{9}{32}\phi_{i+1} - \frac{1}{32}\phi_{i+3}, \quad (4.1)$$

where the filter weights for $\phi_{i\pm 2}$ are zero. The smooth filter function is shown in spectral space in figure 2. In the near-wall region, asymmetric filters are used in the first three grid points for the coarse grid in the wall-normal direction.

In the simulations, the ratio of the test-filter width to the explicit-filter width is chosen to be two, as proposed by Germano *et al.* (1991) for the DSM. The test filter is used only in the calculation of $(C\Delta)^2$ in the DSM, while the explicit filter function is used to determine the RSFS contribution through either the SSM or the ADM. The ratio between the explicit-filter width and the cell size for the coarse grid is two and for the fine grid (128, 97, 96), the ratio is four. This preserves the effective filter width as the grid resolution is increased, as seen in figure 2. The vertical line at low wavenumber represents the grid cutoff (k_{cg}) for the coarse-grid resolution. The filter cutoff wavenumber is the same as the grid cutoff for the coarse grid. For the fine grid, the filter cutoff is held fixed, resulting in a separation between the filter cutoff and grid cutoff (k_{fg}) locations. The grid-cutoff wavenumbers are also shown schematically in figure 1. The ratio of two between the filter width and the cell size for the coarse grid was chosen to prevent the numerical error from the finite-difference scheme from becoming larger than the contribution of the turbulence closure model (Ghosal 1996; Chow & Moin 2003).

5. Solution algorithm

In the computational code, the spatial derivatives are discretized using a fourth-order central-difference scheme on a staggered grid. The convective term is discretized in the skew-symmetric form (Morinishi, Lund, Vasilyev & Moin 1998; Vasilyev 2000) to ensure

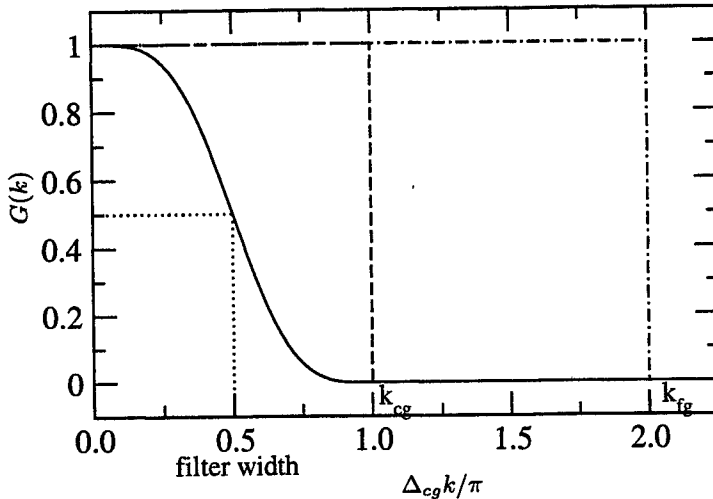


FIGURE 2. The base filter function in spectral space and its relation to the computational grid resolutions. — : filter function, : filter width, - - - : coarse grid resolution, and - - - - : fine grid resolution. The wavenumber k_{cg} represents the grid cutoff wavenumber for the coarse grid, while k_{fg} represents the grid cutoff wavenumber for the fine grid.

conservation of turbulent kinetic energy. The equations are integrated in time using the third-order Runge-Kutta scheme described by Spalart, Moser & Rogers (1991). The diffusion terms in the wall-normal direction are treated implicitly by the Crank-Nicolson scheme. The splitting method of Dukowicz & Dvinsky (1992) is used to enforce the solenoidal condition. The resulting discrete Poisson equation for the pressure is solved in the wall-normal direction using a pentadiagonal matrix solver. In the homogeneous directions, the Poisson equation is solved using a discrete Fourier transform. Periodic boundary conditions are applied in the streamwise and spanwise homogeneous directions, with no-slip conditions at the channel walls. A fixed mean pressure gradient is used to drive the flow. The computational code is compared to a second-order finite-difference code in Gullbrand (2000) and Gullbrand & Chow (2002).

6. Turbulent channel flow simulations

The Reynolds number is $Re_\tau = 395$ and the computational domain is $(2\pi h, 2h, \pi h)$ in (x, y, z) where x is the streamwise direction, y the wall-normal direction, and z the spanwise direction. The computational grid is stretched in the y -direction by a hyperbolic tangent function

$$y(j) = -\frac{\tanh(\gamma(1 - 2j/N_2))}{\tanh(\gamma)} \quad j = 0, \dots, N_2 \quad (6.1)$$

where N_2 is the number of grid points in the wall-normal (j) direction and γ is the stretching parameter, which is set to 2.75. Two computational grids are used; (64,49,48), which corresponds to one-quarter of the DNS resolution in each spatial direction, and (128,97,96), which is half the number of DNS grid points in each direction. The cell size for the coarser grid resolution is $\Delta x^+ = 39$, $\Delta z^+ = 26$, and $0.4 \leq \Delta y^+ \leq 45$. The finer resolution corresponds to the cell size $\Delta x^+ = 19$, $\Delta z^+ = 13$, and $0.2 \leq \Delta y^+ \leq 23$. The ‘plus’ values (wall units) are obtained by normalizing the length scale with the friction

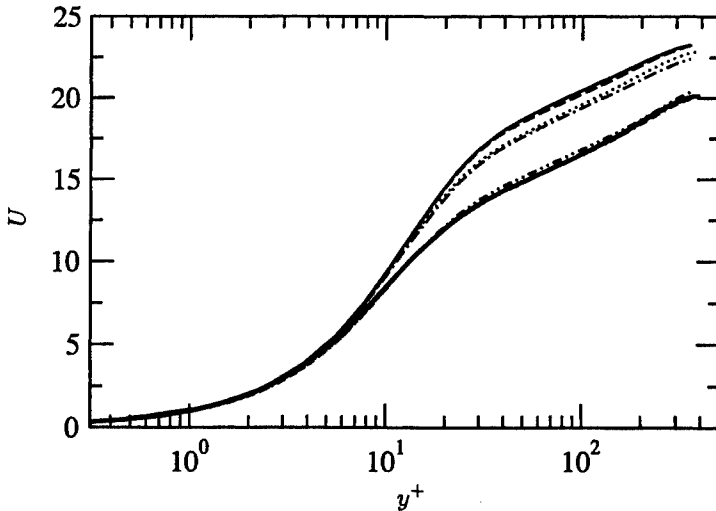


FIGURE 3. Mean velocity profiles using different turbulence closure models. — : DNS, - - : DSM (64,49,48), - · - : DSM (128,97,96), - · - - : DMM (64,49,48), · · · : DMM (128,97,96), - - - - : DRM (64,49,48), and - - - - - : DRM (128,97,96).

velocity and the kinematic viscosity (ν). A statistically stationary solution is obtained after 30 dimensionless time units, and thereafter statistics are sampled during 15 time units. The time is normalized with the friction velocity and channel half-width. The LES results are compared to the unfiltered DNS data of Moser, Kim & Mansour (1999).

7. Results

Figure 3 shows mean velocity profiles from simulations using different RSFS models and different grid resolutions. The filter width is fixed, while the grid resolution is increased. The goal is to obtain a grid-independent LES solution so that the behavior of turbulence closure models can be evaluated. The changes in the predicted mean velocity profiles as the grid resolution is increased are only minor, indicating that the LES solutions are converged. The mean velocities predicted by the DSM are much higher than the DNS results. The DMM improves the results slightly, while the best agreement with the DNS data is predicted by the DRM. This shows the need for a RSFS model when a smooth explicit filter function is applied.

The streamwise velocity fluctuations in figure 4 show the same trend as the mean velocity profiles. However, the differences in the results as the grid is refined are slightly larger than for the mean velocity. The DSM shows the largest overprediction of the peak streamwise velocity fluctuations. The peak value decreases slightly as the grid is refined. This is also observed for the DMM and the DRM. It should be noted that the DRM actually predicts a peak value that is lower than the DNS data. This is very unusual in LES, because most models will overpredict the streamwise velocity fluctuations and underpredict the wall-normal and spanwise fluctuations. However, an underprediction of all velocity fluctuations is to be expected in LES, since LES can be considered as filtered DNS, and if the DNS results filtered, the peak values are expected to decrease.

As pointed out by Winckelmans, Jeanmart & Carati (2002), when LES turbulence intensities (or velocity fluctuations) are compared to DNS data, the LES intensities should

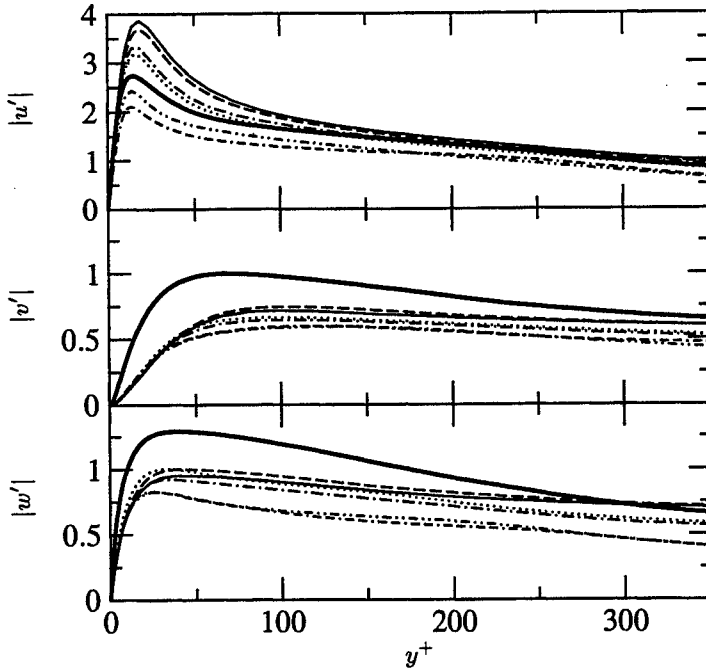


FIGURE 4. Velocity fluctuations in the streamwise $|u'|$, wall-normal $|v'|$, and spanwise $|w'|$ directions. — : DNS, — : DSM (64,49,48), - - : DSM (128,97,96), - - - : DMM (64,49,48), ····· : DMM (128,97,96), - - - - : DRM (64,49,48), and - - - - - : DRM (128,97,96).

include the contribution from the turbulence closure models. However, if a traceless turbulence model like the DSM, or partially-traceless models as the DMM and DRM, are used, it is only the reduced (deviatoric) turbulence intensities of both the DNS and the LES that should be compared. The reduced intensities represent the deviation from isotropy, and the streamwise turbulence intensities are given by

$$-R_{xx} = u'u' - 1/3(u'u' + v'v' + w'w').$$

The reduced turbulence intensities are compared in figure 5. In this paper, both the turbulence intensities and the velocity fluctuations are studied. The reason for investigating both quantities is to show that incorrect conclusions may have been made in previous studies concerning model behavior, since it is usually the uncorrected velocity fluctuations that are compared. As observed in figure 5, the magnitudes of the turbulence intensities show a consistent behavior for all three intensities. The DSM shows the largest overprediction of the peak value. The DMM decreases the predicted peak values slightly, while the DRM predicts peak values that are lower than the DNS. As mentioned earlier, an underprediction of the peak value is expected in LES. When the grid is refined, the peak values decrease slightly for all the models studied. The behavior of the turbulence intensities is not consistent with the observations made for the velocity fluctuations. For the wall-normal and spanwise velocity fluctuations, the DSM predictions are closer to the DNS data than the other models. The DRM predicts velocity fluctuations that are lower than the DNS data in the streamwise direction, while the results in the wall-normal and the spanwise directions show the largest deviation of the models from the DNS re-

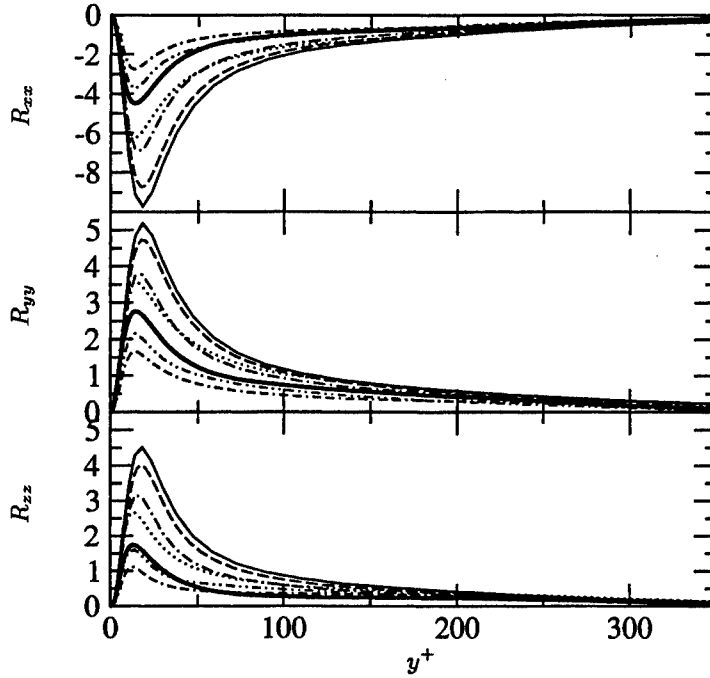


FIGURE 5. Reduced (deviatoric) turbulence intensities in streamwise R_{xx} , wall-normal R_{yy} , and spanwise R_{zz} directions. — : DNS, — : DSM (64,49,48), - - : DSM (128,97,96), - · - : DMM (64,49,48), · · · : DMM (128,97,96), - - - : DRM (64,49,48), and - - - - : DRM (128,97,96).

sults. The velocity fluctuations therefore seem to give a rather confusing message of the DRM behavior, while the turbulence intensities show a consistent behavior for all three intensities.

The modeled shear stresses are shown in figure 6. It is a well-known problem that the DSM does not predict enough shear stress in the near-wall region (Baggett, Jimenez & Kravchenko 1997). As shown in the figure, the total modeled shear stress increases as the level of reconstruction is increased. However, the contribution from the DSM does not change much between the different simulations; the peak value is approximately the same. The increase of modeled shear stress is therefore almost entirely due to the RSFS model.

8. Discussion and conclusions

The true LES approach is investigated in turbulent channel flow using commutative filter functions in all three spatial directions. In the true LES approach, a grid-independent solution to the filtered governing equations is obtained. A computational code using an energy-conserving fourth-order finite-difference scheme is applied and fourth-order commutative filters are used. Simulations of turbulent channel flow were performed at $Re_\tau = 395$. The explicit filter width was kept fixed while the computational grid was refined, to obtain a grid-independent solution. The results using two different grid resolutions show only minor differences, indicating that the LES solutions are converged. The explicit filtering also reduces the numerical errors that are associated with the high-

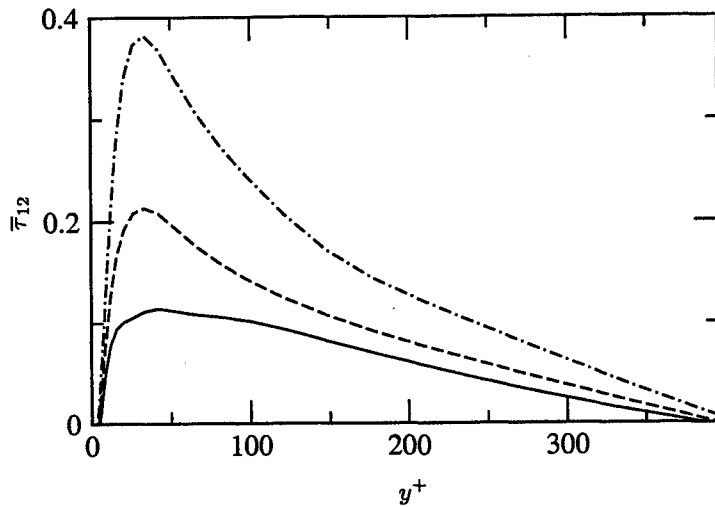


FIGURE 6. Modeled shear stress, $\bar{\tau}_{12}$, using different turbulence closure models for the computational grid (64,49,48). — : DSM, - - - : DMM, - · - : DRM.

wavenumber portion of the spectrum when using non-spectral methods. Therefore, explicit filtering in LES, using high-order commutative filters, results in a numerically-clean environment where turbulence closure models can be investigated in grid-independent LES solutions.

The turbulence closure models investigated are the DSM, DMM and DRM. The models are compared to DNS data for mean velocity profiles, velocity fluctuations, and reduced turbulence intensities. The results show that since the turbulence closure models are traceless (the DSM) or partially traceless (the DMM and the DRM), special care is needed when comparing the turbulence quantities to DNS results. The reduced turbulence intensities represent the deviation from isotropy and show a consistent behavior of the models, while these conclusions cannot be drawn from studying the velocity fluctuations.

The poor agreement between the DNS results and the DSM shows the need for RSFS models when a smooth (in spectral space) explicit filter function is applied. In theory, the RSFS stresses can be exactly reconstructed by an inverse-filtering operation. However, in a non-spectral method, the RSFS stresses cannot be exactly reconstructed, due to numerical errors. The results predicted by the models investigated show a distinct improvement in the predicted quantities, when compared to DNS results, as the level of reconstruction is increased. These improvements are probably due to the increase of modeled shear stress in the near-wall region. The DSM is known not to predict enough shear stress in the near-wall region, and as the level of reconstruction is increased so is the modeled shear stress. The increase is almost entirely due to the RSFS model, since the contribution from the DSM does not change much in the simulations. However, it should be noted that even if an exact reconstruction of the RSFS stresses can be obtained, the results will depend on the USFS model used. The LES results need to be compared to filtered DNS data, since the governing equations are filtered. The accuracy of using the DSM to capture the USFS stresses also needs to be determined.

Acknowledgments

Thanks are extended to Profs. P. Moin and O. V. Vasilyev who contributed through many helpful discussions. Thanks are also due to F. K. Chow for her input.

REFERENCES

- BAGGETT, J., JIMENEZ, J. & KRAVCHENKO, A. G. 1997 Resolution requirements in large-eddy simulations of shear flows. *Annual Research Briefs*, Center for Turbulence Research, NASA Ames/Stanford Univ., 51–66.
- BARDINA, J., FERZIGER, J. H. & REYNOLDS, W. C. 1983 Improved turbulence models based on large eddy simulation of homogeneous, incompressible, turbulent flows. *Tech. Rept. TF-19*, Mech. Engg. Dept., Stanford Univ.
- CABOT, W. 1994 Local dynamic subgrid-scale models in channel flow. *Annual Research Briefs*, Center for Turbulence Research, NASA Ames/Stanford Univ., 143–159.
- CARATI, D., WINCKELMANS, G. & JEANMART, H. 2001 On the modelling of the subgrid-scale and filtered-scale stress tensors in large-eddy simulation. *J. Fluid Mech.* **441**, 119–138.
- CHOW, F. K. & MOIN, P. 2003 A further study of numerical errors in large-eddy simulations. To appear in *J. Comp. Phys.*
- VAN CITTERT, P. 1931 Zum Einfluß der Spaltbreite auf die Intensitätsverteilung in Spektrallinien II. *Zeit. für Physik* **69**, 298–308.
- DUKOWICZ, J. & DVINSKY, A. 1992 Approximate factorization as a high-order splitting for the implicit incompressible-flow equations. *Journal of Computational Physics* **102** (2), 336–347.
- GERMANO, M., PIOMELLI, U., MOIN, P. & CABOT, W. 1991 A dynamic subgrid-scale eddy viscosity model. *Phys. Fluids* **3** (7), 1760–1765.
- GHOSAL, S. 1996 An analysis of numerical errors in large-eddy simulations of turbulence. *J. Comp. Phys.* **125**, 187–206.
- GHOSAL, S. & MOIN, P. 1995 The basic equations for the large eddy simulation of turbulent flows in complex geometry. *J. Comp. Phys.* **118**, 24–37.
- GULLBRAND, J. 2000 An evaluation of a conservative fourth order dns code in turbulent channel flow. *Annual Research Briefs*, Center for Turbulence Research, NASA Ames/Stanford Univ., 211–218
- GULLBRAND, J. 2001 Explicit filtering and subgrid-scale models in turbulent channel flow. *Annual Research Briefs*, Center for Turbulence Research, NASA Ames/Stanford Univ., 31–43.
- GULLBRAND, J. & CHOW, F. 2002 Investigation of numerical errors, subfilter-scale models, and subgrid-scale models in turbulent channel flow simulations. Proceedings of the Summer Program. Center for Turbulence Research, NASA Ames/Stanford Univ.,
- LILLY, D. 1992 A proposed modification of the Germano subgrid-scale closure method. *Phys. Fluids* **4**, 633–635.
- LUND, T. S. 1997 On the use of discrete filters for large eddy simulation. *Annual Research Briefs*, Center for Turbulence Research, NASA Ames/Stanford Univ., 83–95.
- MORINISHI, Y., LUND, T., VASILEV, O. & MOIN, P. 1998 Fully conservative higher order finite difference schemes for incompressible flow. *J. Comp. Phys.* **143**, 90–124.

- MOSER, R., KIM, J. & MANSOUR, N. 1999 Direct numerical simulation of turbulent channel flow up to $Re_\tau = 590$. *Phys. Fluids* **11**, 943–945.
- NAJJAR, F. & TAFTI, D. 1996 Study of discrete test filters and finite difference approximations for the dynamic subgrid-scale stress model. *Phys. Fluids* **8**, 1076–1088.
- PIOMELLI, U., MOIN, P. & FERZIGER, J. 1988 Model consistency in large eddy simulation of turbulent channel flows. *Phys. Fluids* **31**, 1884–1891.
- SARGHINI, F., PIOMELLI, U. & BALARAS, E. 1999 Scale-similar models for large-eddy simulations. *Phys. Fluids* **11**, 1596–1607.
- SMAGORINSKY, J. 1963 General circulation experiments with the primitive equations. *Mon. Weather Rev.* **91**, 99–152.
- SPALART, P., MOSER, R. & ROGERS, M. 1991 Spectral methods for the navier-stokes equations with one infinite and 2 periodic directions. *J. Comp. Phys.* **96**, 297–324.
- STOLZ, S., ADAMS, N. & KLEISER, L. 2001 An approximate deconvolution model for large-eddy simulation with application to incompressible wall-bounded flows. *Phys. Fluids* **13**, 997–1015.
- VASILYEV, O. 2000 High order finite difference schemes on non-uniform meshes with good conservation properties. *J. Comp. Phys.* **157**, 746–761.
- VASILYEV, O., LUND, T. & MOIN, P. 1998 A general class of commutative filters for les in complex geometries. *J. Comp. Phys.* **146**, 82–104.
- WINCKELMANS, G. & JEANMART, H. 2001 Assessment of some models for les without/with explicit filtering. In *Direct and Large-Eddy Simulation IV* (B. Geurts, F. Friedrich & O. Métais, eds.), Kluwer, Dordrecht, 55–66.
- WINCKELMANS, G., JEANMART, H. & CARATI, D. 2002 On the comparison of turbulence intensities from large-eddy simulation with those from experiment or direct numerical simulation. *Phys. Fluids* **14**, 1809–1811.
- WINCKELMANS, G., WRAY, A., VASILYEV, O. & JEANMART, H. 2001 Explicit-filtering large-eddy simulation using the tensor-diffusivity model supplemented by a dynamic smagorinsky term. *Phys. Fluids* **13** (5), 1385–1403.
- ZANG, Y., STREET, R. L. & KOSEFF, J. R. 1993 A dynamic mixed subgrid-scale model and its application to turbulent recirculating flows. *Phys. Fluids* **5**, 3186–3196.
- ZHOU, Y., BRASSEUR, J. & JUNEJA, A. 2001 A resolvable subfilter-scale model specific to large-eddy simulation of under-resolved turbulence. *Phys. Fluids* **13**, 2602–2610.

Wall modeling for large-eddy simulation using an immersed boundary method

By F. Tessicini †, G. Iaccarino, M. Fatica, M. Wang AND R. Verzicco ‡

1. Motivation and objectives

Orthogonal, structured grids allow flow simulations in simple geometries with high efficiency and accuracy. In contrast, complex and realistic flow problems have traditionally required the use of curvilinear or unstructured meshes, which require large computational costs and reduced accuracy due to limited grid smoothness and orthogonality. In recent years an alternative approach which combines the advantages of simple Cartesian grids with the ability to deal with complex geometries has been developed. In this technique, named the immersed boundary method (Fadlun *et al.* (1999)), the complex object is *immersed* in a regular grid and the body effect on the flow is accounted for by prescribing an appropriate body force in the momentum equations in the first computational cell outside the immersed body. This is a *de facto* grid-free numerical method in the sense that the time-consuming construction of the smooth mesh fitted to the body is avoided.

Flows in industrially relevant configurations are often characterized by high Reynolds numbers. A Direct Numerical Simulation (DNS) which resolves all the time and length scales requires grid resolution and computational resources that will not be available in the near future. Turbulence models have to be used to make those simulations feasible. The immersed boundary approach has been used successfully in combination with Large-Eddy Simulation (LES) and Reynolds Averaged Navier-Stokes (RANS) techniques (Iaccarino & Verzicco (2003)). Accurate LES of wall bounded flows, however, requires a near-wall resolution comparable to that for DNS, thus limiting the use of LES to moderate Reynolds numbers. One way to overcome this difficulty is to replace the near-wall region with a wall model which provides the outer LES with approximate wall boundary conditions. In recent years wall models based on turbulent boundary-layer equations and their simplified forms (Balaras, Benocci & Piomelli (1996); Cabot & Moin (2000); Wang & Moin (2002)) have been developed and applied successfully in a number of flow configurations.

The objective of this work is to study the applicability of a simple near-wall model, based on the local equilibrium hypothesis, in the framework of immersed boundary method for LES and to analyze its effect on the flow dynamics. The selected test case is the flow past a 25 degree, asymmetric trailing edge of a model hydrofoil. The Reynolds number based on free-stream velocity U_∞ and the hydrofoil chord C , is $Re_C = 2.15 \times 10^6$. The simulation is performed over the rear 38% of the hydrofoil chord, and the Reynolds number based on the hydrofoil thickness is $Re = 1.02 \times 10^5$. The flow was investigated experimentally by Blake (1975) and numerically by Wang & Moin (2000), who reported that 200 CRAY C-90 CPU hours were needed to advance the simulation by one flow-through time for a fully resolved LES.

† DMA, Università di Roma La Sapienza, Via Eudossiana, 18, 00184, Roma, Italy. Also with INSEAN, Via di Vallerano 139, 00128, Roma, Italy.

‡ DIMeG and CEMeC, Politecnico di Bari Via Re David, 200, 70125, Bari, Italy.

2. Numerical set-up and wall model

The equations used for the present study are the three-dimensional, incompressible, unsteady Navier-Stokes equations with an additional boundary body-force term \mathbf{f} :

$$\frac{D\bar{\mathbf{u}}}{Dt} = -\rho^{-1}\nabla\bar{P} + \nabla \cdot \{\tilde{\nu}[\nabla\bar{\mathbf{u}} + (\nabla\bar{\mathbf{u}})^T]\} + \mathbf{f}, \quad (2.1)$$

$$\nabla \cdot \bar{\mathbf{u}} = 0. \quad (2.2)$$

Here $\bar{\mathbf{u}}$ denotes the filtered velocity, and \bar{P} is the sum of the filtered pressure and the trace of the subgrid-scale stress tensor. The effective viscosity $\tilde{\nu}$ is the sum of the subgrid-scale eddy viscosity and the molecular kinematic viscosity. The subgrid-scale turbulent viscosity is determined by a dynamic procedure and does not require direct specification of any model constant (Germano *et al.* (1991); Lilly (1992)).

The equations are solved by a second-order centered finite-difference solver. Details on the numerical methods and on the expression for \mathbf{f} are given in Fadlun *et al.* (1999). Here it suffices to mention that if the time-discretized version of (2.1) is

$$\bar{\mathbf{u}}^{n+1} - \bar{\mathbf{u}}^n = \Delta t(RHS + \mathbf{f}), \quad (2.3)$$

(with Δt the computational time step and RHS the sum of nonlinear, pressure, and viscous terms), to impose $\bar{\mathbf{u}}^{n+1} = \bar{\mathbf{v}}_b$, the boundary velocity, the body force \mathbf{f} must be,

$$\mathbf{f} = -RHS + \frac{\bar{\mathbf{v}}_b - \bar{\mathbf{u}}^n}{\Delta t}. \quad (2.4)$$

This forcing is active only in the flow region where we wish to mimic the solid body, and it is set to zero elsewhere. In general, the surface of the region where $\bar{\mathbf{u}}^{n+1} = \bar{\mathbf{v}}_b$ does not coincide with a coordinate surface, therefore the value of \mathbf{f} at the node closest to the surface but outside the solid body is linearly interpolated between the value yielding $\bar{\mathbf{v}}_b$ on the solid body and zero in the flow domain. This interpolation procedure is consistent with a centered second-order finite-difference approximation, and the overall accuracy of the scheme remains second-order. The linear interpolation, however, can be used only if the location of this point is inside the linear region of the boundary layer. In order to extend the applicability of the immersed boundary method to higher Reynolds number flows, a two-layer wall modeling approach will be considered instead of the linear interpolation.

Equations (2.1) and (2.2) are solved down to the second grid point from the solid boundaries. From the second grid point to the wall a refined mesh is embedded, and simplified turbulent boundary-layer equations are solved. The boundary-layer equations have the following general form (Balaras, Benocci & Piomelli (1996); Wang & Moin (2002)):

$$\begin{aligned} \frac{\partial}{\partial x_n} \left[(\nu + \nu_t) \frac{\partial \bar{u}_i}{\partial x_n} \right] &= F_i, \quad \text{with} \\ F_i &= \frac{\partial \bar{u}_i}{\partial t} + \frac{\partial \bar{u}_i \bar{u}_j}{\partial x_j} + \frac{\partial \bar{p}}{\partial x_i}, \end{aligned} \quad (2.5)$$

where n denotes the direction normal to the wall and $i = 1, 3$ the wall parallel directions. In the present study only a simplified version of the above model, namely the equilibrium stress balance model obtained by setting $F_i = 0$ in (2.5), was used. The eddy viscosity ν_t is obtained from a simple mixing length eddy viscosity model with near wall damping

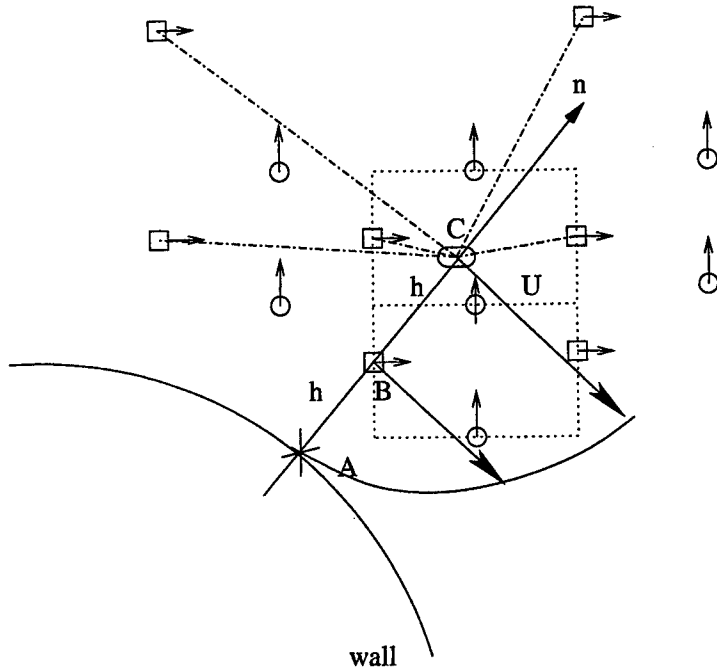


FIGURE 1. Interpolation procedure: \square , streamwise velocity node; \circ , vertical velocity node. n is normal to the wall from first external point B. U is the tangential velocity interpolated at point C, used as boundary condition for the wall model.

(Cabot & Moin 2000; Wang 2002)

$$\frac{\nu_t}{\nu} = \kappa y^+ (1 - e^{-\frac{y^+}{A}})^2, \quad (2.6)$$

where y^+ is the distance to the wall in wall units based on the local instantaneous friction velocity, $\kappa = 0.4$, and $A = 19$. The boundary conditions for the wall model are the LES velocities at the outer edge of the wall-layer and the no-slip condition at $y = 0$. Since in (2.6) the friction velocity u_τ is required to determine y^+ which, in turn, depends on the wall shear stress given by (2.5), an iterative procedure has been implemented to solve (2.5) and (2.6) simultaneously. It is worth mentioning that for a general geometry, an interpolation procedure is needed for the calculation of the tangential velocity in (2.5) since the wall normal does not cross any computational node. The choice of the interpolation points follows the approach used by Balaras (personal communication): all the first external grid nodes are identified, the wall normals are drawn through these points, and the interpolation node is placed on the same segments at twice the distance h (see figure 1). The choice of $2h$ is somewhat arbitrary but, as noted by Balaras, it allows the most compact scheme without involving points inside the body. The fluid velocity at the interpolation point is computed using the inverse distance formula based on the grid points surrounding the interpolation node.

The computational cost of the wall model, including the interpolation procedure, is about 10% of the total computational cost.

The equilibrium stress balance model implies the logarithmic law of the wall for instantaneous velocity at $y^+ \gg 1$ and linear velocity for $y^+ \ll 1$. Figure 2 shows the velocity profiles given by the model when it is used in the low ($Re = 300$) and higher

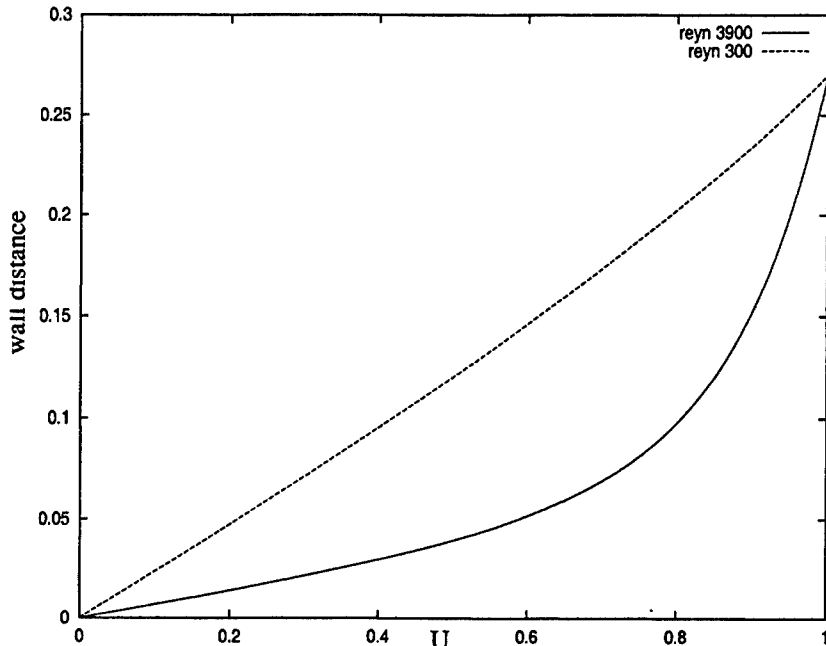


FIGURE 2. Velocity profiles as a function of wall-normal distance, as predicted by (2.5) and (2.6) at two different Reynolds numbers.

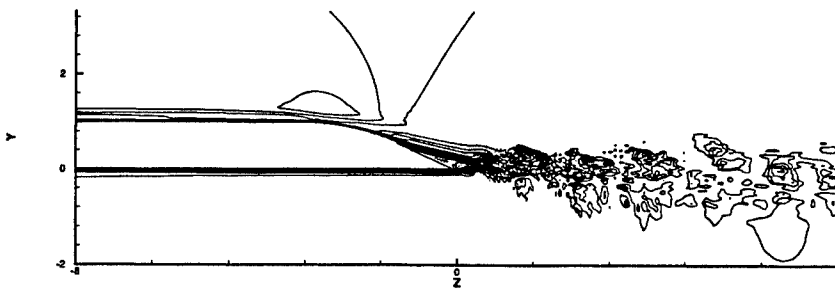


FIGURE 3. Flow past a hydrofoil trailing edge. The contours (-0.2 to 1.2 with increment 0.08) represent the instantaneous streamwise velocity.

($Re = 3900$) Reynolds number cases. In the former case the first interpolation node is located at $y^+ = 5$, while in the latter it is at $y^+ = 30$. It can be observed that the linear interpolation usually adopted in immersed boundary procedures is automatically recovered when the first external node is located in the viscous sublayer of the turbulent boundary layer. In contrast, when the interpolating node is within the log layer, the wall model yields the appropriate velocity profile thus extending the range of applicability of the immersed boundary method in conjunction with LES to the high Reynolds-number regime.

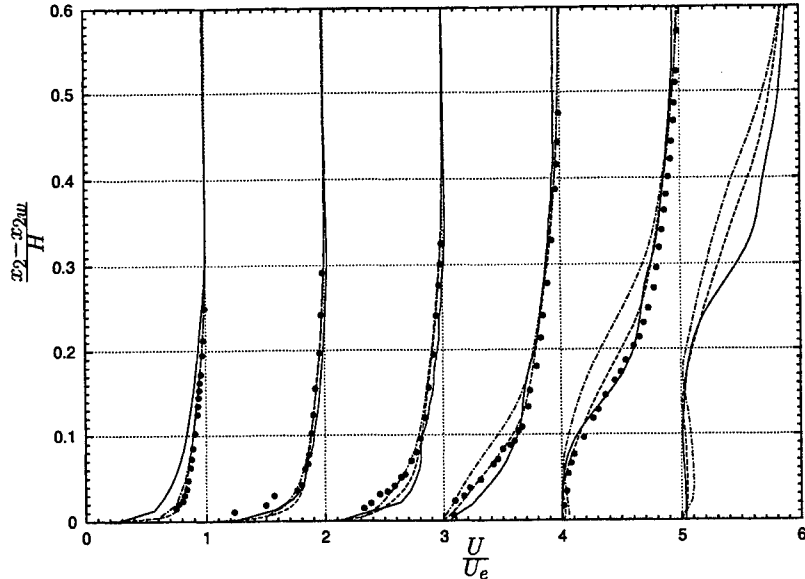


FIGURE 4. Mean velocity magnitude at (from left to right) $x_1/H = -3.125, -2.125, -1.625, -0.625, 0$. •, experiment (Blake 1975); ——, full LES (Wang & Moin 2000); —, present calculation; - - -, LES with wall model (Wang & Moin 2002).

3. Preliminary results and discussion

In the simulation with the wall model the computational domain is $0.25H \times 41H \times 16.5H$, where H denotes the hydrofoil thickness. The grid has $25 \times 206 \times 418$ points, respectively, in the spanwise, cross-stream and streamwise directions. The grid distributions of the Cartesian mesh in the cross-stream and streamwise directions are the same as that used by Wang & Moin (2002) for the straight part of the profile. A uniform mesh with $0.013H$ spacing is used between the upper and lower sides of the hydrofoil in the cross-stream direction. The mesh is uniform in the spanwise direction and non-uniform in the other directions, with nodes clustered around the wall and near the trailing edge in the wake. The distance in wall units from the second off-wall grid point (where the wall model is required to match the local LES velocity) to the wall is in the straight portion of the hydrofoil about $\Delta x_2^+ = 120$. Compared to the full LES performed by Wang & Moin (2000), this simulation has a spanwise domain width that is half of the original one.

In figure 4 the mean velocity magnitude computed using the immersed-boundary technique with wall modeling is compared with the experimental (Blake 1975) and full LES (Wang & Moin 2000) data. Result from the LES of Wang & Moin (2002) on a body-fitted mesh with the same equilibrium stress-balance model is also plotted for reference. The velocity magnitude, defined as $U = (U_1^2 + U_2^2)^{1/2}$, is normalized by its value U_e at the boundary layer edge. The vertical coordinate is measured as the vertical distance to the upper surface. Although considerable discrepancies exist with the experimental and full LES results, compared to the simulation without wall model on the same grid (figure 5), the improvement is evident.

The largest deviation between the present predictions and the full LES solution occurs at $x_1/H = -1.625$ where the second off-wall grid point, used as outer boundary for the wall model, is far from the wall. The location of the outer-boundary for the wall model (first off-wall LES grid point in Wang and Moin (2002) vs. second off-wall point in the

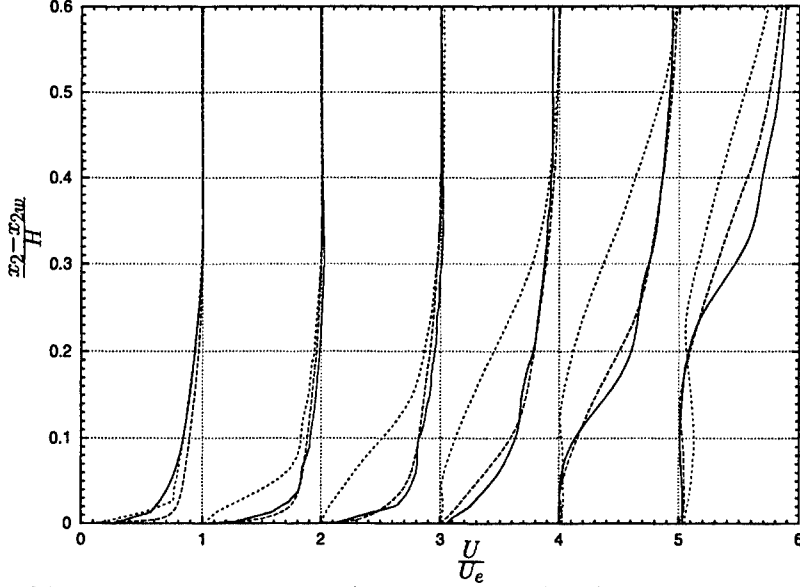


FIGURE 5. Mean velocity magnitude at (from left to right) $x_1/H = -3.125, -2.125, -1.625, -0.625, 0, \dots$, full LES (Wang & Moin 2000); —, present LES with wall model; ---, present LES without wall model.

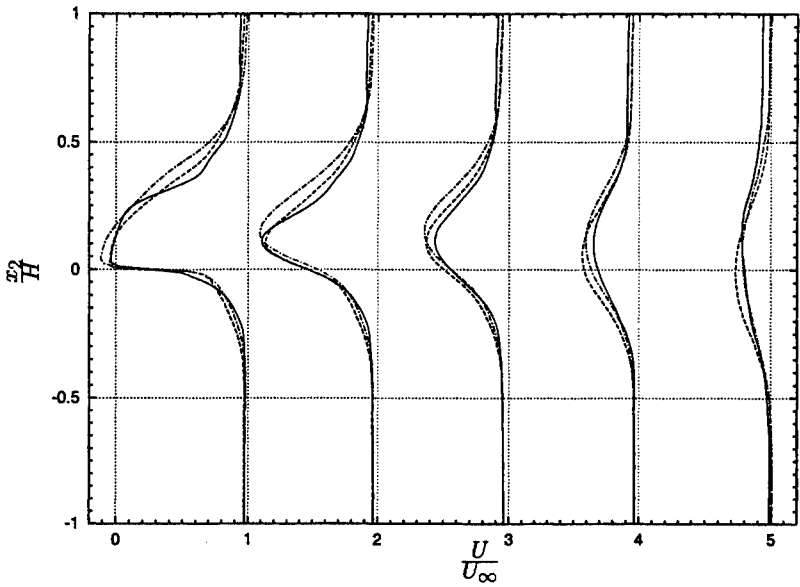


FIGURE 6. Profiles of the normalized mean streamwise velocity in the wake, at (from left to right) $x_1/H = 0, 0.5, 1.0, 2.0, 4.0, \dots$, full LES (Wang & Moin 2000); —, present calculation; ---, LES with wall model (Wang & Moin 2002).

present work) constitutes a major difference between the present model implementation and that of Wang & Moin. This could be the cause for the observed discrepancies between the two wall model solutions, and a grid refinement study in the cross-stream direction is needed to test the sensitivity of the wall model to the outer boundary location. It is noted that the present simulation predicts the separation point near the trailing edge

quite well but a strong deviation from the full LES is observed in the upper part of the trailing-edge station $x_1/H = 0$, possibly due to the small spanwise dimension. As pointed out by Wang & Moin (2002), their spanwise domain size, at half the hydrofoil thickness, was too small. In the present simulation it is even smaller by another 50%. New simulations are underway in order to rectify the above deficiencies and to test the capability of the method to compute the turbulent stresses. Finally, figure 6 depicts the wake profiles in terms of the mean streamwise velocity, which show reasonable agreement with the full LES and previous wall modeling results.

4. Acknowledgments

Fabrizio Tessicini has been partially supported by the Ministero delle Infrastrutture e dei Trasporti in the framework of the INSEAN research plan 2000-2002.

REFERENCES

- BALARAS, E., BENOCCI, C., PIOMELLI, U. 1996 Two-layer approximate boundary conditions for large-eddy simulations. *AIAA J.* **34**, 1111-1119.
- BLAKE, W.K. 1975 *A Statistical Description of Pressure and Velocity Fields at the Trailing-Edge of a Flat Structure*. DTNSRDC Report 4241, David Taylor Naval Ship R. & D. Center, Bethesda, Maryland.
- CABOT, W. & MOIN, P. 2000 Approximate wall boundary conditions in the large-eddy simulation of high Reynolds number flow. *Flow Turb. Combust.* **63**, 269-291.
- FADLUN, E.A., VERZICCO, R., ORLANDI, P. & MOHD-YUSOF, J. 1999 Combined immersed-boundary finite difference methods for three-dimensional complex flow simulations. *J. Comp. Phys.* **161**, 35-60.
- GERMANO, M., PIOMELLI, U., MOIN, P. & CABOT, W.H. 1991 A dynamic subgrid-scale eddy viscosity model. *Phys. Fluids A* **3**, 1760-1765.
- IACCARINO, G & VERZICCO R. 2003 Immersed boundary technique for turbulent flow simulations. To appear in *Applied Mech. Rev.*
- LILLY, D.K. 1992 A proposed modification of the Germano subgrid-scale closure method. *Phys. Fluids A* **4**, 633-635.
- WANG, M., & MOIN, P. 2000 Computation of trailing-edge flow and noise using large-eddy simulation. *AIAA J.* **38**, 2201-2209.
- WANG, M. & MOIN, P. 2002 Dynamic wall modeling for LES of complex turbulent flows. *Phys. Fluids* **14**, 2043-2051.

Towards LES wall models using optimization techniques

By Jeremy A. Templeton, Meng Wang AND Parviz Moin

1. Introduction

Large-eddy simulations (LES) of high Reynolds number flows are difficult to perform due to the need to include a large number of grid points in the near wall region. While LES models the small scales of the flow and resolves the large, dynamically important scales, near the wall, eddies scale with the distance from the wall and move increasingly nearer to the wall as the Reynolds number increases. These eddies are dynamically important despite their small size. Unfortunately, the eddy viscosity sub-grid scale (SGS) models only make a small contribution to the total Reynolds stress. This makes these models invalid near the wall (Jimenez & Moser 2000), unless the LES grid is sufficiently refined to resolve the near-wall vortical structures. Therefore, the number of grid points for an LES scales as Re^2 in an attached boundary layer (Baggett, Jimenez & Kravchenko 1997). This is only a slight improvement on the scaling for a full direct numerical simulation (DNS) of $Re^{9/4}$.

The technique of wall modeling was developed to reduce the Reynolds number scaling of LES resolution so that LES could be applied in practical situations. For recent reviews, see Cabot & Moin (1999) and Piomelli & Balaras (2002). The approach has a long history dating back to atmospheric science and oceanographic applications. Limited by the computational power of the time, Deardorff (1970) was the first to implement a model for the wall layer in an LES of a channel flow at infinite Reynolds number. He implemented constraints on wall-parallel velocities in terms of the wall-normal second derivatives to ensure the LES satisfied the log-law in mean. The wall transpiration velocity was set to zero. The first "modern" wall model was developed by Schumann (1975). It is a modern wall model in the sense that the wall stresses are determined directly by an algebraic model. The wall stresses were found by assuming that they were in phase with the velocity at the first off wall grid point and that the deviation from their mean was proportional to the deviation of the velocity from its mean. Since the flow was in a channel, both the mean wall stresses and mean velocities were known. The transpiration velocity was set to zero. Many improvements to this basic model have been proposed and tested, see e.g. Piomelli *et al.* (1989), Mason & Callen (1986), Grötzschbach (1987), and Werner & Wengle (1991), although none of these attempts produced a wall model robust enough for use in most engineering flows.

To address this robustness issue in wall modeling, several investigators used more elaborate near-wall flow models to compute the wall stresses (see e.g. Balaras *et al.* (1996) and Cabot & Moin (1999)). This type of approach divides the computational domain into two regions: one near the wall and one away from the wall. A simplified set of equations based on turbulent boundary-layer (TBL) approximations are solved on a near wall grid separate from the outer LES grid, subject to boundary conditions determined from the outer LES velocity together with the no-slip wall. The computed wall stress is then provided to the LES as a boundary condition. While this method does require

the solution of an extra set of equations, the simplifications made in these equations makes its cost much less than the evaluation of the LES equations. This method was tested in a plane channel, square duct, and rotating channel by Balaras *et al.* (1996) and in a plane channel and backward-facing step by Cabot & Moin (1999). More recently, Wang & Moin (2002) used a variant of this method to perform an LES of an airfoil trailing edge flow. The results are generally better than those of the algebraic models, since the TBL equations can account for more of the physics of the flow. However, there is insufficient evidence of robustness of this approach, particularly on coarse meshes and at high Reynolds numbers.

The difficulty of formulating a robust wall model was highlighted by Cabot (1996). In that work, a backward facing step LES was performed using the “exact” time series of the wall stress from a resolved LES as the wall model. The results of this approach were not satisfactory and in fact not an improvement over the other types of wall models previously mentioned. This indicates that SGS and numerical errors play an important role in the coarse grid LES, which has not been accounted for by the previous wall models. To investigate this hypothesis and determine what information a wall model must provide to the LES, Nicoud *et al.* (2001) used optimal control techniques to compute the wall stresses in a channel LES at $Re_\tau = 4000$. A cost function was defined to be the difference between the plane-averaged LES streamwise and spanwise velocity fields and their known mean values (log-law in the streamwise direction and zero in the spanwise direction). Adjoint equations were used to determine the cost function derivatives, and iterations were performed at each time step to determine the best wall stress. Since the iterations were not performed over a large time window, this approach was sub-optimal. Linear stochastic estimation (LSE) was then used to determine a feedback law for the wall stresses based on their correlation with LES velocities obtained from the sub-optimal control algorithm.

Many important lessons were learned from this work involving wall models based on optimal control theory. Unfortunately, this approach proves to be impractical due to the high computational cost required for the suboptimal control since it requires both the solution of adjoint equations and many iterations to achieve convergence in the wall stresses. Furthermore, the cost function is based on known target data, making the model non-predictive. Baggett *et al.* (2000) also demonstrated that the LSE models generated from such computations are too sensitive to the numerical parameters to construct a universal LSE coefficient database. The objective of the present work is to develop a low-cost, robust wall model to achieve the accuracy of the sub-optimal control technique without an *a priori* target solution. A cost function based on a Reynolds-averaged Navier Stokes (RANS) solution will be constructed in Section 2 to make the model predictive, and in Section 3, the problem will be formulated in an optimal shape design setting in an attempt to reduce the computational cost. Some test results and discussions are presented in Sections 4 and 5.

2. Cost function

In order to make the wall model predictive, an easy to evaluate cost function near the wall using quantities not known *a priori* must be defined. To this end, a RANS model is used to provide the target velocity. This is motivated by the recognition that the near-wall region of a high Reynolds number boundary layer is more appropriately modeled by

RANS than by a coarse grid LES with filter length larger than the integral scale of the turbulence.

In the present work, the RANS model is obtained from a simplified version of the TBL equation model used by Wang & Moin (2002):

$$\frac{d}{dy} \left[(\nu + \nu_t(y)) \frac{du_i}{dy} \right] = \frac{1}{\rho} \frac{\partial p}{\partial x_i} \Big|_{LES}, \quad i = 1, 3 \quad (2.1)$$

$$\nu_t(y) = \kappa \nu y^+ \left(1 - e^{-y^+/A} \right)^2, \quad y^+ = y u_\tau / \nu.$$

These equations model all Reynolds stresses through a damped mixing length eddy viscosity, and explicitly account for the pressure gradient which is assumed constant across the wall layer and is imposed by the LES. To complete the model, a no slip condition is applied at the wall and the outer boundary is set to be the LES velocity. The resulting velocity profile should be interpreted as the ensemble averaged velocity profile given the local LES state. It can therefore be expected that, on average, the resolved LES should match the RANS solution near the wall. Note that this model is chosen for simplicity in this initial attempt, and there are likely better models for this application that will be explored in future work.

In an overlapped region consisting of N LES grid points in the wall-normal direction, cost functions are devised to match the LES and RANS solutions on average. An attractive method in a statistically stationary flow would be to use a running time average to provide the target velocities. However, if the control authority is restricted to the current time, this approach becomes impractical since the flow at the current time would contribute only a small fraction of the total cost function. This makes it difficult to determine the control since the cost function is insensitive to it. If the control is explicitly computed as a function of time, then adjoint equations have to be integrated backward in time to find a correct solution over a sufficiently large time window which contains enough statistical samples.

An alternative is to use the current state as the statistical sample. Thus, the first cost function is defined to be the \mathcal{L}_2 difference between the LES and RANS states:

$$J_{\mathcal{L}_2} = \int_S \sum_{n=1}^N \left((u_{RANS,1}|_{y_n} - u_{LES,1}|_{y_n})^2 + (u_{RANS,3}|_{y_n} - u_{LES,3}|_{y_n})^2 \right) dS, \quad (2.2)$$

where S is the surface and y_n are the locations of the n overlap points. In this way, a sufficient number of samples of the flow state are used to make a meaningful average. Also, the cost function is based only on quantities at the current time step, so no history information is required. This type of cost function is also compatible with the gradient evaluation methods used in this work (see Section 3).

Other cost functions can also be formulated for this problem. A cost function based on the average deviation of the LES and RANS is:

$$J_A = \left(\int_S \sum_{n=1}^N ((u_{RANS,1}|_{y_n} - u_{LES,1}|_{y_n}) + (u_{RANS,3}|_{y_n} - u_{LES,3}|_{y_n}))^2 dS \right)^{1/2}. \quad (2.3)$$

This cost function is similar to that used by Nicoud *et al.* (2001). However, as shown in Section 4, this cost function performs quite poorly. Analysis of its gradients indicates that they do not capture the sign information correctly in some regions (gradient computation will be discussed in the next section). In order to retain more information and move in

the direction of feedback control, a signed cost function has also been used:

$$J_S = \int_S \sum_{n=1}^N ((u_{\text{RANS},1}|_{y_n} - u_{\text{LES},1}|_{y_n}) + (u_{\text{RANS},3}|_{y_n} - u_{\text{LES},3}|_{y_n})) dS. \quad (2.4)$$

When this cost function is used, the control strategy is shifted to force the cost function to zero rather than minimizing it. It was thought that this approach might better take advantage of the method being used for gradient evaluation, but it only resulted in a moderate improvement (see Section 4).

The choice of N in (2.2) - (2.4) should be made to include as many matching layers as possible while remaining in the region where the RANS model is a reasonable approximation for the given local flow. Furthermore, the LES velocity too close to the wall may involve large errors (Cabot 1996) and thus is not suitable as a RANS boundary condition. In the calculations presented in this article, N has been chosen to be three.

Two important points should now be noted. First, while all the cost functions here are based on matching RANS and LES velocities, other quantities could also be used. These could include matching vorticity or energy fluxes with suitable models. Second, it may not be possible or desirable to reduce the cost function to zero. Doing so could artificially reduce the turbulence fluctuations of the flow. Also, if an inexpensive scheme is required, it may not be possible to fully optimize the solution. Thus, the cost function must act as a suitable quantity for feedback regulation, rather than for minimization.

3. Optimization using shape design techniques

Optimal shape design consists of a set of techniques for optimizing a shape to achieve an engineering objective (e.g. Mohammadi & Pironneau 2001). Several approaches have been developed in this field that have had some success in reducing the computational expense of the optimization procedure. In an attempt to bring these techniques to bear, the wall modeling problem is formulated in this framework.

In general, the formulation is to consider a partial differential equation $A(U, q, a) = 0$ in a region Ω satisfying boundary conditions $b(U, q, a) = 0$ on $\partial\Omega$. The optimization is performed to determine

$$\min_a \{ J(U, q, a) : A(U, q, a) = 0 \forall x \in \Omega, b(U, q, a) = 0 \forall x \in \partial\Omega \} \quad (3.1)$$

for some cost function $J(U, q, a)$. In this formulation, U is the state, q the shape, and a are the control variables. The gradient of the cost function with respect to the control variables is then:

$$\frac{dJ}{da} = \frac{\partial J}{\partial a} + \frac{\partial J}{\partial q} \frac{\partial q}{\partial a} + \frac{\partial J}{\partial U} \frac{\partial U}{\partial q} \frac{\partial q}{\partial a}. \quad (3.2)$$

The standard technique for solving this equation is to use an adjoint method interfaced with a gradient minimization technique. But, as previously noted, this can be expensive and present data storage difficulties in time-accurate computations. Since it is the last term in (3.2) that requires the adjoint evaluation, Mohammadi & Pironneau (2001) suggest the following assumption when the controls and the cost function share the same support:

$$\frac{dJ}{da} \approx \frac{\partial J}{\partial a} + \frac{\partial J}{\partial q} \frac{\partial q}{\partial a}. \quad (3.3)$$

This assumption is called the method of incomplete sensitivities since the sensitivity to

the state gradient is ignored. The use of this method has been explored in this work since it has produced positive results in the optimization of aerodynamic shapes. For examples, see Mohammadi (1999), Mohammadi *et al.* (2000), and Mohammadi & Pironneau (2001), although these are all steady, two-dimensional applications. Since no rigorous proof on the applicability of this technique exists and its usefulness is based on purely empirical studies, it was not known how well it would perform in a full LES. Furthermore, the present cost function is not defined exactly on the support of the control, although it is defined in a small neighborhood of the control. While these factors will produce errors, the gradient evaluation needs only accurately predict the sign of the gradient and capture to some degree the difference in magnitudes of the derivatives with respect to different control parameters. A goal of this work is to determine if the amount of information contained in this gradient is sufficient for application to wall boundary conditions.

In order to apply the incomplete sensitivity assumption, the control must be related to shape design parameters. B-splines spaced evenly along the surface (although not enough to form a complete basis) are used to parameterize deformations normal to the surface. The control parameters, a_i , are then the spline amplitudes. The gradient of the cost function with respect to these parameters can be computed using finite differences by perturbing each parameter by a small value, ϵ , and then using (3.3) to evaluate the gradient based on the current state information. It is not necessary to recompute the actual geometry or grid because all the state variables of interest can be stored and matched to the new surface. The parameter ϵ is chosen *a priori* by making it small enough such that the gradient values are independent of it.

Once the cost function gradient is known, the new spline amplitudes can be computed by

$$a_i^{k+1} = a_i^k - \rho \frac{\partial \mathcal{J}}{\partial a_i}, \quad (3.4)$$

where ρ is a descent parameter set in advance and k is the iteration count. The new shape is computed by adding the surface perturbations to the previous shape. To relate this to the wall stresses, the RANS model is used to compute the correction to the equivalent slip velocity on the original surface:

$$u_{w,i}^c = f_{\text{RANS},i}(y_{\text{new}}), \quad i = 1, 3, \quad (3.5)$$

where f stands for the RANS model given by (2.1). This approach is inspired by a Taylor series expansion about the wall (Mohammadi & Pironneau 2001). In this way, it is not necessary to change the computational geometry of the LES.

The total slip velocity is given by adding the correction $u_{w,i}^c$ to the old wall slip velocity. Corrected wall stresses can then be computed directly by definition

$$\tau_{w,i} = \tau_{w,i}^o + \frac{1}{Re} \frac{-u_{w,i}^c}{\Delta x_2}, \quad (3.6)$$

where Δx_2 is the local wall normal grid spacing.

While this approach avoids the evaluation of a set of adjoint equations, iterations are still required to converge the solution. Additional function evaluations are also often used to determine an optimal choice for ρ at each iteration. In order to make the wall model practical, these costs must be avoided. Therefore, no iterations are performed at each time step. The cost function gradients are computed and used in a feedback manner to provide a correction. Every a_i is reset to zero at each time step. Also, ρ is taken to be a fixed parameter similar to the gain in a feedback controller. To make up for some of this

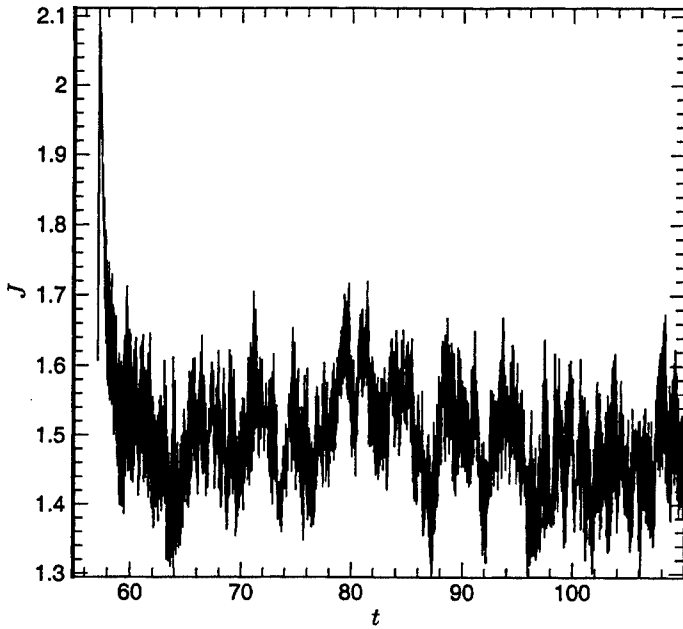


FIGURE 1. \mathcal{L}_2 cost function history.

lost information, a predictor-corrector approach to the control algorithm is used. This is done by using (2.1) to compute a prediction of the wall stress before the optimization is used. It is expected that the prediction will account for the missing physics in the coarse grid LES while the optimization will correct for the numerical and SGS modeling errors. While this approach must be classified as sub-optimal, it is still reasonable to expect a cost function reduction if at each time step the LES velocity is forced in the direction of the reduced cost function.

4. Results

The application of this method to the trailing edge flow simulated previously by Wang & Moin (2000, 2002) has produced mixed results. The first goal is to justify the incomplete sensitivities assumption. The \mathcal{L}_2 cost function history is shown in Figure 1. While the average value is reduced approximately 15% from the initial value, this is not completely out of the range of the cost function fluctuations. It is therefore inconclusive regarding the validity of the assumption. As shown in Figure 2, the predicted wall stress matches the full LES wall stress quite well in some regions for the \mathcal{L}_2 and signed cost functions, but performs poorly in other regions. The separation point is predicted reasonably accurately for both these cost functions. As previously indicated, the average cost function performed more poorly. Figure 3 contains a comparison between the \mathcal{L}_2 cost function results and the predictor alone. The new results are much better in the region near the skin friction peak, although they produce a less smooth skin friction profile, and rather large errors remain in part of the adverse pressure gradient region. Overall, the model demonstrates

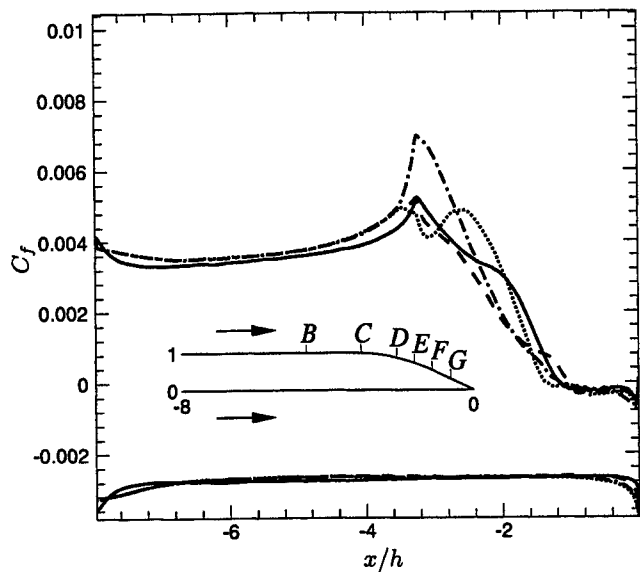


FIGURE 2. Time averaged skin friction over the airfoil surface: -----, \mathcal{L}_2 cost function; - - - , average cost function; ······, signed cost function; ——, full LES of Wang & Moin (2000).

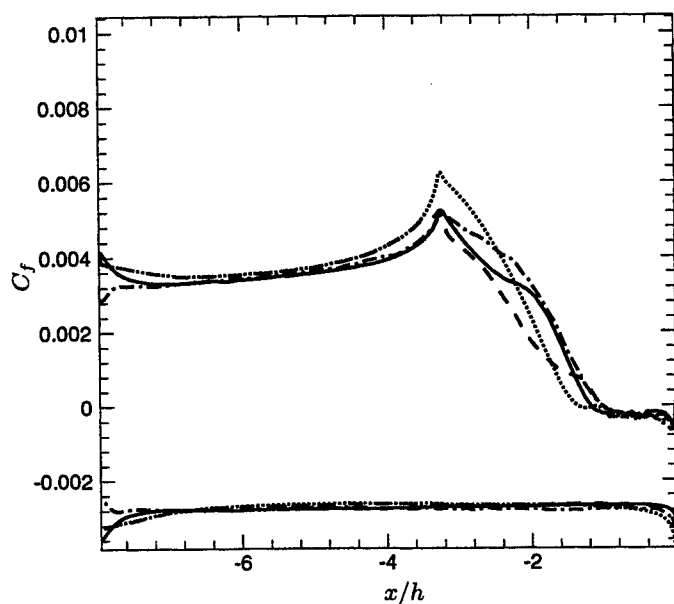


FIGURE 3. Time averaged skin friction over the airfoil surface: -----, \mathcal{L}_2 cost function; ······, predictor only; ——, full LES of Wang & Moin (2000); - - - , TBL model of Wang & Moin (2002).

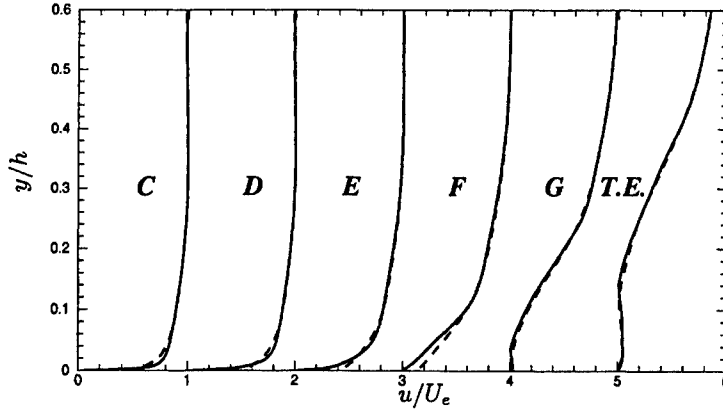


FIGURE 4. Mean velocity magnitude profiles at several trailing edge stations: --- , \mathcal{L}_2 cost function; — , full LES of Wang & Moin (2000). Locations are those indicated in Figure 2. T.E. is the trailing edge point.

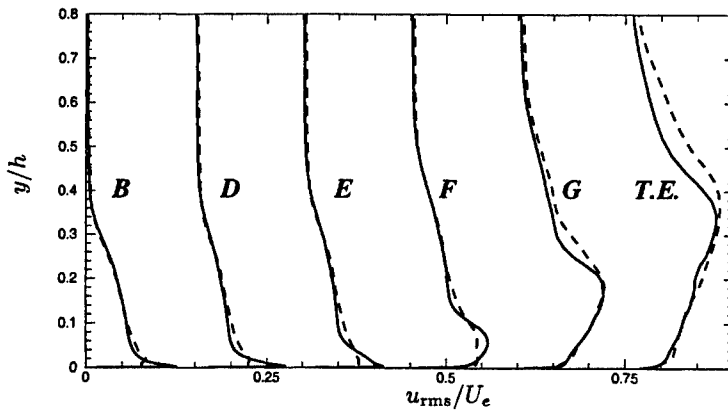


FIGURE 5. Streamwise component of turbulence intensities at several trailing edge stations: --- , \mathcal{L}_2 cost function; — , full LES of Wang & Moin (2000). Locations are those indicated in Figure 2. T.E. is the trailing edge point.

some improvement over the simple wall model used as a predictor, but is less accurate than the full TBL equation model used in Wang & Moin (2002).

Comparison of the velocities between the full LES and wall modeled LES (based on the \mathcal{L}_2 cost function, which produced the best results) are quite good. As shown in Figures 4 and 5, the coarse grid LES is able to match the resolved LES very closely. The main (moderate) discrepancy occurs in the turbulent intensities near the wall. This is not unreasonable since these quantities were not included in the cost function and it may in fact not be possible to capture these regions accurately because the LES grid does not resolve the intensity peak. When compared to the results of Wang & Moin (2002) using only the predictor, the results are found to be comparable and in fact are worse for

the two cost functions not shown. Therefore, it is difficult to draw definitive conclusions about the effect of the gradient based optimization procedure on the velocity field.

5. Channel flow analysis

In order to evaluate the proposed wall model in a more controlled environment, the algorithm has been implemented in the plane channel LES of Nicoud *et al.* (2001). This is a simpler and well known case, so the model can be more readily analyzed. It was immediately noticed that, unlike the trailing edge case, the cost function gradients could not be made independent of the small parameter ϵ used in the finite-difference computation. The gradients monotonically decreased with ϵ until they reached a value of zero. This result indicated that the incomplete sensitivity approach did not accurately capture the gradients in the channel since Nicoud *et al.* (2001) observed non-zero gradients in the sub-optimally controlled channel. The following analysis is used to explain these results, as well as the difficulties encountered with this method in the trailing edge geometry.

Consider a cost function of form

$$J(a) = \int_S f(u(a))dS. \quad (5.1)$$

Since in the current framework, the shape and shape deformations are defined in two dimensions, the surface can be parameterized by taking the y coordinates as a function of x , i.e. $y = g(x)$. Then the cost function becomes

$$J(a) = \int_0^l f(u(x; a))\sqrt{1 + (g'(x))^2}dx. \quad (5.2)$$

Consider a perturbation to this surface parameterized by $\epsilon h(x)$. In the current context, $h(x)$ would correspond to the spline and ϵ to the small change in the control parameter. The new cost function is computed by considering its sensitivity to geometry only, so

$$J(a + \epsilon) = \int_0^l f(u(x; a))\sqrt{1 + (g'(x) + \epsilon h'(x))^2}dx. \quad (5.3)$$

By using a Taylor series expansion, one obtains to $O(\epsilon)$:

$$\sqrt{1 + (g'(x) + \epsilon h'(x))^2} \approx \sqrt{1 + (g'(x))^2} + \epsilon(1 + (g'(x))^2)^{-1/2}g'(x)h'(x). \quad (5.4)$$

When the gradient is computed by taking $(J(a + \epsilon) - J(a))/\epsilon$, the resulting term is

$$\frac{\partial J}{\partial a} \approx \int_0^l f(u(x; a))(1 + (g'(x))^2)^{-1/2}g'(x)h'(x)dx. \quad (5.5)$$

This expression explains the observed cost function gradients. First, it has been demonstrated in both the trailing edge and channel flows that in regions where the surface is flat, the gradients are zero. This is clear since in these regions, $g'(x) = 0$. A similar observation occurs in areas where the surface is a straight line. This is because $g'(x)$ is constant and, in this case, $h(x)$ is symmetric, meaning that whenever $h'(x) > 0$, there is a corresponding x_1 such that $h'(x_1) = -h'(x)$. Thus, unless $f(u(x; a))$ has a very large change between x and x_1 , since $g'(x)h'(x) + g'(x_1)h'(x_1) = 0$ the gradient will be very small.

Finally, it has been observed that in regions of curvature away from the direction of perturbation and for a positive definite $f(u(x; a))$ (such as the L_2 cost function), the

gradient is always positive. This can be seen by examining the product $g'(x)h'(x)$. In these regions, $g'(x)$ is always negative and increases monotonically in magnitude. By the symmetry of $h(x)$, the regions where $h'(x)$ is positive correspond to $g'(x)$ having a smaller magnitude, and the regions where $h'(x)$ is negative correspond to $g'(x)$ having a greater magnitude. Thus, the positive contribution is greater in magnitude than the negative contribution, and hence the gradient is positive since $f(u(x; a))$ is positive and varies less than the curvature.

The sensitivity computed by this method is then almost exclusively dependent on the curvature of the function whose information is contained in $g'(x)$. It is difficult to determine how this information could be useful in changing the state u such that the given cost function is minimized in a rigorous and well defined manner. For any cost function defined as above, the incomplete sensitivity method will act in a way directly related to the curvature of the surface. If a correlation exists between reducing this curvature and reducing the cost function, the method may produce reasonable results. However, there is no reason to believe that, in general, reducing surface curvature will be helpful in wall modeling. In fact, as experience in the channel has demonstrated, a region of no curvature still requires control to obtain an accurate solution. Therefore, it is likely that an alternative method must be found for the general application of a wall model.

6. Conclusions and future work

Wall modeling using control theory is a promising new approach for developing robust wall models which account for not only the unresolved flow physics but also numerical and SGS modeling errors. In the present work, a methodology has been proposed to overcome the deficiencies of the model of Nicoud *et al.* (2001) and make the control-based wall model predictive and practical in terms of computational expense. Two critical components, namely the use of RANS velocity profiles as the near-wall LES target in the cost function and the incomplete sensitivity method for gradient evaluation have been examined and tested in a turbulent trailing edge flow.

Based on the results, it is clear that the assumption of incomplete sensitivities is not appropriate for LES wall models with the type of cost function considered in this work. This is at least partly due to the cost function measuring the LES state in the flow and not at the wall. A cost function that is more sensitive to the geometry could be better suited, but it is unclear how to formulate such a cost function for a wall model. Furthermore, there is evidence suggesting that in applications similar to this, the gradient calculated with incomplete sensitivities may have not only incorrect magnitude but also incorrect sign (Marsden *et al.* 2002). Clearly, a more accurate means is needed to compute the gradient.

The use of a cost function matching a RANS profile near the wall may however prove useful in LES wall modeling. It has a solid physical basis, although the RANS model used here is rather rudimentary. More robust RANS models, such the $k-\omega$ model are being considered. In addition to choosing an appropriate RANS model, the choice of matching quantities is also an important factor in the performance of the model. Matching LES and RANS velocities may prove not to be the best quantity to minimize for optimal performance of the model. Cost functions based on vorticity or energy could better account for dynamics that are more important to the large scales in the LES. An investigation of these cost functions and implementation of a RANS model is underway in a channel flow.

Acknowledgments

This work was supported by the Air Force Office of Scientific Research through contract number F49620-00-1-0111 (Dr. Thomas Beunter, program manager). Computer time was provided by NAS at NASA Ames Research Center and the DOD's High Performance Computing Modernization Program though ARL/MSRC. The authors would like to thank Professors Franck Nicoud and Bijan Mohammadi for many helpful discussions.

REFERENCES

- BAGGETT, J. S., JIMENEZ, J., & KRAVCHENKO, A. G. 1997 Resolution requirements in large-eddy simulation of shear flows. *Annual Research Briefs*, Center for Turbulence Research, Stanford Univ./NASA Ames, 51-66.
- BAGGETT, J. S., NICOUD, F., MOHAMMADI, B., BEWLEY, T., GULLBRAND, J., & BOTELLA, O. 2000 Sub-optimal control based wall models for LES - including transpiration velocity. *Proceedings of the 2000 Summer Program*, Center for Turbulence Research, Stanford Univ./NASA Ames, 331-342.
- BALARAS, E., BENOCCI, C., & PIOMELLI, U. 1996 Two-layer approximate boundary conditions for large-eddy simulations *AIAA J.* **34**, 1111-1119.
- CABOT, W. 1996 Near-wall models in large-eddy simulations of flow behind a backwards facing step. *Annual Research Briefs*, Center for Turbulence Research, Stanford Univ./NASA Ames, 97-106.
- CABOT, W. & MOIN, P. 1999 Approximate wall boundary conditions in the large-eddy simulation of high Reynolds number flow. *Flow, Turbulence and Combustion* **63**, 269-291.
- DEARDORFF, J. W. 1970 Numerical study of three dimensional turbulent channel flow at large Reynolds numbers. *J. Fluid Mech.* **4**, 453-480.
- GRÖTZBACH, G. 1987 Direct numerical and large eddy simulation of turbulent channel flows. in *Encyclopedia of Fluid Mechanics*, Cheremisinoff, N. P. ed., Gulf, West Orange, NJ, Chp. 34, 1337-1391.
- JIMENEZ, J. & MOSER, R. D. 2000 LES: where we are and what we can expect. *AIAA J.* **38**, 605-612.
- MARSDEN, A. L., WANG, M., MOHAMMADI, B. & MOIN, P. 2002 Shape optimization for trailing edge noise control. *Workshop on Geometry, Dynamics and Mechanics in Honour of the 60th Birthday of J.E. Marsden*, Toronto, Canada, August 7, 2002.
- MASON, P. J. & CALLEN, N. S. 1986 On the magnitude of the subgrid-scale eddy coefficient in large eddy simulations of turbulent channel flow. *J. Fluid Mech.* **162**, 439-462.
- MOHAMMADI, B. 1999 Dynamical approaches and incomplete gradients for shape optimization. *AIAA Paper* 99-3374.
- MOHAMMADI, B., MOLHO, J. I. & SANTIAGO, J. G. 2000 Design of minimal dispersion fluidic channels in a CAD-free framework. *Proceedings of 2000 CTR Summer Program*, Center for Turbulence Research, Stanford University/NASA Ames 49-62.
- MOHAMMADI, B. & PIRONNEAU, O. 2001 *Applied Shape Optimization for Fluids*, Oxford University Press.
- NICOUD, F., BAGGETT, J. S., MOIN, P., & CABOT, W. 2001 Large eddy simulation wall-modeling based on suboptimal control theory and linear stochastic estimation. *Phys. Fluids* **13**, 2968-2984.

- PIOMELLI, U., FERZIGER, J., MOIN, P., & KIM, J. 1989 New approximate boundary conditions for large eddy simulations of wall bounded flows. *Phys. Fluids A* **1**, 1061-1068.
- PIOMELLI, U. & BALARAS, E. 2002 Wall-layer models for large-eddy simulations. *Ann. Rev. Fluid Mech.* **34**, 349-374.
- SCHUMANN, U. 1975 Subgrid scale model for finite difference simulations of turbulent flows in plane channels and annuli. *J. Comp. Phys.* **18**, 376-404.
- WANG, M. & MOIN, P. 2000 Computation of trailing-edge flow and noise using large-eddy simulation. *AIAA J.*, **38**, 2201-2209.
- WANG, M. & MOIN, P. 2002 Dynamic wall modeling for large-eddy simulation of complex turbulent flows. *Phys. Fluids*, **14**, 2043-2051.
- WERNER, H. & WENGLE, H. 1991 Large eddy simulation of turbulent flow over and around a cube in a plane channel. *Proceedings of the Eighth Symposium on Turbulent Shear Flows*, 1941-1946.

Optimal aeroacoustic shape design using approximation modeling

By Alison L. Marsden, Meng Wang AND Petros Koumoutsakos

1. Introduction

Reduction of noise generated by turbulent flow past a trailing edge continues to pose a challenge in many aeronautical and naval applications. Aeroacoustics problems related to such applications necessitate the use of large-eddy simulation (LES) or direct numerical simulation in order to capture a wide range of turbulence scales which are the source of broadband noise. Much previous work has focused on development of accurate computational methods for the prediction of trailing-edge noise. For instance, aeroacoustic calculations of the flow over a model airfoil trailing edge using LES and aeroacoustic theory have been presented by Wang & Moin (2000) and were shown to agree well with experiments. To make the simulations more cost-effective, Wang & Moin (2002) successfully employed wall models in the trailing-edge flow LES, resulting in a drastic reduction in computational cost with minimal degradation of the flow solutions. With the recent progress in simulation capabilities, the focus can now move from noise prediction to noise control. The goal of the present work is to apply shape optimization and control theory to the trailing-edge flow previously studied, in order to minimize aerodynamic noise. In this work approximation modeling techniques are applied for shape optimization, resulting in significant noise reduction in several cases.

1.1. *Choice of optimization method*

One general distinction among optimization techniques is between gradient-based methods and non-gradient-based methods. The choice of method for a particular problem depends on factors such as the cost of evaluating the function, the level of noise in the function, and the complexity of implementation. Gradient-based methods generally include adjoint solutions and finite-difference methods. Non-gradient-based methods may include pattern-search methods, approximation models, response-surface methods and evolutionary algorithms. In LES-based aeroacoustic shape design, cost-function evaluations are computationally expensive, and hence the efficiency of the optimization routine is crucial. Therefore, a key consideration is cost minimization when choosing an optimization method.

One of the difficulties in gradient-based optimization methods is the calculation of the gradient of the cost function with respect to the control parameters. The most widely-used gradient method is to solve an adjoint equation in addition to the flow equations, as has been successfully demonstrated by Jameson *et al.* (1998) and Pironneau (1984). However, adjoint methods are difficult to implement for time-accurate calculations, and can present data storage issues. Additionally, adjoint solvers are not portable from one flow solver to another. Because of these factors, the method of "incomplete sensitivities" was initially chosen for the gradient calculation. This method, suggested by Mohammadi & Pironneau (2001), ignores the effects of geometric changes on the flow field when computing the

gradient of a surface-based cost function. This makes it simple to use, and far more cost-effective than solving the full adjoint problem. In fact, only a small additional cost to the flow computation is needed for every iteration. Examples demonstrating the method are given by Mohammadi & Pironneau (2001).

Initially, application of the method of incomplete sensitivities produced seemingly promising results, as presented by Marsden, Wang & Mohammadi (2001). However, on further study the method was found to break down for several important cases. A systematic evaluation of the incomplete-sensitivity method was carried out by comparisons with the "exact" gradient in the case of a single control parameter. It was found that the exact and incomplete gradients do not agree with each other; furthermore, they do not always have the same sign, as shown by Marsden *et al.* (2002). This finding shows that neglecting the state contribution to the gradient is not valid for the problem of trailing-edge noise. We thus conclude that the incomplete sensitivities approach is not adequate for the present application.

In choosing an alternate optimization method, we are concerned with identifying a method that has robust convergence properties and yet is computationally feasible. To this end, the method of approximation modeling was chosen for exploration. Approximation modeling was developed for use in engineering optimization problems which require the use of expensive numerical codes to obtain cost function values. Gradient information for these problems is often difficult or impossible to obtain. In addition, many optimization problems have associated data sets which have error, or cost functions which are noisy. For all of these reasons, there has recently been considerable interest in using approximation modeling for optimization with large engineering simulations.

1.2. Introduction to approximation modeling

Approximation modeling is a family of non-gradient-based methods which rely on model, or surrogate, functions to approximate the actual function. Optimization is performed, not on the expensive actual function but on the model, which is cheap to evaluate. The use of approximation modeling for expensive functions has been demonstrated by Booker *et al.* (1999), Serafini (1998), Chung & Alonso (2002) and others. These surrogates can be polynomials, in which case the models are called "response surface" models, or interpolating functions such as splines or more advanced functions.

As an illustration of this method, let us assume we wish to find a minimum of the function $y = f(x)$ within an allowable domain $x_{min} \leq x \leq x_{max}$. The basic procedure using an approximation-modeling technique is as follows. First, we begin with a set of initial data points $\mathbf{x} = [x_1, x_2, \dots, x_n]$ where the function values are known. We then fit a surrogate function through these points to approximate the actual function. We express the surrogate function as $\hat{y} = \hat{f}(x)$. Because the surrogate function is inexpensive to evaluate, its minimum (within the allowable range of x) can be easily found using standard optimization methods. When the minimum is found, the actual function is evaluated at this point, the surrogate fit is updated, and the process continues iteratively until convergence to a minimum function value.

Approximation-modeling methods have several possible variations. One is the choice of surrogate function. Others include the choice of initial data distribution, and the use of merit functions to ensure a good distribution of the data. In this work, results are presented using approximation-modeling methodology on the model problem of Marsden *et al.* (2001). Details of the optimization procedure are discussed in section 3. In section 4, results are presented for a one-parameter case, for which we compare the performance of several surrogate functions. In section 5 we present results of a calculation using two

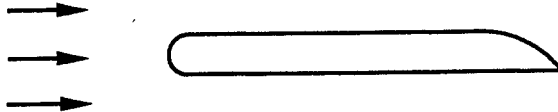


FIGURE 1. Model airfoil used in shape optimization. The right half of the upper surface is allowed to deform.

parameters, and discuss the effects of the initial data set on the final solution. Extension of the method to several parameters is also discussed. Using approximation-modeling methods, a significant reduction in cost function is demonstrated for several one- and two-parameter cases. The method is shown to be robust and computationally affordable. In addition, the method has uncovered a new airfoil shape which gives a greater reduction in noise than previously achieved.

2. Formulation and cost-function definition

We begin by formulating the general optimization problem. Given a partial differential equation $A(\mathbf{U}, \mathbf{q}, \mathbf{a}) = 0$ defined on the domain Ω with control variables \mathbf{a} , state variable \mathbf{U} and design parameters \mathbf{q} , we wish to minimize a given cost function $J(\mathbf{U}, \mathbf{q}, \mathbf{a})$. The control problem can be stated as

$$\min \{ J(\mathbf{U}, \mathbf{q}, \mathbf{a}) : A(\mathbf{U}, \mathbf{q}, \mathbf{a}) = 0 \quad \forall x \in \Omega, \quad b(\mathbf{U}, \mathbf{q}, \mathbf{a}) = 0 \quad \forall x \in \partial\Omega \} \quad (2.1)$$

where $b(\mathbf{U}, \mathbf{q}, \mathbf{a})$ is the boundary condition of the PDE. In our problem, the state equations are the Navier-Stokes equations and the cost function is the acoustic source.

The ultimate goal of this work is to optimize an airfoil shape with fully-turbulent flow at the trailing edge. Because of the cost of LES calculations, the optimization method is first implemented and validated on an unsteady laminar model problem, which is the subject of the present work. The airfoil geometry for the model problem is shown in figure 1 and is a shortened version of the airfoil used in experiments of Blake (1975). The airfoil chord is 10 times its thickness, and the right half of the upper surface is allowed to deform. The flow is from left to right and results presented in this work are at a chord Reynolds number of $Re = 10,000$. Previously, in Marsden *et al.* (2001), results were also presented for $Re = 2,000$, and it was shown that the cost function was easily reduced to zero. The focus of the present work is therefore on the higher Reynolds number.

Before discussion of the optimization method, we outline the derivation of the cost function for the model problem. For unsteady laminar flow past an airfoil at low Mach number, the acoustic wavelength associated with the vortex shedding is typically long relative to the airfoil chord. Noise generation from an acoustically-compact surface can be expressed as follows, using Curle's extension to the Lighthill theory (Curle 1955),

$$\rho \approx \frac{M^3}{4\pi} \frac{x_i}{|\mathbf{x}|^2} \dot{D}_i(t - M|\mathbf{x}|), \quad \dot{D}_i = \frac{\partial}{\partial t} \int_S n_j p_{ij}(\mathbf{y}, t) d^2\mathbf{y} \quad (2.2)$$

where ρ is the dimensionless acoustic density at far field position \mathbf{x} , $p_{ij} = p\delta_{ij} - \tau_{ij}$ is the compressive stress tensor, n_j is the direction cosine of the outward normal to the airfoil surface S , M is the free-stream Mach number, and \mathbf{y} is the source-field position vector. All the variables have been made dimensionless, with airfoil chord C as the length scale, free stream velocity U_∞ as velocity scale, and C/U_∞ as the time scale. The density and pressure are normalized by their ambient values. Note that (2.2) implies the three-

dimensional form of Lighthill's theory, which is used here to compute the noise radiated from unit span of a two-dimensional airfoil. The radiation is of dipole type, caused by the fluctuating lift and drag forces.

The mean acoustic intensity can be obtained from (2.2), as

$$I = \frac{M^6}{16\pi^2|\mathbf{x}|^2} \overline{(\dot{D}_1 \cos \theta + \dot{D}_2 \sin \theta)^2} \quad (2.3)$$

where the overbar denotes time averaging, and $\theta = \tan^{-1}(x_2/x_1)$. To minimize the total radiated power, we need to minimize the integrated quantity

$$\int_0^{2\pi} I(r, \theta) r d\theta = \frac{M^6}{16\pi|\mathbf{x}|} \left(\overline{\dot{D}_1^2} + \overline{\dot{D}_2^2} \right). \quad (2.4)$$

Hence, the cost function is defined as

$$\bar{J} = \overline{\left(\frac{\partial}{\partial t} \int_S n_j p_{1j}(\mathbf{y}, t) d^2\mathbf{y} \right)^2} + \overline{\left(\frac{\partial}{\partial t} \int_S n_j p_{2j}(\mathbf{y}, t) d^2\mathbf{y} \right)^2} \quad (2.5)$$

which corresponds exactly to the acoustic source function.

3. Optimization procedure

In this section, we outline the steps in the algorithm used to optimize the airfoil shape. Our aim is to find the minimum of the cost function defined by (2.5). The cost function, J , depends on control parameters corresponding to the surface deformation. To start the optimization process, the cost function is evaluated for several initial points in the parameter space. The subsequent steps are as follows:

1. Fit a surrogate function through the set of known data points
2. Estimate the function minimum using the surrogate function
3. Evaluate the true function value at the estimated minimum
4. Check for convergence
5. Add new data point to list of known points and go back to 1.

Iterations continue in this way until the parameters have converged to give a final airfoil shape.

The control parameters are defined as follows. Each parameter corresponds to a deformation point on the airfoil surface which must be within the deformation region. The value of each parameter is defined as the displacement of this point relative to the original airfoil shape, in the direction normal to the surface. A positive parameter value corresponds to displacement in the outward normal direction, and a negative value corresponds to the inward normal direction. A spline connects all the deformation points to the trailing-edge point and the left side of the deformation region to give a continuous airfoil surface. Both ends of the spline are fixed. While the surface must be continuous and smooth on the left side, the trailing-edge angle is free to change.

For a given set of parameter values, there is a unique corresponding airfoil shape. To calculate the cost-function value for a given shape, a mesh is generated and the flow simulation is performed until the solution is statistically converged. Because the flow has unsteady vortex shedding, the cost function is oscillatory. In the optimization procedure, the mean cost function \bar{J} (cf. (2.5)) is used, and is obtained by integrating in time until convergence. An example of the oscillatory cost function, and the time-averaged value is shown in figure 2. The case shown corresponds to the original airfoil shape.

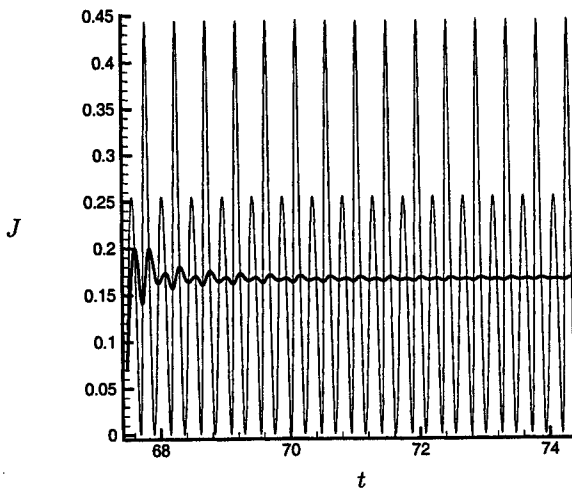


FIGURE 2. Cost function (gray) and mean cost function (solid black) vs. time. Oscillatory cost function is time-averaged until the mean converges. The case shown is for the original airfoil shape.

4. One-parameter results

Results using a single parameter, a , are presented for several surrogate function choices. With a polynomial surrogate function, at least three initial data points are needed. In all one parameter cases presented here, the allowable range of a is $-0.05 \leq a \leq 0.02$. The thickness of the airfoil is 0.1, and the chord length is unity.

Figure 3 shows the evolution of the response surface using a third-order polynomial as the surrogate function. The upper left plot shows the three initial points, and following plots show three iterations on the value of a corresponding to the minimum. With each iteration, the surrogate function evolves to include all known cumulative data. Convergence is reached when the function minimum does not change from one iteration to the next. A least-squares fit of the polynomial is used, so the polynomial does not go exactly through the data points. A total of six function evaluations is required to reach convergence, and a 19% reduction in cost function is achieved.

As expected, an improvement in the function fit is obtained by using a fourth order polynomial, as shown in figure 4. The optimization procedure is the same as for the third order case. A more significant reduction in cost function, 26%, is achieved. However, there is a trade-off in computational cost, since the higher-order polynomial picks up more detail in the function but requires eight function evaluations.

Figure 5 shows results for a single parameter case using a cubic spline as the surrogate function. The optimum airfoil shape corresponding to the minimum cost-function value achieved with the spline fit is shown in figure 6. It is qualitatively similar to the shapes obtained using the polynomial surrogates and these are not shown. Because the surrogate spline is piecewise and fits exactly through the data points, it captures more detail in the function than either polynomial case for the present problem. Similar to the fourth-order polynomial case, the cost function reduction is 27% with 12 function evaluations.

Using only one parameter, we have demonstrated that the approximation modeling

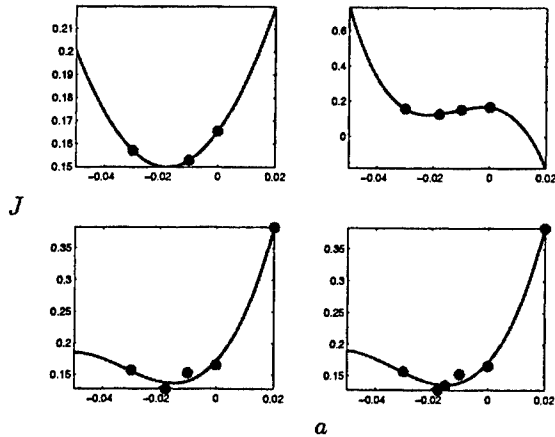


FIGURE 3. Third-order polynomial response surface for one-parameter case. Each plot shows mean cost function \bar{J} vs. shape parameter a where $a = 0$ corresponds to the original shape. Line is surrogate function fit, dots are known function values.

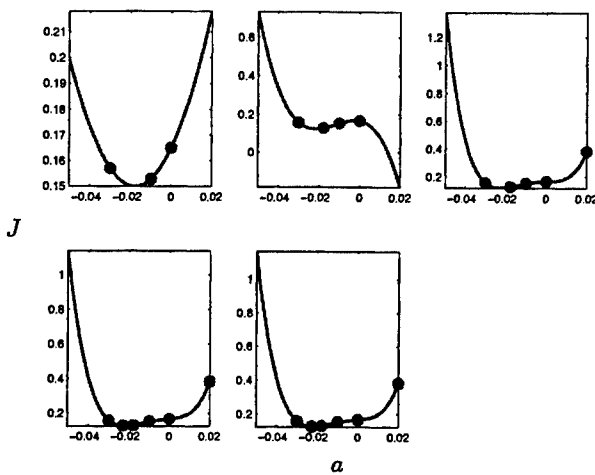


FIGURE 4. Fourth-order polynomial response surface for one parameter case. Each plot shows mean cost function \bar{J} vs. shape parameter a where $a = 0$ corresponds to the original shape. Line is surrogate function fit, dots are known function values.

method is robust and converges to a minimum with a modest number of function evaluations. A significant reduction in cost function has been achieved and the results for all surrogate functions were qualitatively similar. Comparatively, the spline surrogate function resulted in the greatest cost-function reduction. The cases using polynomials emphasize that it is undesirable to use low-order polynomials as global models, since they are unable to capture details of the function such as multiple local minima. However, there is also danger in increasing the order of the polynomial, due to oscillations between the data points known as the "Runge" phenomenon. To avoid these problems, one may wish to use a "trust region" method, in which the polynomial model is restricted to a region near the minimum, where the function is approximately quadratic.

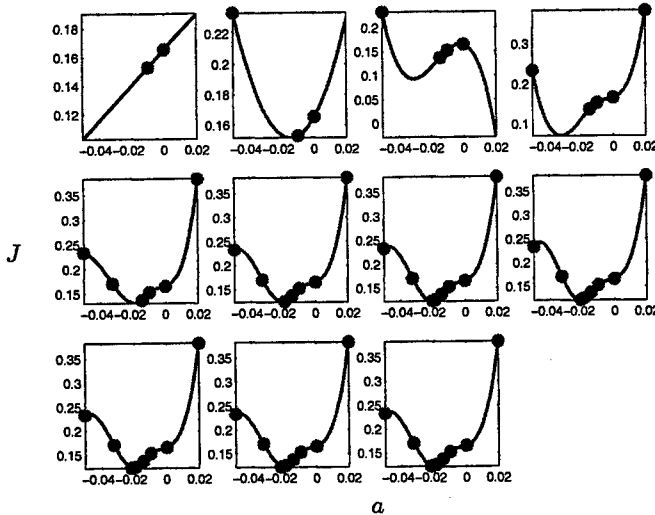


FIGURE 5. One-parameter case with cubic spline as surrogate function. Each plot shows mean cost function \bar{J} vs. shape parameter a , where $a = 0$ corresponds to the original shape. Line is surrogate function fit, dots are known function values.

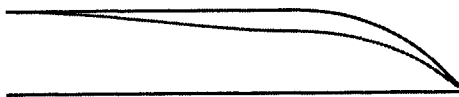


FIGURE 6. Initial (black) and final (gray) airfoil shapes using one parameter with spline as surrogate function.

5. Two parameters

Although the results using one parameter are very promising, the true test is whether the computational cost remains reasonable when the method is extended to more parameters. In this section, results are presented using two parameters, a and b , for which a biharmonic spline was the surrogate function. The deformation points for parameters a and b are evenly spaced in the deformation region of the airfoil surface. A spline is chosen as the surrogate function, based on the results for the one-parameter test case, and the optimization procedure is the same as in the one-parameter case. We also study the effect of choice of initial data on the final solution. Three sets of initial data were used, which we call A, B and C. For all cases, the parameters are limited by $-0.05 \leq a \leq 0.02$ and $-0.035 \leq b \leq 0.02$. The lower limit corresponds to a straight line connecting the left edge of the deformation region and the trailing edge.

The left side of figure 7 shows the initial data points used for the two-parameter case with data set A. Contours of the mean cost function value, \bar{J} , are shown with parameters a and b plotted on the axes. In this case, the initial data points are not chosen to lie in a particular pattern. The final surrogate-function fit is shown on the right side of figure 7. The cluster of points near the minimum shows the convergence of the solution, and the surface has one minimum valley. The cost-function reduction for this case was

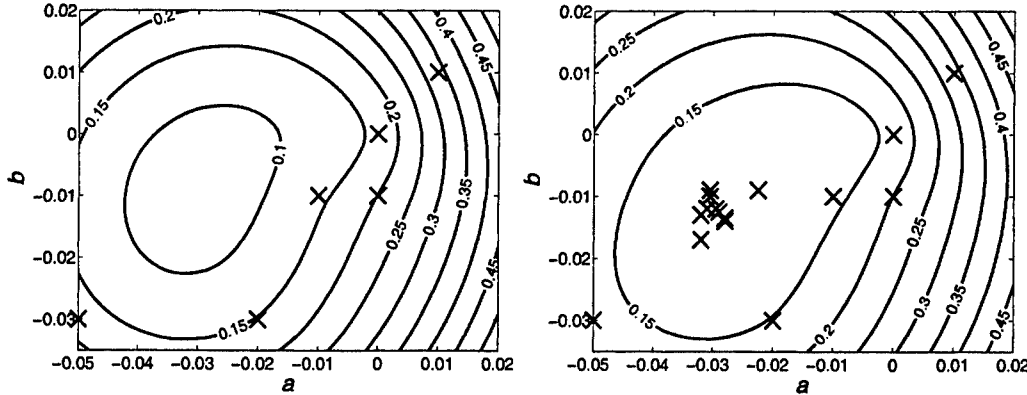


FIGURE 7. Case A: Contours of mean cost function, \bar{J} , vs. parameters a and b for two-parameter case with biharmonic spline as surrogate. Data points marked with \times . Initial data points are shown on left, final converged solution is shown on right.

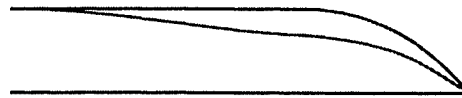


FIGURE 8. Initial (black) and final (gray) airfoil shapes using two parameters with biharmonic spline as surrogate function, data set A.

29% which is a slight improvement over the best one-parameter case. As expected, the two-parameter case requires more function evaluations; 17 evaluations were required for case A. Figure 8 shows the initial and final airfoil shapes for this case.

Contours of the initial surrogate-function fit using data set B are shown on the left of figure 9. In this case, the initial data were chosen in a small star pattern centered around the origin. Like case A, the final surrogate fit, shown in the right of figure 9, has one minimum valley. However, it gives a solution qualitatively very different from case A, suggesting that the actual function has at least two local minima. The optimum airfoil shape for case B is shown in figure 10. In contrast to case A (Fig. 8), the trailing-edge angle in case B has increased instead of decreased. Although the magnitude of the shape deformation is relatively small, the reduction in cost function is significant at 52%. This solution was not previously expected.

Cases A and B show that the initial data set can dramatically impact the final solution, causing the solutions to converge to two distinct local minima. In both cases a viable airfoil shape was found which resulted in a significant cost-function reduction. However, ideally, we desire the solution to converge to the global minimum, and to give the same result independent of the initial data choice. It is, of course, impossible to guarantee convergence to the global minimum, and the cost-function reduction is always limited by the parameter space. However, there are ways to increase our chances of converging to a global minimum and improve robustness. For instance, by choosing an initial data set which covers the entire allowable range of a and b , the solution is not biased toward a minimum in a particular area. To demonstrate this, initial data set C is chosen as a

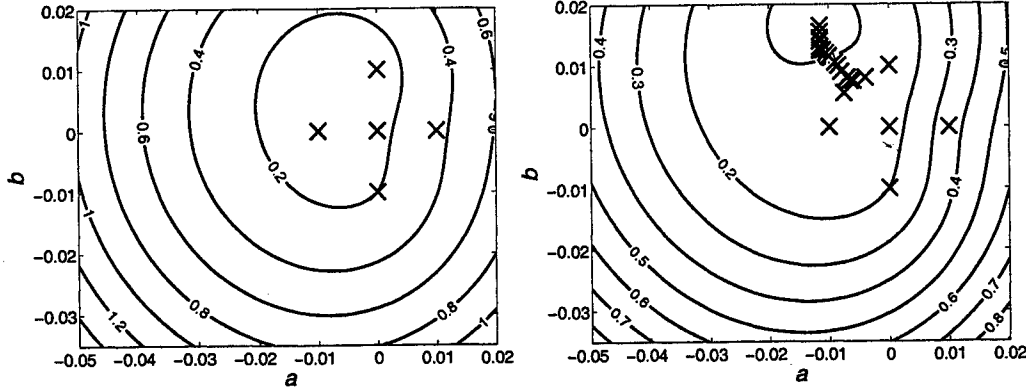


FIGURE 9. Case B: Contours of mean cost function, \bar{J} , vs. parameters a and b for two-parameter case with biharmonic spline as surrogate. Data points marked with x . Initial data points are shown on left, final converged solution is shown on right.

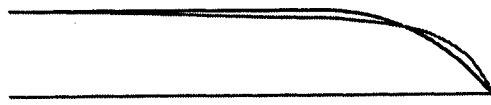


FIGURE 10. Initial (black) and final (gray) airfoil shapes using two parameters with biharmonic spline as surrogate function, data set B.

large star pattern centered around the origin and shown by the surrogate fit in the left of figure 11. The final surrogate fit is shown on the right of figure 11 and this solution gives a cost function reduction of 45%. We notice that the final fit of case C captures two local minima. The final airfoil shape is qualitatively similar to that of case B but the minimum is located in a slightly different position, suggesting that solutions B and C may not be well converged. The total number of function evaluations has been reduced dramatically, from 23 evaluations required for case B to 9 evaluations required in case C.

By introducing a second parameter to the problem, it has been demonstrated that results improve dramatically and the cost of the optimization problem remains manageable. A second parameter also gave the flexibility to find new solutions, as in cases B and C, which are not admissible in the one-parameter space. The importance of choosing an initial data set which spans the parameter space has also been confirmed. It can increase the chance of finding the global minimum and reduce the number of iterations.

The physical reasons for the reduction in cost function can be explained by the vortex-shedding characteristics and associated unsteady forcing on the airfoil. Figure 12 compares vortex-shedding characteristics for the original shape and the final shapes of cases A and C in terms of the instantaneous streamwise velocity. We see that the vortex shedding strength has decreased for both cases A and C compared to the original. As a result, the amplitude of lift fluctuations, which dominate the acoustic dipole source, has been reduced by 12% for case A and 24% for case C. The larger decrease in lift amplitude

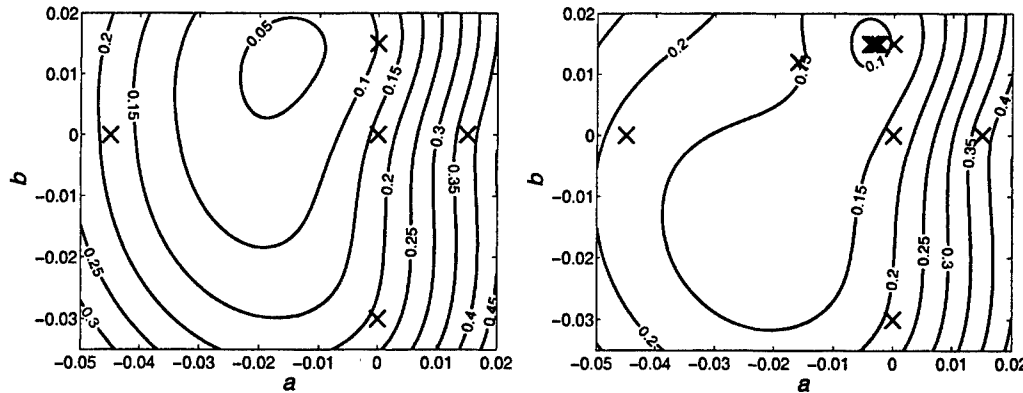


FIGURE 11. Case C: Contours of mean cost function, \bar{J} , vs. parameters a and b for two-parameter case with biharmonic spline as surrogate. Data points marked with \times . Initial data points are shown on left, final converged solution is shown on right.

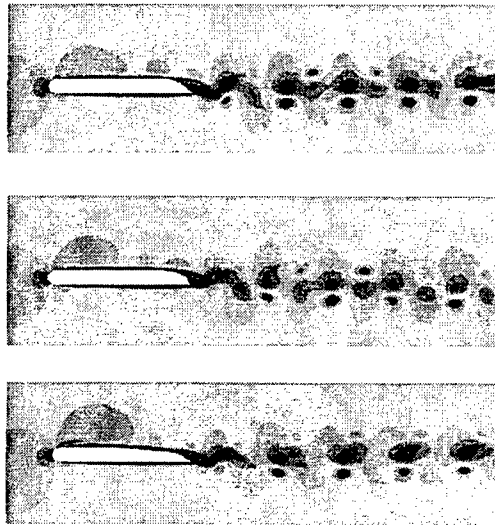


FIGURE 12. Instantaneous streamwise velocity contours for original (top), case C (middle) and case A (lower). Contour levels are the same for all cases, between $-0.4 < u < 1.53$

for case C explains why the reduction in cost function is greater for cases B and C than for case A. The shedding frequencies for all cases are similar. The optimal shape found in case A also shows an increase in mean lift of 40% over the original value, whereas in case C a slight 3% decrease in mean lift is observed. In practical application it is often necessary to ensure that the mean lift is not reduced by the shape optimization. To this end, aerodynamic properties will need to be included using multi-objective optimization methods, which may slightly compromise the large reduction in cost function found in case C.

To extend the method to several parameters, it will be desirable to use a surrogate function which is easy to implement and has good behavior in high dimensions. Many model functions exhibit undesirable behavior such as excessive "wiggles" between data

points when extended to high order. An alternative is the use of kriging functions, a type of interpolating model first introduced in the geostatistics community by South African geologist D. G. Krige. Kriging is based on statistics and random-function theory, and is easy to implement in an arbitrary number of dimensions. The underlying idea is to use a weighted linear combination of values at the sampled data locations to interpolate the function. The best linear estimator is then found by minimizing the error of the estimation. A detailed derivation of the method can be found in Isaaks & Srivastava (1989) and Guinta (2002). Kriging has since been adopted by the optimization community and is now used in many engineering problems.

6. Discussion and future work

A summary of results using several surrogate functions with one and two parameters is presented in table 1. The table clearly shows an improved reduction in cost function with the addition of a second shape parameter. Generally, the cases with greater cost function reduction also require more function evaluations, although a judicious selection of the initial data points can speed up convergence dramatically. It is advantageous to choose initial data which span the entire parameter space. Results using approximation modeling are a nearly two-fold improvement over the results of previous methods presented in Marsden *et al.* (2001).

In future work, the use of kriging functions with several optimization parameters will be explored. Extension to multiple parameters will determine the scalability of this method in terms of the number of function evaluations. It will also determine whether further reductions in cost function are possible, and if the trade-off in computational cost is significant. Additionally, there are several variations on the method used here which could improve convergence and robustness. As shown by Booker *et al.* (1999) and Serafini (1998), the use of a polling step in the algorithm rigorously guarantees convergence to a local minimum. The use of merit functions, as discussed in Torczon & Trosset (1998), to ensure good data distribution will be explored. With this method, a weighting function is employed to determine whether the data points are well distributed throughout the domain. If the data points are clustered together, additional points may be evaluated to improve the surrogate function fit in areas lacking data. To speed up the optimization process, it may be desirable to evaluate the minimum point in parallel with several other points which improve the function fit. These variations of the method will explore the possible cost trade-off between fast convergence to a local minimum and increased chance of reaching a global minimum. The use of multi-objective optimization to include aerodynamic properties (lift and drag) and thickness will also be required in the design of practical trailing-edge shapes.

Once confidence has been gained in the specifics of the approximation-modeling method, optimization of the turbulent trailing-edge flow will be performed. In the turbulent case, the airfoil is not acoustically compact for all the frequencies of interest, and the cost function may need to be reconsidered. Alternatively, an approximation of the cost function can be used so long as it is well correlated with the true acoustic source function. The choice of cost function will be influenced to some degree by whether the objective is to reduce noise in a band of frequencies of primary interest, or to reduce the total radiated power.

surrogate function	parameters	\bar{J}_{orig}	\bar{J}_{optimum}	% reduction	function evaluations
3 rd order polynomial	1	0.166	0.1348	19%	4
4 th order polynomial	1	0.166	0.1223	26%	8
cubic spline	1	0.166	0.1215	27%	12
biharmonic spline, set A	2	0.166	0.1174	29%	17
biharmonic spline, set B	2	0.166	0.0794	52%	23
biharmonic spline, set C	2	0.166	0.0912	45%	9

TABLE 1. Summary of results for several surrogate functions choices with one and two parameters. Cost function reduction and number of function evaluations needed for convergence are compared for all cases.

Acknowledgments

This work was supported by the Office of Naval Research under grant No. N00014-01-1-0423. Computer time was provided by NAS at NASA Ames Research Center and the DoD's HPCMP through ARL/MSRC and NRL-DC.

REFERENCES

- BLAKE, W. K. 1975 A statistical description of pressure and velocity fields at the trailing edge of a flat strut. *Report 4241*, David Taylor NSRDC, Bethesda, MM.
- BOOKER, A. J., DENNIS, J. E., FRANK, P. D., SERAFINI, D. B., TORCZON, V. AND TROSSET, M. W. 1999 A rigorous framework for optimization of expensive functions by surrogates. *Structural Optimization*, **17**, 1–13.
- CHUNG, H. AND ALONSO, J. 2002 Design of a low-boom supersonic business jet using cokriging approximation models. *AIAA Paper 2002-5598*.
- CURLE, N. 1955 The influence of solid boundary upon aerodynamic sound. *Proc. Roy. Soc. Lond. A* **231**, 505–514.
- GUINTA, A. 2002 Use of data sampling, surrogate models, and numerical optimization in engineering design. *AIAA Paper 2002-0538*.
- ISAAKS, E. H. & SRIVASTAVA, M. 1989 *An Introduction to Applied Geostatistics*, Oxford University Press.
- JAMESON, A., MARTINELLI, L. & PIERCE, N. A. 1998 Optimum aerodynamic design using the Navier-Stokes equations. *Theoret. Comp. Fluid Dynamics* **10**, 213–237.
- MARSDEN, A. L., WANG, M. & MOHAMMADI, B. 2001 Shape optimization for aerodynamic noise control. *Annual Research Briefs*, Center for Turbulence Research, NASA Ames/Stanford Univ., 241–247.
- MARSDEN, A. L., WANG, M., MOHAMMADI, B. & MOIN, P. 2002 Shape optimization for trailing edge noise control. *Workshop on Geometry, Dynamics and Mechanics in Honour of the 60th Birthday of J.E. Marsden*, Toronto, Canada, August 7, 2002. <http://www.fields.utoronto.ca/audio/02-03/marsden/marsden/>
- MOHAMMADI, B. & PIRONNEAU, O. 2001 *Applied Shape Optimization for Fluids*, Oxford University Press.

- PIRONNEAU, O. 1984 *Optimal Shape Design for Elliptic Systems*, Springer-Verlag, New York.
- SERAFINI, D. 1998 *A Framework for Managing Models in Nonlinear Optimization of Computationally Expensive Functions*. Ph.D. Thesis, Rice University. cite-seer.nj.nec.com/serafini99framework.html
- TORCZON, V. & TROSSET, M. W. 1998 Using approximations to accelerate engineering design optimization. ICASE TR-98-33 NASA Langley Research Center.
- WANG, M. & MOIN, P. 2000 Computation of trailing-edge flow and noise using large-eddy simulation. *AIAA J.* **38**, 2201–2209.
- WANG, M. & MOIN, P. 2002 Dynamic wall modeling for large-eddy simulation of complex turbulent flows. *Phys. Fluids* **14**, 2043–2051.

Towards sail-shape optimization of a modern clipper ship

By T. Doyle †, M. Gerritsen ‡ AND G. Iaccarino

1. Objective and motivation

Sail-shape optimization is challenging because of the complex coupling between the aerodynamic forces produced by a sailboat's rig and the hydrodynamic forces produced by its hull and underwater appendages: see Marchaj (2000). Yacht designers generally assume a steady-state sailing condition, setting rig forces in equilibrium with hull forces to estimate performance: this assumption forms the basis of widely-used Velocity Prediction Programs or VPPs. Accurate numerical modeling of the complete boat (sails, hulls and appendages) is extremely expensive from a computational point of view, and not practical if many different configurations and flow conditions have to be investigated. In our sail-optimization research, we therefore rely on simplified models to handle the hull forces and the interaction between hull and sail forces. We use CFD to accurately compute the flow past the sails and the aerodynamic forces on the rig.

The typical goal of sail-shape optimization is to produce a configuration that optimizes the velocity made good, VMG (VMG refers to how fast a boat is traveling towards a certain target) for a given apparent wind speed and direction (the apparent wind is the vector sum of the boat velocity and the wind velocity). In many respects, a sail resembles an airplane wing and similarly it generates a lifting force, L , perpendicular to the free stream flow, and a drag force, D , in the direction of the free stream flow. At different apparent wind angles the optimal force configuration will be different. The essential requirement of a sail is to generate a large driving force C_x along the centerline of the boat. Except when sailing dead down wind, this is not possible without producing a heeling force C_y perpendicular to the centerline at the same time. The heeling force must be balanced by the the hull and a side force produced by the underwater appendages. The stability of the hull and the efficiency of the underwater appendages therefore limit the driving power that can be extracted from the wind. The relation between lift and drag, and driving and heeling force is determined by the sail sheeting angle relative to the centerline of the boat. In upwind conditions a sail is set at small sheeting angles meaning that most of the lift produced is directed perpendicular to the centerline, producing a large heeling force and a small driving force. The optimization criterion is therefore generally to maximize the ratio of driving force to heeling force. When a boat turns away from the wind the sheets are eased, which results in the lift contributing more to the driving force and less to the heeling force. Because the hull now needs to balance a smaller heeling force, more lift can be tolerated. When sailing on a beam reach (apparent wind angle of 90 degrees) most of the force produced by the rig acts along the centerline and thus a high lift coefficient is needed. On downwind courses, the only criterion for sail efficiency is maximum drag of the rig.

At present most sail-shape optimization is performed using parametric studies where

† Mech. Eng. Dept, Stanford University

‡ Stanford Yacht Research, Stanford University

design variables such as camber, draft and twist are adjusted in a trial-and-error fashion to maximize a certain performance measure. The performance of a given sail configuration can be evaluated using full-scale testing, wind tunnel testing or numerical simulation. Full-scale testing is accurate, but expensive and time-consuming. Wind-tunnel measurements are also expensive and, in addition, it is difficult to scale real-world performance to model size. Computational Fluid Dynamics (CFD) has the potential to evaluate the performance of a given sail shape accurately. CFD calculations also provide a more detailed description of the flow field than either wind-tunnel testing and full-scale testing, and can therefore contribute to a better understanding of the optimization problem. CFD techniques have been successfully applied to shape-optimization problems in the aerospace industry for a number of years: see Reuther *et al.* (1996), Mohammadi & Pironneau (2001) and Kim *et al.* (2002). A major advantage of using CFD to evaluate the forces produced by a sail is that CFD solvers can be easily integrated with optimization procedures to automatically search for optimized sail shapes.

The goal of our current work is to explore the possibility of using automated optimization algorithms coupled to CFD for sail shape optimization: see Shankaran *et al.* (2002) and Doyle *et al.* (2002). There are two major categories of shape-optimization techniques; adjoint and iterative methods. Adjoint methods calculate the optimal shape via the solution of an adjoint problem obtained from the governing equations describing the fluid flow. This is effective because the cost of an adjoint solution is typically equivalent to that of the original problem and, most importantly, independent of the number of design variables (Kim *et al.* (2002)). The adjoint method has become a popular choice for design problems involving inviscid fluid flow, and has been successfully used for the aerodynamic design of aircraft configurations (Reuther *et al.* (1996)). The major difficulty in using this approach is the definition of the appropriate adjoint equations for viscous flows.

In this work we explore the use of iterative methods. We have chosen two approaches: a classical-gradient based cost-function minimization algorithm and an evolutionary strategy (ES). Both have been successfully applied to shape-optimization problems at the Center for Turbulence Research at Stanford. In the first approach, a cost function characteristic of the performance of the sail is minimized with respect to one or more control parameters. The iterative procedure requires the calculation of the derivatives of the cost function with respect to each of the control parameters at every iteration step. The second optimization approach uses evolutionary algorithms (EAs). EAs are biologically inspired optimization algorithms, imitating the process of natural evolution. EAs do not require gradient evaluations, but use a set of solutions (population) to find the optimal designs. The population-based search allows parallelization, and may avoid premature convergence to local minima. However, the population normally must be large, thus requiring many flow calculations.

Coupling optimization algorithms to CFD calculations requires the integration of various subsystems, such as the grid generation tool, the flow solver, and the optimization algorithm. Initially, we consider a simplified two-dimensional model to facilitate the development of the optimization procedure. We design the procedure so that it can be directly extended to the three-dimensional case. In addition, it is possible that the two-dimensional model will be able to guide the three-dimensional optimization. Once both models have been implemented we will compare the 2D optimization results to the 3D results to evaluate the need for the more expensive 3D calculations.

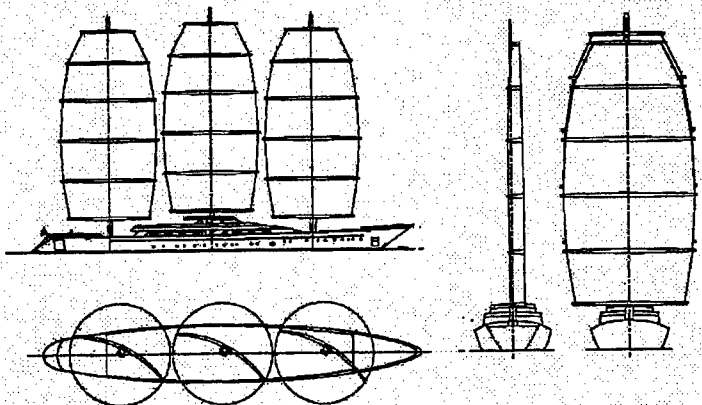


FIGURE 1. Initial geometry.

2. Optimization Approach

2.1. The problem

Because of the complexities involved in developing a general optimization method for sail shapes we start with a relatively simple application: we optimize the yard, camber and sheeting angles of the rig of a modern clipper ship, the Maltese Falcon (figure 1), for upwind performance in moderate winds. The boat has three masts constructed of yards with circular-arc cross-section. The Maltese Falcon will be 87 meters in overall length, with a mast height of 53 meters off the water and a maximum yard length of 22 meters. The rig is based on an original design by W. Proells, which was further developed at Hamburg University in the early 1960's (Wagner (1976)) and is currently being developed by designers from Gerard Dijkstra & Partners and Doyle Sailmakers (Dijkstra (2002)). Wind-tunnel data are available, and eventually real-world measurements will be produced. This will allow a direct assessment of the numerical code.

From a modeling point of view this rig is attractive because the flying shape of the sails will be very close to the shape of the yards. This is due to the construction of the rig, which consists of yards with sails stretched between them. Although the sails will slightly deflect in reality, it is believed that the deformation will not significantly influence the forces on the rig. In addition, the spanwise (vertical) variation of the sail cross section is very limited, and wind-tunnel tests conducted with a model of the rig showed streamlines (visualized using smoke) that were mainly two-dimensional except near the top and bottom of the rig.

2.2. Evolutionary strategies and gradient-based shape optimization

The general objective is the minimization of a properly-constructed cost function, J . The function is characteristic of the performance, and depends on a set of control variables, θ_i . Two optimization algorithms are being developed: a classical gradient-based optimization algorithm and an Evolutionary Strategy.

2.2.1. Gradient-based optimization

The gradient-based optimization procedure requires the evaluation of the derivatives of the cost function with respect to the control parameters in each iteration step. A finite-difference formula is used to calculate the derivatives as:

$$\frac{\partial J}{\partial \theta_i} = \frac{J_{new} - J_{old}}{\Delta \theta_i} \quad (2.1)$$

These derivatives determine the direction of improvement. For the following iteration, a step is taken in this direction and the procedure is repeated until convergence (Mohammadi & Pironneau (2001)):

$$\theta_i^{new} = \theta_i^{old} - \gamma \frac{\partial J}{\partial \theta_i} \quad (2.2)$$

The weighting parameter γ is used to weight the gradient information and changes with cost function and control variables.

It is important to note that during each iteration the number of flow calculations needed is equal to $1 + N$ where N is the number of control variables. Present simulations include 6 control variables and an entire iteration only take a few minutes; three-dimensional simulations, or an increase in the number of control parameters, will make the current procedure computationally expensive.

In our studies, we determined an appropriate γ by trial and error. A comprehensive sensitivity study will be performed in the future.

2.2.2. Optimization using evolutionary strategies

An evolutionary algorithm tries to mimic natural selection to determine the optimal shape. At each step random mutations (changes) to the control variables are attempted and only those solutions that are better than their predecessors are selected in a method that resembles the survival-of-the-fittest natural process. Again a cost function representing performance is defined to compare one solution to another. Our initial implementation is based on a very simple evolutionary strategy called a One + One ES (Sbalzarini *et al.* (2000)). In this scheme an initial solution is calculated J_{parent} ; then each control variable is perturbed (using a random Gaussian distribution with standard deviation σ), and a new solution J_{child} is evaluated. The new solution is compared with the old solution, and if $J_{child} < J_{parent}$ the child becomes the new parent for the next iteration. The standard deviation is adjusted using Rechenberg's 1/5 rule: every $N * L$ iterations (where N is again the number of control variables and L is a constant) the standard deviation is increased (decreased) if the success rate is higher (lower) than 1/5. As the iterations proceed and the optimal solution is approached, the standard deviation continues to drop. In this work, we use $L = 10$. Again, further analysis is necessary to determine the optimal choice.

2.2.3. Sail-shape optimization

When applied to sail-shape optimization the control variables are the parameters that define the sail geometry and configuration with respect to the boat. In our case the relevant control parameters are the camber of the yards and the sheeting angle. Initially we will apply the optimization method to a 2D model of a horizontal cross-section of the rig (taken at mid-mast).

In this study we are interested in optimizing the upwind performance of the Maltese Falcon in moderate winds. As mentioned earlier, defining the cost function is a difficult task in upwind conditions. Ideally the cost function would be the VMG predicted with the use of a VPP, to take into account the hull/sail interaction. At present we do not have access to hull-performance data, so in order to develop our procedure we consider

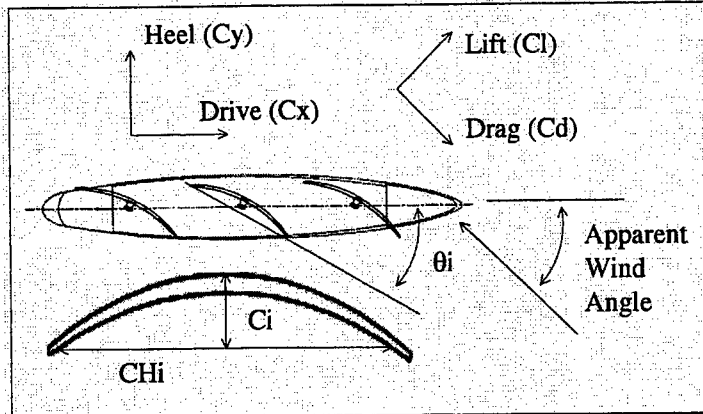


FIGURE 2. Simplified two-dimensional model and definition of the main geometric and flow parameters.

simplified cost functions. Possible simplified cost functions are driving force, ratio of driving force to heeling force, lift produced or ratio of lift to drag.

Our simplified model has nine control parameters: the three sheeting angles (θ_i , $i = 1,2,3$), the three cambers (C_i , $i = 1,2,3$), and the three chord lengths (CH_i , $i = 1,2,3$) as shown in Figure 2. The total force on the rig can be decomposed into lift (C_l) and drag (C_d) or alternatively heeling force (C_y) and driving force (C_x). The other variables in our two-dimensional model are the apparent wind direction and velocity. Initially we consider the chords to be defined by the chord lengths approximately half way up the mast taken from the profile of the original design, but eventually the chord lengths may also be optimized. Because the chord lengths vary in the span-wise direction the spacing between sections at different heights also changes. To date the effect of the spacing (the distance between the 2D sections) has not been investigated but is believed to be an important parameter, and will be the subject of further study.

2.2.4. Flow solution and grid generation

The flow past the sails is calculated using FLUENT 6.0. We use FLUENT's incompressible Reynolds Averaged Navier-Stokes (RANS) solver on non-conformal unstructured grids. In general, unstructured grids (as opposed to structured grids) are more flexible in terms of being able to handle complex and dynamic geometry. Because of the high Reynolds number of the sail flows (of the order of one million), turbulence modeling is required. The turbulence model used in the present calculations is the Spalart-Allmaras turbulence model, which is sufficiently accurate for upwind and close-reaching conditions, and also computationally efficient (Collie *et al.* (2001)). More-sophisticated turbulence models must be used for larger angles of incidence, because of flow separation.

In order to couple FLUENT with our optimization procedure it is necessary to automate the solution process. The automation is accomplished using FLUENT's scripting capability. A central program serves as the interface between the flow solution and the optimization algorithms. The flow-solution interface takes as input the sheeting angles, cambers and chord lengths of each of the sections, together with a description of where each section is placed relative to the center of each mast. A grid is automatically created from the input geometry and then the flow solution is calculated. The entire process takes around 1 minute to produce a solution on a computer with an Athlon 1.2 GHz processor

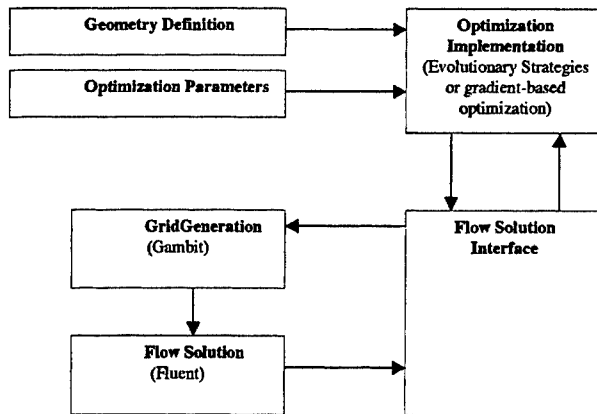


FIGURE 3. Solution Procedure

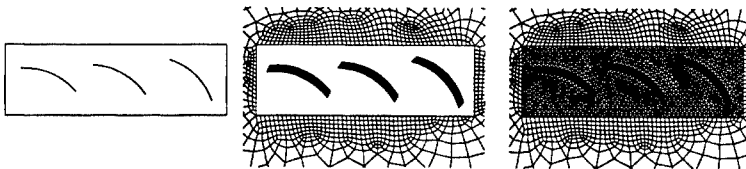


FIGURE 4. Semi-automatic grid generation process steps

using a relatively coarse grid of around 7500 elements. Figure 3 shows a system diagram of the automated solution procedure.

The most challenging aspect of automating the flow solution procedure is the robust and efficient generation of grids to discretize the domain of interest. Here, robust refers to the ability to successfully generate meshes for any possible value of the control parameters. The mesh generation is efficient if it clusters grid points in areas where large gradients of flow variables are expected (such as in the boundary layers) so that a minimal number of grid elements are required to obtain accurate predictions.

The grid generation process starts with defining the three sectional shapes. Once the sections have been defined the region immediately surrounding the sail is clustered densely with grid points in order to properly resolve the boundary layer. Because the gradients are smaller in the stream wise direction than the wall normal direction, we use quadrilateral elements with large aspect ratio. The Spalart-Allmaras turbulence model requires the distance between the first grid point away from the wall to be placed at a non-dimensional distance known as y^+ on the order of 1. After meshing the region immediately adjacent to the sail the remaining domain is discretized using triangular elements. The use of non-conformal grids allows a mismatch between the grid points on the boundary of the inner and outer regions. Fluent uses interpolation to communicate the flow variables from the inner to outer regions.

Triangular elements are used because the algorithm used by Fluent's grid generator Gambit to produce triangular elements is robust, and can handle the varying geometry created by adjusting the camber and sheeting angle of the sections. Quadrilateral elements require fewer elements to discretize the same volume but the current algorithm available in Gambit is not reliable in handling this geometry. We extended the far field

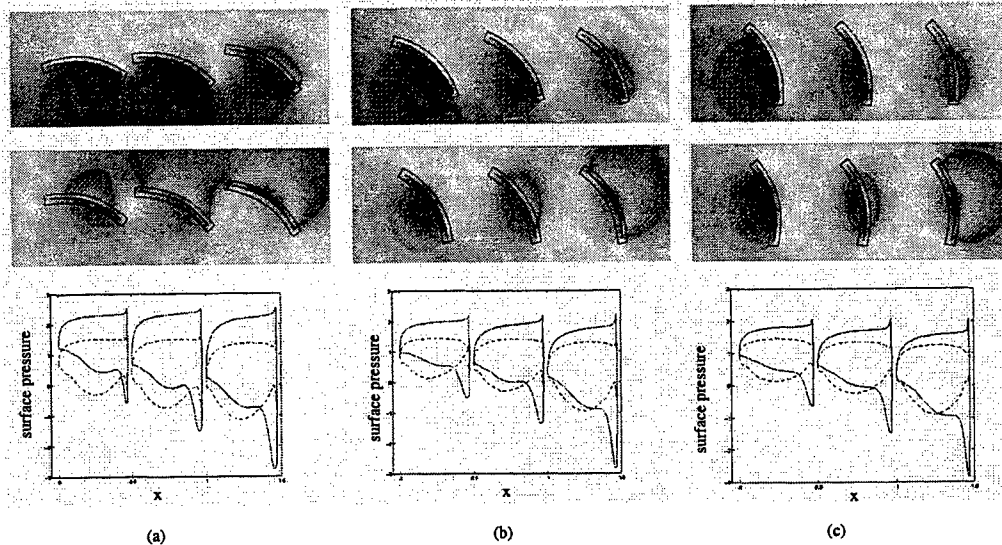


FIGURE 5. Sheeting angle optimization. Top: pressure contours corresponding to J_1 (max C_x). Middle: pressure contours corresponding to J_2 (max C_x/C_y). Bottom: surface pressure distributions; — J_1 - - - J_2 . (a) 30 degrees, (b) 60 degrees and (c) 90 degrees.

region to roughly 20 chord lengths in all directions, and discretized it with quadrilateral elements. The entire process is shown in figure 4.

3. Results

Initial tests were performed on isolated circular arc cross sections to verify our numerical solution method and to gain a better understanding of the aerodynamic properties of such foils. The results were compared to classical theoretical studies. In this section we will focus on two optimization studies.

3.1. Sheeting-angle optimization

The first step in developing an automated sail-shape optimization procedure is to ensure that, for a given apparent wind angle, the sails are set in the optimal configuration. This is straightforward for a single section. Once lift and drag are determined as functions of the angle of attack, the sheeting angle can be set to produce an incidence that optimizes the performance for the given apparent wind direction. With three interacting sections, however, the flow field is dependent on all three sheeting angles and it is not possible to set the optimal sheeting angles *a priori*.

Initially, we consider two simple cost functions J_1 (max C_x) and J_2 (max C_x/C_y): J_1 and J_2 are reasonable choices in upwind and downwind conditions respectively. Optimization runs are performed for both cost functions for apparent wind angles ranging from 30 to 90 degrees. Both optimization strategies were used and lead to identical results with comparable runtime. We present results for apparent wind angles of 30, 60 and 80 degrees in table 1 and figure 5. Table 1 displays the driving force and heeling force coefficients for each apparent wind angle for both cost functions. The optimal sheeting angles are also given. Figure 5 shows plots of static pressure around the sail as well as the pressure distribution on each section.

For all apparent wind angles tested, the cost function J_2 results in more open (larger

Cost Function	Force Coefficient			Sheeting Angle		
	Driving (C_x)	Heeling (C_y)	Aft (θ_1)	Mid (θ_2)	Fore (θ_3)	
$J_1(30)$	0.9304	1.9038	-6.5	-19.3	-31.6	
$J_2(30)$	0.7988	1.4754	-16.0	-26.6	-36.1	
$J_1(60)$	1.4943	1.0116	-42.6	-49.9	-55.8	
$J_2(60)$	1.1327	0.6888	-52.0	-57.3	-60.9	
$J_1(90)$	1.6193	0.3893	-68.4	-70.9	-73.1	
$J_2(90)$	1.2571	0.2499	-77.2	-78.3	-79.6	

TABLE 1. Table 1: Force coefficients and sheeting angles for the optimal sail configuration (the number in parentheses corresponds to the apparent wind angle).



FIGURE 6. Telltales, imagined to be on the leading edge of the aft sail, are shown to lift for the optimal condition predicted using the cost function J_1 , indicating an over-trimmed sail. They stream back for the configuration corresponding to the J_2 optimum, indicating a properly trimmed sail.

angle) sheeting arrangements with a more even pressure coefficient distribution along the length of the sail cross sections. It is interesting to note that if telltales (wool tufts) are imagined to be placed on the leading edge of the sails as shown in Figure 6, cost function J_1 results in an over-trimmed sail with the leeward telltale lifting, while cost function J_2 results in a well trimmed sail with both telltales streaming back.

3.2. Sheetng angle and camber optimization

Initial camber-optimization runs have been performed to investigate the influence of section camber on rig performance. All runs started with sections of 12% camber and the optimal sheeting angles presented in the previous section. In these runs six control parameters are considered: the sheeting angles and the section camber. A summary of the results is presented in table 2. Results are presented only for maximizing the driving force, as problems with convergence of the CFD code prevented conclusive results for optimizing the ratio of driving force to heeling force from being obtained. ratio.

Streamlines are shown in figure 7 for the optimal configurations calculated for maximum driving force. The cambers selected to optimize the driving force are seen to be

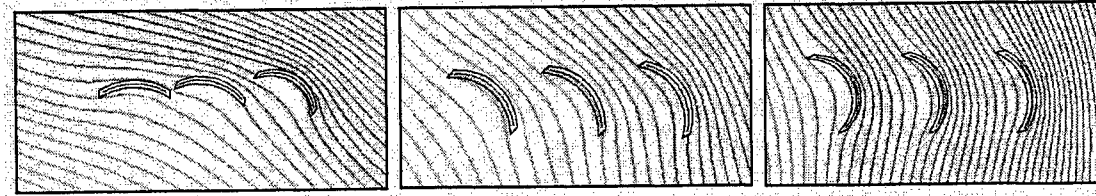


FIGURE 7. Streamlines for maximum driving force for three apparent wind angles: (a) 30 degrees, (b) 60 degrees and (c) 90 degrees.

Cost Function	Force Coefficient		Sheeting Angle			Chamber		
	Driving (C_x)	Heeling (C_y)	Aft (θ_1)	Mid (θ_2)	Fore (θ_3)	Aft (C_1)	Mid (C_2)	Fore (C_3)
$J_1(30)$	1.14	2.35	-0.5	-15.3	-33.5	14.2	16.8	22.8
$J_1(60)$	1.96	1.29	-42.0	-48.6	-58.8	19.4	18.7	26.8
$J_1(90)$	2.39	0.57	-68.2	-71.9	-75.5	30.9	24.4	21.0

TABLE 2. Table 2: Force coefficients, sheeting angles and cambers for the optimal sail configuration (the number in parenthesis corresponds to the apparent wind angle).

greater than the original 12% sections in all cases. For apparent wind angles of 60 degrees and 80 degrees maximizing the driving force can be considered a reasonable cost function but for an apparent wind angle of 30 degrees the heeling force needs to be accounted for. The results for maximizing driving force at 30 degrees are presented as a reference with which to compare the results found in the previous subsection for optimizing the driving force at 30 degrees with only the sheeting angles as control parameters. It is interesting that the optimal sheeting angles are essentially the same as the ones presented before even if the cambers are consistently higher than 12%. Finally, it is interesting to mention that the increase in the performance (as measured by the cost function J_1) ranges from 18% to 32%.

4. Discussion and future work

A CFD-based optimization procedure for sail configuration has been developed and applied to two-dimensional sections of a three-mast clipper ship, the Maltese Falcon.

Optimization runs were conducted using both the gradient-based optimization technique and a scheme based on evolutionary strategies. Both methods converge to the same solution in about the same amount of time, but further studies are required to optimize their performance. The major burden in the gradient-based methods is the calculation of the derivative of the cost functions with respect to the parameters. It is possible that an approximate evaluation of the gradients would be sufficient to drive the optimization process (Mohammadi & Pironneau (2001)).

The value of the parameter γ greatly influences the convergence rate of the gradient-based algorithm. The value we used in this work was found by trial and error. A more thorough sensitivity analysis is required. Within the One + One ES the selection of the initial standard deviation and the constant L should also be investigated. In addition, the One + One ES is the simplest possible ES and there are other strategies that use larger sets of populations to arrive at the optimal configuration.

In this paper we presented the design of our optimization method, and the development of the basic optimization tools. We are currently working on:

- Further validation of the various components of the two-dimensional optimization strategy;
- Development of more realistic cost functions that account for hull forces (and the global force balance) using experimental correlations;
- Refinement of the CFD model to reflect more accurately the aerodynamic characteristics of the rig (three-dimensional effects).

Acknowledgments

TD gratefully acknowledges Gerard Dijkstra (and Associates) for providing the Maltese Falcon geometry.

REFERENCES

- COLLIE, S., GERRITSEN, M. & JACKSON, P. 2001 A review of turbulence modeling for use in sail flow analysis. *School of Engg., Univ. of Auckland, Report No. 603.*
- DIJKSTRA, G. 2002 *Private Communication*
- DOYLE, T., GERRITSEN, M. & IACCARINO, G. 2002 Optimization of yard sectional shape and configuration for a modern clipper ship. *17th Int. Sympo. on Yacht Design and Yacht Construction, Amsterdam.*
- KIM, S., ALONSO, J. & JAMESON, A. 2002 Design optimization of High-Lift Configurations using a viscous continuous adjoint method *AIAA Paper 2002-0844.*
- MARCHAJ, C.A. 2000 *Aero-hydrodynamics of Sailing* 3rd ed. Adlard Coles Nautical, London.
- MOHAMMADI, B. & PIRONNEAU, O. 2001 *Applied Shape Optimization For Fluids*. Oxford University Press.
- REUTHER, J., JAMESON, A., FARMER, J., MARTINELLI, L. & SAUNDERS, D. 1996 Aerodynamic Shape Optimization of complex aircraft configurations via an adjoint formulation *AIAA Paper 96-0094.*
- SBALZARINI, I., SU, L. & KOUOUTSAKOS, P. 2000 Evolutionary optimization for flow experiments *Annual Research Briefs*, Center for Turbulence Research, NASA Ames/Stanford Univ., 31-43.
- SHANKARAN, S., DOYLE, T., GERRITSEN, M., IACCARINO, G. & JAMESON, A. 2002 Improving the design of sails using CFD and optimization algorithms. Presented at *High Performance Yacht Design Conf., Auckland.*
- WAGNER, B. 1976 Sailing ship research at the Hamburg University. A survey of the activities in the years 1961-1967 *Sympo. on the Technical and Economical Feasibility of Commercial Sailing Ships, Liverpool Polytechnic Dept of Maritime Studies, February 1976.*

An experimental investigation of high aspect-ratio rectangular sails

By A. Crook, M. Gerritsen † AND N. N. Mansour

1. Problem statement and relevance of proposed research

The flow around a sail is sensitive to external conditions such as the boat heel, boat speed and atmospheric conditions. The flow may also be Reynolds-number dependent, with typical Reynolds numbers in the range of 1-10 million. Aeroelastic effects of the sail can be important especially in downwind sailing. The performance of the sail is highly dependent on the sail trim. Designing a sail is in many senses more complex than an aircraft wing of high aspect ratio where the ambient conditions are known and are less dynamic. A Velocity Prediction Program (VPP) is used to take into account the performance of the yacht when designing a sail. The VPP solves a set of equations that govern the motion of the yacht. However modelling the aerodynamics of the yacht remains a large problem: see Jackson (1996). Sail performance characteristics usually come from CFD for upwind sails, whereas for downwind sails wind tunnel tests are the preferred method due to the high computational cost of downwind CFD simulations.

At present, VPPs use semi-empirical data to calculate the forces on the hull and sails. An experimental database of sail properties and characteristics would allow the validation of Computational Fluid Dynamics (CFD) codes and their implementation in the VPP.

The fluid dynamics of sails is also poorly understood, although the previous experiments discussed in this brief provide a base from which our knowledge can be further enhanced. The foremost reason for investigating two-dimensional sails is that the flow around three-dimensional sails is highly dependent upon the sail geometry and sailing conditions. For upwind sailing, the sail performance is highly sensitive to sail trim. A three-dimensional model sail is very difficult to trim, and the trim required would change with the varying flow angles and boat heel and direction. A three-dimensional sail experiment also requires that the freestream flow direction change with increasing distance from the foot of the sail. This is necessary to simulate the change in effective wind angle that the sail experiences as it travels through the Earth's atmospheric boundary layer.

Team New Zealand have made use of a twisted-flow tunnel at The University of Auckland in New Zealand (Flay (1996)) for downwind testing of 1/10 scale three-dimensional sail-hull configurations, and this has proved to be very useful in refining existing designs. The flow is twisted using a set of turning vanes, but the twist has to be changed for any change in the boat's speed or heading. For the reasons mentioned, upwind testing of the sail is infeasible.

An experimental investigation of two-dimensional, high-aspect-ratio sails using sail sections representative of that used on modern yachts will therefore provide a generic database that will have a large impact on the sailing industry in terms of providing a database for CFD validation and also enhancing the sail designer's physical understanding of the complex fluid dynamics.

† Stanford Yacht Research, Stanford University

1.1. Sail flow characteristics and the current state of the art

The current state of the art in sail design is different for upwind and downwind sails. For the upwind conditions the camber of the sail and the angle of incidence of the apparent wind to the sail are small, resulting in largely attached flow. A leading-edge separation bubble may be present, especially in the presence of a mast. Wind tunnel testing by racing teams is rare due to the problem of trimming at model scale. Upwind sail performance is highly sensitive to trim because of the small angles of incidence involved, meaning that small changes affect the performance significantly. Upwind sail flow analysis is generally performed using panel methods, and sometimes Euler codes. The design starts as a series of two-dimensional sections that vary with the height of the sail, and that are then blended together to form a three-dimensional sail. The three-dimensional sail is then optimized further by coupling 3D panel methods, some of which can implement twisted onset flow, to a finite-element structural-analysis program to try to predict the flying shape.

Physical understanding of the flow around generic sail sections at representative Reynolds numbers is limited. An enhanced understanding of the flow physics around sail sections is required as a first step to understanding the more complex flow around a three-dimensional upwind sail.

Three-dimensional upwind sails may have separated flow at the head of the sail whilst the flow remains attached elsewhere as a result of the twisted onset flow. This greatly influences the sail design and trim. To reduce separation near the head, the sail is usually twisted also. Generally, strong tip vortices are shed off the head and the foot of the sail. As a result, the induced drag is large, and may contribute as much as 15% of the total boat drag (including hull, rigging and wave drag). Heeling of the boat also significantly affects the performance of the sails. It is also important to understand the sensitivity of the two-dimensional flow to Reynolds number, wind direction, camber and the effects of the mast and its orientation with respect to the sail. Such parameters will affect the transition behaviour of the flow, the size of the leading edge separation bubble if any, and the location of the trailing-edge separation. A correlation of these flow features with the corresponding sail pressure distribution, lift and drag will be invaluable in understanding how to better design sails to provide the greatest amount of forward thrust without exceeding a given rolling moment (Wood and Tan (1978)).

In reaching (i.e. partial-downwind conditions), the angle of incidence is larger. The flow on the main sail and gennaker or spinnaker is complex due to the presence of large scale separation for higher incident wind angles. If the flow is separated at the leading edge it is important to know how large the bubble is and also for what conditions the flow reattaches. At higher angles of incidence, the flow is likely to be unsteady. This unsteady behaviour affects the dynamic behaviour of the sail. Flow simulation requires the use of viscous solvers and turbulence models. Because of their expense and limited expertise in the sailing industry, wind tunnel testing is the preferred method of testing. However, the same limitations of many upwind experiments such as low aspect ratio and purely force and moment data are also seen for the downwind experiments. For the downwind case, it is therefore important to provide flow topology and force/pressure data on sails with realistic camber and high aspect ratio for a range of wind angles and Reynolds numbers.

There have been two seminal series of experiments that have attempted to address some of the fundamental questions regarding 2D sail flows, with and without masts, carried out by Milgram (1971), Milgram (1978) and Wilkinson (1984), Wilkinson (1989) and Wilkinson (1990).

Milgram (1971) investigated highly-cambered (camber ratio (defined as the ratio of

maximum camber to chord) greater than 10) thin airfoils (without masts) with the NACA 65 (Abbott and von Doenhoff (1959), p.386) and $a = 0.8$ (Abbott and von Doenhoff (1959), p.402) mean lines. The experiments were conducted in a water tunnel at three different Reynolds numbers of 6, 9 and 12×10^5 . These high Reynolds numbers were achieved through the use of water as the working fluid and by the use of relatively large-chord sections. The relatively small dimensions of the water tunnel meant that the aspect ratio of the airfoils was low, being equal to approximately 2.2. For highly-cambered sections, a low aspect ratio may cause spanwise three-dimensionality in the separating flow, although this was not addressed in Milgram's report.

Data for the highly-cambered sections is in the form of lift, drag and pitching-moment coefficients for a range of angles of attack. The experimental setup uses dynamometers to measure the forces and moment, with one side of the airfoil clamped and the other side pinned. A consequence of this arrangement is that the airfoil twists under load, with two degrees of twist reported for angles of attack greater than ten degrees.

For the range of camber ratios investigated for the NACA 65 and $a = 0.8$ mean line, the aerodynamic characteristics are similar and do not vary greatly over the limited Reynolds number range in which the tests were conducted. A typical $C_L - \alpha$ plot shows a linear increase in C_L up to 4 degrees angle of incidence, followed by a small drop in C_L and then a recovery in C_L up to approximately 20 degrees. The maximum value of C_L increases with camber ratio for a given thickness distribution as one would expect and ranges between approximately 2 and 2.6. A typical plot of C_D versus C_L shows an almost linear decrease in C_D with C_L until a plateau is reached where C_D is a minimum (approximately 0.06) and fairly constant with C_L until the airfoil stalls and the drag rises sharply. With increasing camber ratio, the sharp increase in drag at the end of the plateau is preceded by a reduction in C_L for increasing C_D . The size of this reversal increases with increasing camber. The pitching-moment coefficient, C_m , defined at the quarter-chord point, is always negative because the center of pressure is significantly aft of the quarter-chord point, and becomes more negative with increasing camber ratio. The slope of the $C_m - \alpha$ through zero angle of incidence is negative, followed by a minimum at around 4 degrees, and then a positive slope before another change in slope just before stall.

These characteristics are different from those of conventional, airfoils with low camber and moderate thickness, the data for which can be found in Abbott and von Doenhoff (1959). Thin airfoil theory predicts pre-stall lift versus angle of incidence fairly well for these sections. For highly cambered, thin sections, the C_L is always less than predicted, with the slope of the curve greater than $2\pi/\text{radian}$ for angles of attack less than the theoretical ideal angle of incidence (defined as the angle of incidence at which the forward stagnation point just lies on the leading edge). The slope is less than $2\pi/\text{radian}$ for angles of attack greater than the ideal angle of incidence (figure 1).

Milgram (1978) tested one mean line (NACA $a = 0.8$) for two different camber ratios (0.12 and 0.15) with circular and elliptic-shaped masts of different diameters. The data are again limited to lift and drag coefficients, although the longitudinal location of the center of pressure is included as a function of C_L . The tests were carried out in the same water tunnel as used Milgram (1971), but without the turbulence screens, which resulted in measured values of C_D for the sections without a mast being 10% higher than in the earlier tests.

The addition of a circular mast with a diameter to chord ratio (d/c) of 0.15, does not significantly change the C_D-C_L behaviour for $CR=0.15$, and extends the C_L range

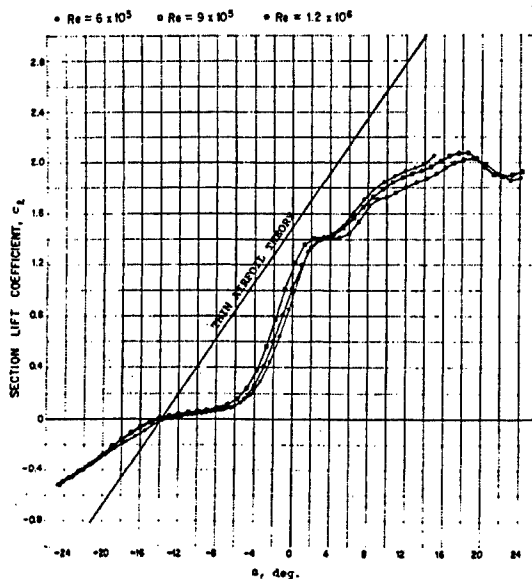


FIGURE 1. Comparison of C_L versus α for NACA 65 mean line with $CR=0.12$ as predicted by thin airfoil theory and measured experimentally (Milgram (1971)).

of the $CR=0.12$ section before the onset of the sharp drag rise. The difference in C_D between the two different camber ratio sections is a slowly increasing function of C_L for the circular mast ($d/c=0.15$). However the addition of an elliptic mast ($d/c=0.17$, where d in this case is the square root of the mast cross-section area), causes the C_D-C_L curve to be shifted to the right for the lower camber ratio meaning that the $CR=0.12$ section has a lower C_D over the whole range in C_L and the difference in C_D between the two increases rapidly with increasing C_L .

The behaviour of C_D versus C_L is a smooth function of d/c over the Reynolds number range investigated ($0.5 - 1.5 \times 10^6$), except for the two largest diameter elliptical masts tested ($d/c=0.31$ and 0.36). For these two masts, C_L/C_D is much larger than would be expected by extrapolating the data from lower values of d/c . This indicates that the large masts are causing a different flow structure to occur with larger regions of separation. The use of trip devices on the elliptical mast with $d/c=0.31$ partly confirms this idea because the drag is reduced with their addition, presumably because of a delayed separation from the mast. For $d/c=0.36$, the effects of adding the trip devices upon the C_D-C_L plot are opposite for the two different Reynolds numbers tested. The data is largely insensitive to Reynolds number over the range examined, except for the $d/c=0.36$ elliptical mast without trip devices.

Milgram concludes that a common range of mast-sail geometries for a broader range of camber ratio still need to be investigated. Also since the value of d/c is typically large near the head of sails, further study of sections at high C_L for large values of d/c is required. The addition of a mast to the sail raises the friction and form drag to the same order of magnitude as the induced drag of the sail, whereas without the mast the friction and form drag would be small by comparison.

Wilkinson (1984) took Milgram's experiments with the mast attached one step further, and measured pressure distributions and velocity profiles for NACA $a = 0.8$ and 63 mean lines with a circular mast attached. Tests with the NACA 63 mean line investigated the

effect of moving the point of maximum camber forward. Wilkinson conducted the tests in the $7' \times 5'$ tunnel at Southampton University, England at Reynolds up to 1.6×10^6 . As with Milgram's tests, a low-aspect-ratio sail was tested to achieve high Reynolds numbers, and therefore three-dimensional flow at high angles of attack cannot be ruled out. Unfortunately neither of the series of experiments report surface-flow visualisation which is an easy tool in determining the large-scale flow structure.

The experiment set out to look at the effects of sail camber distribution, camber ratio, Reynolds number, angle of incidence, mast diameter/chord ratio and mast angle. In total of 216 tests were carried out, and it was concluded that all the pressure distributions could be represented by one universal form of pressure distribution that could be divided into nine regions as shown in figure 2.

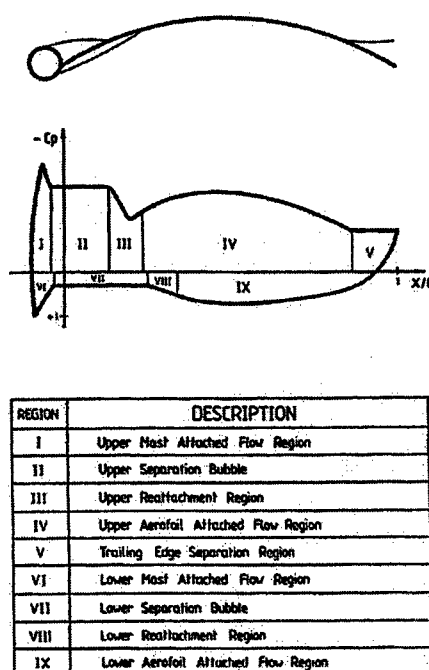


FIGURE 2. Universal pressure distribution: see Wilkinson (1984)

Over the limited Reynolds-number range investigated, little effect was observed. Increasing angle of incidence tended to decrease the base pressure in the upper-surface separation bubble and to shorten the length of the bubble. The pressure distribution also flattened out on the upper surface (region IV), and the position of the trailing-edge separation moved upstream. Increasing d/c has the effect of increasing the size of the separation bubble, flattening out the pressure distribution in region IV and reducing the extent of the trailing-edge separation. Finally, the effect of the two sail shapes tested on the aerodynamic characteristics appears to be small. The pressure recovery at reattachment is larger for the NACA 63, the minimum pressure in region IV occurs further forward, and on the lower surface the pressure distribution is much fuller.

From the review of Milgram and Wilkinson's work, it is obvious that the sections and even the masts tested may not be representative of real sails and masts. Furthermore, the data gained in both series of experiments provided a foundation for understanding

more about sail flows but is limited because three-dimensional flow effects may be large due to the low aspect ratio of the airfoils tested. With modern testing techniques the understanding gained from these seminal experiments can be built upon, further enhancing our understanding of this most complex flow.

2. Research aims and objectives

In summary, the primary aims of this experimental study are to:

- Gain a deeper physical understanding of the flow past upwind and downwind sails under various angles of incidence and Reynolds numbers.
- Create a comprehensive database for validation of numerical solvers and turbulence models that can be used by the (sail) research community and industry at large.

The objectives to achieve these aims for a range of two-dimensional sail sections and apparent wind angles are:

- For select upwind and downwind sections use Particle Image Velocimetry (PIV) to understand the effect of Reynolds number upon the flow topology, which may include the size and structure of leading-edge separation bubbles with and without a mast for the upwind case, location of trailing-edge separation if present, and the structure and frequency of the wake (measured using a hot wire or Laser Doppler Velocimeter (LDV)). Furthermore, the sensitivity of the pressure distribution and sectional lift and drag coefficients (C_L and C_D , respectively) to Reynolds number will be addressed using Pressure Sensitive Paint (PSP) and a wake rake of total-pressure tubes.
- For all six sail sections use a range of tools including surface oil-flow visualization, PSP, oil-film interferometry and/or shear-sensitive liquid crystals, to understand the main flow topology on both surfaces such as mean separation locations and transition location if no leading-edge separation is present.
- To measure sectional lift and drag coefficients, and the skin-friction distribution for all six sail sections, with and without a mast for the upwind cases, and to correlate this with the flow topology.
- For a select upwind case, to investigate in detail the interaction between the mast and sail for a range of sail incidences and effective wind angles with respect to the mast. PIV will be used to measure the flow structure and PSP and the wake rake to measure the section lift coefficient and drag coefficient, respectively.

3. Technical approach

We propose an initial test of six sail and mast configurations, to be conducted in February-June 2003 in the NASA Ames 7' \times 10' tunnel. The configurations are listed in table 1 and shown in figures 4-7. All models will be cambered plates of high aspect ratio, with constant cross section. Initial CFD studies have shown that the aspect ratio must be chosen as 15 or higher to sufficiently reduce three-dimensional effects. Measurements will be taken near mid-span. Alternatively, tangential blowing can be used with wings of lower aspect ratio to achieve higher Reynolds numbers. This option will be investigated.

The thin steel models will be put under tension to reduce the risk of buckling in the tunnel, and will be formed to the desired shape using matching machined blocks placed in compression. The structural package MSC.Nastran will be used to aid the model design, with pressure loads predicted using the CFD package CFX. The sail shape will be formed

Sail Type		Model	7' × 10' tunnel	12' tunnel
Upwind	Genoa (mid-mast height)	Supplied by TNZ	*	
	Mainsail (mid-mast height)	Supplied by TNZ	*	*
	With and without mast		*	
Downwind	Dynarig (Maltese Falcon)	Circular arc 12.5% camber	*	
	Gennaker	Circular arc 20% camber	*	
	Gennaker (TNZ)	Circular arc 25% camber	*	*

TABLE 1. List of sail configurations to be tested

by using thin steel, with two clamping blocks, machined to the desired profile, at each end as shown in figure 3. Appropriate boundary conditions will be applied in Nastran to simulate deforming the steel sheet. The predicted pressure distribution will then be applied to determine the thickness of the steel sheet and the amount of spanwise tension required in order to maintain the sail shape across the span. A small-scale model of the tensioning mechanism with a scaled high-aspect ratio thin steel sail will be constructed to prove the concept. Even with tensioning it is expected that the sail will deflect under aerodynamic load. The flying shape of the sail will therefore be measured using photogrammetric techniques available at NASA Ames. Vibration of the sail sections may also be an issue, particularly for cases where large regions of separated flow exist.

It is planned to test each section shape over a range of angles of incidence, and to determine the sectional pressure and skin friction distribution for each, from which the lift and drag coefficient can be found. In addition the structure of the flow away from the surface will be investigated, with particular emphasis on the regions of separation near the leading and trailing edges.

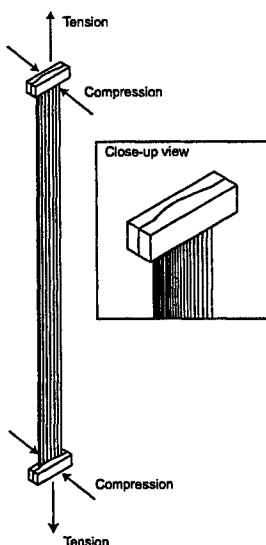


FIGURE 3. High-aspect-ratio 2D sail shape formed by shaped clamps placed under spanwise tension

3.1. Sail geometries

3.1.1. Upwind Sails

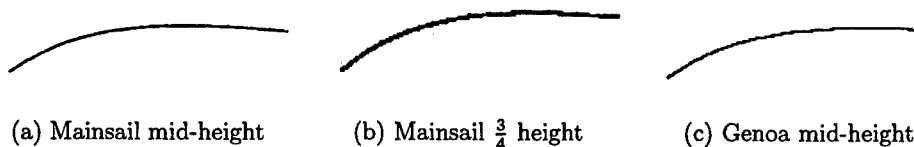


FIGURE 4. Upwind sails. Source: Team New Zealand. All sections shown at 18 degrees apparent wind angle

3.1.2. Reaching and downwind sails

The America's Cup gennaker cross-sections are close to circular arcs with 20-25% camber. We will test 20% and 25% camber. The Dynarig sections are circular arcs with 12.5% camber.

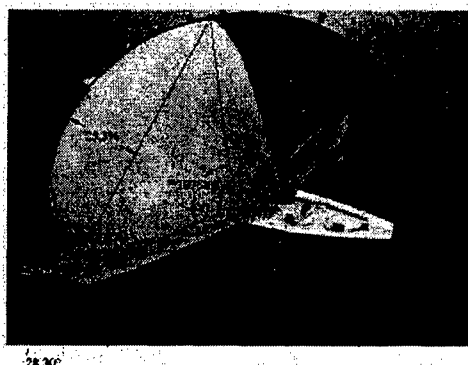


FIGURE 5. Typical TNZ gennaker - 25.3% circular arc. Picture taken in wind tunnel at Auckland



FIGURE 6. Dynarig sail configuration - 12.5% circular arc

3.1.3. Masts

Source: Team New Zealand. Dimensions full-scale (near head) are 200mm \times 150mm.



FIGURE 7. Masts for upwind tests: (a) Cut-off ellipse, (b) Cut-off ellipse, rounded edges.
Source: Team New Zealand

3.2. Experimental facilities and techniques

All models will be tested in the 7' × 10' closed-return wind tunnel at NASA Ames. This wind tunnel is capable of a maximum freestream speed of 200 knots (103 m/s) and has a freestream turbulence intensity of approximately 0.25%. The tunnel will be run at a speed of 30–40 m/s, leading to a chord Reynolds number of approximately half a million. This velocity is low enough to avoid compressibility effects, but high enough to utilize techniques such as PSP which need a reasonable dynamic pressure to work well. The closed-return tunnel also simplifies the process of seeding the tunnel for optical techniques such as PIV and LDV. After the experiments are performed, two designs (one upwind, one downwind) will be tested in the 12' pressurized tunnel at NASA Ames at higher Reynolds numbers, to conduct Reynolds-number sensitivity analyses. Using this tunnel Reynolds numbers of up to 4 million per foot (6 atm pressure) can be achieved at a Mach number of 0.1. Designing a thin sail to withstand such high dynamic pressures will not be an easy task, and performing the tests at a lower pressure of 2 atm (Reynolds number of 1.4 million per foot at Mach 0.1) is more feasible.

3.2.1. Pressure Sensitive Paint (PSP)

PSP will be used on the upper and lower surface of the sail to determine the pressure distribution around the section, and also by integrating the pressure distribution, to calculate the section lift coefficient. PSP is applied to a highly-reflective surface and luminesces when excited molecules in the coating return to a lower energy state due to the collision with an oxygen molecule in a process known as oxygen quenching. Excitation is commonly provided by a UV lamp. The rate of quenching is proportional to the partial pressure of oxygen, which is in turn proportional to the air pressure. PSP is therefore most sensitive to changes in pressure when the dynamic pressure is high and the percentage change in pressure is high with respect to atmospheric pressure.

The ratio of wind-on to wind-off intensity of the emitted light from the PSP is proportional to the ratio of respective pressures under conditions of constant excitation. The constants in the governing equation are derived either before the experiment by measuring the intensity of the PSP for various pressures and temperatures and/or during the experiment by using a reference pressure on the model such as that provided by a pressure transducer. Photogrammetry may then be required to associate the points in the PSP image with those on the model.

Uncertainty in the measurement of pressure can be due to errors in the calibration of the response of the paint to pressure, spatial and temporal variations in illumination and errors in the data processing. By far the largest source of error comes from the uncertainty in the paint's temperature.

Sullivan (2001) states that the accuracy of PSP is 1 mbar with a resolution of 0.5 mbar, and that the typical time response is 0.5 seconds, although 1 μ s has been demonstrated. For further information on PSP, the reader is referred to Bell *et al.* (2001), Mehta *et al.* (2000) and Sullivan (2001).

Illustrations of the ability of PSP to capture the pressure distribution with high resolution over a large area and range of pressure are given in figures 8a and 8b.

3.2.2. Oil-film interferometry

Oil-film interferometry relies on the principle that the rate at which oil thins on a surface is a function of the shear-stress magnitude. There are various incarnations of oil-film interferometry as discussed by Naughton and Sheplak (2000), although the method used

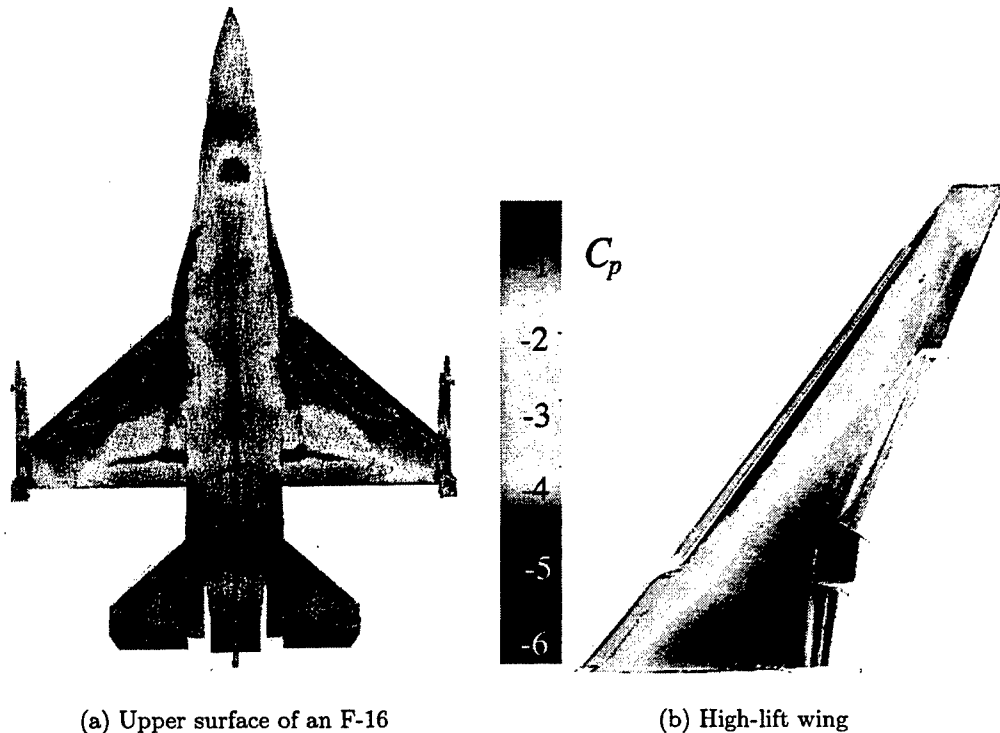


FIGURE 8. Pressure distributions measured using PSP (Bell *et al.* (2001))

at NASA Ames is Fringe Imaging Skin Friction Interferometry (FISF). The interference between the partially-reflected light at the air-oil interface and the light reflected from the model surface will vary between constructive and destructive as the oil film thickness changes. This is observed as a series of light and dark bands or fringes, the spacing of which is proportional to the skin friction (figure 9).

The oil typically used is silicone oil and is applied to the surface in either square patches or drops. The surface should have a high index of refraction (ideally $n = 2$), and therefore glass is ideal. For practical reasons, polished stainless steel or Mylar is often used. The light absorption of aluminium is too low to be used with PSP.

Illumination must be provided by a coherent light source, although the coherence length can be short (a few microns) due to the small thickness of the oil film. Light sources such as fluorescent bulbs, sodium lamps and black lights are often used. Lasers suffer from the expense of special optics and also the problem of specular reflection (speckle) near the surface. Imaging can be achieved using CCD cameras, preferably black and white. Calibration of the oil viscosity and its variation with temperature is necessary, although the measurement of the shear stress is absolute, requiring no additional reference measure. Mehta *et al.* (2000) state that using calibrated oil and with an accurate measurement of the dynamic head and the incident light angle, it is possible to achieve accuracy in the skin friction coefficient, c_f , better than $\pm 5\%$ in magnitude and $\pm 1\%$ in vector direction.

Examples of oil film interferometry applied to wing flows are given in figures 10a and 10b. In figure 10a, oil drops are applied to a wing tip and provide both the magnitude and

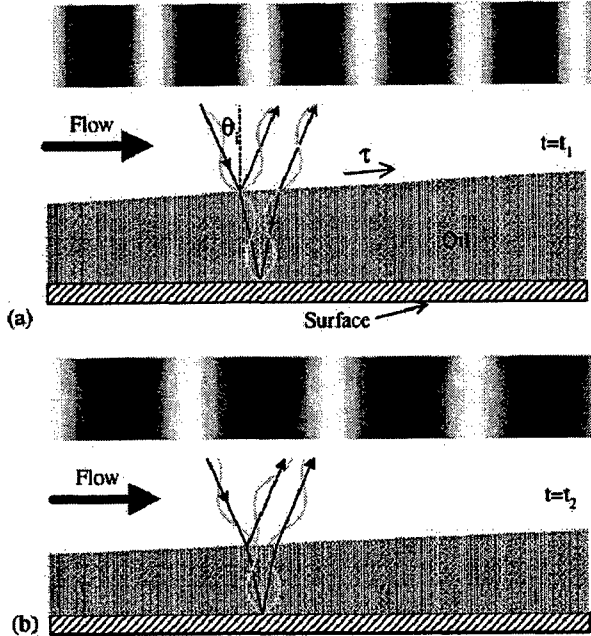
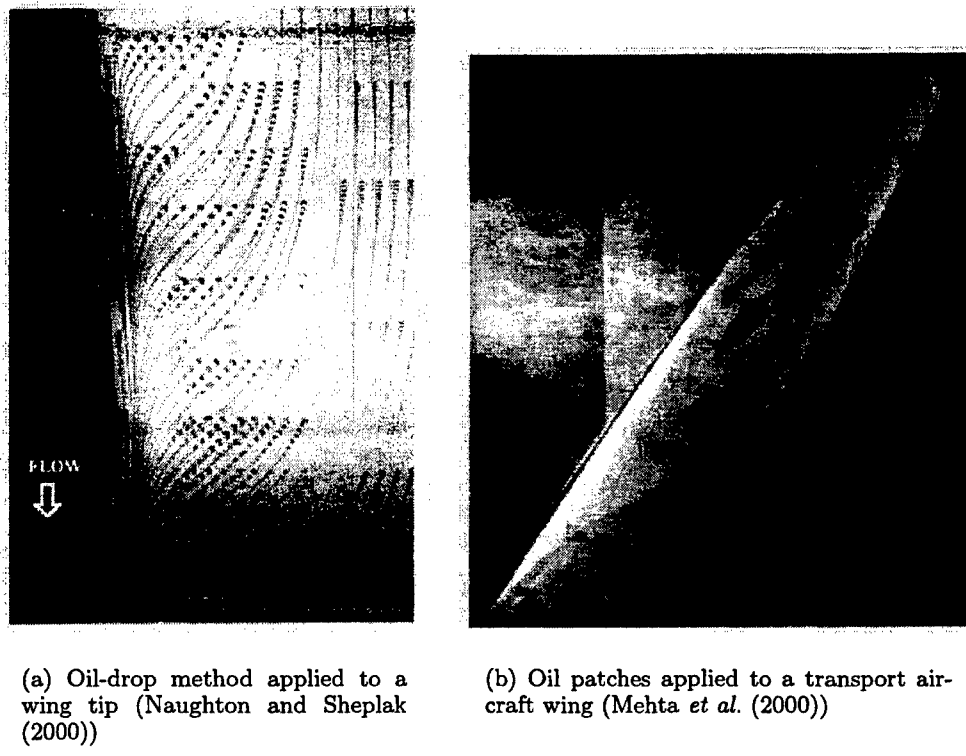


FIGURE 9. Interference fringes produced by Fizeau Interferometry: (a) Constructive interference produces bright bands, whereas (b) destructive interference produces dark bands (Naughton and Sheplak (2000))

direction of the surface shear stress. In figure 10b oil patches are applied to a transport wing to yield the magnitude of the surface shear stresses.

3.2.3. Particle Image Velocimetry (PIV)

Modern PIV calculates the velocity field in a plane by comparing two images containing particles separated by a very short time interval. The flow field of interest is usually illuminated by a thin laser sheet at these two times, with each laser pulse triggering the capture of the particle field using a cross-correlation CCD camera that is placed normal to the plane of the laser sheet (figure 11). This type of CCD camera is capable of capturing two images in very quick succession (usually $10 \mu\text{s}$ apart). A cross-correlation algorithm is then used to locate intensity peaks in both images for small areas (of the order of 64×64 pixels) and this is repeated across the whole image. The peak in the correlation should correspond to the same particle in both images. The distance each particle moves in terms of pixels (and physical space via a calibration) in the time separating the two images can then be calculated, yielding the instantaneous velocity vector in the plane. From this data other properties of the flow, such as vorticity, can be calculated (figure 12), and if sufficient frames are captured, flow statistics such as the rms and mean velocity components and therefore stresses, skewness and kurtosis can be calculated. Extension of the technique to measuring the out-of-plane velocity component, and therefore the full velocity vector, is possible by utilising perspective error. If the CCD camera is placed at 90 degrees to the laser sheet, the angle of view at the edges of the image will decrease from the optimal 90 degrees at the center of the image, and the motion of particles perpendicular to the laser sheet can be detected. Stereoscopic or 3D PIV requires two cross-correlation CCD cameras placed at approximately 40 degrees to the laser sheet.



(a) Oil-drop method applied to a wing tip (Naughton and Sheplak (2000))

(b) Oil patches applied to a transport aircraft wing (Mehta *et al.* (2000))

FIGURE 10. Examples of oil film interferometry applied to aircraft wings

This obviously causes a problem with focus as different parts of the laser sheet are at different distances from the camera lens. This can be overcome by using a large depth of field which results in a small lens aperture and low light intensity at the CCD. The Scheimpflug condition for focusing solves this problem. It states that if the image plane of the CCD sensor and the lens plane are coincident at the focus plane of the lens, then the particles in the laser sheet will be in focus on the CCD sensor.

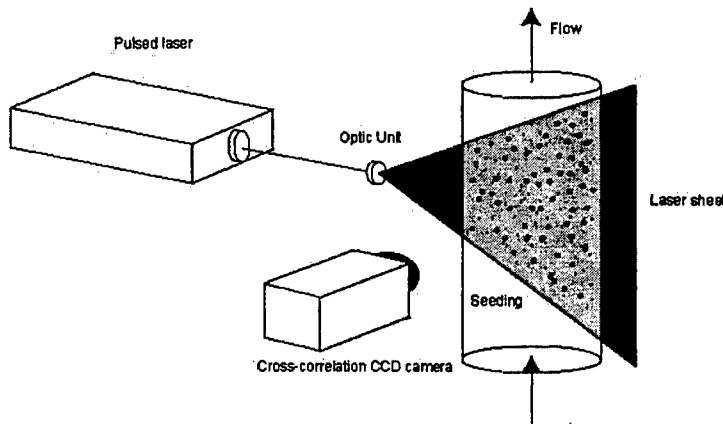


FIGURE 11. Typical 2D PIV setup

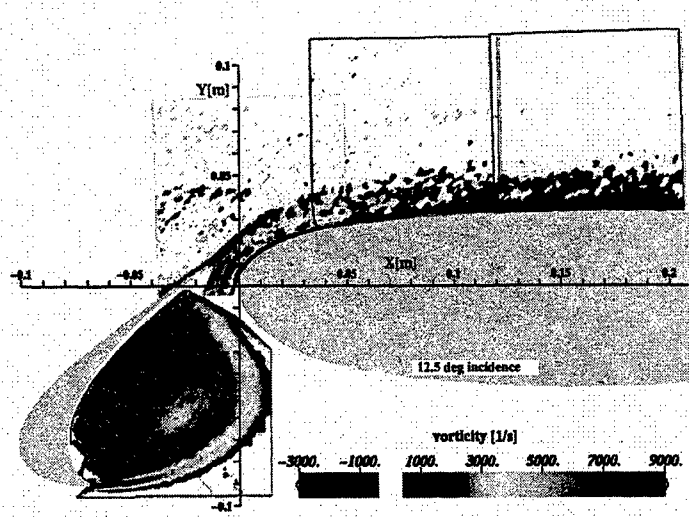


FIGURE 12. Mean spanwise vorticity measured using PIV for a high-lift system (Stanislas *et al.* (2000))

The temporal resolution of PIV is governed by the repetition rate of the laser and the CCD camera. In general these are usually 15–30 Hz, although high speed PIV at frequencies up to 1 MHz is possible using cinematic cameras and high frequency lasers and multiple CCD cameras. Spatial resolution is also limited by the CCD element and the number of pixels and their size. An example of a high-end CCD camera is one with 1280×1024 pixels and a pixel length of $6.7 \mu\text{m}$.

For more information on PIV, the reader is referred to Gharib and Darabi (2000), Grant (1994) and Adrian (1991).

We will determine the pressure distribution, the size of leading-edge bubbles, the trailing-edge separation points and the skin friction in all tests. The pressure distribution will be measured using Pressure Sensitive Paint (PSP). Skin friction will be measured using oil-film interferometry or shear-sensitive liquid crystals. Particle Image Velocimetry (PIV) will be performed on two upwind and two downwind designs to create a detailed picture of the flow past the sail and in the wake. Expertise in all of the measurement techniques described is available at NASA Ames and Stanford.

We will return to the $7' \times 10'$ wind tunnel in late 2003 to test sail shapes for the Maltese Falcon suggested by our optimization algorithm (Doyle *et al.* 2002).

REFERENCES

- ABBOTT, I. H. & VON DOENHOFF, A. E. 1959 *Theory of wing sections. Including a summary of airfoil data*. Dover, New York.
- ADRIAN, R. J. 1991 Particle-imaging techniques for experimental fluid mechanics. *Annu. Rev. Fluid Mech.* **22**, 261–304.
- BELL, J. H., SCHAIRER, E. T., HAND, L. A. & MEHTA, R. D. 2001 Surface pressure measurements using luminescent coatings. *Annu. Rev. Fluid Mech.* **33**, 155–206.
- DOYLE, T., GERRITSEN, M. & IACCARINO, G. 2002 Towards sail shape optimization of a modern clipper ship. *Annual Research Briefs*, Center for Turbulence Research, NASA Ames/Stanford Univ.

- FLAY, R. G. J. 1996 A twisted flow wind tunnel for testing yacht sails. *J. Wind Engng and Indust. Aerod.* **63**, 171–182.
- GHARIB, M. AND DARIBI, D. 2000 Digital Particle Image Velocimetry. In: *Flow Visualization: Techniques and Examples*. (A. J. Smits and T. T. Lim, eds.), Imperial College Press, London.
- GRANT, I. (ED). 1994 *Selected papers on particle image velocimetry*. SPIE Milestone Series MS 99.
- JACKSON, P. S. 1996 Modelling the aerodynamics of upwind sails. *J. Wind Engng and Indust. Aerod.* **63**, 17–34.
- MEHTA, R. D., BELL, J. H., REDA, D. C., WILDER, M. C., ZILLIAC, G. G. & DRIVER, D.M. 2000 Pressure and sensitive coatings. In: *Flow Visualization: Techniques and Examples* (A. J. Smits and T. T. Lim, eds.), Imperial College Press, London.
- MILGRAM, J. H. 1971 *Section data for thin highly cambered airfoils in incompressible flow*. NASA CR-1767, 1971.
- MILGRAM, J. H. 1978 Effects of masts on aerodynamics of sail sections. *Marine Tech.* **15**, 35–42.
- NAUGTHON, J. W. AND SHEPLAK, M. 2001 Modern skin friction measurement techniques: Description, use and what to do with the data. *AIAA Paper* 2000–2521.
- STANISLAS, M., KOMPENHANS, J. & WESTERWEEL, J. 2000 *Particle Image Velocimetry: Progress towards Industrial Application*. Kluwer, Dordrecht.
- SULLIVAN, J. 2001 Temperature and pressure sensitive paint. In: *Advanced Measurement Techniques*, (Sleverding, C.H., ed.) Lecture Series 2001–01, von Karman Institute for Fluid Mechanics.
- WILKINSON, S. 1984 Partially separated flows around 2D masts and sails. Ph.D. thesis, University of Southampton.
- WILKINSON, S. 1989 Static pressure distributions over 2D mast/sail geometries. *Marine Tech.*, **26**, 333–337.
- WILKINSON, S. 1990 Boundary-layer explorations over a two-dimensional mast/sail geometry. *Marine Technology*, **27**, 250–256.
- WOOD, C. J. & TAN, S. H. 1978 Towards an optimum yacht sail. *J. Fluid Mech.* **85**, 459–477.

Turbulence modelling in large-eddy simulations of the cloud-topped atmospheric boundary layer

By M. P. Kirkpatrick

1. Motivation and objectives

This paper discusses turbulence modelling in large-eddy simulations of the cloud-topped atmospheric boundary layer. While our primary focus is on simulations of stratocumulus clouds, most of the discussion is also relevant to other types of cloud. Stratocumulus clouds were chosen because of the important role they play in the Earth's climate, and because the fluid dynamics associated with these clouds has a number of features which researchers have found difficult to model accurately.

Marine stratocumulus clouds cover extensive areas off the west coasts of the large continents in the subtropics. Their presence in these regions is the result of strong static stability due to low sea-surface temperatures and to atmospheric subsidence associated with the descending branch of the Hadley circulation. Due to their high albedo, stratocumulus clouds have a significant effect on the Earth's radiative heat budget. From analysis of satellite data, Klein & Hartmann (1993) calculated top-of-the-atmosphere values of the order of -100 Wm^{-2} for the net cloud radiative forcing over stratocumulus decks. Randall *et al.* (1984) estimated that the global cooling resulting from a 4% increase in areal coverage by marine stratocumulus clouds would offset the expected warming from a doubling of atmospheric carbon dioxide. In addition to their role in the Earth's radiation budget, stratocumulus clouds also affect the dynamics of the atmosphere and oceans. Miller (1997), for example, found that stratocumulus clouds provide a negative-feedback mechanism which reduces the intensity of tropical convection and damps the tropical atmospheric circulation. Similarly, stratocumulus clouds over oceans in the subtropics reduce sea-surface temperatures in these regions by lowering the net surface heat flux. Most atmospheric general circulation models (GCMs) underpredict the amount of subtropical marine stratocumulus (Jakob 1999). In coupled atmosphere-ocean models, this can lead to positive sea-surface temperature biases of up to 5K. Such modelling errors have been shown to have a significant influence on both the predicted circulation (Nigam 1997) and the global radiation budget (Slingo 1990).

The use of large-eddy simulation (LES) to study the planetary boundary layer dates back to the early 1970s, when Deardorff (1972) used a three-dimensional simulation to determine velocity and temperature scales in the convective boundary layer. In 1974 he applied LES to the problem of mixing-layer entrainment (Deardorff 1974) and in 1980 to cloud-topped boundary layers (Deardorff 1980). Since that time the LES approach has been applied to planetary boundary layer problems by numerous authors (see for example Moeng 1986; Mason & Derbyshire 1990; Schumann & Moeng 1991a,b; Brown *et al.* 1994; Saiki *et al.* 2000; Stevens & Bretherton 1999; Stevens *et al.* 2001)

The popularity of the LES technique in atmospheric research is due in part to the difficulties involved with obtaining sufficient field data to develop and test theories concerning the structure and dynamics of the planetary boundary layer. Large-eddy simulations provide three-dimensional time-evolving velocity and scalar fields at a resolution limited

only by computational resources. As such, LES is often used to isolate particular physical processes of interest such as entrainment across the inversion (Stevens *et al.* 2000) or transition from one type of cloud to another (Wyant *et al.* 1997). It is also used to generate databases of different atmospheric flow regimes in order to evaluate, refine and develop parameterisation schemes for use in large-scale models (eg. Lappen & Randall 2001). At the other end of the spectrum, LES is used as a platform on which to develop reliable models of cloud microphysics and radiation (Ackerman *et al.* 2000).

In spite of an increasing reliance on LES as a tool for developing and testing cloud theories and models, there is still considerable uncertainty concerning the fidelity of the simulations themselves. While LES has been shown to be relatively robust for simple cases such as simulations of a clear, convective boundary layer (Mason 1989), model intercomparisons for more complex cases have shown large variations in predictions of important statistics and bulk parameters. For example, in the 1995 Global Energy and Water Cycle Experiment (GEWEX) Cloud System Studies (GCSS) model intercomparison, Bretherton *et al.* (1999) compared simulations of a smoke cloud beneath a temperature inversion. Radiative cooling at the top of the cloud drives convection, which leads to entrainment across the inversion and to growth of the boundary layer. The authors found that the entrainment rates and other statistics predicted by the various LES codes differed by up to a factor of two. Similar entrainment processes occur at the top of stratocumulus clouds, although with the added complexity of latent-heat transfer due to condensation and evaporation of cloud droplets. A second example is the recent intercomparison of simulations of trade-wind cumuli by Stevens *et al.* (2001). Here again, important parameters such as stratiform cloud fraction and the variance of total-water mixing ratio were found to be highly sensitive to the choice of numerical method, spatial resolution and subgrid-scale turbulence model. Bulk parameters such as boundary-layer height, entrainment rate and cloud fraction are important variables in the parameterisations used in global circulation models. It is therefore essential that LES be made robust in its prediction of these variables if it is to be used as a tool for development and tuning of parameterisations for large scale models.

One of the main problem areas in large-eddy simulations of clouds is the accurate representation of processes occurring close to an inversion. Here, strong stable stratification reduces the size of the energetic eddies considerably, so that they are generally poorly resolved by simulations. Bretherton *et al.* (1999), for example, identify an "undulation" length scale given by $z_u = z_i/Ri$ (where z_i is the height of the inversion and Ri the Richardson number) which is of the order 5 – 10 m in a strong inversion. Meanwhile, the grid-cell dimensions used for large-eddy simulations of the planetary boundary layer are typically 25 - 100 m, although, with advances in computer technology, highly-resolved simulations are now becoming possible. Stevens *et al.* (2000), for example, recently performed stratocumulus simulations at grid sizes down to 8 m in the horizontal directions by 4 m in the vertical direction. Even at this resolution, however, they found the predicted entrainment rate and entrainment efficiency to be sensitive to the subgrid model and numerics. A second reason for the difficulties encountered in modelling processes close to an inversion is that the stable stratification tends to damp vertical motions, making the turbulence in this region much more anisotropic than in an unstratified environment. Consequently turbulence models often use one or more corrections to account for the effects of stratification. In clouds, additional buoyancy sources result from energy transfer due to condensation and evaporation of water, and some authors (eg. MacVean & Mason (1990)) recommend applying further corrections to account for these processes.

An alternative to using such corrections is to adopt a dynamic approach, in which the parameters in the subgrid-scale turbulence model are computed at each point in space and time using information contained in the resolved velocity and scalar fields. This approach removes the need to make modelling decisions concerning the coefficients and length scales in the subgrid model. It also removes the need for corrections to account for buoyancy effects since all this information is obtained directly from the resolved flow field.

The dynamic approach, first proposed by Germano *et al.* (1991), has been used with considerable success for complex engineering flows (see Boivin *et al.* 2000; Branley & Jones 2001, for example), however its application to atmospheric flows has been limited. This is due in part to arguments by authors such as Mason & Brown (1999) to the effect that the dynamic procedure is inappropriate for atmospheric applications. These arguments are based on the premise that the dynamic procedure requires a filter cut-off wavenumber in the inertial subrange. This is incorrect. The theory behind the dynamic procedure assumes only that the same subgrid model can be used for both the resolved field and the test-filtered field. It is in fact the Smagorinsky model (Smagorinsky 1963), which is widely used for atmospheric simulations even at very coarse resolutions, whose derivation assumes resolution of the inertial subrange.

Bohnert (1993) tested the dynamic procedure in combination with the Smagorinsky model for simulations of clear and cloud-topped planetary boundary layers. The simulations were performed at a Reynolds number lower than that of a realistic atmospheric boundary layer and used simple parameterisations for cloud physics and radiation. In order to stabilise the model, it was necessary to average the calculated coefficient field over horizontal planes. Nevertheless, these results are encouraging. The dynamic model gave results comparable to, or better, than those obtained using the standard constant-coefficient Smagorinsky model with a Richardson-number correction.

The objective of the present study is to test the dynamic procedure in large eddy simulations of a marine stratocumulus cloud deck. The simulations will be performed at realistic Reynolds and Rayleigh numbers, with conditions matching those measured during the 2001 DYCOMS-II field experiment. This test case has a number of the features discussed above which typically cause difficulties in cloud simulations, namely strong stable stratification, and buoyancy sources within the cloud due to radiation, condensation and evaporation of water droplets. Following Zang *et al.* (1993), we use the mixed model as a base subgrid model, rather than the Smagorinsky model. The mixed model is a combination of the scale-similarity model of Bardina *et al.* (1980) and the Smagorinsky model. The dynamic mixed model of Zang *et al.* has been found to be more stable than the dynamic Smagorinsky model and it is hoped that its use will remove the need for averaging over horizontal planes. This is important in the present case, since horizontal planes close to the cloud-top contain both stably and unstably stratified regions. Horizontal averaging of the calculated model parameters would prevent the dynamic procedure from distinguishing between these two fundamentally different flow regimes.

The author is currently implementing the dynamic mixed model in the LES code, DHARMA, written by David Stevens. This code has performed well in model intercomparisons (see Bretherton *et al.* 1999; Stevens *et al.* 2001) and has also been used for a number of high-resolution simulations (Stevens & Bretherton 1999; Stevens *et al.* 2000, 2002) where it was shown to scale well on massively parallel architectures. In addition, the code has the option to use either standard parameterisations for radiation and cloud

microphysics, or the more complex models of Ackerman *et al.* (1995), which treat the cloud microphysics explicitly and include a detailed treatment of radiative transfer.

In the following, we describe the governing equations, the numerical methods, and the parameterisations and models used in the DHARMA code. We rewrite the governing equations in filtered form and outline a turbulence closure based on the dynamic mixed model of Zang *et al.* Finally we discuss the test case and simulations which will be used to assess the performance of this approach to turbulence modelling in numerical simulations of clouds.

2. Governing equations

The basic equations governing the dynamics of the cloud-topped atmospheric boundary layer comprise equations for conservation of mass, momentum, energy and total water. In addition, radiative heat transfer and cloud microphysics must also be modelled. Cloud microphysics refers to the transitions between vapor, liquid and solid-phase water and the dynamics of the liquid and solid-phase components.

The governing equations are written in the anelastic form of Ogura & Phillips (1962) in which the thermodynamic variables such as pressure p are decomposed into an isentropic base state p_0 (corresponding to a uniform potential temperature θ_0) and a dynamic component. Following Clark (1979), the dynamic component is further decomposed into an initial environmental deviation in hydrostatic balance p_1 and a time-evolving dynamic perturbation p_2 to give

$$p(x, y, z, t) = p_0(z) + p_1(z) + p_2(x, y, z, t). \quad (2.1)$$

The resulting continuous equations written in Cartesian tensor notation are

$$\frac{\partial u_i}{\partial t} + \frac{1}{\rho_0} \frac{\partial(\rho_0 u_i u_j)}{\partial x_j} = -\frac{\partial \Pi}{\partial x_i} + g_i \frac{\theta_{v2}}{\theta_0} + H_{u_i}^{sub} + H_{u_i}^{gw} + H_{u_i}^{coriolis}, \quad (2.2)$$

$$\frac{\partial \theta_l^*}{\partial t} + \frac{1}{\rho_0} \frac{\partial(\rho_0 \theta_l^* u_j)}{\partial x_j} = H_{\theta_l^*}^{sub} + H_{\theta_l^*}^{LS} + H_{\theta_l^*}^{gw} + H_{\theta_l^*}^{rad}, \quad (2.3)$$

$$\frac{\partial q_t}{\partial t} + \frac{1}{\rho_0} \frac{\partial(\rho_0 q_t u_j)}{\partial x_j} = H_{q_t}^{sub} + H_{q_t}^{LS}, \quad (2.4)$$

$$\frac{\partial(\rho_0 u_j)}{\partial x_j} = 0. \quad (2.5)$$

Here u_i is the velocity component in the i direction, ρ is the density, Π is the perturbation pressure p_2/ρ_0 , g_i is the acceleration due to gravity, q_t the total water mixing ratio and $\theta_l^* = (\theta_l - \theta_0)/\theta_0$ is a scaled liquid-water potential temperature. Total-water mixing ratio is the sum of the liquid and vapour mixing ratios,

$$q_t = q_c + q_v = \frac{\rho_c + \rho_v}{\rho_d}, \quad (2.6)$$

where ρ_c , ρ_v and ρ_d are the density of the condensed water, the water vapour and the dry air respectively. Liquid-water potential temperature is defined as

$$\theta_l = \theta - \frac{L q_c}{C_{pd} \pi_0}. \quad (2.7)$$

Here L is the latent heat of vaporisation, C_{pd} is the specific heat at constant pressure

for dry air and $\pi_0 = \left(\frac{p_0}{p_{ref}}\right)^{\frac{R_d}{C_p}}$ with p_{ref} a reference pressure and R_d the gas constant of dry air. The virtual potential temperature θ_v appearing in the buoyancy term of the momentum equations is given by

$$\theta_v = \theta + \theta_0 \left[\left(\frac{R_d}{R_v} - 1 \right) q_v - q_c \right], \quad (2.8)$$

where R_d and R_v are the gas constants of dry air and water vapor respectively.

The interior forcings H are body forces which parameterise the effects of: subsidence H^{sub} ; horizontal large scale advective tendencies H^{LS} ; and the Coriolis force $H^{coriolis}$. In addition, a Rayleigh damping term H^{gw} is applied to the top third of the domain to absorb gravity wave energy. The subsidence and large-scale advective tendencies result from the fact that the LES domain is not isolated, but is embedded within the global circulation. These forcings are generally specified as functions of z/z_i where z is the vertical height, and z_i is the height of the inversion. As an example, in the case of the trade-wind cumulus intercomparison of Stevens *et al.* (2001), the subsidence velocity w_{sub} was specified to vary linearly between 0 at the surface and 6.5 mm s^{-1} at z_i . The subsidence forcings then become,

$$H_{u_i}^{sub} = w_{sub} \frac{\partial u_i}{\partial z}, \quad (2.9)$$

$$H_{\theta_i^*}^{sub} = w_{sub} \frac{\partial \theta_i^*}{\partial z}, \quad (2.10)$$

$$H_{q_i}^{sub} = w_{sub} \frac{\partial q_t}{\partial z}. \quad (2.11)$$

The large-scale advective tendencies were specified as

$$\begin{aligned} \left[\frac{d\theta_i^*}{dt} \right]_{LS} &= -1.1575 \times 10^{-5} \left(3 - \frac{z}{z_i} \right) K s^{-1}, \\ \left[\frac{dq_t}{dt} \right]_{LS} &= -1.58 \times 10^{-8} \left(1 - \frac{z}{z_i} \right) s^{-1}, \end{aligned} \quad (2.12)$$

for $z < z_i$. Above the inversion, the terms were linearly reduced to zero over a distance of 300 m. The Coriolis term is given by

$$H^{coriolis} = [fv, -fu, 0], \quad (2.13)$$

with the Coriolis parameter $f = 2\omega \sin \phi$, where ω is the angular velocity of the Earth and ϕ is the latitude.

3. Filtered equations

In LES, a spatial filter is applied to the governing equations. The application of a spatial filter G to a function f is defined as

$$\bar{f}(\mathbf{x}) = \int_{\Omega} G(\mathbf{x} - \mathbf{x}'; \bar{\Delta}(\mathbf{x})) f(\mathbf{x}') d\mathbf{x}', \quad (3.1)$$

where $\bar{\Delta}$ is the characteristic width of the filter. A box filter is used here as it fits naturally into the finite volume discretisation. The filter width is written in terms of the cell dimensions, $\bar{\Delta} = 2(\Delta_x \Delta_y \Delta_z)^{1/3}$.

Filtering the equations for conservation of momentum and mass yields

$$\frac{\partial \bar{u}_i}{\partial t} + \frac{1}{\varrho_0} \frac{\partial (\varrho_0 \bar{u}_i \bar{u}_j)}{\partial x_j} = - \frac{\partial \bar{\Pi}}{\partial x_i} + g_i \frac{\bar{\theta}_{v2}}{\theta_0} - \frac{\partial \tau_{ij}}{\partial x_j} + \bar{H}_{u_i}^{sub} + \bar{H}_{u_i}^{gw} + \bar{H}_{u_i}^{coriolis}, \quad (3.2)$$

$$\frac{\partial (\varrho_0 \bar{u}_j)}{\partial x_j} = 0. \quad (3.3)$$

Here it is assumed that the isentropic fields ϱ_0 and θ_0 , and the forcings H , vary slowly in space, so that extra moments resulting from the application of the filter to these terms may be neglected. The extra term in the momentum equations is the subgrid-scale stress or SGS tensor,

$$\tau_{ij} = (\bar{u}_i \bar{u}_j - \bar{u}_i \bar{u}_j), \quad (3.4)$$

which represents transport of momentum by subgrid-scale turbulence. This term must be modelled to close the equations. The Smagorinsky eddy-viscosity model (Smagorinsky 1963) assumes that the anisotropic part of the SGS stress tensor is proportional to the large scale strain rate tensor,

$$\tau_{ij} - \frac{1}{3} \delta_{ij} \tau_{kk} = -2\nu_T \bar{S}_{ij}, \quad (3.5)$$

where

$$\bar{S}_{ij} = \frac{1}{2} \left(\frac{\partial \bar{u}_i}{\partial x_j} + \frac{\partial \bar{u}_j}{\partial x_i} \right), \quad (3.6)$$

and that the eddy viscosity ν_T is itself a function of strain rate and filter size,

$$\nu_T = C \bar{\Delta}^2 |\bar{S}|. \quad (3.7)$$

Here $|\bar{S}| = \sqrt{2\bar{S}_{ij}\bar{S}_{ij}}$ and C is the dimensionless model coefficient. In the basic model, C is specified *a priori* and is often written as the Smagorinsky coefficient $C_s = \sqrt{C}$. For incompressible flows, the isotropic part of the SGS stress tensor, τ_{kk} , is absorbed into the pressure term.

For atmospheric simulations this basic model must be modified to account for the effects of stratification. This typically takes the form of a correction to the eddy viscosity to give

$$\nu_T = C \bar{\Delta}^2 |\bar{S}| \sqrt{1 - Ri/Pr_T}, \quad (3.8)$$

where $Ri = N^2/|S|^2$ is a gradient Richardson number and Pr_T is a turbulent Prandtl number. The buoyancy frequency N for dry air is defined as

$$N^2 = -\frac{g}{\theta} \frac{\partial \theta}{\partial z}. \quad (3.9)$$

In the DHARMA code, this formula is modified, following MacVean & Mason (1990), to include the effects of evaporation and condensation.

As discussed in the previous section, while these corrections have been shown to give good results for the relatively simple flows for which they were derived, in more complex flows the results are often highly sensitive to the choice of model coefficients and length scales. Apart from the need to set the model coefficient and length scale *a priori*, the Smagorinsky model has a number of other problems.

(a) The model assumes that the principal axes of the SGS stress tensor are aligned with

the resolved strain-rate tensor whereas analysis of DNS results has shown this not to be the case.

(b) The model does not predict the correct asymptotic behaviour near a solid boundary or in laminar/turbulent transitions.

(c) The model does not allow SGS energy backscatter to the resolved scales.

To overcome item (a) in this list, Bardina *et al.* (1980) proposed a model based on an assumption of similarity between the unresolved scales and the smallest resolved scales. In their "scale similarity model" the subgrid-scale stress is given by

$$\tau_{ij}^a = (\bar{u}_i \bar{u}_j - \bar{\bar{u}}_i \bar{\bar{u}}_j)^a, \quad (3.10)$$

where superscript a specifies the anisotropic part of the tensors. Comparisons with DNS results show that the scale similarity model, which does not require alignment between the SGS stress tensor and the resolved strain-rate tensor, represents the structure of the SGS stress more accurately than does the Smagorinsky model. The model does not, however, dissipate sufficient energy and is usually combined with the Smagorinsky model to form a "mixed model".

Items (b) and (c) were addressed by Germano *et al.* (1991) who proposed a dynamic procedure that calculates the model coefficient dynamically at each point in space and time based on local instantaneous flow conditions. While the procedure can be used with any subgrid model, Germano *et al.* demonstrated the approach with the Smagorinsky model. The resulting dynamic Smagorinsky model has the correct asymptotic behaviour near solid boundaries and in laminar flow, and allows energy backscatter. Unfortunately, values of the predicted model coefficient tend to fluctuate considerably and some form of averaging, usually along homogeneous directions, is required to avoid numerical instability. In the present context, such averaging is problematic since there is no homogeneous direction. The stratocumulus cloud-top contains regions of both stable and unstable stratification within the same horizontal plane.

A number of variants of the dynamic procedure have been proposed to overcome the need for averaging. The localised dynamic models of Ghosal *et al.* (1992) and Piomelli & Liu (1995) are more stable but add to the complexity of the model. Instead, we have chosen to adopt the approach of Zang *et al.* (1993) who used the dynamic procedure with the mixed model as a base model, rather than with the Smagorinsky model. Zang *et al.* tested the dynamic mixed model for rotating stratified flow and reported a significant reduction in fluctuations of the coefficient compared with the dynamic Smagorinsky model. The dynamic mixed model has the added advantage that the scale similarity term removes the restriction of tensor alignment and provides better spectral representation of the subgrid-scale stress.

The mixed model for the subgrid-scale turbulent stress is written

$$\begin{aligned} \tau_{ij}^a &= -2C\bar{\Delta}^2 |\bar{S}| \bar{S}_{ij} + (\bar{u}_i \bar{u}_j - \bar{\bar{u}}_i \bar{\bar{u}}_j)^a \\ &\equiv -2\nu_T \bar{S}_{ij} + (\bar{u}_i \bar{u}_j - \bar{\bar{u}}_i \bar{\bar{u}}_j)^a, \end{aligned} \quad (3.11)$$

where the first term on the right-hand side is the Smagorinsky component of the model while the second term represents the scale similarity component. The dynamic procedure involves the application of a test filter ($\hat{\cdot}$) to the velocity field. By assuming that the same subgrid model can be used to represent the unresolved stresses for both the grid-filtered

and test-filtered fields, an expression is derived for the required parameters,

$$C\bar{\Delta}^2 = -\frac{(L_{ij} - H_{ij})M_{ij}}{2M_{ij}M_{ij}}, \quad (3.12)$$

where

$$L_{ij} = \widehat{\bar{u}_i \bar{u}_j} - \widehat{\bar{u}_i} \widehat{\bar{u}_j}, \quad (3.13)$$

$$H_{ij} = \widehat{\bar{u}_i \bar{u}_j} - \widehat{\bar{u}_i} \widehat{\bar{u}_j}, \quad (3.14)$$

and

$$M_{ij} = \alpha^2 |\widehat{\bar{S}}| \widehat{\bar{S}}_{ij} - |\widehat{\bar{S}}| \widehat{\bar{S}}_{ij}, \quad \alpha = \widehat{\bar{\Delta}} / \bar{\Delta}. \quad (3.15)$$

Using these relations, the momentum equations become

$$\begin{aligned} \frac{\partial \bar{u}_i}{\partial t} + \frac{1}{\varrho_0} \frac{\partial (\varrho_0 \bar{u}_i \bar{u}_j)}{\partial x_j} &= -\frac{\partial \bar{\Pi}}{\partial x_i} + g_i \frac{\bar{\theta}_{v2}}{\theta_0} + \frac{\partial}{\partial x_j} (2\nu_T \bar{S}_{ij} - (\bar{u}_i \bar{u}_j - \bar{\bar{u}}_i \bar{\bar{u}}_j)^a) \\ &+ \bar{H}_{u_i}^{sub} + \bar{H}_{u_i}^{gw} + \bar{H}_{u_i}^{coriolis}. \end{aligned} \quad (3.16)$$

Following a similar argument the spatial filter is applied to the energy equation giving

$$\frac{\partial \bar{\theta}_l^*}{\partial t} + \frac{1}{\varrho_0} \frac{\partial (\varrho_0 \bar{\theta}_l^* \bar{u}_j)}{\partial x_j} = -\frac{\partial \gamma}{\partial x_j} + \bar{H}_{\theta_l^*}^{sub} + \bar{H}_{\theta_l^*}^{LS} + \bar{H}_{\theta_l^*}^{gw} + \bar{H}_{\theta_l^*}^{rad}. \quad (3.17)$$

The SGS energy flux,

$$\gamma = \left(\bar{u}_j \bar{\theta}_l^* - \bar{\bar{u}}_j \bar{\bar{\theta}}_l^* \right), \quad (3.18)$$

is approximated using a mixed model analogous to that used for the momentum equations,

$$\gamma = -\frac{\nu_T}{Pr_{\theta T}} \frac{\partial \bar{\theta}_l^*}{\partial x_j} + \left(\bar{u}_j \bar{\theta}_l^* - \bar{\bar{u}}_j \bar{\bar{\theta}}_l^* \right), \quad (3.19)$$

with the eddy diffusivity computed using the eddy viscosity calculated for the velocities and a turbulent Prandtl number. Substituting into (3.17), the filtered energy equation becomes

$$\begin{aligned} \frac{\partial \bar{\theta}_l^*}{\partial t} + \frac{1}{\varrho_0} \frac{\partial (\varrho_0 \bar{\theta}_l^* \bar{u}_j)}{\partial x_j} &= \frac{\partial}{\partial x_j} \left(\frac{\nu_T}{Pr_{\theta T}} \frac{\partial \bar{\theta}_l^*}{\partial x_j} - \left(\bar{u}_j \bar{\theta}_l^* - \bar{\bar{u}}_j \bar{\bar{\theta}}_l^* \right) \right) \\ &+ \bar{H}_{\theta_l^*}^{sub} + \bar{H}_{\theta_l^*}^{LS} + \bar{H}_{\theta_l^*}^{gw} + \bar{H}_{\theta_l^*}^{rad}. \end{aligned} \quad (3.20)$$

Finally, by analogy, the filtered transport equation for total water is written

$$\begin{aligned} \frac{\partial \bar{q}_t}{\partial t} + \frac{1}{\varrho_0} \frac{\partial (\varrho_0 \bar{q}_t \bar{u}_j)}{\partial x_j} &= \frac{\partial}{\partial x_j} \left(\frac{\nu_T}{Pr_{q T}} \frac{\partial \bar{q}_t}{\partial x_j} - \left(\bar{u}_j \bar{q}_t - \bar{\bar{u}}_j \bar{\bar{q}}_t \right) \right) \\ &+ \bar{H}_{q_t}^{sub} + \bar{H}_{q_t}^{LS}. \end{aligned} \quad (3.21)$$

The turbulent Prandtl numbers, $Pr_{\theta T}$ and $Pr_{q T}$, in the subgrid models for the scalar variables are determined dynamically using the approach of Moin *et al.* (1991). This procedure is similar to that used to calculate the Smagorinsky coefficient outlined above. In this way, all coefficients and length scales in the subgrid-scale models for the flow variables are calculated dynamically, based on information in the resolved scalar and flow fields, and the need for *a priori* specification of parameters and corrections is removed.

4. Microphysics and radiation models

The DHARMA code has the option to use either a standard parameterisation for cloud microphysics, or the more complex explicit model of Ackerman *et al.* (1995). The code includes two standard parameterisations: a bulk-condensation model, in which cloud water q_c is found by inverting Wexler's expressions for saturated vapor pressure (Wexler 1976, 1977) using the method of Flatau *et al.* (1992); and the parameterised microphysics of Wyant *et al.* (1997) which includes a treatment of precipitation.

The cloud microphysics model of Ackerman *et al.* explicitly models the dynamics of two types of particle: condensation nuclei (CN) and water droplets. Particle size distributions are defined by $C(r, \mathbf{x}, t)$ where C_{dr} is the mean number concentration (per unit volume) of particles with radius between r and $r + dr$. A filtered particle-continuity equation is solved for each particle size,

$$\begin{aligned} \frac{\partial \bar{C}}{\partial t} + \frac{\partial (\bar{C} \bar{u}_j)}{\partial x_j} = & \frac{\partial (v_f \bar{C})}{\partial z} + S_n - R_n \bar{C} + \frac{\partial (g_r \bar{C})}{\partial r} \\ & + \frac{1}{2} \int_{r_{min}}^r K_c(r, (r^3 - r'^3)^{1/3}) \bar{C}(r') \bar{C}((r^3 - r'^3)^{1/3}) dr' \\ & - \bar{C} \int_{r_{min}}^{r_{max}} K_c(r, r') \bar{C}(r') dr' \\ & + \bar{H}_C^{sub} + \bar{H}_C^{LS} + \frac{\partial}{\partial x_j} \left(\frac{\rho_0 \nu_T}{Pr_{CT}} \frac{\partial (\bar{C}/\rho_0)}{\partial x_j} - (\bar{u}_j \bar{C} - \bar{u}_j \bar{C}) \right). \quad (4.1) \end{aligned}$$

Here v_f is the particle sedimentation velocity, S_n represents particle creation, R_n is the particle removal rate, g_r is the condensational growth rate and K_c is a coalescence kernel. The first term on the right hand side is the particle flux divergence due to sedimentation. This flux is modelled using the Stokes-Cunningham expression for $Re < 10^{-2}$ and the interpolation of Beard (1976) for higher Re . The second and third terms on the right hand side represent particle creation and transitions between CN and droplets. The fourth term is the divergence in radius-space due to condensation and evaporation. The first integral represents creation of particles due to collisions of smaller particles while the second integral represents the loss of particles due to collisions with other particles. \bar{H}_C^{sub} and \bar{H}_C^{LS} are the subsidence and large-scale advective tendencies similar to those appearing in the gas phase equations. The final term is a turbulent diffusion flux representing the subgrid-scale stresses resulting from the filtering operation. The turbulent Prandtl number Pr_{CT} is set equal to that calculated dynamically for q_t .

Ackerman *et al.* (1995) give further details on modelling of condensation growth, CN activation, total evaporation of droplets, particle collisions and new particle creation. Particle size distributions for CN and droplets are each typically divided into 20 bins with geometrically increasing size such that the particle volume doubles between successive bins.

Because time scales for the cloud microphysics are typically smaller than those for the large-scale dynamics, the microphysics equations are integrated over a series of smaller substeps within each time step of the flow-dynamics model. Also, while the flow-dynamics model uses total-water mixing ratio q_t and liquid-water potential temperature θ_l^* as the thermodynamic variables (see (2.3) and (2.4)), the microphysical model uses the concentration of water vapour G and the potential temperature θ . The equations for

these variables are written

$$\begin{aligned} \frac{\partial \bar{G}}{\partial t} + \frac{\partial (\bar{G}\bar{u}_j)}{\partial x_j} = & - 4\pi \varrho_w \int_{r_{min}}^{r_{max}} r'^2 g_r(r') \bar{C}(r') dr' \\ & + \frac{\partial}{\partial x_j} \left(\frac{\varrho_0 \nu_T}{Pr_{qT}} \frac{\partial (\bar{G}/\varrho_0)}{\partial x_j} - (\bar{u}_j \bar{G} - \bar{\bar{u}}_j \bar{\bar{G}}) \right) \\ & + \bar{H}_G^{sub} + \bar{H}_G^{LS}, \end{aligned} \quad (4.2)$$

$$\frac{\partial (\varrho_0 \bar{\theta})}{\partial t} + \frac{\partial (\varrho_0 \bar{\theta} \bar{u}_j)}{\partial x_j} = \frac{\partial}{\partial x_j} \left(\frac{\varrho_0 \nu_T}{Pr_{qT}} \frac{\partial \bar{\theta}}{\partial x_j} - (\bar{u}_j \bar{\theta} - \bar{\bar{u}}_j \bar{\bar{\theta}}) \right) + \bar{H}_{\theta}^{sub} + \bar{H}_{\theta}^{LS}. \quad (4.3)$$

Here ϱ_w is the density of liquid water and the integral in (4.2) represents vapour exchange with the droplets. The turbulent Prandtl numbers are those calculated for the corresponding variables in the flow-dynamics model.

The fluxes of particles and water vapour across the lower boundary are calculated using Monin-Obukhov similarity functions. Here, the model integrates the surface-layer flux-profile relations of Businger *et al.* (1971) following the method of Benoit (1977). Lateral boundaries are periodic and at the upper boundary the flux divergence is set to zero.

Radiation is modelled in different ways depending on the requirements of the particular study at hand. A simple approach, often used for model intercomparisons, is to parameterise radiation as the sum of two components: a clear-sky radiative-cooling component, typically taken to be a fixed -2 K/day everywhere below the inversion; and a cloud-associated "Beer's Law" component. In the latter, long-wavelength radiative cooling is assumed to be proportional to the liquid-water content and is exponentially attenuated as the overlying liquid-water path increases. The resulting radiative heat flux F_r is then given by

$$F_r(z) = F_r(H) \exp \left(-K_a \int_z^H \varrho_0 q_c dz \right), \quad (4.4)$$

where H is the height of the domain.

A more complex approach models radiative heat transfer following the method of Toon *et al.* (1989). The model computes multiple scattering over 26 solar wavelengths ($0.26 \mu\text{m} < \lambda < 4.3 \mu\text{m}$) and absorption and scattering over 14 infrared wavelengths ($4.4 \mu\text{m} < \lambda < 62 \mu\text{m}$). Blackbody energy beyond those wavelength domains is included to agree with the Stefan-Boltzmann law. An exponential-sum formulation is used to treat gaseous absorption coefficients while the optical properties of particles are determined through Mie calculations in which the complex refractive index for liquid water is used as interpolated from the datasets of Painter *et al.* (1969), Palmer & Williams (1974) and Downing & Williams (1975). The model uses a value for carbon dioxide concentration appropriate to the year of the study. Measurements of the present global annual mean carbon dioxide concentration give a value of approximately 370 ppm by volume ($\approx 10\%$ higher than in the early 1980's). The ozone profile is taken from the *U.S. Standard Atmosphere* (NOAA 1976).

5. Numerical method

The numerical method is described in detail by Stevens & Bretherton (1996). The equations are integrated using a forward-in-time projection method based on a 2nd-order Runge-Kutta scheme similar to that of Bell & Marcus (1992). The integration proceeds as follows:

- advance velocities to $t = n + 1/2$ using explicit Euler
- solve a Poisson equation and do pressure correction at $t = n + 1/2$
- advance scalars to $t = n + 1$
- advance velocity to $t = n + 1$ using a modified trapezoid rule
- solve Poisson equation and do pressure correction at $t = n + 1$

The projection procedure is described in detail by Almgren *et al.* (1998).

The spatial discretisation is performed on a staggered grid (Arakawa C). Second-order central differences are used for diffusion terms and pressure gradients while the advection terms use a modified version of the "Uniform Third-Order Polynomial Interpolation Algorithm" (UTOPIA) of Leonard *et al.* (1993). The modified scheme developed by Stevens & Bretherton (1996) includes additional transverse correction terms which improve the stability of the scheme while maintaining its accuracy. For the scalar equations, the 3D flux limiter of Zalesak (1979) is used to ensure a monotonic solution. Source terms are computed using the second-order accurate method of Smolarkiewicz & Pudykiewicz (1992) and Smolarkiewicz & Margolin (1993). Stevens and Bretherton show that the overall scheme is second-order accurate in space and time, energy-conserving and stable up to a CFL number of 1.0.

At the lower boundary, surface fluxes of momentum, θ_i^* and q_t are calculated using the same similarity relations as those used for water vapour and particle fluxes (see Section 4). The lateral boundaries are periodic while the top boundary uses a rigid lid. As discussed above, numerical problems due to gravity waves reflecting from the top boundary are prevented by using a Rayleigh damping layer in the upper third of the domain.

6. Future plans

The performance of the dynamic mixed model will be tested using a series of simulations of a nocturnal marine stratocumulus cloud deck. The particular test case chosen is the DYCOMS-II field experiment which took place off the coast of San Diego in July, 2001. DYCOMS-II is an acronym for "Dynamics and Chemistry of Marine Stratocumulus – Phase II: Entrainment". The purpose of the experiment was to collect data for use in testing large-eddy simulations of nocturnal stratocumulus. In particular, the experiment focused on cloud-top processes involved in entrainment.

The domain to be used for the simulations has size $3.2 \text{ km} \times 3.2 \text{ km} \times 1.5 \text{ km}$ and is periodic in the horizontal directions. Two sets of simulations will be performed: one set using the dynamic mixed model and the other using the classical Smagorinsky model with the standard corrections. Each set comprises a series of simulations at grid resolutions ranging from coarse resolution (32 m horizontal by 16 m vertical grid size) to very fine resolution (4 m horizontal by 2 m vertical). Previous studies (eg. Stevens *et al.* 2000) indicate that all energetic scales will be resolved in the very fine resolution simulations, so that these simulations can reasonably be used as a benchmark for comparing the performance of the subgrid-scale turbulence models.

Comparisons will be made with a view to answering the following questions:

- 1) Does the dynamic mixed model more accurately represent the subgrid-scale turbulence,

in the sense that it reduces the difference between the coarser grid solutions and the benchmark solution?

2) How do the subgrid-scale stresses predicted by the dynamic model compare with those of the standard model? Does the dynamic model, for example, predict a Richardson-number dependence in regions of stable stratification similar to that used in the standard model?

3) How does the dynamic model perform for simulations in which the inertial subrange is not well resolved?

For coarser simulations in which the inertial subrange is not resolved, Stevens *et al.* (1999) found that the turbulent kinetic energy equation approach gives results which are less dependent on grid resolution than those obtained using a Smagorinsky model. A possible future study would test the performance of a turbulence closure scheme in which the dynamic procedure is used to determine the coefficients in the turbulent kinetic energy equation.

REFERENCES

- ACKERMAN, A. S., HOBBS, P. V. & TOON, O. B. 1995 A model for particle micro-physics, turbulent mixing, and radiative transfer in the stratocumulus-topped marine boundary layer and comparisons with measurements. *J. Atmos. Sci.* **52**, 1204–1236.
- ACKERMAN, A. S., TOON, O. B., STEVENS, D. E., HEYMSFIELD, A. J., RAMANATHAN, V. & WELTON, E. J. 2000 Reduction of tropical cloudiness by soot. *Science* **288** (5468), 1042–1047.
- ALMGREN, A. S., BELL, J. B., COLELLA, P., HOWELL, L. H. & WELCOME, M. L. 1998 A conservative adaptive projection method for the variable density incompressible Navier-Stokes equations. *J. Comp. Phys.* **142**, 1–46.
- BARDINA, J., FERZIGER, J. H. & REYNOLDS, W. C. 1980 Improved subgrid scale models for large eddy simulation. *AIAA Paper* 80-1357.
- BEARD, K. V. 1976 Terminal velocity and shape of cloud and precipitation drops aloft. *J. Atmos. Sci.* **33**, 851–864.
- BELL, J. B. & MARCUS, D. L. 1992 A 2nd-order projection method for variable-density flows. *J. Comp. Phys.* **101**, 334–348.
- BENOIT, R. 1977 Integral of surface-layer profile-gradient functions. *J. Appl. Met.* **16**, 859–860.
- BOHNERT, M. 1993 A numerical investigation of cloud-topped planetary boundary layers. PhD thesis, Stanford University.
- BOIVIN, M., SIMONIN, O. & SQUIRES, K. D. 2000 On the prediction of gas-solid flows with two-way coupling using large eddy simulation. *Phys. Fluids* **12**, 2080–2090.
- BRANLEY, N. & JONES, W. P. 2001 Large eddy simulation of a turbulent non-premixed flame. Submitted to *Combustion and Flame*.
- BRETHERTON, C. S., MACVEAN, M. K., BECHTOLD, P., CHLOND, A., COTTON, W. R., CUJXART, J., CUIJPERS, H., KHAIROUTDINOV, M., KOSOVIC, B., LEWELLEN, D., MOENG, C. H., SIEBESMA, P., STEVENS, B., STEVENS, D. E., SYKES, I. & WYANT, M. C. 1999 An intercomparison of radiatively driven entrainment and turbulence in a smoke cloud ; as simulated by different numerical models. *Quart. J. Royal Meteor. Soc.* **125** (554/pt.B), 391–423.
- BROWN, A. R., DERBYSHIRE, S. H. & MASON, P. J. 1994 Large-eddy simulation of

- stable atmospheric boundary-layers with a revised stochastic subgrid model. *Quart. J. Royal Meteor. Soc.* **120** (520), 1485–1512.
- BUSINGER, J. A., WYNGAARD, J. C., IZUMI, Y. & BRADLEY, E. F. 1971 Flux-profile relationships in the atmospheric surface layer. *J. Atmos. Sci.* **28**, 181–189.
- CLARK, T. L. 1979 Numerical simulations with a three-dimensional cloud model: Lateral boundary condition experiments and multicellular severe storm simulations. *J. Atmos. Sci.* **36**, 2191–2215.
- DEARDORFF, J. W. 1972 Convective velocity and temperature scales for the unstable planetary boundary layer and Rayleigh convection. *J. Atmos. Sci.* **27**, 1211–1213.
- DEARDORFF, J. W. 1974 Three-dimensional numerical study of turbulence in an entraining mixed layer. *Bound.-Layer Meteorol.* **7**, 199–226.
- DEARDORFF, J. W. 1980 Stratocumulus-capped mixed layers derived from a three-dimensional model. *Bound.-Layer Meteorol.* **18**, 495–527.
- DOWNING, H. D. & WILLIAMS, D. 1975 Optical constants of water in the infrared. *J. Geophys. Res.* **80**, 1656–1661.
- FLATAU, P. J., WALKO, R. L. & COTTON, W. R. 1992 Polynomial fits to saturation vapor pressure. *J. Appl. Met.* **12**, 1507–1513.
- GERMANO, M., PIOMELLI, U., MOIN, P. & CABOT, W. H. 1991 A dynamic subgrid-scale eddy viscosity model. *Phys. Fluids A* **3** (7), 1760–1765.
- GHOSAL, S., LUND, T. S. & MOIN, P. 1992 A dynamic localization model for large-eddy simulation of turbulent flows. *Manuscript 139*, Center for Turbulence Research, NASA Ames/Stanford Univ.
- JAKOB, C. 1999 Clouds in the ECMWF re-analysis. *J. Climate* **12**, 947–959.
- KLEIN, S. A. & HARTMANN, D. L. 1993 The seasonal cycle of stratiform clouds. *J. Climate* **6**, 1587–1606.
- LAPPEN, C. L. & RANDALL, D. A. 2001 Toward a unified parameterization of the boundary layer and moist convection. Part III: Simulations of clear and cloudy convection. *J. Atmos. Sci.* **58**, 2052–2072.
- LEONARD, B. P., MACVEAN, M. K. & LOCH, A. P. *NASA Tech. Memo.* 1060555.
- MACVEAN, M. K. & MASON, P. J. 1990 Cloud-top entrainment instability through small-scale mixing and its parameterization in numerical-models. *J. Atmos. Sci.* **47**, 1012–1030.
- MASON, P. 1989 Large-eddy simulation of the convective atmospheric boundary-layer. *J. Atmos. Sci.* **46**, 1492–1516.
- MASON, P. J. & BROWN, A. R. 1999 On subgrid models and filter operations in large eddy simulations. *J. Atmos. Sci.* **56**, 2101–2114.
- MASON, P. J. & DERBYSHIRE, S. H. 1990 Large-eddy simulation of the stably-stratified atmospheric boundary-layer. *Bound.-Layer Meteorol.* **53**, 117–162.
- MILLER, R. L. 1997 Tropical thermostats and low cloud cover. *J. Climate* **10**, 409–440.
- MOENG, C. H. 1986 Large eddy simulation of a stratus-topped boundary layer. Part I: Structure and budgets. *J. Atmos. Sci.* **43**, 2886–2900.
- MOIN, P., SQUIRES, K., CABOT, W. & LEE, S. 1991 A dynamic subgrid-scale model for compressible turbulence and scalar transport. *Phys. Fluids A* **3**, 2746–2757.
- NIGAM, S. 1997 The annual warm to cold phase transition in the eastern equatorial Pacific: Diagnosis of the role of stratus cloud-top cooling. *J. Climate* **10**, 2447–2467.

- NOAA 1976 U.S. Standard Atmosphere. NOAA-S/T 76-1562, Washington, D.C., 227 pp.
- OGURA, Y. & PHILLIPS, N. 1962 Scale analysis of deep and shallow convection in the atmosphere. *J. Atmos. Sci.* **19**, 173–179.
- PAINTER, L. R., BIRKHOFF, R. D. & T., A. E. 1969 Optical measurements of liquid water in the vacuum ultraviolet. *J. Geophys. Res.* **51**, 243–251.
- PALMER, K. F. & WILLIAMS, D. 1974 Optical properties of water in the near infrared. *J. Opt. Soc. Amer.* **64**, 1107–1110.
- PIOMELLI, U. & LIU, J. 1995 Large eddy simulation of rotating channel flows using a localized dynamic model. *Phys. Fluids* **7**, 839–848.
- RANDALL, D. A., COAKLEY, D. A. C. W., FAIRALL, C. W., KROPFLI, R. A. & LENSCHOW, D. H. 1984 Outlook for research on subtropical marine stratiform clouds. *Bull. Amer. Meteor. Soc.* **65**, 1290–1301.
- SAIKI, E. M., MOENG, C. H. & SULLIVAN, P. P. 2000 Large-eddy simulation of the stably stratified planetary boundary layer. *Bound.-Layer Meteorol.* **95**, 1–30.
- SCHUMANN, U. & MOENG, C. H. 1991a Plume fluxes in clear and convective boundary layers. *J. Atmos. Sci.* **48**, 1746–1757.
- SCHUMANN, U. & MOENG, C. H. 1991b Plume fluxes in clear and convective boundary layers. *J. Atmos. Sci.* **48**, 1758–1770.
- SLINGO, A. 1990 Sensitivity of the Earth's radiation budget to changes in low clouds. *Nature* **343**, 49–51.
- SMAGORINSKY, J. 1963 General circulation experiments with the primitive equations, I. The basic experiment. *Mon. Weath. Rev.* **91**, 99–164.
- SMOLARKIEWICZ, P. K. & MARGOLIN, L. G. 1993 On forward-in-time differencing for fluids : Extension to a curvilinear framework. *Mon. Weath. Rev.* **121** (6), 1847–1859.
- SMOLARKIEWICZ, P. K. & PUDYKIEWICZ, J. A. 1992 A class of semi-lagrangian approximations for fluids. *J. Atmos. Sci.* **49**, 2082–2096.
- STEVENS, B., ACKERMAN, A. S., ALBRECHT, B. A., BROWN, A. R., CHLOND, A., CUXART, J., DUYNKERKE, P. G., LEWELLEN, D. C., MACVEAN, M. K., NEGERS, R. A. J., SANCHEZ, E., SIEBESMA, A. P. & STEVENS, D. E. 2001 Simulations of trade wind cumuli under a strong inversion. *J. Atmos. Sci.* **58**, 1870–1891.
- STEVENS, B., MOENG, C. H. & SULLIVAN, P. P. 1999 Large-eddy simulations-of radiatively driven convection: Sensitivities to the representation of small scales. *J. Atmos. Sci.* **56**, 3963–3984.
- STEVENS, D. E., ACKERMAN, A. S. & BRETHERTON, C. S. 2002 Effects of domain size and numerical resolution on the simulation of shallow cumulus convection. Submitted to *J. Atmos. Sci.*
- STEVENS, D. E., BELL, J. B., ALMGREN, A. S., BECKNER, V. E. & RENDLEMAN, C. A. 2000 Small-scale processes and entrainment in a stratocumulus marine boundary layer. *J. Atmos. Sci.* **57**, 567–581.
- STEVENS, D. E. & BRETHERTON, C. S. 1996 A forward-in-time advection scheme and adaptive multilevel flow solver for nearly incompressible atmospheric flow. *J. Comp. Phys.* **129**, 284–295.
- STEVENS, D. E. & BRETHERTON, C. S. 1999 Effects of resolution on the simulation of stratocumulus entrainment. *Quart. J. Royal Meteor. Soc.* **125** (554/pt.B), 425–439.
- TOON, O. B., MCKAY, C. P., ACKERMAN, T. P. & SANTHANAM, K. 1989 Rapid

- calculation of radiative heating rates and photodissociation rates in inhomogeneous multiple-scattering atmospheres. *J. Geophys. Res.-Atmos.* **94** (D13), 16287–16301.
- WEXLER, A. 1976 Vapor pressure formulation for water in range 0 to 100°C. *J. Res. Natl. Bur. Stand.* **80A**, 775–785.
- WEXLER, A. 1977 Vapor pressure formulation for ice. *J. Res. Natl. Bur. Stand.* **81A**, 5–20.
- WYANT, M. C., BRETHERTON, C. S., RAND, H. A. & STEVENS, D. E. 1997 Numerical simulations and a conceptual model of the stratocumulus to trade cumulus transition. *J. Atmos. Sci.* **54**, 168–192.
- ZALESAK, S. T. 1979 Fully multidimensional flux-corrected transport algorithms for fluids. *J. Comp. Phys.* **31**, 335–362.
- ZANG, Y., STREET, R. & KOSEFF, J. R. 1993 A dynamic mixed subgrid-scale model and its application to recirculating flows. *Phys. Fluids A* **5**, 3186–3196.

Secondary shear instability as a source of turbulence in the solar tachocline

By K. Petrovay[†]

1. Introduction

The tachocline is a thin layer in the interior of the Sun characterized by stable stratification and a strong rotational shear in both the radial and latitudinal directions. This layer is thought to be of crucial importance in the origin of solar activity phenomena. The origin and character of turbulence in this layer is poorly known, even though turbulence has an important role in determining the overall structure of the tachocline. Owing to the strongly stable stratification, the mean radial shear is stable, while the horizontal shear is expected to drive predominantly horizontal, quasi-2D motions in thin slabs. However, here I suggest that a major source of 3D overturning turbulent motions in the tachocline is the secondary shear instability due to the strong, random vertical shear arising between the uncorrelated horizontal flows in neighbouring slabs. A simplified one-dimensional model is presented for the tachocline in this case. It is found that Maxwell stresses due to an oscillatory poloidal magnetic field of a few hundred gauss are able to confine the tachocline to a thickness of a few megameters. The integral scale of the 3D overturning turbulence is the buoyancy scale, on the order of 10 km and its velocity amplitude is a few m/s, yielding a vertical turbulent diffusivity on the order of $10^8 \text{ cm}^2/\text{s}$.

The enormous spatial scales of astrophysical flows, such as the flows in stellar interiors and atmospheres, lead to extremely high Reynolds numbers, so these flows are usually strongly turbulent. Studying the flows in the "star in our backyard", the Sun, offers a chance to study turbulent flows in conditions and parameter regimes way beyond the reach of laboratory experiments, terrestrial observations, and often even direct numerical simulations. Further importance to these studies is given by the influence the Sun exerts on the cosmic environment of our planet, determining space weather, and indirectly influencing the terrestrial climate.

The rich variety of solar activity phenomena is the product of a magnetohydrodynamic dynamo operating in the Sun. It is currently thought that a thin layer of the solar interior, known as the tachocline, plays a crucial role in the solar dynamo mechanism, and it can be essentially regarded as the seat of the dynamo. Yet the fluid dynamical properties of this layer are poorly known —in fact even its existence has only been known for little more than a decade, from helioseismic measurements.

From the fluid dynamicist's point of view, the tachocline is an MHD shear flow in the azimuthal direction in a thin, rotating spherical shell with both radial and latitudinal shear and a strongly stable stratification (Richardson number $\sim 10^3$). It is situated at $0.69 R_\odot$ ($1 R_\odot = 698 \text{ Mm}$ is the solar radius) and its thickness is less than a few percent of R_\odot (Kosovichev, 1996). There are indications that at high latitudes the tachocline is situated at slightly shallower depths, $r = 0.705 R_\odot$, and it may also be marginally thicker,

[†] Eötvös University, Department of Astronomy, Budapest, P.O. Box 32, H-1518 Hungary

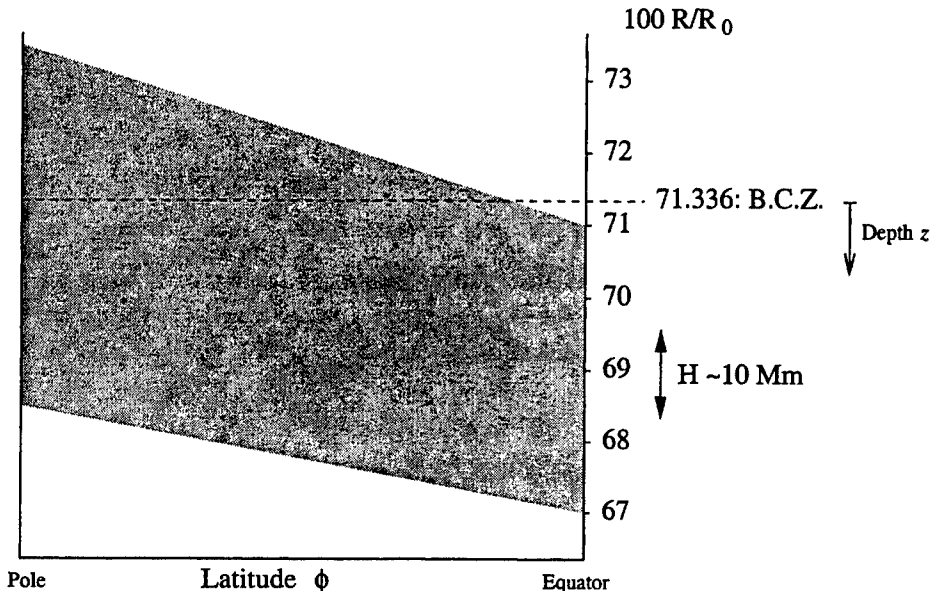


FIGURE 1. Sketch of the geometry of the solar tachocline (proportions distorted)

(Basu & Antia, 2001) —cf. figure 1. The radiative interior below the tachocline rotates like a rigid body, while the convective zone lying above it is characterized by a latitudinal differential rotation which can be regarded independent of depth to a first approximation. The tachocline itself is defined as the transitional layer between these two regimes. The rigid rotation rate of the interior equals the rotation rate of the convective envelope at an intermediate heliographic latitude of about 35° , so the radial shear changes sign at this latitude in the tachocline.

The differential rotation in the convective zone is driven by turbulent angular momentum transport due to nondiagonal terms of the Reynolds stress tensor, which in turn arise as a consequence of the effect of the Coriolis force on turbulence. As pointed out by Spiegel & Zahn (1992), in the absence of turbulence and magnetic fields this differential rotation should penetrate deep ($\sim R_\odot$) into the radiative interior below. The empirical fact that the tachocline is quite thin thus implies the presence of a strongly anisotropic (predominantly horizontal) transport of angular momentum. This may either be due to anisotropic turbulence or to Maxwell stresses in a predominantly horizontal magnetic field. While strongly anisotropic (horizontal) turbulence is the natural expectation in a stably stratified shear layer, the actual calculations (Garaud, 2001b; Miesch, 2002) show that the horizontal motions arising from a weak nonlinear instability of the latitudinal shear do not lead to an efficient transfer of angular momentum. This leaves us with magnetic fields as the prime candidate to confine the tachocline to its observed size.

Depending on the value of the magnetic diffusivity, this magnetic field may either be a weak permanent, primordial field pervading the solar interior, or the strong oscillatory

field generated by the solar dynamo. A magnetic field oscillating with a circular frequency $\omega_{\text{cyc}} = 2\pi/P$, ($P = 22$ years is the solar cycle period) is known to penetrate a conductive medium only down to a skin depth of

$$H_{\text{skin}} = (2\eta/\omega_{\text{cyc}})^{1/2} \quad (1.1)$$

where η is the magnetic diffusivity. Basu & Antia (2001) have recently calibrated the thickness of the tachocline: the scale height resulting from their fitting profile is $H \sim 10$ Mm. Accepting this value it follows that for $\eta \lesssim 10^8$ cm²/s the dynamo field cannot penetrate the tachocline, and we can expect the tachocline to be pervaded by the internal primordial field. On the other hand, for $\eta \gtrsim 10^9$ cm²/s the tachocline dynamics should be governed by the dynamo field. As the associated diffusive and Lorentz timescales are also very different, these two cases basically correspond to the case of "slow" and "fast" tachocline, discussed in the literature (Gilman, 2000; Brun, 2001).

This shows that turbulence plays a key role in determining the structure of the tachocline. Unfortunately, while the thermal stratification in the tachocline is relatively well known (as summarized in Section 2 below), its fluid dynamical properties, including the precise profile of the rotational flow $v(r, \theta)$, the meridional flow, and the characteristics of turbulence, are very poorly constrained by observations. Direct numerical simulations of stratified shear flows are currently limited to much lower values of the Richardson and Reynolds numbers (Jacobitz & Sarkar, 1998). In consequence, we need to rely on theoretical arguments concerning the properties of turbulent motions in such conditions. On the basis of such arguments, simplified one- or two-dimensional models may be constructed for the mean flow, or appropriate subgrid closure schemes may be constructed for full 3D large-eddy simulations. In the lack of sound theoretical foundations for subgrid closures, all tachocline models published to date have either simply ignored turbulence (Rüdiger & Kitchatinov, 1997, MacGregor & Charbonneau, 1999, Garaud, 2001a), or assumed arbitrary fixed scalar turbulent diffusivities in 2D mean flow models (Forgács-Dajka & Petrovay, 2001, Forgács-Dajka & Petrovay, 2002) and in LES (Miesch, 2001, 2002).

The aim of the present work is to attempt to remedy this situation by considering, on the basis of the known stability criteria, the possible sources of turbulence in a strongly stably stratified shear flow with both vertical and horizontal shear, and discussing the expected properties of the turbulence generated by it, on the basis of a dimensional analysis of the $K-\epsilon$ equations. As our analysis does not consider the effects of spherical geometry, rotation, or magnetic fields, it should only be regarded as a first step towards a more comprehensive theoretical analysis of the problem of turbulence in the solar tachocline. These theoretical arguments can be found in Section 3. Then, in Section 4, as an illustration of the use of such theoretical considerations, our prescription for calculating the turbulent diffusivity in the tachocline, equation (3.6), is incorporated in a simplified one-dimensional model for the tachocline. The results show that Maxwell stresses due to an oscillatory poloidal magnetic field of a few hundred gauss (a rather moderate value) are able to confine the tachocline to a thickness of a few megameters. Finally, Section 5 concludes the paper by discussing the implications of this result.

2. Conditions in the tachocline

The thermal stratification of the Sun is quite accurately known from a comparison of standard solar models with helioseismic inversion results. Various characteristic timescales and diffusivities in the tachocline region are plotted in figure 2. As mentioned

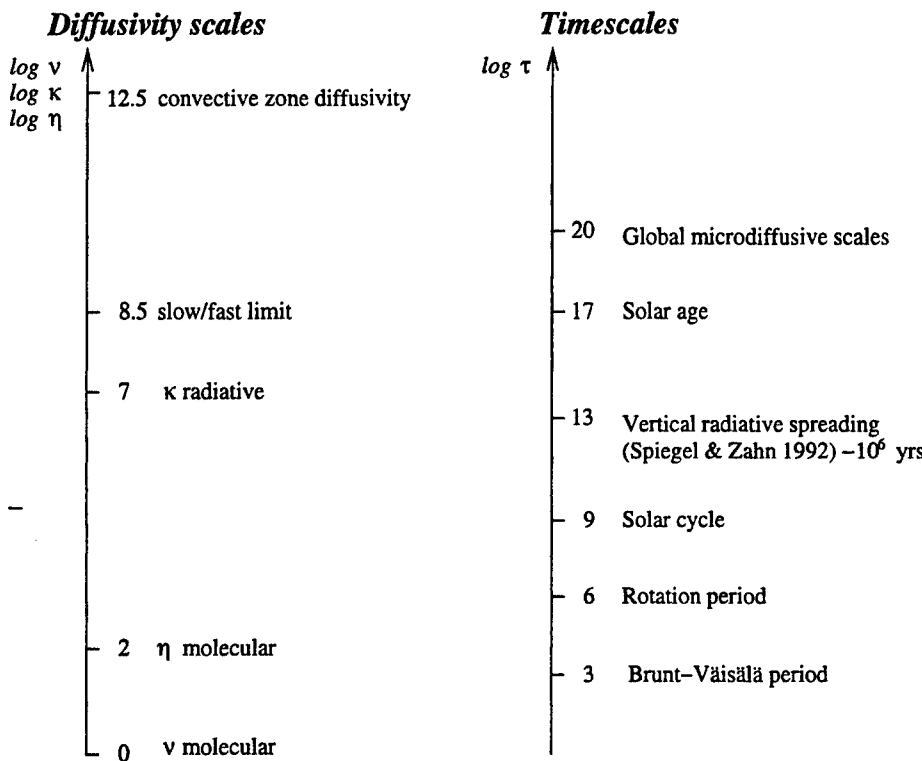


FIGURE 2. Characteristic diffusivities and timescales in the solar tachocline (CGS units)

above, the solar radius is $R_\odot = 698$ Mm, the outer 29 % of which comprises the convective zone (CZ). Owing to the high efficiency of convective energy transport, this convective envelope is nearly adiabatically (isentropically) stratified, i.e. the superadiabatic lapse rate $0 < \Delta \nabla = \nabla - \nabla_{\text{ad}} \ll 1$.[†] The radiative interior below the convective zone is characterized by significant negative values of $\Delta \nabla$. For rough estimates, a useful approximation in the tachocline region (i.e. near the top of the radiative zone) is $\Delta \nabla \sim -0.015 z$ [Mm], where $z = r_{\text{bcz}} - r$ is the depth below the bottom of the convective zone at a radius value of $r_{\text{bcz}} = 0.71 R_\odot$. On the other hand, the pressure scale height in this region is $H_P = -P dz/dP \sim 50$ Mm. With $g = 5 \cdot 10^4$ cm²/s, this yields a Brunt-Väisälä frequency

$$N_{\text{BV}}^2 [\text{s}^{-2}] = -\Delta \nabla \frac{g}{H_P} \sim 1.5 \cdot 10^{-7} z [\text{Mm}], \quad (2.1)$$

i.e. in the mid-tachocline, at $z = H \sim 10$ Mm (if the Basu & Antia, 2001, calibration of H is accepted) $N_{\text{BV}} \sim 10^{-3}$ s⁻¹.

A displaced mass element will then oscillate around its equilibrium position under the action of buoyancy on a timescale $N_{\text{BV}}^{-1} \sim 1000$ s. The amplitude of the oscillation is

[†] ∇ is standard astrophysical notation for the lapse rate $d \ln T / d \ln P$.

clearly $\sim v_z/N_{\text{BV}}$, so in the presence of turbulent motions, these motions will be limited to a vertical scale $l_b = K^{1/2}/N_{\text{BV}}$, called the *buoyancy scale*. ($K = \overline{v_z^2}$ is the kinetic energy in the vertical component of motions.) On the other hand, as an elementary estimate gives $\nu \sim K^2/\epsilon$ for the vertical turbulent diffusivity, one has $l_b \sim (\nu/N_{\text{BV}})^{1/2}$. Vertical overturning motions on scales exceeding l_b will be strongly damped by gravity wave emission.

3. The secondary shear instability

The pole-equator difference in the rotational rate of the convective zone is about 30 % of the equatorial rotation rate. Taking half of this value to be the characteristic amplitude of the differential rotation (cf. eq. (3.3) below), we have a differential rotation amplitude of $\Delta v \sim 3 \cdot 10^4 \text{ cm/s}$ at the top of the tachocline. This value is clearly also roughly the amplitude of the vertical velocity difference across the tachocline, so the characteristic vertical shear is

$$S \sim \Delta v/H \sim 3 \cdot 10^{-5} \text{ s}^{-1} \quad (3.1)$$

This yields a Richardson number $\text{Ri} = N_{\text{BV}}^2/S^2 \sim 10^3$. This enormous value shows that the vertical shear cannot directly drive turbulence in the tachocline.

Buoyancy, however, cannot stabilize the horizontal shear. While linear stability analysis (Dziembowski & Kosovichev, 1987, Charbonneau *et al.*, 1999) shows that the horizontal shear is marginally stable in the nonmagnetic case, nonlinear effects and magnetic fields are known to lead to instability (Garaud, 2001b; Miesch, 2001, 2002). The motions driven by the horizontal shear instability are predominantly horizontal, and their spatial scale is

$$l_h \sim R_\odot, \quad (3.2)$$

while their velocity scale v_h is determined by the amplitude Δv of the horizontal shear at the given depth:

$$v_h \sim \Delta v = R_\odot \frac{[\omega(z, \theta = 0) - \omega(z, \theta = \pi/2)]}{2} \quad (3.3)$$

OVERTURNING TURBULENT MOTIONS IN THE VERTICAL DIRECTION ARE IMPEDED BY THE STABLE STRATIFICATION, THEIR SCALE BEING LIMITED TO l_b . OWING TO THE LOW VERTICAL DIFFUSIVITY, HOWEVER, THE HORIZONTAL MOTIONS WILL BE CHARACTERIZED BY A LIMITED VERTICAL CORRELATION LENGTH

$$l_c \sim (\nu l_h/v_h)^{1/2}. \quad (3.4)$$

The random horizontal flows driven by the shear will then be limited to thin sheets of thickness l_c , the motion in neighbouring sheets being independent. This will give rise to random vertical shear between neighbouring sheets, of amplitude

$$S_2 \sim v_h/l_c \sim (v_h^3/\nu l_h)^{1/2} \quad (3.5)$$

This *secondary vertical shear* is much stronger than the primary (mean) vertical shear, the corresponding Richardson number being $\text{Ri}_2 = g\Delta\nu l_h/H_P v_h^3$. Substituting here the characteristic values of the parameters, we find that $\text{Ri}_2 < 0.25$, i.e. the secondary shear is unstable, if

$$\nu < \nu_{\text{cr}} = \frac{v_h^3}{4l_h N_{\text{BV}}^2} = 10^{-4} \frac{v_h^3 [\text{CGS}]}{z [\text{Mm}]} \quad (3.6)$$

In the mid-tachocline this value is $\nu_{\text{cr}} \sim 10^8 \text{ cm}^2/\text{s}$, much higher than the molecular value, so we expect that the secondary shear is strongly unstable.

What is the characteristic amplitude of the turbulent motions driven by the secondary shear instability? In principle, this could be derived from a K - ϵ model (or, more, generally, from a Reynolds stress model —cf. Mansour, Kim & Moin, 1999). Assuming plane parallel geometry for simplicity, the relevant equations are of the general form

$$\frac{\partial K}{\partial t} = P_K - D_K - \frac{\partial F_K}{\partial z} \quad (3.7)$$

$$\frac{\partial \epsilon}{\partial t} = P_\epsilon - D_\epsilon - \frac{\partial F_\epsilon}{\partial z} \quad (3.8)$$

Here, the non-local fluxes or third order moments (TOMs) are

$$F_K = \overline{v_z^3} \quad (3.9)$$

$$F_\epsilon = \overline{v_z \epsilon_l} \quad (3.10)$$

ϵ_l being the local dissipation rate, while ϵ is the mean dissipation. The production terms are usually modelled as

$$P_K = \frac{\nu}{2} S_2^2 \quad (3.11)$$

$$P_\epsilon = C_P \frac{\epsilon}{K} P_K \quad (3.12)$$

while, assuming an ideal gas and the Boussinesq approximation $\rho'/\rho = -T'/T$ (prime denotes fluctuations), the dissipation/sink terms read

$$D_K = \epsilon + g \overline{v_z T'} \quad (3.13)$$

$$D_\epsilon = C_{D1} \frac{\epsilon^2}{K} + C_{D2} \frac{\epsilon}{K} g \overline{v_z T'} \quad (3.14)$$

(The first terms on the r.h.s. represent viscous dissipation, while the second terms correspond to gravity wave emission. Note that in a subadiabatic environment $\overline{v_z T'} > 0$, i.e. downmoving fluid parcels are hotter than average.)

Performing a dimensional analysis on these equations we find that the diffusive timescale, corresponding to the non-local terms, is $d^2/\nu \gtrsim d^2/\nu_{\text{cr}} \sim 10^{10} \text{ s}$, while the timescale associated with the shear production term is $K/\nu S_2^2 \sim N_{\text{BV}}/S_2^2 \sim N_{\text{BV}} l_h \nu / v_h^3 \sim 10^{-5} \nu < 10^3 \text{ s}$. This implies that the transport terms can be neglected in the K - ϵ equations. Under such conditions the equations have no stationary solution, as the values of the constants C_P , C_{D1} and C_{D2} are different in general. The intensity of turbulence will then keep increasing until the turbulent diffusivity reaches the critical value ν_{cr} , when further shear production is switched off.

We thus conclude that the secondary vertical shear instability can be expected to drive overturning turbulence to the level $\nu = \nu_{\text{cr}}$ on a short timescale. The turbulence generated by this mechanism may then be crudely represented by the vertical diffusivity value given by eq. (3.6).

4. Tachocline model

We now proceed to develop a simple one-dimensional model for the solar tachocline, assuming that the secondary shear instability discussed in the previous section is the

only source of turbulence in the tachocline region. Our computational domain will be restricted to the top of the radiative interior, below r_{bcz} .

From figure 2 it is apparent that the convective zone is characterized by extremely high turbulent diffusivities. Due to the Coriolis force, the Reynolds stress tensor also has significant nondiagonal components in the convective envelope. These components imply an angular momentum transport which is thought to be the main driver of solar differential rotation. Based on the discussion of the previous section we expect that the amplitude of turbulence in the tachocline is much lower than in the CZ. Thus, from the point of view of tachocline modelling, it is not unrealistic to regard the latitudinal differential rotation at $r = r_{bcz}$ as a given boundary condition imposed at the top of the region of interest. This is tantamount to assuming that differential rotation is driven by a highly effective mechanism in the convective zone which is not seriously influenced by the processes in the tachocline.

As the layer studied is thin, we also adopt a plane parallel representation for it, with constant density. (The effects of density stratification are only implicitly taken into account by its role in determining the turbulent viscosity, eq. (3.6).)

Thus, we regard the following model problem. Consider a plane parallel layer of incompressible fluid of density ρ , where the viscosity ν and the magnetic diffusivity η depend on z only. At $z = 0$ where z is the vertical coordinate (corresponding to depth in the solar application we have in mind) a periodic horizontal shearing flow is imposed in the y direction:

$$v_{y0} = v_0 \cos(kx)$$

(so that x will correspond to heliographic latitude, while y to the longitude). We assume a two-dimensional flow pattern ($\partial/\partial y = 0$) and $v_x = v_z = 0$ (no ‘meridional flow’). An oscillatory horizontal ‘poloidal’ field is present in the x direction, given by

$$V_p = \frac{1}{(4\pi\rho)^{1/2}} \frac{\partial A}{\partial z} \quad (4.1)$$

(in Alfvénic units). The ‘toroidal’ (i.e. y) component A of the vector potential obeys the corresponding component of the integral of the induction equation, which in our case simplifies to a diffusion equation:

$$\frac{\partial A}{\partial t} = \frac{\partial}{\partial z} \left(\eta \frac{\partial A}{\partial z} \right) \quad (4.2)$$

The upper boundary condition $A = A_0$ at $z = 0$ fixes the poloidal field amplitude.

The evolution of the azimuthal components of the velocity and the magnetic field is described by the corresponding components of the equations of motion and induction, respectively. Introducing $v = v_y$ and using Alfvén speed units also for the toroidal magnetic field

$$b = B_y (4\pi\rho)^{-1/2}, \quad (4.3)$$

these can be written as

$$\frac{\partial v}{\partial t} = V_p \cos(\omega t) \frac{\partial b}{\partial x} + \frac{\partial}{\partial z} \left(\nu \frac{\partial v}{\partial z} \right) \quad (4.4)$$

$$\frac{\partial b}{\partial t} = V_p \cos(\omega t) \frac{\partial v}{\partial x} + \frac{\partial}{\partial z} \left(\eta \frac{\partial b}{\partial z} \right) \quad (4.5)$$

where we have taken into account that, owing to the thinness of the tachocline, the

vertical derivatives dominate the diffusive terms. As the imposed poloidal field V_p is independent of x , Fourier transforming (4.4) and (4.5) in terms of x yields the same equations for the Fourier amplitudes \hat{v} and \hat{b} , except that $\partial/\partial x$ is substituted by ik :

$$\frac{\partial v}{\partial t} = ikbV_p \cos(\omega t) + \frac{\partial}{\partial z} \left(\nu \frac{\partial v}{\partial z} \right) \quad (4.6)$$

$$\frac{\partial b}{\partial t} = ikvV_p \cos(\omega t) + \frac{\partial}{\partial z} \left(\eta \frac{\partial b}{\partial z} \right) \quad (4.7)$$

(Hats are omitted to simplify notation.) For a rough estimate, we write $\pi b/P$ for the l.h.s. of (4.7), then substitute the resulting expression of b into (4.6), take the real part, and omit the factor $\cos^2(\omega t)$ in the first term on the r.h.s.:

$$\frac{\partial v}{\partial t} = -k^2 V_p^2 P v + \frac{\partial}{\partial z} \left(\nu \frac{\partial v}{\partial z} \right) \quad (4.8)$$

The equations to solve are thus (4.1), (4.2) and (4.8), with the turbulent diffusivities $\nu = \eta = \nu_m + \nu_{cr}$ given by equation (3.6) with the identification $v_h = v$. ν_m is a minimal diffusivity value (“molecular diffusivity”).

The simplified form of the first term in equation (4.8) will not allow a correct reproduction of the periodic part of the time dependence. The important point is, however, that this sink term, representing the reduction of horizontal shear by Maxwell stresses, has the right amplitude and the correct scaling with V_p , P , v , and k , so it may be expected to reproduce well the cycle-averaged flow amplitude as a function of z , which is our main interest here. Indeed, solving our equations for the case of constant diffusivities ν and η , the results are in a remarkably good agreement with the fully consistent solutions in spherical geometry, presented in Forgács-Dajka & Petrovay (2002).

The equations were solved numerically by a finite difference scheme second-order accurate in time. All quantities were set to zero at the lower boundary, situated at $z_0 = 60$ or 30 Mm below r_{bcz} , while the boundary conditions applied at top ($z = 0$) were $v = v_0 = 3 \cdot 10^4$ cm/s and different prescribed values for A_0 . As equation (3.6) is singular at $z = 0$, ν was set to a high finite value ν_{max} here. For ν_m we used the value 10^7 cm²/s. This is much higher than the actual molecular diffusivities in the tachocline, but using a realistic value would lead to forbiddingly long integration times. Similarly, a too high value for ν_{max} would lead to very short timesteps, also increasing the computing time to unaffordable values. Test runs with varying values of ν_{max} and ν_m , however, show that these choices do not significantly distort the results.

Starting from an arbitrary initial state, the system was allowed to evolve until very nearly periodic behaviour sets in (in about 10^4 years, depending on the value of ν_m), then average quantities for one 11-year half-cycle were computed and plotted as functions of depth (Figs. 3 and 4).

5. Discussion

In the case with a very weak magnetic field (left-hand column in figure 3), it is straightforward to show that equation (4.8) with ν given by (3.6) admits the analytic solution

$$v = v_0 \left[1 - \left(\frac{z}{z_0} \right)^2 \right]^{1/4}, \quad (5.1)$$

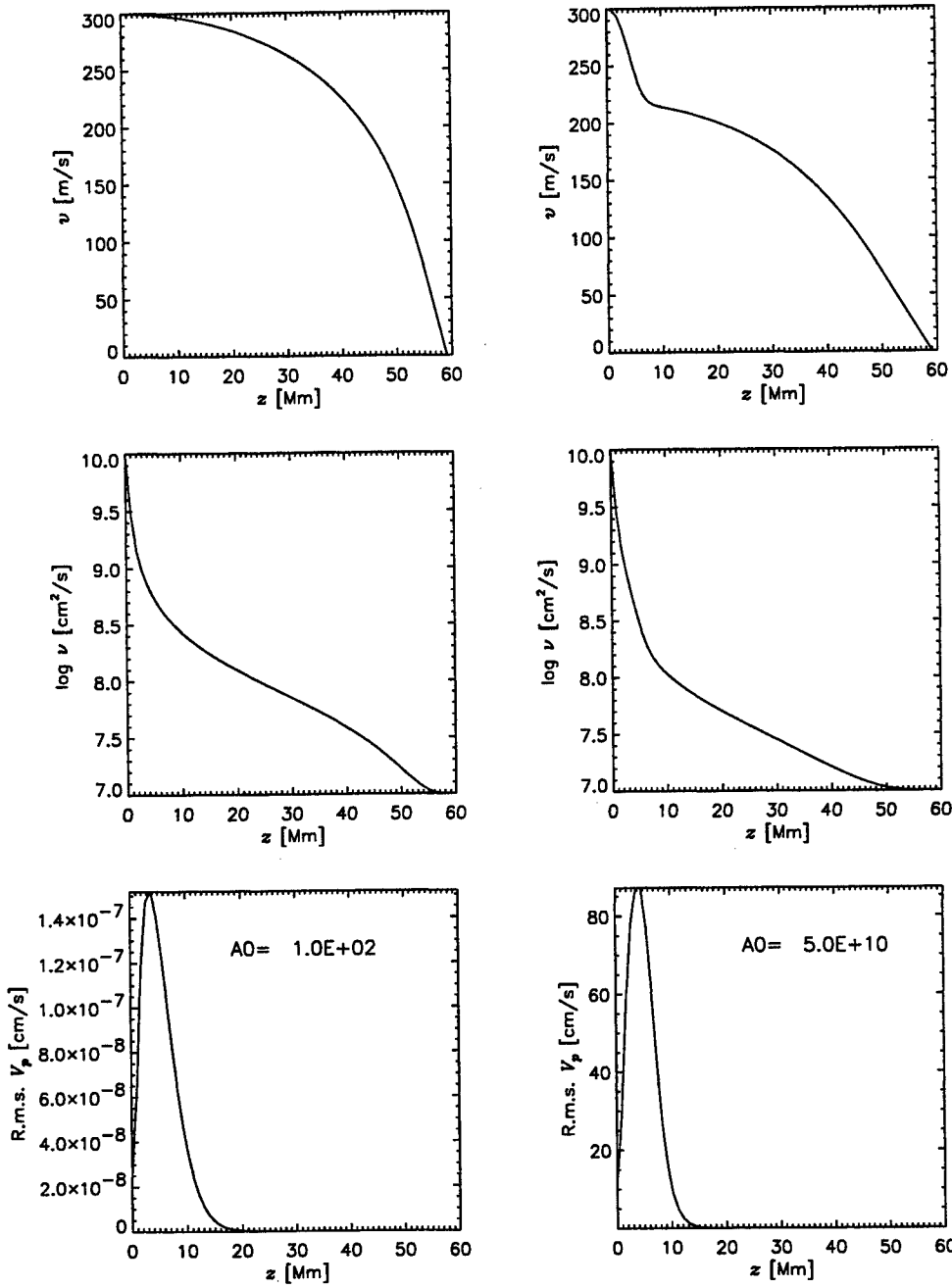


FIGURE 3. Horizontal differential rotation amplitude $v = v_h$, as defined in eq. (3.3) (top row), vertical turbulent diffusivity v (middle row), and poloidal magnetic field in Alfvénic units (bottom row), averaged over a solar half-cycle, as functions of depth below the convective zone, for a very low (left-hand column) and a medium (right-hand column) value of the field strength imposed at the top. Note that by coincidence, in the solar tachocline the field strength in gauss is roughly equal to the corresponding Alfvén speed in cm/s.

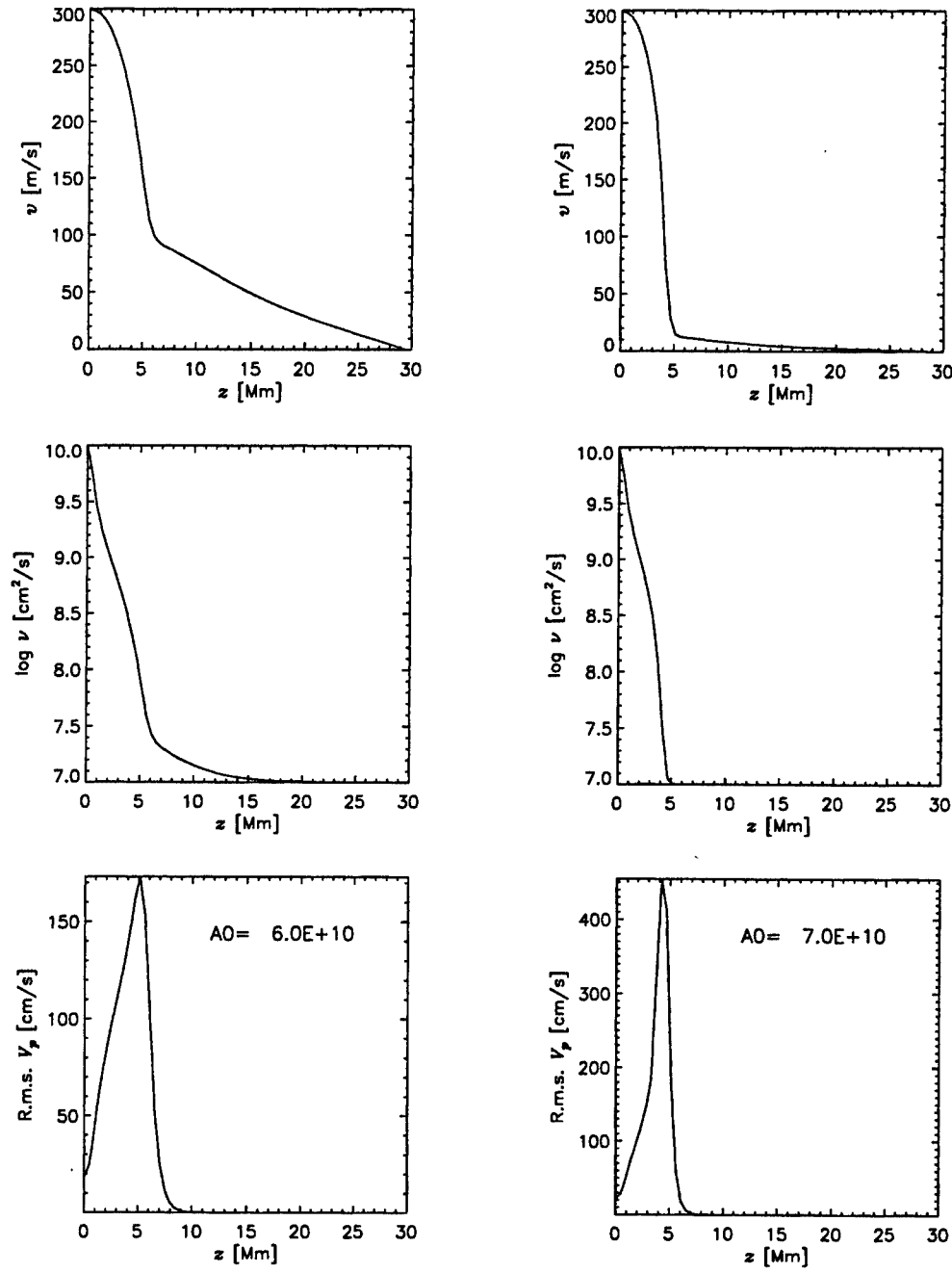


FIGURE 4. Same as figure 3 for two higher field strength values.

confirmed by the numerical calculations. This essentially means that in this case the shear penetrates as far down into the radiative interior as the placement of the lower boundary condition allows. The weak magnetic field itself only penetrates down to the skin depth given by equation (1.1), as expected. It is worth noting that the poloidal field

shows a non-monotonic behaviour with depth in all cases, reaching its maximum at some finite z value. This is due to the variable diffusivity: the horizontal field lines tend to “pile up” where the diffusivity is significantly reduced.

From the right-hand column of figure 4 we can see that a poloidal magnetic field of a few hundred gauss (peak strength 500 G) can confine the tachocline to a thickness of barely 4 Mm. This field strength is quite realistic: the total poloidal flux in the tachocline in this case is comparable to the flux through the solar surface, as required. Nevertheless, the resulting thin tachocline seems to be at odds with the results of Basu & Antia (2001), and is also hard to reconcile with the gradual depletion of lithium in the atmospheres of Sun-like stars during their lifetimes. Lithium is destroyed by nuclear reactions in layers below $z \sim 40$ Mm only, so a mixing characterized by a diffusivity of at least $10^3 \text{ cm}^2/\text{s}$ must be present as far down as that depth. While our prescription $\nu_m = 10^7 \text{ cm}^2/\text{s}$ does not allow a firm statement on this issue, the very sharp cutoff of the ν -curve in the figures under discussion does not seem to indicate that any significant level of turbulence could be maintained at such great depths.

One might think that an intermediate field strength might lead to a somewhat thicker tachocline. This is, however, not the case: an inspection of the full series of results in our figures clearly shows that a weaker field simply results in an “aborted tachocline”, i.e. the horizontal shear is first reduced by a factor depending on the field strength in a thin layer of a few Mm, but below that layer, as the magnetic field is damped by the skin effect, it follows the field-free solution (5.1), with a lower amplitude. It remains to be seen, whether such a two-tiered ν -profile can yield an equal or better fit to helioseismic data than the more conventional profiles, used e.g. by Basu & Antia (2001).

One obvious shortcoming of the present models is their simplified treatment of the time development and of the geometry. The development of more realistic, axially symmetric spherical models employing the viscosity formula (3.6) is in progress.

Acknowledgements

I thank Nagi Mansour, Sasha Kosovichev, and Alan Wray for their warm hospitality during my stay at Ames. This paper owes much to discussions with them and with Mark Miesch. This work was supported in part by the OTKA under grant no. T032462.

REFERENCES

- BASU, S. & ANTIA, H. M. 2001 A Study of Possible Temporal and Latitudinal Variations in the Properties of the Solar Tachocline. *Mon. Not. Roy. Astr. Soc.* **324**, 498–508.
- BRUN, A. S. 2001 In *Helio- and Asteroseismology at the Dawn of the Millennium*, p. 273. ESA Publ. SP-464.
- CHARBONNEAU, P., DIKPATI, M. & GILMAN, P. A. 1999 Stability of the Solar Latitudinal Differential Rotation Inferred from Helioseismic Data. *Astroph. J.* **526**, 523–537.
- DZIEMBOWSKI, W. & KOSOVICHEV, A. 1987 Low Frequency Oscillations in Slowly Rotating Stars III: Kelvin-Helmholtz Instability. *Acta Astr.* **37**, 341.
- FORGÁCS-DAJKA, E. & PETROVAY, K. 2001 Tachocline Confinement by an Oscillatory Magnetic Field. *Solar Phys.* **203**, 195–210.
- FORGÁCS-DAJKA, E. & PETROVAY, K. 2002 Dynamics of the Fast Solar Tachocline I: Dipolar Field. *Astron. Astroph.* **389**, 629–640.

- GARAUD, P. 2001a Dynamics of the Solar Tachocline I: An Incompressible Study. *Mon. Not. Roy. Astr. Soc.* **329**, 1–18.
- GARAUD, P. 2001b Latitudinal Shear Instability in the Solar Tachocline. *Mon. Not. Roy. Astr. Soc.* **324**, 68–76.
- GILMAN, P. A. 2000 Fluid dynamics and mhd of the solar convection zone and tachocline: Current understanding and unsolved problems. *Solar Phys.* **192**, 27–48.
- JACOBITZ, F. G. & SARKAR, S. 1998 The effect of nonvertical shear on turbulence in a stratified medium. *Phys. Fluids* **10**, 1158–1168.
- KOSOVICHEV, A. G. 1996 Helioseismic Constraints on the Gradient of Angular Velocity at the Base of the Solar Convection Zone. *Astroph. J.* **469**, L61–L64.
- MACGREGOR, K. B. & CHARBONNEAU, P. 1999 Angular Momentum Transport in Magnetized Stellar Radiative Zones. IV. Ferraro's Theorem and the Solar Tachocline. *Astroph. J.* **519**, 911–917.
- MANSOUR, N. N., KIM, J. & MOIN, P. 1989 Near-Wall $k-\epsilon$ Turbulence Modeling. *AIAA Journal* **27**, 1068–1073.
- MIESCH, M. S. 2001 Numerical Modeling of the Solar Tachocline. I. Freely Evolving Stratified Turbulence in a Thin Rotating Spherical Shell. *Astroph. J.* **562**, 1058–1075.
- MIESCH, M. S. 2002 Numerical Modeling of the Solar Tachocline. II. Forced Turbulence with Imposed Shear. *Astroph. J.* to be published
- RÜDIGER, G. & KITCHATINOV, L. L. 1997 The Slender Solar Tachocline: A Magnetic Model. *Astr. Nachr.* **318**, 273–279.
- SPIEGEL, E. A. & ZAHN, J.-P. 1992 The Solar Tachocline. *Astron. Astroph.* **265**, 106–114.

Numerical simulation of 2D compressible heat-driven convection

By K. V. Parchevsky †

1. Introduction

We study the properties of heat-driven compressible turbulent convection. Two problems were considered. The first concerns an industrial application: numerical simulation of the sedimentation of a polydisperse suspension in a convectively unstable medium using a perfect gas equation of state. It is shown that convection acts as a size filter, separating particles into settled and suspended fractions with respect to particle radius. Heat driven convection can thus be used for separation of suspensions with a cut-off particle radius depending on the temperature difference only.

The second problem concerns the large scale numerical simulation of compressible convection in the solar convection zone. Here the 2D compressible hydrodynamic equations were solved by an explicit MacCormack scheme. An equation of state including real-gas effects (the OPAL equation of state) was used. Large dynamical structures were observed in the simulation which can be identified with solar supergranulation. A power spectrum of g-mode solar oscillations, excited by turbulent convection, was also obtained.

Convection plays an important role in many fields of applied physics as well as in industry. The first part of this work is devoted to studying sedimentation of a polydisperse suspension in a convectively unstable medium. Many technological processes use sedimentation for size separation of the particles in suspension. Thus, the settling behavior of polydisperse suspensions is a matter of great importance. Furthermore, very often the particles are settling in a non-static medium. In industrial applications unwelcome motions of the medium can sometimes be reduced, but in many cases the motion is significant and must be taken into account. This motion may have a preferred direction, as in a pipe flow; in other cases there is no preferred direction, as in the case of thermal convection. Since, if we do not make special efforts to stabilize the temperature, convection arises almost everywhere, knowledge of convective influences on the sedimentation process would be extremely important.

The second part of this work is a 2D numerical simulation of large scale compressible convection in the solar convection zone. Convection is one of two main mechanisms of energy transport in the Sun, the other being radiation. The dynamics of the convection zone determines such global phenomena as differential rotation, the solar dynamo, excitation of 5-min. solar oscillations, granulation, and supergranulation. On the surface of the Sun convection appears as the granulation network. Using local correlation tracking methods one can map the horizontal velocities. Supergranules can be seen on such a map; without such processing the supergranulation pattern is smoothed by the movements of individual granules. The aim of this research is to simulate solar convection in a spatial region containing many granules in order to study granule evolution in time and to deduce the supergranulation pattern using the movements of separate granules. Our

† Crimean Astrophysical Observatory, Crimea 98409, Ukraine

simulations were designed to answer the following important question in solar physics: Is supergranulation a surface phenomenon, or it is caused by the deep subphotospheric structure of the second helium ionization zone? In order to include the effects of helium ionization, the OPAL equation-of-state tables were used to calculate the thermodynamic state.

2. Governing hydrodynamic equations

Two dimensional viscous compressible convection is simulated by solution of the compressible Navier-Stokes equations. We write the equations in terms of dimensionless variables

$$\begin{aligned} x &\rightarrow \frac{x}{L}, \quad t \rightarrow \frac{a_0}{L}t, \quad \rho \rightarrow \frac{\rho}{\rho_0}, \quad p \rightarrow \frac{p}{p_0}, \\ u &\rightarrow \frac{u}{a}, \quad T \rightarrow \frac{T}{T_0}, \quad T_0 = \frac{p_0}{\rho_0 R}, \quad a_0^2 = \frac{\gamma p_0}{\rho_0} \end{aligned}$$

where R is the gas constant. Subscript 0 indicates that the values are those in a reference state, taken to be the state at the top boundary.

Dimensionless parameters R_e , P_r and F_r , given by the following expressions

$$R_e = \frac{\rho_0 a_0 L}{\mu}, \quad P_r = \frac{\mu c_p}{\kappa}, \quad F_r^2 = \frac{a_0^2}{gL}$$

represent Reynolds, Prandtl, and squared Froude numbers respectively, where μ is the viscosity, κ is the thermal conductivity, g is the gravitational acceleration, a is the speed of sound, and L is the characteristic size of the computational region.

The equations to be solved are

$$\begin{aligned} \frac{\partial \rho}{\partial t} + \frac{\partial}{\partial x}(\rho u) + \frac{\partial}{\partial y}(\rho v) &= 0 \\ \frac{\partial}{\partial t}(\rho u) + \frac{\partial}{\partial x}\left(\rho u^2 + \frac{p}{\gamma} - \tau_{xx}\right) + \frac{\partial}{\partial y}(\rho uv - \tau_{xy}) &= 0 \\ \frac{\partial}{\partial t}(\rho v) + \frac{\partial}{\partial x}(\rho uv - \tau_{xy}) + \frac{\partial}{\partial y}\left(\rho v^2 + \frac{p}{\gamma} - \tau_{yy}\right) + \frac{\rho}{F_r^2} &= 0 \quad (2.1) \\ \frac{\partial E}{\partial t} + \frac{\partial}{\partial x}\left[u\left(E + \frac{p}{\gamma} - \tau_{xx}\right) - v\tau_{xy} + \dot{Q}_x\right] + \\ + \frac{\partial}{\partial y}\left[v\left(E + \frac{p}{\gamma} - \tau_{yy}\right) - u\tau_{xy} + \dot{Q}_y\right] + \frac{\rho v}{F_r^2} &= 0 \end{aligned}$$

where τ_{ij} is the viscous stress tensor

$$\tau_{xx} = \frac{2}{3} \frac{1}{R_e} \left(2 \frac{\partial u}{\partial x} - \frac{\partial v}{\partial y} \right), \quad \tau_{yy} = \frac{2}{3} \frac{1}{R_e} \left(2 \frac{\partial v}{\partial y} - \frac{\partial u}{\partial x} \right), \quad \tau_{xy} = \tau_{yx} = \frac{1}{R_e} \left(\frac{\partial u}{\partial y} + \frac{\partial v}{\partial x} \right)$$

The rate of heat transfer is written in accordance with Fourier's law

$$\dot{Q}_x = -\frac{1}{R_e P_r (\gamma - 1)} \frac{\partial T}{\partial x}, \quad \dot{Q}_y = -\frac{1}{R_e P_r (\gamma - 1)} \frac{\partial T}{\partial y}$$

In the case of an ideal gas, $p \sim \rho T$, the pressure p can be expressed in terms of the total

energy per volume unit E as follows

$$\frac{p}{\gamma} = (\gamma - 1) \left(E - \frac{(\rho u)^2 + (\rho v)^2}{2\rho} \right)$$

where $\gamma = c_p/c_v$ is the adiabatic exponent, ρ is the density, and u and v are the x and y velocity components. In our solar convection simulation p is calculated from a real-gas equation of state through interpolation in the OPAL tables.

At the Reynolds numbers characterizing the solar convection zone, the flow will be turbulent. A turbulent viscosity μ_t and a turbulent thermal conductivity κ_t are introduced to approximate the effects of turbulence:

$$\mu_t = \rho \Delta^2 \sqrt{\left(\frac{\partial u}{\partial y} \right)^2 + \left(\frac{\partial v}{\partial x} \right)^2}, \quad \kappa_t = \frac{c_p \mu_t}{P_{rt}}$$

where Δ is the mixing length and P_{rt} is the turbulent Prandtl number ($P_{rt} = 0.9$ for air). Since we want to account for subgrid turbulence, Δ represents a characteristic grid cell size, and we take $\Delta^2 = \Delta x \Delta y$. To add turbulence to the dimensionless equations (2.1) the following changes are made:

$$\begin{aligned} \frac{1}{R_e} &\rightarrow \frac{1}{R_e} + \frac{1}{R_{et}}, \quad \frac{1}{R_e P_r} \rightarrow \frac{1}{R_e P_r} + \frac{1}{R_{et} P_{rt}} \\ \frac{1}{R_{et}} &= \frac{\mu_t}{\rho_0 a_0 L} = C \rho \Delta^2 \sqrt{\left(\frac{\partial u}{\partial y} \right)^2 + \left(\frac{\partial v}{\partial x} \right)^2} \end{aligned}$$

where $C = 0.2$ is an empirical dimensionless constant.

The governing equations are written in divergence form and can be expressed as a single vector equation:

$$\frac{\partial \mathbf{q}}{\partial t} + \frac{\partial \mathbf{F}}{\partial x} + \frac{\partial \mathbf{G}}{\partial y} + \mathbf{S} = 0 \quad (2.2)$$

The vector of dependent variable $\mathbf{q} = (\rho, \rho u, \rho v, E)^T$. An explicit MacCormack scheme is directly applied to Eq. (2.2) as follows:

Predictor step:

$$\begin{aligned} \mathbf{q}_{j,k}^* &= \mathbf{q}_{j,k}^n - \frac{\Delta t}{\Delta x} (\mathbf{F}_{j+1,k}^n - \mathbf{F}_{j,k}^n) - \frac{\Delta t}{\Delta y} (\mathbf{G}_{j,k+1}^n - \mathbf{G}_{j,k}^n) - \Delta t \mathbf{S}_{j,k}^n \\ \mathbf{F}_{j,k}^n : \quad 0 \leq j \leq N_x + 1, \quad \mathbf{G}_{j,k}^n : \quad 0 \leq j \leq N_x & \quad 0 \leq k \leq N_y \\ 0 \leq k \leq N_y & \quad 0 \leq k \leq N_y + 1, \quad 0 \leq k \leq N_y \end{aligned}$$

Corrector step:

$$\begin{aligned} \mathbf{q}_{j,k}^{n+1} &= \frac{1}{2} \left[\mathbf{q}_{j,k}^n + \mathbf{q}_{j,k}^* - \frac{\Delta t}{\Delta x} (\mathbf{F}_{j,k}^* - \mathbf{F}_{j-1,k}^*) - \frac{\Delta t}{\Delta y} (\mathbf{G}_{j,k}^* - \mathbf{G}_{j,k-1}^*) - \Delta t \mathbf{S}_{j,k}^n \right] \\ \mathbf{F}_{j,k}^* : \quad 0 \leq j \leq N_x - 1, \quad \mathbf{G}_{j,k}^* : \quad 1 \leq j \leq N_x - 1 & \quad 1 \leq j \leq N_x - 1 \\ 1 \leq k \leq N_y - 1 & \quad 0 \leq k \leq N_y - 1, \quad 1 \leq k \leq N_y - 1 \end{aligned}$$

This scheme has second order accuracy in both space and time.

Convection is driven by the temperature gradient between the top and bottom boundaries. Dirichlet boundary conditions are applied at the top and bottom:

$$T_{top} = T_0 = 273.15K, \quad u_{top} = v_{top} = 0,$$

$$T_{bottom} = T_0 + \Delta T, \quad u_{bottom} = v_{bottom} = 0$$

To calculate the pressure and density on the top and bottom boundaries we use the following procedure. We have temperature, pressure, and density at the inner nodes of the computational domain. On the boundary we have a given fixed temperature and zero velocities as boundary conditions. Assuming that the temperature changes linearly across one cell, we can write the following system of equations for the bottom boundary

$$\begin{aligned}\frac{dp}{dy} &= -\frac{\gamma g}{F_r^2} \rho \\ p &= \rho RT \\ T &= T_{bottom} - \frac{\Delta T}{\Delta y} y,\end{aligned}$$

where $R = p_1/\rho_1 T_1$ is the local gas constant and $\Delta T = T_{bottom} - T_1$ is the temperature difference between the bottom and top of the cell. We assume that the gas is perfect locally, that is, that the gas constant is constant in the cell. This system of equations can be solved analytically for ρ :

$$\rho = \rho_1 \left(\frac{T_{bottom}}{T_1} - \frac{\Delta T}{T_1 \Delta y} \right)^{\frac{\gamma g \Delta y}{R F_r^2 \Delta T} - 1}$$

Similar conditions can be written for the top boundary. Lateral boundary conditions are taken to be periodic.

As an initial condition we choose a hydrostatic state with a linear temperature gradient

$$\begin{aligned}T(y) &= 1 + \Delta T(1 - y) = T_{bottom} - y \Delta T \\ \rho(y) &= [1 + \Delta T(1 - y)]^{\frac{\gamma / F_r^2 - \Delta T}{\Delta T}} \\ p(y) &= \rho(y) T(y) = [1 + \Delta T(1 - y)]^{\frac{\gamma}{F_r^2 \Delta T}}\end{aligned}$$

where in our dimensionless variables $T_{top} = p_{top} = \rho_{top} = 1$. To provide a "soft" start of the convection without shock waves we introduce a seed velocity field of small amplitude A:

$$\begin{aligned}u(x, y) &= A \sin(2\pi x) \cos(\pi y) \\ v(x, y) &= -A \cos(2\pi x) \sin(\pi y)\end{aligned}$$

A is chosen so that absolute seed velocities are 10^5 times smaller than the final hydrodynamic velocities.

3. Simulation of sedimentation

We choose air at standard conditions as the compressible viscous medium for hydrodynamic simulation. A square computational region is used with side $L = 10\text{ m}$ and consists of 50×50 nodes. Convection is driven by the temperature gradient between the top and bottom boundaries. The temperature of the top boundary is set to 0 degrees Celsius ($T_{top} = 273.15\text{ K}$). The computational region is heated from the bottom. Calculations were carried out for two cases: $\Delta T = 20\text{ K}$ and $\Delta T = 50\text{ K}$. The suspension consists of 50,000 small cement particles ($\rho = 2200\text{ kg/m}^3$). Particle radii are assumed to

be lognormally distributed

$$q(r) = \frac{1}{r\sigma\sqrt{2\pi}} \exp \left[-\frac{1}{2} \left(\frac{\ln r - \ln \bar{r}}{\sigma} \right)^2 \right] \quad (3.1)$$

with the following parameters: $\bar{r} = 1$, $\sigma = 1/2$. Radii of the particles were chosen in such a way that the settling time of particles with the most probable radius from the height $L = 10$ m in a static medium is equal to 1 minute. Usually a suspension of small particles is made by breaking. It can be shown (Kolmogorov (1941)) that particles of such a suspension have a lognormal distribution of radii. When the hydrodynamic system reaches a stationary state the small particles of the suspension are randomly distributed in the computational region. We start the particle positions at random values y uniformly distributed on the interval $0 \leq y < 1$. Rather than using the standard random number generators, which are almost always *linear congruential generators* and do not satisfy our requirements for random number generators, we used instead the procedure ran2() from Press et. al. (1992). It uses a combination of three random generators with an additional shuffle which breaks up serial correlations. To obtain a random value x with predefined normalized density distribution function $q(x)$ from a uniformly distributed random number y the following nonlinear equation must be solved for x

$$\int_0^x q(\xi) d\xi = y$$

The velocities and positions of the suspension particles are calculated simultaneously with the solution of the hydrodynamic equations (2.1). The particle velocity has two components: (i) a constant settling rate

$$u_{\text{settling}} = \frac{2}{9} \frac{\Delta\rho}{\mu} gr^2$$

which depends on the particle radius r , gravitational acceleration g , and medium parameters, and (ii) the hydrodynamic velocity of the motion of the medium $\mathbf{v}_{\text{hydro}} = (u, v)$. The total weight $P(t)$ of settled matter is recorded during the numerical experiment. Settled particles are excluded from further calculations.

The numerical simulation provides both a sedimentation curve $P(t)$ (the total weight of settled matter versus time) and also information about the radii of settled and suspended particles. To obtain the particle sizes of these two fractions we have to calculate the particle radius distribution function. It can be obtained from the sedimentation curve, for settling without convection, by solution of the following integral equation of the first kind

$$\int_0^{r^*(t)} q(r) \left[1 - \left(\frac{r}{r^*(t)} \right)^2 \right] dr = 1 - P(t), \quad r^* = \sqrt{\frac{9\mu L}{2\Delta\rho g t}} \quad (3.2)$$

This is an ill-posed inverse problem, and we are forced to use special regularizing algorithms to solve it. We used the Tikhonov regularization method (Tikhonov & Arsenin (1979), Tikhonov et. al. (1990)). Details of this method for the reconstruction of a particle radius distribution function can be seen in Parchevsky (2000a) and Parchevsky (2001). This approach is based on calculation of the first derivative from the empirical cumulative distribution function $F_e(x)$ (Parchevsky (2000b)) and can be described as follows. The

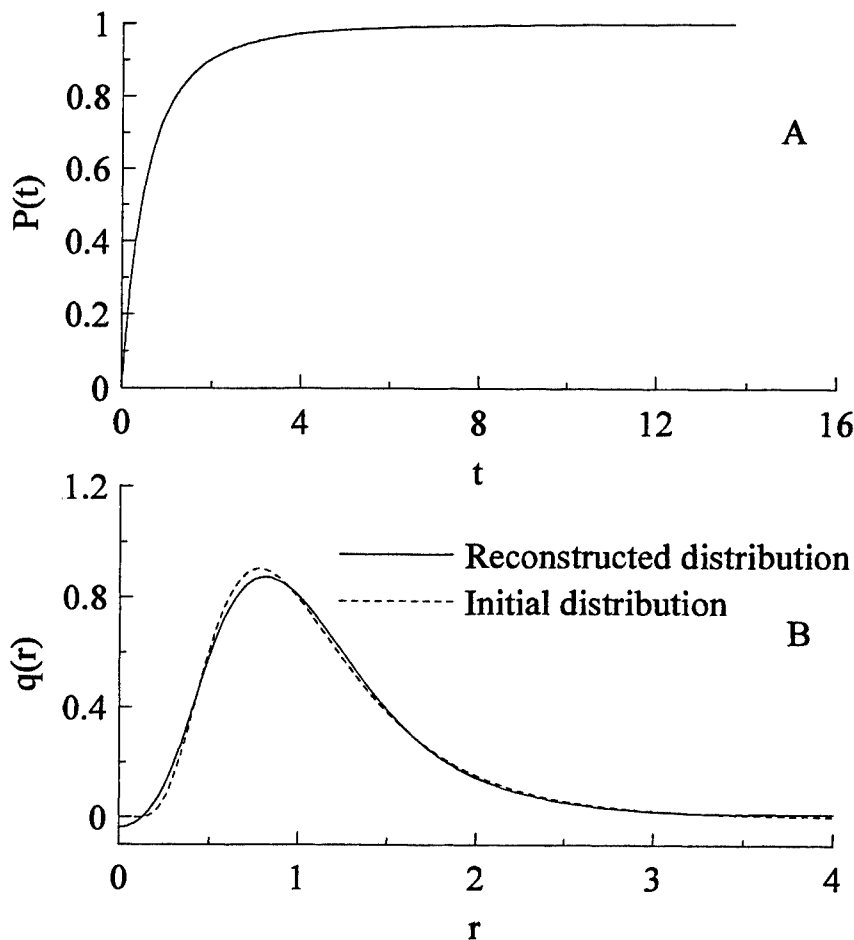


FIGURE 1. Reconstruction of particle radius distribution from the sedimentation curve in the case of a static medium. Time and radius are given in normalized units.

probability density distribution and cumulative distribution are related by the formula

$$\int_0^x q(\xi) d\xi = F_e(x) \quad (3.3)$$

To obtain $q(x)$ we have to substitute an empirical normalized cumulative distribution

$$F_e(x) = \begin{cases} 0, & x < x_1 \\ \frac{i}{N}, & x_i \leq x < x_{i+1} \\ 1, & x \geq x_N \end{cases}$$

calculated from the experimental sample (x_1, x_2, \dots, x_N) , in the right hand side Eq. (3.3) and then solve the integral equation.

4. Numerical simulation of solar convection

We carried out 2D simulations of solar compressible convection in a rectangular region $47.95 \text{ Mm} \times 7.99 \text{ Mm}$ with a mesh of 600×100 nodes. The density ratio was

$\rho_{bottom}/\rho_{top} = 1800$. The full system of hydrodynamic equations was integrated by an explicit MacCormack scheme. The total simulation time equals 9.317 days of solar time (775000 iterations). After a transient period of 265000 iterations, the temperature, velocity, and density were stored every 104 seconds. A movie of the temperature map as a function of time was produced from this data.

For the numerical simulation of solar convection we used the same code as for the sedimentation simulation except for the equation of state. The simulation does not include radiative transport, but employs the realistic OPAL equation of state, which is more important to include than radiation for our purposes.

Since chemical composition in the convection zone is uniform we use the OPAL tables for fixed chemical composition X and Z (hydrogen and heavy element abundance respectively). In the simulated hydrodynamic equations we use ρ and E (mass density and total energy density) as dependent variables. The OPAL tables are constructed to use ρ and T as input parameters. To speed up the interpolation process the OPAL tables were inverted with respect to T and internal energy density ϵ and reinterpolated on logarithmically uniform ρ and ϵ grids. Cubic interpolation was used for this procedure. This eliminates the need for searching in the tables.

The velocity of the fluid in the superadiabatic zone (immediately below the photosphere) is sufficiently high that we have to use a fully compressible code. The computational domain is chosen so that the horizontal size is comparable to the supergranule size and the vertical size to the density scale height. The grid is chosen to be sufficiently fine for good spatial resolution.

5. Results and discussion

1. Sedimentation.

Our computational procedure consists of three steps: (i) numerical simulation of the convection until the system reaches a statistically stationary state, (ii) calculation of the sedimentation curve, (iii) reconstruction of the particle radius distribution from the sedimentation curve and from the samples of particle radii of both settled and suspended fractions. We simulated sedimentation of an identical particle distribution in a static medium as well, results of which are shown in Fig. 1. The dashed line in Fig. 1b represents the initial particle radius distribution (3.1), and the solid line represents the particle radius distribution reconstructed from the sedimentation curve shown in Fig. 1a obtained by solution of Eq. (3.2). One can see a good agreement of initial and reconstructed distributions.

Convective motions of the medium lead to the following effects. The fine dispersed fraction of the suspension remains suspended much longer than without convection, and some particles with sufficiently small radii never settle at all. The mass of the suspended fraction depends on the average convective velocity of the medium, which in turn depends on the temperature difference between the top and bottom boundaries. A greater temperature difference (and convective velocity), leads to a greater mass of suspended matter. The results of our numerical simulation of sedimentation in the presence of compressible convection are shown in Fig. 2. For comparison we show results of sedimentation in a static medium in the same figure. The curves were calculated for two temperature differences between the top and bottom boundaries: $\Delta T = 20\text{ K}$ and $\Delta T = 50\text{ K}$. Time is given in normalized units. The asymptotes are calculated by extrapolating the curve

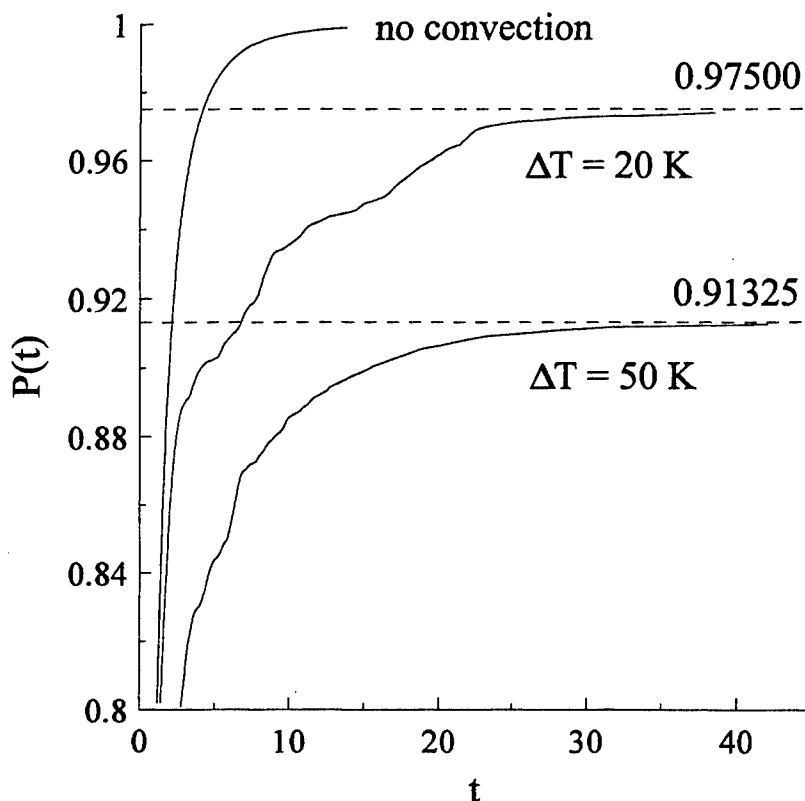


FIGURE 2. Sedimentation curves showing the mass fraction of settled matter versus time in the presence of 2D compressible convection. Asymptotes show the mass fraction of suspended particles which will never settle. For comparison the sedimentation curve of the same suspension in a static medium is also shown.

$P(1/t)$ to the y axis, at which the ordinate of the intersection point is taken as the asymptotic value.

The distribution of particle radii in the settled and suspended fractions is a matter of great interest. Normally, experiments provide only a sedimentation curve. In numerical simulation the radii of settled particles are available as well, so we have samples of radii of settled and suspended particles for every moment of time. The problem of reconstruction of the particle radius distribution is reduced to the problem of reconstruction of the probability density function from a sample of finite size, and we can use the approach discussed above. Results are shown in Fig. 3. Dashed lines represent the particle radius distribution in the suspended and settled fractions. These curves were obtained from the samples of particle radii. Thick solid lines represent the initial particle radius distribution. If this were a laboratory experiment, only a sedimentation curve (as in Fig. 2) would be available, and the particle radius distribution curve would have to be constructed from it. If we reconstruct the particle radius distribution from the sedimentation curve, it is clear that we shall not obtain the correct radius distribution because convection distorts the result of radius reconstruction. Thin solid lines in Fig. 3 represent particle radius distri-

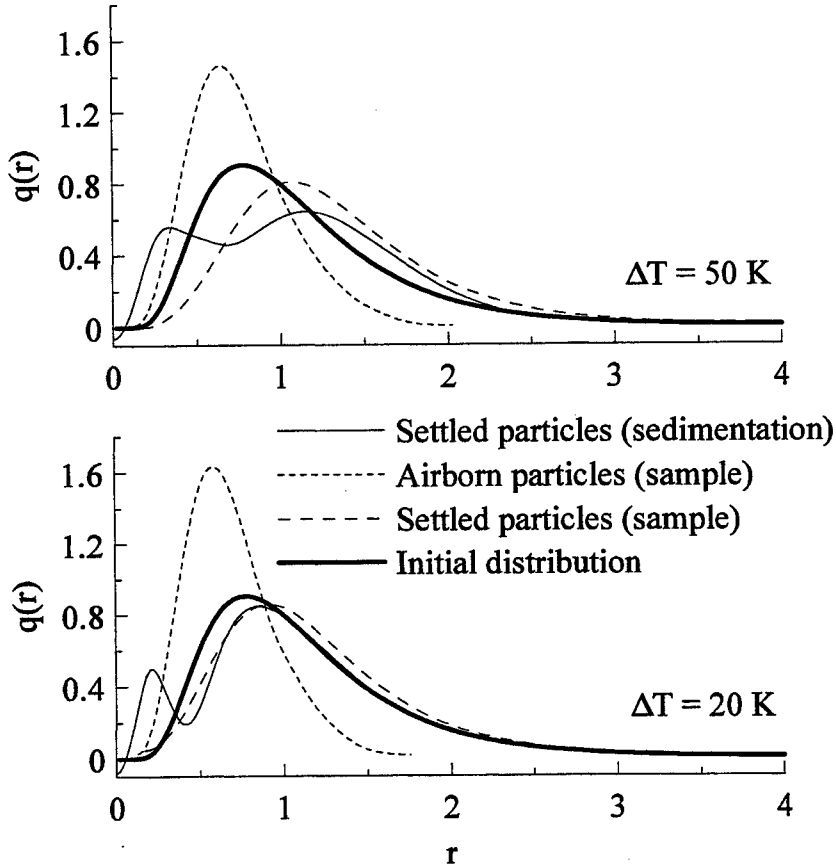


FIGURE 3. Numerical results of reconstruction of the particle radius distribution function of suspended and settled fractions.

butions obtained from the sedimentation curve by solution of integral equation (3.2). One can see a gap for small radii, because these particles remain suspended and do not settle. This is detected as a lack of particles with small radii. Thus, convection acts as a size filter which separates particles by radius. The average (and most probable) particle radius of the suspended and settled fractions depends on the temperature difference between the top and bottom boundaries. A separation technology based on the simultaneous action of sedimentation and convection would have a cut-off particle radius controlled by the temperature difference between the top and bottom boundaries.

2. Solar convection.

Results of the numerical simulation of solar convection are shown in Fig. 4. Color denotes a temperature difference between the medium and a reference model with a linear temperature profile. Blue denotes regions with temperatures smaller than the reference model, and red denotes regions with temperature higher than the reference model. Arrows show the direction and amplitude of the fluid motion. The ratio of horizontal to vertical domain length is 6:1.

A characteristic feature of solar convection is a fast cooling of solar matter in the subsurface layer and the resulting formation of downdrafts. These are cool compact

structures descending with high velocity (10.43 ± 0.05 km/s) and penetrating deep inside quieter regions. Such downdrafts form the boundaries of separate granules. Hot matter rises in the center of the granules at comparatively low speed (5.27 ± 0.02 km/s). The whole pattern is shifting continuously. Representative granule lifetimes are 10-15 min.

To study granule motion we plot a so-called time-spatial diagram. We choose a horizontal slice of the computational region at a fixed depth and plot its evolution with time. Time-spatial diagrams for temperature and velocity components at a depth of 0.56 Mm are shown in Fig. 5. Characteristic feather-like structures are formed due to the horizontal movement of downdrafts. The deep blue color of these feather-like structures on the temperature plot indicates their low temperature. Corresponding blue structures on the vertical velocity map show that the matter is descending. On the total velocity map these regions are red, indicating above average velocity. This indicates that in general the cold matter is descending faster than the hot matter is rising. All left branches of the feather-like structures on the horizontal velocity map are red, meaning horizontal movement to the right, and all right branches are blue, meaning horizontal movement to the left. All branches have nearly the same slope, indicating that they move horizontally with the same velocity. Horizontal movement of downdrafts is caused by advection of the small-scale granulation pattern by the slower large-scale motion of rising hot matter near the surface.

Observations show the existence of large-scale structures on the surface — meso- and super-granulation. These structures are not seen directly since the velocities are low and the pattern is clouded by higher-velocity small-scale granule motions. Supergranulation can be seen only on the horizontal velocity maps of granules or on the time-spatial diagrams. Such large-scale structures arise naturally in our numerical simulations. Fig. 6 shows a large-scale time-spatial diagram where structures with a characteristic size of 15-20 Mm and a lifetime of 50-60 hours are clearly seen.

Highly turbulent subsurface convection excites acoustic and gravitational waves. To find standing wave patterns in our model and determine their dispersion relation (wavelength versus frequency) we plot 2D Fourier transforms of a large-scale time-spatial diagram similar to the one shown in Fig. 6, but computed for a depth of 6.234 Mm. The result is shown in Fig. 7 where the so-called $k - \omega$ diagram is presented. Inverse wavelength λ^{-1} in Mm^{-1} is along the horizontal axis and frequency ν in mHz is along the vertical axis. This figure presents a power spectrum of g-modes excited by turbulent convection. One can clearly see three ridges similar to those that are seen in the power spectrum of 5-min solar oscillations. A similar $k - \omega$ diagram plotted for a depth of 0.56 Mm does not show ridges, just a larger total acoustic power. This may be due to an insufficient length of simulated time and high noise due to motions associated with granulation.

Acknowledgements

I gratefully acknowledge Dr. Alan Wray for helpful advice about code optimization for parallel computing and fruitful discussions.

REFERENCES

- KOLMOGOROV, A.N. 1941 About logarithmically normal particle size distribution law at breaking. *Dokl. Akad. Nauk SSSR* **31**, 99-101, (in Russian).

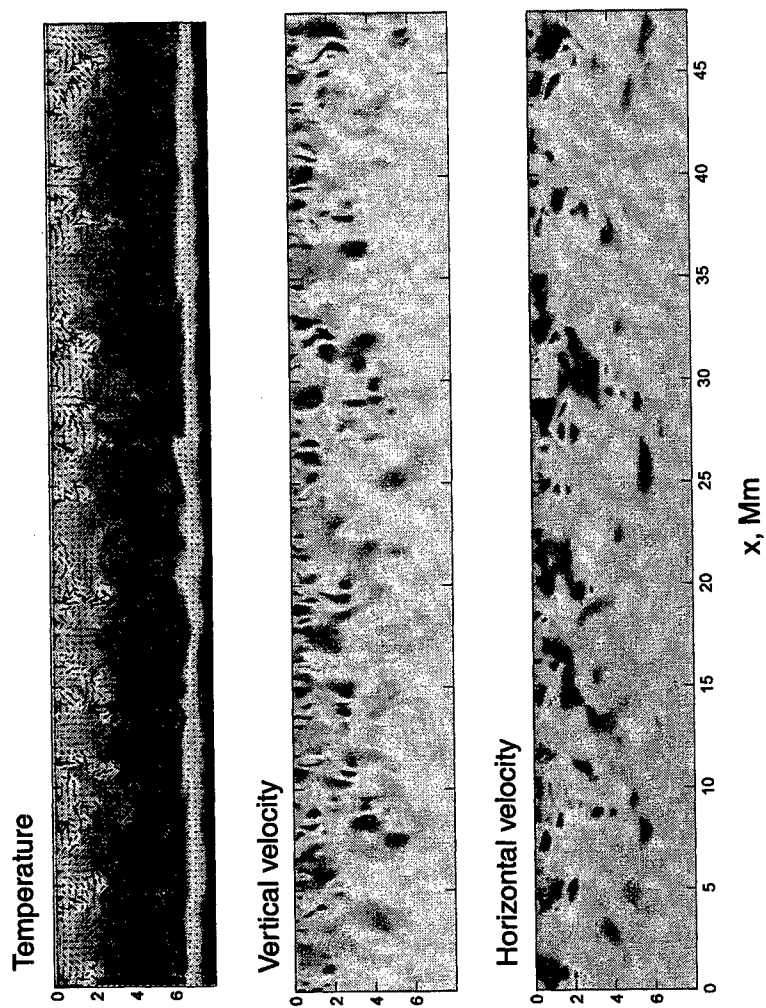


FIGURE 4. Maps of the difference of computed temperature and reference model temperature and vertical and horizontal velocity components for $t = 223.6155$ hours on a 600×100 grid.

- PRESS, W.H., TEUKOLSKY, S.A., VETTERLING, W.T. & FLANNERY, B.P. 1992 Numerical Recipes in C *Cambridge University Press*, 998 pp.
- TIKHONOV, A.N. & ARSENIN, V.J. 1979 Methods of Solution of Ill-posed Problems. *Moscow: Nauka*, 286 pp., (in Russian).
- TIKHONOV, A.N., GONCHARSKY, A.V., STEPANOV V.V. & JAGOLA, A.G. 1990 Numerical Methods of Solution of Ill-posed Problems. *Moscow: Nauka*, 332 pp., (in Russian).

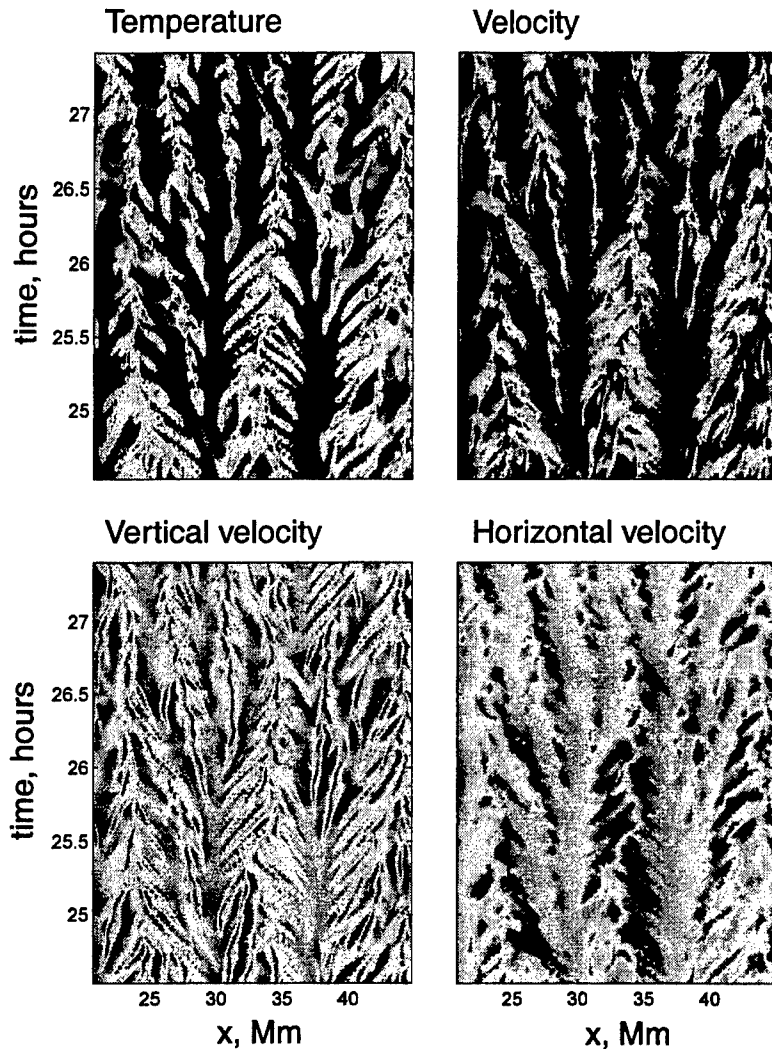


FIGURE 5. Time-spatial diagrams for the temperature, total velocity, and vertical and horizontal velocity components at a depth 0.56 Mm counted from the upper boundary.

- PARCHEVSKY, K.V. 2000 A new method for the reconstruction of the particle radius distribution function from the sedimentation curve. *Chemical Engineering Journal* **80**, 73-79.
- PARCHEVSKY, K.V. 2001 Numerical simulation of sedimentation in the presence of 2D compressible convection and reconstruction of the particle-radius distribution function. *Journal of Engineering Mathematics* **41**, 203-219.
- PARCHEVSKY, K.V. 2000 Using regularizing algorithms for the reconstruction of growth rate from the experimental data. *Ecological Modelling* **133**, 107-115.

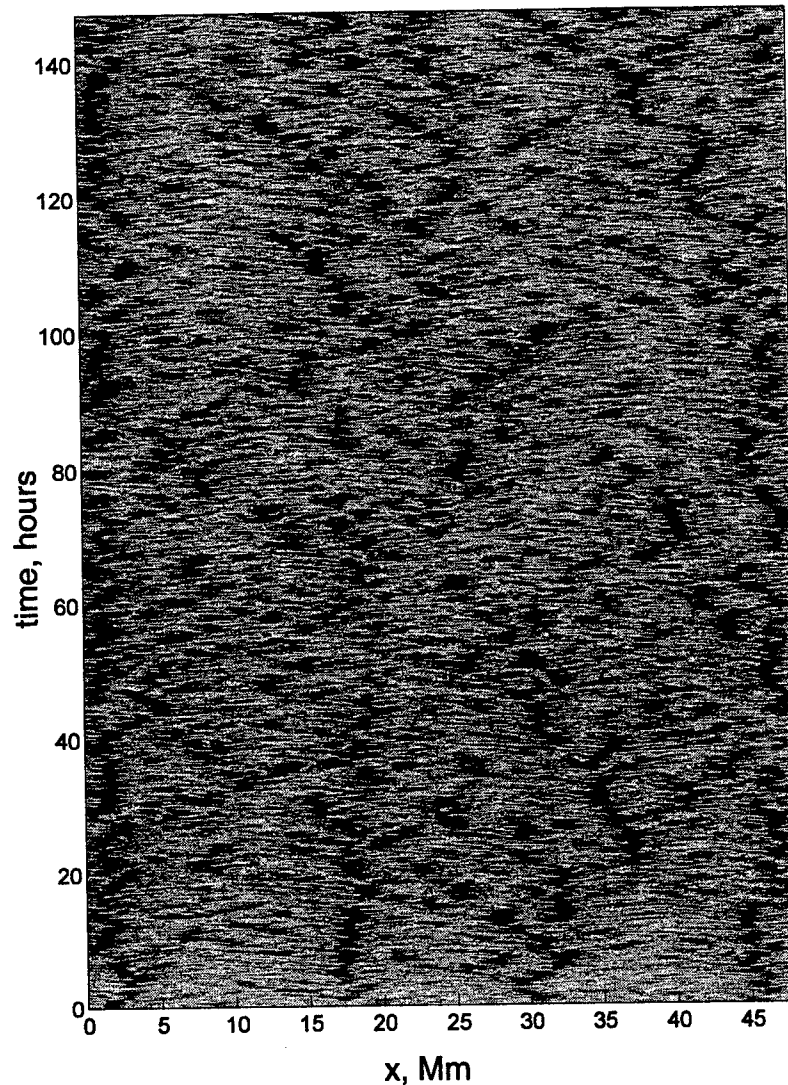


FIGURE 6. Large-scale time-spatial diagram for the temperature at a depth of 0.56 Mm.
Large-scale structures identified with the supergranules are clearly seen.

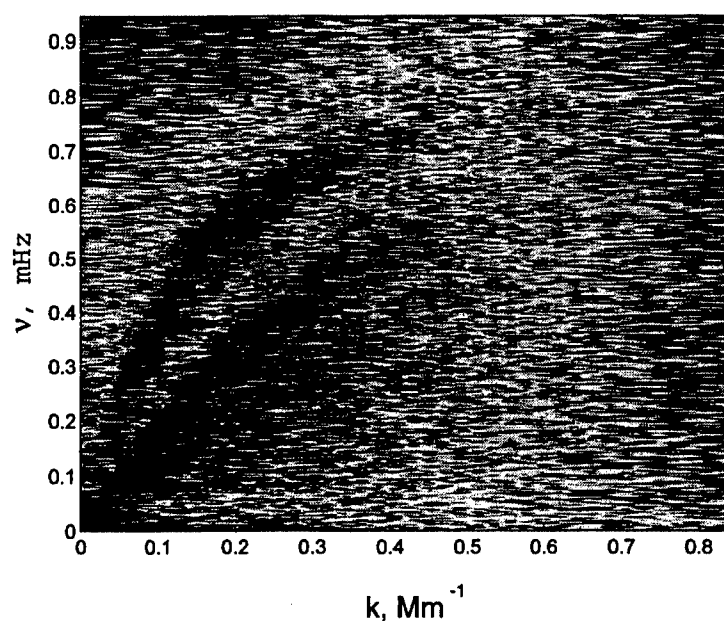


FIGURE 7. Power spectrum of g-modes excited by turbulent convection.

Numerical simulation of magnetoconvection in a stellar envelope

By S. D. Ustyugov AND A. N. Andrianov †

1. Introduction

One of the main problems in the physics of the Sun is the interaction between convection and magnetic fields. Convective motions in stellar envelopes span a substantial radial distance from the convectively unstable region into the adjacent stable zones and can distort the magnetic field into concentrated flux sheets and tubes in which the magnetic pressure is comparable to the gas pressure (see Hurlburt & Toomre (1988)). On the other hand, magnetic fields can be sufficiently strong to suppress convection on granular and supergranular scales. The dynamics of such couplings is strongly nonlinear, and the flow spans many scale heights in the vertical direction and weakens the stable thermal stratification. Studies of convection in the presence of magnetic fields have already shown effects arising from compressibility, revealing distinctive asymmetries between upward and downward flows. Convection penetrates into the underlying stable layers as downward-directed plumes (see Hurlburt et.al. (1986)). Here we consider compressible convection in three spatial dimensions in the presence of an externally imposed magnetic field. We study penetrative convection within relatively simple configurations consisting of two layers with well-posed boundary conditions. We include all diffusive processes and do not model the unresolved scales.

2. Initial model and equations

We shall consider penetrative convection in a compressible stellar envelope in the presence of an imposed magnetic field. We assume that this envelope experiences uniform gravitational acceleration directed downward, and possesses constant thermal conductivity, a constant magnetic diffusivity, and a constant shear viscosity.

The stratification consists of an unstable layer bounded below by a stable polytrope. This configuration mimics the lower part of the solar convection zone and the upper radiative zone. The initial distribution of temperature, density, and pressure are expressed as

$$T = T_\alpha + \frac{z - z_\alpha}{K_\alpha}, \quad \frac{\rho}{\rho_\alpha} = \left(\frac{T}{T_\alpha} \right)^{m_\alpha}, \quad \frac{P}{P_\alpha} = \left(\frac{T}{T_\alpha} \right)^{m_\alpha+1} \quad (2.1)$$

for the unstable ($\alpha = 1$) and stable ($\alpha = 2$) layers. Here the polytropic indices m_α are

given by $m_\alpha + 1 = g K_\alpha / R F_T$, where R is the gas constant, K_α is the coefficient of thermal conductivity, and F_T is the total energy flux. Convective instability occurs when $m_\alpha < m_c$, where m_c , the critical polytropic index, depends on the ratio of specific heats

† Keldysh Institute of Applied Mathematics, Moscow, Russia

γ . For perfect a monoatomic gas ($\gamma = 5/3$), $m_c = 3/2$. We take $m_1 = 1$ in the unstable layer and $m_2 = 3$ in the stable layer.

We have solved the equations of three-dimensional, fully compressible nonlinear magnetoconvection. We use cartesian coordinates $x = x_1, y = x_2, z = x_3$, where the positive z -axis points downwards. The equations of motion are as follows: conservation of mass,

$$\frac{\partial \rho}{\partial t} + \frac{\partial}{\partial x_i} (\rho u_i) = 0, \quad (2.2)$$

conservation of momentum,

$$\frac{\partial \rho u_i}{\partial t} + \frac{\partial}{\partial x_j} \left[\delta_{ij} \left(P + \frac{1}{2} B_k B_k \right) + \rho u_i u_j - \tau_{ij} - B_i B_j \right] - \rho g \delta_{i3} = 0, \quad (2.3)$$

conservation of energy,

$$\begin{aligned} \frac{\partial \rho E}{\partial t} + \frac{\partial}{\partial x_j} \left[\rho u_j \left(\frac{1}{2} u_i u_i + \epsilon + \frac{P}{\rho} - g x_3 \right) - u_i \tau_{ji} - K \frac{\partial T}{\partial x_j} \right] \\ - \frac{\partial}{\partial x_j} \left[\eta B_i \left(\frac{\partial B_i}{\partial x_j} - \frac{\partial B_j}{\partial x_i} \right) + B_i (B_j u_i - B_i u_j) \right] = 0, \end{aligned} \quad (2.4)$$

and the induction equation,

$$\frac{\partial B_i}{\partial t} + \frac{\partial}{\partial x_j} \left[u_j B_i - u_i B_j - \eta \left(\frac{\partial B_i}{\partial x_j} - \frac{\partial B_j}{\partial x_i} \right) \right] = 0. \quad (2.5)$$

These are augmented by the equation of state for a perfect gas,

$$P = R\rho T, \quad (2.6)$$

and expressions for the total energy per unit mass,

$$E = \epsilon + \frac{1}{2} u_i u_i - g x_3 + \frac{1}{2} \frac{B_i B_i}{\rho}, \quad (2.7)$$

and the viscous stress tensor,

$$\tau_{ij} = \mu \left(\frac{\partial u_i}{\partial x_j} + \frac{\partial u_j}{\partial x_i} - \frac{2}{3} \delta_{ij} \frac{\partial u_l}{\partial x_l} \right). \quad (2.8)$$

Here ρ , T , P , and ϵ are density, temperature, pressure, and specific internal energy, and B_i denotes components of the magnetic field.

We write the equations in dimensionless form and take our unit of length to be the depth of the unstable layer d . The time unit $d/(Rd\beta_1)$ is related to the sound travel time across the unstable layer, where β_1 is the initial temperature gradient within the unstable layer. The magnetic field is scaled by \hat{B} , the value of the initially uniform vertical magnetic field.

The evolution of the system depends on some physical and geometrical parameters. We define the computational box to extend in a horizontal plane from $x = y = 0$ to $x = y = A$, where A is the aspect ratio of the unstable layer, and vertically from $z = z_1$

to $z = z_3$. The depth of the unstable layer is unity in our units. The density contrast χ_2 is the ratio of the density at the bottom of the unstable layer ($z = z_2$) to that at the top:

$$\chi_2 = \frac{\rho(z_2)}{\rho(z_1)} \quad (2.9)$$

The Prandtl number, which gives the ratio of viscous to thermal diffusivity, is defined as

$$\sigma = \frac{\mu c_p}{K} \quad (2.10)$$

The degree of instability in the unstable layer is given by the Rayleigh number

$$R_a = (m_1 + 1)(m_c - m_1)(m_c + 1)^{-1} \sigma_1^{-1} \lambda^2 z^{2m_1 - 1}, \quad (2.11)$$

where λ is the ratio of the sound speed to the thermal diffusion time and σ_1 is the Prandtl number in the unstable layer. Since R_a depends on vertical position in the unstable layer, we evaluate it at the center, taking

$$\hat{R}_a = R_a \left(z_1 + \frac{1}{2} \right). \quad (2.12)$$

as a nominal Rayleigh number.

The strength of the imposed magnetic field and its effect on convective stability can be measured by the Chandrasekhar number

$$Q = B^2 \frac{d^2}{\mu \eta} \quad (2.13)$$

The magnetic Prandtl number (the ratio of magnetic to thermal diffusivity) is defined as

$$\zeta = \eta \rho c_p / K \quad (2.14)$$

3. Numerical method

For the numerical simulation we have used an explicit TVD method, second order accurate in space with the time advance using a three-step Runge-Kutta scheme (see Yee et.al. (1990), Shu (1989)). Our algorithm uses equations in conservative form for advection, wave propagation, and diffusion processes. The 3-D compressible time-dependent MHD equation with source term can be written as

$$\frac{\partial U}{\partial t} + \frac{\partial F}{\partial x} + \frac{\partial G}{\partial y} + \frac{\partial H}{\partial z} = S, \quad (3.1)$$

The dependent variable U is vector of conserved variables, and F, G, H are vectors of flux in the three space directions. Let

$$U_t = L(U)_{i,j,k}, \quad (3.2)$$

be the semi-discrete form of (3.1) at point (i, j, k) , where L is the spatial discretization operator

$$\begin{aligned} L_{i,j,k} = & -\frac{1}{\Delta x} (F_{i+1/2} - F_{i-1/2}) - \frac{1}{\Delta y} (G_{j+1/2} - G_{j-1/2}) \\ & - \frac{1}{\Delta z} (H_{k+1/2} - H_{k-1/2}) + S_{i,j,k}, \end{aligned} \quad (3.3)$$

The numerical flux, for example in the x direction, is defined as

$$F_{i+1/2} = \frac{1}{2} (F_{i+1} + F_i + P_{i+1/2} \Phi_{i+1/2}). \quad (3.4)$$

The last term $P_{i+1/2} \Phi_{i+1/2}$ is a nonlinear dissipation, and the quantity $P_{i+1/2}$ is the right eigenvector matrix $\partial F / \partial U$ using, for example, Roe's approximate average state.

The components $\phi_{i+1/2}^l$ of vector $\Phi_{i+1/2}$ can be written as

$$\phi_{i+1/2}^l = \frac{1}{2} \psi(a_{i+1/2}^l) (g_{i+1}^l + g_i^l) - \psi(a_{i+1/2}^l + \gamma_{i+1/2}^l) \alpha_{i+1/2}^l, \quad (3.5)$$

$$\gamma_{i+1/2}^l = \frac{1}{2} \psi(a_{i+1/2}^l) (g_{i+1}^l - g_i^l) / \alpha_{i+1/2}^l \quad \text{if } \alpha_{i+1/2}^l \neq 0, \quad (3.6)$$

$$\gamma_{i+1/2}^l = 0 \quad \text{if } \alpha_{i+1/2}^l = 0. \quad (3.7)$$

The $a_{i+1/2}^l, l = 1, \dots, 7$, are the characteristic speeds of $\partial F / \partial U$ evaluated at some symmetric average of U_i and U_{i+1} . The function ψ is an entropy correction to $|a_{i+1/2}^l|$. The $\alpha_{i+1/2}^l$ are elements of $R_{i+1/2}^{-1}(U_{i+1} - U_i)$.

The limiter function g_i^l can be expressed as

$$g_i^l = \text{minmod}(2a_{i-1/2}^l, 2a_{i+1/2}^l, \frac{1}{2}(a_{i-1/2}^l + a_{i+1/2}^l)). \quad (3.8)$$

For the thermal conductivity we have applied an explicit multistage numerical scheme. This scheme is absolutely stable and is described in detail by Zhukov et.al. (1993). The numerical scheme has been tested widely and used successfully in earlier work (see Ustyugov & Andrianov (2002)). We have carried out computations in a cube with 128 mesh points in each direction on 256 processors of the parallel machine with cluster architecture MBC 1000M. The computer program was parallelized using the NORMA system (see Andrianov et.al. (2001)). The Norma program was then compiled using Fortran and the MPI library. A typical simulation requires on this cluster 50 hours to advance the solution well past its start-up transient.

4. Boundary and Initial conditions

We impose periodic boundary conditions with period A for all variables in x and y . On the upper and lower surfaces we use stress-free boundary conditions:

$$B_x = B_y = \partial B_z / \partial z = u_z = \partial u_x / \partial z = \partial u_y / \partial z = 0, \quad (4.1)$$

i.e., vertical velocities, together with the horizontal components of both the viscous and magnetic stresses, vanish at the upper and lower surfaces. The temperature is held fixed on the upper surface, and its vertical derivative is imposed on the lower. These conditions require

$$T = T_1 \text{ at } z = z_1, \quad (4.2)$$

$$\partial T / \partial z = 1/K_2 \text{ at } z = z_3, \quad (4.3)$$

We introduce a small-amplitude velocity perturbation over several wavenumbers within the unstable layer. The main parameters are fixed at the commonly used values of

$$\gamma = 5/3, \sigma = 1, \zeta = 0.25, K = 0.05, Q = 144 \quad (4.4)$$

5. Results

We study the effects of compressibility and magnetic fields on the penetration of convection into the region of stable stratification that lies below a stellar convection zone. Our results show that penetrative convection exhibits a distinct asymmetry between upflow and downflow; the downward flow is concentrated into strong localized plumes which deeply penetrate into the lower stable zones and involve large positive density fluctuations (Figure 1). Compressibility leads to significant pressure fluctuations and results in enhanced buoyancy-driving in regions of downflow. The upward flows span significantly wider regions and are distinctly weaker than downflows but not negligible.

Convection tends to sweep the initially uniform vertical magnetic field into concentrated magnetic flux tubes and sheets with significant magnetic pressure (see also Weiss et.al. (1996)). The motion in downdrafts in the stable region are considerably less vigorous in the regions of magnetic sheets (Figure 2). Buoyancy and the Lorentz force retard downward flow, and magnetic pressure produces partial evacuation of matter which enhances buoyancy-braking in flux sheets (Figure 3).

In the upper unstable region, variations of velocity are much weaker. Velocity magnitudes indicate slowly modulated convection. The cellular flows display prominent narrow regions with downward flows surrounded by broader regions of upflow. The magnetic fields concentrate into flux tubes and sheets also, but the motion in downdrafts in this region is slower than in the stable layers. There are large variations of magnetic field intensity between regions with flux sheets and those with upward flow. In the penetrative region these variations are weaker and the magnetic field is concentrated mainly in flux tubes. (Figure 4).

6. Conclusions

In this report we have studied formation and development of penetrative convection in stellar envelopes in the presence of imposed magnetic fields. We have revealed a complex, time-varying flow field with compressible convection interacting with the magnetic field

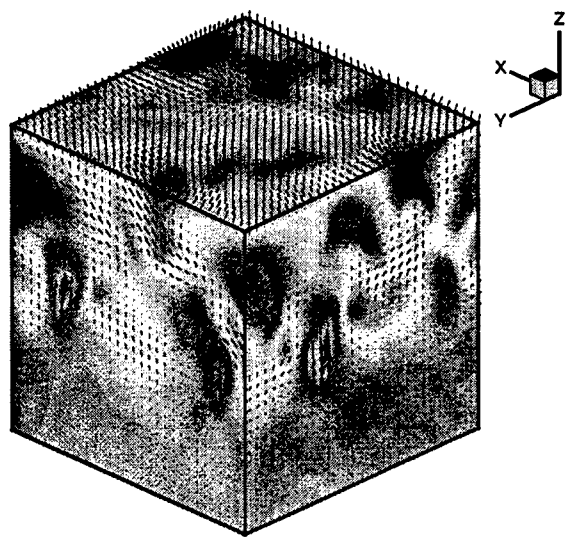


FIGURE 1. Velocity fields and levels of the vertical component of velocity (denoted by color).

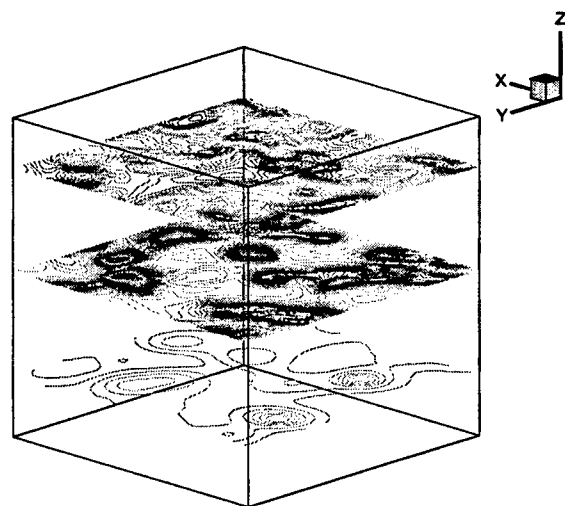


FIGURE 2. Distribution levels of the vertical component of velocity.

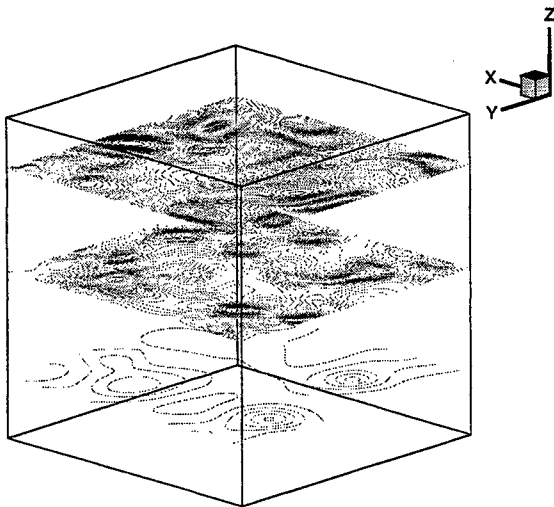


FIGURE 3. Distribution levels of the vertical component of magnetic field.

in an unstable layer bounded below by stably a stratified polytrope. On one side, convection sweeps the magnetic field into flux tubes and sheets, and on the other side magnetic pressure regulates the velocity of flow in downdrafts. In the future we will explore magnetoconvection for other initial parameters: aspect ratio, strength of magnetic field, Prandtl number, etc. We also plan to include a real-gas equation of state and opacity relations in our computer program.

7. Acknowledgments

This work has been supported by CTR. The authors thank Alexander G. Kosovichev from HEPL, Stanford University, Nagi N. Mansour and Alan Wray from NASA Ames Research Center, for help and very useful discussions.

REFERENCES

- HURLBURT, N.E., TOOMRE, J. & MASSAGUER, J. M. 1986 Nonlinear compressible convection penetrating into stable layers and producing internal gravity waves. *ApJ* **311**, 563-577.
- HURLBURT, N.E., & TOOMRE, J. 1988 Magnetic fields interacting with nonlinear compressible convection. *ApJ* **327**, 920-932.
- WEISS, N. O., BROWNJOHN, D. P., MATTHEWS, P. C. & PROCTOR, M. R. E. 1996 Photospheric convection in strong magnetic fields. *MNRAS* **283**, 1153-1164.
- YEE, H. C., KLOPFER, G. H., & MONTAGNE, J.-L. 1990 High-resolution shock-capturing schemes for inviscid and viscous hypersonic flows. *JCP* **88**, 31.

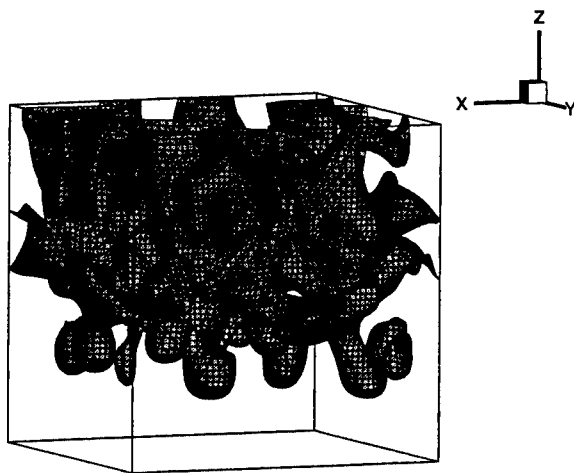


FIGURE 4. Iso-surface of the vertical component of magnetic field.

- SHU, S.- W. 1989 Efficient implementation of essentially non-oscillatory shock-capturing schemes.II *JCP* **83**, 32.
ZHUKOV, V. T., ZABRODIN, A. V., & FEODORITOVA, O. B. 1993 *Comp. Maths. Math. Phys.* **33**, 1099.
ANDRIANOV, A. N., EFIMKIN, K. N., LEVASHOV, V. Y. & SHISHKOVA, I. N. 2001
Lecture Notes in Computer Science **2073**, July.
USTYUGOV, S. D. & ANDRIANOV, A. N. 2002 *HYP 2002 (in press)*.

Vortex dynamics and angular momentum transport in accretion disks

By H. Lin, J. A. Barranco † AND P. S. Marcus ‡

1. Introduction

One of the prominent open problems in astrophysics is the mass and angular momentum transport in protoplanetary (accretion) disks. A typical disk is a few hundred AU (astronomical unit, $1\text{AU} = 1.5 \times 10^{13}\text{cm}$) in size. It is mainly composed of hydrogen and helium gas, and the thickness-to-radius ratio (aspect ratio) is usually ~ 0.1 and increases slowly with radius (a flared disk). Originating from the collapse of a rotating spherical cloud under the gravitational pull of its central star (see, e.g. Cassen & Moosman (1981), Terebey, Shu & Cassen (1984)), the disk has an azimuthal velocity field that can be described, provided being pressureless and steady, by the formula $V_\phi(r) = \sqrt{GM/r}$ (Keplerian velocity; here we have adopted a cylindrical coordinate system (r, ϕ, z) , z is the axis of rotation, G is the constant of gravitation, and the central star of mass M can be treated as a point of gravitation at the origin for dynamics at sufficiently large radii). This velocity profile is simply given by the balance of gravitational and centrifugal force, which are the two dominant forces in the disk.

A central issue of the disk dynamics is how mass and angular momentum are radially transported. Mass accretion is supported, even though not directly confirmed, by infrared observation. However, as gas particles travel toward the star, they have to give up or transport outward their angular momentum. Because the only external force acting on the disk is the gravitation of the central star, which is no source of external torque, this transport shall only occur between parts of the disk by internal interactions. It is this mechanism that remains unknown and defines the scope of this research.

2. The averaged equation for angular momentum transport

To illustrate the problem we give a simple yet revealing analysis. Because the characteristic Reynolds number of the disk is extremely high (around 10^{14}), we can safely ignore viscosity for large scale dynamics and apply Euler's equation for the momentum as

$$\frac{D\mathbf{v}}{Dt} = -\frac{1}{\rho} \nabla p - \nabla \Phi, \quad (2.1)$$

where Φ is the gravitational potential of the central star, and the equation is described in an inertia frame. To look at the evolution of the angular momentum, we combine the azimuthal momentum equation with the continuity equation, and multiply the resulting equation by r to yield

$$\frac{\partial \rho v_\phi r}{\partial t} + \frac{1}{r} \frac{\partial \rho v_\phi v_r r^2}{\partial r} + \frac{\partial \rho v_\phi^2 r}{\partial \phi} + \frac{\partial \rho v_\phi v_z r}{\partial z} = -\frac{\partial p}{\partial \phi}. \quad (2.2)$$

† Department of Astronomy, University of California, Berkeley

‡ Department of Mechanical Engineering, University of California, Berkeley

Note that $\rho v_\phi r$ is the angular momentum, and the equation is now in conservative form. Next we define an integral operation as

$$\langle \cdot \rangle \equiv \int_{-\infty}^{+\infty} \int_0^{2\pi} \cdot r d\phi dz. \quad (2.3)$$

Under this operation equation (2.2) becomes simply

$$\frac{\partial \langle \rho v_\phi r \rangle}{\partial t} + \frac{\partial \langle \rho v_\phi v_r r \rangle}{\partial r} = 0. \quad (2.4)$$

In the integrations we have already made use of the periodicity in ϕ , and the assumption that v_z vanishes at $z = \pm\infty$. Further integrating equation (2.4) in the radial direction yields

$$\frac{\partial}{\partial t} \int_{r_1}^{r_2} \langle \rho v_\phi r \rangle dr = - \langle \rho v_\phi v_r r \rangle |_{r=r_1}^{r=r_2}. \quad (2.5)$$

Not surprisingly, equation (2.5) reasserts angular momentum conservation in the integral form, and for an outward (or zero) angular momentum transport at a given radial location, it requires that

$$\langle \rho v_\phi v_r r \rangle \geq 0. \quad (2.6)$$

The inequality (2.6) constrains the type of flow we can have on top of the Keplerian field. To see this let us decompose the velocity field into the sum of the base Keplerian flow, and deviations from it:

$$v_\phi = V_k(r) + \tilde{v}_\phi, \quad v_r = \tilde{v}_r, \quad (2.7)$$

where $V_k(r) \equiv \sqrt{GM/r}$, and v_z is not used in the analysis here. We also define the rate of accretion as

$$\dot{m} = - \langle \rho \tilde{v}_r \rangle, \quad (2.8)$$

which is the rate of mass flow across certain radius r , and a positive \dot{m} means inward mass flow and accretion. Substituting (2.7, 2.8) into equation (2.6) yields

$$-V_k \dot{m} + \langle \rho \tilde{v}_\phi \tilde{v}_r \rangle \geq 0. \quad (2.9)$$

Equation (2.9) gives important guidance. First, for accretion ($\dot{m} > 0$), the correlation $\langle \rho \tilde{v}_\phi \tilde{v}_r \rangle$ should be positive. Second, the accretion rate suggested by observation ($\sim -10^{-9}$ to -10^{-7} solar mass per year) provides a constraint on the magnitude of the deviations through the relation (2.9), namely,

$$\langle \rho \tilde{v}_\phi \tilde{v}_r \rangle \geq V_k \dot{m}. \quad (2.10)$$

This means the flow has to transport enough angular momentum out to cancel that carried in by the accretion flow.

The next question is: what mechanism can generate a flow, with the required magnitude, sign of correlation, and most importantly, that is self-sustaining. This is the motivation of this work. The immediate candidate is a self-sustaining turbulence, possibly originating from a hydrodynamic instability. (Remember that the characteristic Reynolds number is on the order of 10^{14} .) This has become the pursuit of many works in the past decade. Nonetheless, there has not been much success in this search of turbulent flow (or any other kind of chaotic, or simply convective flow) in accretion disks, and we shall discuss this matter in the last section. While not ruling out other possibilities, our

proposal in this work is that, because vortices are known to be efficient agents for transporting angular momentum, and because they are known to be ubiquitous in flows with differential rotation, we look for vortices in the accretion disks as a possible candidate of the desired flow. This we will discuss in the next section.

3. Vortex dynamics in rotating shear flow

Coherent vortices exist in both terrestrial and extraterrestrial flows. Prominent examples are the Great Red Spot on Jupiter, and the Couette-Taylor vortices which result from an instability of Couette flow between rotating cylinders. In this section we discuss their relevance to angular momentum transport, and the protoplanetary disks.

Vortices transport angular momentum in various ways. In case of the Couette-Taylor vortices, they transport angular momentum outward (toward the outer cylinder) by a positive correlation $\langle v_\phi v_r \rangle$, similar to what we have discussed in the previous section. However, the vortices themselves are stationary swirls and they do not migrate.

An alternative way is more interesting, and less discussed in the literature: vortices can move in space, and convect angular momentum as they stir the flow. Certainly in this case there exists a non-trivial correlation $\langle v_\phi v_r \rangle$ as well.

A very straightforward analysis on vortex migration is given by Schecter & Dubin (1999). In this analysis, they derived from linear theory not only the direction, but also the speed of migration of point vortices driven by a background vorticity gradient. As a result, even though the global angular momentum is conserved, the angular momentum field is convected. Before we start to discuss its relevance in the context of the disks, let us use an example in the context of geophysical flow to better illustrate the idea. We consider a channel (figure 1) in a rotating system with variable Coriolis force, known as the “ β -effect”. Suppose that we are in the quasi-geostrophic regime, and the governing equation is simply given by Ertel’s conservation law (see, e.g. Pedlosky (1987)):

$$\frac{Dq}{Dt} = \frac{\partial q}{\partial t} + u \frac{\partial q}{\partial x} + v \frac{\partial q}{\partial y} = 0, \quad (3.1)$$

where

$$q = \nabla^2 \psi - \frac{\psi}{L_R^2} + \beta y \quad (3.2)$$

is the potential vorticity, ψ is the stream function which satisfies $u = -\partial \psi / \partial y$, $v = \partial \psi / \partial x$, $\nabla^2 \psi = \omega_z$, and L_R is the dimensionless Rossby deformation radius. For a flow at rest, the potential vorticity is a stationary yet non-constant field $q_b = \beta y$. It is straightforward to verify by integration by parts that

$$\frac{\partial}{\partial t} \int_A q dx dy = 0, \quad (3.3)$$

and

$$\frac{\partial}{\partial t} \int_A qy dx dy = 0, \quad (3.4)$$

where A is the section of the domain contained in the channel, and we have assumed periodicity in the x direction. Following Schecter & Dubin (1999), we define a q -weighted altitude as

$$\langle y \rangle = \frac{\int_A qy dx dy}{\int_A q dx dy}. \quad (3.5)$$

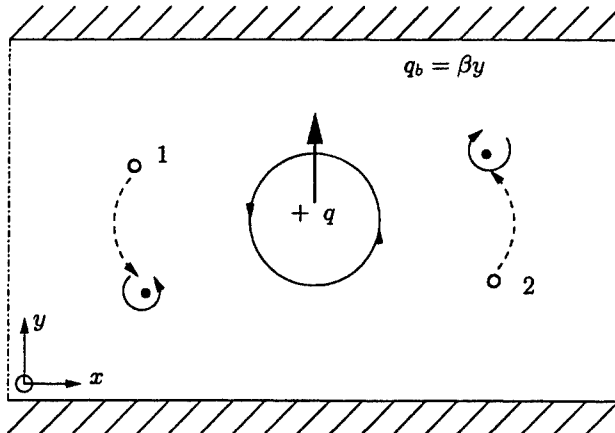


FIGURE 1. A diagram for vortex migration.

Now we may suppose that there is a constant- q patch located at the center of the flow field. Note that, a positive q -patch means a counter-clockwise circulation, a low pressure center, or a cyclone; on the other hand, a negative q -patch means a clockwise circulation, a high pressure center, or an anti-cyclone. We may decompose the q -weighted altitude into contributions from the background flow and the vortex patch, as

$$\langle y \rangle = \frac{\int_A q_b y dx dy + \int_A q_v y dx dy}{\int_A q dx dy} = \text{constant}, \quad (3.6)$$

As the vortex mixes (convects) the flow around, and because q is a material field, the contribution of the background potential vorticity q to the weighted altitude $\langle y \rangle$ is reduced. Consequently, an anti-cyclone ($q < 0$) has to move down, or an cyclone ($q > 0$) has to move up, to compensate for the change and conserve $\langle y \rangle$. (Note also that the area of the patch is preserved, from the divergence-free condition.) In these situations, the horizontal (x direction) symmetry of the vortex is clearly broken, and a non-trivial $\langle uv \rangle$ correlation has been created to exchange angular momentum. (A detailed calculation is theoretically difficult and best via numerical computation.)

The above seemingly mysterious mathematical explanation becomes clear when we take a close look at the physical processes. Take for example the case of a cyclonic vortex $q > 0$. We follow a certain particle 1 (figure 1), which has originally a zero relative vorticity (w.r.t. the rotating system), and which is convected down on the left side of the vortex patch by the vortex. As the βy contribution in the potential vorticity decreases along with y , the vorticity part $(\nabla^2 - 1/L_R^2)\psi$ must undergo an increase to conserve the potential vorticity. Consequently, a small cyclonic vorticity is created. Similarly a particle 2 traveling upward on the right side has its β -potential increased, and has to create a small anti-cyclonic vorticity as the compensation. The velocity field generated by these two small vorticities, which can be deduced from the Biot-Savart law, points upward on the patch. The same qualitative conclusion can be established for every point around the patch, the collective effect of the generated velocity field convects the cyclonic patch to a higher altitude, and an anti-cyclonic patch to a lower one.

This physical interpretation applies not only to the above case, but also to more general situations involving coherent vortices. We can now look at its implications to our problem at hand, which, like other more general situations, does not have the clean cut conservation laws like those of (3.3) and (3.4), and which cannot be reduced to a single

variable of ψ . Nonetheless, Ertel's theorem still holds (see also Pedlosky (1987)):

$$\frac{D}{Dt} \left(\frac{\omega}{\rho} \cdot \nabla s \right) = 0, \quad (3.7)$$

where D/Dt is the material derivative, ω is the absolute vorticity as observed in an inertia frame, and s is the specific entropy. To arrive at (3.7) only two assumption were used: i) the viscous force is ignorable, and ii) the dissipation time scale is much longer compared with the characteristic dynamics, such that entropy is material. We may further assume that the vertical vorticity ω_z and entropy gradient $\partial s/\partial z$ are the dominant ones compared with those in the azimuthal and radial directions†; then Ertel's equation becomes

$$\frac{D}{Dt} \left(\frac{\omega_z}{\rho} \frac{\partial s}{\partial z} \right) \approx 0. \quad (3.8)$$

The term $1/(\rho \partial s / \partial z)$ plays a similar role to that of βy , or the background vorticity gradient in Schechter & Dubin (1999), with its (slower) variation in the radial direction. It is the purpose of this project to study the evolution of vortices under such a thermodynamic background. (The disk has also a background vorticity gradient associated with the Keplerian flow, which influence we shall study in the future.) Certainly, the problem is much more complicated because the flow is compressible (we have a gas disk), and $\frac{1}{\rho} \frac{\partial s}{\partial z}$ is a thermodynamically evolving field rather than a static one. Our approach is outlined as the following. First, we study the general forms of long-lived (coherent) vortices in the disk. The analytical part of this problem has been given in Barranco, Marcus & Umurhan (2000), and shall not be repeated here. Second, we study the evolution of the such vortices under the influence of an entropy and density gradient in the radial direction, which are conjectured to exist in the disks. The vortices may or may not move radially, but the thermodynamic gradient can surely break their azimuthal symmetry and introduce velocity correlation. Last but not the least, we study the formation of these vortices, in part to verify the Rossby wave theory outlined in Lovelace *et al.* (1999). Currently, we are making progress on identifying various types of coherent vortices. We study the problem with numerical methods and our first results are presented in the next section.

4. Numerical scheme and results

Scalings in the protoplanetary disk is a complicated matter and was done in Barranco, Marcus & Umurhan (2000). Here we simply list the equations to solve, namely

$$\frac{\partial \bar{\rho} \mathbf{v}}{\partial t} + (\bar{\rho} \mathbf{v} \cdot \nabla) \mathbf{v} = -2\bar{\rho} \Omega \hat{k} \times (\mathbf{v} - \bar{\mathbf{v}}) - \nabla \tilde{p} - \bar{\rho} \Omega^2 z \hat{k}, \quad (4.1)$$

$$\nabla \cdot (\bar{\rho} \mathbf{v}) = 0, \quad (4.2)$$

$$\rho c_v \frac{DT}{Dt} = -p \nabla \cdot \mathbf{v} + \frac{T - \bar{T}}{\tau_{rad}}, \quad (4.3)$$

$$p = \rho R T \quad (4.4)$$

† Note that $\partial s/\partial z \gg \partial s/\partial r$, $\partial s/\partial r$ is a standard assumption for optically thick disks. For the vorticity, as we will see in the next section, we will presumably set it to have a dominant component in the vertical direction. However, we do not exclude the situation that these assumptions may not be valid, and whose influence is best found through the simulations.

where the “bar-ed” quantities are the base state, which are exact solutions of the full Euler’s equations, and the tilde quantities are the deviations from the base state, namely $\tilde{\rho} = \rho - \bar{\rho}$, $\tilde{p} = p - \bar{p}$. Also \hat{k} is the unit vector in the z direction, R is the gas constant used in the equation of state, and Ω is the local angular velocity, *i.e.* that of the rotating frame these equations are described in.

The base state is determined judiciously by our choice of the thermodynamic background of the disk. For the current work, we will always choose a background that is stably stratified, that is to say,

$$\frac{\partial \bar{s}}{\partial z} \sim \frac{\partial}{\partial z} \left(\frac{\bar{p}}{\bar{\rho}^\gamma} \right) > 0. \quad (4.5)$$

The simplest way is to set the background flow to be isothermal, *i.e.* $\bar{T} = T_o = \text{constant}$. Then from the equation of state $p = \rho RT$ and hydrostatic balance in the vertical direction, one can easily obtain that

$$\bar{\rho} = \rho_o(r) \exp \left(-\frac{z^2}{2H_o^2} \right), \quad (4.6)$$

and the pressure base state is simply $\bar{\rho}RT_o$. In the above equation $\rho_o(r)$ is an arbitrary function of r whose form is determined from other physical argument (*e.g.* the well known “minimum-mass solar nebula” assumption proposed by Hayashi (1981)), and the scale height follows the standard definition $H_o \equiv c_s/\Omega$. Clearly the corresponding entropy field satisfies the requirement of stable stratification, and the density has the favorable exponentially decaying form for the assumption (to be made later) of the finite thickness of the disk. For the base state velocity, we assume that \bar{v} is simply the Keplerian shear in a rotating frame, *i.e.*

$$\bar{v} = \frac{3}{2}\Omega y, \quad (4.7)$$

where y is the local radial coordinate.

The energy equation (4.3) simply manifests conservation of entropy $Ds/Dt = 0$, plus a small correction due to radiation. The radiation is naively modeled as the temperature perturbation $T - \bar{T}$ decaying on a time scale of τ_{rad} , which itself is exponentially decaying in z , *i.e.* there is more radiation toward the top and bottom layer of the disk, following an optically thick assumption. This modeling of radiation is certainly an over-simplification. However, because we are requiring that the thermodynamics does not deviate much from adiabatic process, the radiation time scale τ_{rad} is set to be very large and its effect is only detectable for very long runs†.

We solve equation (4.1-4.3) numerically with a parallel, pseudo-spectral (nonlinear terms calculated in physical space) code. The code is doubly periodic in the vertical and azimuthal direction, and Chebyshev in the radial direction. We use a time-splitting algorithm, with the leap-frog method for advection. The code is not dealiased, and equation (4.2) is satisfied through a τ -method. We would like to mention that the periodicity in z is artificial, which means we are stacking identical disks on top of each other. However, as the density of the disk $\bar{\rho}$ is decaying exponentially with z , we presume that the interaction of the disks via the low density gas on the interfaces does not have a significant influence on the disk proper.

† As a matter of fact, we assume $\tau_{rad} \sim 10,000$ years in the middle plane at 1 AU, and $\tau_{rad} < \text{year}$ near “top” or “bottom” of the disk; however at those places the gas has very low density and the dynamical influence is presumably small.

As a side note, the immediate advantage of solving this set of equations is that the pressure operator becomes elliptical via the anelastic assumption (4.2), and is solved through a Helmholtz solver. Nonetheless when needed, we can implement a semi-implicit scheme and solve a more broadly applicable set of equations in the future.

Our first results are presented in the following.

4.1. Coherent columnar vortices

In this set of numerical experiments we explore semi-two-dimensional vortices. For simplicity we specify the thermodynamic background to be isothermal, and we assume that there is no radial variation in $\bar{\rho}$ and \bar{p} , *i.e.* $\rho_o = \text{constant}$. The radial variation will only be needed when we come to the study of vortex evolution under such a background gradient.

For each height z , we specify identically an elliptical vortex patch satisfying the Moore-Saffman formula (Saffman (1992)) for two-dimensional, steady vortices embedded in shear flow, namely

$$\frac{\tilde{\omega}_z}{\sigma} = \lambda \frac{\lambda + 1}{\lambda - 1}. \quad (4.8)$$

Here $\tilde{\omega}_z$ is the constant vorticity patch superimposed on the shear flow, $\sigma = \frac{3}{2}\Omega$ is the shear rate of the background, and $\lambda \equiv b/a$ is the ratio of the semi-axis of the elliptical patch, with b in the radial direction and a in the azimuthal direction. For a vorticity patch with a strength equal to that of the shear flow, this formula gives an aspect ratio of roughly 0.5. For the vertical direction, we make the pressure and density to initially satisfy the hydrostatic balance.

The result agrees with those previously found in the two-dimensional, quasi-geostrophic cases, *e.g.* in Marcus (1993). We found that prograde vortices with a strength on the order of the background shear (or higher) maintain their coherence very well (figure 2); whereas adverse vortices or prograde vortices that are not strong enough are destroyed by the shear (figure 3). Owing to the setup of the stable stratification, the vertical velocity remained to be very small (as we put disturbances in the form of white noise to test the robustness of the vortex) in both cases. We are currently running tests to confirm that the vertical motion follows closely to that of the linear Brunt-Väisälä oscillation. These cases showed that even away from the quasi-geostrophic limit a shear flow can well support coherent vortices.

4.2. Merger of columnar vortices

Merging of vortices to form a larger one is speculated to be one of the possible mechanisms for the formation of coherent vortices. We demonstrate this by putting two columnar vortices in different positions of the shear flow, and let them approach each other. As we initially specify the shear flow to be positive for the upper half domain (in the radial direction) and negative in the lower half domain, the differential motion brings the vortices together, and they eventually merge to form a larger one that is of the same strength (in vorticity), but approximately double the area of the patch. The resulting vortex is again stable and coherent. This result shows that the merging of smaller vortices to form larger ones is a viable mechanism to form large, coherent vortices.

4.3. Three-dimensional vortices

Even though we have obtained stable forms of coherent columnar vortices, they are simply the quasi-two-dimensional analogs of two-dimensional vortices. In the environment of

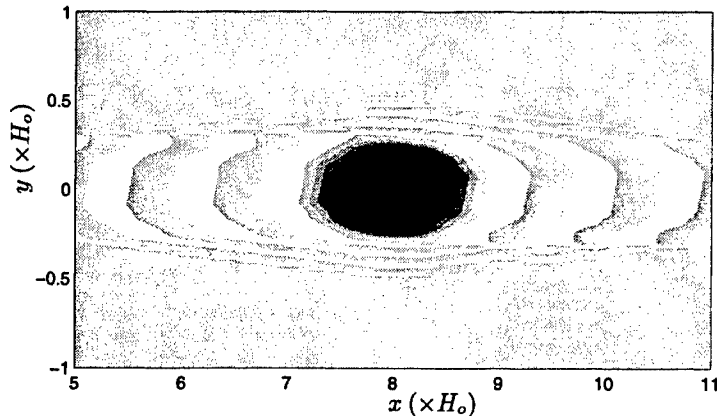


FIGURE 2. A typical stable prograde vortex. In this figure x is the local azimuthal coordinate, y is the local radial coordinate, and the contour of the vertical vorticity ω_z at the middle plane $z = 0$ is plotted. The dark elliptical patch at the center of the graph is our prograde vortex (corresponding to a vorticity "hole"). The boundary of the vortex patch oscillates with small amplitude (which is only best seen through animation), whereas the patch itself is stable. The computational resolution is $128 \times 128 \times 32$.

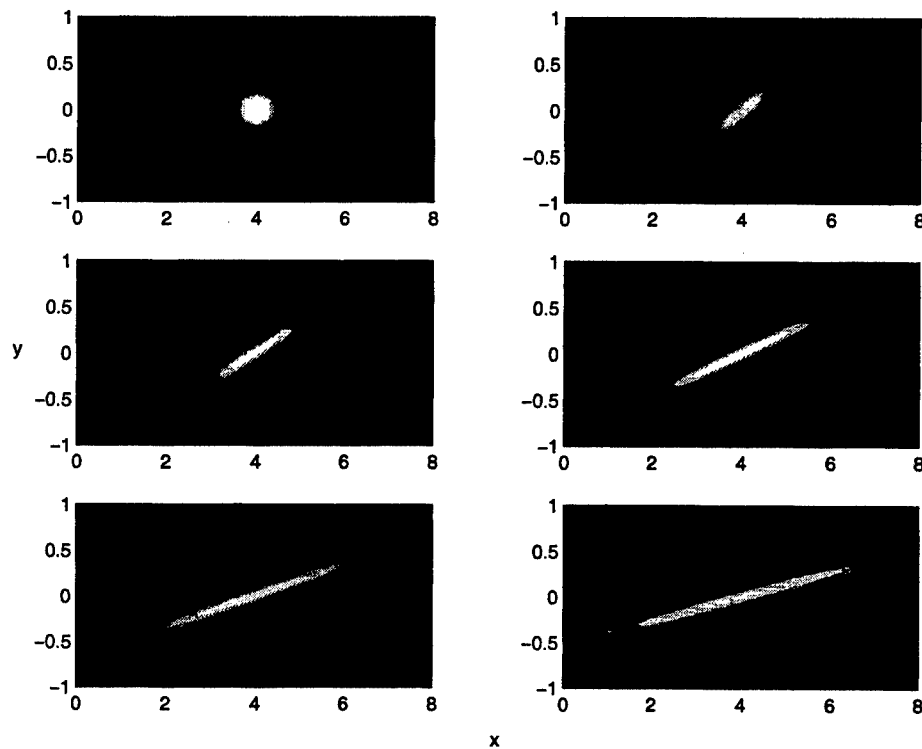


FIGURE 3. The same plot as in figure 1, but with an adverse vortex (the white patch in the first graph) instead of a prograde one. The sequence in time goes from left to right, and top to bottom; the total length of the run is about 1.6 of a turn-around time (one turn-around time equals one orbital period, or a year, in this case), and the frames are evenly divided in time. Clearly the vortex patch is stretched by the shear on the scale of turn-around time.

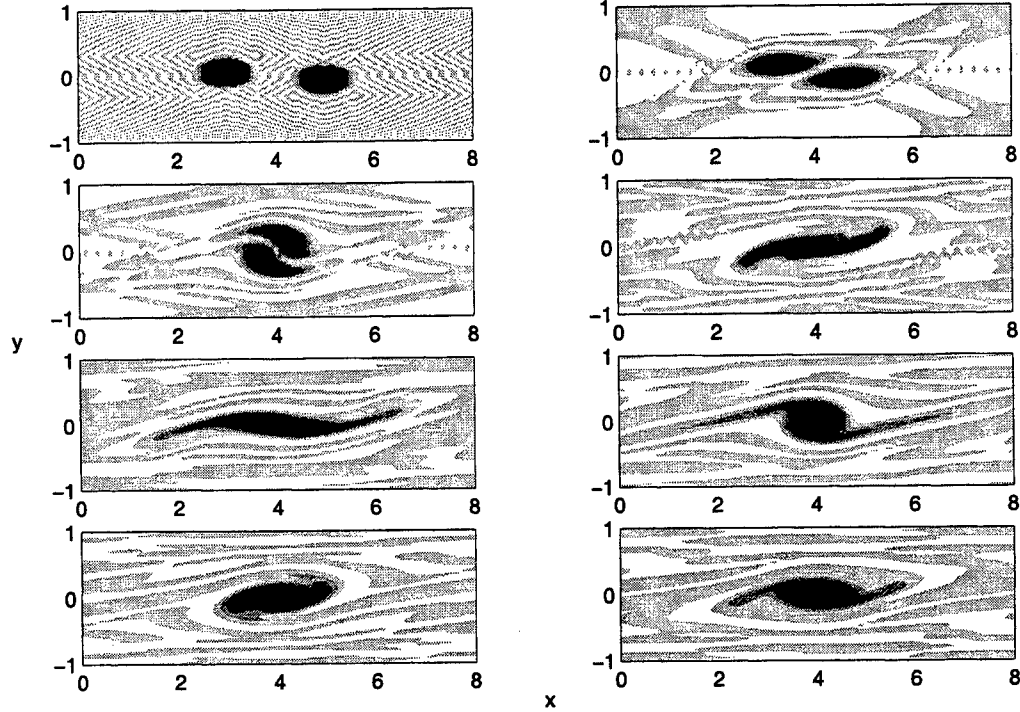


FIGURE 4. An exemplary vortex merger. As usual x and y ($\times H_o$) represent the azimuthal and radial direction, respectively. The dark patches are the prograde vorticity at the middle plane $z = 0$. Sequence in time goes from left to right, and top to bottom. The length of the run is 3 years.

the accretion disk with an order-unity Rossby number, it is of great interest to find “real” three-dimensional, coherent vortices. Three-dimensional vortices are much less understood than their two-dimensional counterparts, and much more difficult to study. Their significance lies also in their relation to planetesimal formation (see Barranco & Marcus (2000)).

Our first aim is to find pancake-like vortices, a cartoon of which can be found in figure 3 of Barranco & Marcus (2000). The character of this type of vortex is the circulation in the vertical direction within the vortex, which, we speculate, should be close to a thermal wind balance, *i.e.* the balance of the rotational effects with baroclinicity in the vertical ($r - z$) plane. We specify the initial condition to be the same as the columnar vortices in previous subsections, but reduce the strength of vorticity exponentially with height. Unfortunately, after observing similar vertical circulation pattern (as that in the cartoon) for a short duration (about a half of the turn-arounds time), the vertical cells begin to break into smaller ones, and eventually the vortex reduce in strength and decays. A possible reason can be that the background is too-strongly stratified, that a vertical circulation cannot self-sustain. Our only conclusion so far is that, the vertical setup of the background flow has a significant influence on the vortex dynamics. We will explore different combinations of thermodynamic background and vorticity initialization in the future.

5. Discussions and future work

In this report we have described the problem of angular momentum transport in the accretion disks, as well as our approach and preliminary results to this problem. Much is needed to be done in the future, following the plan we have outlined at the end of section 3. First we need to obtain a steady form of a three-dimensional, stable vortex structure. Next, as the problem that is directly associated with the purpose of this project, we need to study the evolution of such vortices under the influence of a radial thermodynamic background, the purpose of which would be to break the azimuthal symmetry of the flow and provide a non-trivial velocity correlation to transport angular momentum.

Even though we have shown strong interest in vortex dynamics as a proposed mechanism for angular momentum transport, the possibility of the existence of turbulence (or, in general, other non-vortical flow) can never be ruled out. The Rayleigh stability criterion[†] can only be applied to the disk with much caution, because of complications in the disk (*e.g.* compressibility, stratification, baroclinicity, among others) that are not considered in the linear instability analysis. Furthermore, different boundary conditions easily modify the stability of a system. Nonetheless, the disk does have to satisfy some constraints, like those proposed in equations (11) and (12) in Stone & Balbus (1996); these constraints emphasize the importance of azimuthal structures (*i.e.* non-homogeneity in the azimuthal direction), without which the flow cannot be self-sustaining. In the future we will explore the possibility of turbulent flow in the disk; or, similar to the situation of the Great Red Spot on the Jupiter, that of vortices embedded in turbulent flow. Our special advantage would be that our numerical method resolves the full three-dimensional flow with vertical structures, rather than the vertical homogeneity that was assumed in Rayleigh analysis, and many other works.

Acknowledgments

The authors thank Karim Shariff, Alan Wray and Yuan-nan Young of CTR for help and very useful discussions.

REFERENCES

- BARRANCO, J. A. & MARCUS, P. S. 2000 Vortices in protoplanetary disks and the formation of planetesimals. In *Proceedings of the 2000 Summer Program*. Center for Turbulence Research, Stanford University.
- BARRANCO, J. A., MARCUS, P. S. & UMURHAN, O. M. 2000 Scalings and asymptotics of coherent vortices in protoplanetary disks. *Proceedings of the 2000 Summer Program*. Center for Turbulence Research, Stanford University.
- CASSEN, P. & MOOSMAN, A. 1981 On the formation of protostellar disks. *ICARUS* **48**, 353-376.
- CHANDRASEKHAR, S. 1981 *Hydrodynamic and Hydromagnetic Stability*. Dover.
- HAYASHI, C. 1981 Structure of the solar nebula, growth and decay of magnetic fields and effects of magnetic and turbulent viscosities on the nebula. *Prog. Theor. Phys. Suppl.* **70**, 35-53.

[†] See *e.g.* Chandrasekhar (1981). Because the Keplerian flow has its angular momentum increasing with radius, the criterion states that it is linearly stable.

- LOVELACE, R. V. E., LI, H., COLGATE, S. A. & NELSON, A. F. 1999 Rossby wave instability of Keplerian accretion disks. *ApJ* **513**, 805-810.
- MARCUS, P. S. 1984 Simulation of Taylor-Couette flow, part 1 and 2. *J. Fluid Mech.* **146**, 45-113.
- MARCUS, P. S. 1993 Jupiter's Great Red Spot and other vortices. *Annu. Rev. Astron. Astrophys* **31**, 523-573.
- PEDLOSKY, J. 1987 *Geophysical Fluid Dynamics*. Springer-Verlag.
- SAFFMAN, P. G. 1992 *Vortex Dynamics*. Cambridge University Press.
- SCHECTER, D. A. & DUBIN, D. H. E. 1999 Vortex motion driven by a background vorticity gradient. *Phys. Rev. Lett.* **83**:11, 2191-2194.
- STONE, J. M. & BALBUS, S. A. 1996 Angular momentum transport in accretion disks via convection. *ApJ* **464**, 264-372.
- TEREBEY, S., SHU, F. H. & CASSEN, P. 1984 The collapse of the cores of slowly rotating isothermal clouds. *ApJ* **286**, 529-551.

Interaction between turbulent flow and free surfaces

By Y.-N. Young, F. E. Ham, M. Herrmann AND N. N. Mansour

1. Motivation and objectives

Fluids with interfaces are ubiquitous in fields ranging from geophysics and engineering to applied physics and biology. In various setups, the interface instability has been studied by masters such as Faraday, Fermi, Lighthill, Miles, Rayleigh and Taylor, just to name a few. Interaction of turbulent flow with a fluid interface, however, is much less understood compared to the stability problem. This is due to the complexity of wave-turbulence interaction, and the wide dynamical range to be covered. A classic example is the wind over water problem in oceanography, where a wind (turbulent or laminar) blows over the sea surface. In a solitary moment at the beach, one immediately sees that the dynamical range is at least four decades as large waves of length meters break into small droplets of millimeter sizes.

The amplification of free-surface waves driven by a mean shear flow can be dominated by a critical layer instability, caused by the resonance between the surface waves and the wind (Miles 1957; Alexakis, Young & Rosner 2002a). Non-linear analysis can illuminate the initial amplification period (Alexakis, Young & Rosner 2002b), however, the breaking of growing waves and the ensuing mixing cannot be easily understood in this manner.

Thus our motivation in this project is to carefully investigate the challenging problem of turbulence interaction with fluid interfaces. Specifically, we will develop and utilize tools and models to examine how the mixing of fluids and momentum proceed and partition among the different fluids. The following interim objectives are proposed:

- development of underlying numerical method for LES – based on the second-order Cartesian adaptive finite-volume method of Ham et al. (2002),
- integration of free-surface methodology – based on the level set method,
- sub-grid scale model implementation and development

2. Mathematical formulation

We treat the incompressible, immiscible two-fluid system as a single fluid with strong variations in density and viscosity in the neighborhood of the interface. The continuity and momentum equations for such a variable density flow can be written in conservative form as:

$$\frac{\partial \rho}{\partial t} + \frac{\partial \rho u_j}{\partial x_j} = 0, \quad (2.1)$$

$$\frac{\partial \rho u_i}{\partial t} + \frac{\partial \rho u_j u_i}{\partial x_j} = -\frac{\partial p}{\partial x_i} + \frac{\partial \tau_{ij}}{\partial x_j} + \rho g_i + \sigma \kappa \delta(d) n_i, \quad (2.2)$$

where u_i is the fluid velocity, ρ the fluid density, p the pressure, τ_{ij} the viscous stress tensor, g_i the acceleration due to gravity, σ the surface tension coefficient, κ the local free

surface curvature, δ the Dirac delta function evaluated based on d the normal distance to the surface, and n_i the unit normal at the free surface.

When the density can be written $\rho = \rho(\phi)$ where $\phi(x_i, t)$ is a level set function that is evolved to describe the location of the interface, the application of chain rule to the continuity equation yields:

$$\frac{d\rho}{d\phi} \left(\frac{\partial\phi}{\partial t} + u_j \frac{\partial\phi}{\partial x_j} \right) + \rho \frac{\partial u_j}{\partial x_j} = 0 \quad (2.3)$$

For the case of constant density except in the neighborhood of the zero level set – e.g. $\rho = \rho^+ H(\phi) + \rho^- (1 - H(\phi))$ – then the solution of the continuity equation can be decomposed into the solution of the following:

$$\frac{\partial\phi}{\partial t} + u_j \frac{\partial\phi}{\partial x_j} = 0 \Big|_{\phi=0} \quad (2.4)$$

$$\frac{\partial u_j}{\partial x_j} = 0 \quad (2.5)$$

Eq. 2.4 is the standard evolution equation for the level set function, and eq. 2.5 is the incompressible continuity equation.

In a similar way, the application of chain rule to the momentum equation allows the decomposition of the momentum equation into the solution of the level set equation, eq. 2.4, and the solution of the following momentum equation:

$$\rho \frac{\partial u_i}{\partial t} + \rho \frac{\partial u_j u_i}{\partial x_j} = - \frac{\partial p}{\partial x_i} + \frac{\partial \tau_{ij}}{\partial x_j} + \rho g_i + \sigma \kappa \delta(d) n_i \quad (2.6)$$

Note that the level set formulation results in a system of governing equations that can no longer be written in conservative form. Thus, when the finite volume method is applied to this system, we cannot expect to achieve discrete conservation of mass (ρ) and momentum (ρu_i) in the region of the interface. It is the hope of the level set formulation that these errors in conservation are mitigated by the more accurate tracking of the interface that is possible with the smoothly-varying level set function. Recent developments to the level set method that improve its conservation properties – specifically the particle level set method of Enright, Fedkiw, Ferziger & Mitchell (2002) – will also be investigated and are described in a later section of this brief.

3. Numerical Method

The system described by eqs. 2.4 - 2.6 is commonly solved on a structured staggered grid using finite difference methods, where coupling between the velocity field and pressure occurs naturally. In the present work, we will develop a finite volume method suitable to solve the system on a collocated grid. This will allow the use of both Cartesian structured grids with local refinement, and fully unstructured grids. The spatial arrangement of variables is shown in Figure 1. The arrows at the faces in the figure represent the location of the face-normal velocity, U_f .

The following numerical method is proposed. First, the level set function is advanced in time by solving the following semi-implicit second-order discretization of the level set equation:

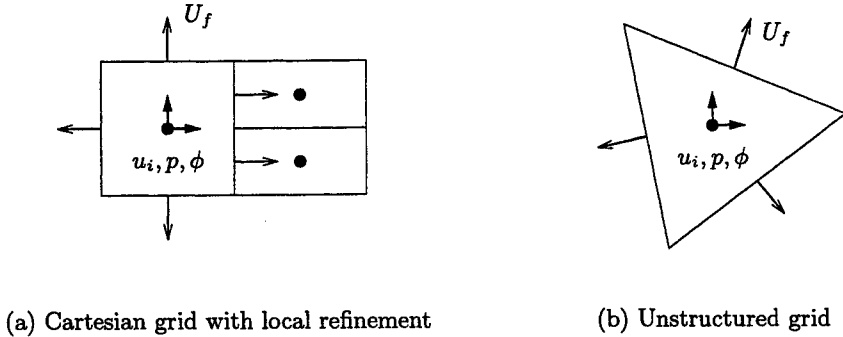


FIGURE 1. Spatial location of variables for collocated discretization.

$$\frac{\phi^{n+1} - \phi^n}{\Delta t} + \frac{1}{V} \sum_f \left(\frac{3}{2} U_f^n - \frac{1}{2} U_f^{n-1} \right) A_f \left(\frac{1}{2} \phi_f^n + \frac{1}{2} \phi_f^{n+1} \right) = 0 \quad (3.1)$$

where A_f is the face area. Note that the face-normal velocities, U_f , are used to advance the level set function. The required face values of the level set function, ϕ_f , are interpolated from the cell-centered ϕ values using a second order ENO scheme (Sussman, Smereka and Osher 1994).

At this point, the level set function is re-initialized to a signed distance function by solving the following equation to steady-state:

$$\frac{\partial \phi}{\partial \tau} + sgn(\phi) (|\nabla \phi| - 1) = 0. \quad (3.2)$$

In practice, only a few time steps are required, and the equation need only be solved in a band about the zero level set (Peng, Merriman, Osher, Zhao & Kang 1999).

With the level set advanced, properties can be calculated based on the level set at the mid-point of the time interval:

$$\rho^{n+1/2} = \rho \left(\frac{1}{2} (\phi^n + \phi^{n+1}) \right) \quad (3.3)$$

$$\mu^{n+1/2} = \mu \left(\frac{1}{2} (\phi^n + \phi^{n+1}) \right) \quad (3.4)$$

In the present investigation, we use a smoothed property variation in the region of the zero level set as described by Sussman, Smereka & Osher (1994).

The momentum and continuity equations are then solved using a fractional-step method similar to that described in Kim & Choi (2000). Specific attention must be paid, however, to the discrete form of force terms that have rapid spatial variation, specifically the surface tension forces added to the momentum equation in the neighborhood of the interface. A fractional step discretization of the momentum equation proceeds as follows.

Advance the momentum equation to solve for CV-centered pseudo-velocities \hat{u}_i^{n+1} using:

$$\rho^{n+1/2} \left(\frac{\hat{u}_i^{n+1} - u_i^n}{\Delta t} \right) = -\frac{\delta p}{\delta x_i}^{n-1/2} + R_i^{n+1/2}, \quad (3.5)$$

where all other terms in the momentum equation have been incorporated into the right hand side term R_i , approximated at the midpoint of the current time step.

Following Kim and Choi (2000), a second pseudo-velocity field denoted by a superscript * is then calculated:

$$u_i^{*n+1} = \hat{u}_i^{n+1} + \Delta t \frac{1}{\rho^{n+1/2}} \frac{\delta p}{\delta x_i}^{n-1/2} \quad (3.6)$$

This starred velocity field is then interpolated to the faces:

$$U_f^{*n+1} = \overline{u_i^{*n+1}}^f - \Delta t \left(\frac{\overline{R_i^{n+1/2}}^f}{\rho^{n+1/2}} - \frac{R_f^{n+1/2}}{\rho_f^{n+1/2}} \right), \quad (3.7)$$

where $\overline{(\cdot)}^f$ is a second-order interpolation operator that yields a face-normal component from two CV-centered vectors. The divergence of these face velocities is then used as the source term in a variable-coefficient Poisson equation for the pressure:

$$\frac{1}{\Delta t} \sum_f U_f^{*n+1} A_f = \sum_f \frac{1}{\rho_f^{n+1/2}} \frac{\delta p}{\delta n}^{n+1/2} A_f. \quad (3.8)$$

With the Poisson equation solved, the face-normal and CV-centered velocity fields are corrected as follows, completing the time advancement:

$$U_f^{n+1} = U_f^{*n+1} - \Delta t \frac{1}{\rho_f^{n+1/2}} \frac{\delta p}{\delta n}^{n+1/2} \quad (3.9)$$

$$u_i^{n+1} = u_i^{*n+1} - \Delta t \frac{1}{\rho^{n+1/2}} \frac{\delta p}{\delta x_i}^{n+1/2} \quad (3.10)$$

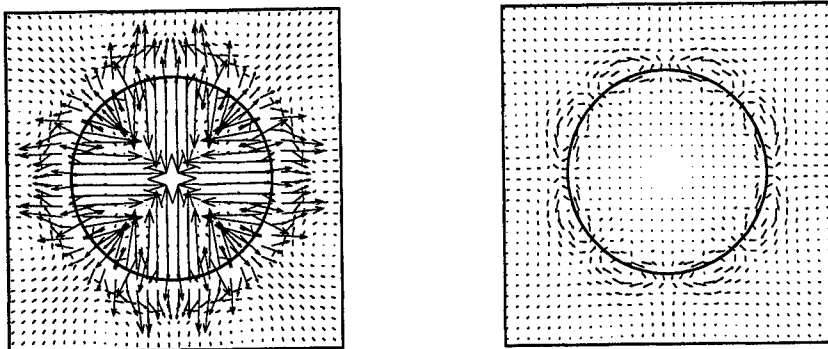
Following this correction, the face-normal velocity components will exactly conserve mass. The CV-centered pressure gradient required in eq. 3.10 is reconstructed from the face-normal components using a second-order reconstruction operator,

$$\frac{\delta p}{\delta x_i}^{n+1/2} = \rho^{n+1/2} \frac{\overline{1}^f \frac{\delta p}{\delta n}^{n+1/2}}{\overline{\rho_f^{n+1/2}}^f}. \quad (3.11)$$

In the present work we use a face-area weighted average. At this point the time step is completed, and the algorithm would cycle back to eq. 3.1.

A critical difference between the present formulation and the formulation of Kim and Choi is in the calculation of the starred face-normal velocities (eq. 3.7). Kim and Choi assume that:

$$\frac{\overline{R_i^{n+1/2}}^f}{\rho^{n+1/2}} \approx \frac{R_f^{n+1/2}}{\rho_f^{n+1/2}}. \quad (3.12)$$



(a) eq. 3.12 assumed for surface tension (b) eq. 3.13 assumed for surface tension

FIGURE 2. Comparison of calculated velocity field around a cylindrical drop for two different formulations of the surface tension forces.

This is an $O(\Delta x^2)$ approximation, seemingly consistent with the overall accuracy of the method, and significantly simplifies the calculation of the Poisson equation source term. In the present investigation, however, it was found that when surface tension forces were introduced in the region of the zero level set, this approximation could lead to large non-physical oscillations in the CV-centered velocity field. To solve this problem, the surface tension forces must be calculated at the faces, and then averaged to the CV centers, i.e.:

$$\frac{R_i^\sigma}{\rho} \equiv \frac{\overline{R_f^\sigma}^{x_i}}{\rho_f} \quad (3.13)$$

With this calculation of the surface tension forces, we can no longer make the assumption of eq. 3.12, and the additional terms must be included in the calculation of U_f^* and thus in the Poisson equation source term.

4. Results

4.1. Surface tension formulation

To illustrate the importance of a proper handling of the surface tension forces, figure 2 compares the calculated velocity field around a cylindrical drop with surface tension using the two different formulations. Figure 3 compares the normalized pressure and velocity along a horizontal line through the center of the drop for the same two calculations. Clearly the formulation that assumes eq. 3.13 is superior. Although the steady velocity field for this problem should be exactly zero, even with the new formulation we do observe eight small vortices arranged symmetrically around the perimeter of the drop. These “parasitic currents” have been observed by other investigators (Tryggvason *et al.* 2001). For the improved face-based surface-tension formulation, the maximum induced velocity is on the order of $0.001\sigma/\mu$, consistent with the observations of others using staggered structured codes.

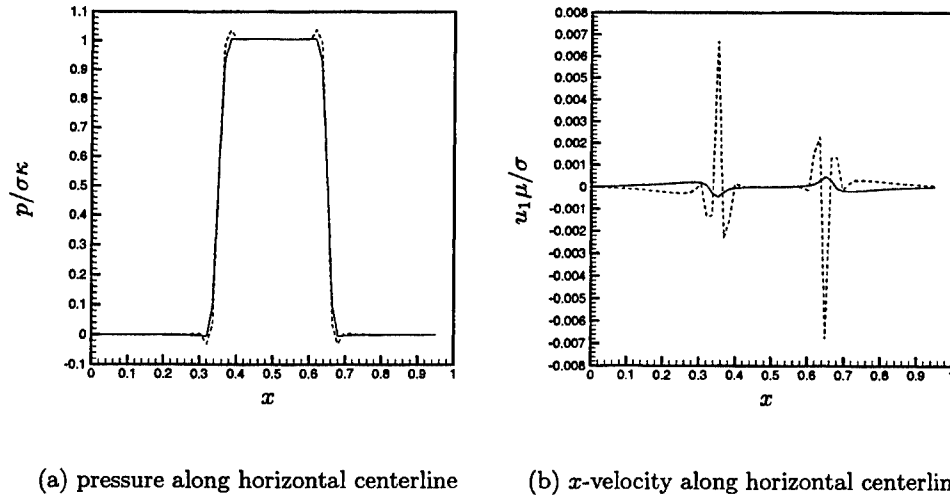
(a) pressure along horizontal centerline (b) x -velocity along horizontal centerline

FIGURE 3. Cylindrical drop computation: Comparison of a) calculated pressure and b) calculated CV-centered velocity through the horizontal centerline of the drop: --- eq. 3.12 assumed for surface tension; — eq. 3.13 assumed for surface tension.

4.2. Adaptive mesh refinement and coarsening

Because of the substantial variations in resolution requirement, some sort of local refinement capability is considered essential to the success of this investigation. In the present work, the adaptive Cartesian method of Ham et al. (2002) is being developed to solve the system described by eqs. 2.4 - 2.6.

To illustrate the potential of the method, figure 4 shows the adapted mesh that results when the Rayleigh-Taylor instability is calculated with a simple isotropic adaptation criteria in the region of the zero level set. The development of a more optimal flow and level set adaptation criterion is an ongoing part of this investigation.

5. The particle level set method

As a compliment to the numerical development presented in the previous sections, the potential of the particle level set method of Enright, Fedkiw, Ferziger & Mitchell (2002) to improve the conservation properties in the region of the free surface is also being investigated.

In the particle level set method, massless Lagrangian particles are placed in a band around the zero level set and used to correct the level set evolution. Initially, particles of the same signs as the level set function values are placed within this band. Each particle (with coordinate \vec{x}_p) is advanced according to the local velocity

$$\frac{d\vec{x}_p}{dt} = \mathbf{u}(\vec{x}_p), \quad (5.1)$$

where $\mathbf{u}(\vec{x}_p)$ is the interpolated velocity at the particle position.

As in Enright, Fedkiw, Ferziger & Mitchell (2002), each particle is given a sign (s_p), a radius (r_p), and an individual level set function ϕ_p defined as

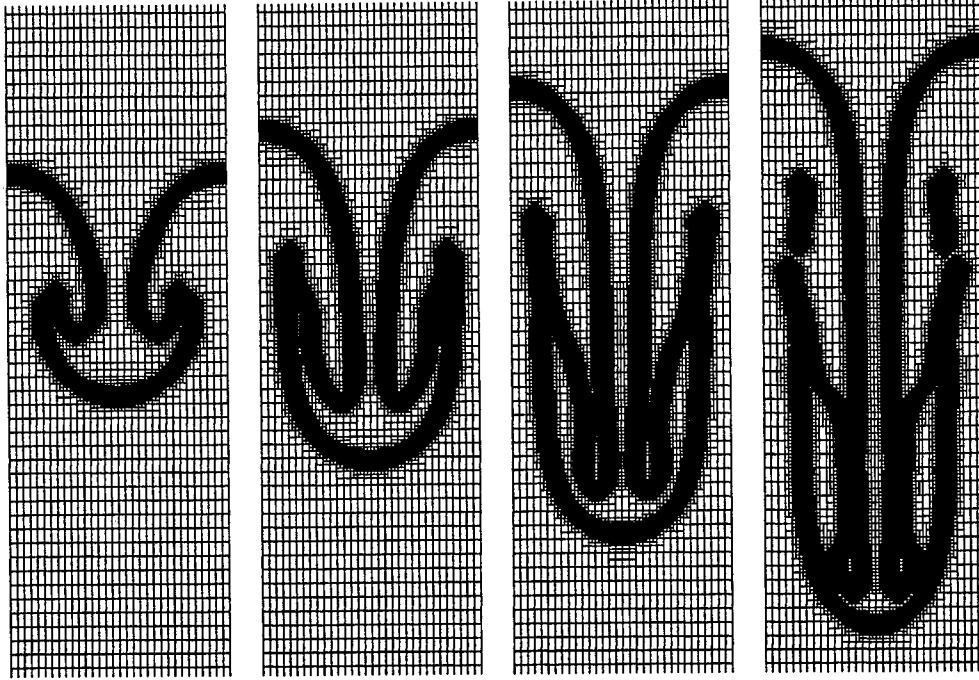


FIGURE 4. 2D Rayleigh-Taylor instability: Calculated evolution of the mesh in the region of the free surface.

$$\phi_p(\vec{x}) = s_p(r_p - |\vec{x} - \vec{x}_p|). \quad (5.2)$$

The sign of each particle is assigned once initially, and the radius of each particle is determined according to the algorithm in Enright, Fedkiw, Ferziger & Mitchell (2002). At each time step, errors made in the level set function leads to displacement of particles; some may end up on the wrong side relative to the zero level set. Explicitly, a particle is found to be on the wrong side if

$$\phi(\vec{x}_p) \times s_p < 0. \quad (5.3)$$

Once the particle is found to be on the wrong side, it will be defined as an escaped particle if the following condition is met

$$-\phi(\vec{x}_p) \times s_p > r_p. \quad (5.4)$$

Following the algorithm in Enright, Fedkiw, Ferziger & Mitchell (2002), only the escaped particles contribute to correcting the level set. The correction is made by reassigning the values of the level set ϕ according to the following rules: for a given set of escaped positive particles (E^+) and a level set ϕ , the maximum of the level set values from all escaped positive particles (E^+) is picked as the projected level set value $\phi^+(\vec{x})$

$$\phi^+(\vec{x}) = \max_{p \text{ in } E^+} (\phi_p(\vec{x}), \phi^+(\vec{x})) \quad (5.5)$$

with $\phi^+(\vec{x})$ first initialized with $\phi(\vec{x})$.

Similarly for escaped negative particle, given a set of escaped negative particles (E^-)

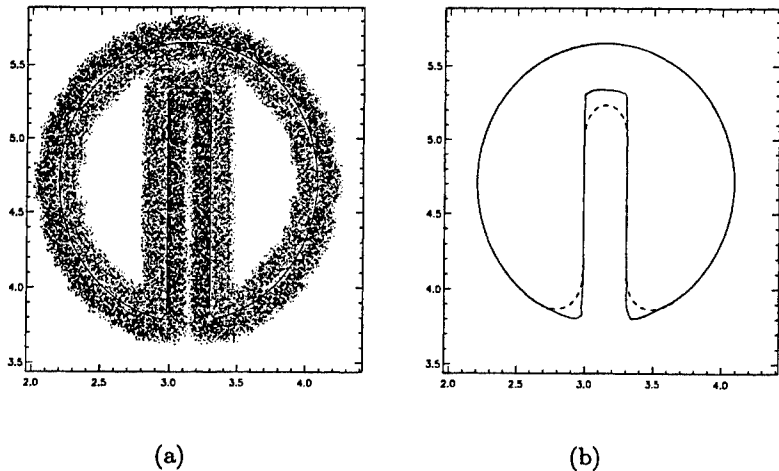


FIGURE 5. (a) Initial level set on a uniform grid of resolution 128×128 . Particles are also included.
 (b) After one revolution: — with particle correction; - - - without particle correction.

and a level set ϕ , the minimum of the level set values from all escaped negative particles is the projected level set value $\phi^-(\vec{x})$

$$\phi^-(\vec{x}) = \min_{p \text{ in } E^-} (\phi_p(\vec{x}), \phi^-(\vec{x})) \quad (5.6)$$

with $\phi^-(\vec{x})$ first initialized with $\phi(\vec{x})$. The corrected level set value is then determined as the value that is closer to the interface

$$\phi(\vec{x}) = \begin{cases} \phi^+ & \text{if } |\phi^+| \leq |\phi^-| \\ \phi^- & \text{if } |\phi^+| > |\phi^-|. \end{cases} \quad (5.7)$$

To ensure that the level set remains as close to the boundary between positive and negative particles as possible, the particle correction is conducted after both the transport of the level set and the re-initialization.

Results from the standard test of Zalesak's disk are shown in figure 5. After one revolution, the level set with particle correction still retains the sharp corners compared with the results without particle correction where the corners are severely smoothed and eroded. Such results are consistent with those presented in Enright, Fedkiw, Ferziger & Mitchell (2002) for equivalent numerical resolution.

5.1. Additional geometrical information

A potential improvement to the particle level set method is to incorporate more geometric information into each particle. From differential geometry, the geometric properties such as the line element/surface element of the level set also evolve as the level set is transported. A simple idea then is to associate each particle with such geometric properties of the level sets that the particles reside on. Specifically, at time $t = 0$, with each particle a line element vector \mathbf{l} is defined as the derivative of the distance \mathbf{r} on the curve parameterized by λ

$$\mathbf{l} \equiv \frac{\partial \mathbf{r}}{\partial \lambda}, \quad (5.8)$$

where \mathbf{r} is related to the fluid flow by

$$\frac{d}{dt} \mathbf{r} = \mathbf{u}(\mathbf{r}, t). \quad (5.9)$$

It follows that the line element \mathbf{l} satisfies the following equation

$$\dot{l}_i = W_{ij} l_j, \quad (5.10)$$

where $W_{ij} \equiv \frac{\partial u_i}{\partial x_j}$ and the dot is the time derivative. Higher order derivatives are needed for computation of curvature. At $t = 0$, we define \mathbf{a} as

$$\mathbf{a} = \frac{\partial \mathbf{l}}{\partial \lambda}. \quad (5.11)$$

This leads to the following equations for each component of \mathbf{a}

$$\dot{a}_i = W_{ij} a_j + W_{ijkl} l_j l_k, \quad (5.12)$$

where $W_{ijk} \equiv \frac{\partial^2 u_i}{\partial x_j \partial x_k}$. Denoting the length of \mathbf{l} as $\xi \equiv |\mathbf{l}|$, we can calculate the curvature of the level set associated with each particle as $\kappa \equiv \xi^{-3} \epsilon_{ijk} n_i l_j a_k$, where the Einstein summation is assumed for repeated indexes, ϵ_{ijk} is the delta function, and n_i is the normal vector. With this additional information, we may modify how we correct the level set according to the escaped particles. For example, we may incorporate the normal vectors and the curvature into the particle level set function ϕ_p . The simplest modification, just using the line element \mathbf{l} , is to write the particle level set function as

$$\phi'_p(\vec{x}) = s_p(r_p - |\mathbf{n}_p \cdot (\vec{x} - \vec{x}_p)|), \quad (5.13)$$

where \mathbf{n}_p is the normal vector to the level set where the particle belongs. Figure 6 shows how ϕ_p (equation 5.2) compares with ϕ'_p for a positive particle ($s_p = 1$). The dashed line is where $\phi_p = 0$ and the solid line is where $\phi'_p = 0$.

Whenever a particle escapes and is used to correct the level set function, the shortest distance between the grid point and all the zero particle levels will be used to correct the value of the level set function. To test this idea, we advect a circular level set by a single vortex in two-dimensions. Inside a unit box, the mixing flow is described by the stream function

$$\Psi = \frac{1}{\pi} \sin^2(\pi x) \sin^2(\pi y), \quad (5.14)$$

and the corresponding velocity

$$u = \frac{1}{2}(\sin(2\pi y) - \sin(2\pi y) \cos(2\pi x)), \quad v = \frac{1}{2}(-\sin(2\pi x) + \cos(2\pi y) \sin(2\pi x)). \quad (5.15)$$

The initial condition is a circle of radius 0.15 located at (0.5, 0.75) (cf Enright, Fedkiw, Ferziger & Mitchell (2002)), and the numerical resolution is 128×128 .

The improvement is significant when two level sets move toward each other within distances less than two grid spacings. More small-scale structures are retained using ϕ'_p

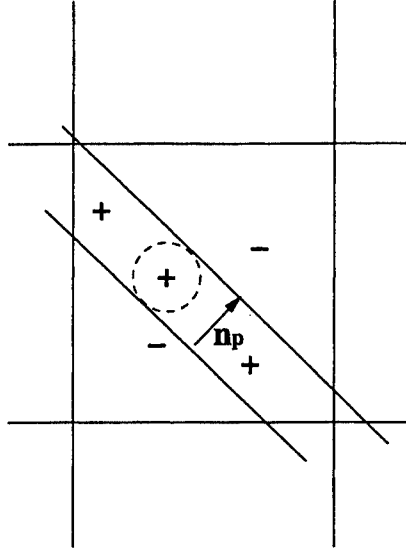


FIGURE 6. Particle level set ϕ'_p and ϕ_p for a positive particle inside a cell.

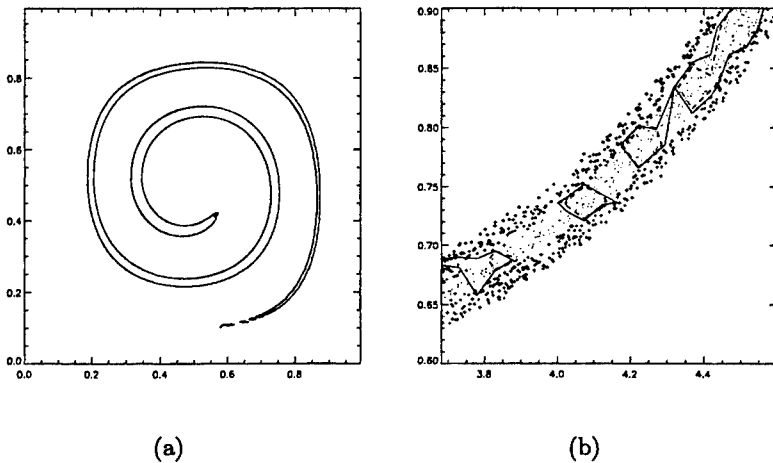


FIGURE 7. Advection of a circle by a single vortex. (a) The level set at $t = 2.8$. The solid line is using equation 5.12 for particle correction, and the dashed line is based on equation 5.2. (b) Detail of the level sets with particles superimposed.

for particle correction (solid line in fig. 7b) than the correction based on ϕ_p (dashed line in fig. 7b). Eventually the numerical limitation sets in and annihilation of level sets occurs for both simulations using ϕ_p or ϕ'_p .

6. Future plans

At the time of writing, the Cartesian adaptive code is undergoing a period of validation where a series of 2D and 3D free surface problems will be investigated, including bubble oscillation, interaction and breakup problems, and the 2D and 3D Rayleigh-Taylor in-

stability. In the context of this validation, a flow and level set based adaptation criterion similar to the interpolation error based criterion described in Ham et al. (2002) will be developed. Eventually it is planned to incorporate the particle level set into the Cartesian adaptive code, and compute the interaction between a turbulent boundary layer and free surface with overturning waves.

REFERENCES

- ALEXAKIS, A., YOUNG, Y.-N. & ROSNER, R. 2002 Shear instability of fluid interfaces: stability analysis. *Phys. Rev. E* **65** 026313.
- ALEXAKIS, A., YOUNG, Y.-N. & ROSNER, R. 2002 Weakly non-linear analysis of wind-driven gravity waves. *J. Fluid Mech.* submitted.
- ENRIGHT, D., FEDKIW, R., FERZIGER, J. & MITCHELL, I. 2002 A Hybrid Particle Level Set Method for Improved Interface Capturing. *J. Comput. Phys.*, to appear.
- HAM, F. E., LIEN, F. S. & STRONG, A. B. 2002 A Cartesian grid method with transient anisotropic adaptation. *J. Comput. Phys.* **179**, 469-494.
- KIM, D. & CHOI, H. 2000 A Second-Order Time-Accurate Finite Volume Method for Unsteady Incompressible Flow on Hybrid Unstructured Grids *J. Comput. Phys.* **162**, 411-428.
- MILES, J. 1957 On the generation of surface waves by shear flows. *J. Fluid Mech.* **3**, 185.
- PENG, D., MERRIMAN, B., OSHER, S., ZHAO, H. & KANG M. 1999 A PDE-based fast local level set method. *J. Comput. Phys.* **155**, 410-438.
- RHIE, C.M., & CHOW, W.L. 1983 Numerical study of the turbulent flow past an airfoil with trailing edge separation. *AIAA J.* **21**, 1525.
- SUSSMAN, M., SMEREKA, P. & OSHER, S. 1994 A level set approach for computing solutions to incompressible two-phase flow. *J. Comput. Phys.* **114**, 146-159.
- TRYGGVASON, G., BUNNER, B. ESMAEELI, A., JURIC, D., AL-RAWAHI, N., TAUBER, W., HAN, J., NAS, S. & JAN, Y.-J. 2001 A Front-Tracking Method for the Computations of Multiphase Flow *J. Comput. Phys.* **169**, 708-759.

Simulation of flows over wavy rough boundaries

By A. Nakayama † AND K. Sakio ‡

1. Motivation and objectives

Numerical calculation of large-scale flows appearing in the natural environment almost always involves simplification of the boundary geometry. It is not only impossible, but also meaningless, to represent all the details of the terrain with trees and vegetation, not to mention smaller objects like little stones in simulating a wind field in a localized area, or irregular bank and bed forms of natural meandering rivers. Flows in rivers and oceans have, in addition, a complex boundary on the free surface, whose shape is not just given but determined by the motion of water. The overall effects of small and random irregularities are accounted for as roughness, but larger undulations would have to be considered a part of the boundary shape. In fact the roughness and the boundary shape cannot be distinguished so easily. The numerical resolution of the flow field requires determination of what is to be considered roughness and what should be considered as the boundary shape. If the small-scale irregularities are smoothed out, the motion associated with the details is lost. In the context of large-eddy simulation (LES), this will give rise to additional subgrid-scale stresses. It has been pointed out by Nikora et al. (2001) that the small details of irregularities of even the time-averaged flow near the rough bed of an open channel must be treated by spatial averaging, which also leads to an additional stress. In simulation of the atmospheric boundary layer over a forest canopy, the extra resistance due to the roughness of the canopy is added in the flow (e.g. Yamada (1982)). In an LES, it is found (Brown, Hobson & Wood (2001) and Chow & Street (2002)) that these additional stresses need to be distributed over a much larger area in order to obtain the correct logarithmic law for an atmospheric boundary layer.

Various studies of numerical simulation of smooth-surface wall flows have indicated that proper representation of the near-wall flow is essential for accurate reproduction of the main flow. Proper representation of the flow near rough and irregular boundaries can also be very important in computation of flows over rough surfaces. The main objectives of the present work is to study the effects of smoothing of the boundary on the large-eddy simulation as well as filtering of small-scale fluctuations of the flow, and to investigate modeling methods of the subgrid scale stresses and the boundary conditions when the boundary geometry is complex and irregular. We do this by conducting a direct simulation of model flow over a wavy boundary with distinct length scales. Small waves are used to simulate the surface irregularities that large-eddy simulations may not be able to resolve. A large body of work on rough surface flows does not address the effects of smoothing boundary shapes and we look at the simulation results from this point of view. Effects of smoothing the free-surface waves have been pointed out by Hodges & Street (1999). A model for inviscid surface waves has been proposed by Dimas & Fialkowski (2000). Extension of the present line of work to moving wavy surfaces can be applied to free-surface fluctuations as well.

† Division of Global Environment Development Science, Kobe University

‡ Dept. Civil Engineering and Architecture, Kobe University

TABLE 1. Parameters for simulation calculation.

Case	Grid cells	$L_x \times L_y \times H$	λ	δ	λ'	δ'	Re_H
Case 1	$192 \times 128 \times 96$	$3 \times 2 \times 1$	1.0	0.05	—	—	6760
Case 2	$384 \times 128 \times 96$	$3 \times 2 \times 1$	1.0	0.05	0.2	0.02	6760

2. Results

2.1. Direct simulation of flow over wavy rough surface

In order to study the effects of small boundary irregularities, a direct numerical simulation of a model flow with a "simplified" complex boundary has been conducted. It is a flow over a wavy surface containing two modes of two-dimensional cosine waves with different wave lengths and amplitudes. The smaller waves simulate undulations or roughness that a LES computation cannot resolve but whose effects should be reflected in the resolved flow field. Therefore, additional computation is performed for the case without the smaller waves. Flows over wavy walls have been studied both experimentally (e.g. Hudson, Dykhno & Hanratty (1996) and Gong, W., Taylor, P. A. & Doernbrack (1996)) and numerically (e.g. Krettenauer & Schumann (1992) and Maass & Schumann (1994)) as a case of rough surface itself. We repeat the simulation of this flow as a verification of our computation and as the basis for evaluating further effects of smaller waviness. It is the same as the flow in a channel with wavy surface computed by Maass & Schumann (1994), except the upper boundary in the present flow is a free-slip boundary approximating a free surface. A free surface flow over wavy bottom of much higher Reynolds number has also been simulated by Calhoun & Street (2001) using a LES method and the basic flows may be compared with these calculations. The present simulation results and the filtered fields of the simulated flows will provide basic data for examining the effects of the boundary irregularities.

The computational domain, the definition of symbols and the computational grids for the two simulation cases are shown in Figure 1. One in every four of $192 \times 128 \times 96$ grid lines of Case 1 and $384 \times 128 \times 96$ grid lines of Case 2 on the three bounding surfaces are shown. The values of the parameters are shown in Table 1. The parameters for Case 1 of the single-mode wavy surface are identical to those of Maass & Schumann (1994) and the ratio of the wave amplitude to the wave length is 0.05 with a maximum slope of 0.31. The present flow domain consists of three wavelengths compared with four in Maass & Schumann (1994). Case 2 is a flow over the same wavy surface with smaller waves superimposed. The wavelength λ' and the amplitude δ' of the smaller waves are one fifth and two fifths of the main waves, respectively. These are respectively approximately 150 and 30 viscous units based on the average shear stress. The bulk Reynolds number Re_H defined by the average velocity U_m and the flow depth H is 6760 and is the same as Maass & Schumann (1994).

The numerical method used in these simulations is the same as that explained in Yokojima & Nakayama (2001), which is essentially the same as the method of Zang, Street & Koseff (1994). It is a fractional step method formulated on the collocated grid arrangement in general curvilinear coordinates. For the present configuration of the flow, one of the coordinates is taken to conform to the wavy surface on the bottom and the flat

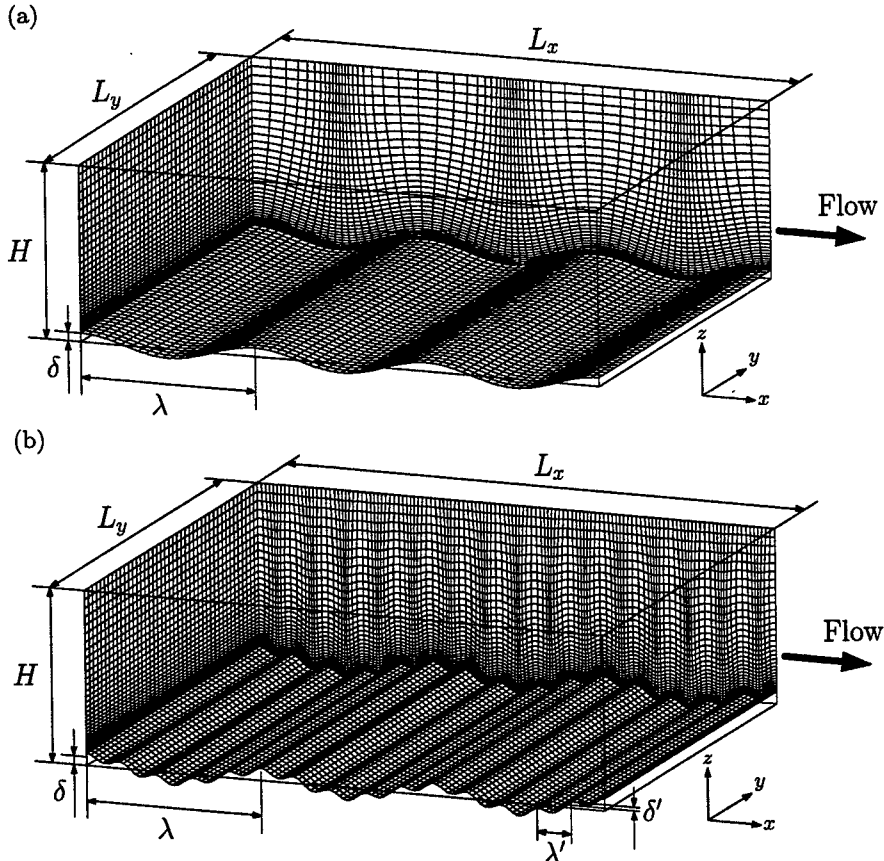


FIGURE 1. Computational domain and grids (every four grid lines shown) : (a) Case 1; (b) Case 2.

upper boundary and the second coordinate is taken so that it is close to orthogonal to the first as close as possible without much distortion in the main flow domain. Approximate orthogonality near the solid boundary is important to capture the motion accurately in this region.

The boundary conditions are no-slip on the bottom wavy walls, free slip on the upper boundary and periodic in the streamwise and cross flow directions. In order to shorten the initial flow development time, the current calculation was first started with the result of our earlier DNS calculation of straight open-channel flow (Nakayama & Yokojima (2001)) as the initial flow over one period of the large waves.

2.2. Mean flow and filtered mean flow

The mean-flow properties of the simulated flows are shown in Figures 2 and 3. The flow configuration of present Case 1 is the same as those of Maass & Schumann (1994) and Calhoun & Street (2001). Particularly the Reynolds number of the present calculation is the same as that of Maass & Schumann (1994) and detailed comparisons are made in Figure 2. The only difference between these two calculations is that the boundary condition on the top. The present calculation, similar to Calhoun & Street (2001), does not have a boundary layer there. The two results are seen to be sufficiently close to each

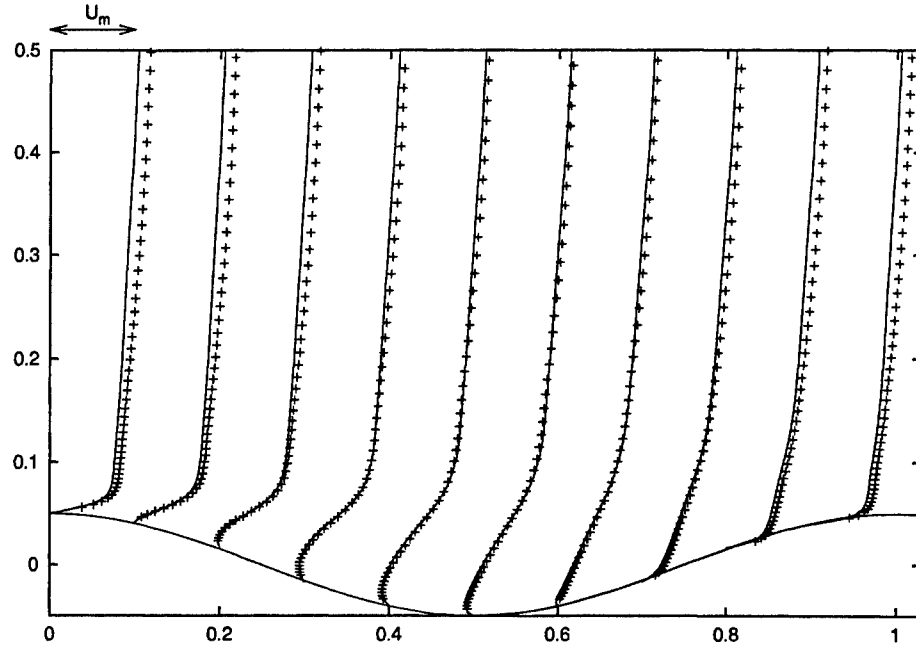


FIGURE 2. Mean velocity profiles of Case 1 compared with calculation of Maass & Schumann (1994). — : present simulation, . + : Maass & Schumann (1994)

other. Slightly lower velocity of the present calculation in the center region is due to the absence of the boundary layer on the upper boundary.

Figures 3(a) and (b) show the mean velocity vectors of the present two simulation cases in the lower half of the middle one third of the calculation region. The flow is separated in both cases and the dividing streamlines are shown in dotted lines. These may roughly be thought of as the effective boundaries for the flow away from the bottom boundary. It is noted that the dividing streamline for Case 2 shows undulations that are of opposite phase to that of the boundary shape, and somewhat smoothed and shifted upward.

A LES simulation of flows like that of present Case 2 that does not resolve the small waviness is not to reproduce the flow over the large waviness alone like that of Case 1. Instead, one would like to obtain a flow that corresponds to the filtered flow field of Case 2. Figure 3(c) is the flow field obtained by filtering the flow of Case 2 with filter length equal to the wavelength of the small waves. The filter function is a rectangular top-hat of horizontal to vertical side ratio equal to the ratio of the wave length to the height. In the filtering process, the flow outside the actual flow domain is excluded by a conditioning function discriminating the flow region and outside; thus only velocities from within the flow domain contribute to the filtered result. This filtering method with a conditioning function may not be the best choice in actual LES simulations, due mainly to the non-commutativity with spatial differentiations, but its important consequences will be representative of possible filters to be used in a LES. The location (represented by the elevation) of the original boundary is also filtered in the same way and shown in a solid line. With the filter length chosen to be equal to the wave length of the small waves, the small-scale motions due to the small waves are removed. The recirculation

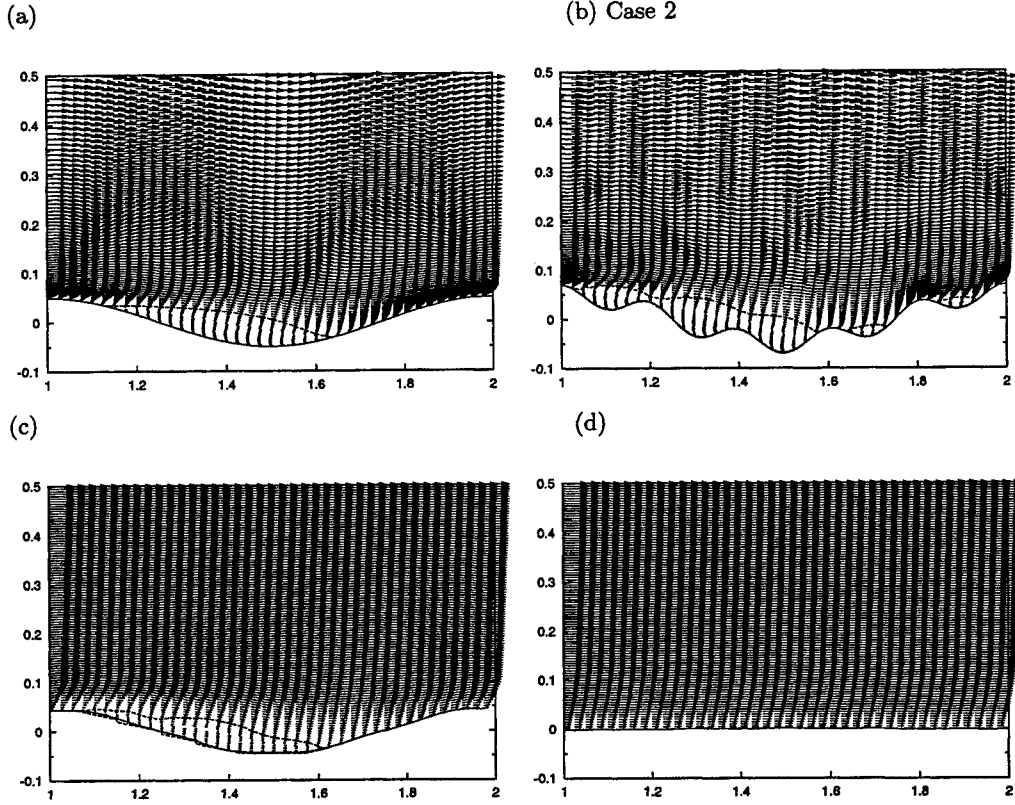


FIGURE 3. Mean velocity distributions of the simulated and filtered flows: (a) Case 1; (b) Case 2; (c) Case 2 filtered with filter size $\lambda' \times 2\delta'$; (d) Case 2 filtered with filter size $\lambda \times 2\delta$: separation streamline

region is smaller but the flow above the separated region retains similarity implying usefulness of a LES type simulation over such complex boundary. Figure 3(d) shows the result of filtering with scale equal to the wave length of the large waves. It is now almost uniform and may be thought a flow over flat rough surface. It is noted that the filtered velocity on the filtered boundary is not exactly equal to zero. Figures 4(a) and (b) are the semi-logarithmic plots of the velocity profiles of Figure 3(c) and (d) at four streamwise positions with the friction velocity determined by filtering the wall stresses and the wall pressure in the direction parallel to the smoothed boundary. The solid line is the rough-surface boundary layer profile with the equivalent roughness height taken to be equal to $k = 2(\delta + \delta')$, the height from the bottom to the top of the boundary of Case 2. The roughness height Reynolds number $k^+ = u_{\tau s} k / \nu$ is 106, where $u_{\tau s} = \sqrt{\tau_s / \rho}$ is the friction velocity determined from the filtered wall resistance which corresponds to the overall pressure gradient and is 0.0127. It is seen that the results with the filter size $\lambda' \times 2\delta'$ vary considerably from a fixed logarithmic profile but those with the large filter size are close to the well-known rough-surface profile, except a slight overshoot near $zu_{\tau s} / \nu = k^+$. The distribution of the filtered resistance τ_s is shown in Figure 5. It is distributed over distances from the smoothed boundary comparable to the filter height and its variation is much larger than the average.

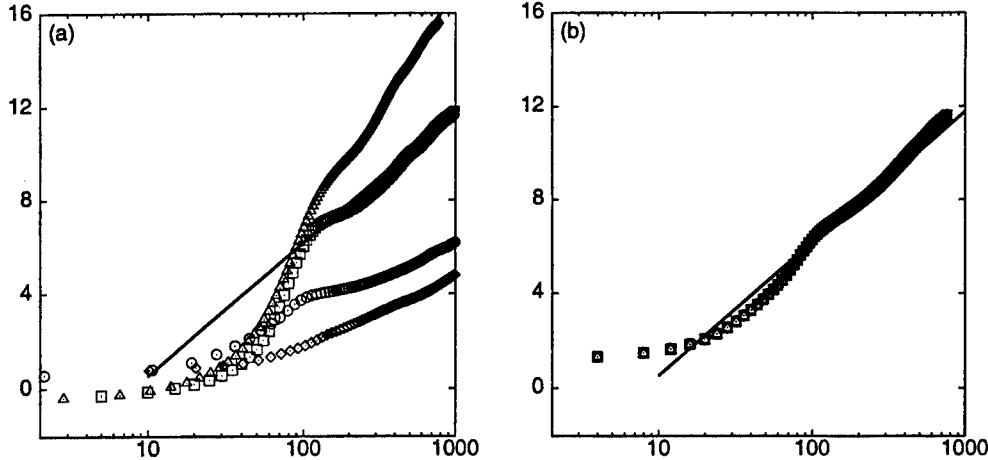


FIGURE 4. Semi-logarithmic plot of the filtered mean velocity distributions: (a) Case 2 with filter size $\lambda' \times \delta'$; (b) Case 2 with filter size $\lambda \times \delta$. $\circ: x/\lambda = 1.0$; $\square: x/\lambda = 1.25$; $\triangle: x/\lambda = 1.5$; $\diamond: x/\lambda = 1.75$; —: rough surface log-law with roughness height equal to the total variation of the wavy wall

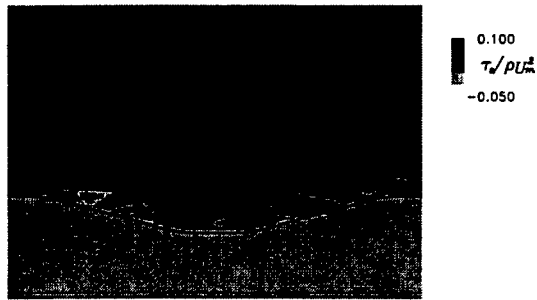


FIGURE 5. Distribution of the component of the filtered wall stresses in the direction tangent to the smoothed boundary.

2.3. Instantaneous features of simulated flows

Figure 6 shows a feature of the instantaneous flows in terms of the distributions of the secondary flow velocity vectors at five cross stream planes in the center one third of the flow. It is seen that the instantaneous flow structure of Case 1 shows quite strong and large structures extending into the middle of the channel. These are like the streamwise vortices seen by Calhoun & Street (2001) in a LES calculation at a much higher Reynolds number. In Case 2 with small boundary waviness, the scale of the fluctuations appears to be smaller and they do not extend as far into the channel main flow as Case 1. The disturbances due to the small waviness appear to destroy and break up many of the larger vortical structures. Although not shown, the filtered flow of Case 2 has even weaker structures.

Figure 7 further shows the iso-surfaces of the second invariant of the instantaneous velocity gradient tensor. They are known to show the vortical structures more directly.

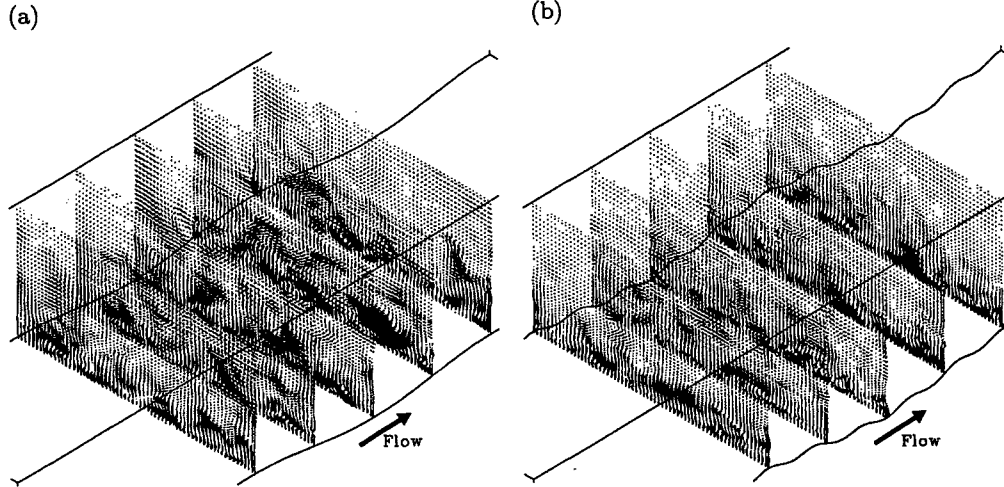


FIGURE 6. Secondary flow velocity vectors in the cross-stream planes in the center one third of the flow: (a) Case 1; (b) Case 2.

The streamwise structures seen in Case 1 are similar to those seen by Calhoun & Street (2001). Most of them originate from the ridges and extend over distances comparable to the wave length. In Case 2 the structures appear to be disturbed by the smaller waviness and are broken into smaller scale motions.

2.4. Subgrid scale stresses and effects of boundary smoothing and flow filtering

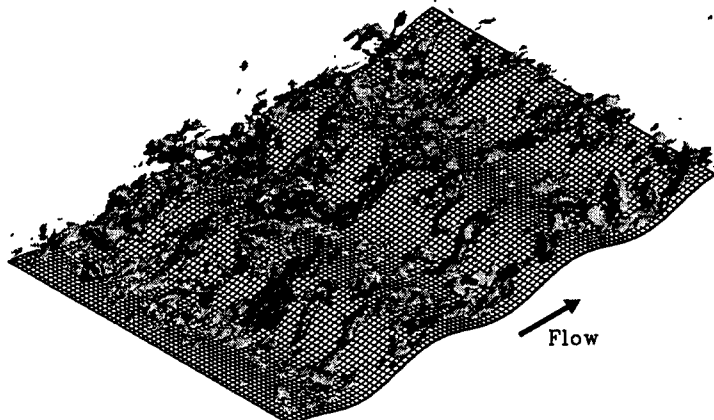
In order to gain an idea about the magnitudes and the distribution of the sub-grid stresses that one will have to deal with in a LES simulation of flows like that influenced by small waviness of the boundary, subgrid stresses are computed from the simulated flow field. In conventional LES, the effects of the subgrid scale motion are represented by the subgrid stress

$$\tau_{ij} = -\overline{u_i u_j} + \overline{u_i} \overline{u_j} \quad (2.1)$$

where u_i is the instantaneous velocity vector, and the overbar indicates a spatial filtering. Sample distributions of component τ_{13} at one instant of time in a $x - y$ plane are shown in Figure 8 in shaded contour plots. Here subscript 3 is used to mean the z -direction and is upward from the wavy bottom surface. Figures 8(a) and (b) are obtained by using the same filtering method used earlier for the mean quantities so that the boundary of Case 2 is smoothed at the same time. While these are only samples we see that the sub-grid stresses in Case 2 are of larger magnitude. High stress regions are seen downstream of the ridges of the main waves. Figure 8(c) shows the sub-grid scale stresses when the filtering is performed only in the spanwise direction which is the direction of flow homogeneity. Filtering this way retains the small-scale variations and the boundary geometry is not smoothed. This is not what one models in a LES which does not resolve the small waviness, but is shown here for comparison.

In order to further see the effects of boundary smoothing, we look at the difference of the two simulations on an instantaneous basis. The two simulations are statistically independent and the instantaneous difference does not necessarily represent the instantaneous effects of the small waviness. Nonetheless it will show a possible picture of the effects and we have plotted one example of the difference distribution in a $x - z$ plane in

(a)



(b)

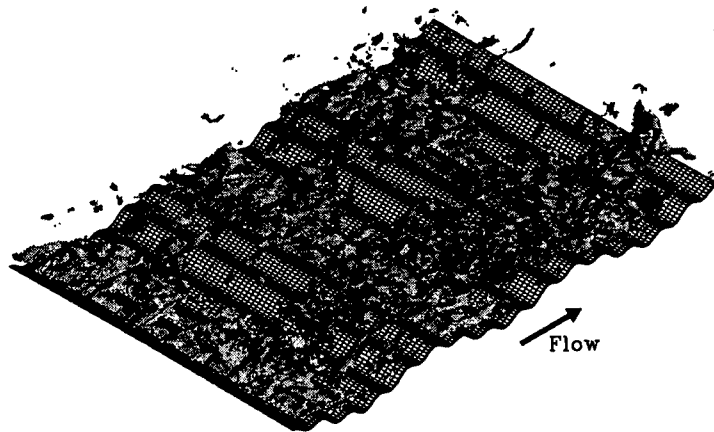


FIGURE 7. Iso-surface of second invariant of velocity gradient tensor: (a) Case 1; (b) Case 2.

Figure 9. It shows that strong fluctuations with scales comparable to the small waves are seen in the near wall region, particularly downstream of the ridges of the main waves. What is important is that these perturbations burst up into the main part of the channel. This bursting is the reason that the effects of roughness, if introduced as an external force must be input in regions much larger than the roughness height.

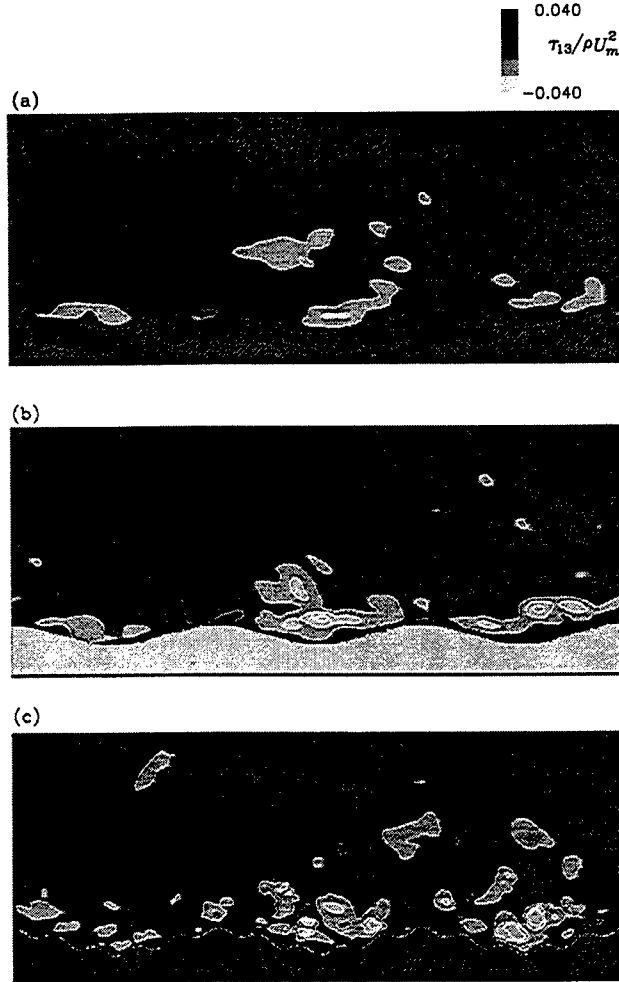


FIGURE 8. Instantaneous subgrid scale shear stress distribution: (a) Case 1; (b) Case 2 with filter $\lambda' \times \delta'$; (c) Case 2 with spanwise filtering; (b) and (c) are at the same time and in the same plane.

3. Considerations for LES of flows over complex boundaries

In a LES simulation of a flow in a complex domain that cannot be resolved by the computational grid, smoothing of the boundary must be done explicitly or implicitly. We interpret that the boundary is smoothed when the spatial filtering is applied to flow quantities. In order to help model this, we denote the filtered and smoothed velocity of the original velocity u_i by \bar{u}_i , and identify the motion lost by boundary smoothing by δu_i and fluctuation lost by the spatial filtering by u'_i . \bar{u}_i cannot explicitly be given by a linear operation on u_i alone. This is a difficulty in formulating smoothing of the boundary, but we may write

$$u_i = \bar{u}_i + u'_i + \delta u_i, \quad (3.1)$$

An additional difficulty is that there are differences in the domains on which these quantities are defined. u_i is defined in the original unsmoothed flow domain D , while \bar{u}_i is

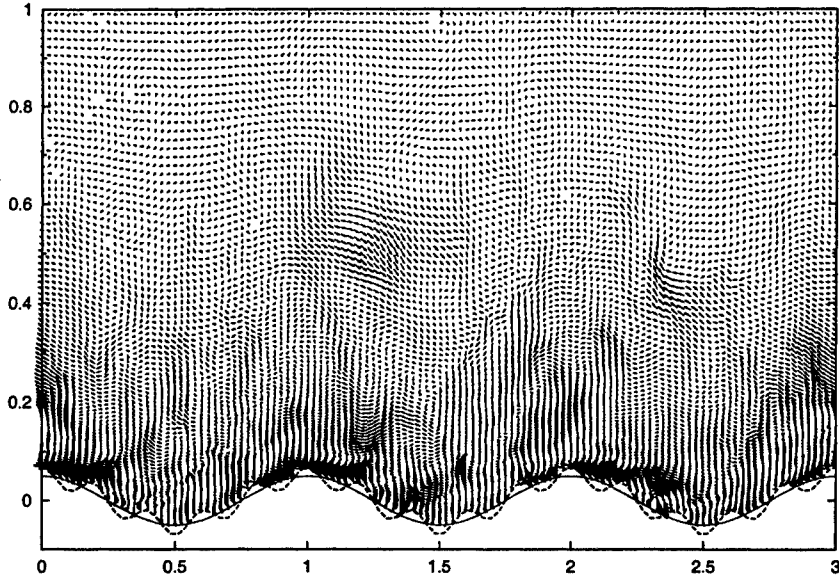


FIGURE 9. Difference between the instantaneous velocity vectors in Case 1 and Case 2.



FIGURE 10. Subgrid scale shear stress of the difference velocity of Case 1 and Case 2.

defined in the smoothed domain \tilde{D} and δu_i can be defined in the intersection of these two domains. We interpret Eq(3.1) in the smoothed domain \tilde{D} by assuming some extrapolated flow u_i outside D .

The equations for \bar{u}_i may then be obtained by filtering the original equations of motion and by replacing the boundary conditions with those on the smoothed boundary. The results will be the same as the usual LES equations

$$\frac{\partial \bar{u}_i}{\partial t} + \frac{\partial \bar{u}_i \bar{u}_j}{\partial x_j} = -\frac{1}{\rho} \frac{\partial \bar{p}}{\partial x_i} + \frac{\partial}{\partial x_j} \left(\nu \frac{\partial \bar{u}_i}{\partial x_j} - T_{ij} \right) \quad (3.2)$$

and the boundary conditions are applied on the smoothed boundary \tilde{B} . The subgrid scale stress appearing in these equations is denoted by T_{ij} to emphasize that it includes the boundary smoothing effects and is given by

$$T_{ij} = -\bar{\bar{u}_i \bar{u}_j} + \bar{u}_i \bar{u}_j - \bar{\bar{u}_i u'_j} - \bar{\bar{u}_j u'_i} - \bar{u}'_i \bar{u}'_j$$

$$-\overline{\tilde{u}_i \delta u_j} - \overline{\tilde{u}_j \delta u_i} - \overline{\delta u_i u'_j} - \overline{\delta u_j u'_i} - \overline{\delta u_i \delta u_j}. \quad (3.3)$$

The first half is the same as the usual Leonard, cross and Reynolds stress terms due to filtering and the terms in the next line contain δu_i . These may be considered the effects of smoothing of the boundary. There are terms showing interactions between the filtering and smoothing and the stresses due to smoothing alone. δu_i is a quantity related to the smoothing of the boundary. If we define a measure of deviation of the smoothed boundary from the original position such as the mean square of the deviation, a model for the statistical quantities involving δu_i may be constructed. We will examine some of these terms from the present direct simulation of a model flow.

In order to know δu_i , additional equations will have to be solved. Since the difference velocity field we saw in the previous subsection can be thought of as one realization of δu_i , we computed the stresses associated with it

$$\eta_{ij} = -\overline{\delta u_i \delta u_j} + \overline{\delta u_i \delta u_j}. \quad (3.4)$$

The results are plotted in Figure 10. It shows that the magnitudes are slightly smaller than the subgrid scale stresses due to filtering and distributed in a broader region.

If usage of the instantaneous δu_i is to be useful, we will need to be able to calculate it. One way of doing this is to assume a (fictitious) unfiltered velocity field \tilde{u}_i within the smoothed boundary, that is, \tilde{u}_i satisfies the Navier-Stokes equations in the smoothed domain. Then the equations for δu_i may be obtained by taking the difference of the equations for u_i and \tilde{u}_i in the intersection region of D and \tilde{D}

$$\frac{\partial \delta u_i}{\partial t} + \frac{\partial \tilde{u}_j \delta u_i}{\partial x_j} + \frac{\partial \tilde{u}_i \delta u_j}{\partial x_j} + \frac{\partial \delta u_i \delta u_j}{\partial x_j} = -\frac{1}{\rho} \frac{\partial \delta p}{\partial x_i} + \nu \frac{\partial^2 \delta u_i}{\partial x_j \partial x_j} \quad (3.5)$$

where δp is the difference in the pressures in the original flow and the smoothed flow. Since δu_i is expected to be significant only near the region where the boundary is altered, this equation may be linearized in most of the smoothed flow. But it should be noted that δu_i may not be of small scale and may not be negligible in regions away from the boundary. The boundary condition for δu_i may be applied on \tilde{B} and is $u_i - \tilde{u}_i$ with some extrapolation for u_i . Even if it is not possible to solve for δu_i , it should be possible to solve for its filtered values or the stress η_{ij} .

4. Conclusions and future work

A direct simulation of an idealized flow with wavy surfaces consisting of distinct length scales has been conducted. The results have been analyzed in view of how an LES simulation that does not resolve the small details of the boundary shapes must be done. Using the filtering and boundary smoothing method considered in the present work, the surface stresses on the original boundary are spread as external forces over the area corresponding to the filter size and the filtered velocity field does not satisfy the original no-slip condition on the smoothed boundary. The filtered velocity profiles indicate some form of similarity, but the precise form still needs to be examined. In addition to the stresses due to the original surface stresses, motion removed by the boundary smoothing introduces additional stresses that extend into the region where there was no original solid boundary. A possible method of modeling these stresses based on decomposition of the velocity field into the filtered field and the parts lost by the boundary smoothing and the filtering, has also been presented. The obvious step of future work is to complete the analysis of the simulation results. The averages should include, not only the conventional

averages but filter averages with alternative filtering and smoothing methods, and all quantities that arise in the filtering and smoothing process. Models for these terms and the boundary conditions must be constructed. Then one can do an actual LES calculation for the present flow with the appropriate models and evaluate the results.

REFERENCES

- BROWN, A.R., HOBSON, J.M. & WOOD, N. 2001 Large-eddy simulation of neutral turbulent flow over rough sinusoidal ridges. *Boundary-Layer Meteorology* **98**, 411-441.
- CALHOUN, R.J. & STREET, R.L. 2001 Turbulent flow over wavy surface: Neutral case. *J. GOP. Res.* **106**, 9277-9293.
- CHOW, F.K. & STREET, R.L. 2002 Modeling unresolved motions in LES of field-scale flows *15th symp. on Boundary Layers and Turbulence*, American Meteorological Society, 432-435, Wageningen, The Netherlands.
- DIMAS, A.A., & FIAŁKOWSKI, L.T. 2000 Large-Wave Simulation (LWS) of Free-Surface Flows Developing Weak Spilling Breaking Waves. *J. Comp. Phys.* **159**, 172-196.
- GONG, W., TAYLOR, P. A. & DOERNBRACK 1996 Turbulent boundary-layer flow over fixed aerodynamically rough two-dimensional sinusoidal waves. *J. Fluid Mech.* **312**, 1-37.
- HODGES, B. R. & STREET, R. L. 1999 On Simulation of Turbulent Nonlinear Free-Surface Flows. *J. Comp. Phys.* **151**, 425-457.
- HUDSON, J. D., DYKHNO, L. & HANRATTY, T. J. 1996 Turbulence production in flow over a wavy wall. *Experiments in Fluids* **20**, 257-265.
- KRETTENAUER, K., & SCHUMANN, U. 1992 Numerical Simulation of Turbulent Flow Over a Wavy Boundary. *J. Fluid Mech.* **237**, 261-299.
- MAASS, C., & SCHUMANN, U. 1994 Numerical simulation of turbulent convection over wavy terrain. *Direct and Large-Eddy Simulation I*, ed. by P.R. Voke, L. Kleiser and J.-P. Chollet, 287-297, Kluwer Academic.
- NAKAYAMA, A. & YOKOJIMA, S. 2001 Direct numerical simulation of the fully developed open-channel flow at subcritical Froude numbers DNS/LES Progress and Challenges, Third AFOSR International Conference Arlington, Texas 2001, 569-576.
- NIKORA, V., GORING, D., McEWAN, I. & GRIFFITHS, G. 2001 Spatially averaged open-channel flow over rough bed. *J. Hydr. Engrg. ASCE* **127**, 123-133.
- YAMADA, T. 1982 A numerical model study of turbulent airflow in and above forest canopy. *J. Meteor. Soc. Japan* **60**, 439-454.
- YOKOJIMA, S. & NAKAYAMA, A. 2001 Development and verification of finite difference method based on collocated grid in generalized coordinate system for direct and large edy simulations. *Annual J. Hydraulic Eng. JSCE* **45**, 565-570.
- ZANG, B. R., STREET, R. L. & KOSEFF, J. R. 1994 A non-staggered grid, fractional step method for time-dependent incompressible Navier-Stokes equations in curvilinear coordinates. *J. Comp. Phys.* **114**, 18-33.

Image-based computational modeling of blood flow in a porcine aorta bypass graft

By V. Favier AND C. A. Taylor †

1. Motivation and objectives

Even though pathological factors are known to characterize the development of vascular diseases, mechanical factors play a major role in their localization and progression. For example, fluid mechanic factors contribute to the initiation of atherosclerosis: plaque formation is more likely to occur in recirculation areas, downstream of arterial bifurcations and bends. It has been observed that, beside mediating the generation of diseases, local hemodynamic parameters enhance their growth. In complex flow areas, low wall shear stresses and high residence time are thought to exacerbate the chemical processes of wall thickening and clotting (cell proliferation in the inner layer of the vessels, surface damage of the endothelium cell layer at the interface of blood and the vessels, Dilley, Mc Geachie & Prendergast 1988; Gewertz *et al.* 1992).

Understanding these phenomena is important not only in research on diseases but also in surgery planning and in the development of artificial devices. Obstruction and failure of a bypass-graft operation may occur if the chemical reactions for thrombosis are activated at the wound where the bypass is added, and can further be maintained because of the sensitivity of the human cardiovascular system to a foreign body and favorable local hemodynamics, like flow stasis.

Numerous studies, both experimental and numerical, have focused on assessing these hypotheses and characterizing the level of importance of fluid quantities in the past few years. Nevertheless, how fluid mechanics and diseases interact remains unclear due to the variety of parameters required to describe the full physics of blood flow.

Non-invasive magnetic resonance imaging (MRI) and ultrasound techniques have been applied to *in vitro* studies on simple geometries (pipes, branches,...) and have shown their ability to measure accurate velocities and characterize flow patterns (Botnar *et al.* 2000). Significant progress in those imaging tools now make it possible to visualize large areas of the cardiovascular tree, observe moving vessel walls and measure velocities *in vivo*.

Numerical simulation is a very attractive tool to access fluid parameters that are difficult to obtain experimentally (full velocity fields, shear stresses,...). Moreover, numerical techniques enable the investigation of the effect of geometric and flow-rate modifications in the studied model. Computations of blood flow in idealized models of the cardiovascular system have been extensively studied. Perktold and colleagues examined blood flow in rigid and deformable models of carotid arteries (Perktold, Resch & Peter 1991; Perktold & Rappitsch 1995). Taylor *et al.* quantified blood flow in an idealized model of the human abdominal aorta under resting and exercise conditions (Taylor, Hughes & Zarins 1998a; Taylor, Hughes & Zarins 1999). Others examined blood flow in models of the end-to-side anastomosis (downstream connection of the end of a bypass graft to side of a host artery, Milner *et al.* 1998; Taylor, Hughes & Zarins 1998b).

† Stanford University, Mechanical Engineering & Surgery

Velocity profile comparisons between *in vitro* experiments and computation of blood flow using the same geometry have been successful in idealized models and also more complex cases. Taylor, Hughes & Zarins (1996), Milner *et al.* (1998), Cebral & Lohner (2001) have extracted realistic models of vessels from volumetric MRI or computed tomography (CT) in order to reproduce the complex anatomy of a patient.

Nevertheless, the combination of medical imaging techniques to extract geometric models and numerical simulation in *in vitro* cases only enables one to study pulsatile blood flow with significant assumptions about inflow boundary conditions. Measuring physiological flow waveforms *in vivo* and using them as data input to the experiment or the simulation does not insure that the velocity profile is realistic.

Ku *et al.* 2002 used a Dacron band to create a restriction (stenosis) in the descending thoracic aorta of pigs and then bypassed this stenosis with a Dacron graft. This aorto-aorta bypass graft was imaged using magnetic resonance angiography (MRA) and blood-flow velocity was measured in the aorta above the proximal connection of the graft to the aorta, using phase-contrast magnetic resonance imaging (PC-MRI). This flow velocity data was used to calculate the volumetric flow rate which in turn was used to prescribe fully-developed pulsatile flow boundary conditions (based on Womersley theory) at the inlet of the computational model. Computed flow rates in the bypass graft and native aorta compared favorably to the flow rates obtained from PC-MRI measurements in these locations. A limitation of this prior investigation is that a Womersley boundary condition was employed, and the effect of this idealized boundary condition on blood-flow rate and velocity patterns was not examined.

In this paper, we describe the effect of inflow boundary conditions on flow rate and velocity in the porcine aorto-aorta bypass model. We compare results of computational solutions performed using a Womersley inflow boundary condition and inflow velocity mapped directly from the PC-MRI data (*in vivo* experiments by Ku *et al.* 2002).

2. Methods

The anatomic model is constructed from MRA data as follows. A vessel path is identified and two-dimensional slice planes are positioned along this path in the volumetric image data. A level-set method is used to extract closed curves representing the vessel boundary in each two-dimensional plane (Wang *et al.* 1999). A surface is lofted through these curves and a solid model constructed. (see figure 1).

An automatic finite-element mesh generator is used to discretize the solid model (SCOREC, Rensselaer Polytechnic Institute). For the calculations described herein, a 1.2 million tetrahedral element mesh was used (figure 1).

As a first approximation we assume that the vessel walls are rigid and that blood behaves as a Newtonian fluid (Taylor *et al.* 1999). With these simplifications, the incompressible Navier-Stokes equations describe the problem.

$$\begin{aligned} u_{i,i} &= 0 \\ u_i + u_j u_{i,j} &= -(p_{,i}/\rho) + \tau_{ij,j} + f_i \end{aligned} \quad (2.1)$$

The density ρ is constant, u_i is the i^{th} component of the velocity, p the pressure, f_i the prescribed body force, and τ_{ij} the viscous stress tensor given by $\tau_{ij} = \nu(u_{i,j} + u_{j,i})$, $\nu = \mu/\rho$ is the kinematic viscosity.

Velocity and pressure are solved using a stabilized finite-element method (Taylor *et al.* 1998, Jansen *et al.* 2000). A traction-free boundary condition is used at the outlet.

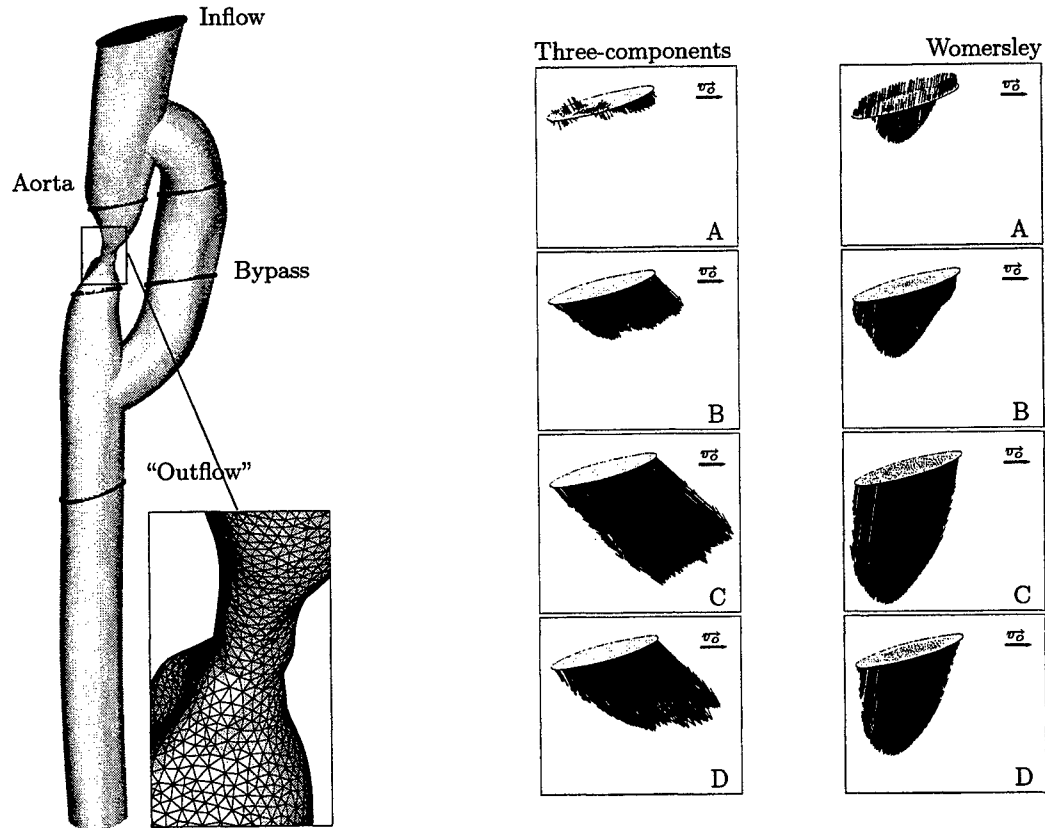


FIGURE 1. Pig anatomy and mesh at the stenosis (left). Cross-sections where flow rate is measured are shown. Measured velocity profiles at the inlet for times A, B, C and D in the cardiac cycle. Corresponding Womersley velocity profiles (right). Reference vector: $\vec{v}_o = 10 \text{ cm.s}^{-1}$.

Two different pulsatile velocity profiles are imposed at the inlet of the calculation domain: the actual velocities measured using PC-MRI (including in-plane components,) or an idealized Womersley velocity profile derived from the measured flow rate.

Womersley theory is based on the analytical solution of the Navier-Stokes equations in the case of a fully-developed pulsatile flow in a straight circular cylinder (of radius R). Keeping these assumptions in mind, it can be applied to blood flow: when the flow rate, $\dot{Q}(t)$, is known, the axial velocity profile can be derived. Given the period of the cardiac cycle ($T = 2\pi/\omega$), a Fast Fourier Transform is used to extract the frequency content of the flow waveform.

The Fourier coefficients B_n and the Womersley velocity profile in terms of the radius r and the time t are

$$\dot{Q}(t) = \sum_{n=0}^N B_n e^{in\omega t}; u(r, t) = \frac{2B_o}{\pi R^2} \left[1 - \left(\frac{r}{R} \right)^2 \right] + \sum_{n=1}^N \frac{B_n}{\pi R^2} \left[\frac{1 - \frac{J_o(\alpha_n \frac{r}{R} i^{3/2})}{J_o(\alpha_n i^{3/2})}}{1 - \frac{2J_1(\alpha_n i^{3/2})}{\alpha_n i^{3/2} J_o(\alpha_n i^{3/2})}} \right] e^{in\omega t}$$

where J_o and J_1 are Bessel functions, and $\alpha_n = R\sqrt{(n\omega)/\nu}$.

The Womersley number, α_1 , takes the value of 10.8 in our simulations. The period is

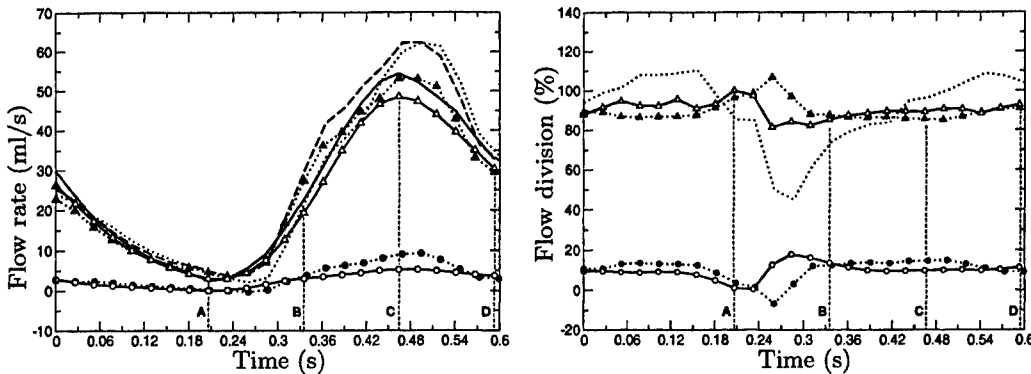


FIGURE 2. Flow rate versus time (left), flow rate ratio versus time (right). — : inflow (data), : outflow (data), —○— : aorta (simulation), ···●··· : aorta (data), —△— : bypass (simulation), ···▲··· : bypass (data), --- : outflow (data aorta + bypass). Time A: end diastole, time B: mid-systole, time C: peak systole, time D: mid-diastole

$T = 0.62$ s. The Reynolds number measured at the inlet varies from 50 at end diastole (time A, figure 2) to 1300 at peak systole (time C, figure 2).

From measured data we calculate the flow rate (figure 2, full line, left). As we do not have a circular inlet, we first calculate the Womersley velocities for a constant radius, R , corresponding to the maximum radius of the lumen. The resulting velocity profile is then mapped on the real geometry. In this model, the measured inflow cross-section is not normal to the vessel path, so that the velocity vectors need to be reoriented. The shape of the velocity profile is kept similar (with zero values at the boundaries and a maximum at the centroid of the vessel), and the flow rate is conserved, leading to a "quasi-Womersley" profile. The measured three-component and idealized velocity profiles are shown on figure 1 (left and right side cross-section respectively) at four representative times in the cardiac cycle (see time A, B, C and D on figure 2). In contrast to the measured three-component velocity profile, which is fairly uniform, the Womersley solution is characterized by a smooth profile. The descending aorta is curved in such a way that the in-plane component of the velocity vectors for the three-component data is not negligible and a large quantity of blood enters the bypass graft.

3. Results

3.1. Flow rates

Comparison of the flow division in the simulation and in the experiment show a maximum of 10% discrepancy at peak systole, both in the bypass (figure 2 left, triangles) and in the aorta (figure 2 left, circles). We notice on this graph that the measured flow rate is always larger than the result of the simulation. The flow rate in the simulation was extracted from measurements of the three components of the velocity at the location of the inlet, whereas the data plotted at the location of the aorta and the bypass correspond to through-plane velocity measurements only. The flow rate measured further downstream of the stenosis ("Outflow") with the through-plane technique is also higher than that given by the three-components velocity measurements (figure 2 left, dashed line). Furthermore, the sum of the measured flow rate in the aorta and the bypass (figure 2 left, dotted

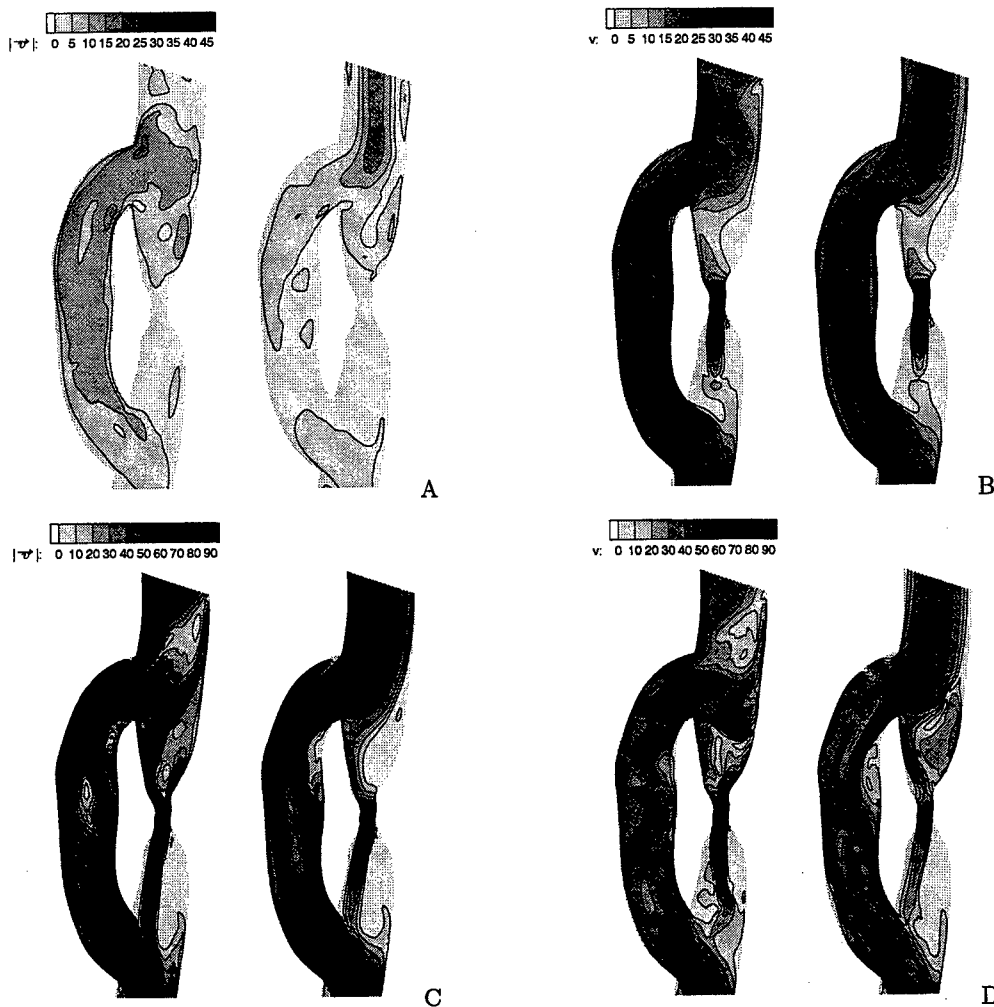


FIGURE 3. Transversal cross-section: comparison of the velocity magnitude (in $\text{cm} \cdot \text{s}^{-1}$) for the three component case (right) and the Womersley case (left) at times A, B, C, D

line) is not equivalent to that measured (with the same measurement technique) at the outlet (figure 2 left, dashed line). Assuming that the segmentation process of the vessel boundary does not add any error, this difference can be due to a small change in the physiological state of the pig (peak systole is slightly shifted), or illustrates the fact that the vessel wall is compliant.

As the flow division between the two branches is not dependent on which measurement technique was employed, we can still compare simulation and imaging data (figure 2, right). On average, in the simulation, 9.7% of the fluid that enters the domain goes into the aorta (open circles) and 10.5% in the experiment (plain circles). The majority of blood flows into the bypass: 90.3% in the simulation (open triangles) versus 89.5% in the experiments (plain triangles). Due to pulsatile effects, the flow division varies slightly during the cardiac cycle, and particularly at end-diastole, between the deceleration and acceleration phases.

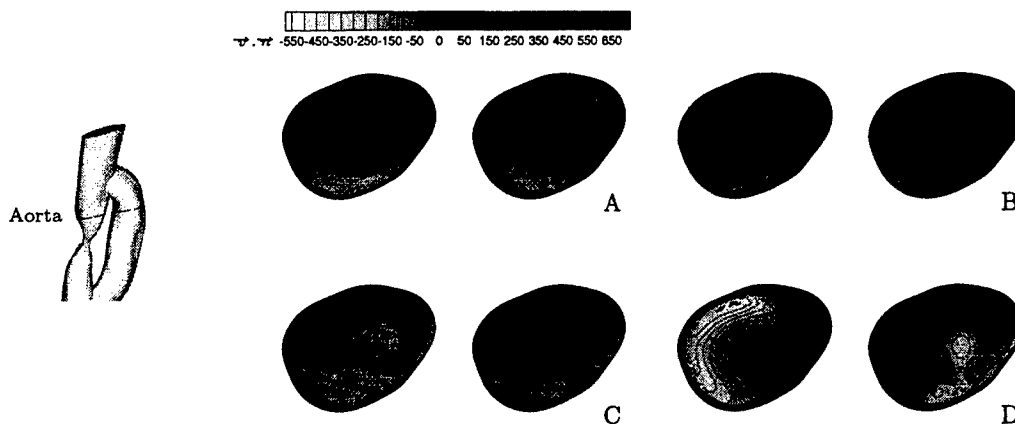


FIGURE 4. Aorta cross-section (above the stenosis): comparison of the through-plane velocity ($\vec{v} \cdot \vec{n}$ in mm.s^{-1}) in the three-components case (left) and the Womersley case (right)

Within the generally-accepted 10% error band in MRI measurements, the flow rates in the calculation and the data compare favorably.

3.2. Influence of inflow profiles: three components and Womersley

In order to characterize the influence of inflow boundary conditions, we will focus on four representative times in the cardiac cycle (time A, B, C and D, figure 2).

A basic observation that has been previously made in the configuration of a tight stenotic vessel (Khalifa & Giddens 1981) is that a non-periodic behavior from cycle to cycle appears upstream and downstream of the stenosis. Even though the physiological Reynolds numbers at the inflow are small, the reduction in area at the stenosis is large (85%) and pulsatile effects excite vortex shedding. In our model, in addition to the "simple restriction case" studies, the aperiodic stenotic jet is also influenced by the high-velocity fluid coming from the bypass. Both the three-component and the Womersley inlet boundary conditions show this phenomenon. As a consequence, we will focus only on averaged-velocity comparisons between experiment and numerics. We consider the 35 periods following the usual five periods required to initialize the simulation (i.e. about four flow-through times).

The velocity-magnitude field across the domain is plotted in figure 3 for the three-component case (left side of the figure) and for the Womersley case (right side). As expected close to the inflow, one can clearly observe the variations induced by using two different velocity profiles as a boundary condition. At all characteristic times the isocontours of the velocity in the Womersley case are aligned with the vessel centerline at the inlet, whereas the inlet velocity in the three-component case is oriented towards the bypass. This fact locally modifies the fluid mechanics in the domain, but global parameters such as the flow division in the branches are identical in the two cases. The same general features of the flow can be recognized: during systole (acceleration phase, times B and C), a large recirculation zone appears above the stenosis, while high velocities are measured at the stenotic jet. On the inside wall of the bypass graft, the region of separation classically found in curved vessels is observed. Comparing local velocities in the two simulations, we find some variations in the recirculation area above the stenosis, mainly in the deceleration phase (time D, figures 3 and 4). When the flow rate is high, a large vortex is generated above the stenosis (times B and C, figures 3 and 4). In both cases the size of this vortex is similar. During the deceleration phase and later (times D

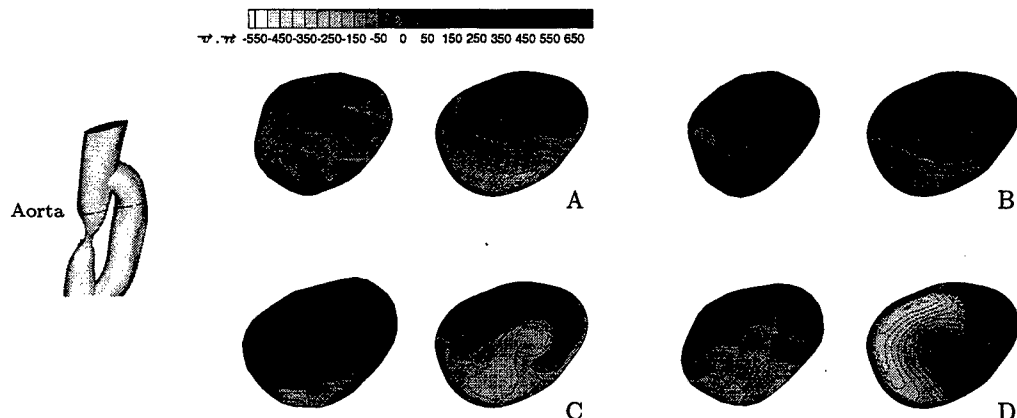


FIGURE 5. Aorta cross-section (above the stenosis): comparison of the through-plane velocity ($\vec{v} \cdot \vec{n}$ in $\text{mm} \cdot \text{s}^{-1}$) in experiments (left) and the simulation in the three-components case (right).

and A, 3), the flow is more perturbed and vortex shedding occurs, leading to different behavior in the two cases. In the bypass graft, at all times in the cardiac cycle, the extent of the separation region is more pronounced in the Womersley case. On figure 3, the jet is also influenced by the boundary conditions downstream of the stenosis.

Using physiological boundary conditions has an impact on local velocity. Whether these variations of the flow field are large enough to cause, or modify the development of, thrombosis is still an open question.

3.3. Comparison of experiment and simulation

Figure 5 shows the through-plane velocity obtained in the simulation (in the "realistic" three-component case) and in the experiments at an aortic cross-section above the stenosis. The velocities are similar, which is consistent with what we observed above: the flow rates in the experiments and in the calculations compare well. When comparing local velocity patterns, the results do not agree. The maxima of the velocity are shifted between the data and the simulation (time D, figure 5).

The comparison is not conclusive. On the experimental data, the isocontours of the velocity are noisy, particularly at end-diastole and during the acceleration phase (times A and B, figure 5). At peak systole and mid-diastole (times C and D, figure 5), the velocity profiles corresponding to the experiments look erratic and do not reflect the complexity of the contours found in the simulation.

Steinman (2002) reports in a review that MRI is likely to fail when measuring sudden local changes in the flow field and in the presence of complex flow patterns. To add to the difficulty of measuring accurate velocity fields *in vivo* (the pig has to be kept in the same physiological state), the possible sources of error in the procedure involved in the simulation are numerous. The volumetric images (MRA), as well as the two-dimensional MRI data, need to be segmented in order to build the geometric model and to extract the velocity vectors at a specific location. Even using an automatic segmentation program to avoid human subjectivity, an error of a few pixels may induce some variations in the calculation and in comparing the velocity profiles.

4. Conclusion and future plans

From measurements of the velocity vectors in the aortic vessel, above the restriction, we observe that its characteristics differ from the analytical solution of a pulsatile flow. We have demonstrated numerically that the flow field in the domain is modified when using one inflow condition or the other. We believe that using the "true" velocity profile as a boundary condition in the simulation is essential when trying to understand the evolution of diseases. In one of the experiments, a clot formed in the separation region in the bypass, a typical region of the flow where we obtained differences in the velocity between the two cases. While the measured division of the flow rate between the two passages is well predicted in the simulation, detailed flow patterns do not seem to be captured properly by the measurements. More complex *in vitro* experiments, with large flow variations, should be considered for validation purposes. Further, the influence of variations in geometry should be evaluated.

REFERENCES

- BOTNAR, R., RAPPITSCH, G., SCHEIDECKER, M. B., LIEPSCH, D., PERKTOLD, K. & BOESIGER, P. 2000 Hemodynamics in the carotid artery bifurcation: A comparison between numerical simulation and *in vitro* MRI measurements. *J. Biomech.* **33**, 137–144.
- CEBRAL, J. R. & LOHNER, R. 2001 From medical images to anatomically accurate finite element grids. *Int. J. Num. Methods Engng.* **21**, 985–1008.
- DILLEY, R. J., MC GEACHIE, J. K. & PRENDERGAST, F. J. 1988 A review of the histologic-changes in vein-to-artery grafts with particular reference to intimal hyperplasia. *Arch. Surg.* **123**, 691–696.
- GEWERTZ, B. L., GRAHAM, A., LAWRENCE, P. F., PROVAN, J. & ZARINS, C. K. 1992 Diseases of the vascular system. *Essentials of general surgery*, Lippincott Williams & Wilkins, Philadelphia, pp. 328–347.
- JANSEN, K. E., WHITING, C. H. & HULBERT, G. M. 2000 A generalized-alpha method for integrating the filtered Navier-Stokes equations with a stabilized finite element method. *Comput. Meth. Appl. Mech. Engrg.* **190**, 305–319.
- KHALIFA, A. M. A. & GIDDENS, D. P. 1981 Characterization and evolution of post-stenotic flow disturbances. *J. Biomech.* **14**, 279–296.
- KU, J. P., DRANEY, M. T., ARKO, F. R., LEE, W. A., CHAN, F., PELC, N. J., ZARINS, C. K. & TAYLOR, C. A. 2002 *In Vivo* validation of numerical predictions of blood flow in arterial bypass grafts. *Ann. of Biomed. Engng.* **30**, 743–752.
- MILNER, J. S., MOORE, J. A., RUTT, B. K., & STEINMAN, D. A. 1998 Hemodynamics of human carotid artery bifurcations: Computational studies with models reconstructed from magnetic resonance imaging of normal subjects. *J. Vasc. Surg.* **28**, 143–156.
- PERKTOLD, K. & RAPPITSCH, G. 1995 Computer-simulation of local blood-flow and vessel mechanics in a compliant carotid-artery bifurcation model. *J. Biomech.* **28**, 845–856.
- PERKTOLD, K., RESCH, M. & PETER, R. 1991 Three-dimensional numerical analysis of pulsatile flow and wall shear stress in the carotid artery bifurcation. *J. Biomech.* **24**, 409–420.

- STEINMAN, D. A. 2002 Imaged-based computational fluid dynamics modeling in realistic arterial geometries *Ann. Biomed. Engrg.* **30**, 483–497.
- TAYLOR, C. A., DRANEY, M. T., KU, J. P., PARKER, D., STEELE, B. N., WANG, K. & ZARINS, C. K. 1999 Predictive medicine: Computational techniques in therapeutic decision-making. *Computer Aided Surgery* **4**, 231–247.
- TAYLOR, C. A., HUGUES, T. J. R. & ZARINS, C. K. 1996 Computational investigations in vascular disease. *Computers in Physics* **10**, 224–232.
- TAYLOR, C. A., HUGUES, T. J. R. & ZARINS, C. K. 1998 Finite element modeling of flow in arteries. *Comput. Methods Appl. Mech. Engrg.* **158**, 155–196.
- TAYLOR, C. A., HUGUES, T. J. R. & ZARINS, C. K. 1998 Finite element modeling of 3-dimensional pulsatile flow in the abdominal aorta: relevance to atherosclerosis. *Ann. Biomed. Engrg.* **26**, 1–13.
- TAYLOR, C. A., HUGUES, T. J. R. & ZARINS, C. K. 1999 Effect of exercise on hemodynamic conditions in the abdominal aorta. *J. Vasc. Surg.* **29**, 1077–89.
- ZARINS, C. K. & TAYLOR, C. A. 1998 Hemodynamic Factors in Atherosclerosis *Vascular surgery: a comprehensive review* (W. S. Moore, ed.) Saunders Company/Elsevier, Amsterdam, pp. 97–110.
- WANG, K. C., DUTTON, R. W. & TAYLOR, C. A. 1999 Level Sets for vascular model construction in computational hemodynamics *IEEE Engineering in Medicine and Biology* **18**, 33–39.

Hemodynamic changes induced by stenting in elastic arteries

By F. Nicoud †

1. Motivation and objectives

Angioplasty, with or without endovascular stenting, is a promising, minimally-invasive technique that can be used as treatment of occlusive disease in medium to large arteries. It has been applied extensively in the coronary, renal, and peripheral vascular systems. The use of intravascular stents tends to lower the complication rate. Although re-stenosis rates as high as 15-30 % after six months for human coronary arteries have been observed; see e.g. Rau *et al.* (1998). One possible explanation for this observation relies on the hemodynamic modifications induced by the prosthesis. Changes in wall shear stress are believed to induce endothelial dysfunction, ultimately leading to intimal hyperplasia and re-stenosis. Davies *et al.* (2001) suggest that magnitude of the shear stress is of secondary importance to the spatial and temporal fluctuations of this quantity.

In vivo testing performed by Vernhet *et al.* (2001), Vernhet *et al.* (2000), Rolland, Charifi & Verrier (1999) show that endovascular stenting induces a large modification of the arterial compliance and thus may drastically modify the propagation of arterial waves by introducing artificial reflexions. The first objective of this study is therefore to assess the amount of pressure-wave reflexion related to the endovascular stenting of an elastic artery. For this purpose, the stented section of the vessel is modeled as an elastic duct, whose compliance is less than the non-stented artery. We intent to clarify the extent of reflexion that can be expected, depending on the characteristics of both the stent and the host vessel. Another expected effect of the compliance mismatch induced by stenting is to modify the details of the blood motion in the stented area. Specifically, the wall shear stress (averaged over the cardiac cycle) might be changed, as well as the level of its systo-diastolic variations. For high enough Reynolds numbers, one also expects recirculation zones to appear with larger residence times. The second objective of this paper is thus to clarify the changes in the blood motion that can be expected in relation to endovascular stenting. Note that this study deals with the global effect of the compliance mismatch, neglecting the details of the prosthesis structure (struts). Consistently, the prosthesis is modeled as a uniform (elastic) tube with its own compliance.

2. The pressure-wave point of view

2.1. Basic equations

The general one-dimensional (1D) equations describing the pulsatile blood flow (mass and momentum conservation) in compliant arteries are well known since the work of Hughes & Lubliner (1973):

$$\frac{\partial A}{\partial t} + \frac{\partial Au}{\partial x} = 0, \quad \frac{\partial u}{\partial t} + u \frac{\partial u}{\partial x} = -\frac{1}{\rho} \frac{\partial P}{\partial x} - \frac{f_v}{\rho} u \quad (2.1)$$

† University of Montpellier II, CC51, 34095 Montpellier Cedex 5, France

where u and P are the averages (over the cross section of the artery) of the velocity along the x -direction and the pressure (relative to that outside the duct) pressure respectively, A is the area of the cross section, ρ is the blood density and $f_v u/\rho$ stands for the viscous drag. Assuming that the velocity and pressure fluctuations are small enough to neglect non-linear terms and introducing the state equation of the artery $A = A(P)$, we obtain

$$\frac{\partial P}{\partial t} + \frac{A}{A'} \frac{\partial u}{\partial x} = 0, \quad \frac{\partial u}{\partial t} + \frac{1}{\rho} \frac{\partial P}{\partial x} + \frac{f_v}{\rho} \frac{u}{A'} = 0 \quad (2.2)$$

where A' stands for the derivative of the cross-sectional area with respect to the pressure ($A' \equiv dA/dP$), that is, the compliance. The non-linear formulation (2.1), although more general than (2.2), suffers from several drawbacks. Indeed, since it has to be solved in the time domain, the viscous-drag term must be assessed by using the Poiseuille assumption for the velocity profile instead of the more accurate frequency-dependent Womersley (1955) solution. Moreover, any viscoelastic wall behavior is difficult to account for since A' may depend on the frequency of the perturbation in this case. In contrast, the linear formulation (2.2) can be solved in Fourier space, and the abovementioned physical behavior (frequency-dependent velocity profile and viscoelasticity) can be included without difficulty. Consistently, Reuderink *et al.* (1989) have shown that better overall accuracy is obtained by using the linear formulation. In the course of the present study, u and P will be taken as the solution of (2.2).

Considering a sector whose diameter and compliance do not depend on the space variable x and letting $P = \hat{P} \exp(-j\omega t)$ and $u = \hat{u} \exp(-j\omega t)$, where $j^2 = -1$ and ω is the angular frequency of the wave, the classical wave equation $d^2\hat{P}/dx^2 + k^2\hat{P} = 0$ can be easily derived, the complex wave number being $k = \sqrt{\omega(\rho\omega + jf_v)}A'/A$ and the wave speed being $c = \omega/k$. The general solution within a homogeneous segment is then

$$\hat{P} = P^+ e^{jk(x-x_0)} + P^- e^{-jk(x-x_0)}, \quad \hat{u} = \frac{k}{\rho\omega + jf_v} (P^+ e^{jk(x-x_0)} - P^- e^{-jk(x-x_0)}) \quad (2.3)$$

where x_0 is the abscissa of the left boundary of the sector and P^+ and P^- correspond to the amplitude of the forward and backward pressure waves. Their values are determined to satisfy the boundary conditions at $x = x_0$ and $x = x_0 + L$, where L is the length of the sector.

2.2. Modeling the endovascular stenting

To model the wave reflexion induced by an endovascular stent placed in an elastic artery, three successive homogeneous segments are considered, each having its own set of constant area and compliance (see figure 1). Each physical quantity in sector number i ($i = 1, 2, 3$) is denoted by index i . Conservation of the total flow rate and energy at the interfaces 1–2 and 2–3 requires, for $j = 1, 2$:

$$A_j \hat{u}_j(x_{0_j} + L_j) = A_{j+1} \hat{u}_{j+1}(x_{0_{j+1}}), \quad \hat{P}_j(x_{0_j} + L_j) = \hat{P}_{j+1}(x_{0_{j+1}}). \quad (2.4)$$

Two boundary conditions, at $x = x_{0_1} = 0$ and $x = x_{0_3} + L_3$, are needed to close the problem. To assess the stent response without spurious wave reflexion, non-reflecting boundary conditions are prescribed at both sides, leading to $P_1^+ = 1$ and $P_3^- = 0$. The four remaining wave amplitudes, viz. $P_2^+, P_3^+, P_1^-, P_2^-$, are determined by solving (2.4) for $j = 1, 2$. The complex coefficient of wave reflexion due to the stent is then defined as

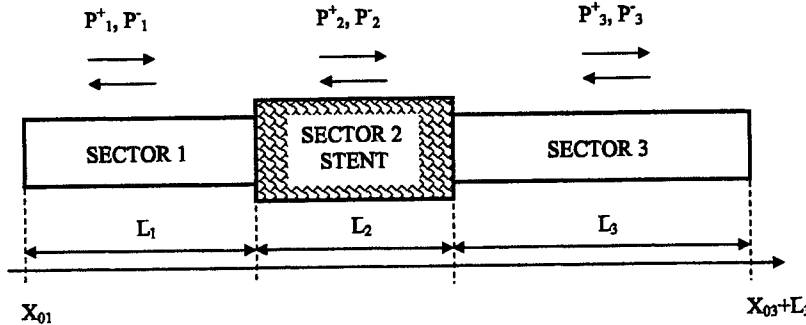


FIGURE 1. Schematic of the three homogeneous sectors used to model an artery stenting in terms of waves.

$R_{\text{stent}} = \exp(-2jk_1 L_1) P_1^- / P_1^+$. After some algebra we find

$$R_{\text{stent}} = \frac{A_2 K_2 (A_1 K_1 - A_3 K_3) \cos(k_2 L_2) - j(A_1 K_1 A_3 K_3 - (A_2 K_2)^2) \sin(k_2 L_2)}{A_2 K_2 (A_1 K_1 + A_3 K_3) \cos(k_2 L_2) - j(A_1 K_1 A_3 K_3 + (A_2 K_2)^2) \sin(k_2 L_2)} \quad (2.5)$$

where $K_i = k_i / (\rho\omega + j f_{v_i})$. A typical value of the speed of propagation of waves in (human) arteries being a few meters per second, the wavelength is usually a few meters. On the other hand, the length scale of the stent is most likely equal to a few centimeters, meaning that the numerical value of the dimensionless parameter $k_2 L_2$ is small compared to unity. Moreover, since the goal of this study is to assess the wave reflexion related to the endovascular prosthesis, one can assume that there is no reflexion in the absence of a stent, i.e. when $A_1 K_1 = A_3 K_3$ (in other words, we assume that the host artery is perfectly homogeneous). Finally, we obtain the following first-order expression for the reflexion coefficient:

$$R_{\text{stent}} = \frac{j(1 - \Lambda^2)}{2\Lambda} k_2 L_2 + O((k_2 L_2)^2), \quad \Lambda = \frac{A_1 K_1}{A_2 K_2} \quad (2.6)$$

This relation shows that the theoretical reflexion induced by an endovascular prosthesis decreases with the length of the stent and increases with the frequency of the wave. Moreover the reflexion coefficient is zero when $\Lambda = 1$, i.e. $A_1 K_1 = A_2 K_2$. Assuming that viscous effects can be neglected in the reflexion process makes Λ and k_2 real numbers with $\Lambda = \sqrt{A_1 A'_1 / A_2 A'_2}$ and $k_2 L_2 = \omega \sqrt{\rho A'_2 / A_2 L_2}$. Equation (2.6) then leads to a convenient formula to assess the amount of wave reflexion:

$$R_{\text{stent}} \simeq j\omega \sqrt{\rho} \frac{A_2 A'_2 - A_1 A'_1}{2\sqrt{A_1 A'_1}} \frac{L_2}{A_2}. \quad (2.7)$$

From this relation, the amount of wave reflexion is related to the geometrical/mechanical mismatch induced by the stenting and to a stent shape factor L_2/A_2 , as well as to the flow conditions. Moreover, it shows that a stent satisfying the relation $A_2 = A_1 A'_1 / A'_2$ produces no wave reflexion. The compliance A'_2 of the stent being always smaller than the compliance A'_1 of the host artery, it follows that overdilation ($A_2 > A_1$) tends to reduce the amount of reflected waves. For physiological and mechanical data obtained from animal experimentation (see section 3.3), we find out that the modulus of R_{stent} is not larger than a few percent.

3. Numerical approach

The simple 1D analysis provided in section 2 cannot be used to gain insights about the details of the fluid motion modifications related to the artery stenting. Of significant interest are the perturbations in wall shear stress induced by the compliance mismatch. In the 1D description of the blood flow, the shear stress is modeled by assuming that the shape of the velocity profile is known. Such knowledge is attainable only when the flow is varying weakly along the streamwise direction. However, in the case of stenting, no reasonable assumption regarding the shape of the velocity profile within the transition area can be formulated *a priori* and the multi-dimensional flow equations must be solved.

The incompressible unsteady Navier-Stokes equations are solved by the NSIKE code developed at University of Montpellier and INRIA by Medic & Mohammadi (1999). The solver is based on the projection method of Chorin (1967) with finite element discretization. A third order low storage Runge-Kutta approach is used for the time-stepping. At each sub steps, the computation of the intermediate velocity is done explicitly and the stabilization of the convection terms is based on the Positive Streamwise Invariant (PSI) residual distribution scheme proposed by Deconinck *et al.* (1993) and Paillere, Carette & Deconinck (1994). Specifically, a mixed Galerkin/PSI formulation has been used in order to minimize the numerical dissipation while ensuring the stability of the solution. Moving boundaries are accounted for by the Arbitrary Lagrangian Eulerian formulation. This code has been extensively validated by Medic & Mohammadi (1999), who computed classical test cases such as the flow over a 2D flat plate, within a closed cavity, and over a backward-facing step. Specific unsteady test cases have been performed in the course of this study, two of which are presented in sections 3.1 and 3.2. The numerical setup used to study the effects of the endovascular stenting is then described in section 3.3.

3.1. Pulsed pipe flow

We consider the pulsatile flow of an incompressible Newtonian fluid (kinematic viscosity ν) within a rigid, straight circular pipe of radius R_0 and length L . For a pulsed flow rate of the form $Q(t) = Q_0 + Q_1 \exp(j\omega t)$, where ω is the pulsation and Q_0 and Q_1 stand for the steady and pulsed parts of the flow rate, the (complex) velocity profile may be written following Womersley (1955) as

$$u(r, t) = \frac{2Q_0}{A_0} \left(1 - \frac{r^2}{R_0^2} \right) + \frac{Q_1}{A_0} \frac{1 - \frac{J_0(\alpha r/R_0)}{J_0(\alpha)}}{1 - \frac{2J_1(\alpha r/R_0)}{\alpha J_0(\alpha)}} \quad (3.1)$$

where $A_0 = \pi R_0^2$ is the cross section area and $\alpha = j^{3/2}W_0$, where $W_0 = R_0\sqrt{\omega/\nu}$ is the Womersley parameter. Due to the incompressibility constraint, the solution does not depend on the abscissa x along the pipe. The present test case consists in imposing the velocity profile (3.1) at the inlet of the computational domain ($x = 0$) together with a zero-pressure boundary condition at the outlet ($x = L$), and checking the ability of the code to preserve the analytical solution throughout the pipe. Starting with a zero-velocity, constant-pressure field, four cycles were computed in order to reach a proper periodic state. The results shown correspond to $L/R_0 \simeq 53$ and $W_0 \simeq 10.63$. The mean bulk Reynolds number based on R_0 and Q_0/A_0 is $R_b = 320$ while the flow-rate ratio is $Q_1/Q_0 = 0.5$. Under these conditions, the flow reverses. The numerical solution obtained by solving the Navier-Stokes equations in cylindrical form with a mesh of 169×21 grid points (169 nodes in x , 21 along the radial direction r) is virtually 1D (no dependence

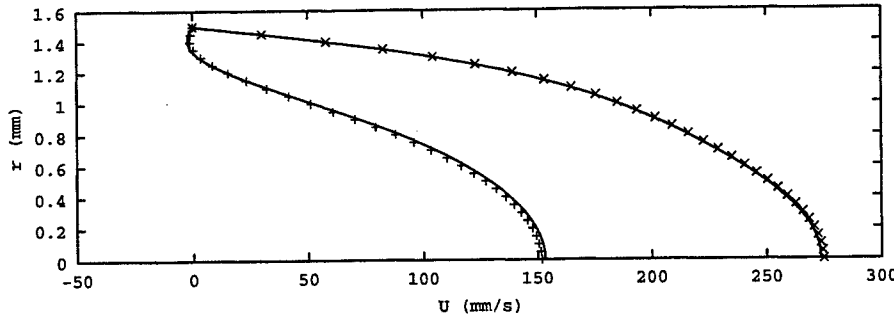


FIGURE 2. Analytical (lines) and numerical (symbols) velocity profiles at \times :systole and $+$:diastole.

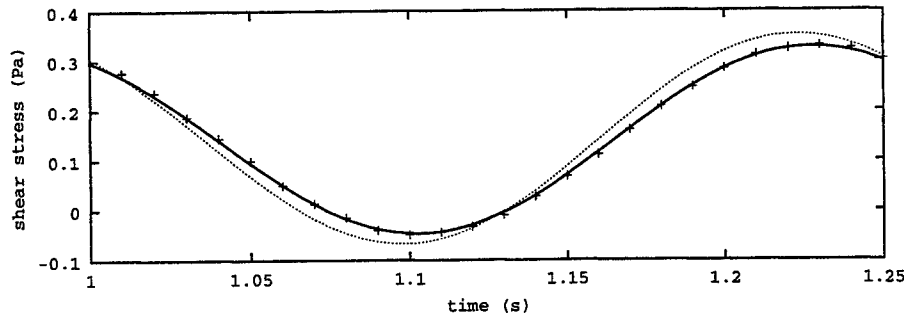


FIGURE 3. Analytical (lines) and numerical (symbols) wall shear stress as a function of time.
 —, finite differences applied to (3.1); ······, analytical differentiation of (3.1).

along the longitudinal coordinate x , not shown). The overall comparison between analytical and numerical velocity profiles is good, as shown in figure 2. Eventually, the wall shear stress obtained numerically is in good agreement with that expected over the period of time. Figure 3 shows that the agreement between the wall shear stress given by the numerical solution and that obtained by formally differentiating (3.1) is fairly good (less than 10 % error). The agreement becomes virtually perfect when the gradient of the analytical profile (3.1) is evaluated using second-order finite differences with the same resolution as that used in the simulation.

3.2. Wall-induced channel flow

The computational domain now extends from $x = 0$ to $x = 25$ streamwise and from $y = 0$ to $y = h$ cross stream. A symmetry condition is imposed at both boundaries $x = 0$ and $y = 0$ while zero pressure is prescribed at the section $x = 25$. The boundary at $y = h$ is a moving straight

wall which remains parallel to the x -axis and whose (complex) position as a function of time t is given by $h(t) = h_0(1 + \epsilon e^{-j\omega t})$. In this expression, h_0 is the mean distance between the wall and the symmetry plane $y = 0$ and ϵ fixes the amplitude of the wall oscillation. Seeking a stream function of the form $\Psi = xF(\eta)e^{-j\omega t}$, where η is the reduced coordinate $\eta = y/h(t)$, one may derive the following equation for the function F :

$$F'''' + \frac{h'h}{\nu}(\eta F''' + 2F'') + \frac{j\omega}{\nu}h^2F'' = 0. \quad (3.2)$$

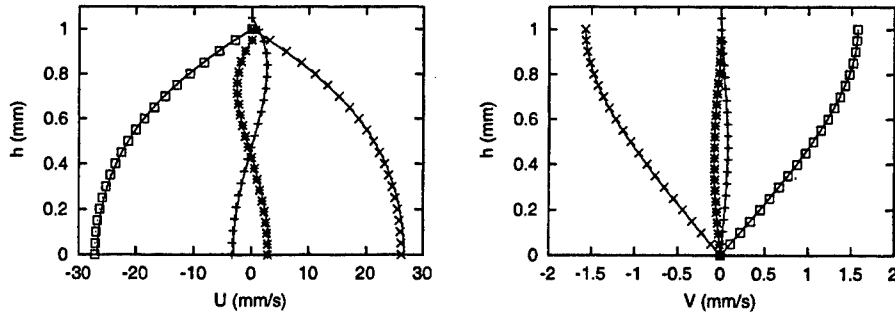


FIGURE 4. Analytical (symbols) and numerical (lines) streamwise (left) and normal wise (right) velocity profiles at times +, $t = 0$; \times , $t = T/4$; *, $t = T/2$ and \square , $t = 3T/4$.

Recall that the velocity components are given by $u = \partial\Psi/\partial y$ and $v = -\partial\Psi/\partial x$ so that the boundary conditions $v(x, 0) = \partial u/\partial y(x, 0) = 0$, $u(x, h) = 0$ and $v(x, h) = h' = -j\omega eh_0 e^{-j\omega t}$ lead to $F(0) = F''(0) = 0$, $F'(1) = 0$ and $F(1) = j\omega\epsilon h_0$ respectively. Expanding F as power series of the (small) parameter ϵ , viz. $F/\epsilon = F_0 + \epsilon F_1 + O(\epsilon^2)$ leads to the following first order solution

$$F_0 = j\omega h_0 \frac{\eta - \sinh(\alpha\eta)/\alpha \cosh \alpha}{1 - \tanh(\alpha)/\alpha} \quad (3.3)$$

where $\alpha = j^{3/2}W_0$ is proportional to the Womersley parameter $W_0 = h_0\sqrt{\omega/\nu}$. Figure 4 shows the comparison between the first-order analytical solution and the numerical profiles for $x = 11.875$, $\epsilon = 0.05$ and $W_0 = 2.8$. The agreement is good for the four phases considered which correspond to the uppermost position ($t = 0$), the most negative wall speed ($t = T/4$), the wall bottom position ($t = T/2$) and the maximum wall speed ($t = 3T/4$) respectively. Note that for the values of the parameters selected, the first-order correction ϵF_1 is negligible compared to F_0 so that the approximate solution, (3.3) is relevant to the test case.

3.3. Computational domain

Since our objective is to investigate the global effect of the compliance mismatch induced by stenting, the endovascular prosthesis is modeled as a uniform duct (the details of the struts are not represented) whose wall is not compliant. Such a “prosthesis” is inserted within an elastic artery with compliant wall, as shown in figure 5. We suppose that the computational domain is sufficiently short to neglect any variation of the host artery characteristics. Moreover, the flow rate entering the domain is taken similarly to section 3.1, viz. $Q(x_{\text{inlet}}, t) = Q_0 + Q_1 \exp(j\omega(t - x_{\text{inlet}}/c))$, where ω is the pulsation, x_{inlet} is the abscissa of the inlet section, and Q_0 and Q_1 stand for the steady and pulsed parts of the flow rate. The mechanical and geometrical data were obtained from animal experimentation performed by Vernhet *et al.* (2001): the angular frequency is $\omega = 8\pi$ (only the first harmonic of the temporal evolution of the flow rate is kept as a first approximation), the mean artery radius is $R_0 = 1.5$ mm, the distensibility coefficient of the non-stented artery is $A'/A = 20.7 \times 10^{-6} \text{ Pa}^{-1}$ and the length of the stent is set to $L_{\text{stent}} = 13$ mm. At the stent level, the compliance measured is small enough (six times smaller than in the host vessel) to be neglected in this exploratory study (rigid prosthesis).

In the real world, the motion of the vessel boundary results from the coupling between

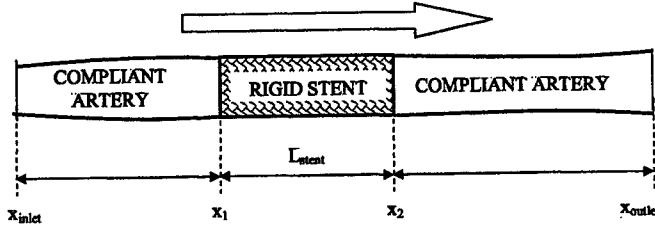


FIGURE 5. Schematic of the computational domain.

the fluid and wall mechanics and the local radius is related mainly to the pressure field. Such a coupling is difficult to handle, because the density of blood and tissue are of the same order and the rheology of the vessels is far from well understood. Besides, we are mostly interested in the response of the fluid mechanics to wall-motion perturbations induced by the compliance mismatch. In this framework, the fluid/wall coupling problem can be avoided by prescribing the wall motion *a priori*. Since the flow rate is harmonic with angular frequency ω , the wall displacement for an elastic uniform artery without reflexion may be written as

$$R(x, t) = R_0 \left(1 + \epsilon e^{j(\omega t - kx)} \right), \quad k = \frac{\omega}{c}, \quad (3.4)$$

where the wave number k is related to the speed of the (forward) pressure wave c . The animal experimentation of Vernhet *et al.* (2001) suggests $\epsilon = 0.05$, meaning that the amplitude of the wall displacement is close to $2\epsilon R_0 = 0.15$ mm. The speed of propagation is chosen real (no viscous-damping effect accounted for). Moreover, its real part is fixed by stating that, the non-stented artery being uniform along the streamwise direction, the mass-flow rate at any section $x = L$ should be the time-lagged version of the mass flow rate at $x = x_{\text{inlet}}$. The conservation of mass applied to the artery sector $0 < x < L$ then implies that:

$$Q_1 e^{j\omega(t-(x_{\text{inlet}}+L)/c)} = Q_1 e^{j\omega(t-x_{\text{inlet}}/c)} + 2\pi \int_{x_{\text{inlet}}}^{x_{\text{inlet}}+L} R \frac{dR}{dt} dx \quad (3.5)$$

Making use of (3.4) and keeping only first-order terms in ϵ to assess the integral in (3.5), we obtain the following expression for the speed of propagation of the pressure wave:

$$c = \frac{Q_1}{2A_0\epsilon} + O(1), \quad A_0 = \pi R_0^2 \quad (3.6)$$

From the physiological data obtained by Vernhet *et al.* (2001), the following values were used for the flow rate: $Q_0 \simeq 2413 \text{ mm}^3/\text{s}$ and $Q_1 \simeq 1761 \text{ mm}^3/\text{s}$. Equation (3.6) then leads to $c \simeq 2492 \text{ mm/s}$. With $\omega = 8\pi$, the corresponding wavelength is $\lambda \simeq 623 \text{ mm}$. In the case where the vessel is stented between abscissae x_1 and x_2 (see figure 5), the wall displacement is zero for $x_1 < x < x_2$:

$$R(x, t) = R_0 \left(1 + \epsilon f(x) e^{j(\omega t - kx)} \right) \quad (3.7)$$

where the damping function is $f(x) = [1 - \tanh(x - x_1)]/2$ for $x < (x_1 + x_2)/2$ and $f(x) = [1 + \tanh(x - x_2)] \exp(jk(x_2 - x_1))/2$ for $x > (x_1 + x_2)/2$. Equation (3.7) gives the wall displacement for an elastic stented artery, assuming that the speed of propagation within the prosthesis is infinite (since the wall is not compliant). Note that L_{stent}/λ

being very small, (2.7) can be used to estimate the reflexion coefficient under the mechanical conditions considered. This latter relation leads to $|R_{\text{stent}}| \simeq 2\%$. As a result, the pressure field is related mostly to the forward pressure wave, which justifies the fact that no backward-propagating wave is accounted for in (3.7). Besides, the length of the transition zone between the elastic artery and the stent is of order 3 mm (this is a direct consequence of the damping function $f(x)$ used in 3.7). This value is in agreement with the observations made during the animal experimentations of Vernhet *et al.* (2001) and showing that the buffer region is close to one diameter long. Finally, the radius of the non-compliant prosthesis is set to the medium artery radius R_0 (no overdilation). An over dilated prosthesis can be represented by the following wall displacement:

$$R(x, t) = R_0 \left(1 + \epsilon f(x) e^{j(\omega t - kx)} \right) + (1 - f(x)) \delta R_{\text{stent}} \quad (3.8)$$

where the damping function is defined as in (3.7) and δR_{stent} is the amount of overdilation.

4. Numerical results

Several 2D axisymmetric simulations have been performed, based on the computational domain and wall motion described in section 3.3. In all cases, the bulk Reynolds number based on the steady part of the flow rate Q_0 and the mean radius R_0 is close to $R_b = 102$. The Womersley number is $W_0 = 3.36$. The velocity profile is imposed at the inlet section $x = x_{\text{inlet}}$ following the (complex) Womersley solution in elastic tubes:

$$\begin{aligned} u_{\text{inlet}} &= \frac{2Q_0}{\pi R(x_{\text{inlet}}, t)^2} \left(1 - \frac{r^2}{R(x_{\text{inlet}}, t)^2} \right) + \frac{Q_1}{\pi R(x_{\text{inlet}}, t)^2} \frac{1 - J_0(\alpha y)/J_0(\alpha)}{1 - 2J_1(\alpha)/\alpha J_0(\alpha)} e^{j\omega(t-x_{\text{inlet}}/c)} \\ v_{\text{inlet}} &= j\omega \epsilon R_0 \frac{y - 2J_1(\alpha y)/\alpha J_0(\alpha)}{1 - 2J_1(\alpha)/\alpha J_0(\alpha)} e^{j\omega(t-x_{\text{inlet}}/c)} \end{aligned} \quad (4.1)$$

where $y = r/R(x, t)$ is the reduced radial coordinate ($0 \leq y \leq 1$). A zero-constraint condition is used at the outlet section $x = x_{\text{outlet}}$. In order to assess the effect of the inlet/outlet boundary conditions on the results, computational domains with two different lengths have been considered. Two different spatial resolutions were also used, to assess the spatial discretization errors. The main characteristics of the calculations performed are given in table 1 where Δx is the grid spacing in the streamwise direction in the area $x_1 < x < x_2$ and Δr refers to the grid spacing in the radial direction. Runs R1 and R2 correspond to reference calculations without endovascular prosthesis, the artery being fully rigid (no wall displacement) for R1 and elastic for R2. Labels R3 and R4 correspond to runs with stenting, the overdilation being non-zero only for the latter where $\delta R_{\text{stent}} = \epsilon R_0$ (the stent radius is equal to the artery radius at systole). When present, the stent is between $x_1 = 34$ mm and $x_2 = 47$ mm. Runs whose label contains 'a' have been performed with a longer computational domain than others. Labels containing letter 'b' correspond to runs with finer mesh in the radial direction. In all cases, four cardiac cycles were computed first, in order to reach a periodic state. A fifth cycle was then computed in order to analyze the results and compare the different physical/numerical configurations.

Time evolutions of the flow rate at inlet and outlet sections are shown in figure 6 for case R2. The constraint that was introduced in section 3.3 in order to set the speed of propagation of the pressure wave is fulfilled satisfactorily. Indeed, the flow rate at $x = x_{\text{outlet}}$

Run	Wall motion	η	δR_{stent}	x_{inlet}	x_{outlet}	Δx	Δr	# of grid points
R1	$R(x, t) = R_0$	0.0	N/A	0	80	0.075	0.286	3528
R2	(3.4)	0.05	N/A	0	80	0.075	0.286	3528
R3	(3.7)	0.05	0.0	0	80	0.075	0.286	3528
R4	(3.8)	0.05	0.075	0	80	0.075	0.286	3528
R2a	(3.4)	0.05	N/A	-30	110	0.075	0.286	4368
R3a	(3.7)	0.05	0.0	-30	110	0.075	0.286	4368
R3b	(3.7)	0.05	0.0	0	80	0.050	0.286	5208

TABLE 1. List of the axisymmetric calculations performed, with their main numerical characteristics and the equations governing the wall motion. Lengths and abscissae are in mm.

is the signal at $x = x_{\text{inlet}}$ with a time lag close to $(x_{\text{outlet}} - x_{\text{inlet}})/c \simeq 80/2492 \simeq 0.032$ s. In absence of an endovascular prosthesis, all the physical quantities are self-similar, with a constant speed of propagation c along the computational domain. Due to the wall displacement (3.4), the wall shear stress is not constant in the streamwise direction, as shown in figure 7 at four different instants. Instead it alternately increases and decreases along the domain, depending on the phase considered. Note that the harmonic displacement (3.4) is never apparent, because the length of the computational domain (80 mm) is small compared to the wavelength (see also figure 9, top row). In spite of this, the numerical solution depends only weakly on the length of the whole domain, as shown in figure 8, which compares the wall shear stress from runs R2 and R2a. Only small disagreement is visible, close to the upstream end of the R2 domain (the smallest one). There is virtually no difference between the two runs in the central region. The same conclusion can be drawn in the case of a stented artery by comparing runs R3 and R3a (not shown). Thus, regarding the effects of the vessel stenting, the numerical results do not depend on the details of the implementation of the boundary conditions. In the case where the vessel is not compliant, there should be no time lag between shear-stress signals at different locations, because the exact Womersley profile is imposed at $x = x_{\text{inlet}}$. Accordingly, the wall shear stress is mainly uniform over the streamwise distance in case R1 (see figure 7).

The shape of the computational domain for cases R2, R3 and R4 is shown in figure 9 for times $t = nT$ (corresponding to systole at the inlet section) and $t = (n+1/2)T$ (diastole). The non-compliant region which represents the endovascular prosthesis is clearly visible (cases R3 and R4) in the central region. However, the over-dilated stent (R4) is hardly visible at systole since $\delta R_{\text{stent}} = \epsilon R_0$ in this case. The contours of streamwise velocity show that the flow accelerates when the cross-sectional area decreases. The effect of the wall-motion mismatch on the wall shear stress is shown in figure 10. At systole, this quantity is larger in the medium part of the stented region ($x \simeq 40$ mm) than in the

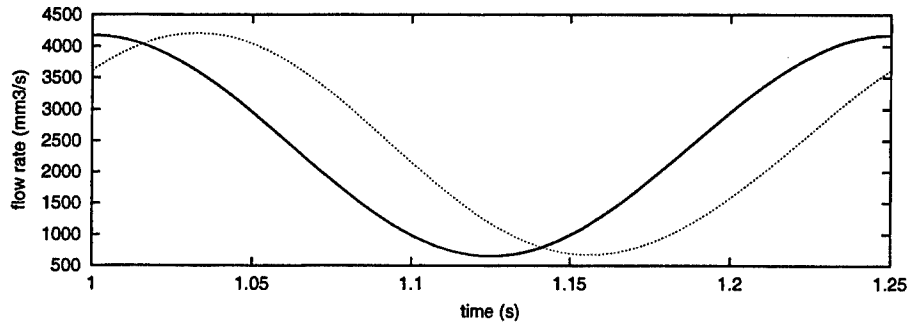


FIGURE 6. Time evolutions of the flow rate at sections — : $x = x_{\text{inlet}}$ and : $x = x_{\text{outlet}}$ for the case R2.

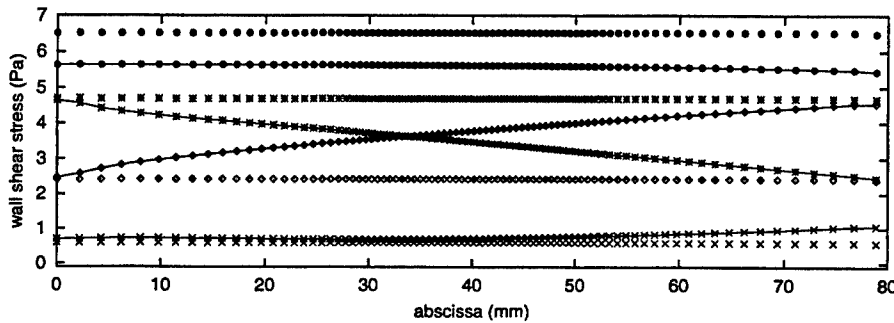


FIGURE 7. Wall shear stress for runs R1 (symbols) and R2 (lines with symbols) at times: • : $t = nT$, ◊ : $t = (n + 1/4)T$, × : $t = (n + 1/2)T$ and * : $t = (n + 3/4)T$.

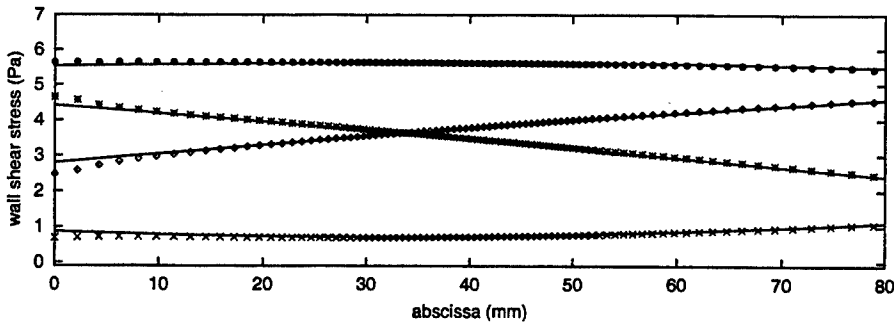


FIGURE 8. Wall shear stress for runs R2 (symbols) and R2a (—) at times: • : $t = nT$, ◊ : $t = (n + 1/4)T$, × : $t = (n + 1/2)T$ and * : $t = (n + 3/4)T$.

non-stented artery. This is consistent with the fact that the cross-sectional area in R3 and at systole is smaller in the prosthesis zone (see figure 9). At diastole, the cross-sectional area within the stent is larger and the wall shear stress is smaller. In the transition zones between the endovascular prosthesis and the elastic artery, the stress experiences larger fluctuations, especially at systole. Extra stress is generated in the upstream transition zone, which acts as a convergence ($x \approx 35$ mm). Conversely, the downstream buffer region acts as a divergence at systole and tends to decrease the stress. Accordingly, the wall shear stress turns out to be locally smaller than its value in the non-stented artery ($x \approx 47$ mm). The transition zones have less effect at diastole, when the flow rate is

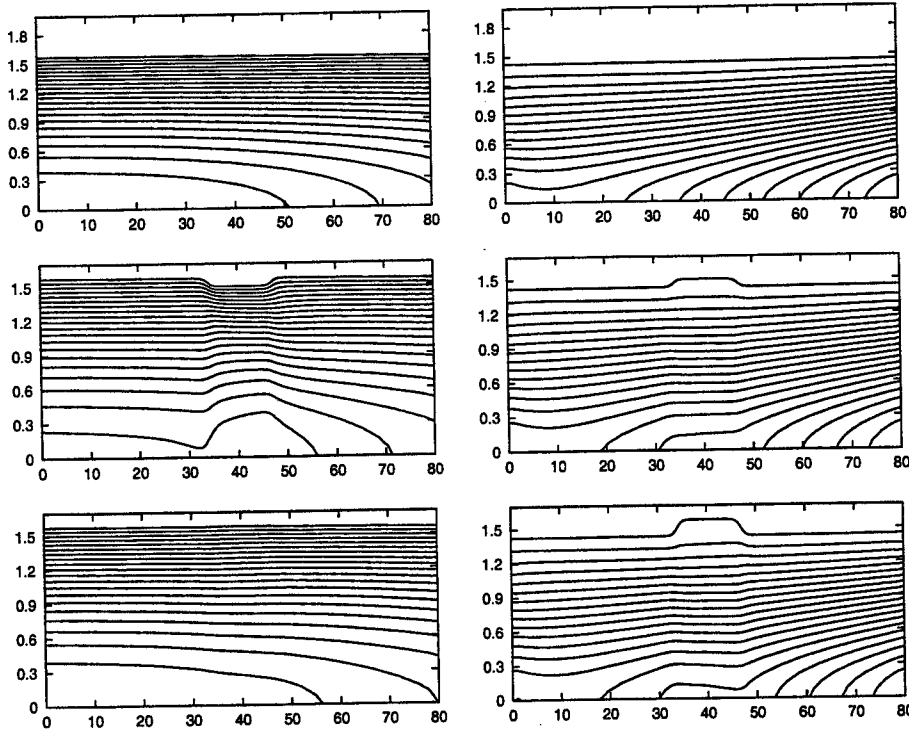


FIGURE 9. Shape of the computational domain at systole (left column) and diastole (right column) for the runs R2 (top row), R3 (medium row) and R4 (bottom row). The isolines of the streamwise velocity are plotted. The streamwise and radial coordinates are expressed in millimeters. The aspect ratio R_0/L has been multiplied by 35 for convenience.

smaller. Note finally that using a finer mesh produces only small changes in wall shear stress (compare runs R3 and R3b). Thus the numerical errors are much smaller than the physical effects related to the stent. Figure 11 shows the time dependence of the stress near $x = (x_1 + x_2)/2 \approx 40$ mm. The amplitude of this quantity over the cardiac cycle is larger for the stented vessel than for the elastic artery. It is worth noting that although the length of the stent is very small compared to the wavelength, the amplitude of the wall shear stress in case R3 behaves more like case R1 (fully rigid tube) and less like case R2 (elastic tube). The over-dilated prosthesis, by avoiding the increase in shear stress at systole (there is no geometry discontinuity at systole for the case R4; see figure 9), drastically limits the increase in stress amplitude.

5. Conclusions

This theoretical/numerical study suggests that over-dilated stents produce less hemodynamic perturbations. From the pressure-wave point of view, the optimal overdilation is proportional to the compliance ratio. Moreover, because the reflexion coefficient is proportional to the stent-to-wavelength ratio, it is most likely that the amount of wave reflexion remains rather small. An easy-to-use formula is provided to estimate the reflexion coefficient from knowledge of the compliance before and after stenting. From the local hemodynamic point of view, the amplitude of the wall shear stress is drastically increased (by 45-50 % at the stent level, possibly more in the transition regions) by

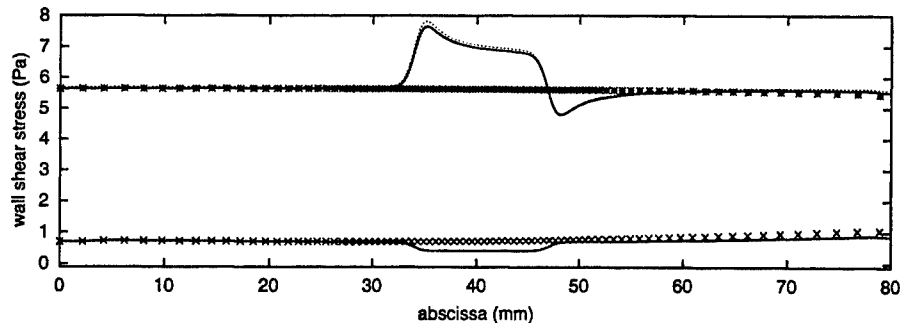


FIGURE 10. Wall shear stress for runs R2 (symbols), R3 (—) and R3b (·····) at times *: $t = nT$ and x: $t = (n + 1/2)T$

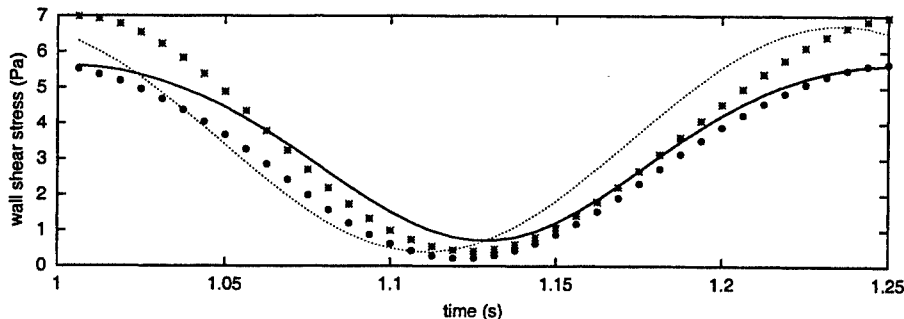


FIGURE 11. Wall shear stress versus time for runs ·····: R1, —: R2, *: R3 and •: R4 at $x \approx 40$ mm.

stenting. This result supports the idea that stenting can induce endothelial dysfunction via hemodynamic perturbations. The amplitude of the fluctuations in wall shear stress over the cardiac cycle are not as large when a (slight) over-dilatation is used.

REFERENCES

- CHORIN, J. A. 1967 A numerical method for solving incompressible viscous flow problems. *J. Comp. Phys.* **2**, 12–26.
- DAVIES, P., SHI, C., DEPAOLA, N., HELMKE, B. & POLACEK, D. 2001 Hemodynamics and the focal origin of atherosclerosis. A spatial approach to endothelial structure, gene expression, and function. *Annu. N.Y. Acad. Sci.* **947**, 7–16.
- DECONINCK, H., STRUIJS, R., BOURGOIS, G. & ROE, P. 1993 *Compact advection schemes on unstructured grids*. Von Karman Inst. Lecture Series 1993-04.
- HUGHES, T. & LUBLINER, J. 1973 On the one-dimensional theory of blood flow in the larger vessels. *Math. Biosci.* **18**, 161–170.
- MEDIC, G. & MOHAMMADI, B. 1999 NSIKE – an incompressible Navier-Stokes solver for unstructured meshes. *INRIA Res. Rept.* 3644.
- PAILLERE, J.-C., CARETTE, C. & DECONINCK, H. 1994 *Multidimensional upwind and SUPG methods for the solution of the compressible flow equations on unstructured grids*. VKI Lecture Series 1994-05.
- RAU, T., SCHOFER, J., SCHLUTER, M., SEIDENSTICKER, A., BERGER, J. & MATHEY,

- D.G. 1998 Stenting of non acute total coronary occlusions: predictors of late angiographic outcome. *J. Am. Coll. Card.* **31**, 275–280.
- REUDERINK, P. J., HOOGSTRATEN, H. W., SIPKEMA, P., HILLEN, B. & WESTERHOF, N. 1989 Linear and nonlinear one-dimensional models of pulse wave transmission at high Womersley numbers. *J. Biomech.* **22**, 819–827.
- ROLLAND, P. H., CHARIFI, A. B. & VERRIER, C. 1999 Hemodynamics and wall mechanics after stent placement in swine iliac arteries: comparative results from six stent designs. *Radiology* **213**, 229–246.
- VERNHET, H., DEMARIA, R., OLIVA-LAURAIRE, M. C., JUAN, J. M., SÉNAC, J. P. & DAUZAT, M. 2001 Changes in wall mechanics after endovascular stenting in rabbit aorta: comparison of three different stent designs. *Am. J. Roent.* **176**, 803–807.
- VERNHET, H., JUAN, J.M., DEMARIA, R., OLIVA-LAURAIRE, M.C., SÉNAC, J.P. & DAUZAT, M. 2000 Acute changes in aortic wall mechanical properties after stent placement in rabbits. *J. Vasc. Inter. Rad.* **11**, 634–638.
- WOMERSLEY, J.R. 1955 Oscillatory motion of a viscous liquid in a thin-walled elastic tube—I: The linear approximation for long waves. *Phil. Mag. (Series 7)* **45**, 199–221.

Wavelet analysis of blood flow singularities by using ultrasound data

By Philippe May

1. Motivation and objectives

The effects of blood flow turbulence are of great clinical importance in both medical and surgical areas. For example, several biological research fields have focused on the role played by turbulence on cell and tissue behavior. It is now well established that the transition to turbulence is expected to be dependent on flow pulsatility and on the nature of the arterial wall. There is evidence suggesting that the effect of pulsatility on transition to flow turbulence is common in a wide variety of arterial flows and several studies support this view (Winter 1984; Ku 1997). In addition, the presence of an intra-arterial singularity such as a stenosis, an aneurysm or a thrombosis is known to greatly increase the probability of transition to turbulence downstream of the singularity.

In the study of vascular physiology, Nerem (1993) demonstrated the decrease of cell proliferation and the alteration of cell morphology when vascular endothelium is exposed to laminar shear stress. This laminar blood flow induces endothelial cells to exhibit a non-reactive phenotype. Davies *et al.* (2001) demonstrated *in vitro* that disturbed flows induce greater variability of gene expression from cell to cell than do undisturbed laminar flows. Microgravity experiments have shown that the low-turbulence culture environment (simulated with the NASA Bioreactor) promotes the formation of large, three-dimensional cell clusters and has provided insight into better understanding of normal and cancerous tissue development (Gao *et al.* 1997; Radin *et al.* 2001). Because high turbulence levels can damage cells (Davies *et al.* 1986), the determination and control of the turbulence levels that optimize expression of differentiated function and tissue development is of great importance.

At a larger vascular scale, the location of atherosclerotic lesions near branches, bifurcations, and curvatures of arteries has long been identified. For instance, Ku *et al.* (1985) found a strong correlation between flow disturbances and arterial susceptibility to the development of atherosclerosis plaque. Tsao *et al.* (1996) demonstrated that the effects of flow in inhibiting atherogenesis appear to be mediated in part by the endothelium-derived nitric oxide (NO). Bluestein *et al.* (1999, 2000) demonstrated the correlation between the generation of shed vortices downstream of an arterial singularity, and with both the local platelet deposition and the free emboli of platelet aggregates. These local hemodynamics are widely believed to impact vascular diseases, from the development and progression of vascular lesions to the production of the thromboemboli and the cholesterolemboi that cause heart attacks and strokes.

For all of these reasons, but not limited to, the analysis of the intra-vascular blood flow behavior requires a much better understanding under simulated and physiological conditions, with the needed development of devices and tools to accurately determine the turbulence levels of blood flow in real-time.

For this purpose, an ideal system to study is the generation of turbulence downstream of a singularity: the generated turbulence is strong and, has in many various fields, important implications of increasing the accuracy of real-time detection procedures.

In biology and medicine there are usually differences amongst individuals when studying the time evolution of physiological parameters of a non-pathological human group. Therefore, the use of dimensionless numbers to describe biological flow disturbances is of higher relevance in conducting biological research flow studies. Since a Reynolds' number (Re) is usually defined for steady flow through rigid tubes, it may not reflect the actual fluid behavior of intra-vascular pulsatile flow. The Womersley' number (Wo) which includes the pulsatile and frequency behavior of the flow is a better parameter, but has the same limitation as Re . Because biological fluid dynamics invariably involves the interaction of visco-elastic and active tissue with viscous incompressible non-Newtonian fluid, this interaction can not be neglected in biological fluid mechanics research and computation of biological models, as pointed out by Peskin *et al.* (1995) with the immersed boundary method; and considered in their studies by Ye *et al.* (1999).

Since Leonardo Da Vinci's studies of cardiovascular systems by using a simple aortic glass model to simulate flow dynamics (Gharib *et al.* 2002), - 400 years ahead of Osborn Reynolds' famous pipe flow visualization studies -, the real-time detection of blood flow behavior has gained more and more importance. This requires non-invasive and safe vascular imaging techniques of the highest resolution in space and time. Since Schmidt *et al.* (1970), significant advances in ultrasonic flow measurements have been made. Ultrasonics are widely used in both medical and surgical areas (Cloutier *et al.* 1990), and this device demonstrated in fluid mechanics its utility where opaque flow fields preclude the use of optically-based diagnostic tools (Johari *et al.* 1998; Nowak 2002).

When analysing a scientific image, the main goal is to describe it quantitatively. This goal is difficult to achieve without the use of mathematical tools because human interpretation can often be subjective. Recently, there has been increasing interest in the study of scaling behavior in irregular objects: the velocity field of fully developed turbulent flows (Farge *et al.* 1988; Meneveau 1991; Muzy *et al.* 1991; Frisch 1995; Arnéodo *et al.* 1995), financial time-series (Mantegna *et al.* 2000), telecommunication traffic (Abry *et al.* 2002), medical time-series (West 1990), random walks associated with DNA sequences (Arnéodo *et al.* 1996).

Adapting the methodology of Farge (1992); Arnéodo *et al.* (1995), and in order to analyze scaling behavior and singularities in pulsatile blood flows as previously done by May *et al.* (2001a,b, 2002), the goal of this study is to use the wavelet signal processing strategy on bidimensional vascular data:

- In part I, adapting the work of Farge (1992) & later Kailas *et al.* (1999), the basic methodology is outlined to examine the 2D wavelet transform of vascular flow images at various scales, especially when the images indicated the presence of intervals during which the blood flow pattern downstream of the lesion contains shedding vortices. Kailas *et al.* (1999) made this analysis from images taken of a mixing layer (Roshko 1954; Bloor 1964).
- In part II, adapting the work of Arnéodo *et al.* (1995) & Haase (2000), the wavelet transform modulus maxima (WTMM) method is applied on the same data for extracting singularities of the velocity field by analyzing all vertical 1D cross sections of each image (Figure 1).

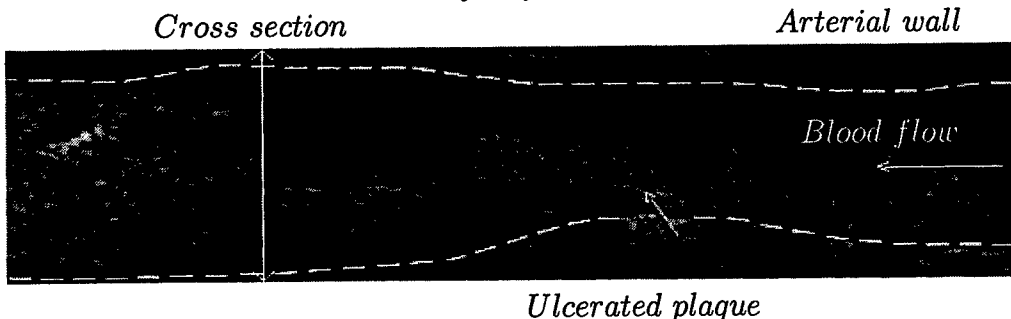


FIGURE 1. Turbulence induced by an ulcerated plaque located in a carotid artery and imaged by Doppler ultrasound (General Electric Corporation, LaConte (2002)).

2. Methods

2.1. Ultrasound data used

Ultrasound datasets were recorded upstream and downstream of an ulcerated atherosclerosis plaque located in the human carotid artery (LaConte 2002). The basic variable of the images, $f(x)$ is the grey-scale intensity correlated with the blood flow velocity, and x is the two-dimensional position vector. The images were digitized with 512×128 pixels and 8 bit accuracy providing 256 grey levels of image intensity.

2.2. The Fourier transform

The Fourier transform has long been a principle analytical tool in various fields such as linear systems, optics, probability theory, quantum physics, antennas, and signal analysis. This mathematical tool originally was used for analysis of stationary signals and systems. The Fourier transform, with its wide range of applications, like many other mathematical tools, has its limitations. For example, this transformation cannot be applied to non-stationary signals. These signals have different characteristics at different times or space coordinates. The modified version of the Fourier transform, referred to as short-time (or time-variable) Fourier transform, can resolve some of the problems associated with non-stationary signals but does not address all the issues of concern. The Fourier transform is a classical tool for measuring the regularity of a function $f(x)$ by investigating the asymptotic decay of its Fourier transform $\hat{f}(w)$ as $w \rightarrow \infty$. However, since all local information is unlocalized by the Fourier transform, the asymptotic decay can only give overall information about singularities within the interval considered.

2.3. The wavelet transform

By definition, wavelet analysis acts as a mathematical microscope which allows one to zoom in on the fine structure of a signal, or, alternatively, to reveal large scale structures by zooming out. Therefore, when a signal or a process contains some form of scale invariance or some self-reproducing property under dilatation, wavelets are useful in identifying them. The wavelet transform (WT) of a real valued function f , according to the analysing mother wavelet ψ , is defined as the convolution product of the scaled and shifted mother wavelet ψ with $f(x)$ (Goupillaud *et al.* 1984),

$$T_\psi[f](a, b) = \frac{1}{a} \int_{-\infty}^{+\infty} f(x)\psi\left(\frac{x-b}{a}\right)dx, \quad (a, b \in \mathbb{R}, a > 0) \quad (2.1)$$

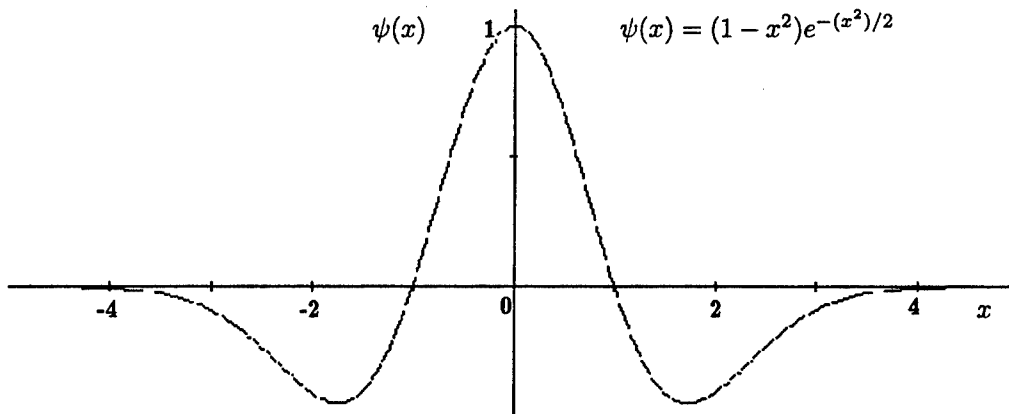


FIGURE 2. The Mexican hat mother wavelet.

The wavelet transform (WT) decomposes a signal $f(x) \in L^2(\mathbb{R})$ hierarchically in terms of elementary components $\psi\left(\frac{x-b}{a}\right)$, which are obtained from a single mother function $\psi(x)$ by dilatations and translations. Here a denotes the scale parameter and b is the shift parameter. The crucial point is to choose $\psi(x)$ to be well localized both in physical and Fourier space. In contrast to Fourier analysis, the WT does not lose information about the position of transient phenomena and irregular structures. In order to detect singular behavior one has to choose an analyzing wavelet $\psi(x)$ that is orthogonal to polynomials of up to order n . The first n moments of $\psi(x)$ are vanishing (Mallat *et al.* 1992).

$$\int_{-\infty}^{+\infty} x^k \psi(x) dx = 0, \quad (0 \leq k < n) \quad (2.2)$$

2.4. The Gaussian functions

A very common way to build admissible wavelets of arbitrary order n is to successively differentiate a smoothing function. Confining to singularities, a family of real valued wavelets constructed from a Gaussian distribution $\psi_0(x)$ has proven to be very effective and has good scale-space localization,

$$\psi_0(x) = e^{-x^2/2}, \quad \psi_n(x) = \frac{d^n}{dx^n} \psi_0(x), \quad (n \in \mathbb{Z}) \quad (2.3)$$

The mother wavelet adopted here is the second derivative of the Gaussian function: the Mexican hat (Figure 2), which was the first function used to computationally detect multiscale edges (Witkin 1983),

$$\psi(x) = (1 - x^2)e^{-x^2/2}, \quad (2.4)$$

The wavelet transform is successfully applied to non-stationary signals for analysis and processing and provides new techniques which deserve special attention in the area of fractal analysis and synthesis since they can be used to extract *microscopic* information on their scaling properties. Fractals have a complex geometrical shape and are charac-

terized by a non-integer dimensionality defined as follows: the minimum number N of balls of size ε required to cover the set completely behaves like,

$$N(\varepsilon) \propto \frac{1}{\varepsilon^D}, \quad (\varepsilon \rightarrow 0) \quad (2.5)$$

where D is the *fractal dimension*.

In this respect, every point is associated with a singular behavior. Fractals are invariant under a group of self-affine transformations including translations and dilatations which are the basic operations in wavelet theory.

2.5. Detection of signal singularities

A standard way of characterizing irregular distributions is to extract *macroscopic* information about the underlying hierarchical structure and to statistically describe the scaling properties using concepts such as the generalized fractal dimensions D and the multifractal spectrum $f(\alpha)$. Wavelet analysis represents a generalization of the standard box-counting technique. It allows the estimation of the entire spectrum of singularities $D(h)$ (h is the Hölder exponent) of fractal distributions as well as functions.

In order to locally characterize the irregularity of an object, one generally uses the notion of Hölder exponent h . This exponent can be seen as a measurement of the strength of the singularity behavior of a given function $f(x)$ around a given point $x = x_0$. It is defined as the greatest exponent h so, that f is *Lipschitz h* at x_0 , and x_0 is a singularity called *cusp* with Hölder exponent $h(x_0)$. For example, $f(x) = \sqrt{x}$ has a *cusp* at $x_0 = 0$ with Hölder exponent $h(0) = 1/2$, the Heaviside function has a “jump” at $x_0 = 0$ with $h(0) = 0$. In that sense, the Hölder exponent generalizes the notion *order of differentiability* and measures the strength of irregularities in the function or in its derivative. f is said to be *Lipschitz h* at x_0 if and only if there exists a constant C and a polynomial $P(x)$ of order smaller than h so that, for all x in a neighborhood of x_0 (Mallat 1998),

$$|f(x) - P(x - x_0)| \leq C|x - x_0|^h. \quad (2.6)$$

The higher the exponent $h(x_0)$, the more regular the function f . In the case where f is made up of an accumulation of singular behavior (which is the case in a fractal function), the direct estimation of $h(x_0)$ and the estimation of the singularity spectrum $D(h)$ of a singular function f , requires the multifractal formalism (Frisch 1995; Arnéodo *et al.* 1995), which provides a “global” method for estimating this singularity spectrum based on the computation of a partition function. It can be shown (Mallat *et al.* 1992) that for *cusp* singularities, the location of the singularity can be detected, and the related exponent can be recovered from the scaling of the WT along the so-called maxima line, converging towards the singularity. This is a line where the WT reaches local maximum (with respect to the position coordinate). Connecting such local maxima within the continuous wavelet transform “landscape” gives rise to the entire tree of maxima lines. It incorporates the main characteristics of the WT: the ability to reveal the hierarchy of (singular) features, including the scaling behaviour. This Wavelet Transform Modulus Maxima (WTMM) tree has been used for defining the partition function based multifractal formalism,

$$Z(q, a) = \sum_i |T_\psi[f](x_i(a), a)|^q, \quad (2.7)$$

where q are the moments of the measure distributed on the WTMM tree.

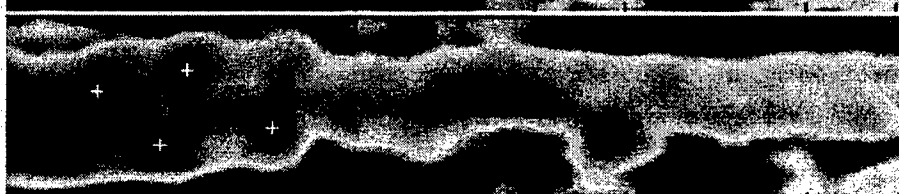
Rawdata*2D Wavelet transform* $a = 0.1$  $a = 2$  $a = 6$ *2D Wavelet transform and isolines* $a = 0.1$  $a = 2$  $a = 6$ 

FIGURE 3. Vortex street induced by an ulcerated plaque located in a carotid artery and imaged by Doppler ultrasound (General Electric Corporation, LaConte (2002)).

Rawdata

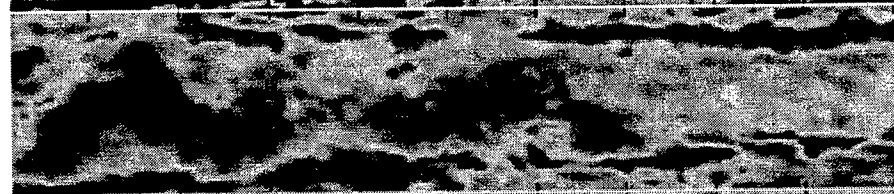


2D Wavelet transform

$a = 0.1$



$a = 2$



$a = 6$



2D Wavelet transform and isolines

$a = 0.1$



$a = 2$



$a = 6$



FIGURE 4. Wake induced by an ulcerated plaque located in a carotid artery and imaged by Doppler ultrasound (General Electric Corporation, LaConte (2002)).

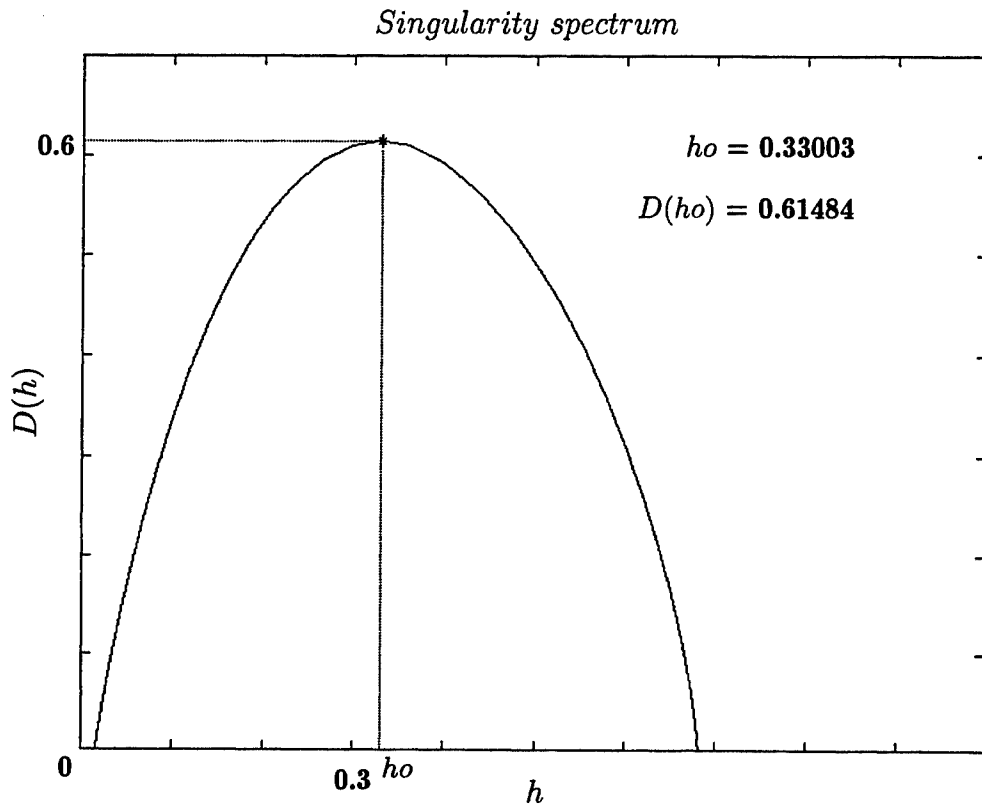


FIGURE 5. Singularity spectrum of a vertical cross section, (analysing wavelet ψ_2).

Arnéodo *et al.* (1995) demonstrated that all the local maxima $x_i(a)$ of $|T_\psi[f](x, a)|$ can be considered as a function of x and proved that, for a large class of fractal functions, $Z(q, a)$ follows a power law scaling

$$Z(q, a) \sim a^{\tau(q)}, \quad a \rightarrow 0^+ \quad (2.8)$$

The $Z(q, a)$ is the partition function of the q -th moment of the measure distributed over the wavelet transform maxima at the scale a considered and the exponents $\tau(q)$ are related to the $D(h)$ singularity spectrum (Figure 5) through the Legendre transform

$$D(h) = \min_q (hq - \tau(q)). \quad (2.9)$$

Haase (2000) successfully applied the WTMM method to turbulent data from an axisymmetric jet with helium at low temperature (Chabaud *et al.* 1994) previously used to analyze turbulent intermittency. The range of Hölder exponent h was between 0 and 0.8, with the most frequent exponent h found for the maximum of the spectrum close to the classical Kolmogorov value of $1/3$.

3. Results

3.1. First description of the ultrasound data used

A Doppler ultrasound image of an ulcerated plaque located in the wall of a carotid artery is shown in Figure 1. The velocity blood flow is digitized with a lighter shade of gray scale. The real-time analysis of the blood flow behavior during each heart cycle, indicates the presence of intervals during which the blood flow pattern downstream of the lesion contains shedding of vortices. Upstream of the lesion, the flow is radially uniform except in the boundary layer near the wall of the artery. As reported by Owsley (2000), the flow of the plaque is wave-like with a velocity variation wavelength that can be related, under ideal static lesion symmetry conditions, to the Strouhal vortex shedding rate frequency, $f_s = S(v_p/d_p)(A_p/A_c)^{1.5}$. Here $S = 0.2$ is the Strouhal number ($S = f_s \cdot d_p/v_p$), v_p is the average upstream flow velocity, d_p is the proximal artery diameter, A_p and A_c are the proximal and lesion-constrained artery cross sectional areas respectively (Owsley 2000). In practice, the lesion morphology is neither symmetric nor static in time. For $d_p = 3.18$ mm, using the ranges of values $30 < v_p < 60$ cm/s and $2 < (A_p/A_c) < 9$, the vortex shedding frequencies are ranged between 50 and 1000 Hz (Owsley 2000). This downstream turbulence dissipates blood flow kinematic energy to the artery wall through boundary layer effects and is able to promote morphological changes of the cellular tissue surrounding the artery. Using these velocity values, the estimated Reynolds number in two smooth and rectilinear pipes with a diameter of 3 to 5 mm is respectively $239_{Re_{min}}$ and $795_{Re_{max}}$. With $\rho = 1060 \text{ kg/m}^3$ and $\mu = 0.004 \text{ kg/(m.s)}$.

In a purely oscillating case, according to Hino *et al.* (1983), the oscillating flow remains stable for $Re < 400$, for $400 < Re < 800$ the flow undergoes a periodically transition between laminar and turbulent states; finally, it becomes fully turbulent for $Re > 800$.

3.2. Part I: the 2D wavelet transform

The WT was used on ultrasound images taken at the middle of a heart cycle when the existence of blood flow coherent structures, mostly generated downstream of a singularity, is unambiguous. Figures 3 and 4 depict two different states of the shedding vortices produced and the WT at three different scales (0.1, 2 & 6). In addition, the isolines of each WT were represented to clarify our purpose. At the smallest scale $a = 0.1$, the fine scale structure is apparent and in comparison with the raw data the coherent structures are easily identified. However as a increases we can easily identify, at each scale, the regions of stronger and weaker gradients. In Figure 3 the vortices (white cross) and the connectedness between them are clearly shown for the scales larger than $a = 2$. In Figure 4 the connectedness of the two main wakes are evident in the raw data. Again for scales larger than $a = 2$, a discontinuity is observed between the two main wakes. The same flow characteristics were seen for all the images taken at the middle of a heart cycle. These results demonstrated that the WT captures the profile of the sharp density gradients more clearly than the raw data.

3.3. Part II: singularity signal analysis in ultrasound images

The WTMM method was applied to the 512 vertical cross sections of each image (Figure 1) in order to compute the singularity spectrum (Figure 5) of each 1D signal cross section.

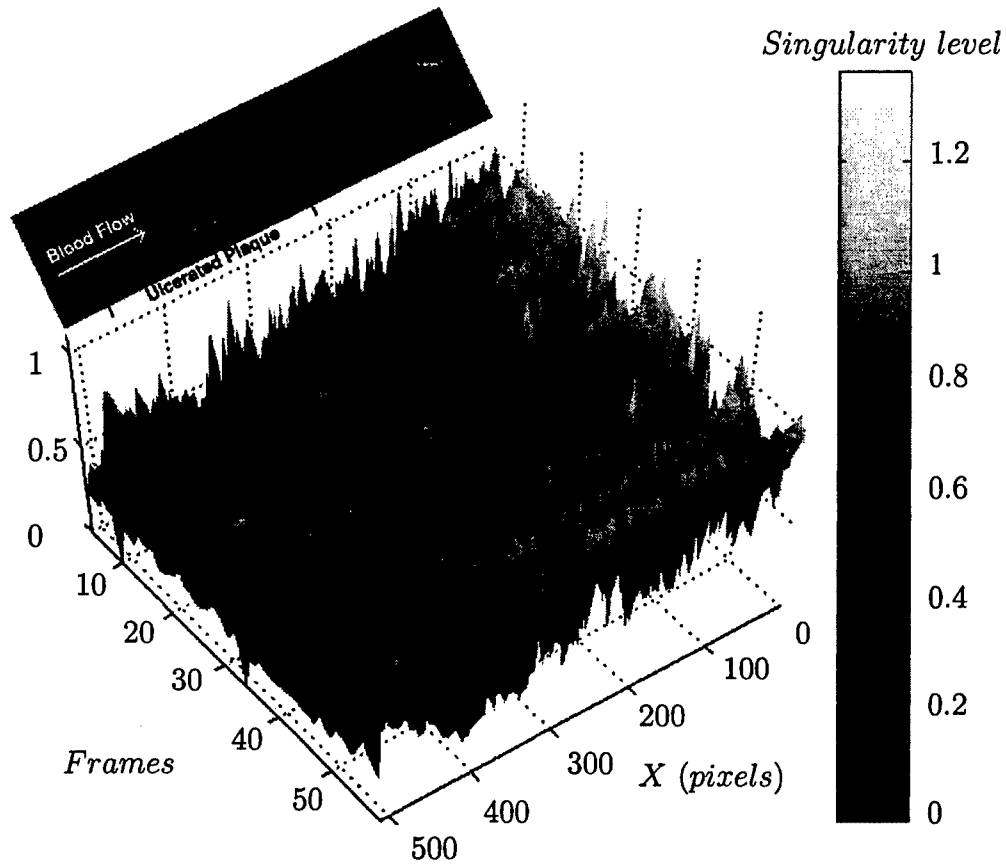


FIGURE 6. 3D representation of the singularity levels calculated for all the frames.

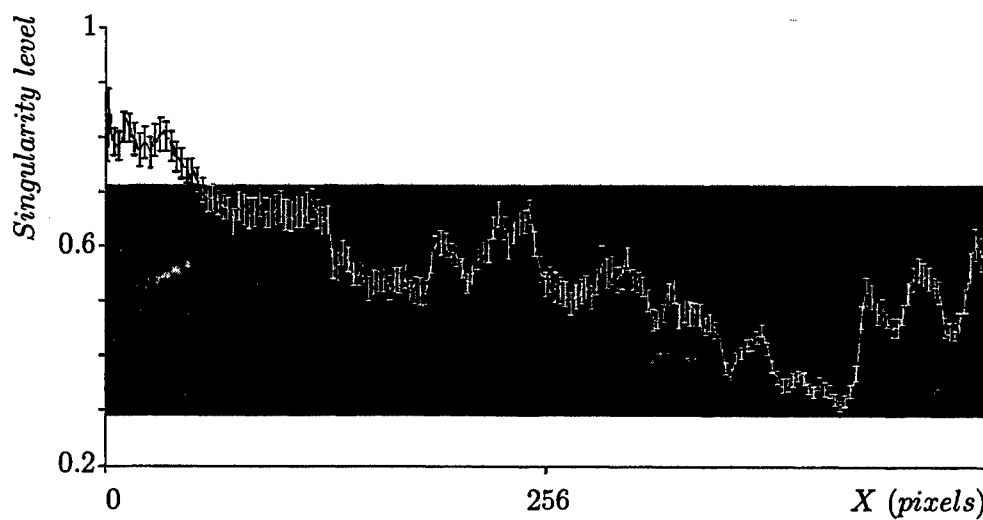


FIGURE 7. Means and SEM of the singularity levels calculated for all the frames.

A numerical code (May *et al.* 2001b)‡ was used to compute the variation of the Hölder exponent h and of $D(h)$. These computations allowed the representation of the singularity level of each 1D signal cross section as a function of the position X and of the time/frame (3D graphical representation of Figure 6). The means of the singularity level of each 1D signal cross section in function of the position X are shown in Figure 7 with an ultrasound frame in the background. As observed by Owsley (2000), after visualizing the ultrasound data, Figure 6 and Figure 7 showed the constant decrease of the singularity level for the upstream region over the plaque for all frames. This singularity decrease is in good comparison with the turbulence decrease of a boundary layer over a two-dimensional bump, experimentally observed by Webster *et al.* (1996).

4. Future plans

The present study has employed a numerical analysis method which is used in other research areas in studying fluid mechanics. In particular, singularity information was extracted from one- and two-dimensional data by this method. This wavelet based method is able to capture the real-time complex biological flows behavior and for instance to evaluate the effect of pharmacological drugs on hemodynamics, and thus its validity should be checked using other flow data behavior taken from simulation and/or experimental biological fluid mechanics. Future work will focus on the validation of this wavelet analysis method with simulation data of biological fluid mechanics.

Acknowledgments

General Electric Corporation is gratefully acknowledged for providing the ultrasound data used in this study. The author wishes to thank Professor David Donoho (Statistics Department, Stanford University) for the wavelet software package "WaveLab". Special thanks to Dr. Y. Dubief for sharing his knowledge of turbulence and for his corrections and helpful comments on the manuscript. I am also thankful to Dr. C.M. White and Dr. J.S. Hur for the helpful corrections and suggestions on the manuscript.

‡ All computations were realized with a numerical code based on a collection of Matlab function files included in the WaveLab 802 package (Pr. David Donoho, Statistics Department, Stanford University).

REFERENCES

- ABRY, P. & BARANIUK, R. & FLANDRIN, P. & RIEDI, R. & VEITCH, D. 2002 Multiscale nature of network traffic. *IEEE Signal Processing Magazine* **19**(3), 28-46.
- ARNÉODO, A. & ARGOUL, F. & BACRY, E. & ELEZGARAY, J. & MUZY, J.F. 1995 *Ondelettes, Multifractales et Turbulences*. Diderot, Arts et Sciences, Paris, New-York, Amsterdam.
- ARNÉODO, A. & D'AUBENTON-CARAFA, Y. & BACRY, E. & GRAVES, P.V. & MUZY, J.F. & THERMES, C. 1996 Wavelet-based fractal analysis of DNA sequences. *Physica D* **96**, 291-320.
- BLOOR, M.S. 1964 The transition to turbulence in the wake of a circular cylinder. *J. Fluid Mech.* **21**, 290.
- BLUESTEIN, D. & GUTIERREZ, C. & LONDONO, M. & SCHOEPHOERSTER, R.T. 1999 Vortex Shedding in Steady Flow Through a Model of an Arterial Stenosis and its Relevance to Mural Platelet Deposition. *Annals of Biomedical Engineering* **27**, 763-773.
- BLUESTEIN, D. & RAMBOD, E. & GHARIB, M. 2000 Vortex Shedding as a Mechanism for Free Emboli Formation in Mechanical Heart Valves. *Journal of Biomedical Engineering* **122**, 125-134.
- BROWN, G.L. & ROSHKO, A. 1974 On density effects and large structures in turbulent mixing layers. *J. Fluid Mech.* **64**, 775-816.
- CHABAUD, B. & NAERT, A. & PEINKE, J. & CHILLÀ, F. & CASTAING, B. & HEBRAL, B. 1994 Transition toward developed turbulence. *Phys. Rev. Lett.* **73**, 3227-3230.
- CLOUTIER, G. & LEMIRE, F. & DURAND, L.G. & LATOUR, Y. & LANGLOIS, Y.E. 1990 Computer evaluation of Doppler spectral envelope area in patients having a valvular aortic stenosis. *Ultrasound Med. Biol.* **16**(3), 247-260.
- LA CONTE, K. 2002 Courtesy of LaConte Kirstin, Global Clinical Marketing Program Manager, *GE Ultrasound*, Milwaukee, WI, October 2002.
- DAVIES, P.F. & REMUZZI, A. & GORDON, E.J. & DEWEY, C.F. & GIMBRONE, M.A. 1986 Turbulent Fluid Shear Stress Induces Vascular Endothelial Turnover In Vitro. *Proceedings of the National Academy of Sciences* **83**, 2114-2117.
- DAVIES, P.F. & SHI, C. & DEPAOLA, N. & HELMKE, B.P. & POLACEK, DC. 2001 Hemodynamics and the focal origin of atherosclerosis: a spatial approach to endothelial structure, gene expression, and function. *Ann. N. Y. Acad. Sci.* **947**, 7-16.
- FARGE, M. & RABREAU, G. 1988 Transformée en ondelettes pour détecter et analyser les structures cohérentes dans les écoulements turbulents bidimensionnels. *C.R. Acad. Sci. Paris Série II* **307**, 1479-1486.
- FARGE, M. 1992 Wavelet transforms and their applications to turbulence. *Ann. Rev. Fluid Mech.* **24**, 395-457.
- FRISCH, U. 1995 *Turbulence*. Cambridge Univ. Press, Cambridge.
- GAO H. & AYYASWAMY P.S. & DUCHEYNE P. 1997 Dynamics of a microcarrier particle in the simulated microgravity environment of a rotating-wall vessel. *Microgravity Sci. Technol.* **10**(3), 154-165.
- GHARIB, M. & KREMERS, D. & KOOCHESFAHANI, M.M. & KEMP, M. 2002 Leonardo's vision of flow visualization. *Experiments in Fluids* **33**, 219-223.
- GOUPILLAUD, P. & GROSSMANN, A. & MORLET, J. 1984 Cycle-octave and related transforms in seismic signal analysis. *Geoexploration* **23**(1), 85-102.

- HAASE, M. 2000 Extracting singularities in turbulent flow with real and complex wavelets. In *Proceedings of the Science and Art Symposium 2000*. Eds A. Gyr, P.D. Koumoutsakos and U. Burr. Kluwer Academic Publishers, 1-11.
- HINO, M. & KASHIWAYANAGI, M. & NAKAYAMA, A. & HARA, T. 1983 Experiments on the turbulence statistics and the structure of a reciprocating flow. *J. Fluid Mech.* **131**, 63.
- JAFFARD, S. 1997 Multifractal Formalism for Functions Part I: Results Valid For All Functions. *SIAM Journal on Mathematical Analysis.* **28**(4), 944 - 970.
- JOHARI, H. & DURGIN, W.W. 1998 Direct measurement of circulation using ultrasound. *Experiments in Fluids.* **25**, 445-454.
- KAILAS, S.V. & NARASIMHA, R. 1999 The eduction of structures from flow imagery using wavelets Part I. The mixing layer. *Experiments in Fluids.* **27**, 167-174.
- KU, D.N. & GIDDENS, D.P. & ZARINS, C.K. & GLAGOV, S. 1985 Pulsatile flow and atherosclerosis in the human carotid bifurcation. Positive correlation between plaque location and low and oscillating shear stress. *Arteriosclerosis.* **5**, 293-301.
- KU, D.N. 1997 Blood flow in arteries. *Annu. Rev. Fluid Mech.* **29**, 399-343; *Atherosclerosis* **5**, 289-302.
- LIN D.C, & HUGHSON R.L. 2001 Modeling heart rate variability in healthy humans: a turbulence analogy. *Phys. Rev. Lett.* **86**(8), 1650-1653.
- MALLAT, S. & HWANG, W.L. 1992 Singularity detection and processing with wavelets. *IEEE Trans. Image Proc.* **38**(2), 617-643.
- MALLAT, S. 1998 A wavelet tour of signal processing. Academic Press, San Diego.
- MANTEGNA, R.N. & STANLEY, H.E. 2000 *An introduction to Econophysics*. Cambridge Univ. Press, Cambridge.
- MAY, P. & GERBAULT, O. & ARROUVEL, C. & REVOL, M. & SERVANT, J.M. & VICAUT, E. 2001 Nonlinear analysis of arterial oscillated flow in experimental stenosis and microsurgical anastomosis. *J. Surg. Res.* **99**(1), 53-60.
- MAY, P. & SERVANT, J.M. & VICAUT, E. "Procédé d'analyse d'un événement tel qu'une intervention chirurgicale sur un vaisseau sanguin", French patent BRFR 0109145, 10 july 2001. PCT/FR02/02419.
- MAY, P. & ARROUVEL, C. & REVOL, M. & SERVANT, J.M. & VICAUT, E. 2002 Detection of hemodynamic turbulence in experimental stenosis: an in vivo study in the rat carotid artery. *J. Vasc. Res.* **39**(1), 21-29.
- MENEVEAU, C. 1991 Analysis of turbulence in the orthonormal wavelet representation. *J. Fluid Mech.* **232**, 469-520.
- MUZY, J.F. & BACRY, E. & ARNÉODO, A. 1991 Wavelets and multifractal formalism for singular signals: application to turbulence data. *Phys. Rev. Lett.* **67**, 3515-3518.
- MUZY, J.F. & BACRY, E. & ARNÉODO, A. 1994 The multifractal formalism revisited with wavelets. *Int. J. Bif. and Chaos.* **4**, 245-302.
- NARASIMHA, R. & SAXENA, V. & KAILAS S.V. 2002 Coherent structures in plumes with and without off-source heating using wavelet analysis of flow imagery. *Experiments in Fluids.* **33**, 196-201.
- NEREM, R.M. 1993 Hemodynamics and the Vascular Endothelium. *ASME Journal of Biomechanical Engineering.* **115**, 510-514.
- NOWAK, M. 2002 Wall shear stress measurement in a turbulent pipe flow using ultrasound Doppler velocimetry. *Experiments in Fluids.* **33**, 249-255.
- OWSLEY, N.L. 2000 Array phonocardiography. In *Adaptive Systems for Signal Process-*

- ing, Communications, and Control Symposium 2000. AS-SPCC. The IEEE 2000 , 31-36.
- PESKIN, C.S. & MCQUEEN, D.M. 1995 A general method for the computer simulation of biological systems interacting with fluids. *Symp. Soc. Exp. Biol.* **49**, 265-276.
- RADIN, S. & DUCHEYNE, P. & AYYASWAMY, P.S. & GAO H. 2001 Surface transformation of bioactive glass in bioreactors simulating microgravity conditions. Part I: experimental study. *Biotechnol. Bioeng.* **75(3)**, 369-378.
- ROSHKO, A. 1954 On the Development of turbulent wakes from vortex streets *NACA Report.* **1191**, 124-132.
- SCHMIDT, D.W. & TILMANN, P.M. 1970 Experimental study of sound-wave phase fluctuations caused by turbulent wakes. *J. Acoustic. Soc. Am.* **47**, 1310-1324.
- SPENCE, J.D. & PERKINS, D.G. & KLINE, R.L. & ADAMS, M.A. & HAUST, M.D. 1984 Hemodynamic modification of aortic atherosclerosis. Effects of propranolol vs hydralazine in hypertensive hyperlipidemic rabbits. *Atherosclerosis.* **50(3)**, 325-333.
- TSAO, P.S. & BUITRAGO, R. & CHAN, J.R. & COOKE, J.P. 1996 Fluid flow inhibits endothelial adhesiveness. Nitric oxide and transcriptional regulation of VCAM-1. *Circulation* **94(7)**, 1682-1689.
- WEBSTER, D.R. & DEGRAAFF, D.B. & EATON, J.K. 1996 Turbulence characteristics of a boundary layer over a two-dimensional bump. *J. Fluid Mech.* **320**, 53-69.
- WEST, B.J. 1990 Physiology in fractal dimension: error tolerance. *Annals of Biomedical Engineering.* **18**, 135-149.
- WINTER, D.C. & NEREM, R.M. 1984 Turbulence in pulsatile flows. *Annals of Biomedical Engineering.* **12**, 357-369.
- WITKIN, A. 1983 Scale space filtering. In *Proc. Int. Joint. Conf. Artificial. Intell.* Espoo, Finland, 1983.
- YE, T. & MITTAL, R. & UDAYKUMAR, H.S. & SHYY, W. 1999 An Accurate Cartesian Grid Method for Viscous Incompressible Flows with Complex Immersed Boundaries. *Journal of Computational Physics* **156**, 209-240.

Flow around cactus-shaped cylinders

By Sharon Talley and Godfrey Mungal †

1. Motivation and objectives

This study combines biology and fluid mechanics to understand mechanisms that organisms use to cope with flows in their environment. Because organisms are selected in and by the flow conditions of their environment, their study can provide insight into novel mechanisms of controlling flow given certain constraints such as body size, basic shape (bluff vs. streamlined), and structural properties. Large desert succulents, such as the saguaro cactus, *Carnegiea gigantea* (Cactaceae), experience high wind velocities in their natural habitat and have converged on a common surface geometry of longitudinal cavities and spines (figure 1a). At the highest wind velocities in their natural habitat and when in danger of being uprooted by wind forces, saguaros with typical diameters of 0.5 m experience flows at Reynolds number (Re) up to 10^6 . Being stationary organisms that must cope with high wind speeds from all directions, their shape is constrained to a cylindrical bluff body, and they likely rely on their complex surface geometry to affect the surrounding flow. Given that the shape and surface characteristics of an object influences the surrounding airflow, natural selection by wind may favor bluff body morphologies that reduce forces exerted by wind gusts (i.e. drag and fluctuating side-force). In this paper, we address the complex surface geometry of saguaros by experimentally examining the effect of longitudinal cavity depth on flow past circular cylinders ($Re \approx 2 \times 10^4$ to 2×10^5). Because of the broad nature of this interdisciplinary research, we provide background information on the physical attributes of saguaros, evidence of wind as a natural selective agent and flow around circular cylinders.

1.1. Saguaro background

The size, shape, surface characteristics and material properties prescribe a structure's (e.g. saguaro) ability to withstand high flow velocities. From a fluid mechanical perspective, saguaros can be viewed as giant cylindrical structures having complex surface geometry and a hemispherical free end. The main cylindrical trunks of adult saguaros reach heights of 8 m to over 15 m (Hodge 1991) and diameters of 0.3 m to over 0.8 m (Benson 1981). Age, climatic conditions and soil properties govern the size of saguaros; therefore, saguaro size can differ with environment. Information from one study area suggest that aspect ratios (*height/diameter; h/d*) of saguaros are height/ age dependent (Niklas and Buchman 1994). Saguaro taller than 4.5 m in height have (*h/d*) ratios between 12 and 23 and are relatively more slender than shorter saguaros, which have aspect ratios between 5 and 12 (*h/d*).

The complex surface geometry of saguaros is caused by longitudinal cavities and spines. Ten to 30 v-shaped longitudinal cavities (ribs) span the length of the trunk (Hodge 1991). The number of cavities depends on the trunk diameter; new cavities are added or deleted (figure 1a) to maintain a fraction cavity depth (l/d - depth of the cavity divided by the diameter of the cylinder) of 0.07 ± 0.0015 at approximately 1.5 m in height (Geller and

† Mech. Engg. Dept, Stanford University.

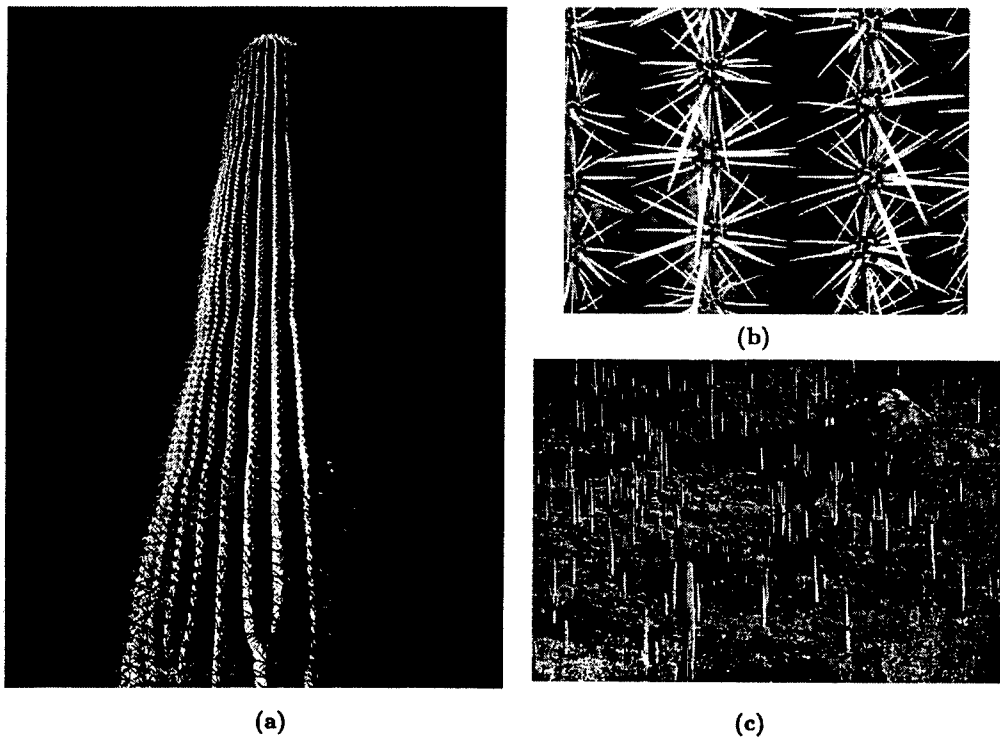


FIGURE 1. (a) Adult saguaro trunk showing the addition of cavities, (b) spines, and (c) saguaro forest

Nobel 1984). Cavity depth may increase higher up the trunk (personal observations). Cavity junctures (apices) have staggered clusters of 15 to 30 spines 2.5 to 7.6 cm long (Benson 1981; figure 1b).

Structural properties determine its load capacities and other factors that can interact with flow phenomena (natural resonance frequency and ability to flex causing aeroelastic responses). The root to soil interface likely determines a saguaro's load capacity, because toppled saguaros usually are found uprooted rather than broken at the trunk (see Talley *et al.* 2001 for structural strength of saguaro tissue). Saguars have a shallow root system, which provides poor root anchorage and is believed to allow the toppling of saguaros during strong winds (Hodge 1991). While saguaros greater than a 1 m in diameter, may have natural frequencies between 4 and 10 Hz (Niklas 2002, personal communication), no studies have reported the forces required to topple saguaros, their behavior and flexibility in wind or their resonance frequency in soil. A morphologically similar species to the saguaro is the Mexican cardón, (*Pachycereus pringlei*), which has a more extensive root system of a deep bayonet-like central root and shallow lateral roots (Niklas *et al.* 2002). Anchorage is believed to be primarily provided by the central root system, which does not grow proportionately in girth or depth with growth of the trunk. Niklas (2002) argues that in an environment where water is extremely limited, as the cardón increases in size the root's function may shift more towards water absorption than anchorage because death by dehydration is more likely than toppling by wind. However, the likelihood of being toppled by wind depends on wind occurrences in their habitat, and other mechanisms may be responsible for their ability to withstand high wind velocities.

For wind to be a natural selective agent on saguaros, saguaros must be exposed to

wind, high wind velocities must occur in their habitat, and wind forces must affect their reproductive success. High wind velocities occur within the distribution of saguaros and frequently enough to affect their reproductive success. During a 9-year period, the maximum wind velocity recorded was 38 ms^{-1} , and velocities exceeding 22 ms^{-1} occurred almost every month (Bulk 1984; For a 0.5 m diameter saguaro, these wind velocities give Re of 1.3×10^6 and 7.3×10^5 , respectively). The saguaro cactus can live for 150 years and requires 30 to 50 years to attain reproductive maturity, suggesting that high wind velocities need only occur every 30 to 50 years to be an important selective agent. Saguaros are likely exposed to winds because their desert habitat supports few if any other tall plants to provide shelter from the wind (figure 1c).

Substantial circumstantial evidence suggests that wind affects the reproductive success of saguaros by toppling them and causing their premature mortality (figure 1c, Benson 1981, Alcock 1985, Pierson and Turner 1998). It is likely that most of the saguaros that are toppled are large plants; however, enough young saguaros are toppled by wind to be documented (see figure 1c in Talley *et al.* 2001). Information on the occurrence of toppling events and on the wind velocities required to topple saguaros is lacking. The best-documented cases of mortality due to windfall are briefly mentioned in two different papers. (*i*) From 1941 to 1944, 2% of the saguaros in a 130 ha area were toppled by wind, and in 1945, 7% of the remaining saguaros in the same 130 ha area were toppled (Steenbergh and Lowe 1983). (*ii*) In August 1982, over 140 saguaros in a 15 ha area were toppled by wind velocities reported to be greater than 28 ms^{-1} (Pierson and Turner 1998). The fact that some saguaros are toppled by gusts, while many others remain standing is consistent with the natural selection scenario.

1.2. Flow around circular cylinders

Much is known about flows past circular cylinders, and below we provide a short review of flow phenomena relevant to the fluid mechanics of the saguaro's shape. Saguaros have the shape of a circular cylinder augmented with longitudinal cavities (the effect of spines is a future topic) and a hemispherical free end. For simplicity, we will focus flow around two-dimensional cylinders and then discuss free end effects. For an introduction to basic fluid mechanics, see White (1994, chapter 7).

Drag coefficient, C_D , curves of spheres and cylinders have four distinct Re flow ranges (figure 2a), which are distinguished by changes in C_D caused by boundary layer phenomena including separation and transition from laminar to turbulent flow (Roshko 1961, Achenbach 1977, Farell 1981). In the subcritical regime, the boundary layer is laminar and separates at an angle from the front stagnation point of about 80° . In the critical regime, C_D drops as the laminar boundary layer separates further downstream (to about 100°). The lowest C_D on the curve, occurring within the critical range, is the critical Re (figure 2a). At the critical Re , turbulent reattachment occurs, causing a bubble which delays separation (to about 140°). In the supercritical regime, C_D rises as the reattachment bubble shrinks and moves upstream. In the transcritical regime, C_D is almost independent of Re and the boundary layer becomes turbulent before separation.

Comparisons of C_D curves of smooth and uniformly rough cylinders reveals that rough cylinders have C_D curves to the left of smooth cylinders and, therefore, experience the critical range at lower Re (Achenbach 1971). Roughness promotes turbulent transition (surface roughness size is quantified by the parameter k_s/d , the height of the roughness divided by the diameter of the cylinder), and generally, the greater the roughness, the greater the shift of the C_D curve to the left. Although a greater degree of uniform surface roughness promotes an earlier critical Re , it is accompanied by a smaller drop in C_D and

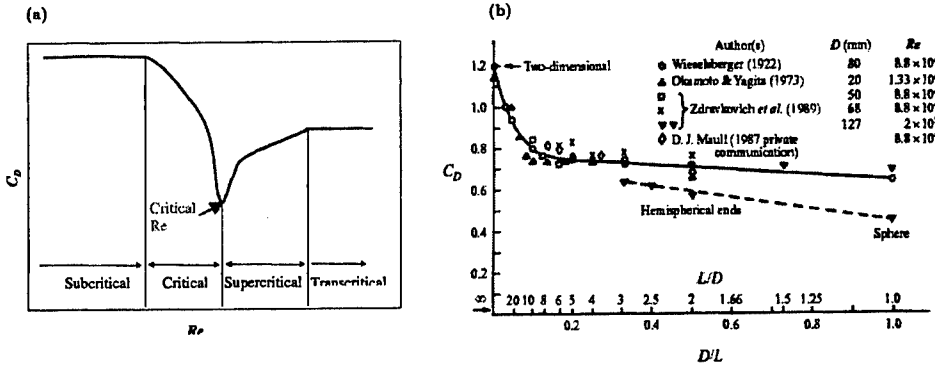


FIGURE 2. (a) Four ranges of flow past circular cylinders and (b) Drag coefficient of circular cylinders differing in aspect ratio of in terms of (Zdravkovich *et al.* 1989).

a shorter critical Re range. In addition, uniformly rough cylinders often have higher C_D than smooth cylinders in the postcritical ranges. Therefore, the C_D reduction afforded by uniform surface roughness occurs for a very limited Re range and at a cost of higher C_D in the postcritical regime.

Distributed surface roughness and complex surface geometries (i.e. dimples) can affect the shape of the C_D curve without the same limit in the range of C_D reduction and cost of higher C_D in the postcritical regime as occurs with uniformly rough cylinders. For example, distributed strips of roughness on cylinders promotes early transition without a rapid rise in C_D in the supercritical range (Nakamura and Tomonari 1982). Complex surface geometry, such as dimples on a cylinder (similar to those on a golf ball; Bearman & Harvey 1993), also induce early transition and extend the critical range. The dimpling geometry may be effective at tripping the laminar boundary layer while inhibiting the thickening of the turbulent boundary layer (Mehta and Pallis 2001). Thus, C_D depends not only on the size of surface roughness but also on the shape (geometry) and distribution of surface roughness. Although many surface modifications have been studied to reduce drag on circular cylinders, to our knowledge, none have examined spanwise v-shaped cavities with l/d greater than 0.035. Our study is motivated by the saguaro cactus and other tall succulents that have a l/d of 0.07. In this paper, we compare unsteady drag and lift of smooth and uniformly rough cylinders ($k_s/d = 1.74 \times 10^{-3}$ and 8.41×10^{-3}) to cylinders differing in cavity depth ($l/d = 0.035, 0.07, 0.105$).

Cylinders with free ends generally have lower C_D than two-dimensional cylinders (figure 2b; Zdravkovich *et al.* 1989). The effect of free ends on C_D depends on aspect ratio. For $l/d < 1$, the lower the aspect ratio the greater the effect of the free ends. For cylinders with both ends free, free-end effects appear to be beneficial for aspect ratios (h/d) < 30 . This may also be the case for cylinders with one free end; Fox, Apelt, and West (1993) reported that at an aspect ratio equal to 30 there is still a considerable decrease in the mean and fluctuating forces. The average aspect ratio of saguaros is unknown; however, aspect ratios likely range between 5 and 23 (h/d). Therefore, the effect of free ends should not be discounted. The saguaro has one free end that is hemispherical. Note that in figure 2b, hemispherical ends give a larger decrease in C_D than flat ends. Cavities on the hemispherical free end, such as those on a saguaro, may provide even a larger decrease in C_D than a smooth-hemispherical free end.

1.3. Significance

With our interdisciplinary approach, we address the fluid mechanics of a novel surface geometry and fundamentals in biology. This is the first study to our knowledge to examine how spanwise v-shaped cavities (l/d up to 0.105) can affect flow around cylinders. Research on the effect of surface augmentation on flow around bluff bodies is important to many applications, such as chimneystacks, towers, and marine risers. In biology, fundamental concepts in evolutionary ecology are addressed by examining whether natural selection by wind has optimally shaped stationary organisms to reduce potentially damaging wind forces (drag and fluctuating side-force). Surprisingly few have studied the fluid mechanics of biological organisms, especially terrestrial and stationary organisms, with bluff bodies. No studies have reported accounts that bluff-bodied organisms reduce drag by surface roughness (Vogel 1981). Surface roughness has been argued an unlikely adaptation to control drag, because the reduction in C_D afforded by the surface roughness is accompanied by an increase in C_D at higher Re (Denny 1988 and Vogel 1981). However, an increase in C_D in a Re range that is rarely, if ever, experienced by the organism in question should have no effect on its evolution. Moreover, complex surface roughness affects the C_D curve differently than uniform roughness, and other forces and flow phenomena (i.e. drastic changes in C_D , fluctuating side-forces, and vibration frequencies) may be important but overlooked selective agents on the shape of organisms.

2. Experimental arrangement and methods

2.1. Test cylinders

Circular cylinders 76.2 cm in length (cylinders spanning the tunnel) and 57.5 cm in length (flat-capped, free-ended cylinders) were manufactured from RenShape 460 modeling board. All cylinders were 9.98 cm in diameter. Six surfaces were examined: one smooth, two uniformly rough ($k_s/d = 1.74 \times 10^{-3}$, 8.41×10^{-3}), and three different depths of 24 spanwise v-shaped cavities ($l/d = 0.035$, 0.07, and 0.105). Uniform roughness, $k_s/d = 1.74 \times 10^{-3}$ and 8.41×10^{-3} , was provided by commercial 100 and 36 grit sandpaper, respectively. Sheets of sandpaper were attached to the smooth cylinder with double-sided adhesive tape, adding a thickness less than 2 mm. The sandpaper spanned the cylinder to $\pm 130^\circ$ with respect to the flow direction (0°). The 24 cavities on the cylinder were 15° apart cut at included angles of 124° , 82.5° , and 60° for the 0.035, 0.07, and 0.105, respectively.

2.2. Experimental arrangement in wind tunnel

Figure 3 shows the experimental configuration. Experimental measurements were performed in a low-speed blower tunnel with a test section 76.2 cm high by 76.2 cm wide at flow velocities from 4 to 29.5 ms^{-1} ($Re \approx 2 \times 10^4$ to 2×10^5). Geometric blockage was 13% (d /width of the test section). In all experiments, cylinders were mounted vertically between aluminum endplates (3.35 mm thick). To eliminate direct contact between endplates and cylinders, endplates were fixed 2.54 cm below the roof and 2.54 cm above the floor. Endplates were $8d$ long by $7d$ wide with a distance between the cylinder axis and the leading edge of $3.5d$ (Szepessy 1994). Aspect ratio between the endplates was 7.08 (h/d) for cylinders spanning the tunnel and 5.47 (h/d) for cylinders with free ends. The portion of all cylinders that were between the endplate and the closest wall (i.e. 0.066 for cylinders spanning the tunnel and 0.033 for free-ended cylinders) had a smooth surface, and their contribution was neglected in the force calculations.

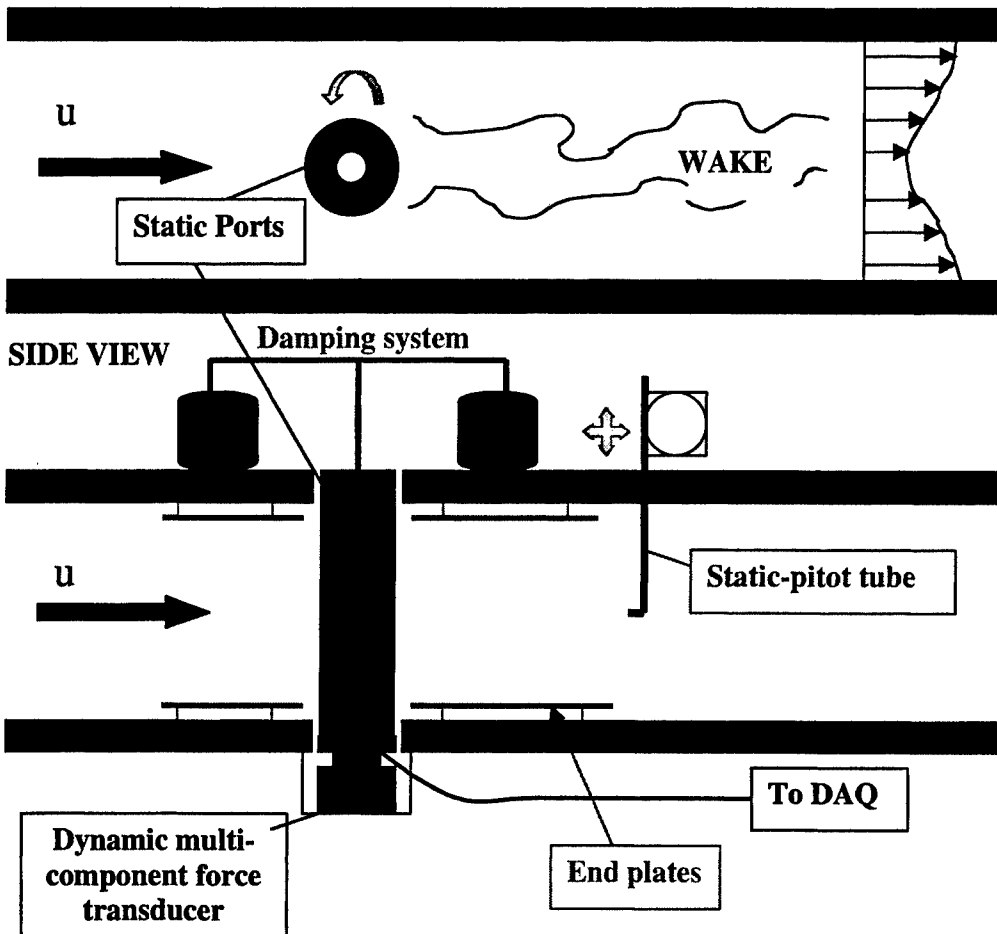
TOP VIEW

FIGURE 3. Experimental configuration.

2.3. Pressure distribution

Cylinders were equipped with at least 16 static-pressure ports of less than 1-mm diameter. At 19.1 cm, 31.8 cm, 44.5 cm, and 57.2 cm from base of the cylinders, there were a series of four static ports located 90° apart from one another. For cylinders with cavities, the 16 static ports were located on the middle of the cavity wall. Cavity cylinders were equipped with two additional static ports 44.5 cm from the base, one of which was located on the apex of the cavity juncture and the other in the trough (valley) of the cavity. The three static-port locations along the cavities were used to determine pressure differences with the different orientations of the cavity to the flow. Only the cylinders spanning the tunnel were measured for pressure distribution. Cylinders were mounted on a turntable and rotated 15° between sampling periods. Pressure measurements were made using a differential pressure transducer at a sampling rate of 500 Hz for a total of 150,000 samples for each velocity.

2.4. Direct force and vortex shedding measurements

Force measurements were obtained directly using a dynamic multi-component force transducer (MC3A-6-250, Advanced Mechanical Technology, Inc, Watertown, MA). The cylinders were attached to a metal plate that was directly attached to the force transducer. The transducer was rigidly attached to the tunnel. The MC3A-6-250 transducer has six channels; three channels measure forces in the three directions (drag, lift, and weight) and three channels measure moments about the different directions. Channels have a 2% or less crosstalk which had to be corrected for due to the cylinder length creating large moments, and hence, causing considerable errors in force measurements. Correction factors were obtained through comprehensive calibrations using a pulley system and a series of weights. Wires were attached to the cylinder at three or more different spanwise locations (to correct for moment crosstalk contribution) for both the drag and lift directions.

The MC3A-6-250 transducer is not rigid and allowed the cylinder to displace (approximately 1 cm) when under maximum wind loads. To prevent large amplitude vibrations due to vortex shedding, the free end of the cylinders spanning the tunnel (ends were outside the tunnel roof; figure 3), was attached to a floating dampening system. No corrections were made for damping in the force calculations. No damping system was employed for free-ended cylinders (see discussion). Using a spectrum analyzer, we measured the resonance frequencies of the cylinders. Cylinders spanning the tunnel had a natural frequency of 8 Hz, and the flat-capped cylinders had a natural frequency of 20 Hz.

The mounting mechanism did not allow different orientations of the cavities to the flow, so all cylinders had the cavity apices facing the flow. A total of 150,000 samples at a sampling rate of 500 Hz were measured for up to 30 different velocities (from 4 to 29.5 ms^{-1}) for each cylinder. Velocity was obtained using a Pitot-static tube attached to a differential pressure transducer. Vortex-shedding frequency (f) was measured by counting the peaks of the fluctuating lift forces and presented as the Strouhal number ($St = f^*d/U$, where U is the velocity). Blockage corrections were made for the C_D and velocity calculations using formulas from Allen and Vincenti (1944). Blockage corrections were not applied to the lift coefficient, C_L . The root-mean-square (r.m.s.) lift coefficient, $C_{L'}$, was calculated using the r.m.s. of the lift fluctuations (L').

3. Results

3.1. Pressure distribution

Pressure distributions at $Re = 110,000$ for the cylinders spanning the tunnel are shown in figure 4a. There is greater pressure recovery for cylinders with cavities than for the smooth and rough cylinders. The cylinders with cavities have greater negative pressures on the sides of the cylinder. Pressure recovery appears to increase with increasing cavity depth while the negative pressures on the sides of the cylinder appear not to be affected by cavity depth. The pressure distribution depends somewhat on the orientation of the cavity to the flow. When the cavity trough faced the flow, static pressures were very similar to those when the wall faced the flow. Conversely, when apex was facing the flow, static pressures differed from those when the wall or cavity trough faced the flow. The largest differences were for pressures on the front and sides of the cylinders. figure 4b shows the pressure distribution at different locations along the cavity for the 0.07 l/d cylinder.

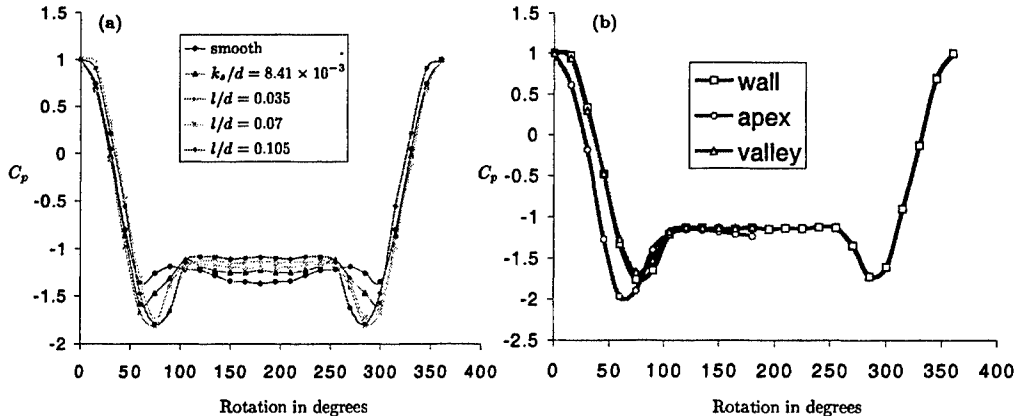


FIGURE 4. (a) pressure distribution of all cylinders at $Re = 110,000$ and (b) pressure distribution from different locations along the cavity for the $0.07 l/d$ cylinder.

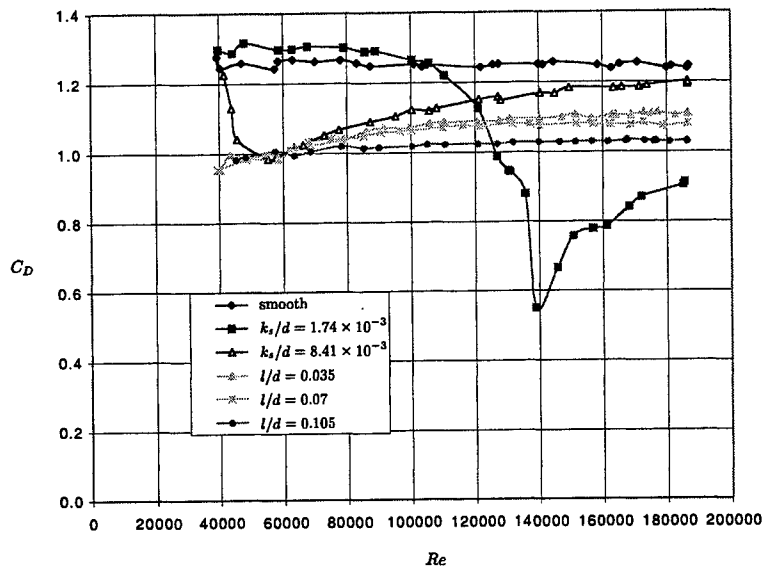
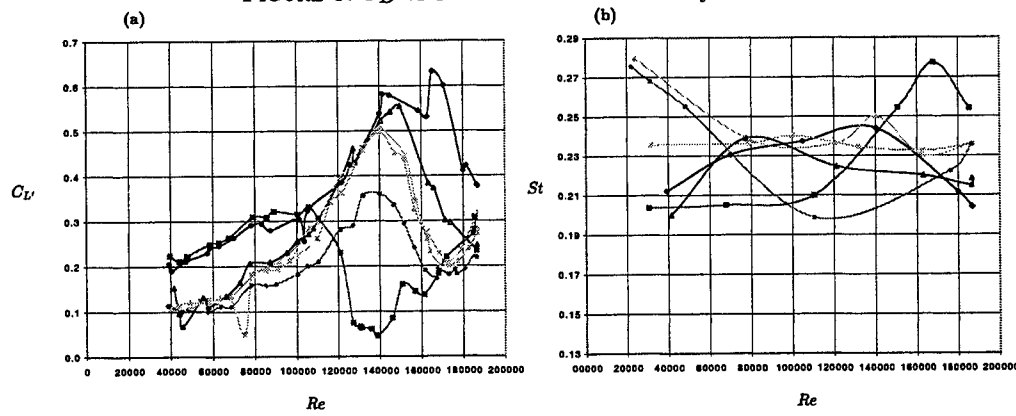
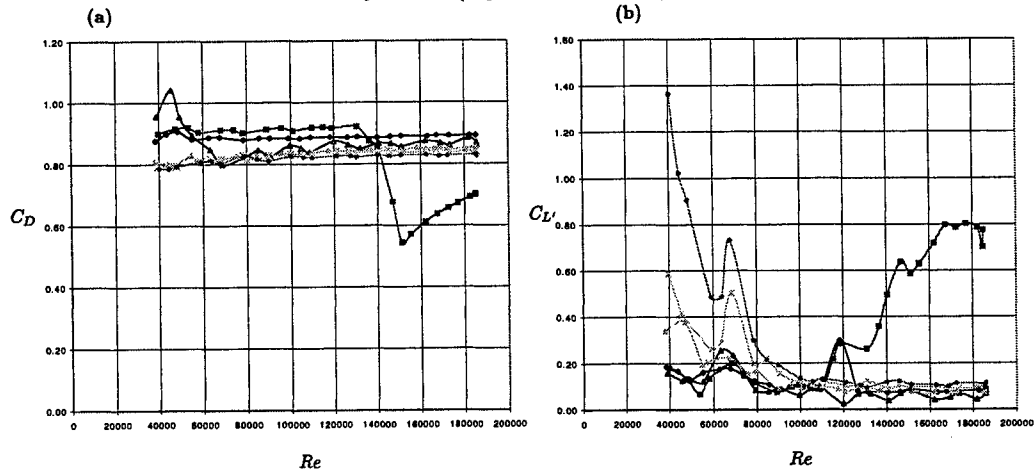
3.2. Drag, lift and vortex shedding

C_D vs. Re for the test cylinders are shown in figure 5. Note that C_D values were calculated using only the portion of the cylinder between the endplates (neglecting the smooth portions of the cylinder between the endplate and the nearest wall) and, therefore, the C_D values are higher than those reported elsewhere. However, trends in the magnitude of the drop in C_D and the critical Re for the two uniformly rough cylinders are in close agreement with those reported in Güven, Farrell, and Patel (1980). The cavity cylinders have no obvious critical Re . At the highest Re , the C_D for the cavity cylinders asymptotically approaches C_D values of 1.13, 1.09, 1.04 for the 0.035, 0.07, and 0.105 l/d cylinders, respectively.

$C_{L'}$ plotted against Re is shown in figure 6a. The $C_{L'}$ values for a smooth cylinder are in agreement with those reported in Norberg (2001). The cavity cylinders had lower values of $C_{L'}$ than the smooth and the $k_s/d = 8.41 \times 10^{-3}$ cylinder. The cavity cylinders had lower values of $C_{L'}$ than the $k_s/d = 1.74 \times 10^{-3}$ cylinder from Re of 2.0×10^4 to 1.0×10^5 . The $k_s/d = 1.74 \times 10^{-3}$ cylinder had the lowest $C_{L'}$ values from Re of 1.2×10^5 to 1.6×10^5 . For the two uniformly rough cylinders, the lowest $C_{L'}$ value corresponds to their critical Re . Plots of unsteady drag and lift as a function of time (1 s) for different Re , show that variation is a function of vortex-shedding frequency and the natural frequency of the model. For all the cavity cylinders and the $k_s/d = 1.74 \times 10^{-3}$ cylinder, the variation in drag and lift was dominated by the vortex-shedding frequency. Conversely, for the smooth and $k_s/d = 8.41 \times 10^{-3}$ cylinder, the variation in drag had a greater amplitude of lower frequencies that mirrored the natural resonance frequency of the model (data not shown). St plotted against Re for the test cylinders is shown in figure 6b. There is little variation in St with Re for all cylinders. The cylinders with cavities have slightly higher St from $Re = 2 \times 10^4$ to 6×10^4 . No trends with C_D and $C_{L'}$ curves were obvious.

3.3. Free-end effects

Drag coefficients of flat-capped cylinders were less than their corresponding two dimensional cylinders (figure 7a); however, the trends in C_D curves for flat cylinders were similar to the trends of their corresponding two-dimensional cylinders. The flat-capped cylinders had no damping system. Consequently, cylinders experienced oscillations arising from the free end effect.

FIGURE 5. C_D vs Re for two-dimensional cylinders.FIGURE 6. (a) $C_{L'}$ vs Re for two-dimensional cylinders and (b) St vs Re for two-dimensional cylinders (legend see figure 5).FIGURE 7. (a) C_D vs Re for free-ended cylinders and (b) $C_{L'}$ vs Re for free-ended cylinders (legend see figure 5).

ing from the lack of stiffness in the force transducer. The large amplitude vibrations of the resonance frequency likely affected the C_L' curves (figure 7b) and vortex shedding.

4. Discussion

4.1. Pressure distribution

The greater pressure recoveries for cylinders with cavities than for smooth and rough cylinders suggests a decrease in drag for cylinders with cavities. The pressure recoveries differed slightly with location of the static port along the cavity and orientation of the cavity to the flow. When the apex of cavity juncture faced the flow, there were greater negative pressures on sides of the cylinders and slightly less pressure recovery, indicating slightly higher drag.

4.2. Drag, lift and vortex shedding

In general, an increase in cavity depth causes a decrease C_D . Over the entire Re range (2×10^4 to 2×10^5), the cylinders with cavities had lower C_D values than the smooth cylinder. Conversely, before their critical range, both uniformly rough cylinders had higher C_D values than the smooth cylinder. The cylinders with cavities had lower C_D values than the rough $k_s/d = 8.41 \times 10^{-3}$ cylinder with the exception of small Re range from 5×10^4 to 7×10^4 where all had equal values. For Re up to 1.2×10^5 , the cavity cylinders had lower C_D values than the $k_s/d = 1.74 \times 10^{-3}$ cylinder. Although roughness, $k_s/d = 1.74 \times 10^{-3}$, caused a larger C_D reduction at higher Re , cavities induce a lower C_D at lower Re and the reduction is sustained as C_D is almost independent of Re . Analogous to surface roughness, the cavities likely serve to trip turbulent transition but at an lower Re . The flat curves of the cavity cylinders have no obvious critical Re , which suggests that the transition to turbulence occurred at Re less than 2×10^4 . The fact that C_D does not drop rapidly with Re (as it does for the uniformly rough and smooth cylinders) may be biologically important to saguaros because rapid changes in force can damage a structure. The extent of the C_D reduction at higher Re remains unanswered. We suspect that the cavities have flow benefits up to Re on the order of 10^6 , because this range of C_D reduction likely corresponds to potentially damaging Re that saguaros commonly experience in their natural habitat with a possible added safety factor for those rarer, higher velocity gusts (30 ms^{-1}). For example, if a 0.5 m diameter saguaro commonly experiences gusts of 22 ms^{-1} and is likely to experience a top gust of 30 ms^{-1} at least once every 30 years, the C_D of saguaros is likely to have C_D reductions extending to 7×10^5 and possible further.

C_D values of saguaros may be influenced by factors not examined in this study. Depending on the orientation of the cavities to the flow, the C_D values for cavity cylinders likely differ somewhat from those reported in figure 5. When the cavity or cavity walls are facing the flow compared to the apex facing the flow, there is less negative pressures at the sides of the cylinders and base pressure recovery is slightly better. Since we tested only with cavity apices pointing into the flow for all cavity cylinders, the C_D values may be somewhat overestimated. We also expect that axial flow and angle of attack may be important factors in the drag reducing capability of cavities on saguaros. It is conceivable that the cavities induce axial flow (which may be induced from the free end). For cylinders spanning the tunnel, axial flow was most likely inhibited because cavities were filled in at the ends of the cylinders making the cylinders smooth between the endplates and the closest wall. Visualization experiments carried out in a low-speed smoke tunnel

suggest that longitudinal cavities affect axial flow and the symmetry of vortex shedding (Talley *et al.* 2001).

For the entire Re range, the cavity cylinders had a lower magnitude of fluctuating side-force than the smooth cylinder, and this was almost always the case for the $k_s/d = 8.41 \times 10^{-3}$ cylinder. For Re up to 1.1×10^5 , the cylinders with cavities had a lower magnitude of fluctuating side-force than the $k_s/d = 1.74 \times 10^{-3}$ cylinder. The ability to dampen fluctuating side-forces may be particularly important in keeping saguaros upright since large fluctuations in forces may break or dislodge roots. Variances in the unsteady drag and fluctuating side-forces correspond to the vortex shedding. All cylinders were attached to the same damping system and corrections were not made for damping and differences in the weights of the cylinders. The natural frequency of all cylinders was ≈ 8 Hz and resonance contributed slightly to variations in the unsteady drag and fluctuating side-forces. For the cavity cylinders and the $k_s/d = 1.74 \times 10^{-3}$ cylinder, the natural frequencies were less evident in the waveforms of the unsteady drag and fluctuating side-forces. The differences in amplitudes at resonance frequencies excited by vortex shedding needs to be investigated further.

4.3. Free-ended cylinders

The reduction in drag due to free-end effects is likely due to the low aspect ratio of the flat-capped cylinders ($5.5 h/d$). In nature, aspect ratios of saguaros likely fall between 5 and 23 (h/d). Free-end effects on drag have been shown to be important for aspect ratios ($h/d < 30$) (Zdravkovich *et al.* 1989), suggesting that end effects may be important for saguaros. Furthermore, hemispherical ends, such as those on saguaros, are likely to have even a greater effect on drag reduction (figure 2b). Longitudinal cavities may promote axial flow (Talley *et al.* 2001) and hemispherical caps with longitudinal cavities may cause even a further reduction in drag and fluctuating side-forces. This will be addressed in future studies.

Results for the flat-capped cylinders were obtained without a damping system. Recall that the force transducer used for the measurements lacks stiffness, allowing the cylinder to vibrate. In order to reduce structural vibration interactions with vortex shedding, a damping system needs to be employed. For the free-end cylinders, it is difficult to attach a damping system without affecting the flow conditions at the free end. Several attempts were made to control vibrations without affecting flow around the free end, but none were successful. We lowered the natural frequency of the model by filling the model with lead and copper; this brought the natural frequency down from 20 to 10 Hz; however, the amplitude was still great enough to interfere with the measurements. Next, we tried elastic dampers by making rubber, neoprene, and cork gaskets that varied in thickness; however, the benefit afforded by the elastic damping was counteracted by hysteresis effects. We also attached a damping system to the sides of the cylinder using piano wires that were pulled tight with weights (figure 8a). This added stiffness to the lift direction, but did not greatly improve the amplitude of the resonance vibrations. We stiffened the same system by using thicker wire in the tunnel and rods outside the tunnel, but this allowed only marginal improvement in the lift direction and no improvement in the drag direction.

5. Future studies

A new damping system will be employed to control natural resonance (figure 8b). Because the damping system will affect flow around the free end, experiments will be

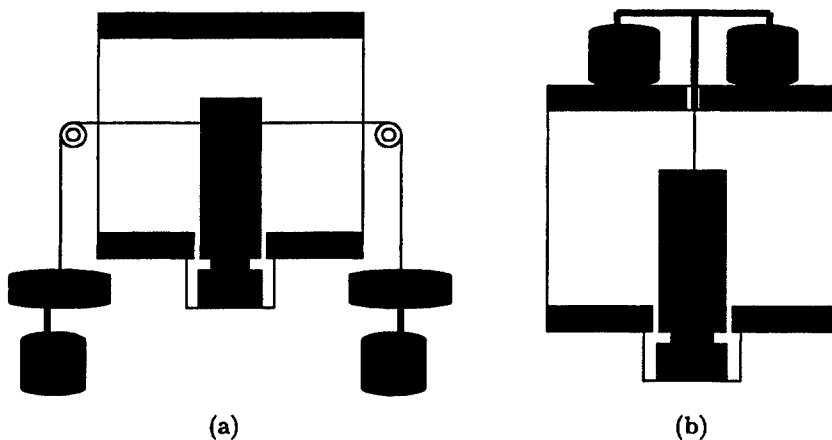


FIGURE 8. Damping systems (a) with wires and weights and (b) with rod from ceiling of tunnel.

performed with and without a damping system. Further work is required to assess the effect of longitudinal cavities in the range of Re relevant to the saguaro as well as with models that allow axial flow (i.e. hemispherical caps). Future experiments will obtain C_D curves over a range of Re from 2×10^4 (for computational comparisons) to 1×10^6 (limit of wind velocities in the saguaro habitat) and will include the effect of hemispherical caps and spines. Research may also include angle of attack, flexibility of the body and vortex induced vibrations.

Much about the physical characteristics of saguaros and their behavior in the wind remains elusive. Simple field measurements of aspect ratio and longitudinal changes in cavity depth need to be made. For structural interactions with wind, the natural frequency of a saguaro cactus needs to be measured in their natural habitat (sandy and/or rocky soils) both under dry and wet conditions. Saguars may have mechanisms to avoid vortex shedding frequencies coming into resonance with the natural bending frequencies. Simple video recordings of the saguaro during the monsoon, will provide information on the behavior of the saguaro in high wind velocities. Structural deformations and motion of the saguaro in wind may add or alleviate forces caused by the wind. Furthermore, bending of the saguaro stem in the wind may increase axial flow in cavities and my alleviate pressure recovery at the base.

6. Acknowledgements

This work is sponsored by the Center for Turbulence Research, Stanford University and NASA Ames. We are grateful to everyone that has made this work possible. We especially thank Dr. Parviz Moin, Dr. Peter Bradshaw, Dr. Nagi Mansour, Dr. John Eaton, Dr. Rabindra Mehta, Ross Bishop, Dr. Georgi Kalitzin, Ralf Socher, Gianluca Iaccarino, Larry Siebold, Alex Hsu, Loren Rideout, Simon Song, Bruce MacGregor, Vijay Somandepalli, Dr. Haecheon Choi, Dr. Javier Jiménez, Dr. Joel H. Ferziger, Tamer Zaki, and Gorazd Medic.

REFERENCES

- ACHENBACH, E. 1971 Influence of surface roughness on the cross-flow around a circular cylinder. *J. Fluid Mech.* **46**, 321-335.
- ACHENBACH, E. 1977 The effects of surface roughness on the heat transfer from a circular cylinder to the cross flow of air. *Int. J. Heat Mass Transf.* **20**, 359-362.
- ALCOCK, J. 1985 *Sonoran Desert Spring*. University of Chicago Press.
- ALLEN, H. J. & VINCENTI, W. G. 1944 Wall interference in a two-dimensional-flow wind tunnel, with consideration of the effect of compressibility. *NACA Report 782*.
- BEARMAN, P. W. & HARVEY, J. K. 1993 Control of circular cylinder flow by the use of dimples. *AIAA J.* **31**, 1753-1756.
- BENSON, L. 1981 *The Cacti of Arizona*. The University of Arizona Press.
- BULK, H. C. 1984 The Maximum Daily Wind Gust Speed Climatology at Sky Harbor Airport, Phoenix Arizona. *The Laboratory of Climatology, Arizona State Univ. Report 18*.
- DENNY, M. W. 1988 *Biology and the Mechanics of the Wave-Swept Environment*. Princeton University Press.
- FARELL, C. 1981 Flow around fixed circular cylinders: fluctuating loads. *ASCE J. Eng. Mech. Div.* **107**, 565-573.
- FOX, T. A., APELT, C. J. & WEST, G. S. 1993 The aerodynamic disturbance caused by the free-ends of a circular cylinder immersed in a uniform flow. *J. Wind Eng. Ind. Aerodyn.* **49**, 389-400.
- GELLER, G. N. & NOBEL, P. S. 1984 Cactus ribs: influence on PAR interception and CO_2 uptake. *Photosynthetica* **18**, 482-494.
- GIBSON, A. C. & NOBEL, P. S. 1986 *The Cactus Primer*. Harvard University Press.
- GÜVEN, O., FARELL, C. & PATEL, V. C. 1978 Surface-roughness effects on mean flow. *J. Fluid Mech.* **98**, 673-701.
- HODGE, C. 1991 *All About Saguaros*. Hugh Harelson/Arizona Highways, Phoenix.
- MEHTA, R. D. & PALLIS, J. M. 2001 Sports ball aerodynamics: effects of velocity, spin and surface roughness. *Materials and Science in Sports Conference*, Coronado, CA.
- NAKAMURA, Y. & TOMONARI, Y. 1982 Effects of surface roughness on the flow past circular cylinders at high Reynolds numbers. *J. of Fluid Mech.* **123**, 363-378.
- NIKLAS, K. J. 2002 Wind, size, and tree safety. *J. Arboric.* **28**, 84-93.
- NIKLAS, K. J. & BUCHMAN, S. L. 1994 The allometry of saguaro height. *Am. J. Bot.* **81**, 1161-1168.
- NIKLAS, K. J., MOLINA-FREANER, F., TINOCO-OJANGUREN, C. & PAOLILLO, D. J. 2002 The biomechanics of *Pachycereus pringlei* root systems. *Am. J. Bot.* **89**, 12-21.
- NOBEL, P. S. 1994 *Remarkable Agaves and Cacti*. Oxford University Press.
- NORBERG, C. 2001 Flow around a circular cylinder: Aspects of fluctuating lift. *J. Fluids Struct.* **15**, 459-469.
- PIERSON, E. A. & TURNER, R. M. 1998 An 85-year study of saguaro (*Carnegiea gigantea*) demography. *Ecology* **79**, 2676-2693.
- ROSHKO, A. 1961 Experiments on the flow past a circular cylinder at very high Reynolds number. *J. Fluid Mech.* **10**, 345-356.
- STEENBERGH, W. F. & LOWE, C. H. 1983 *Ecology of the Saguaro III*. National Park Service.

- SZEPESSY, S. 1994 On the spanwise correlation of vortex shedding from a circular cylinder at high Reynolds number. *Phys. Fluids* **6**, 2406-2416.
- TALLEY, S., IACCARINO, G., MUNGAL, G. & MANSOUR, N. 2001 An experimental and computational investigation of flow past cacti. *Annual Research Briefs*. Center for Turbulence Research, NASA Ames/Stanford Univ., 51-63.
- VOGEL, S. 1981 *Life in Moving Fluids*. Princeton University Press.
- ZDRAVKOVICH, M. M., BRAND, V. P., MATTHEW, G. & WESTON, A. 1989 Flow past short circular cylinders with two free ends. *J. Fluid Mech.* **203**, 557-575.

Numerical simulation of turbulent polymer solutions

By Y. Dubief

1. Introduction

Drag reduction using polymer additives in wall-bounded flows poses many challenges to our understanding of turbulence and polymer dynamics, due to the large spectrum of scales involved. Up to 80% of drag reduction can be obtained with ultra-dilute solutions of polymers with high molecular weight, for which each molecule is several orders of magnitude smaller than the smallest turbulent scale of the flow. Owing to this range of scales, numerical simulations as the ones presented here can tackle such flows only by using a continuum model for the polymer dynamics (Sureshkumar *et al.* 1997). The validity of the most popular models was assessed by comparing the evolution of polymer stress with Brownian dynamic (BD) simulations in simple shear, extensional or rotational flows (Herrchen & Öttinger 1997) but not in turbulent flows. For the latter, the validation has so far been limited to qualitative comparisons of turbulent statistics with experimental data, and only, to the knowledge of the author, for small drag reductions. Even though the agreement of the existing simulations is good, the extension of this type of comparison to higher drag reduction is therefore necessary, but not sufficient. It remains to be demonstrated that the polymer dynamics predicted by the model is consistent with corresponding BD simulations. The present paper uses, for one of the very first times, the two types of comparison to discuss the limitation of the numerical schemes used to solve the model.

For drag-reduced flows with polymers, turbulent statistics have been extensively characterized by experiments. Thus Warholic *et al.* (1999) established the existence of two distinct statistical regimes. For a given polymer molecule, the mean-velocity profile experiences an upward shift of its log-law region for the smallest concentration, up to a drag reduction (*DR*) of the order of 40%. This regime is referred to as the Low-Drag Reduction (LDR) regime. A further increase in concentration leads to a change in the slope of the log law which defines the High-Drag Reduction (HDR) regime. As more polymers are added, the flow tends toward an asymptotic state, called the Maximum Drag Reduction (MDR) regime, for which drag is slightly higher than the laminar state (Virk & Mickley 1970). The components of the Reynolds stress tensor $\overline{u_i u_j}$ decrease in magnitude when scaled with outer variables (here, the centerline mean velocity of the Poiseuille flow U_c and the channel half-width h) as *DR* increases. Yet the diminution of the rms u' of the streamwise velocity fluctuations is small compared to v' , w' or \overline{uv} and it results in an increase of the maximum of u'^+ in the wall region ($+$ denotes the scaling by inner variables based on the skin-friction velocity u_τ and the viscosity ν). LDR produces the largest maximum values of u'^+ whereas the peak seems to reduce back to the $DR = 0\%$ case at HDR and MDR. In this latter regime, Warholic *et al.* (1999) measured a vanishing Reynolds stress $-\overline{uv}$ as MDR is approached. The authors concluded that the polymer stress has to be the only source of energy which prevents relaminarization occurring. A more recent experiment by Ptasiński *et al.* (2001) supports the decreasing

trend of the Reynolds stress but found it to be non-negligible at MDR. It indicates that turbulence structures did not fully vanish in their experiments, adding more confusion as to how MDR could be defined.

In order to simulate all regimes of drag reductions, it has to be assumed that a viscoelastic model can be used. The first simulation of this kind by Sureshkumar *et al.* (1997), using the FENE-P model, proved to reproduce the shift of the log law in the mean-velocity profile, the increase of streamwise velocity fluctuations and reduction of transverse fluctuations observed at LDR. Sureshkumar *et al.* used spectral methods while recent results (Min *et al.* 2001; Dubief & Lele 2001) have shown that finite differences can produce similar results. By improving the robustness of the temporal scheme used in Dubief & Lele (2001) to solve the FENE-P model, it is shown in this paper that a state very similar to the one observed experimentally at HDR can be achieved. The comparison with experiments is extended to coherent structures in the near-wall region.

2. Numerical method

2.1. Formalism

Polymer dynamics has typical length scales much smaller than the smallest turbulent flow scales. Using traditional numerical schemes for flow simulation makes the explicit resolution of molecules unfeasible with current computer facilities; therefore the polymer field has to be modeled. The evolution of polymers is predicted from bead-spring (dumbbell) models. Each dumbbell is subject to the hydrodynamic forces exerted by the flow on the beads, the spring force and Brownian forces. The balance of forces gives an evolution equation for the end to end dumbbell vector \mathbf{q} , known as the FENE (Finitely Extensible Nonlinear Elastic) model. A constitutive approach is obtained by taking the Brownian motion into account, using a phase average of the product of the \mathbf{q} -components, which defines the conformation tensor $c_{ij} = \langle q_i q_j \rangle$. The hydrodynamic and relaxation (spring) forces are explicitly simulated; the latter force can be estimated with various models. The model used here is the FENE-P model, where P stands for the Peterlin function, f , defining the following set of equations

$$\partial_t c_{ij} + u_k \partial_k c_{ij} = c_{kj} \partial_k u_i + c_{ik} \partial_k u_j - \frac{1}{We} (f c_{ij} - \delta_{ij}), \quad (2.1)$$

$$f = \frac{1}{1 - c_{kk}/L^2}. \quad (2.2)$$

The parameter L is the maximum polymer extension and the Weissenberg number, We , the ratio of the polymer to the flow time scales and ensures the non-dimensionality of (2.1). Finally the contribution of polymers to the flow is brought in the momentum equations via the divergence of the polymeric stress tensor τ_{ij} ,

$$\tau_{ij} = \frac{1}{We} (f c_{ij} - \delta_{ij}), \quad (2.3)$$

yielding the viscoelastic momentum equations,

$$\partial_t u_i + u_j \partial_j u_i = -\partial_i p + \frac{\beta}{Re} \partial_j \partial_j u_i + \frac{1-\beta}{Re} \partial_j \tau_{ij}, \quad (2.4)$$

where β is the ratio of the solvent viscosity η_s to the total viscosity η . The last term in the r.h.s. of (2.4) is the contribution of the viscoelastic stress to the flow.

2.2. Spatial derivatives

The numerical code was described by Dubief & Lele (2001). The numerical method follows that of Min *et al.* (2001). Velocities are discretized on a staggered grid while the pressure and the polymeric tensors c_{ij} and τ_{ij} are located at the cell-center. Velocity derivatives are computed using second-order finite-difference schemes. To maintain good resolution, the polymeric stress derivatives are calculated with a non-dissipative fourth-order compact scheme. The advection terms of (2.1) are solved using a compact upwind scheme similar to Min *et al.* (2001), modified to guarantee at least third-order accuracy. Using the following upwinding coefficient,

$$\varepsilon = \frac{1}{2}(s^- + s^+), \quad (2.5)$$

where s^- and s^+ are the sign of the velocity at the interface of the cell, the compact scheme writes

$$(2 + 3\varepsilon)\phi'_{i-1} + 8\phi'_i + (2 - 3\varepsilon)\phi'_{i+1} = \frac{1}{6\Delta} [(-1 - \varepsilon)\phi_{i-1} + 2\varepsilon\phi_i + (1 - \varepsilon)\phi_{i+1}], \quad (2.6)$$

Like any upwind scheme, it introduces numerical dissipation at small scales, which proves to stabilize the solution of (2.1). However, as mentioned by Min *et al.* (2001), an extra dissipation has to be locally added, wherever the tensor c_{ij} is not positive-definite, i.e. when $\det(c_{ij}) < 0$. The number of nodes affected by the local artificial dissipation (defined in Min *et al.* 2001; Dubief & Lele 2001) depends on the strength of the flow, the length and Weissenberg number of the polymers and the coefficient of local artificial dissipation (LAD). The worst case is the uncoupled case as will be shown later; as much as 20% of grid points may have $\det(c_{ij}) < 0$ for high L and We . In drag-reduced flows, the number of points requiring LAD drops to significantly smaller fractions, of the order of 5% and less for LDR, and less than 1% for HDR. Further insight on this issue will be given in section 3.

2.3. Time-stepping technique

The numerical method used to solve (2.4) is based on a semi-implicit, fractional-step method (Le & Moin 1991). The Newtonian viscous stress in the wall-normal direction is advanced in time with the Crank-Nicolson scheme, while all other terms in (2.1) and (2.4) are advanced with a third-order Runge-Kutta (RK3) method. After solving (2.1) at time (l), the resulting algorithm is

$$\frac{u_i^{(*)} - u_i^{(l-1)}}{\Delta t} = -\gamma_l N_i^{(l-1)} - \zeta_l N_i^{(l-2)} + \alpha_l (L_i^{(l)} + L_i^{(l-1)} + T_i^{(l)} + T_i^{(l-1)}) \quad (2.7)$$

$$\partial_k \partial_k \phi = \frac{1}{\alpha_l \Delta t} \partial_k u_k^{(*)} \quad (2.8)$$

$$u_i^{(l)} = u_i^{(*)} - \alpha_l \Delta t \partial_i \phi \quad (2.9)$$

In (2.7), N , L and T denote the non-linear, viscous and polymeric terms, respectively. The index l is the substep of the RK3 and γ_l , ζ_l and α_l the corresponding coefficients:

$$\begin{aligned}\gamma_1 &= \frac{8}{15}; & \zeta_1 &= 0; & \alpha_1 &= \frac{4}{15} \\ \gamma_2 &= \frac{5}{12}; & \zeta_2 &= -\frac{17}{60}; & \alpha_2 &= \frac{1}{15} \\ \gamma_3 &= \frac{3}{4}; & \zeta_3 &= -\frac{5}{12}; & \alpha_3 &= \frac{1}{6}\end{aligned}$$

The use of a fully-explicit scheme for the time derivative in (2.1) appeared to be unstable under strong magnitude of turbulence or for large We . The relaxation force is extremely stiff when the trace c_{ii} approaches L^2 . Small time steps are then required to diminish numerical errors that might induce some local extensions to become larger than L^2 (Dubief & Lele 2001). From (2.1), it can be inferred that the simulation diverges to infinity when the Peterlin function (2.2) turns negative. Previous studies have used fully or semi-implicit scheme in order to avoid this issue. For FENE dumbbell simulations, Herrchen & Öttinger (1997) implemented a second order semi-implicit predictor-corrector scheme. The implicit part of this scheme yields a cubic equation for the length of the polymer which has a unique root within the physical bounds $q^2 \in]0; L^2[$. A similar method can be applied to the trace of (2.1) in which the relaxation term is solved implicitly and the stretching terms explicitly. Following the same numerical scheme as for the momentum equations (2.4), the time advancement of (2.1) is

$$\begin{aligned}\frac{c_{ij}^{(l)} - c_{ij}^{(l-1)}}{\Delta t} &= \gamma_l R_{ij}^{(l-1)} + \zeta_l R_{ij}^{(l-2)} \\ &\quad - \alpha_l \left[\frac{1}{We} \left(\frac{c_{ij}^{(l)}}{1 - c_{kk}^{(l)}/L^2} - \delta_{ij} \right) + \frac{1}{We} \left(\frac{c_{ij}^{(l-1)}}{1 - c_{kk}^{(l-1)}/L^2} - \delta_{ij} \right) \right],\end{aligned}\quad (2.10)$$

where

$$R_{ij}^{(l)} = -u_k^{(l)} \partial_k c_{ij}^{(l)} + (c_{ik}^{(l)} \partial_k u_j^{(l)} + c_{kj}^{(l)} \partial_k u_i^{(l)}) \quad (2.11)$$

By summing the equations for the diagonal components and using the variable $\psi^{(l)} = 1 - c_{kk}^{(l)}/L^2$, equation (2.10) can be simply recast into a second-order polynomial,

$$\begin{aligned}(\psi^{(l)})^2 + \left[\frac{\alpha_l \Delta t}{We} \left(2 + \frac{1}{\psi^{(l-1)}} - \frac{6}{L^2} \right) \right. \\ \left. + \frac{\Delta t}{L^2} (\gamma_l R_{ii}^{(l-1)} + \zeta_l R_{ii}^{(l-2)}) - \psi^{(l-1)} \right] \psi^{(l)} - \frac{\alpha_l \Delta t}{We} = 0,\end{aligned}\quad (2.12)$$

whose roots are real and of opposite sign. It can be shown that the unique positive root

$$\psi^{(l)} = \frac{1}{2} \left(-b + \sqrt{b^2 + 4 \frac{\alpha_l \Delta t}{We}} \right), \quad (2.13)$$

approaches zero as

$$\psi^{(l)} \sim \frac{2\alpha_l \Delta t}{b^2 We}, \quad (2.14)$$

when $b \gg 1$ (b is the coefficient of $\psi^{(l)}$ in 2.12). Note that this scheme can ensure only

that the trace is upper bounded ($\psi > 0$) but may allow negative values of c_{kk} ($\psi > 1$). The latter situation occurs wherever

$$\underbrace{\frac{\alpha_l \Delta t}{We} \left(1 + \frac{1}{\psi^{(l-1)}} - \frac{6}{L^2} \right)}_I - \psi^{(l-1)} + \underbrace{1 + \frac{\Delta t}{L^2} (\gamma_l R_{ii}^{(l-1)} + \zeta_l R_{ii}^{(l-2)})}_II > 0 \quad (2.15)$$

is not satisfied. In this equation, the term I is strictly positive for any $\psi^{(l-1)} \in]0; 1[$ when $L^2 > 3$, while II is subject to fluctuations in both the advection and the stretching terms of c_{ij} , which render the value of II with respect to I difficult to predict in a turbulent flow. Even though a positive Δt can always be found to ensure that (2.15) is satisfied, we are interested in time steps of the order of the time step of the flow when the *CFL* number is of the order of unity. The time constraint of the compact upwind scheme (2.6) requires *CFL* = 0.5 (Min *et al.* 2001), which turns out to be too high for the computation of (2.10). At this *CFL* number, the solution of the polymer field exhibit strong oscillations at high wavenumbers. For our flow conditions, *CFL* = 0.25 was enough to get rid of the high frequency oscillations, and marginal differences were found with results calculated at *CFL* = 0.025. These two simulations gave approximately the same fraction of grid points at which c_{ij} was not positive-definite. In order to get more insight in the behavior of the term II in (2.15), a simulation was performed without the advection term, so that the polymers do not move with the flow; it was found that the determinant of c_{ij} was negative for only $\sim 10^{-3}\%$ of the nodes for *CFL* = 0.25 and that (2.15) was always satisfied. In this numerical experiment, it can be argued that there is not enough stretching to create a breakdown of (2.15), since the small-scale structures are advected and the polymers are not. The simulation discussed in the next section, where the Eulerian advection is replaced by a Lagrangian, does not experience any loss of positiveness of the conformation tensor. The Eulerian advection can therefore be identified as the major cause of instabilities and unphysical solutions in the computation of the discrete evolution equations of c_{ij} , 2.10). It should be noted that the conditions (2.15) and $\det(c_{ij}) > 0$ are necessary but not sufficient. We are currently investigating a modification of the procedure of Min *et al.* (2001) for which the lost of positiveness is defined as $(\lambda_k(\mathbf{x}) \geq 0; k = 1, 3$, where $\lambda_k(\mathbf{x})$ is the k^{th} eigenvalue of $c_{ij}(\mathbf{x})$.

3. ‘Eulerian vs. Lagrangian’ or the problem of pure advection

The FENE-P equations are derived from molecular theories, which predicts the evolution of a single molecule as a function of hydrodynamic, entropic and Brownian forces. In this particular framework, particles move with the flow and the advection term in (2.1) reproduces this motion in the macroscopic formalism. In the Stanford group working on polymers, Mr. V. Terrapon is in charge of Brownian Dynamic simulation of polymer molecules represented as particles moving with the flow. This method allows the study of the effects of the flow on polymers without back-coupling, due to the inadequate number of particles ($\sim 10^5$ in a minimal channel flow unit). The comparison of this microscopic approach with our macroscopic formalism can be made simply by solving (2.1) without the advection terms on the particles which are advected in a Lagrangian manner (called hereafter Particle-Tracking, PT):

$$\frac{d\mathbf{x}_p}{dt} = \mathbf{u}(\mathbf{x}_p), \quad (3.1)$$

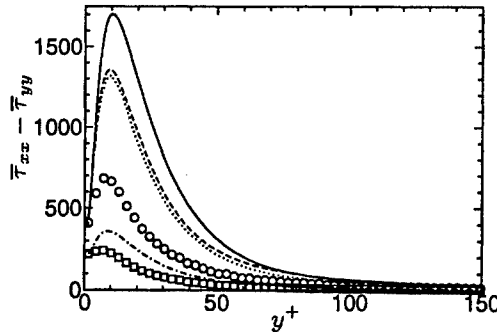


FIGURE 1. Normal stress profiles of the viscoelastic simulation compared to the particle-tracking (PT) simulation. All simulations are run at $We_\tau = 35$. $L = 60$: —, $64 \times 129 \times 32$; - - -, $96 \times 151 \times 48$; ······, $128 \times 257 \times 128$; \circ , PT. $L = 30$: ——, $96 \times 151 \times 48$; □ PT.



FIGURE 2. Snapshots of c_{kk}/L^2 in the $y-z$ plane for different resolutions, from left to right: $64 \times 129 \times 32$; $96 \times 151 \times 48$; $128 \times 257 \times 128$. Only the lower half of the channel is shown. The scale goes from white (0%) to black (90%).

where \mathbf{x}_p is the location of a particle in the flow. The simulations are run with identical polymer and flow parameters: $L = 60$ and 30 , $We = 3.0$, $\beta = 1$. In the PT simulation, the average is performed over small bins in the wall-normal direction. The mean normal stress is plotted as a function of y^+ in figure 1. For both polymer lengths, the overestimation of the Eulerian method is obvious, and the averaging due to the bins for the PT statistics has a very small effect compared to the magnitude of the discrepancy. For stiff polymers ($L = 30$), the difference is slightly smaller than for $L = 60$. In the latter case, increasing the number of grid points brings the macroscopic solution closer to the microscopic one, yet the error remains large. Figure 2 displays snapshots of c_{kk} in cross-planes for three different resolutions. The finer the resolution, the thinner the regions of highly-stretched polymer. For the coarsest grid, the discretized solution does predict high stretch of the vortices; however this phenomenon is spread over several grid points, yielding these large dark regions. The diffusion is not only due to the use of artificial dissipation. Obviously, the conformation tensor equations generate small scales and sharp gradients that are of energetic importance to the polymer dynamics. As the discretized Navier-Stokes equations behave in LES by increasing the streak dimensions to fit a coarse grid, the discretized equation (2.1) seems to adjust its physics to the grid.

As was implied in the previous section, the advection term cannot be handled without dissipation and was found to cause unphysical solutions. Taken alone as a pure advection equation, such an equation is known to produce extremely sharp gradients, impossible to

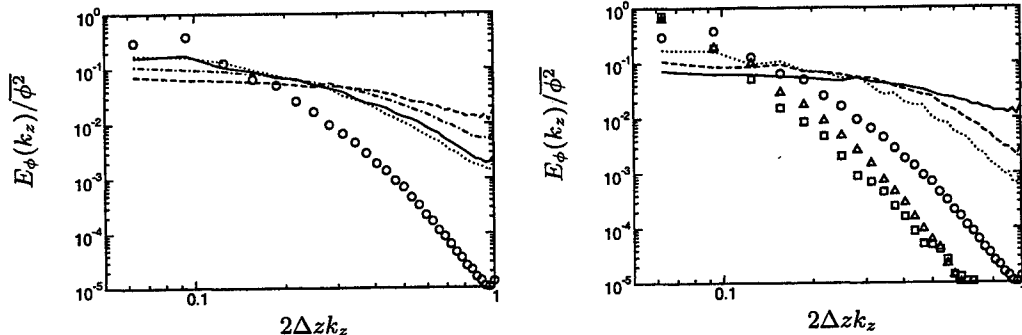


FIGURE 3. Spectral distributions of the streamwise velocity and polymer stress fluctuations. *Left:* $DR = 0\%$. \circ : u ; —: τ_{xx} ; - - -: τ_{yy} ; ·····: τ_{zz} ; ——: τ_{xy} . *Right:* Symbols and lines show spectra of wall-normal velocity and polymer stress, respectively. \circ , —: $DR = 0\%$, \triangle , - - -: $DR = 20\%$; \square , ·····: $DR = 65\%$. The spectra are normalized by their respective variance.

capture numerically without any artifacts such as artificial diffusion. In the conformation tensor equations, the stretching and entropic terms relate to scales imposed by the flow, from the largest to the Kolmogorov scale ($\eta = \nu^{3/4}/\varepsilon^{1/4}$, where ε is the dissipation rate), and the relaxation time controlled by the Weissenberg number. Intuitively, it could be assumed that small eddies would create thin regions of polymer stretch and, in such a case, advection is likely to act on these regions to produce smaller scales. How small depends merely on a diffusive phenomenon, which is not explicit in (2.1), since the diffusion of polymer molecules in the solvent is extremely low. A rough estimation of a Schmidt number would be $10^5 \sim 10^6$. The stretching and entropic terms indicate that the behavior of a polymer molecule is not related to its neighbors but depends on the flow scales it experiences locally. Therefore, as a first approximation, it is tempting to draw an analogy between (2.1) and a passive-scalar equation at very high Schmidt number ($Sc = \nu/\kappa$, where κ is the scalar diffusion), with the addition of a source term containing the hydrodynamic and entropic forces.

The spectral properties of the passive-scalar equation,

$$\partial_t \theta + u_j \partial_j \theta = \frac{1}{ScRe} \partial_j \partial_j \theta, \quad (3.2)$$

were first studied by Batchelor (1959) and Batchelor *et al.* (1959). At small scales, their analysis predicts two distinct behaviors of the passive-scalar spectrum depending on the value of Sc relative to unity. For $Sc < 1$, they found that the spectrum of the variance of scalar fluctuations advected by the velocity scales from the inertial subrange should decay as $E_\theta(k) \sim k^{-17/3}$, for wavenumbers greater than $k_B = Sc^{3/4}/\eta$. For $Sc \gg 1$, the theory predicts the so-called Batchelor spectrum,

$$E_\theta \sim k^{-1}, \quad (3.3)$$

valid from the Kolmogorov wavenumber up to the Batchelor wavenumber,

$$k_B = \frac{Sc^{1/2}}{\eta}. \quad (3.4)$$

If the conformation tensor equations (2.1) were to be derived including the actual diffusion of polymers, the length scale would be 10^{-2} to 10^{-3} smaller than η , assuming that the effect of the source term could be disregarded. The analogy with the passive scalar

finds some support in the comparison of spectral distributions of the polymer stress to those of velocity. Figure 3 displays spectra, which are normalized by their respective variance to make comparisons easier. It is striking that the polymer stress contains considerable energy at the highest wavenumbers resolved. This result is not surprising since polymers are expected to be mostly affected by small scales. However this plot demonstrates that our resolution i ($\Delta z^+ = 4.5$) is far from sufficient in the uncoupled case ($DR = 0\%$). The local character of the artificial dissipation used to stabilize the advection term is equivalent to a MILES approach, which could be defined as a large-eddy simulation where the subgrid-scale model is embedded in the numerical scheme. All the energy contained at the highest wavenumbers is contaminated by the dispersion of our finite difference schemes. An energy backscatter could be a solid assumption to explain the discrepancy with PT simulations (Fig 1). Also plotted in figure 3 is the evolution of the spectra of v and τ_{yy} with increasing DR . The reduction in the small scale energy of the velocity field allows polymer stress spectra to drop faster at high wavenumbers, although the decay is obviously very different from that of the velocity. At HDR, the decay of spectral energy or τ_{ij} is sufficient that a fairly coarse grid can be used. An ongoing resolution study for this regime suggests that the coarsest grid used in figure 1 gives results in good agreement with simulations at higher resolution.

The implementation of a subgrid-scale model for the advection term only is currently being investigated, and it has so far been found to improve the solution regarding the loss of positiveness of c_{ij} . Statistics are being gathered to assess the effect on polymer-stress statistics.

4. Results

In this section, three simulations are discussed. The Reynolds number based on the channel half-width and the centerline velocity is 7500, which translates into $h^+ = 295$ when $DR = 0\%$. This study aims at comparing the solution obtained with a minimal channel flow and the one computed from a domain four times the length and span of a minimal channel flow. These simulations respectively predict $DR = 67\%$ and $DR = 47\%$ with $L = 60$, $\beta = 0.9$ and $We_\tau = 84$. A third simulation using the large computational domain is also presented, for which the length and Weissenberg number are increased ($L = 100$, $We_\tau = 120$). The drag reduction is 60%. All simulations are performed on grid with a constant resolution of $\Delta x^+ = 15$, $\Delta y^+ = 0.1 - 8$ and $\Delta z^+ = 9$, when normalized by the skin friction at $DR = 0\%$.

4.1. Velocity statistics

The effect of the domain size on the mean velocity is quite dramatic (figure 4). While the minimal channel predicts an MDR regime, the larger domain produces a regime which appears to be close to the lower bound of the HDR regime. It is obvious that the HDR regime is populated by very-large-scale structures that have an impact on the drag and therefore need to be resolved. The fact that turbulence does not vanish in the minimal channel flow demonstrates that these very large scales are yet not of the highest importance for the dynamics of the flow. Our hope to achieve MDR by increasing the polymer length and elasticity has not been rewarded, but the trend is encouraging. Also plotted in figure 4 are the data obtained by Dr. White and Mr. Somendapalli, who take care of the experimental study at Stanford. The agreement is very good for $DR = 47\%$ and a departure is observed for the MDR case near the centerline. The experiment has been shown to have strong inhomogeneities in the polymer distribution across the

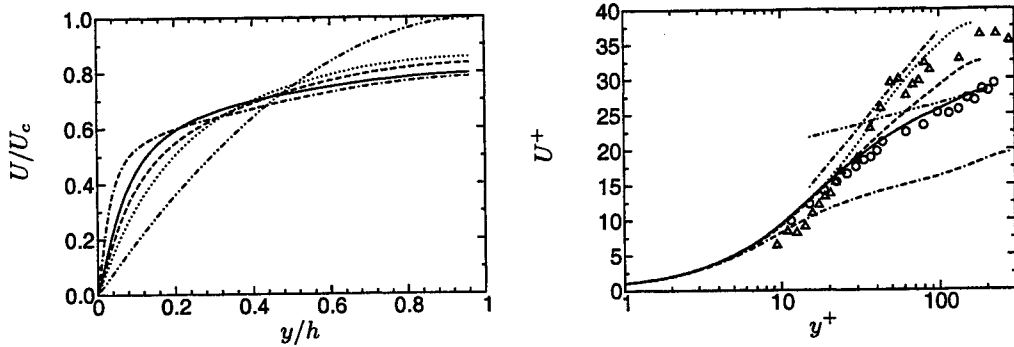


FIGURE 4. mean-velocity profiles in outer (left) and inner (right) variables. Simulations on the large domain: ·····, $DR = 0\%$; —, $DR = 47\%$; -·-, $DR = 60\%$; ·····, $DR = 67\%$. Minimal domain: ·····, $DR = 45\%$; △, $DR = 67\%$. Experimental data: ○, $DR = 45\%$; △, $DR = 67\%$. Analytical profiles: —, Virk's asymptote $U^+ = 11 \ln y^+ + 17$; — (left), Poiseuille profile; —··· (right), translated log law $U^+ = 2.5 \ln y^+ + 15$

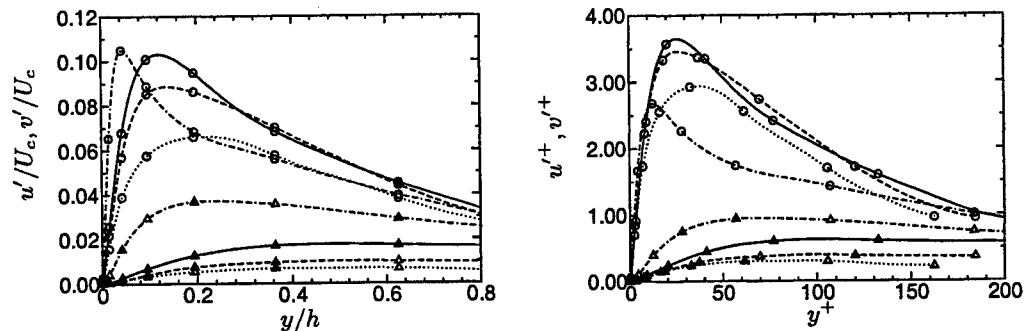


FIGURE 5. RMS of velocity fluctuations in outer (left) and inner (right) variables. Lines as defined in figure 4. ○ : u' ; △ : v' .

boundary layer, resulting in the existence of turbulent structures in the outer region of the flow. The near-collapse of the mean velocity profile in the minimal channel with Virk & Mickley (1970)'s asymptote can be attributed to the insufficient length and span of the outer region. As seen in figure 4, mean-velocity profiles at HDR retain a shape typical of turbulence rather than tending toward the laminar profile.

The turbulent intensities decrease as drag reduction increases, as shown in figure 5 (left). The peak of u' shifts away from the wall, but its magnitude decreases slowly compared to v' (w' behaves as v' and consequently is omitted from the plot for clarity). This difference is clear when inner scaling is used. In drag reduced flow, the maximum of u'^+ is actually higher or comparable with the $DR = 0\%$ case, as found in experiments (Warholic *et al.* 1999; Ptasinski *et al.* 2001). These plots suggest that extremely long and elastic polymers are needed to damp the turbulence, according to the prediction of the FENE-P model. At HDR, the polymer stress (not shown here) is low and therefore the inability of the FENE-P model to predict MDR for polymers, which are more elastic and concentrated than a typical PEO solution, indicates that internal modes may no longer be ignored. The major interest of the minimal channel flow experiment is to understand where the energy which sustains the turbulence comes from. The Reynolds stress, when normalized by outer length scales, diminishes by an order of magnitude in the upper HDR regime (figure 6). In inner variables, the Reynolds stress appears to be

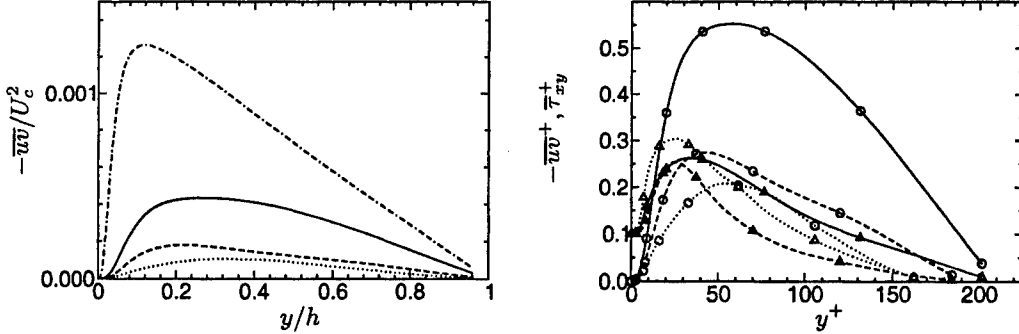


FIGURE 6. *Left:* Reynolds stress normalized by outer variables. *Right:* Reynolds stress \circ and polymer stress \triangle normalized by inner variables. Lines as defined in figure 4

only reduced by a factor of 4 for $DR = 67\%$, which is consistent with Ptasiński *et al.* (2001) but disagrees with Warholic *et al.* (1999) who found a near-zero Reynolds stress at MDR. The contribution of the polymer stress in the balance,

$$-\frac{\bar{uv}}{u_\tau^2} - \left(1 - \frac{y}{h}\right) + \frac{\beta}{u_\tau^2 Re} \frac{\partial U}{\partial y} + \frac{1-\beta}{u_\tau^2 Re} \bar{\tau}_{xy} = 0, \quad (4.1)$$

is of the same order as the Reynolds stress in our simulations of HDR, even larger in the case of the minimal channel. In spite of the incomplete physics simulated in the minimal channel, such simulation provides extremely valuable information about what MDR could be. Thus it can be surmised that MDR is purely a near-wall phenomenon, since $\bar{\tau}_{xy}^+$ is larger than $-\bar{uv}^+$ from the wall up to $y^+ = 70$. Considering the weak magnitude of the turbulent intensities, the polymer dynamics is likely to be driven by shear-dominant event. It should be noted that Warholic *et al.* (1999) and Ptasiński *et al.* (2001) suggested also that MDR is sustained by polymer stress alone.

4.2. Structure of the HDR turbulence

Using an appropriate vortex-identification scheme (the Q -criterion in the present case, $Q = (\Omega_{ij}\Omega_{ij} - S_{ij}S_{ij})/2$, Dubief & Delcayre 2000), figure 7 illustrates the dramatic modification of coherent vortical structures between the Newtonian flow and the HDR regime. At HDR, near-wall vortices are weaker and more horseshoe-type vortices can be found. The weakening of the vortices has also been observed by our experimental group, together with an increase of streak dimensions as depicted by the contours of the polymer stretch c_{kk} at the wall. Due to the no-slip condition, the dynamics of c_{kk} at the wall is driven by $\partial u / \partial y$. So far, the streamwise coherence of the streaks has not been determined either experimentally or numerically. Experimental data indicate that they could be several thousands of wall units long. Also shown in figure 7, the polymer stretch $\sqrt{c_{kk}}/L$ in the channel flow (contours on the side walls) exhibits completely different patterns for the Newtonian simulation and the HDR regime. In the former, regions of high stretch are observed to extend in the wall-normal direction and they are found to correlate with upwash and downwash motions of the flow (not shown here). For the HDR regime the polymer field is organized in thin layers which seem to denote the energetic activity of the polymers in the near-wall region.

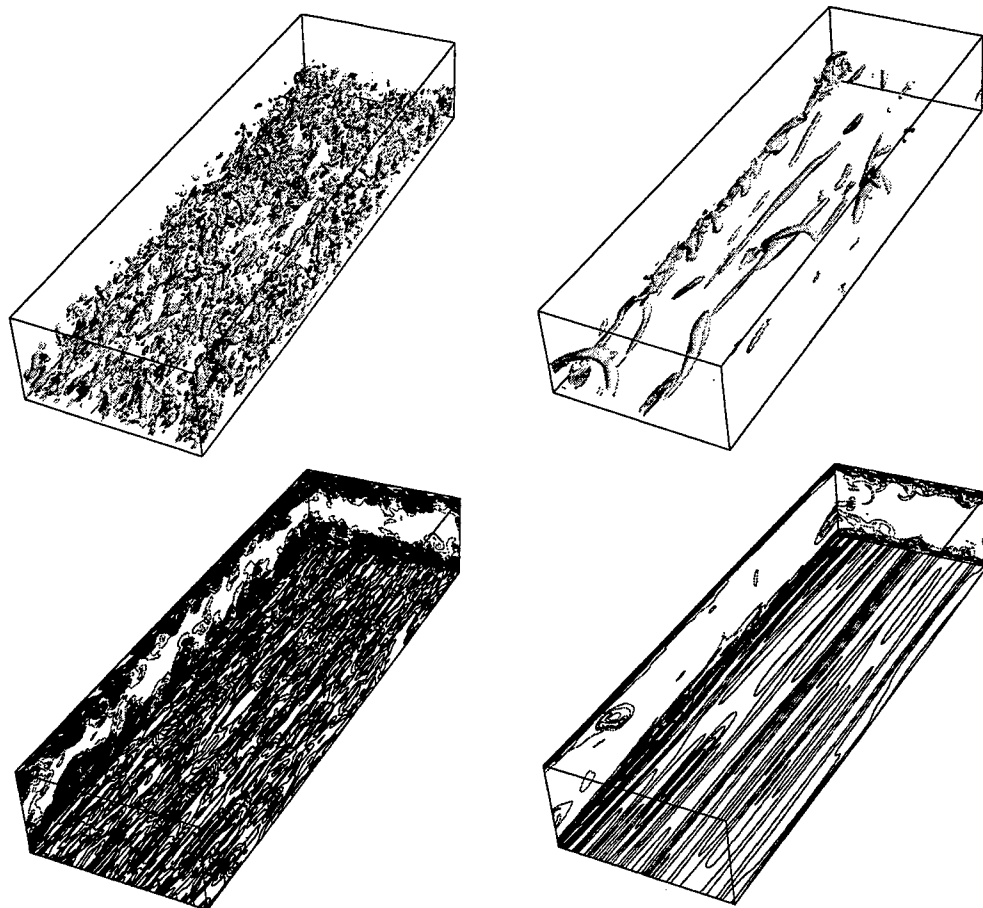


FIGURE 7. Snapshot of vortices (*top*) and polymer stretch (*bottom*) for the Newtonian case (*left*) and HDR (*right*). The vortices are identified with the Q -criterion: $Q = 0.5h^2/U_c^2$ for the Newtonian flow and $Q = 0.08h^2/U_c^2$ for HDR.

5. Perspectives

The simulation of turbulent viscoelastic flows requires overcoming many obstacles, and the present work only partially resolves the major issues. Although desirable, the implementation of a subgrid scale for the advection in the conformation tensor equation is not expected to resolve the discrepancy between the Eulerian and Lagrangian approaches. This study has at least shown the importance of solving scales close to Kolmogorov with as little dissipation for the polymer stress as possible. The size of the computational domain is another issue addressed by this paper. It is not clear how long the channel needs to be, since experimental observations indicate that streaks might be coherent over several thousands wall units. Nevertheless, it is remarkable that, in spite of a simplistic model and unresolved (large and small) scales, our simulations reproduce many features observed experimentally in the HDR regime.

Based on our results obtained experimentally and numerically at the macroscopic and microscopic levels, some advances have been made regarding the understanding of the phenomenon of drag reduction with polymer additives. In publications to appear, it will

be demonstrated that polymer drag reduction is purely a near-wall phenomenon, which affects almost exclusively quasi-streamwise vortices.

The support of DARPA is gratefully acknowledged.

REFERENCES

- BATCHELOR, G. K. 1959 Small-scale variation of convected quantities like temperature in turbulent fluid. part 1. general discussion and the case of small conductivity. *J. Fluid Mech.* **5**, 113–133.
- BATCHELOR, G. K., HOWELLS, I. D. & TOWNSEND, A. A. 1959 Small-scale variation of convected quantities like temperature in turbulent fluid. part 1. the case of large conductivity. *J. Fluid Mech.* **5**, 134–139.
- DUBIEF, Y. & DELCAYRE, F. 2000 On coherent-vortex identification in turbulence. *J. of Turbulence* **1** (011).
- DUBIEF, Y. & LELE, S. K. 2001 Direct numerical simulation of polymer flow. *Center For Turbulence Research*, NASA Ames/Stanford Univ., 197–208.
- HERRCHEN, M. & ÖTTINGER, H. C. 1997 A detailed comparison of various FENE dumbbell models. *J. Non-Newtonian Fluid Mech.* **68**, 17–42.
- LE, H. & MOIN, P. 1991 An improvement of fractional step methods for the incompressible Navier-Stokes equations. *J. Comp. Phys.* **92**, 369–379.
- MIN, T., YOO, J. Y. & CHOI, H. 2001 Effect of spatial discretization schemes on numerical solutions of viscoelastic fluid flows. *J. Non-Newtonian Fluid Mech.* **100**, 27–47.
- PTASINSKI, P. K., NIEUWSTADT, F. T. M., VAN DEN BRULE, B. H. A. A. & HULSEN, M. A. 2001 Experiments in turbulent pipe flow with polymer additives at maximum drag reduction. *Flow, Turbulence and Combustion* **66** (2), 159–182.
- SURESHKUMAR, R., BERIS, A. N. & HANDLER, R. A. 1997 Direct numerical simulations of turbulent channel flow of a polymer solution. *Phys. Fluids* **9** (3), 743–755.
- VIRK, P. S. & MICKLEY, H. S. 1970 The ultimate asymptote and mean flow structures in Tom's phenomenon. *Trans. ASME E: J. Appl. Mech.* **37**, 488–493.
- WARHOLIC, M. D., MASSAH, H. & HANRATTY, T. J. 1999 Influence of drag-reducing polymers on turbulence: effects of Reynolds number, concentration and mixing. *Exp. Fluids* **27**, 461–472.

Flat-plate boundary-layer transition in hypersonic flows

By C. Stemmer

1. Motivation and objective

Knowledge on transitional flows at elevated Mach numbers is very limited due to the immense difficulty in conducting experiments – be it wind-tunnel or free-flight. Therefore, direct numerical simulation provides a very powerful tool to gain significant insight into these high-temperature flows. These high-temperature hypersonic flows become chemically reacting creating additional challenges for the modeling of chemical reactions and the thermodynamic properties of such flows. The simulation of laminar-turbulent transition in boundary-layer flows for entry scenarios can deliver estimates of flight-relevant physical properties such as drag and heat transfer important for the flight path design and the design of the heat shield of an entry vehicle, respectively.

Early efforts to investigate hypersonic flows involved rockets in free-flight experiments, where qualitative results were obtained for the transition location (see Schneider (1999)). These experiments, according to Schneider, are not very reliable in terms of quantitativeness since the angle of attack is not measured accurately enough. Recent efforts to investigate hypersonic flows include Ma=21 experiments by a Russian group, Mironov & Maslov (2000), at Novosibirsk, which can serve as a qualitative comparison to the presented direct numerical simulations. Free-flight hypersonic experiments are not to be expected in the near future due to the sheer cost involved.

Direct numerical simulations with high-order finite-difference schemes shall be employed to unveil some of the important mechanisms in the evolution of laminar-turbulent transition in flat-plate boundary-layer flows. The differences between transition assuming ideal-gas and chemically-reacting flows is the main goal of this ongoing investigation.

2. Numerical method

The well-documented numerical method developed by Adams (1996), Adams (1998) and Adams (2000) for turbulent compression-ramp flow is employed for the high Mach-number simulations. The discretization is on the base of the conservative, compressible Navier-Stokes equations. The mesh is uniform in the downstream direction and variable in the wall-normal direction allowing for the collocation of grid points at the boundary-layer edge. The numerical method is a compact one and sixth-order accurate in space with periodic boundary conditions in the spanwise direction. The time advancement is done with a Runge-Kutta time integration scheme of third order accuracy. Very sharp gradients that cannot be resolved through the numerical scheme are captured in all three spatial directions through a hybrid ENO-scheme singling out the regions where it needs to be applied only. For the incorporation of the chemical and thermal high-temperature effects, the modeling of Stemmer & Mansour (2001) is used.

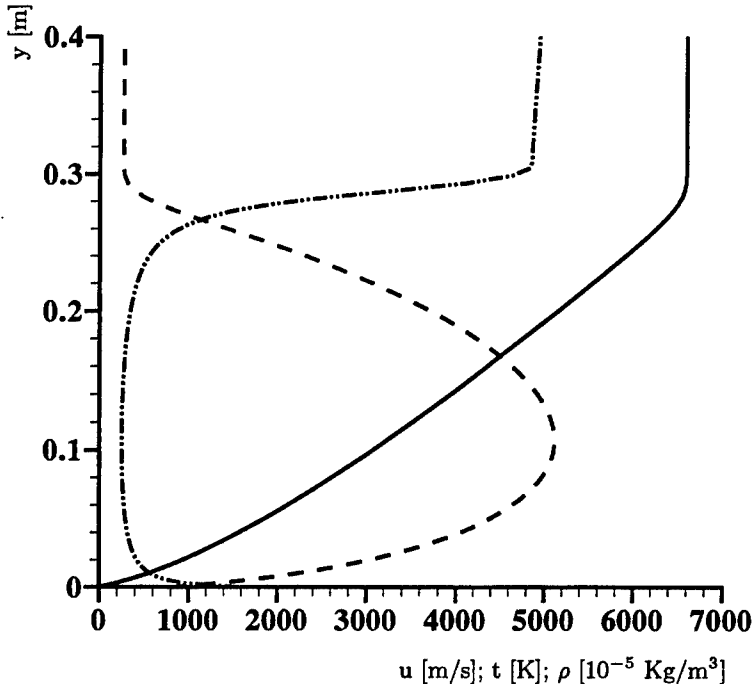


FIGURE 1. Wall-normal profiles of streamwise-velocity, temperature and density for $\text{Re}_x = 4 \cdot 10^6$ in dimensional units. Note that the density has been multiplied by a factor of 10^5 to show on the graph.

Disturbances are introduced at the wall through a disturbance strip. Blowing and suction is applied simultaneously to ensure that zero net mass is introduced at any one time step (see Eißler, (1995))

$$\begin{aligned} (\rho v)|_{wall} &= Ag(z, t) \frac{81}{16} \zeta^3 (3\zeta^2 - 7\zeta + 4), \quad 0 \leq \zeta \leq 1, \\ (\rho v)(2 - \zeta)|_{wall} &= -A(\rho v). \end{aligned} \quad (2.1)$$

The function $g(z, t)$ is a trigonometric function in time and space.

The dimensional quantities of the Ma=20 flow at free-stream conditions at an altitude of H=50km are $U_\infty = 6596 \text{ m/s}$, $\rho_\infty = 1.027 \cdot 10^{-3} \text{ Kg/m}^3$, $T_\infty = 270.65 \text{ K}$ and the viscosity is $\mu_\infty = 1.703 \cdot 10^{-5} \text{ Kg/(m \cdot s)}$ according to the US Standard Atmosphere (1976). An isothermal case is investigated with $T_{wall} = 3T_\infty = 811.95 \text{ K}$.

The ideal gas boundary layer equations, Anderson (1989), were solved for the starting solution of the base-flow calculations. The wall-normal profiles of downstream velocity (u), temperature (t) and density (ρ) are shown in figure 1. The sharp rise in density at the boundary-layer edge ($y=0.29 \text{ m}$) is a prominent feature of the boundary-layer profiles, which underlines the necessity of a fine resolution at that wall-normal position.

For the present simulation, a resolution of $1500 \times 240 \times 6$ points in x , y and z -direction are used. This yields a resolution of $\Delta x = 0.066$, $\Delta y_{min} = 7.717 \cdot 10^{-3}$ and $\Delta z = 0.146$, where the lengths are made dimensionless with the boundary-layer thickness $\delta_1 = 0.2197 \text{ m}$.

In deviation to the ideal gas case, vibrational degrees of freedom were incorporated in the code for the calculation of the thermodynamic properties.

3. Stability properties

After Lees & Lin (1946) had laid the foundation of a compressible stability theory through an asymptotic viscous approach, Mack (1969) developed the full parallel theory for finite Reynolds numbers. The stability properties are evaluated through linearization of the complete Navier-Stokes equations in a locally parallel flow. The disturbances are assumed to be harmonic in nature

$$q'(x, y, z, t) = q(y) \exp [i(\alpha x + \beta z - \alpha c t)], \quad (3.1)$$

where $q = \{u, v, w, \rho, p, t\}$. The wave numbers α and β are complex in the most general sense and describe temporal as well as spatial growth. The reader is kindly referred to Gaster (1965) for the transformation of spatial amplification rates into temporal amplification rates and vice versa.

Mack's original computer code for ideal-gas flows was available to produce the presented stability results for the $Ma=20$ flow. Mack normalizes the stability results with the Reynolds number defined as

$$R_x = \sqrt{Re(x)} = \sqrt{\left(\frac{\tilde{\rho} \tilde{U} \tilde{x}}{\tilde{\mu}} \right)}, \quad (3.2)$$

where variables with a tilde denote dimensional variables. The wall-normal coordinate \tilde{y} is non-dimensionalized through

$$\eta = \tilde{y} \cdot \frac{R_x}{\tilde{x}}. \quad (3.3)$$

The boundary-layer thickness for this case is $\eta(\delta) \approx 29.1$.

The frequency parameter F is defined as $F = f 2\pi \tilde{\mu} / (\tilde{\rho} \tilde{U}^2)$. For the dimensionless frequency of $F = 3.6416 \cdot 10^{-5}$, the dimensional frequency is $f = 15.2$ KHz. Firstly, two-dimensional disturbances are investigated since they turn out to be the most amplified waves for the chosen frequency. The spatial amplification rate $-\alpha_i$ over a wide range of Reynolds numbers is shown in figure 2 compared to two-dimensional disturbances with a slightly higher frequency. For the higher frequency, the same pattern appears but is shifted to smaller Reynolds numbers R_x . Two local peaks of the spatial amplification can be identified at $R_x \approx 1000$ and $R_x \approx 2250$. Comparing the eigenfunctions for the pressure p at these respective Reynolds numbers, one can identify the first peak with a first mode disturbance (according to the classification by Mack). At these high Mach numbers, the areas of instability merge and the amplification rate shows unstable waves as the eigenfunctions switch to a second mode disturbance. The peak at $R_x \approx 2250$ is associated with such a disturbance exhibiting a zero in its wall-normal amplitude profile. The number of zeros is one less than the mode number given by Mack. At $R_x \approx 3500$, the third mode is present with a slightly lower peak in the amplification rates. Downstream of $R_x \approx 4000$, the two-dimensional disturbance will encounter damping as the amplification rate $-\alpha_i$ becomes negative for this frequency.

The phase velocities of the unstable eigensolution is shown in figure 3. Inviscid theory predicts a phase speed of $c_{ph} = 1 - \frac{1}{Ma} = 0.95$ which is very close to the observed phase velocities of $c_{ph} \approx 0.98$ which in turn is very close to the free-stream velocity. Every peak in the spatial amplification rates coincides with a local minimum in the phase velocities.

Wall-normal profiles of the eigensolutions of the stability problem are shown at the local Reynolds number of $R_x = 1000$ (first mode disturbance) in figure 4. This two-dimensional mode represents the first peak in figure 2. The eigenfunctions of the downstream velocity

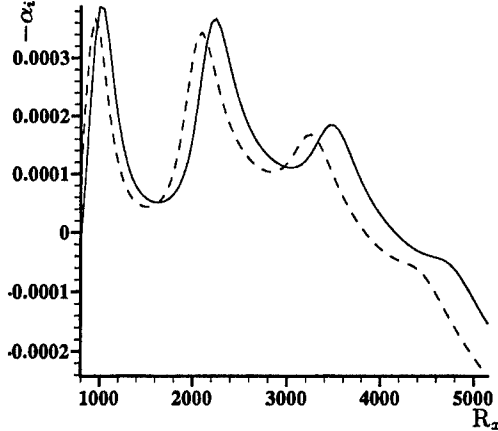


FIGURE 2. spatial amplification rates $-\alpha_i$ vs. the downstream direction for two-dimensional disturbances at $F=3.6416 \cdot 10^{-5}$ (—) and $F=3.9 \cdot 10^{-5}$ (---)

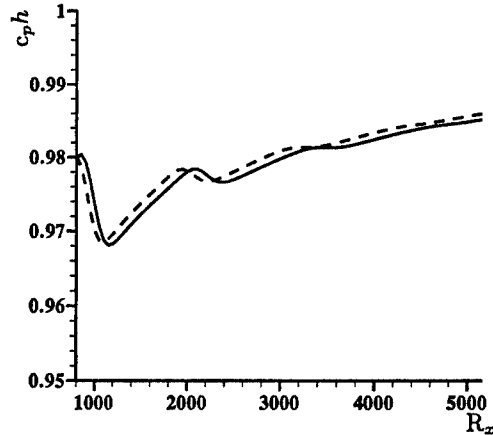


FIGURE 3. phase velocity $c_p h$ vs. the downstream direction for two-dimensional disturbances at $F=3.6416 \cdot 10^{-5}$ (—) and $F=3.9 \cdot 10^{-5}$ (---)

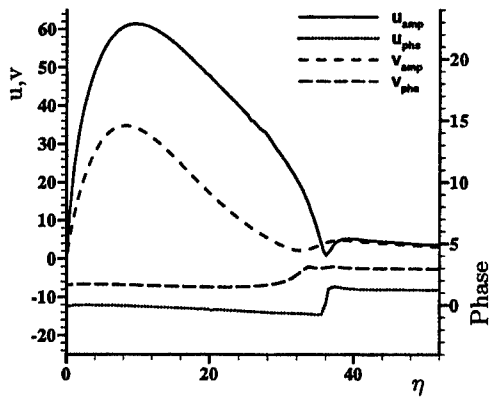


FIGURE 4. u and v eigensolutions at $R_x=1000$ for two-dimensional disturbances at $F=3.6416 \cdot 10^{-5}$. u_{amp} (—), v_{amp} (---), u_{phs} (····), v_{phs} (—·—).

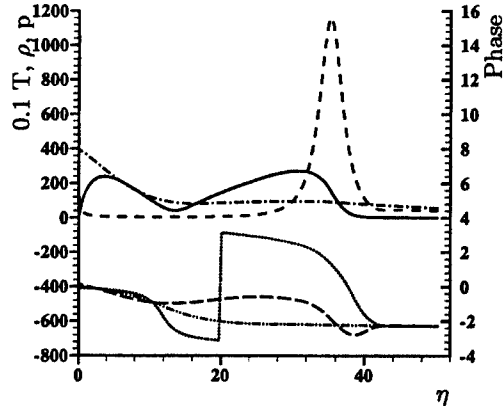


FIGURE 5. t , ρ and p eigensolutions at $R_x=1000$ for two-dimensional disturbances at $F=3.6416 \cdot 10^{-5}$. t is scaled by a factor of 0.1. t_{amp} (—), ρ_{amp} (---), p_{amp} (—·—), t_{phs} (····), ρ_{phs} (—·—), p_{phs} (—·—·—).

u and the wall-normal velocity v both show a distinct maximum inside the boundary layer and a second, much smaller maximum outside the boundary layer typical for the first mode disturbance. The pressure (see figure 5) has no zero in its profile distinguishing the first mode eigenfunction.

At the local Reynolds number of $R_x=2450$, the second mode disturbance is the most unstable eigenmode. The wall-normal profiles of the eigensolutions of the stability equations are shown in figure 6 and 7. For higher Mach-numbers, the second mode is generally strongly amplified. For the high Mach number chosen, the amplification rates of the two-dimensional first and second modes are very close.

In figure 6, the eigenfunctions for the downstream velocity u and the wall-normal ve-

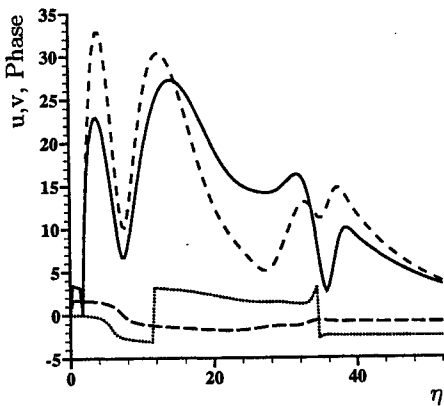


FIGURE 6. u and v eigensolutions at $R_x=2450$ for two-dimensional disturbances at $F=3.6416 \cdot 10^{-5}$. u_{amp} (—), v_{amp} (---), u_{phys} (.....), v_{phys} (-·-·).

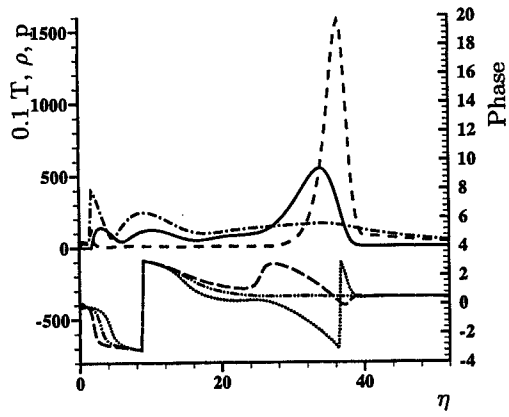


FIGURE 7. t , ρ and p eigensolutions at $R_x=2450$ for two-dimensional disturbances at $F=3.6416 \cdot 10^{-5}$. t is scaled by a factor of 0.1. t_{amp} (—), ρ_{amp} (---), p_{amp} (—·—·), t_{phys} (.....), ρ_{phys} (—·—), p_{phys} (—·—·).

locity v are shown together with their phase distribution for that local Reynolds number. Compared to the earlier station $R_x = 1000$ (figure 4), the eigenfunctions now show a double peak inside the boundary layers. As one goes further downstream (not shown here), the number of maxima inside the boundary layer increases. The pressure as shown in figure 7 shows a phase shift of π at $\eta=4$ identifying the second mode. It can be noted, that the density eigenfunction looks almost identical to the case at $R_x = 1000$.

The results for the third mode at $R_x = 2800$ will be shown together with the simulation results further into the report.

The importance of the three-dimensional modes for the above described conditions is discussed by means of figure 8 showing the dependence of the amplification rate on the obliqueness angle of the disturbance φ . Four downstream locations are shown. For $R_x = 800$, before the first-mode instability sets in, there is almost no dependence on the obliqueness angle for the damped waves. As the first-mode instability is at its peak at $R_x = 1000$, low obliqueness waves are almost as unstable as the two-dimensional disturbance up to approximately 20° . The amplification rates drops continuously down to neutral at about $\varphi = 65^\circ$. For $R_x = 2250$, the picture is very similar to the station where the first-mode instability is at its maximum.

The presented stability results are based on a non-reacting ideal-gas flow. The effects of the chemical reactions have been studied among others by Johnson, Seipp & Candler (1998), which have found that chemical reactions can diminish amplification rates and delay transition. This coincides with other work on chemically reacting flow.

4. Results

The simulations have been carried out under free-flight conditions at an altitude of $H=50$ Km (compare page 390 for the dimensional properties). The disturbances were introduced at a Reynolds number of $R_x = 2250$ ($x=58$). An acoustic disturbance is introduced which propagates towards the upper boundary at the Mach angle of $\theta \approx 3^\circ$. This accounts for the elevated amplitudes in the presented results for $y > 0.3$.

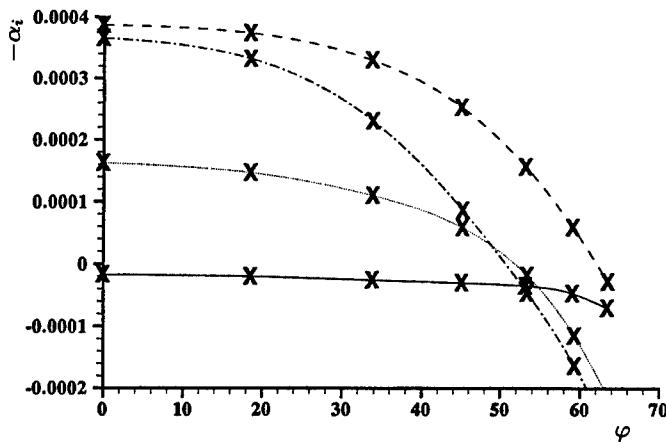


FIGURE 8. spatial amplification rate $-\alpha_i$ vs. wave propagation angle φ for $F = 3.6416 \cdot 10^{-5}$.
 $R_x = 800$ (—), $R_x = 1000$ (---), $R_x = 2000$ (.....), $R_x = 2250$ (—·—).

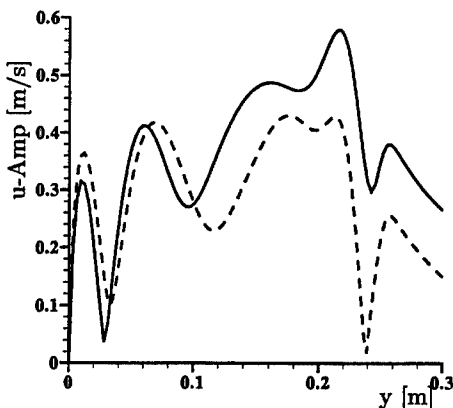


FIGURE 9. Comparison of simulation (—) and Linear Stability results (---) of the downstream velocity u at $R_x = 2800$

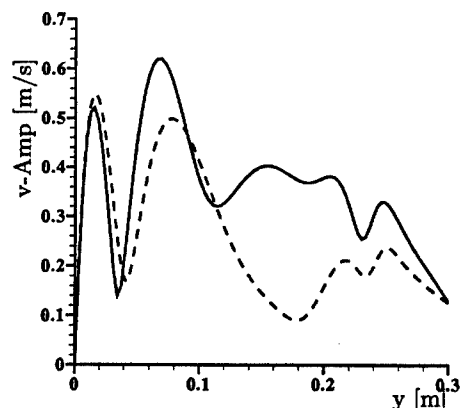


FIGURE 10. Comparison of simulation (—) and Linear Stability results (---) of the wall-normal velocity v at $R_x = 2800$

The results for the most-amplified two-dimensional disturbance are compared with the stability results acquired through Mack's stability code in figures 9-12 at $R_x = 2800$. The downstream velocity (u) in figure 9 shows very close agreement to the theoretical results reproducing the phase shift at the right wall-normal distances. The way the disturbances are introduced opens the possibility of the presence of multiple instability waves with the same frequency but differing wave numbers.

The deviation from the theoretical results can be explained through the inclusion of the vibrational modes in the calculation of the thermodynamic properties. In areas of high temperature (above ~ 3000 K), this will alter the temperature profile compared to the ideal-gas case. This happens at $0.2 < y < 0.3$ for $R_x = 2800$ and can explain the differences there.

The wall-normal velocity (v) is presented in figure 10, pressure (p) and density (ρ) are

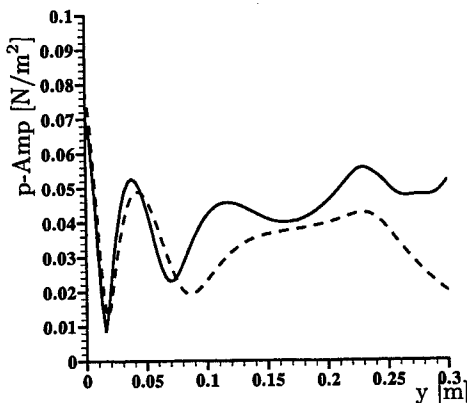


FIGURE 11. Comparison of simulation (—) and Linear Stability results (---) of the pressure p at $R_x = 2800$

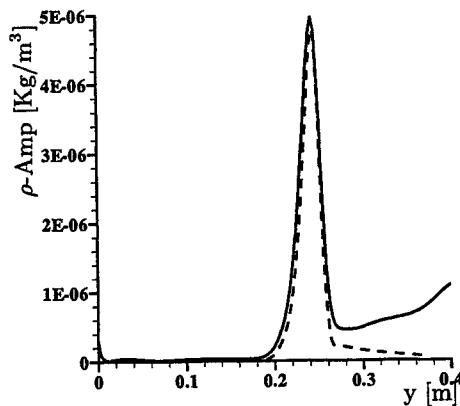


FIGURE 12. Comparison of simulation (—) and Linear Stability results (---) of the density ρ at $R_x = 2800$

shown in figure 11 and figure 12, respectively. The temperature results are qualitatively the same as the presented results.

The amplification rate given by the stability theory results is $\alpha_i = -0.0186[1/m]$ and the rate obtained from the simulation is $\alpha_i = -0.017[1/m]$.

5. Conclusions and future work

It has been shown that the numerical method presented is capable of tackling the hypersonic transition problem proposed. The results of the Linear Stability Theory match well with the simulation results for a third mode unstable two-dimensional disturbance.

Fundamental and oblique transition scenarios for the described $Ma=20$ flow will be performed. Simulations will be undertaken to provide for chemical and thermal non-equilibrium conditions.

To mimic closer the introduction of disturbances in an experimental environment, a point source disturbance, Stemmer (2001), will be introduced. Therefore, a single frequency with all possible spanwise wave numbers can be excited simultaneously leaving the flow to naturally amplify the unstable components of the disturbance.

Laminar-turbulent transition scenarios under varying disturbance conditions will be investigated to understand more about the physical behaviour of chemically reacting flows in transition on a flat plate.

REFERENCES

- ADAMS, N. A. 1996 A high-resolution hybrid compact-ENO scheme for shock-turbulence interaction problems. *J. Comp. Phys.* **127**, 27-51.
- ADAMS, N. A. 1998 Direct numerical simulation of turbulent compression ramp flow *Theor. and Comp. Fluid Dyn.* **12**, 109-129.
- ADAMS, N. A. 2000 Direct simulation of the turbulent boundary layer along a compression ramp at $M=3$ and $Re_\theta=1685$. *J. Fluid. Mech.* **420**, 47-83.
- ANDERSON, J. D. 1989 *Hypersonic and high temperature gas dynamics*. AIAA publication.
- BLOTTNER, F. G., JOHNSON, M. & ELLIS, M. 1971 *Chemically reacting viscous flow program for multi-component gas mixtures*. Sandia Natl. Laboratories, SC-RR-70-754.
- EISSLER, W. 1995 *Numerische Untersuchungen zum laminar-turbulenten Strömungs-umschlag in Überschallgrenzschichten*. Dissertation, Universität Stuttgart.
- GASTER, M. 1965 A note on a relation between temporally increasing and spatially increasing disturbances in hydrodynamic stability. *J. Fluid. Mech.* **22**, 222-224.
- HIRSCHFELDER, J. O., CURTISS, C. F. & BIRD, R. A. 1964 *Molecular theory of gases and liquids*. Wiley, New York.
- JOHNSON, H. B., SEIPP, T. G. & CANDLER, G. V. 1998 Numerical study of hypersonic reacting boundary layer transition on cones *Physics of Fluids*. Vol. **10**, 2676-85.
- LEES, L. & LIN, C. C. 1945 *Investigation of the stability of the laminar boundary layer in a compressible fluid*. NACA TN 1115.
- MIRONOV, S. G. & MASLOV, A. A., 2000 Experimental study of secondary stability in a hypersonic shock layer on a flat plate. *J. Fluid. Mech.* **412**, 259-277.
- MACK, L.M., 1969 *Boundary-layer stability theory*. JPL Report 900-277 Rev. A, Jet Propulsion Laboratory, Pasadena, USA.
- PARK, C. 1989 A review of reaction rates in high temperature air. *AIAA Paper 89-1740*.
- SARMA, G. S. R. 2000 Physico-chemical modeling in hypersonic flow simulation. *Prog. Aerospace Science* **36**, 281-349.
- SCHNEIDER, S. P. 1999 Flight data for boundary-layer transition at hypersonic and supersonic speeds. *J. of Spacecraft and Rockets* **36**, 8-20.
- STEMMER, C. 2001 *Direct numerical simulation of harmonic point source disturbances in an airfoil boundary layer with adverse pressure gradient*. Dissertation, Universität Stuttgart.
- STEMMER, C. & MANSOUR, N.N. 2001 DNS of transition in hypersonic boundary-layer flows including high-temperature gas effects. *Annual Research Briefs 2001*, Center for Turbulence Research, NASA Ames/Stanford University., 143-150.
- STUCKERT, G. K. & REED, H. L. 1991 Unstable branches of a hypersonic, chemically reacting boundary layer. *Boundary Layer Transition and Control*; Proceedings of the Conference, Univ. of Cambridge, UK, Apr. 8-12, 1991, 19.1-19.13.
- U.S. Standard Atmosphere*, U.S. Government Printing Office, Washington, D.C., 1976.
- VINCENTI, W. G. & KRUGER, C. H. 1982 *Introduction to physical gas dynamics*, Krieger, Malabar, FL.
- WILKE, S. P. 1950 A Viscosity equation for gas mixtures. *J. Comp. Phys.* **18**, 517-519.

Simple stochastic model for laminar-to-turbulent subcritical transition

By Sergei Fedotov †, Irina Bashkirtseva ‡ AND Lev Ryashko ‡

1. Motivation and objectives

The main purpose of this paper is to study the effects of stochastic perturbations on a non-normal dynamical system mimicking laminar-to-turbulent subcritical transition. The mechanism of non-normal transient linear growth has received much attention, both experimentally and theoretically, during the past decade, especially after the seminal work of Trefethen *et al.* (1993). The main reason is that this explains the onset of turbulence when the laminar flow passes to a turbulent regime without linear instability. Non-normality of the linearized Navier-Stokes evolution operator leads to the transient growth of velocity disturbances, even though the steady mean flow is linearly stable. A typical example of such transient growth is the function $t \exp(-t)$. Let us remind that the matrix A is normal, if $AA^* = A^*A$, where $*$ denotes the Hermitian transpose, otherwise it is non-normal. The nonlinear interactions lead to a further amplification of the initially small but finite disturbances. Nonlinear terms play a vital role in the redistribution of energy to those disturbances which exhibit a linear transient growth. Thus the transition to turbulence is not a consequence of the linear instability of the stationary laminar flow; rather, it is the result of the interaction of the non-normality-producing transient amplification of velocity perturbations and energy-conserving nonlinearities driving the system into the basin of attraction of the turbulent regime. A comprehensive review of the up-to-date results on such interactions and the resulting onset of shear-flow turbulence can be found in the review by Grossmann (2000) and the book by Schmid and Henningson (2001).

Several theoretical studies have been devoted to stochastically-forced dynamical systems involving a non-normal operator (Farrel & Ioannou 1993; Bassam & Dahlem 2001). It has been found that these systems have an extraordinary sensitivity to random perturbations, which leads to a great amplification of the variances. However, this research has focused only on linear non-normal systems.

The objective of this paper is to study the interaction between the following three factors: non-linearity, non-normality, and stochastics. In order to gain some insight into this problem, we shall examine the role of external noise in a simple non-normal dynamical system mimicking laminar-to-turbulent subcritical transition

$$\begin{aligned} \frac{du}{dt} &= -2\epsilon u + (u^2 + v^2)^{\frac{1}{2}} v, \\ \frac{dv}{dt} &= -\epsilon v + u - (u^2 + v^2)^{\frac{1}{2}} u, \end{aligned} \quad (1.1)$$

where u and v mimic streamwise vortices and streamwise streaks respectively; ϵ is a small parameter, chosen in analogy with the inverse Reynolds number. This dynamical system

† Also, Department of Mathematics, UMIST, Manchester, U.K.

‡ Department of Mathematical Physics, Ural State University, 620083 Ekaterinburg, Russia

has been suggested by Trefethen *et al.* (1993) as a simple model explaining the subcritical transition of a flow obeying the Navier-Stokes equations. It should be noted that several other low-dimensional models have been proposed to explain the onset of a turbulent regime for high Reynolds numbers (e.g. Gebhardt & Grossmann 1994, Baggett *et al.* 1995, 1997). The dynamical system (1.1) has three stable equilibrium points including $(0, 0)$. The main feature of the system (1.1) is that for $\varepsilon \ll 1$ the linearized evolution operator for the fixed point $(0, 0)$ is a highly-non-normal matrix that leads to a large transient growth of $v(t)$ prior to an eventual exponential decay. It can easily be found that for the non-zero initial conditions $u(0) = \varepsilon u_0$ and $v(0) = 0$, the solution of the linearized equations is of the form $v(t) = u_0(e^{-\varepsilon t} - e^{-2\varepsilon t})$, $u(t) = \varepsilon u_0 e^{-2\varepsilon t}$. The function $v(t)$ achieves a maximum of order one, on a time scale of order ε^{-1} . Furthermore, although both eigenvalues are negative ($\lambda_1 = -\varepsilon$; $\lambda_2 = -2\varepsilon$), finite fluctuations with exceedingly low amplitude can excite the transition from the fixed point $(0, 0)$. The main problem here is to find the minimum amplitude of all fluctuations capable to excite this transition and its dependence on the parameter ε of the form ε^α . The threshold exponent α is found to be 3. This tells us that the basin of attraction of $(0, 0)$ shrinks very rapidly as $\varepsilon \rightarrow 0$ (Chapman 2002).

2. Non-normal dynamical system with noise

One of the purposes of this paper is to understand how random perturbations can affect the dynamics of the non-normal system (1.1). We simply add two generic uncorrelated Gaussian white-noise terms to the right-hand side of (1.1). The dynamical system (1.1) can then be written in the form of the stochastic differential equations (Gardiner 1996)

$$\begin{aligned} du &= (-2\varepsilon u + (u^2 + v^2)^{\frac{1}{2}} v) dt + (2\delta)^{\frac{1}{2}} dW_1(t), \\ dv &= (-\varepsilon v + u - (u^2 + v^2)^{\frac{1}{2}} u) dt + (2\delta)^{\frac{1}{2}} dW_2(t), \end{aligned} \quad (2.1)$$

where $W_1(t)$ and $W_2(t)$ are the uncorrelated standard Wiener processes. Here we assume for simplicity that the intensity of the noise parameter, δ , is the same for both stochastic terms.

For the deterministic system (1.1) only small but finite initial perturbations can escape from the basin of attraction for a fixed point at the origin. In this case the main problem is to answer the question "What are the minimum amplitude of the form ε^α and the threshold exponent α for transition to turbulence?". In the stochastic case the key question is "What is the long-time effect of adding noise terms to the nonlinear non-normal dynamical system?". Due to the highly sensitive way that non-normal systems are affected by random perturbations, we can expect that the presence of noise on the right-hand side of (1.1) may lead to a transition, even for zero initial conditions

$$u(0) = 0, \quad v(0) = 0. \quad (2.2)$$

We believe that this is physically significant since in practical situations random fluctuations may often be what induce the subcritical transition in fluid flow. To illustrate the stochastic sensitivity of the non-normal system (2.1), consider its linear approximation

$$\begin{aligned} du &= -2\varepsilon u dt + (2\delta)^{\frac{1}{2}} dW_1(t), \\ dv &= (-\varepsilon v + u) dt + (2\delta)^{\frac{1}{2}} dW_2(t) \end{aligned} \quad (2.3)$$

with zero initial conditions (2.2). This is a relatively simple stochastic dynamical system in which the variable $u(t)$ is the Ornstein-Uhlenbeck process, with well-known statistical properties, while $v(t)$ is the non-Markov random process whose properties can be easily found (Gardiner 1996). The second moments are very important statistical characteristics of the system (2.3), since they mimic the kinetic energy of fluid flow. One can find the following explicit representations for them:

$$\begin{aligned} m_1(t) &\equiv Eu^2(t) = \frac{\delta}{2\varepsilon}(1 - e^{-4\varepsilon t}), \\ m_2(t) &\equiv Eu(t)v(t) = -\frac{2\delta}{3\varepsilon^2}e^{-3\varepsilon t} + \frac{\delta}{2\varepsilon^2}e^{-4\varepsilon t} + \frac{\delta}{6\varepsilon^2}, \\ m_3(t) &\equiv Ev^2(t) = \left(-\frac{\delta}{\varepsilon^3} - \frac{\delta}{\varepsilon}\right)e^{-2\varepsilon t} + \frac{4\delta}{3\varepsilon^3}e^{-3\varepsilon t} - \frac{\delta}{2\varepsilon^3}e^{-4\varepsilon t} + \frac{\delta}{\varepsilon} + \frac{\delta}{6\varepsilon^3}, \end{aligned}$$

where E denotes the expectation operator. The limiting values $\bar{m}_i = \lim_{t \rightarrow \infty} m_i(t)$ are

$$\bar{m}_1 = \frac{\delta}{2\varepsilon}, \quad \bar{m}_2 = \frac{\delta}{6\varepsilon^2}, \quad \bar{m}_3 = \frac{\delta}{\varepsilon} + \frac{\delta}{6\varepsilon^3}. \quad (2.4)$$

From (2.4) we can see that owing to the non-normality of the system (2.3) as $\varepsilon \rightarrow 0$ for constant δ , all second moments tend to infinity. The stationary second moment \bar{m}_3 exhibits the highest degree of sensitivity. Even for very weak noise, say $\delta \sim \varepsilon^2$ then $\bar{m}_3 \rightarrow \infty$ as $\varepsilon \rightarrow 0$.

It is instructive to investigate the effect that non-normality has on the probability of exit from the zero-attraction point. This problem is closely related to the famous ‘Kramer’s exit problem’ which concerns the escape of random trajectories of a stochastic dynamical system from the domain of attraction of the underlying deterministic dynamical system (Gardiner 1996). We have calculated numerically the empirical exit probabilities of random trajectories from the neighborhood of the zero point $U = \{(u, v) : u^2 + v^2 \leq 0.01\}$ up to $t = 10$. The results in figure 1 demonstrate that even for a very small intensity of noise ($\delta = 10^{-3}$) the exit probability p_e is close to unity. In particular, for $\varepsilon = 2^{-5} \approx 0.03$ and $\delta = 5 \times 10^{-5}$ the exit probability is greater than 0.6. For $\delta = 2 \times 10^{-4}$ the probability p_e is greater than 0.8. For $\delta = 10^{-3}$ this probability is very close to one.

An analytical treatment of the stochastic dynamical system (2.1) is rather difficult, although some approximations are possible, and indeed useful (see (4.3) for the slowly-varying energy of the non-normal system). We have performed simulations of random trajectories of (2.1) for different values of ε and δ . Our numerical results show that, either by increasing the intensity of noise δ or by decreasing the non-normality parameter ε , the stochastic system (2.1) undergoes a series of phase transitions. We have found three qualitatively different regimes. For a fixed value of ε , this phenomenon can be interpreted as a noise-induced transition. A detailed discussion can be found in the excellent book by Horsthemke & Lefever (1984).

Figures 2 and 3 illustrate these transitions in terms of stochastic trajectories of the non-normal dynamical system for $\varepsilon = 10^{-2}$ and $\delta = 10^{-4}$ (figure 2), $\delta = 10^{-2}$ (figure 3). For very small values of δ ($\delta < 10^{-12}$), we have observed that the random trajectory is concentrated around the equilibrium point at $(0, 0)$. As δ increases, the trajectory then begins to become more concentrated in the vicinity of one of the non-trivial fixed points (Fig. 2). Further increase of the noise intensity parameter δ leads to the stochastic orbits containing all three fixed points (Fig. 3). It should also be noted that these noise-induced

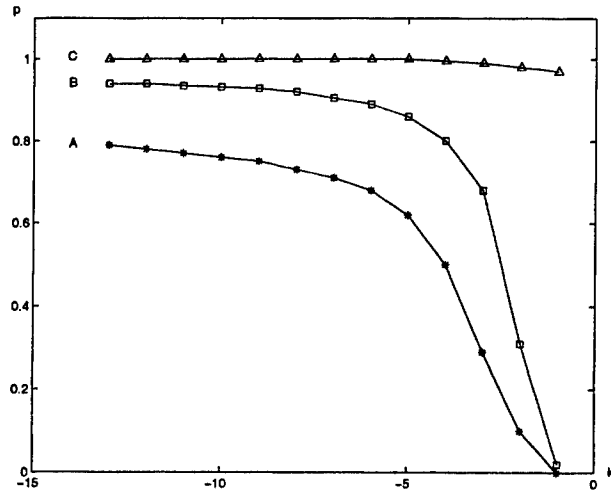


FIGURE 1. The exit probability p_e as a function of non-normal parameter $\varepsilon = 2^{-k}$. Curves A, B and C correspond to $\delta = 5 \cdot 10^{-5}, 2 \cdot 10^{-4}, 10^{-3}$.

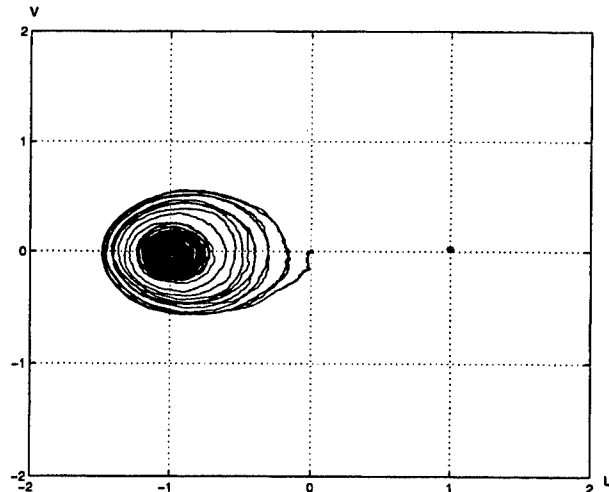


FIGURE 2. The stochastic trajectory for $\varepsilon = 10^{-2}, \delta = 10^{-4}$; initial conditions: $u(0) = 0$ and $v(0) = 0$.

transitions can also be analyzed in terms of the extrema of the stationary probability density $p_{st}(u, v)$ (Horsthemke & Lefever 1984).

3. Underlying Hamiltonian structure

The behavior of the trajectories when the values of ε and δ are small can be explained by the existence of a Hamiltonian structure in (2.1). If we introduce the Hamiltonian function

$$H(u, v) = \frac{1}{3} (u^2 + v^2)^{\frac{3}{2}} - \frac{1}{2} u^2, \quad (3.1)$$

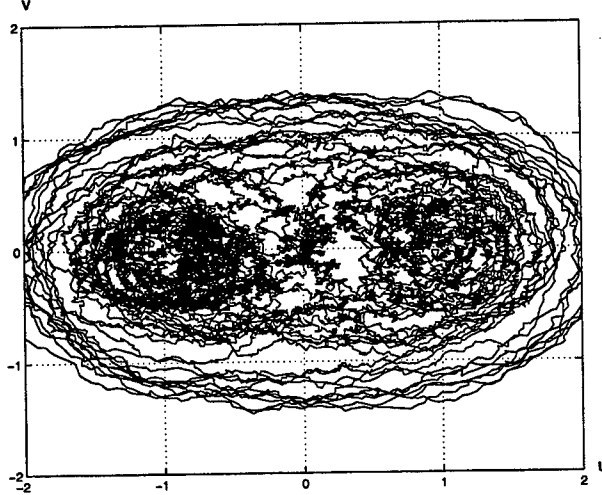


FIGURE 3. The stochastic trajectory for $\varepsilon = 10^{-2}, \delta = 10^{-2}$.

then the dynamical system (2.1) can be rewritten as

$$\begin{aligned} du &= -2\varepsilon u dt + \frac{\partial H}{\partial v} dt + (2\delta)^{\frac{1}{2}} dW_1(t), \\ dv &= -\varepsilon v dt - \frac{\partial H}{\partial u} dt + (2\delta)^{\frac{1}{2}} dW_2(t). \end{aligned} \quad (3.2)$$

In the limits $\varepsilon \rightarrow 0$ and $\delta \rightarrow 0$, the system (3.2) becomes conservative, so

$$\frac{du}{dt} = \frac{\partial H}{\partial v}, \quad \frac{dv}{dt} = -\frac{\partial H}{\partial u}, \quad (3.3)$$

and, therefore, $H(u, v) = E = \text{const}$. The phase trajectories $u(t)$ and $v(t)$ of (3.3) move along the level set

$$C(E) = \{(u, v) : H(u, v) = \frac{1}{3}(u^2 + v^2)^{\frac{3}{2}} - \frac{1}{2}u^2 = E\}. \quad (3.4)$$

with the speed

$$V(u, v) = \left(\frac{\partial H}{\partial v}, -\frac{\partial H}{\partial u} \right). \quad (3.5)$$

It follows from the existence of the Hamiltonian (3.1) that the trajectories are periodic, and that the period of the oscillations $T(E)$ can be found to be

$$T(E) = \int_{C(E)} |V(u, v)|^{-1} ds, \quad (3.6)$$

where the integral is taken along the level curves $C(E)$.

In figure 4 we plot the one-parameter family of curves generated by (3.4) that gives us the full phase portrait of the conservative system (3.3). There are three equilibrium points, at $(0, 0)$ and $(\pm 1, 0)$. One can see that the phase portrait is similar to that of the Duffing equation without dissipation. Linearization of (3.3) at $(1, 0)$ and $(-1, 0)$ gives us the period 2π . While moving out, the periodic trajectories have longer periods and tend to infinity as we approach the saddle connection. The situation is more complicated in the presence of dissipative terms. An addition of the two terms $-2\varepsilon u$ and $-\varepsilon v$ changes

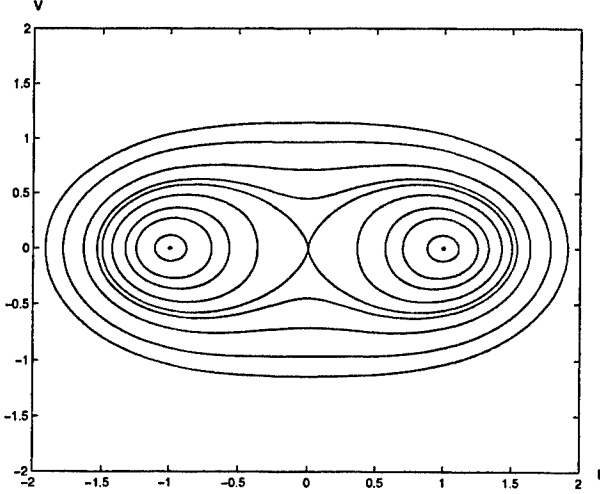


FIGURE 4. The phase portrait of the conservative system (3.3).

the direction of the vector field in an alternative way, to that of the dissipative Duffing equation. Of course, the global effect is to destroy the closed orbits. In particular, the fixed point $(0, 0)$ becomes linearly stable, but the width of its basin of attraction decreases as ε^3 .

4. Stochastic differential equation for the energy

In a further analysis of the effect of randomness and dissipation, it is of interest to consider the reduced equation for energy. In the general case ($\varepsilon \neq 0, \delta \neq 0$) the energy of the system $E = H(u, v)$ is not a constant, but rather a random function of time. If we apply the Itô formula for $E = H(v, u)$ (Gardiner 1996) we can obtain the governing equation for the energy,

$$\begin{aligned} dE = & \left(-2\varepsilon \frac{\partial H}{\partial u} u - \varepsilon \frac{\partial H}{\partial v} v + \delta \frac{\partial^2 H}{\partial u^2} + \delta \frac{\partial^2 H}{\partial v^2} \right) dt \\ & + (2\delta)^{\frac{1}{2}} \frac{\partial H}{\partial u} dW_1(t) + (2\delta)^{\frac{1}{2}} \frac{\partial H}{\partial v} dW_2(t). \end{aligned} \quad (4.1)$$

It is clear that for small values of both the dissipation parameter ε , and the noise parameter δ , after some transient period of time, the phase trajectories of (3.2) will be very close to the level curves $C(E)$. There are three different families of periodic orbits, separated by the saddle connection (see Fig. 4). Let us denote those components of the level set by $C_i(E)$ ($i = 1, 2, 3$). The overall dynamics of (2.1) can be viewed as a composition of a fast motion along the level curve $C_i(E)$ and of a slow motion normal to the energy levels with the possible transitions, for example, from $C_1(E)$ to $C_3(E)$. In this case one can eliminate the fast motion to derive an equation for the slowly-varying energy $E(t)$. It is well known (Gardiner 1996) that the fast variables can be eliminated when there exists a stationary distribution function, independent of small parameters. Let us introduce the following normalized measure corresponding to the fast motion (Freidlin 1996) along the energy-level curve $C_i(E)$

$$\rho_i(u, v) = \frac{1}{T_i(E) |V(u, v)|}. \quad (4.2)$$

The equation for the energy $E(t)$ can be derived as follows. Let us multiply the equation (4.1) by the measure (4.2), and integrate along the level curve $C_i(E)$ (Freidlin 1996). The equation for $E(t)$ then takes the form of a one-dimensional stochastic differential equation

$$\frac{dE}{dt} = S_i(E) - D_i(E) + \sigma_i(E) \frac{dW}{dt}, \quad (4.3)$$

where the rate of energy supply due to the noise is

$$S_i(E) = \frac{\delta}{T_i(E)} \int_{C_i(E)} \left(\frac{\partial^2 H}{\partial u^2} + \frac{\partial^2 H}{\partial v^2} \right) |V(u, v)|^{-1} ds, \quad (4.4)$$

while the rate of removal of energy by dissipation can be written as

$$D_i(E) = \frac{\varepsilon}{T_i(E)} \int_{C_i(E)} \left(2 \frac{\partial H}{\partial u} u + \frac{\partial H}{\partial v} v \right) |V(u, v)|^{-1} ds. \quad (4.5)$$

The intensity of noise is

$$\sigma_i^2(E) = \frac{\delta}{T_i(E)} \int_{C_i(E)} |V(u, v)| ds. \quad (4.6)$$

The details of the derivation of the above formula can be found in the book by Freidlin (1996). For very small values of ε and δ , most of the probability is concentrated on the level curves $C_i(E)$. We have in essence a deterministic motion with speed V along the level curves. In general, we have stochastically-sustained oscillations for which the energy generation $S_i(E)$ due to the noise, and the dissipation $D_i(E)$, are in balance with the stochastic term, whose intensity $\sigma_i(E)$ is a function of energy itself.

5. Conclusions and future work

In summary, we have investigated the effects of the additive Gaussian perturbations on a non-normal dynamical system mimicking laminar-to-turbulent subcritical transition both analytically and numerically. We have derived explicit representations for the second moments and found that the dynamical system with a non-normal transient linear growth is highly sensitive to the presence of weak random perturbations. We have calculated numerically the empirical exit probabilities of random trajectories from the neighborhood of a zero fixed point. We have found that even for very small values of the intensity of noise parameter ($\delta = 10^{-3}$) the exit probability is close to unity. We have also found that an increase of the intensity of noise parameter, or a decrease of the non-normality parameter, will lead to certain qualitative changes in the behavior of the trajectories. This can be interpreted as noise-induced phase transitions. By using the Itô formula and the adiabatic elimination procedure, we have derived a stochastic equation governing the slow evolution of the energy of the system.

We believe that the study of the impact of noise on non-normal dynamical systems is physically significant, since, in practical situations, random fluctuations may often be what induce the subcritical transition in fluid flow. The transition appears to become an essentially random event. The generic feature of laminar-to-turbulent transition in shear flow is that it does not have a critical, reproducible Reynolds number (see Grossman 2000). Regarding the model (2.1), it should be noted that its nonlinearity is quite different from that of the Navier-Stokes equations: therefore, it does not really describe the laminar-to-turbulent transition in fluid flow. However, it gives the general features of

such transition involving transient growth, and the interaction between non-linear and stochastic modes. The stochastic dynamic system (2.1) is fundamentally different from the deterministic one (1.1) that has only two degrees of freedom. We can regard (2.1) as an *effective* dynamical system with many degrees of freedom in which two variables u and v play the role of order parameters, while the stochastic noise terms approximate other degrees of freedom and their influence on u and v . Further research is needed to identify the statistical characteristic of the noise terms in (2.1).

Acknowledgments

Useful conversations with John Dold are gratefully acknowledged. S.F. thanks Parviz Moin and Heinz Pitsch for their kind invitation to the Center for Turbulence Research.

REFERENCES

- BAGGETT, J. S., DRISCOLL, T. A. & TREFETHEN, L. N. 1995 A mostly linear model of transition to turbulence. *Phys. Fluids* **7**, 833–846.
- BAGGETT, J. & TREFETHEN, L. 1997 Low-dimensional models of subcritical transition to turbulence. *Phys. Fluids* **9**, 1043–1053.
- BASSAM, B. & DAHLEH, M. Energy amplification in channel flows with stochastic excitation *Phys. Fluids* **13**, 3258–3269.
- CHAPMAN, S. J. 2002 Subcritical transition in channel flow. *J. Fluid Mech.* **451**, 35–97.
- FARRELL, B. F. & IOANNOU, P. J. 1993 Stochastic forcing of the linearized Navier-Stokes equations. *Phys. Fluids* **5**, 2600–2609
- FREIDLIN, M. 1996 *Markov Processes and Differential Equations: Asymptotic Problems*. Birkhauser, Basle.
- GARDINER, C. W. 1996 *Handbook of Stochastic Methods*. 2nd ed. Springer, Berlin.
- GBEHARDT, T. & GROSSMANN, S. 1994 Chaos transition despite linear stability. *Phys. Rev. E* **50**, 3705–3709.
- GROSSMANN, S. 2000 The onset of shear flow turbulence. *Rev. Mod. Physics* **72**, 603–618.
- HORSTHEMKE, W. & LEFEVER, R. 1984 *Noise-Induced Transitions*. Springer, Berlin.
- SCHMID, P. J. & HENNINSON, D. S. 2001 *Stability and Transition in Shear Flows*. Springer, Berlin.
- TREFETHEN, L. N., TREFETHEN, A. E., REDDY, S. C. & DRISCOLL, T. A. 1993 Hydrodynamic stability without eigenvalues. *Science* **261**, 578–584.

An analytical model for predicting airfoil self-noise using wall-pressure statistics

By M. Roger †, S. Moreau ‡ AND M. Wang

1. Motivation and objectives

Broadband self-noise or trailing-edge noise is due to the scattering of boundary-layer vortical disturbances into acoustic waves at the trailing edge of an airfoil. As the only airfoil noise contribution in a homogeneous stationary flow, it is a matter of primary interest when addressing the problem of the noise generated by fans, wind turbines and high-lift devices. Simple aeroacoustic prediction tools dedicated to trailing-edge noise, that could be integrated in a design cycle, are a current need for manufacturers. In the context of industrial applications, a minimum degree of relevance is required, but the fine details of the scattering process are not expected to be reproduced exactly. A consistent model only has to provide reliable A-weighted levels, which means a realistic distribution of noise intensity with both frequency and angle of radiation, accurate enough for a definition in terms of decibels. Such tools can be deduced from analytical models and could be used in conjunction with incompressible flow computations, according to the acoustic analogy as stated by Ffowcs Williams & Hawkings (1969).

As a result of the scattering of a boundary layer turbulent flow, self noise can be related either to the vortical, hydrodynamic velocity field around the trailing-edge or to the induced hydrodynamic pressure field on the airfoil surface. The first approach, based on the velocity field, is outlined by Ffowcs Williams & Hall (1970) and was applied by Wang & Moin (2000) using large-eddy simulation results as input. The second approach, based on the induced wall pressure, has been developed and applied, for instance by Brooks & Hodgson (1981) and Amiet (1976), but rarely addresses the connection with computational results. It is supported by experimental evidence, as pointed out by Brooks, Marcolini & Pope (1989) and Roger & Moreau (2002).

The present work is an extension of Amiet's original formulation of trailing-edge noise based on fully analytical derivations. A back-scattering, leading edge correction is developed, yielding a modified chordwise distribution of the acoustic sources induced by the scattering mechanism. Furthermore, a three-dimensional extension is provided. The full solution has the advantage of accounting for all the effects of a finite chord length. The study is aimed at predicting airfoil self noise from wall pressure fluctuations computed by incompressible LES. In that sense, the present formulation is an alternative to the one proposed by Ffowcs Williams & Hall (1970), and has the advantage that both the actual chord length and any subsonic motion of the surrounding fluid are accounted for.

† Ecole Centrale de Lyon (ECL), France
‡ VALEO Motors and Actuators, France

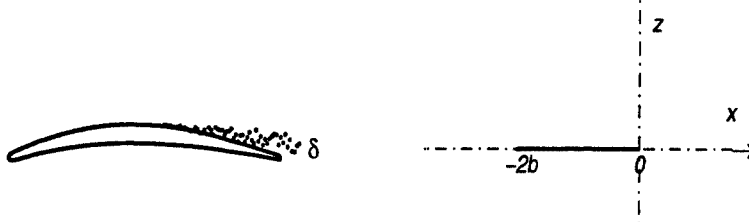


FIGURE 1. Flat-plate model of an airfoil with moderate camber and thickness. The boundary layer vorticity (thickness δ) is represented by equivalent convected pressure fluctuations.

2. Results

2.1. Far-field power spectral density

In the present analytical model, the airfoil is reduced to a flat plate with zero thickness and angle of attack, with a chord length $c = 2b$ and a span L . The space is described by the streamwise coordinate x , the spanwise coordinate y and the normal z coordinate. The trailing edge is at $x = 0$ (figure 1). The fluid is moving uniformly with velocity U along the chordwise direction $x > 0$. The corresponding Mach number $M = U/c_0$ with c_0 the speed of sound is assumed subsonic. The acoustic wavenumber $k = \omega/c_0$ is related to the convective wavenumber $K = \omega/U$ by the relationship $k = KM$.

The power spectral density of the far field sound pressure radiated from the airfoil due to the lift fluctuations induced by trailing-edge scattering can be expressed in the following way, extending the results of Amiet (1975):

$$S_{pp}(\vec{x}, \omega) = \left(\frac{\omega z L b}{2\pi c_0 S_0^2} \right)^2 \frac{1}{b} \int_{-\infty}^{\infty} \Pi_0 \left(\frac{\omega}{U_c}, K_2 \right) \operatorname{sinc}^2 \left\{ \frac{L}{2b} \left(\bar{K}_2 - \bar{k} \frac{y}{S_0} \right) \right\} \left| I \left(\frac{\bar{\omega}}{U_c}, \bar{K}_2 \right) \right|^2 d\bar{K}_2 \quad (2.1)$$

with:

$$\operatorname{sinc}(t) = \frac{\sin(t)}{t}$$

In this formula, I is the radiation integral associated with a two-dimensional Fourier component of the incident hydrodynamic wall pressure field, with hydrodynamic wavenumbers K_1 and K_2 respectively in the streamwise and spanwise directions. This incident field is assumed frozen when convected past the trailing edge, which selects the value of the streamwise wavenumber $K_1 = \omega/U_c$. U_c is the convection speed, related to U by the factor $\alpha = U/U_c > 1$. $S_0 = \sqrt{x^2 + \beta^2(y^2 + z^2)}$ is the corrected distance to the far field point \vec{x} , with $\beta^2 = 1 - M^2$, and (\cdot) stands for quantities made nondimensional by multiplying by b . Π_0 is the energy of the incident wall pressure fluctuations at angular frequency ω for a given spanwise wavenumber. It is deduced from the full cross spectral density function of the incident wall pressure $\Pi(K_1, K_2, \omega)$:

$$\Pi_0 \left(\frac{\omega}{U_c}, K_2 \right) = \int_{-\infty}^{\infty} \Pi(K_1, K_2, \omega) dK_1 \quad (2.2)$$

In (2.2), Π represents a huge amount of information hardly tractable in experiments. Only accurate numerical methods, such as Direct Numerical Simulation or Large Eddy Simulation, are able to provide the necessary data by explicitly computing the wall pressure fluctuations associated with most of the turbulent eddies carrying the energy

of the vortical flow. Yet the full statistics Π appears not to be necessary for the present acoustic formulation. Indeed let's introduce:

$$\Pi(K_1, K_2, \omega) = \frac{1}{4\pi^2} \int \int \Omega_{pp}(\eta_1, \eta_2, \omega) e^{i(K_1\eta_1 + K_2\eta_2)} d\eta_1 d\eta_2 \quad (2.3)$$

where Ω_{pp} is the cross-spectral density between signals at two points on the airfoil with separations η_1 and η_2 in the streamwise and spanwise directions. Then let's define the functions A and B as in Singer (1996):

$$A(\eta_1, \omega) = \frac{\Omega_{pp}(\eta_1, 0, \omega)}{\Phi_{pp}(\omega)} \quad B(\eta_2, \omega) = \frac{\Omega_{pp}(0, \eta_2, \omega)}{\Phi_{pp}(\omega)} \quad (2.4)$$

where Φ_{pp} is the wall pressure spectrum corresponding to the incident hydrodynamic fluctuations only, assumed statistically homogeneous in the trailing-edge area. Without any further assumption on the wall pressure statistics, equation (2.2) then becomes accounting for (2.3) and (2.4):

$$\Pi_0\left(\frac{\omega}{U_c}, K_2\right) = \int_{-\infty}^{\infty} \Pi(K_1, K_2, \omega) dK_1 = \frac{\Phi_{pp}}{2\pi} \int_{-\infty}^{\infty} B(\eta_2, \omega) e^{iK_2\eta_2} d\eta_2$$

The more tractable parameter in connection with model experiments is the wall pressure field coherence between two points on the airfoil surface:

$$\gamma^2(\eta_1, \eta_2, \omega) = \frac{|\Omega_{pp}(\eta_1, \eta_2, \omega)|^2}{\Phi_{pp}^2(\omega)}$$

Therefore, the coherence can be identified to the squared chordwise and spanwise correlation functions A and B , respectively, as the separation η_2 or η_1 is set to zero. If the following corrected correlation length $l_y(\omega)$ is introduced:

$$l_y(K_2, \omega) = \int_0^{\infty} \sqrt{\gamma^2(0, \eta_2, \omega)} \cos(K_2\eta_2) d\eta_2$$

a final expression can be derived for the energy of the incident wall pressure fluctuations at frequency ω for a given spanwise wavenumber:

$$\Pi_0\left(\frac{\omega}{U_c}, K_2\right) = \frac{1}{\pi} \Phi_{pp}(\omega) l_y(K_2, \omega) \quad (2.5)$$

Functions Φ_{pp} and l_y are the minimum informations about the wall pressure statistics, needed for acoustic calculations. They are easy to measure on a model airfoil by means of a set of wall pressure transducers, spanwise distributed at a short distance upstream of the trailing edge. Such transducers, when located beneath a fully turbulent boundary layer, measure a priori the full wall pressure field, including the acoustic contamination from the trailing-edge scattering. However the acoustic pressure is typically 20 decibels below the hydrodynamic pressure associated with the convected turbulence. Thus the measured pressure can be assimilated to the hydrodynamic pressure only in this case. This is confirmed by the values of the convection speed measured by Roger & Moreau

(2002). As a consequence, trailing-edge transducers provide the same information as that computed in incompressible LES.

2.2. Radiation integral

Calculating the distant sound field with (2.1) still requires the computation of the radiation integral $I(\bar{\omega}/U_c, \bar{K}_2)$, which holds for a unit gust of reduced wavenumber vector $(\bar{K}_1 = \bar{\omega}/U_c, \bar{K}_2)$, at angular frequency ω . This vector defines an incident hydrodynamic oblique gust of unit pressure:

$$P_0 = e^{-i\bar{K}_1 X} e^{-i\bar{K}_2 Y}$$

with $X = x/b$ and $Y = y/b$, leading to a three-dimensional scattering problem. The equation for the corresponding scattered pressure is:

$$\frac{\partial^2 p'}{\partial x^2} + \frac{\partial^2 p'}{\partial z^2} + \frac{\partial^2 p'}{\partial y^2} - \frac{1}{c_0^2} \left(\frac{\partial}{\partial t} + U \frac{\partial}{\partial x} \right)^2 p' = 0$$

together with the boundary condition of no cross-flow on the airfoil surface and the cancellation of P_0 in the wake according to the Kutta condition. The solution is sought in the form:

$$\begin{aligned} p'(x, y, z, t) &= P(x, y, z) e^{i\omega t} \\ P(x, y, z) &= p(x, z) e^{i(kM/\beta^2)x} e^{-iK_2 y} = p(X, Z) e^{iM\bar{\mu}X} e^{-iK_2 Y} \end{aligned}$$

with $\bar{\mu} = \bar{K}M/\beta^2$. Introducing $Z = \beta z/b$, the equation becomes:

$$\frac{\partial^2 p}{\partial X^2} + \frac{\partial^2 p}{\partial Z^2} + \bar{\kappa}^2 p = 0 \quad \text{in which} \quad \bar{\kappa}^2 = \bar{\mu}^2 - \frac{\bar{K}_2^2}{\beta^2} \quad (2.6)$$

with

$$\frac{\partial p}{\partial Z}(X, 0) = 0 \quad -2 < X < 0$$

$$p(X, 0) = -e^{-i(\bar{K}_1 + M\bar{\mu})X} \quad X > 0$$

Supercritical gusts, corresponding to positive values of $\bar{\kappa}^2$ (i.e. real $\bar{\kappa} = \sqrt{\bar{\mu}^2 - \bar{K}_2^2/\beta^2}$), thus a hyperbolic equation, are known to radiate efficiently, whereas subcritical gusts, for which $\bar{\kappa} = -i\kappa'$ is imaginary ($\kappa' = \sqrt{(\bar{K}_2^2/\beta^2) - \bar{\mu}^2}$), are less efficient. The differential equation for p has no exact solution but can be solved by successive iterations. The first iteration is performed by assuming that the airfoil extends towards infinity in the upstream direction instead of the leading edge location $X = -2$. A Schwarzschild's problem is obtained, whose basic solution is summarized in the appendix. This first solution has been derived by Amiet (1976) in the case of two-dimensional gusts. Later Amiet (1978) refined the solution to account for the radiation effect of the incident pressure. The corresponding scattered field must be corrected to behave properly upstream. This is made by adding a leading edge back-scattered field ensuring a zero total disturbance potential for $X < -2$. The correction is calculated assuming that the airfoil now extends

towards infinity in the downstream direction from the leading edge, which leads to another Schwarzschild's problem by a straightforward change of variables. The technique has been described by Amiet (1975) dealing with the similar problem of the noise generated when upstream turbulence impinges on the leading edge of an airfoil. Generally speaking, the Schwarzschild's solution holds for the pressure disturbance when applied at the trailing edge and for the velocity potential ϕ when applied at the leading edge, with:

$$-\frac{b}{\rho_0 U} P = \frac{\partial \phi}{\partial X} + i \bar{K} \phi$$

The new items with respect to the original papers are the additional leading edge back-scattering correction for trailing-edge noise and the extension to three-dimensional scattering, accounting for subcritical gusts. The Schwarzschild's iterative procedure provides the value of p on the airfoil surface, used to calculate the radiation integral I . Only the final results are given here.

I can be written as $I = I_1 + I_2$, where I_1 stands for the main scattering from the trailing edge and I_2 for the back-scattering from the leading edge.

The first term for a supercritical gust, already obtained by Amiet (1978) in the two-dimensional case, is given by:

$$I_1 = -\frac{e^{2iC}}{iC} \left\{ (1+i)e^{-2iC} \sqrt{\frac{B}{B-C}} E^*[2(B-C)] - (1+i)E^*[2B] \right\} \quad (2.7)$$

with:

$$C = \bar{K}_1 - \bar{\mu} \left(\frac{x}{S_0} - M \right) \quad \text{and} \quad B = \bar{K}_1 + M \bar{\mu} + \bar{\kappa}$$

The correction term derived in the present work is:

$$I_2 = H \left(\{ e^{4i\bar{\kappa}} [1 - (1+i)E^*(4\bar{\kappa})] \}^c - e^{2iD} + i[D + \bar{K} + M\bar{\mu} - \bar{\kappa}]G \right) \quad (2.8)$$

with

$$\begin{aligned} G &= (1+\epsilon) e^{i(2\bar{\kappa}+D)} \frac{\sin(D-2\bar{\kappa})}{D-2\bar{\kappa}} + (1-\epsilon) e^{i(-2\bar{\kappa}+D)} \frac{\sin(D+2\bar{\kappa})}{D+2\bar{\kappa}} \\ &\quad + \frac{(1+\epsilon)(1-i)}{2(D-2\bar{\kappa})} e^{4i\bar{\kappa}} E^*(4\bar{\kappa}) - \frac{(1-\epsilon)(1+i)}{2(D+2\bar{\kappa})} e^{-4i\bar{\kappa}} E(4\bar{\kappa}) \\ &\quad + \frac{e^{2iD}}{2} \sqrt{\frac{2\bar{\kappa}}{D}} E^*(2D) \left[\frac{(1+i)(1-\epsilon)}{D+2\bar{\kappa}} - \frac{(1-i)(1+\epsilon)}{D-2\bar{\kappa}} \right] \end{aligned}$$

and

$$D = \bar{\kappa} - \bar{\mu} x/S_0 \quad H = \frac{(1+i)e^{-4i\bar{\kappa}}(1-\Theta^2)}{2\sqrt{\pi}(\alpha-1)\bar{K}\sqrt{B}} \quad \epsilon = \frac{1}{\sqrt{1+1/(4\bar{\kappa})}}$$

$$\Theta = \sqrt{\frac{A_1}{A}} \quad A_1 = \bar{K}_1 + M\bar{\mu} + \bar{\kappa} \quad A = \bar{K} + M\bar{\mu} + \bar{\kappa}$$

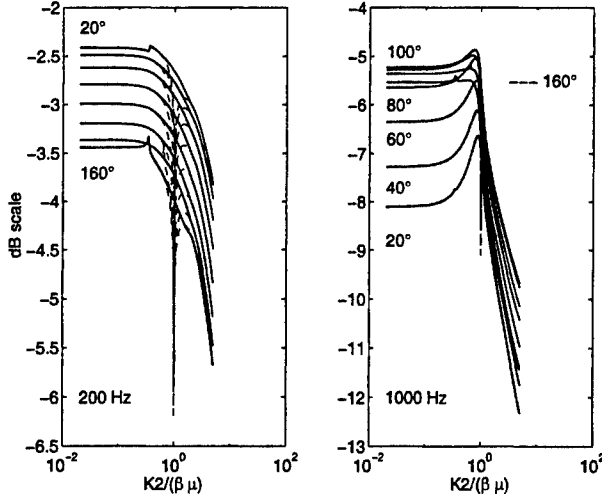


FIGURE 2. Profiles of the radiation integral $|J|$ in nondimensional variables, for radiation angles θ (in 20° increment) with respect to the flow direction in the mid-span plane. $M = 0.05$. - - regularization off, — regularization on.

In both equations (2.7) and (2.8), the complex function E^* stands for a combination of Fresnel integrals C_2 and S_2 given in Abramowitz & Stegun (1970) and is defined as:

$$E^*(x) = \int_0^x \frac{e^{-it}}{\sqrt{2\pi t}} dt = C_2(x) - iS_2(x)$$

$\{\cdot\}^c$ stands for quantities whose imaginary part needs to be multiplied by the empirical corrective factor ϵ . The latter has been determined numerically to yield an analytical form for the back-scattering radiation integral.

Equivalent results have been derived for a subcritical gust, leading to the following expressions:

$$I_1 = -\frac{e^{2iC}}{iC} \left\{ e^{-2iC} \sqrt{\frac{A'_1}{\bar{\mu}(\frac{x}{S_0}) - i\bar{\kappa}'}} \Phi^* \left(\sqrt{2i(\bar{\mu}(\frac{x}{S_0}) - i\bar{\kappa}')} \right) - \Phi^* \left(\sqrt{2iA'_1} \right) \right\} \quad (2.9)$$

and

$$I_2 = \frac{e^{-2iB}}{B} H' \left\{ A' \left(e^{2iB} \left[1 - \text{erf}(\sqrt{4\bar{\kappa}'}) \right] - 1 \right) + \sqrt{2\bar{\kappa}'} \left(\bar{K} + (M - \frac{x}{S_0})\bar{\mu} \right) \frac{\Phi^*(\sqrt{-2iB})}{\sqrt{-iB}} \right\} \quad (2.10)$$

with

$$H' = \frac{(1+i)(1-\Theta'^2)}{2\sqrt{\pi}(\alpha-1)\bar{K}\sqrt{A'_1}} \quad \Theta' = \sqrt{\frac{A'_1}{A'}}$$

$$A'_1 = \bar{K}_1 + M\bar{\mu} - i\bar{\kappa}' \quad A' = \bar{K} + M\bar{\mu} - i\bar{\kappa}'$$

In both equations (2.9) and (2.10), a new complex function Φ^* is introduced that is

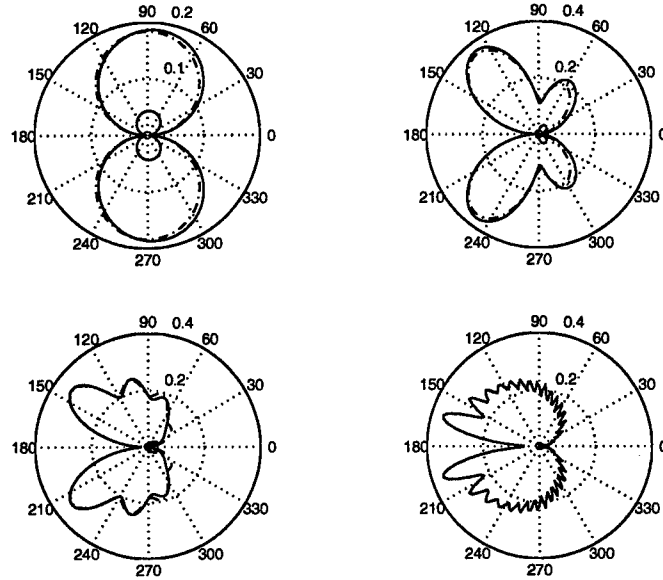


FIGURE 3. Directivity patterns for parallel gusts. From left to right and top to bottom: $kc = 1, 5, 10, 50$ for comparison with Howe (2001). $M = 0.05$, $\bar{K}_2 = 0$. — full solution, - - main term, — back-scattering (small lobes at center).

related to the complex E^* by:

$$\Phi^\circ(Z) = \frac{1}{\sqrt{\pi}} \int_0^{Z^2} \frac{e^{-z}}{\sqrt{z}} dz \quad \text{and} \quad \Phi^\circ(\sqrt{i x}) = \sqrt{2} e^{i\pi/4} E^*(x)$$

Sample non-dimensional K_2 -profiles of I for an observer in the mid-span plane ($y = 0$) are given in figure 2. A regularization procedure has been applied to smooth out the sharp cuts in the profiles between the supercritical and subcritical expressions understood as asymptotic solutions. The cuts are due to the breakdown of the analytical solution as the frequency parameter $\bar{\kappa}$ or $\bar{\kappa}'$ becomes exactly zero. The procedure is achieved by matching linearly the values of the derivative $\partial I / \partial K_2$ from both sides of the cuts and then re-calculating the profile. Subcritical gusts, for higher values of K_2 ($\bar{K}_2 / (\beta \bar{\mu}) > 1$), are cut-off in the sense that their efficiency is lower than the one of supercritical gusts and decreases with increasing K_2 . However their contribution to the sound field is not zero.

Calculations are made here with $c = 13 \text{ cm}$ and $M = 0.05$. At 200 Hz ($kc = 0.48$), $|I|$ is a slowly decreasing function of θ , whereas at 1000 Hz ($kc = 2.4$), it increases with θ until 100° and then decreases. The dashed horizontal segment in the right plot shows the level at 160° for small K_2 .

Typical directivity patterns in the mid-span plane for parallel and supercritical, oblique gusts are plotted in figures 3 and 4, respectively. The back-scattering has a noticeable effect on the radiation of parallel gusts only at low frequencies, as shown in figure 3. These results agree very well with similar calculations by Howe (2001) in the case of vanishing Mach number for hydroacoustic applications. They correspond to the left, flat part of the plots in figure 2. Figure 4 shows the effect of gust obliqueness on the full solution. Increasing K_2 makes the radiation to beam in an oblique direction upstream,

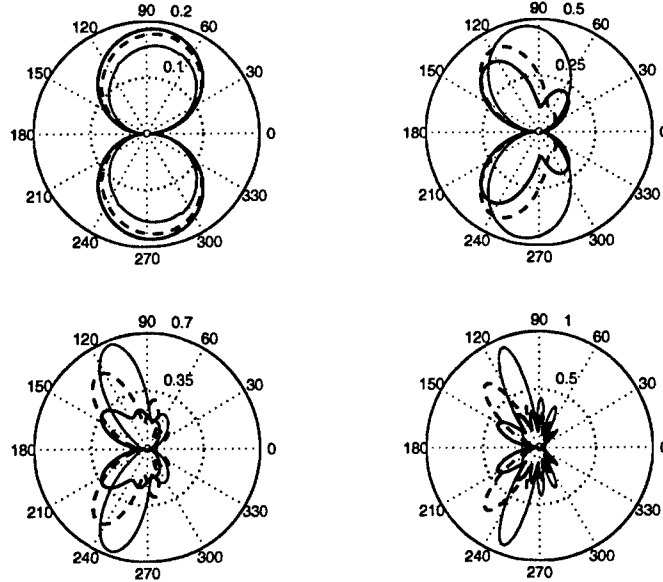


FIGURE 4. Directivity patterns for oblique gusts. From left to right and top to bottom: $k_c = 1, 5, 10, 20$. $M = 0.05$, $\bar{K}_2/(\beta \bar{\mu}) = 0.05$ —, 0.5 - - , 0.85 - · - .

more sharply as frequency increases. This effect corresponds to the hump in the radiation profiles of figure 2 for 1000 Hz.

A simplified version of the present formulation has been previously reported by Roger & Moreau (2002), for an observer in the mid-span plane. The squared function sinc of formula (2.1) was approximated by a Dirac delta function, which is valid for large aspect ratios. S_{pp} , Φ_{pp} and l_y were measured separately on a mock-up in an anechoic open-jet wind tunnel, in order to evaluate the ratio $S_{pp}/(\Phi_{pp} l_y)$. The latter was compared to its theoretical value according to the simplified equation. The measured directivity, integrated over the frequency range attributed to broadband self noise, was also compared to averaged calculations. Sample results are reported in figure 5. The airfoil chord makes a 13° angle with respect to the direction of the mean flow. An encouraging agreement is found, suggesting that the approach is reliable. The remaining discrepancies can be due to either the difficulty of evaluating the convection speed and spanwise coherence length at all frequencies of interest in the experiment, or to the simplification in the analytical model. This motivated the present research.

3. Future plans

The present theory only addresses the question of the transfer function between the hydrodynamic wall pressure and the far field acoustic pressure. The wall pressure statistics defined by Φ_{pp} and l_y and needed as input must be known from either flow measurements or computations. It is not available from RANS calculations that are routinely used by most industrial manufacturers. However, it can be provided by incompressible LES.

The next step, still in progress, is to improve the validation procedure and to use LES results to compute the aforementioned statistical parameters. More precisely, a new experiment with an increased width of the open jet has been designed at Ecole Centrale de Lyon, in order to minimize the installation effects pointed out by Moreau et al (2001).

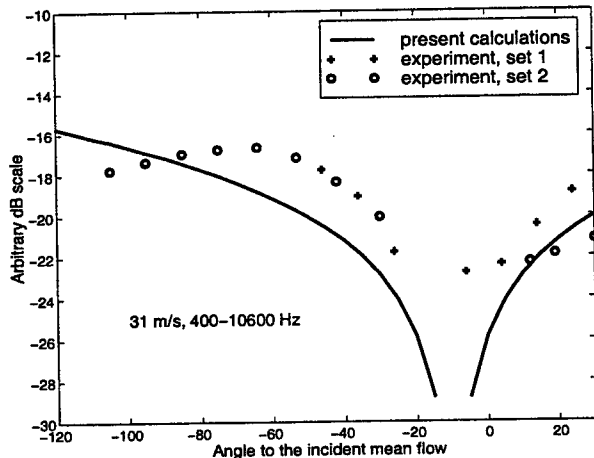


FIGURE 5. Measured versus predicted directivity of the trailing-edge broadband noise due to turbulent boundary layers. Negative angles correspond to an observer facing the suction side.

A simulation of the experimental mean flow has been made with the help of a RANS code. This flow field will be used to provide boundary conditions for an LES, carried out in a smaller domain within the potential core of the jet. First, the LES results will be compared to the measured wall pressure statistics. In the second step, the radiated sound will be calculated using (2.1) and compared to the sound actually measured in the experiment.

4. Appendix

Let Φ be a two-dimensional scalar field solution of the following wave problem:

$$\begin{aligned} \frac{\partial^2 \Phi}{\partial x^2} + \frac{\partial^2 \Phi}{\partial z^2} + \mu^2 \Phi &= 0 \\ \Phi(x, 0) &= f(x) \quad x \geq 0 \\ \frac{\partial \Phi}{\partial z}(x, 0) &= 0 \quad x < 0 \end{aligned}$$

Then for any $x < 0$:

$$\Phi(x, 0) = \frac{1}{\pi} \int_0^\infty G(x, \xi, 0) f(\xi) d\xi$$

with:

$$G(x, \xi, 0) = \sqrt{\frac{-x}{\xi}} \frac{e^{-i\mu(\xi-x)}}{\xi - x}$$

This result, known as Schwarzschild's theorem and given in Landahl (1961), leads to mathematical solutions that are equivalent to the ones obtained by Adamczyk (1974) using the Wiener-Hopf technique. Strictly speaking, the theorem holds for half-plane

problems. When applied to an airfoil with finite chord length, it must be used within an iterative procedure involving alternative corrections. According to Amiet (1975), the first two iterations are enough in the problem of the noise generated by the impingement of upstream turbulence on an isolated airfoil. The same is assumed to hold here. The iterations are referred to as main scattering and back-scattering in the text.

REFERENCES

- ABRAMOWITZ, M. & STEGUN, I.A. 1970 *Handbook of Mathematical Functions*. Dover, New York.
- ADAMCZYK, J.J. 1974 *The passage of an infinite swept airfoil through an oblique gust*. NASA CR-2395.
- AMIET, R.K. 1975 Acoustic radiation from an airfoil in a turbulent flow. *J. Sound Vib.* **41**, 407–420.
- AMIET, R.K. 1976 Noise due to turbulent flow past a trailing edge. *J. Sound Vib.* **47**, 387–393.
- AMIET, R.K. 1978 Effect of the incident surface pressure field on noise due to turbulent flow past a trailing edge. *J. Sound Vib.* **57**, 305–306.
- BROOKS, T.F. & HODGSON, T.H. 1981 Trailing-edge noise prediction from measured surface pressures. *J. Sound Vib.* **78**, 69–117.
- BROOKS, T.F., MARCOLINI, M.A. & POPE, D.S. 1989 *Airfoil self-noise and prediction*. NASA RP-1218.
- FFOWCS WILLIAMS, J.E. & HAWKINGS, D.L. 1969 Sound generation by turbulence and surfaces in arbitrary motion. *Phil. Trans. Roy. Soc. A* **264**, 321–342.
- FFOWCS WILLIAMS, J.E. & HALL, L.H. 1970 Aerodynamic sound generation by turbulent flow in the vicinity of a scattering half-plane. *J. Fluid Mech.* **40**, 657–670.
- HOWE, M.S. 2001 Edge-source acoustic Green's function for an airfoil of arbitrary chord, with application to trailing-edge noise. *Q. J. Mech. Appl. Math.*, **54**, pp. 139–155.
- LANDAHL, M. 1961 *Unsteady transonic flow*. Pergamon Press, New York.
- MOREAU, S., IACCARINO, G., ROGER, M. & WANG, M. 2001 CFD analysis of flow in an open-jet aeroacoustic experiment. *Annual Research Briefs*, Center for Turbulence Research, NASA Ames/Stanford Univ., 343–351.
- ROGER, M. & MOREAU, S. 2002 Trailing edge noise measurements and prediction for a subsonic loaded fan blade. *AIAA Paper 2002-2460*.
- SINGER, B.A. 1996 *Turbulent wall-pressure fluctuations: new model for off-axis cross-spectral density*. NASA CR 198297.
- WANG, M., & MOIN, P. 2000 Computation of trailing-edge flow and noise using large-eddy simulation. *AIAA J.* **38**, 2201–2209.

Turbulence modeling in an immersed-boundary RANS method

By Georgi Kalitzin AND Gianluca Iaccarino

1. Motivation and Background

Virtually all the applications of the Immersed Boundary (IB) technique have been in the low-Reynolds number regime (up to 10^4) either as Direct Numerical Simulations (DNS) or Large Eddy Simulations (LES). For those applications simple off-boundary conditions (usually based on linear interpolations) are used for the velocity fields to account for the effect of the *immersed* boundary on the flow field: see Fadlun *et al.* (2000) and Verzicco *et al.* (2000). The application of IB to industrially relevant turbulent flows at high Reynolds numbers requires its adaptation in the framework of the Reynolds-Averaged Navier-Stokes equations.

When IB is used in conjunction with RANS additional care must be devoted to the application of suitable turbulence models. In particular, classical approaches (e.g. models of $k-\epsilon$ type) are based on differential equations for turbulent scalars that characterize a velocity and a length scale which, in turn, define the eddy-viscosity. Those quantities typically exhibit large gradients and local extrema in the near vicinity of solid walls; for example the turbulent kinetic energy has a peak in the logarithmic layer and decays quadratically towards solid walls. It is evident that the straightforward application of an off-wall linear interpolation would introduce errors in the representation of such a quantity; on the other hand, even at high Reynolds numbers, provided that the grid resolution is sufficient, a linear interpolation for the velocity would still be consistent with the linear behavior of the velocity in the viscous sublayer.

Previous investigations by Majumdar *et al.* (2001) of more sophisticated off-wall boundary conditions, mainly for flows at low Reynolds number, did not demonstrate a conclusive advantage over the simpler linear interpolation. Furthermore, a linear interpolation scheme can easily be recast in a fully-implicit form, thus introducing no time step limitation or additional stiffness for steady-state problems. The implicit treatment of more sophisticated interpolation schemes (quadratic, inverse-distance based, etc.) introduce non-linearities that may have an impact on the robustness and overall stability of the computational procedure.

In this paper we focus on the development of IB conditions for turbulence models and the initial validation of an IB RANS solver. The application consists of a turbine blade passage for which detailed DNS results are available (see Kalitzin *et al.* (2002)). The paper compares the IB technique with a standard body-fitted method to isolate the effect of the off-wall boundary conditions on the results. A three-dimensional test case of a turbine blade with a 10% tip gap is included to demonstrate the potentials of the IB technique for more complicated situations.

A major concern in applying the IB technique to high-Reynolds number flow is the resolution of thin boundary layers on curvilinear bodies using Cartesian grids. This resolution issue will be addressed in future work with a grid-refinement technique. The present paper considers coarse-grid solutions to demonstrate that smooth surface distri-

butions of pressure and friction can be obtained with the present IB technique. To model turbulence, we first considered the model of Spalart and Allmaras (1992) and the $k-g$ models, discussed by Kalitzin (1997) because of their simple wall boundary conditions. The $k-\omega$ model of Wilcox (1993) was implemented at a later stage. The test case considered is not sensitive to the turbulence model, especially for the grid used. Thus, the objective of considering several turbulence models is to show that these models can be used in conjunction with the IB technique.

2. Flow solver and turbulence models

The steady-state incompressible Reynolds-averaged Navier-Stokes equations are solved using a second-order, cell-centered finite-volume scheme on Cartesian non-uniform grids. The momentum equation is solved sequentially for each component of an intermediate velocity. The divergence of this velocity field provides the source term of a Poisson equation for a pressure correction (SIMPLE procedure, Vandoormaal *et al.* (1984)) which enforces a solenoidal velocity field. The eddy viscosity is obtained from an one-equation or two-equation turbulence model which is solved separately from the mean flow. The equations are linearized and solved in a fully-implicit fashion, resulting in a linear algebraic system of the form:

$$a_p^n \phi_p^{n+1} + \sum_{l=w,e,s,n,b,t} a_l^n \phi_l^{n+1} = S_p^n \quad (2.1)$$

where ϕ is either one of the velocity components, the pressure or a turbulence variable. While the usual boundary conditions (inflow, outflow, periodicity and solid walls) are applied at the boundary of the computational domain, the curvilinear solid body is placed entirely or partly within the computational domain and immersed using the IB procedure described in section 2.1. The system is then solved using a LU-type decomposition or a Krylov iterative solver; the computer program is based on Ferziger and Perić (2002).

2.1. Immersed Boundary Approach

The IB-methodology is based on the work of Fadlun *et al.* (2000) and Verzicco *et al.* (2000). It has been suitably modified to work in the current RANS environment. In a preliminary step, a given geometry which is described with a closed polygon in 2D and an STL file in 3D is overlaid on a Cartesian non-uniform mesh. The computational cells in the fluid and in the solid body are tagged as *internal* and *external* cells, respectively. The cells containing both fluid and solid body are tagged as *interface* cells (figure 1). In this phase, care must be taken to ensure that the layer of interface cells completely surrounds the immersed surface. Once all the cells are tagged, the distance from the wall is computed if needed for later use by the turbulence models.

The equations that is solved for the variables ϕ in the interface cells is:

$$\alpha_b^n \phi_p^{n+1} + \sum_{l=w,e,s,n,b,t} \alpha_l^n \phi_l^{n+1} = 0 \quad (2.2)$$

where the α 's are the interpolation weights. These weights are computed from the *base* cells (i.e. the internal cells) and the *target* cells (i.e. the internal cells surrounding each base cell). The base and target notation is commonly used for *Chimera* grids. The weights are computed once, at the start of the calculation, and stored.

Equation (2.2) represents the discrete form of the direct-forcing approach proposed by Fadlun *et al.* (2000). The interpolation is applied to the velocity components and to the

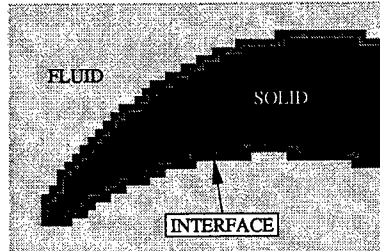


FIGURE 1. Result of the cell-tagging procedure for the Immersed Boundary Technique

turbulent scalars. The pressure equation is not modified and no boundary conditions are enforced at the immersed boundary. This has proven to be effective in producing smooth pressure distributions, even for thin airfoils such as the one presented in the Results section. Alternative treatments of the pressure have been attempted but further analysis is required to identify improvements to the current approach.

2.2. Spalart-Allmaras turbulence model

The model of Spalart and Allmaras (1992) exhibits good convergence properties and has a remarkably accurate response to pressure gradient. It consists of one transport equation for a modified eddy-viscosity, $\tilde{\nu}$:

$$\vec{u} \cdot \text{grad } \tilde{\nu} = \frac{1}{c_{b3}} \left[\text{div} ((\nu + \tilde{\nu}) \text{grad } \tilde{\nu}) + c_{b2} (\text{grad } \tilde{\nu} \cdot \text{grad } \tilde{\nu}) \right] + Q \quad (2.3)$$

in which the source term Q is:

$$Q = c_{b1}(1 - f_{t2})\tilde{S}\tilde{\nu} + \left(\frac{c_{b1}}{\kappa^2}f_{t2} - c_{w1}f_w \right) \left(\frac{\tilde{\nu}}{d} \right)^2 \quad (2.4)$$

The eddy viscosity is:

$$\mu_t = \rho\tilde{\nu}f_{v1} \quad (2.5)$$

The model damping functions, auxiliary relations and trip term are defined as:

$$f_{v1} = \frac{\chi^3}{\chi^3 + c_{v1}^3}, \quad f_{v2} = 1 - \frac{\chi}{1 + \chi f_{v1}}, \quad \chi = \frac{\tilde{\nu}}{\nu} \quad (2.6)$$

$$f_w = g \left[\frac{1 + c_{w3}^6}{g^6 + c_{w3}^6} \right]^{\frac{1}{6}}, \quad g = r + c_{w2}(r^6 - r), \quad r = \frac{\tilde{\nu}}{\tilde{S}\kappa^2 d^2} \quad (2.7)$$

$$\tilde{S} = S + \frac{\tilde{\nu}}{\kappa^2 d^2} f_{v2}, \quad S = \sqrt{2\Omega_{ij}\Omega_{ij}}, \quad f_{t2} = c_{t3} \exp(-c_{t4}\chi^2) \quad (2.8)$$

in which d is the distance to the nearest wall, κ the von Kármán constant and S the vorticity expressed in terms of the rotation tensor $\Omega_{ij} = \frac{1}{2}(\frac{\partial u_i}{\partial x_j} - \frac{\partial u_j}{\partial x_i})$. Finally, the model

closure coefficients are:

$$c_{b1} = 0.1355, \quad c_{b2} = 0.622, \quad c_{b3} = 2/3, \quad c_{v1} = 7.1 \quad (2.9)$$

$$c_{w1} = \frac{c_{b1}}{\kappa^2} + \frac{1 + c_{b2}}{c_{b3}}, \quad c_{w2} = 0.3, \quad c_{w3} = 2, \quad c_{t3} = 1.2, \quad c_{t4} = 0.5 \quad (2.10)$$

The wall boundary condition is:

$$\tilde{\nu}_t = 0. \quad (2.11)$$

2.3. Wilcox $k-\omega$ model

The $k-\omega$ model of Wilcox (1993) is implemented in its original form. The 1998 version of the model (see 2nd ed.) contains certain correction terms which will be considered at a later stage. The transport equations for the turbulent kinetic energy k and the specific dissipation rate $\omega \propto \epsilon/k$ are:

$$\frac{\partial(\rho u_i k)}{\partial x_i} = \frac{\partial}{\partial x_i} \left[(\mu + \frac{\mu_t}{\sigma_\omega}) \frac{\partial \omega}{\partial x_i} \right] + P_k - \rho k \omega, \quad (2.12)$$

$$\frac{\partial(\rho u_i \omega)}{\partial x_i} = \frac{\partial}{\partial x_i} \left[(\mu + \frac{\mu_t}{\sigma_\omega}) \frac{\partial \omega}{\partial x_i} \right] + \alpha \frac{\omega}{k} P_k - \beta \rho \omega^2. \quad (2.13)$$

The eddy viscosity is:

$$\mu_t = \rho \frac{k}{\omega} \quad (2.14)$$

The model coefficients are:

$$\sigma_\omega = 2.0, \beta^* = 0.09, \alpha = 5/9, \beta = 0.075$$

The wall boundary condition for k is:

$$k = 0. \quad (2.15)$$

The specific dissipation rate tends asymptotically to infinity at the wall as $\sim 1/y^2$. Wilcox (1993) describes the numerical errors associated with the numerical integration of ω up to the wall. Menter (1993) suggested to use the following boundary condition:

$$\omega = \frac{60\nu}{\beta_1 y_1^2} \quad (2.16)$$

where y_1 is the distance from the wall to the center of the first cell above the wall.

2.4. Near-wall behavior

This section focuses on the near-wall behavior of the turbulence models presented above, in particular on the treatment of the wall boundary condition in the framework of the immersed boundary.

The modified eddy viscosity $\tilde{\nu}$ is zero at the wall and it has the property of varying in a nearly linear fashion from the wall throughout the law-of-the-wall layer thus decreasing the sensitivity to grid resolution and wall clustering (Durbin and Pettersson Reif (2001)). The linearity of $\tilde{\nu}$ makes it straightforward to implement the Spalart-Allmaras model with the immersed boundaries, using in the interface cells the same linear interpolation stencil used for the velocity components. Inside the body the modified eddy viscosity $\tilde{\nu}$ is set to zero.

The turbulent kinetic energy k and the specific dissipation rate ω in the $k-\omega$ model

vary in the viscous sublayer as $\sim y^{3.23}$ and $\sim 1/y^2$, respectively. At the current stage the linear interpolation method is applied directly to k . This may, however, not be sufficiently accurate, and further investigation is required. ω is set in the interface cells to the value computed with (2.16). Some of the cell centers may lie exactly on the wall, which would lead to undefined values in those cells. The minimal distance y in equation (2.16) is limited by an arbitrary small constant which could be related to the Reynolds number. This basically cuts off the ω value at the wall. In the cells inside the body, ω is set to the value defined by this arbitrary constant.

In an alternative approach, we investigate the transformation of the ω -equation to a different independent variable that is more suitable for use with immersed boundaries. Kalitzin (1997) suggests recasting the ω -equation in terms of the variable $g = 1/\sqrt{\beta^* \omega}$: then

$$\frac{\partial(\rho u_i g)}{\partial x_i} = \frac{\partial}{\partial x_i} \left[\left(\mu + \frac{\mu_t}{\sigma_g} \right) \frac{\partial g}{\partial x_i} \right] - \alpha \frac{g}{2k} P_k + \frac{\beta \rho}{2g\beta^*} - \left(\mu + \frac{\mu_t}{\sigma_g} \right) \frac{3}{g} \frac{\partial g}{\partial x_i} \frac{\partial g}{\partial x_i}. \quad (2.17)$$

In the viscous sublayer g varies linearly with the distance to the wall. At the wall g is zero, and the interpolation stencil used for the mean velocities can be applied in the interface cells.

In the continuous space the above transformation leads to identical eddy viscosity values, whereas when the discretized equations are solved this is not the case. Numerical dissipation is in particular influential in regions of large gradients and poor resolution. g increases away from the wall as shown for the flat plate in figure 2b. However, the outer part of the boundary layer is usually less resolved than the near-wall region. The diffusion of g from the free stream into the boundary layer is in contrast to ω diffusing from the boundary layer to the freestream. To investigate the effect of this, the $k-\omega$ and $k-g$ models have been combined into a two-layer formulation (hybrid model) where the latter is used only in the vicinity of solid walls.

2.5. Implementation of the hybrid model

At the start of the computation, each cell is marked with an integer array γ which identifies the equations to be solved. In the near-wall region, where the g equations is to be solved, γ is set to 1, elsewhere it is set to 0. The distance to the wall is used to define the near-wall region. The implicitly-discretized turbulence equations can be written as:

$$a_p^n \phi_p^{n+1} + \sum_{l=w,e,s,n,b,t} a_l^n \phi_l^{n+1} = RHS_p^n \quad (2.18)$$

where the variable ϕ is g or ω depending on the array γ . The coefficients a_l^n and the right hand side RHS_p^n , which depend on the variable ϕ^n from the previous iteration n , are computed according to the g - or ω -equation, respectively. Thus, the source term S_p^n which is included in RHS_p^n is computed as:

$$S_p^n = \left(-\alpha \frac{\phi_p^n}{2k} P_k + \frac{\beta \rho}{2\phi_p^n \beta^*} \right) \gamma_p + \left(\alpha \frac{\phi_p^n}{k} P_k - \beta \rho (\phi_p^n)^2 \right) (1 - \gamma_p) \quad (2.19)$$

The convective and diffusion terms contain the dependent variable from two adjacent cells. The dependent variable in the cell l adjacent to cell p is computed from:

$$\tilde{\phi}_l^n = (\Gamma_{gg} + \Gamma_{\omega\omega}) \phi_l^n + \Gamma_{gw} \left(\frac{1}{\sqrt{\beta^* \phi_l^n}} \right) + \Gamma_{\omega g} \left(\frac{1}{\beta^* (\phi_l^n)^2} \right) \quad (2.20)$$

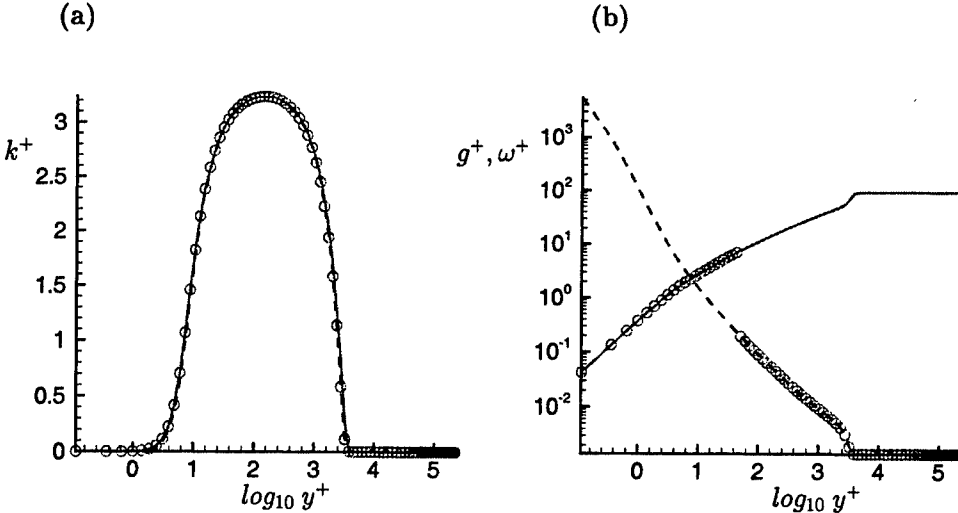


FIGURE 2. (a) Turbulent kinetic energy and (b) length scale variable for flat plate (--- $k-\omega$, —— $k-g$, ○ hybrid (every cell centered value plotted))

with $\Gamma_{gg} = \gamma_p \gamma_l$; $\Gamma_{gw} = \gamma_p(1 - \gamma_l)$; $\Gamma_{wg} = (1 - \gamma_p)\gamma_l$; $\Gamma_{ww} = (1 - \gamma_p)(1 - \gamma_l)$; Only one of these indicators is non-zero and equal to one. In the case of an interface cell, Γ_{gg} and Γ_{ww} are zero and ϕ_l^n is converted into $\tilde{\phi}_l^n$.

Implicitness at the interface is achieved by modifying the coefficients a_l^n with $\tilde{a}_l^n = a_l^n \tilde{\phi}_l^n / \phi_l^n$; only at the interface \tilde{a}_l^n is not equal a_l^n . At the interface the coefficient \tilde{a}_l^n is $\tilde{a}_l^n = a_l^n \omega^n / g^n$ and $\tilde{a}_l^n = a_l^n g^n / \omega^n$ for $\Gamma_{wg} = 1$ and $\Gamma_{gw} = 1$, respectively. If the interface is close to the wall, the algebraic system becomes unstable as ω tends to infinity and g to zero. Therefore ω is treated explicitly at the interface:

$$a_p^n \phi_p^{n+1} + \sum_{l=w,e,s,n,b,t} \tilde{a}_l^n \phi_l^{n+1} (1 - \Gamma_{wg}) = S_p^n - a_l^n \phi_l^n \Gamma_{wg} \quad (2.21)$$

Figures 2 and 3 show the results of a calculation of flow over a flat plate with the $k-\omega$, $k-g$ and the hybrid model. The turbulent kinetic energy in figure 2a and the velocity profile in 3a are almost identical although the shear stress at the wall is slightly smaller for the $k-\omega$ model, resulting in a larger U^+ in the defect layer. Figure 2b demonstrates the second scalar of the hybrid model following g near the wall and switching at a prescribed location to ω . The convergence is very similar for all three models as shown in figure 3b.

2.6. Wall models

High near-wall grid resolution is usually required to perform RANS simulation using the discussed turbulence models; the accepted rules in meshing turbulent boundary layers are: (i) the y^+ of the first cell center should not be greater than 1 and (ii) about 20 cells should be located inside the boundary layers. A careful selection of turbulence model might reduce those restrictions. However, it is reasonable to expect that for high Reynolds numbers Cartesian mesh will not fully resolve the boundary layers. Computing skin friction in the usual way on such grids may result in values incorrect by several order of magnitude. Therefore, the velocity fields are post-processed using a wall model of the form:

$$u/u_\tau = \frac{1}{\kappa} \ln(1 + \kappa y^+) + c(1 - e^{-y^+/d^+} - \frac{y^+}{d^+} e^{-b y^+}) \quad (2.22)$$

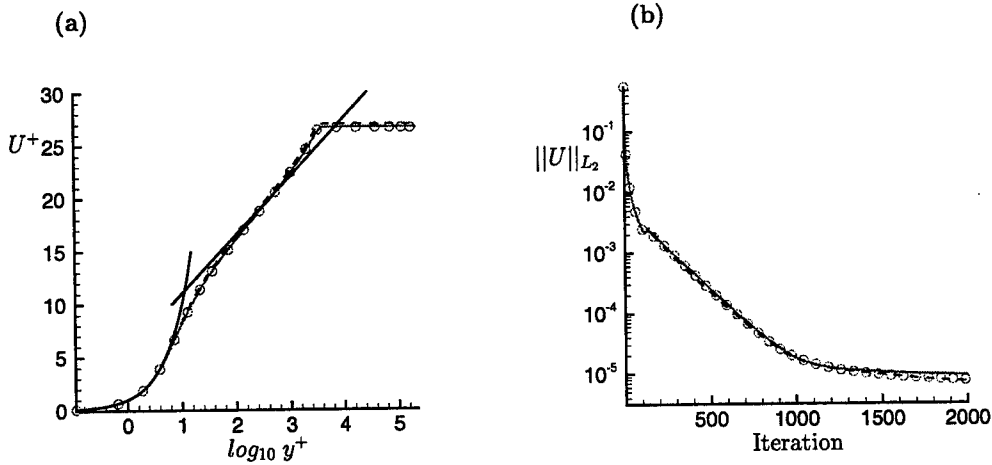


FIGURE 3. (a) Velocity and (b) convergence of L_2 norm of velocity residual for flat plate
(--- $k-\omega$, —— $k-g$, ○ hybrid (selected values are plotted))

$$b = \frac{1}{2} \left(\frac{d^+ \kappa}{c} + \frac{1}{d^+} \right) \quad (2.23)$$

$$c = \frac{1}{\kappa} \ln \left(\frac{E}{\kappa} \right) \quad (2.24)$$

where κ , E and d^+ assume the values of 0.4187, 9.793 and 11 respectively. This expression, due to Reichardt (1951), reproduces the logarithmic layer and the linear sublayer with a continuous switch in the buffer region.

The formulation (2.22) is used to compute u_τ using the (tangential) velocity u at a certain distance (δ) from the immersed surface (this *de facto* corresponds to the creation of a *body-fitted* grid line). The friction velocity u_τ and the formulation (2.22) are used to estimate the tangential velocity in the interface cell (at a distance $\delta_i < \delta$). Note that, if the interface cell is very close to the surface, the above approach returns a linear velocity interpolation consistent with the *standard* immersed boundary technique. The choice of the distance δ is obviously critical for the application of this procedure. Preliminary results have been obtained using δ equal to the largest distance from the wall in all the interface cells.

3. Results and discussion

The IB/RANS solver is applied to turbulent flow inside the T106 turbine blade passage. This test case has been studied extensively using DNS for various inflow conditions (Kalitzin *et al.* (2002)). The focus of the present study is to investigate the feasibility of the IB approach for this flow, and its accuracy in representing surface quantities like pressure and skin friction. The representation of the latter using the IB-approach has not been discussed previously in the literature. Comparison are made with body-fitted results obtained with FLUENT and the DNS data for a turbulence-free inlet.

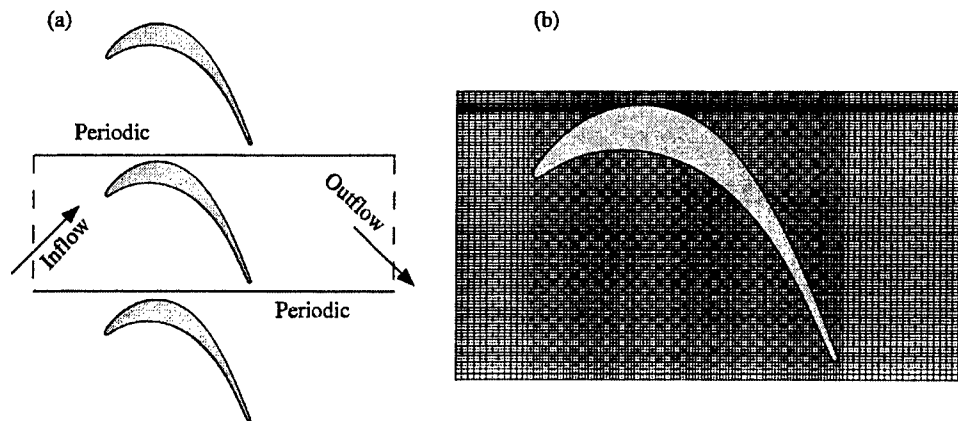


FIGURE 4. (a) Computational domain and (b) computational grid 186×110

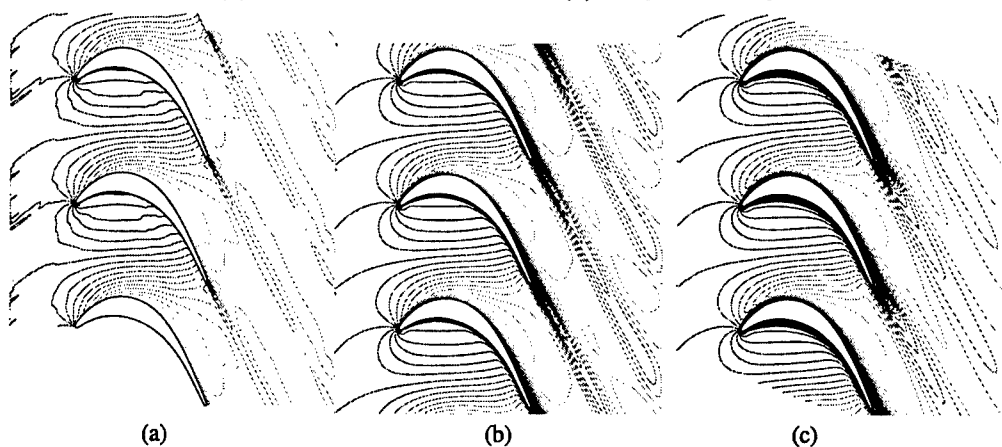


FIGURE 5. Comparison of the velocity magnitude in the blade passage. (a) DNS, (b) Immersed Boundary / SA model and (c) Body-fitted / SA model.

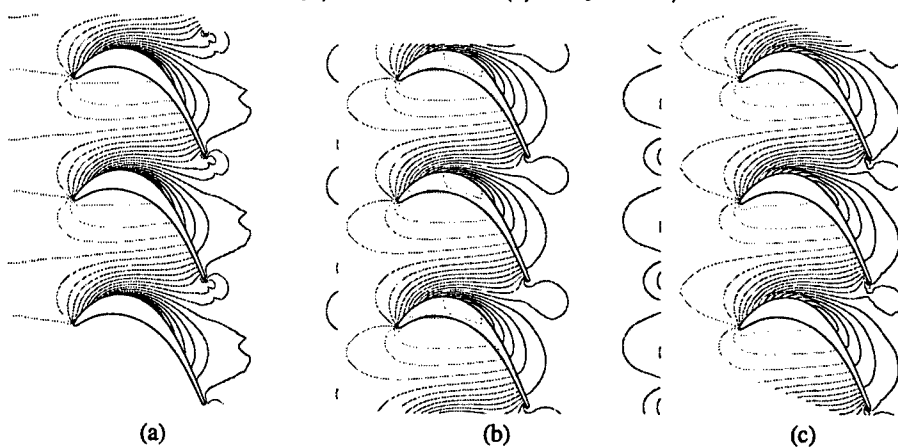


FIGURE 6. Comparison of the pressure coefficient in the blade passage; (a) DNS, (b) Immersed Boundary / SA model and (c) Body-fitted / SA model.

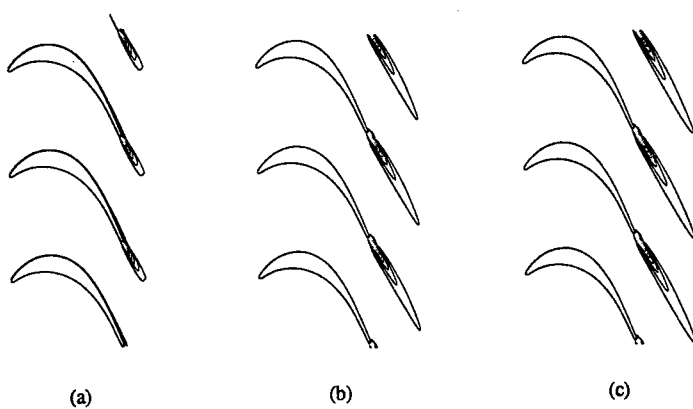


FIGURE 7. Turbulent kinetic energy in the blade passage; (a) DNS, (b) Immersed Boundary / $k-\omega$ model, (c) Immersed Boundary / $k-g$ model.

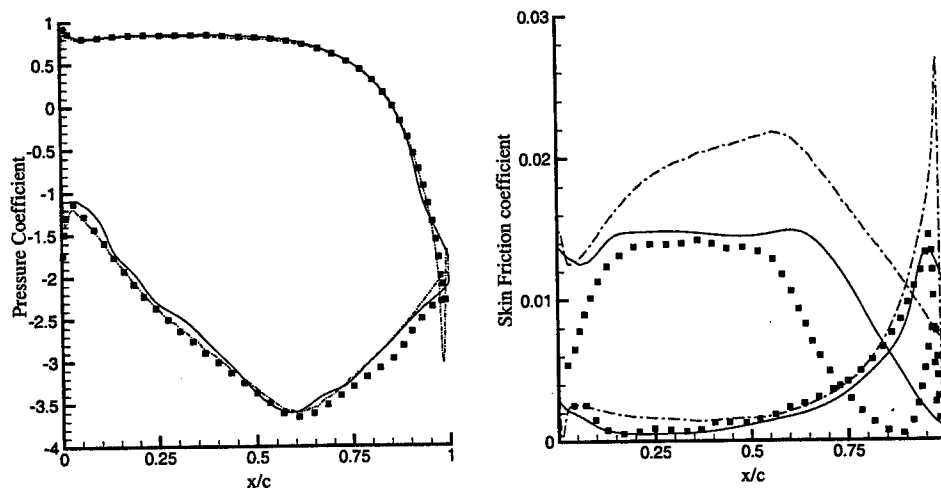


FIGURE 8. Surface pressure distribution (left), skin friction distribution (right). ■ DNS,
— Immersed Boundary / SA model - - - Body-fitted / SA model.

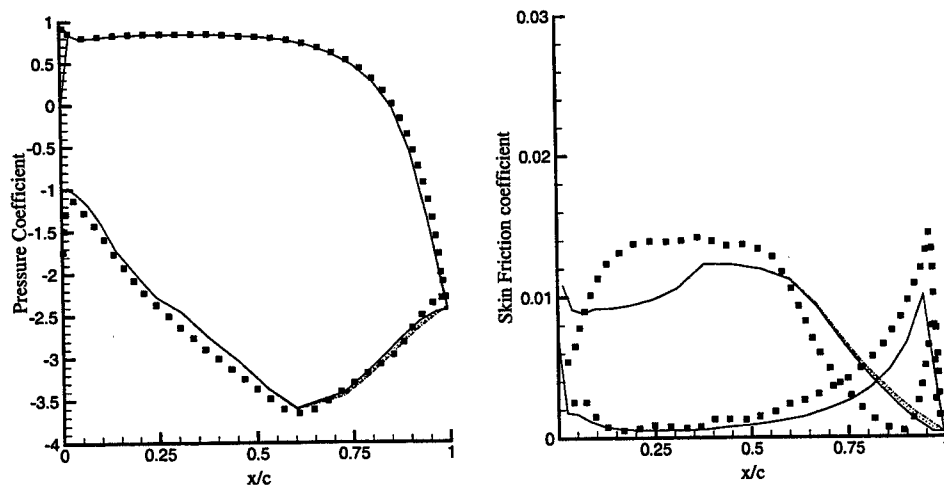


FIGURE 9. Surface pressure distribution (left), skin friction distribution (right). ■ DNS,
— $k-\omega$ model, - - - $k-g$ model, hybrid model. RANS is with Immersed Boundaries.

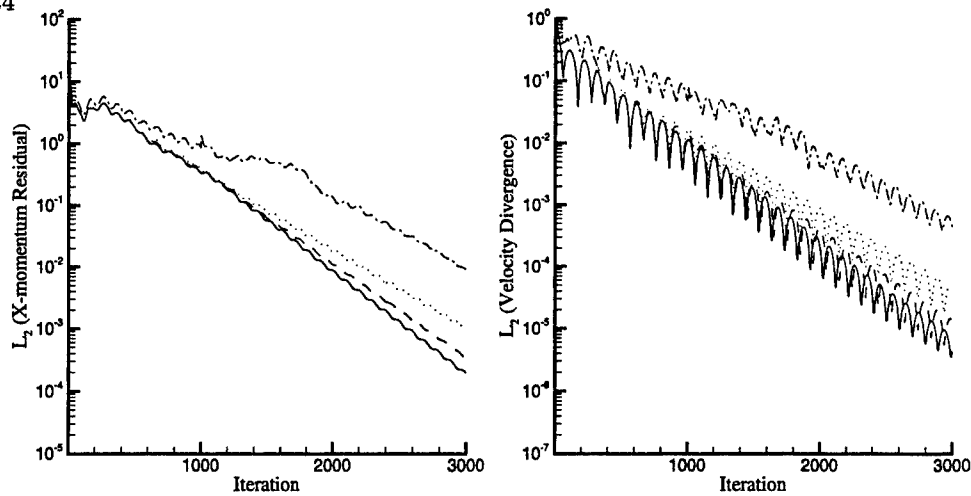


FIGURE 10. Convergence history for IB method. Velocity (left), Velocity divergence (right).
 — $k-\omega$, - - - $k-g$, hybrid, - · - SA

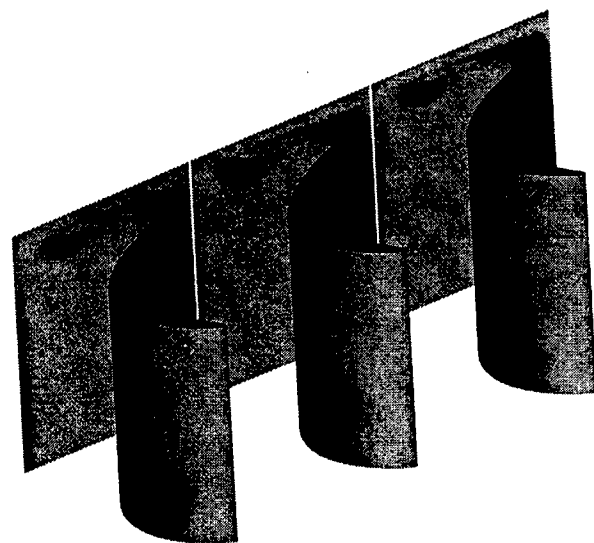


FIGURE 11. Velocity distribution in the wake of the three-dimensional blade with 10% tip gap showing traces of a vortex and trailing edge separation, IB method.

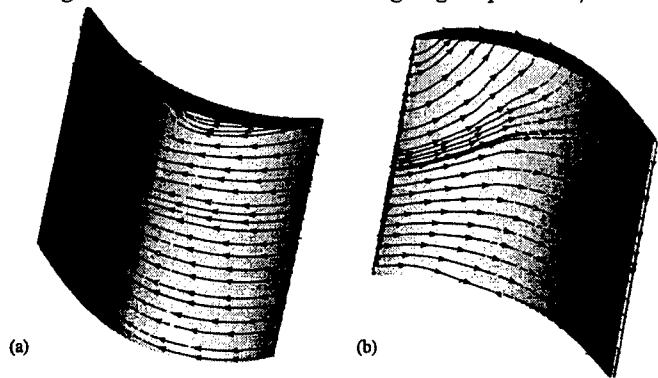


FIGURE 12. Friction lines on the surface of the three-dimensional blade: (a) suction side (b) pressure side, IB method.

A sketch of the computational setup and the grid is shown in figure 4. The IB and body-fitted calculations are carried out on a Cartesian mesh of (186×112) cells and a comparable unstructured mesh of about 20,000 elements, respectively. The Reynolds number is $Re = 148,000$. The T106 case is extremely challenging for the current IB-approach because of the large pressure difference between the suction and pressure sides of the blade. The airfoil is extremely thin and only a few cells (ranging from 4 to 15) are inside it.

Contours of the velocity magnitude are shown in figure 5. The overall qualitative agreement among the DNS, the IB and the body-fitted RANS calculations is satisfactory, even though the latter two methods predict a thicker boundary layer towards the trailing edge on the upper side of the airfoil. This is caused by the under-resolution of the boundary layers. However, the agreement between the IB and body-fitted results is good. Figure 6 demonstrates that the IB technique is able to predict accurate pressure distributions in the passage. The region near the leading edge is particularly challenging for the IB method due to the sharp pressure gradient and strong surface curvature. The comparison of the turbulent kinetic energy contours to the DNS, shown in figure 7, is satisfactory although the DNS predicts a higher level of turbulent kinetic energy on the upper side of the airfoil. Transition is missed by the RANS simulations.

A quantitative assessment of the IB method is shown in figure 8. The wall pressure distribution agrees well among the DNS, the IB and the body fitted RANS calculations, the latter two using the Spalart-Allmaras model. Differences among the skin friction distributions are more substantial. The RANS simulations do not show the sharp increase in the final 10% portion of the blade, which is caused by transition. Interestingly, the IB calculation shows friction levels that are overall closer to the DNS, especially on the lower side of the airfoil. This might be due to differences in the implementation details of the Spalart-Allmaras model or to differences in the post-processing.

Figure 9 shows wall-pressure and skin-friction distributions for the $k-\omega$ variants. The hybrid model has been run with the g -equation in the near-wall region wrapped around the blade. This layer is $0.1C_x$ thick, where C_x is the axial chord of the blade. Only slight discrepancies are observable in the skin friction, on the upper wall near the trailing edge. The pressure is slightly better predicted than using the Spalart-Allmaras model.

The convergence of the IB method is plotted in Figure 10. The steady state is achieved in about 2,000 iterations. The IB interpolation has no negative impact on convergence to the steady state.

The flow around a three-dimensional version of the blade geometry, embedded between an endwall and a tip gap of 10% of the blade chord, is shown in Figure 11. This flow was computed to demonstrate the potential of the IB method for complex flows. The tip gap adds substantial complexity to the flow with the formation of a strong tip vortex. The skin-friction lines on the blade surface, shown in Figure 12, reveal that the three-dimensionality of the flow starts at 50% span. The flow separates at the trailing edge and there is a strong tip leakage flow from the pressure side to the suction side.

The main objective of future work is the evaluation of the accuracy of the present IB approach. A local grid refinement will be implemented to resolve of the boundary layers. Future work will also include an investigation of coarse grid behavior of turbulence models in conjunction with the linear interpolation procedure of the IB method.

REFERENCES

- DURBIN, P. A. & PETTERSSON REIF, B. A. 2001 *Statistical Theory and Modeling for Turbulent Flows*. Wiley, New York.
- FADLUN, E. A., VERZICCO, R., ORLANDI, P. & MOHD-YUSOF, J. 2000 Combined immersed-boundary/finite-difference methods for three-dimensional complex flow simulations. *J. Comp. Phys.* **161**, 35–60.
- FERZIGER, J. H. & PERIĆ, M. 2002 *Computational Methods for Fluid Dynamics*. 3rd ed. Springer, Berlin.
- KALITZIN, G. 1997 Validation and development of two-equation turbulence models. In *Validation of CFD codes and assessment of turbulence models*. (W. Haase et al., eds.). Notes on Numerical Fluid Mechanics Series Vol. 57. Vieweg, 1997.
- KALITZIN, G., WU, X. & DURBIN, P. A. 2002 DNS of fully turbulent flow in a LPT passage. Presented at *5th Int. Sympo. on Engg Turbulence Modelling and Meas. (ETMM5)*, Mallorca, Spain.
- MAJUMDAR, S., IACCARINO, G. & DURBIN P. A. 2001 RANS solver with adaptive structured boundary non-conforming grids. *Annual Research Briefs*, Center for Turbulence Research, NASA Ames/Stanford Univ., 353–366.
- MENTER, F. R. 1993 Zonal two equation $k - \omega$ turbulence model predictions. *AIAA paper* 93-2906.
- REICHARDT, H. 1951 Vollständige Darstellung der turbulenten Geschwindigkeitsverteilung in glatten Leitungen. *Z. Math. Mech.* **31**, 11.
- SPALART, P. R. & ALLMARAS, S. R. 1992 A one-equation turbulence model for aerodynamic flows. *AIAA paper* 92-439.
- VANDOORMAAL, J. P., & RAITHBY, G. D. 1984 Enhancements of the SIMPLE method for predicting incompressible fluid flows. *Num. Heat Transf* **7**, 147–163.
- VERZICCO, R., MOHD-YUSOF, J., ORLANDI, P. AND HAWORTH, D. 2000 LES in complex geometries using boundary body forces. *AIAA J.* **38**, 427–433.
- WILCOX D.C. 1993 *Turbulence modeling for CFD*. 1st ed. DCW Industries, La Cañada.

Skin-friction estimation at high Reynolds numbers and Reynolds-number effects for transport aircraft

By A. Crook

1. Motivation and objectives

Accurate performance estimation is essential for any aircraft, either civil or military. Although both types of aircraft will operate at transonic cruise conditions for a portion of a typical flight, the civil transport aircraft is largely optimized for this condition above all others.

The purpose of this research brief is to conduct a brief review of skin-friction estimation over a range of Reynolds numbers, as this is one of the key parameters in performance estimation and Reynolds number scaling. If it is concluded that the available data are of insufficient quality, it is proposed to undertake an experiment to measure incompressible flat-plate skin friction directly over a large range of Reynolds numbers up to Reynolds numbers representative of flight conditions.

The flow around modern aircraft can be highly sensitive to Reynolds number. Elsenaar (1988a) provides a pragmatic criterion for defining sensitivity: "Reynolds number effects are large when they affect significantly the design (performance) of an aircraft as derived from sub-scale wind tunnel testing. Three drag counts variation in drag-creep will be significant for a transport type aircraft, but irrelevant for a maneuvering condition of a fighter aircraft." For a transport aircraft, the wing is the component most sensitive to Reynolds number change. Figure 1 shows the flow physics typically responsible for such sensitivity, which include boundary layer transition, shock / boundary-layer interaction and trailing-edge boundary-layer separation for transonic cruise conditions and the same features for a high-lift configuration in addition to confluent boundary layers, possible re-laminarization and leading-edge separation bubbles.

The nature of the interaction between a shock wave and an attached boundary layer depends largely upon whether the boundary layer is laminar or turbulent at the foot of the shock. For a laminar boundary layer, separation of the boundary layer will occur for a relatively weak shock and upstream of the freestream position of the shock. The majority of the pressure rise in this type of shock / boundary-layer interaction, generally described as a λ shock, occurs in the rear leg. The interaction of the rear leg with the separated boundary layer causes a fan of expansion waves that tend to turn the flow toward the wall, and hence re-attach the separated boundary layer. This is in contrast to the interaction between a turbulent boundary layer and a shock wave, in which the majority of the pressure rise occurs in the front leg of the shock wave. The expansion fan that causes reattachment of the laminar separated boundary layer is therefore not present, and the turbulent boundary layer has little tendency to re-attach.

Herein lies the problem of predicting the flight performance of an aircraft when the methods used to design the aircraft have historically relied upon wind tunnels operating below flight Reynolds number, together with other tools such as Computational Fluid Dynamics (CFD), empirical and semi-empirical methods and previous experience of similar design aircraft. Industrial wind tunnels such as the NASA 12ft and 11ft, Boeing Transonic

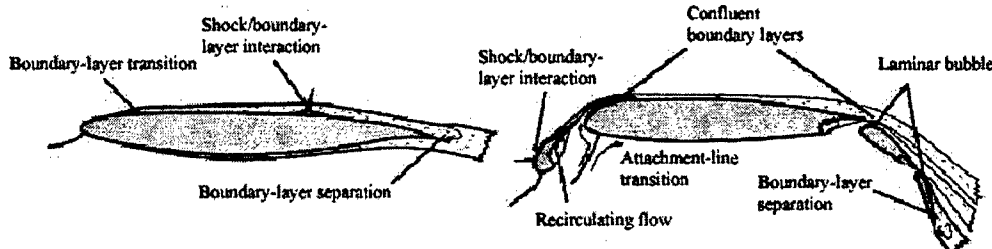
A. Crook

FIGURE 1. Flow features sensitive to Reynolds number for a cruise and high-lift configuration
(Mack & McMasters (1992))

Wind Tunnel (BTWT) and the DERA (now QinetiQ) 5m can only achieve a maximum chord Reynolds number of between 3×10^6 and 16×10^6 , compared with a typical value of 45×10^6 for cruise conditions. Therefore historically, results from wind tunnels have to be extrapolated to flight conditions in a process known as Reynolds-number scaling.

Comparison of wind tunnel and flight test results requires great caution as true Reynolds number effects, defined by Elsenaar (1988a) as the "change in flow development with Reynolds number for a particular configuration in free air," must be separated from scale and pseudo-Reynolds number effects that are a result of wind tunnel testing. Scale effects are characterised by Haines (1994) as those due to the model geometric fidelity and aeroelastic effects. The geometric fidelity of the model will not be as high as one would like because it is not possible to reproduce the many fine details of the aircraft at a small scale. This effect can be particularly important for military aircraft with external stores as discussed by Haines (1994), although it can be equally important for transport aircraft where the engines are not normally represented and the width of the slat and flap tracks may be larger than those scaled correctly, in order to withstand the high aerodynamic loads encountered in a high-lift configuration. Aeroelastic effects are also important because the model is rigid compared to the relatively flexible structure of the aircraft. The model wing is designed for 1g cruise conditions with the geometric twist matched to that of the wing at the same conditions in flight. Any deviation from this operating condition, such as a variation in the tunnel dynamic head (to vary Reynolds number) or C_L will mean that the twist of the model and aircraft wings will be different. Correction for aeroelastic effects must be made if the true Reynolds-number effects are to be shown.

Pseudo-Reynolds-number effects are related to the wind tunnel facility. Wind-tunnel models are generally supported rather than free flying and the flow around them is constrained by the tunnel walls, and therefore support and wall interference must be accounted for correctly. The freestream flow may also have a different turbulent length scale, turbulence intensity and spectrum to that occurring in the atmosphere. Other effects which can be wrongly interpreted as Reynolds number effects include the tunnel calibration, buoyancy effects, thermal equilibrium and humidity, as discussed by Haines (1994).

Haines & Elsenaar (1988) define two types of scale effect: indirect and direct, based upon the definition by Hall (1971) of scale effects being "the complex of interactions between the boundary layer development and the external inviscid flow." Direct and indirect Reynolds number effects are represented schematically in figure 2 and defined by Haines & Elsenaar (1988) as follows:

- Direct Reynolds-number effects occur as a consequence of a change in the boundary-

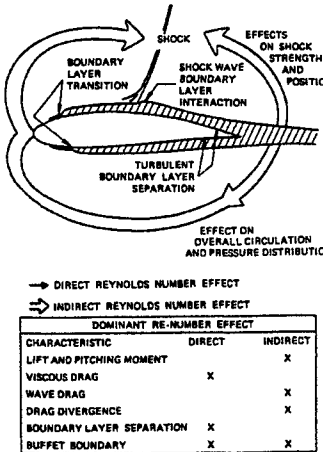


FIGURE 2. Schematic representation of direct and indirect Reynolds number effects (Elsenaar (1988a))

layer development for a fixed (frozen) pressure distribution. Examples of "direct" effects range from the well-known variation of skin friction with Reynolds number for a given transition position to complex issues such as changes in the length of a shock-induced separation bubble for a given pressure rise through a shock.

- Indirect Reynolds number effects are associated with changes in the pressure distribution arising from changes with Reynolds number in the boundary-layer and wake development. An example of an indirect effect is when changes in the boundary-layer displacement thickness with Reynolds number lead to changes in the development of supercritical flow, and hence in shock position and shock strength. Therefore, a change in wave drag with Reynolds number at a given C_L or incidence, can appear as an indirect Reynolds-number effect.

Haines (1987) provides a historical review of scale effects up to 1987, and gives examples of aircraft where direct effects dominated the wing flow, and indirect effects were probably small. The examples given are those of the VC-10 and X-1 aircraft, and correlation between wing pressure distributions in the wind tunnel and in flight are good. It is observed that the shock position in flight is slightly aft of that found in the tunnel test for these test conditions, when the flow is attached, with little or no trailing edge separation, and is turbulent. The reason for this behaviour in these two cases is the thinning of the boundary layer with increasing Reynolds number, with the displacement thickness being roughly proportional to $Re^{-\frac{1}{6}}$. The effective thickness of the wing therefore decreases and the effective camber increases with increasing Reynolds number. The shock wave will move downstream with reduced viscous effects until the limiting case of inviscid flow is reached. If however, C_L is kept constant for a given Mach number, and the Reynolds number varied, the increased aft loading must be compensated by a decrease in the load over the front of the aerofoil. This is generally accomplished by a decrease in the angle of incidence, which normally results in the forward movement of the shock wave. The final outcome of these opposing effects will depend upon their relative strength, as demonstrated by Elsenaar (1988b).

When the flow is attached or mostly attached, indirect Reynolds-number effects appear to be small. However, when the flow is separated large variations in the pressure

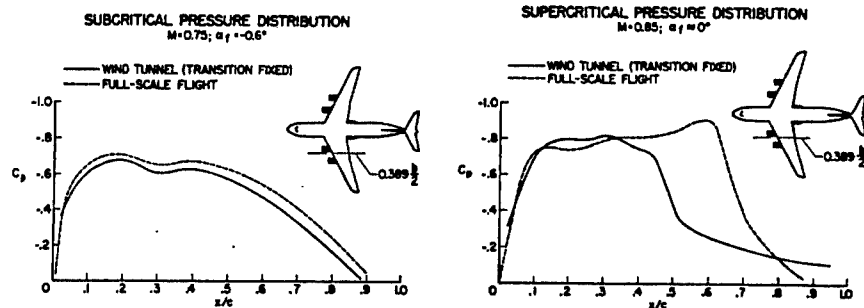


FIGURE 3. Comparison of C-141 wing pressure distributions between wind tunnel and flight for, (a) subcritical and (b) supercritical flow(Elsenaar (1988b))

distribution can result with varying Reynolds number *i.e.* indirect effects can be large as demonstrated in figure 3. Aside from the separation that can occur due to an adverse pressure gradient at the trailing edge, shock-boundary layer interaction is one of the primary causes of separation in transonic flight. Following the work of Pearcey *et al.* (1968) such flow separations are classed as either type A or B.

Elsenaar (1988b) describes the differences between type A and type B separation, and states that the final state is the same both, namely a boundary-layer separation from the shock to the trailing edge. However, the mechanism by which this final state is achieved, differs for the two. For a type A separation, the bubble that forms underneath the foot of the shock grows until it reaches the trailing-edge. The type B separation has three variants, with the common feature being a trailing edge separation that is present before the final state is reached. The final state is reached when the separation bubble and trailing-edge separation merge.

The type B separation is considered to be more sensitive to Reynolds number than type A. This is partly because the trailing-edge separation is dependent upon the boundary-layer parameters such as its thickness and displacement thickness. Furthermore, it was shown by Pearcey & Holder (1954) that the supersonic tongue that exists in a shock-boundary interaction is the dominant factor in the development of the separation bubble, and that the incoming boundary layer is less important. Moreover, the local shock Mach number that causes shock-induced separation is a weak function of the freestream Mach number. Relevant to wind tunnel-to-flight scaling is the possibility that at sufficiently high Reynolds numbers, the trailing edge separation will disappear and the type B flow that is observed in wind tunnels becomes a type A separation at flight conditions.

The behaviour of the trailing-edge separation and that of the separation bubble are highly coupled, with the trailing-edge separation amplified by the upstream effects of the shock-boundary layer interaction. The trailing-edge separation will modify the pressure distribution in a Reynolds-number-dependent manner, and this in turn will alter the shock strength and the conditions for separation at the foot of the shock. This will then affect the boundary layer at the trailing edge. The sensitivity to Reynolds number of this interaction process will be dependent upon the pressure distribution and hence the type of aerofoil (Elsenaar (1988b)). It is also argued that most pre-1960 aerofoils show a rapid increase in shock strength with increasing Mach number and angle of incidence. By implication viscous effects would be small, and the dominant effect would be lengthening of the shock-induced separation bubble. By contrast, modern supercritical aerofoils are designed to limit the variation in shock-wave strength and have higher aft loading and

hence greater pressure gradients over the rear of the aerofoil. Viscous effects will therefore be more important for these aerofoils and there performance more sensitive to Reynolds number.

As demonstrated by figure 3, estimation of aircraft performance and characteristics based upon data from wind-tunnel tests at low Reynolds number can lead to flight performance that is worse than that predicted. In the case of the C-141, the wing pressure distribution in flight shows that the shock is further aft than predicted by the wind tunnel tests. This increased aft loading meant that the pitch characteristics of the wing were very different in flight to that predicted and this necessitated a complete re-design of the wing. There are many examples of where flight performance is worse than predicted using wind tunnel tests at lower Reynolds numbers, some of which are given by Wahls (2001). Examples include higher than expected interference drag of the F-111 airframe, the lack of performance benefit for the DC-10 using a drooped aileron and recently the wing-drop phenomenon of the F/A-18E/F Super Hornet (Stockesberry (2001)). The flight performance need not be worse than predicted from wind tunnel data, with the example given by Wahls (2001) of the increased cruise speed of the C-5A due to a delayed drag rise in flight.

The fact that the flight performance is better than predicted means that the design point was calculated incorrectly and raises the possibility that the design is overly conservative. The financial incentives for designing and predicting the flight performance of an aircraft at high Reynolds numbers are large. This is true not only for the aircraft manufacturer, who has to meet certain performance guarantees or face stiff financial penalties or a costly re-design, but also for the aircraft operator. Mack & McMasters (1992) reported that a 1% reduction in drag equates to several million dollars in savings per year for a typical fleet of aircraft. Bocci (1979) examined what performance might be lost by designing an aerofoil at a typical test Reynolds number of 6×10^6 instead of a typical full-scale Reynolds number of 35×10^6 . The results were gained by calculating the 2D transonic flow over an aerofoil section, and it was found that:

(a) The C_L for the section designed (using CFD) to operate at $Re_c = 6 \times 10^6$, but simulated at $Re_c = 35 \times 10^6$ is 4% higher for the same Mach number and shock strength on the upper surface.

(b) For the aerofoil section designed (using CFD) for a Reynolds number of 35×10^6 , the improvement in C_L is 13% over the section designed and simulated at a Reynolds number of 6×10^6 .

The accurate prediction of flight performance would also save time in the development process by reducing the number of wind-tunnel hours, flight-test hours and design iterations. The use of CFD has helped reduce the upward trend in the number of wind-tunnel hours required to develop an aircraft (Beach & Bolino (1994)), although approximately 20,000 wind tunnel hours were still required to develop the Boeing 777-200.

Differences between predicted and flight performance have led to many different methods of simulating the flight Reynolds number flow using low Reynolds number testing facilities. In flight, transition normally occurs near the leading edge of the wing, and the boundary layer interacting with the shock wave is therefore turbulent. In wind tunnels, it is possible for the boundary layer to remain laminar over a large percentage of the chord, and therefore a laminar boundary layer-shock interaction may occur. These two types of interaction are vastly different in their nature, and therefore the flow is generally tripped. For many years the standard method of transition fixing was to place narrow, sparse bands of carborundum or ballotini at chordwise positions of between 0.05c and

0.07c. This worked well for many aerofoils pre-1960, but not for the highly-aft-loaded sections such as the C-141 where a trailing edge separation exists. The sensitivity of a type B flow to transition location and the degree of roughness is discussed by Haines (1987) for the NPL 9240 and 9241 sections, whose only difference is a very slight change in the upper-surface thickness aft of the point of maximum thickness. The pressure distribution of the NPL 9241 shows that a small incipient trailing-edge separation exists at Mach 0.6, which is not present for the NPL 9240. The $C_L - M$ plot for the two sections shows that when fine sparse roughness is used at 10-15% chord the behaviour of the two is similar. However, the differences are large when coarse roughness is used close to the leading edge, and the effects of a shock-induced separation on the break in the lift data are greater for the 9241 section.

The increased sensitivity of type B flows to scale effects led to steps being taken to simulate the high-Reynolds-number flow more accurately by reducing the non-dimensional boundary-layer thickness on the model to a value close to that found in flight. One method of achieving this is known as aft-fixing, allowing the boundary layer to remain laminar and thin over the forward part of the wing and then fixing transition aft of where it occurs naturally in flight, but far enough ahead of the shock wave to avoid any local interaction of the shock and the transition trip. This technique has proved to be capable of alleviating the rear separation found in model tests for $2 \times 10^6 < Re_c < 6 \times 10^6$, which are not expected to occur in flight (Haines (1987)).

Three-dimensional effects complicate the use of the aft-fixing technique on typical high-aspect-ratio transport aircraft wings. Near the wing root there is often a double-shock pattern with the intersection point to the single outboard shock often close to the kink-section of the wing. The leading shock in the double-shock pattern is often close to the leading edge of the wing, and therefore the aft-fixing technique will not be applicable. Furthermore, the transition mechanism in a three-dimensional flow is different from a two-dimensional flow where the Tollmien-Schlichting instability is the primary cause. In a three-dimensional flow, cross-flow instability and leading-edge contamination can also contribute to transition. Transition also occurs near to the leading edge at the wing tip, and therefore if the aft-fixing transition method is to be used on a swept wing, the trip strip must be cranked and then only the mid-section of the wing is represented adequately. Elsenaar (1988b) discusses the effect of transition fixing upon the local sweep angle of the shock, and how this is important for drag evaluation because of the sensitivity of compressibility drag to small variations in shock strength and sweep angle.

Alternative techniques to the aft-fixing method are discussed briefly by Elsenaar (1988b) and include vortex generators, boundary-layer suction and geometry modification on the sub-scale model. Haines & Elsenaar (1988) and Haines & Elsenaar (1988b) discuss detailed methodologies for simulating the full-scale behaviour of an aircraft wing using sub-flight Reynolds-number facilities, and moreover what the most important simulation criteria should be, given that it is unlikely to be able to simulate them all. The simulation criteria listed by Haines & Elsenaar (1988b) are:

- (a) Shock position
- (b) Shock strength
- (c) Non-dimensional momentum thickness at the wing trailing edge
- (d) Non-dimensional length of the shock-induced separation bubble
- (e) Boundary-layer shape factor at a position close to the trailing edge on the upper surface, or at any other position where separations are anticipated

Even with complex simulation methodologies, the flight performance and character-

istics of an aircraft can be hard to predict using low-Reynolds-number facilities. This led to the recognition of the need for high-Reynolds-number testing facilities such as the National Transonic Facility (NTF) at NASA Langley and the European Transonic Windtunnel (ETW) in Cologne, Germany. Both tunnels can operate at cryogenic temperatures using Nitrogen and from low Mach numbers (0.15-0.2) to supersonic Mach numbers (1.2-1.3). Importantly, they can operate at Reynolds numbers greater than that achieved in flight by typical transport aircraft, and are capable of varying temperature, pressure and velocity independently, allowing the separation of Reynolds number effects from aeroelastic effects.

Despite the existence of the NTF and ETW, industrial and commercial wind tunnels are still required to carry out the majority of the development work for a new aircraft because of their relatively high productivity. The ETW and NTF are viewed as research tunnels where Reynolds-number scaling methodologies can be developed and an aircraft design checked before its first flight. The requirement for Reynolds-number scaling methods has therefore not diminished with the advent of high-Reynolds-number facilities.

To further understand the effects of scale upon aircraft performance and to establish a capability to account for them during the design process, the High Reynolds number Aerodynamic Research Project (HiReTT) was commenced in January 2000 as part of the European Fifth Framework Programme. This project combined with others funded by the EC is part of a strategy that aims to make European aeronautics the World leader by the year 2020 (Argüelles *et al.* (2001)).

The specific objectives of HiReTT are listed by Rolston (2001) and include the testing of a modern aircraft research configuration with and without control devices at high Reynolds numbers and particularly at high subsonic Mach numbers. The database gained will be fully corrected for interference effects by evaluating and developing new and existing methods in the ETW and by using CFD. The results from the ETW will also be compared with the predictions of modern CFD methods, with a view to producing guidelines to enable CFD to predict such flows.

The US does not at present have such a research program dedicated to Reynolds number scaling, although between 1994 and 2000 the NASA Advanced Subsonic Transport (AST) program funded research into Reynolds number scaling using the NTF. There is undoubtedly a great deal of experience in scaling techniques in the US, with 57% of research investigations in the NTF since 1985, concentrating on subsonic transport aircraft (Wahls (2001)). Much of the data and knowledge however remains undisclosed due to its proprietary nature.

The current status of Reynolds-number scaling can be assessed from a number of recent publications resulting from the use of the NTF (Curtin *et al.* (2002) and Clark and Pelkman (2001)) and ETW (Rolston (2001), Quest *et al.* (2002), and Hackett *et al.* (1999)). The full details are too long to discuss in this brief, but an attempt at a summary is provided herein.

(a) Angle of incidence at cruise, drag-rise Mach number, C_L and C_M are all functions of Reynolds number. Comparison of data from the NTF and ETW with flight measurements is very good for cruise conditions.

(b) The effect of Reynolds number on drag can be predicted if the empirical relationship is matched to drag measured at a Reynolds number of 8-10 million or above.

(c) The shape of drag polar varies with Reynolds number up to flight Reynolds numbers of approximately 40 million, although vortex generators reduce the variation slightly.

(d) Drag-rise Mach number is increased with increasing Reynolds number, indicating

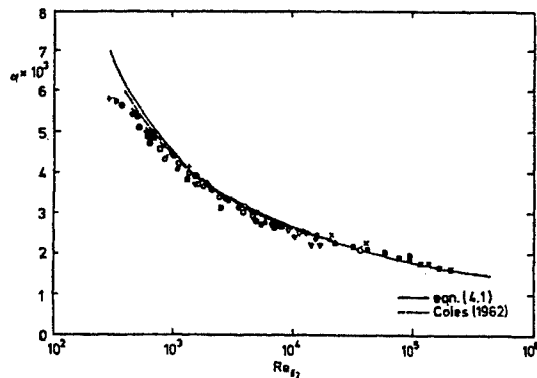


FIGURE 4. Comparison of flat plate skin friction data with the relationships of Fernholz (1971) and Coles (1962) (Fernholz & Finley (1996))

that higher Reynolds number testing would predict a higher cruise Mach number than that achieved using a tunnel such as the Boeing Transonic Wind Tunnel (BTWT).

(e) The effect of vortex generators on drag at cruise varies with Reynolds number, causing a higher drag at low Reynolds numbers and having very little or a slightly beneficial effect at flight Reynolds numbers. Vortex generators also have little effect on spanwise loading at flight Reynolds numbers, compared with a large effect at low Reynolds numbers. This indicates that if wing loads were developed from low Reynolds number data, an unnecessary structural weight penalty would be paid.

(f) Buffet onset is very difficult to predict, and is often difficult to measure in a wind tunnel because the model dynamics and that of the aircraft are very different.

Drag estimation is an important part of the design process, and involves the prediction of wave drag, vortex-induced drag and viscous drag, with the latter contributing approximately 50% to the total drag during cruise (Thibert *et al.* (1990)). A simple estimate of the scaled viscous drag is often gained by using a combination of form factors and flat plate skin friction formulae once the transition location is known. This method relies upon an accurate description of the skin friction coefficient, c_f , from low Reynolds numbers found in wind tunnels to flight Reynolds numbers.

2. Skin friction estimation

There is a variety of empirical and semi-empirical relationships for the prediction of the turbulent incompressible skin friction on a flat plate. Common methods such as those based upon the $\frac{1}{7}$ -th power law and the logarithmic law (Schlichting (1968)) relate c_f to Re_x and suffer from the difficulty of an unknown origin.

Fernholz & Finley (1996) compare measurements of flat-plate skin friction from a variety of sources for $300 < Re_\theta < 212 \times 10^3$ to the empirical relationship of Coles (1962) and the semi-empirical relationship of Fernholz (1971) as shown in figure 4. Agreement with the experimental data is within $\pm 5\%$ in the range $600 < Re_\theta < 212 \times 10^3$, although the agreement is better at higher Reynolds numbers.

More recently, Watson *et al.* (2000) carried out a comparison of the semi-empirical relationships of Ludwig & Tillmann (1950), Spalding (1962), Kármán-Schoenherr (Schoenherr (1932)) and Fernholz (1971) as shown in figure 5. The methods of Kármán-Schoenherr and Spalding show opposite trends at low and high Reynolds numbers with the inter-

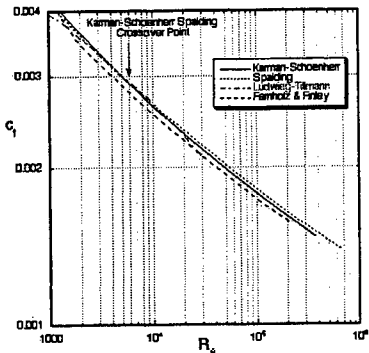


FIGURE 5. Flat plate skin friction correlations and theories (Watson *et al.* (2000))

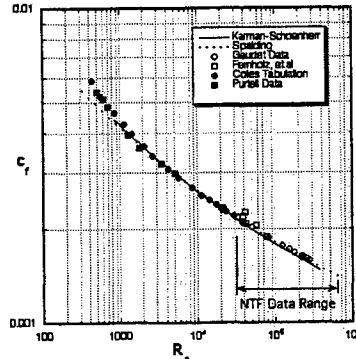


FIGURE 6. Comparison of the flat plate data with the correlations and theories (Watson *et al.* (2000))

section point at Re_θ between 6000 and 7000. The relationship of Fernholz consistently underpredicts the skin friction compared to the other methods. The skin friction predicted by Ludwieg-Tillmann matches that of Kármán-Schoenherr for Re_θ between 3000 and 20000. Both the methods of Spalding and Fernholz rely upon the logarithmic law and hence the von Kármán constant κ and the additive constant, B . Watson *et al.* (2000) report that the method of Spalding incorrectly predicts the skin friction if the usual value of κ is used. This is because the relationship relies upon Spalding's sublayer-buffer-log profile which does not take the wake region into account correctly. Despite this, the relationships of Kármán-Schoenherr and Spalding are observed to be the best fit to the data of Coles (1962) and Gaudet (1984) shown in figure 6.

The relationships of Spalding and Kármán-Schoenherr are used for comparison with the data taken in the National Transonic Facility (NTF) at NASA Langley in 1996. Although a flat-plate experiment was originally proposed by Saric & Peterson (1984), it posed too many problems in the high-dynamic-pressure environment of the NTF. An axisymmetric body, 17ft long, for which transverse-curvature effects are small ($\delta/R = 0.25$) was therefore tested at Mach numbers between 0.2 and 0.85 and unit Reynolds numbers from 6×10^6 to 94×10^6 per foot. Skin friction was measured using three different techniques: a skin friction balance, Preston tubes and velocity profiles from which the skin friction was inferred by the Clauser method. The last method relies upon the validity of the logarithmic law and the constants used, which have been a subject of debate over the last decade, and one that is still not settled. Hites *et al.* (1997) compared the skin friction velocity u_τ measured by a near-wall hot wire, a microfabricated hot wire on the wall, and a conventional hot wire on the wall to that obtained by measuring the velocity profile using a hot wire and applying the Clauser technique. In all cases, the measured u_τ is higher than that predicted by the Clauser technique. The prediction of u_τ is also sensitive to the values of κ and B used in the log-law, with a ± 0.5 change in the slope $1/\kappa$ resulting in a 12% difference in u_τ . The comparison of the measured values of u_τ to that predicted by the Clauser method should however be treated with care as significant errors can occur, even for microfabricated devices, due to thermal conduction to the substrate and connecting wires.

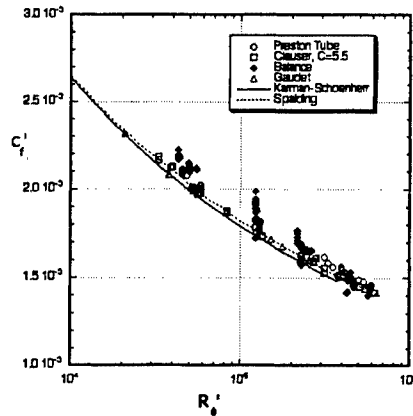


FIGURE 7. Comparison of three measurement techniques of skin friction with the data of Gaudet (1984) and with the predictions of Kármán-Schoenherr and Spalding (Watson *et al.* (2000))

Compressibility effects on the skin friction are removed using the van Driest transformation (Van Driest (1951)) for the velocity-profile data and the Sommer and Short T' method (Sommer & Short (1955)) for the Preston-tube data. Using the Van Driest transformation for the velocity profile at the highest Reynolds number condition yielded an incompressible Re_θ of 619,800.

Data obtained using the skin friction balance exhibits a large degree of scatter and these data were therefore not relied upon. The data from the Preston tubes and velocity profiles shows good agreement, and yields a best fit relationship of $c_f = 0.0097Re_\theta^{-0.144}$ shown in figure 7. The scatter of the data around this fit is $\pm 1\%$, with the fit 1% above the Spalding value and 3% above the Kármán-Schoenherr value at $Re_\theta=600,000$. It equals the Spalding value at $Re_\theta=30,000$.

Skin friction measured in two facilities using the near-wall technique and oil-film interferometry is compared by (Österlund *et al.* (1999)) for Re_θ up to 27000. The data compare well with the correlation of Fernholz (1971) and the logarithmic skin-friction law using $\kappa = 0.384$ and $B = 4.08$. However, the range of Re_θ considered is too small, and the maximum Reynolds number too low, to draw conclusions about the suitability of the correlation and logarithmic skin friction law at high Reynolds number.

3. Conclusions

Reynolds number scaling remains a topic that receives a great deal of attention 50 years after such effects were first observed. The advent of high Reynolds number tunnels such as the NTF and ETW has not lessened the need for good Reynolds number scaling techniques, but has provided the facilities in which to test new methods and aircraft designs before their first flight, helping to reduce risk. Comparison of flight data with that taken in such tunnels is good for cruise conditions. However, buffet onset is still very difficult to predict, due primarily to the fact that the wind tunnel model and support dynamics are very different to the real aircraft.

The accurate prediction of drag at flight Reynolds number using low Reynolds number wind tunnels remains a challenge, and it appears that a Reynolds number of 8-10 million or above is required if empirical methods are to be used for extrapolation to flight conditions. The error in the extrapolation is likely to be higher than the variation of c_f with Reynolds number predicted by the best empirical methods discussed. It is therefore concluded that the measurements of skin friction taken in the NTF over a very large range of Reynolds number match the predictions of Spalding and Kármán-Schoenherr well enough for skin friction extrapolation purposes. The direct and accurate measurement of skin friction however remains very challenging, although microfabricated skin friction devices are proving promising.

REFERENCES

- ARGÜELLES, P., BISCHOFF, M., BUSQUIN, P., DROSTE, B. A. C., EVANS, R., KRÖLL, W., LAGARDÉRE, J-L., LINA, A., LUMSDEN, J., RANQUE, D., RASMUSSEN, S., REUTLINGER, P., ROBINS, R., TERHO, H. & WITTLÖV, A. 2001 European aeronautics: A vision for 2020. European Commission.
- BEACH, H. L., JR. & BOLINO, J. V. 1994 National planning for aeronautical test facilities. *AIAA Paper* 94-2474.
- BOCCI, A. J. 1979 Aerofoil design for full scale Reynolds number. *ARA Memo* 211.
- CLARK, R. W. & PELKMAN, R. A. 2001 High Reynolds number testing of advanced transport aircraft wings in the National Transonic Facility. *AIAA Paper* 2001-0910.
- COLES, D. 1962 The turbulent boundary layer in a compressible fluid. *R-403-PR*, Rand Corp.
- CURTIN, M. M., BOGUE, D. R., OM, D., RIVERS, S. M. B., PENDERGRAFT, O. C., JR., & WAHLS, R. A. 2002 Investigation of transonic Reynolds number scaling on a twin-engine transport. *AIAA Paper* 2002-0420.
- ELSENAAR, A. Observed Reynolds number effects: Airfoils and high aspect ratio wings. ELSENAAR, A., BINION, T. W. & STANEWSKY, E. 1988 Reynolds number effects in transonic flow. *AGARDograph AG-303*, 17-49.
- ELSENAAR, A. Introduction. ELSENAAR, A., BINION, T. W. & STANEWSKY, E. 1988 Reynolds number effects in transonic flow. *AGARDograph AG-303*, 1-6.
- FERNHOLZ, H. H. 1971 Ein halbempirisches Gesetz für die Wandreibung in kompressiblen turbulenten Grenzschichten bei isothermer und adiabater Wand. *ZAMM* **51**, 149-149.
- FERNHOLZ, H. H. & FINLEY, P. J. 1996 The incompressible zero-pressure gradient turbulent boundary layer: An assessment of the data. *Prog. Aerospace Sci.* **32**, 4, 245-311.
- GAUDET, L. 1984 Experimental investigation of the turbulent boundary layer at high Reynolds number and a Mach number of 0.8. *TR 84094*, Royal Aircraft Establishment.
- HACKETT, K., BURNELL, S. & ASHILL, P. 1999 Aerodynamic scale effects on a transport aircraft model at high subsonic speed. *AIAA Paper* 99-0305.
- HAINES, A. B. 1987 27th Lanchester memorial lecture: Scale effect in transonic flow. *Aeronautical Jnl.*, August/September 1987, 291-313.
- HAINES, A. B. 1994 Scale effects on aircraft and weapon aerodynamics. *AGARDograph AG-323*.

- HAINES, A. B. & ELSENAAR, A. 1988 An outline of the methodology. Boundary layer simulation and control in wind tunnels. *AGARD Advisory Report AR-224*, 96-110.
- HAINES, A. B. & ELSENAAR, A. 1988 Transport-type configurations. Boundary layer simulation and control in wind tunnels. *AGARD Advisory Report AR-224*, 139-163.
- HALL, M. G. 1971 Scale effects in flows over swept wings. *AGARD CP 83-71*.
- HITES, M., NAGIB, H. & WARK, C. 1997 Velocity and wall shear stress measurements in high Reynolds number turbulent boundary layers. *AIAA Paper 97-1873*
- LUDWIEG, H. & TILMANN, W. 1950 Investigations of the wall shearing stress in turbulent boundary layers. *NACA TM-1285*. National Advisory Committee for Aeronautics.
- MACK, M. D. & McMASTERS, J. H. 1992 High Reynolds number testing in support of transport airplane development. *AIAA Paper 92-3982*.
- ÖSTERLUND, J. M., JOHANSSON, A. V., NAGIB, H. M. & HITES, M. H. 1999 Wall shear stress measurements in high Reynolds number boundary layers from two facilities. *AIAA Paper 99-3814*.
- PEARCEY, H. H. & HOLDER, D. W. 1954 Examples of shock induced boundary layer separation in transonic flight. *Aeronautical Research Council Technical Report R & M No. 3012*.
- PEARCEY, H. H., OSBORNE, J. & HAINES, A. B. 1968 The interaction between local effects at the shock and rear separation - a source of significant scale effects in wind tunnel tests on aerofoils and wings. *AGARD CP 35*, Paper 11.
- QUEST, J., WRIGHT, C. N. & ROLSTON, S. 2002 Investigation of a modern transonic transport aircraft configuration over a large range of Reynolds numbers. *AIAA Paper 2002-0422*.
- ROLSTON, S. 2001 High Reynolds number tools and techniques for civil aircraft design. *AIAA Paper 2001-2411*.
- SARIC, W. S. & PETERSON, J. B., JR. 1984 Design of high Reynolds number flat plate experiments in the NTF. *AIAA Paper 84-0588*.
- SCHLICHTING, H. 1968 *Boundary Layer Theory*. McGraw-Hill.
- SCHOENHERR, K. E. 1932 Resistance of flat surfaces moving through a fluid. *Trans. SNAME* **40**, 279-313.
- SOMMER, S. C. & SHORT, B. J. 1955 Free-flight measurements of turbulent boundary layer skin friction in the presence of severe aerodynamic heating at mach numbers from 2.8 to 7.0. *NACA TN-3391*.
- SPALDING, D. B. 1962 A new analytical expression for the drag of a flat plate valid for both turbulent and laminar regimes. *Int. Jnl. Heat and Mass Transf.* **5**, 1133-1138.
- STOOKESBERRY, D. 2001 CFD modeling of the F/A-18E/F abrupt wing stall - a discussion of the lessons learned. *AIAA Paper 2001-2662*.
- THIBERT, J. J., RENEAUD, J. & SCHMITT, R. V. 1990 ONERA activities on drag reduction. *Proceedings of the 17th Congress of the ICAS*. 1053-1059.
- VAN DRIEST, E. R. 1951 Turbulent boundary layer in compressible fluids. *Jnl. Aeronautical Sci.* **18**, 3, 145-160.
- WAHLS, R. A. 2001 The National Transonic Facility: A research retrospective. *AIAA Paper 2001-0754*.
- WATSON, R. D., HALL, R. M. & ANDERS, J. B. 2000 Review of skin friction measurements including recent high Reynolds number results from NASA Langley NTF. *AIAA Paper 2000-2392*.

*Center for Turbulence Research
Annual Research Briefs 2002*

APPENDIX

Roster

NAME/TERM	AREA OF RESEARCH
POSTDOCTORAL FELLOWS	
CHA, Dr. Chong 4/00-9/02	(Ph.D. Mechanical Engineering, 2000, University of Washington) Turbulent combustion
CROOK, Dr. Andrew 1/02-present	(Ph.D. Aerospace Engineering, 2001, Univ. of Manchester, UK) Fluid mechanics of high aspect-ratio sails
DUCHAMP DE LAGENESTE, Dr. Laurent 2/00-present	(Ph.D. Fluid Mechanics, 1999, Ecole Centrale de Lyon, France) LES for premixed combustion
FAVIER, Dr. Valerie 10/00-9/02	(Ph.D. Combustion, 2000, Inst. National Sciences Appliques de Rouen, France) Cardiovascular fluid mechanics
GULLBRAND, Dr. Jessica 1/00-present	(Ph.D. Mechanical Engineering, 1999, Lund Institute of Technology, Sweden) Large eddy simulation
HAM, Dr. Frank 6/02 – present	(Ph.D. Mechanical Engineering, 2001, University of Waterloo, Canada) LES on unstructured grids & simulation of multiphase flows
HERRMANN, Dr. Marcus 3/02 – present	(Ph.D. Mechanical Engineering, 2001, University of Technology Aachen, Aachen, Germany) Turbulent combustion
HUR, Dr. Joseph 7/02 – present	(Ph.D. Chemical Engineering, 2001, Stanford) Protein folding and unfolding
KIRKPATRICK, Dr. Michael 4/02 – present	(Ph.D. Mechanical Engineering 2000, University of Sydney, Aust.) Turbulence modeling in LES of clouds
KNAEPEN, Dr. Bernard 7/02 – present	(Ph.D. Physics, 1999, University of Brussels, Belgium) MHD turbulence
LIN, Dr. Hao 8/01-present	(Ph.D. Mechanical Engineering, 2001, UC Berkeley) Protoplanetary disks

NAME/TERM	AREA OF RESEARCH
MAY, Dr. Phillippe 5/02 – present	(Ph.D. Microsurgery & Biophysics, 2001, University of Paris) Biological Fluid Mechanics
RIPOLL, Dr. Jean-Francois 1/02 - present	(Ph.D. Applied Mathematics, 2001, University of Bordeaux, France) Radiation Modeling
STEMMER, Dr. Christian 8/01-present	(Ph.D. Aerospace Engineering, 2001, Univ.of Stuttgart, Germany) Hypersonic flows
TALLEY, Dr. Sharon 1/01-present	(Ph.D. Biology, 1999, University of Utah) Biological fluid mechanics
TROUILLET, Dr. Phillippe 3/00-9/02	(Ph.D. Mechanical Engineering, 2000, University of Poitiers, France) Turbulent combustion
USTYUGOV, Dr. Sergei 11/02-present	(Ph.D. Computational Physics, 1999, Keldysh Institute of Applied Math, Russia) Solar Dynamics
YOUNG, Dr. Yuan-Nan 9/02 – present	(Ph.D. Astronomy & Astrophysics, 2000, University of Chicago) Turbulence in multi-phase flows
SR. RESEARCH ASSOC.	
WANG, Dr. Meng 9/92-present	(Ph.D. Mech. Engr., 1989, University of Colorado) Aeroacoustics, LES
FATICA, Dr. Massimiliano 10/95-present	(Ph.D. Fluid Mechanics, 1995, Univ. of Rome, Italy) Parallel computing
RESEARCH ASSOCIATES	
APTE, Sourabh, Dr. 9/00-present	(Ph.D. Engineering, 2000, Pennsylvania State University) Large eddy simulation of multiphase flows
IACCARINO, Gianluca 4/98-present	(Masters Aeronautical Engineering, 1994, University of Naples, Italy) Turbulence modeling
CONSTANTINESCU, Dr. George 11/99-present	(Ph.D. Environmental Eng. 1998 University of Iowa) LES for complex geometries
DUBIEF, Dr. Yves 5/01-present	(Ph.D. Fluid Mechanics, 2000, Institute National Polytechnique de Grenoble, France) Polymer Drag Reduction
KALITZIN, Dr. Georgi 1/97 - present	(Ph.D. Mechanical Engineering, 1992 University of Magdeburg, Germany) Turbulence Modeling & Numerical Methods
KASSINOS, Stavros 1/97 - present	(Ph.D. Mechanical Engineering, 1994, Stanford) Turbulence Modeling & MHD Turbulence
PITSCH, Dr. Heinz 4/99 - present	(Ph.D. Mechanical Eng., 1998, University of Technology Aachen, Germany) Turbulent Combustion

NAME/TERM	AREA OF RESEARCH
SCHLUTER, Dr. Jorg, 10/00-present	(Ph.D. Mechanical Engineering, 2000, CERFACS, France)
SR. VISITING FELLOWS	
ABARZHI, Dr. Snezhana 9/02 - present	Landau Institute for Theoretical Physics, Moscow
CHO, Dr. JUNGEON 7/02 – 8/02	University of Wisconsin
FEDOTOV, Dr. Sergei 9/02-11/02	Univ. Manchester Inst. of Science and Technology, U.K.
GOROKHOVSKI, Dr. Mikhail 2/02 – 4/02	University of Rouen, France
KLIMENKO, Dr. Alex 1/ 02 - 2/02	University of Queensland, Australia
LAZARIAN, Dr. Alex 7/02 – 8/02	University of Wisconsin
MAJUMDAR, Dr. Sekhar 6/01- 5/02	National Aerospace Laboratories Bangalore, India
MOHAMMADI, Prof. Bijan 1 /02 – 2/02, 8/02	University of Montpellier, France
NAKAYAMA, Dr. Akihiko 6/02 – 12/02	Kobe University, Japan
NICOUD, Dr. Frank 7/02 – 8/02	University of Montpellier, France
PARCHEVSKY, Konstantin 11/02 – 12/02	Crimean Astrophysical Observatory, Ukraine
PETROVAY, Dr. Kristof 9/02 – 10/02	Eotvos University, Hungary
SR. RESEARCH FELLOWS	
JIMENEZ, Prof. Javier 1987-present	University of Madrid, Spain
KOUMOUTSAKOS, Dr. Petros 8/94-present	Swiss Federal Institute of Technology, Switzerland
VISITING RESEARCHERS	
DEL ALAMO, Juan Carlos 7/02-9/02	University of Madrid, Spain
CAMGUILHEM, Benoit 3/02-7/02	Ecole Polytechnique, Paris, France
	Large eddy simulation
	Large eddy simulation

NAME/TERM		AREA OF RESEARCH
TESSICINI, Fabrizio 7/02-9/02	INSEAN, Italy	Large eddy simulation
SAKIO, Koji 6/02-12/02	Kobe University, Japan	Large eddy simulation
GRADUATE STUDENTS		
BHASKARAN, Rathakrishnan 6/02 – 12/02	(Stanford University)	Plasma flow control
CHEUNG, Lawrence 6/02 – 9/02	(Stanford University)	Turbulent acoustics
DOYLE, Tyler 1/02 - 9/02	(Stanford University)	Optimization techniques
HONEIN, Albert 9/02 – 12/02	(Stanford University)	Large eddy simulation of compressible flows
TSENG, Yu-Heng 6/02 – 12/02	(Stanford University)	Numerical modeling of coastal ocean

2002 ADVISORY COMMITTEE

Prof. Ron F. Blackwelder (Chair)
University of Southern California

Dr. Joe Adams, VP Eng. Tech.
United Technologies-Pratt & Whitney

Dr. Marvin E. Goldstein, Chief Scientist
NASA Glenn Research Center

Prof. Brian Launder
University of Manchester

Prof.. Sidney Leibovich
Cornell University

Prof. Phillip Marcus
University of California at Berkeley

Dr. Pat Purtell
Office of Naval Research

Prof. Richard A. Matzner,
Center for Relativity, U of Texas at Austin

Dr. Charles Smith
NASA Marshall Space Flight Center

Dr. Julian Tishkoff
Air Force Office of Scientific Research

Prof. Forman Williams
University of California, San Diego

Dr. Thomas Beutner (observer)
Air Force Office of Scientific Research

Dr. Julian Hunt
University College – London, England

2002 STEERING COMMITTEE

Prof. Paul A. Durbin
Mechanical Engineering, Stanford University

Prof. Sanjiva K. Lele
Mechanical Engineering Aeoronautics &
Astronautics, Stanford University

Prof. Javier Jiménez
Sr. Research Fellow, Center for Turbulence Research,
Professor, University of Madrid

Dr. Nagi N. Mansour
Deputy Director, Center for Turbulence Research
NASA Ames Research Center

Prof. Parviz Moin
Director, Center for Turbulence Research
Professor, Mechanical Engineering, Stanford.

Prof. Norbert Peters
Mechanical Engineering, Stanford University

Prof. William C. Reynolds
Professor, Mechanical Engineering, Stanford.

Dr. Karim Shariff
Research Scientist, NASA Ames Research Center